

A - OPERATION AND ECONOMICS

- THE COSTS OF CHARGING ELECTRIC VEHICLES IN POLAND** **A1**
E. Sendek-Matysiak, H. Rzędowski
- ANALYSIS OF THE TRAFFIC PARAMETERS ON A SECTION IN THE CITY OF THE NATIONAL ROAD DURING SEVERAL YEARS OF OPERATION** **A12**
A. Bąkowski, L. Radziszewski
- MIXED FUZZY-LOGIC AND GAME-THEORETICAL APPROACH TO JUSTIFY VEHICLE MODELS FOR SERVICING THE PUBLIC BUS LINE** **A26**
V. Naumov, L. Bekmagambetova, Z. Bitileuova, Z. Zhanbirov, I. Taran

B - MECHANICAL ENGINEERING

- DETERMINATION OF THERMOMECHANICAL STRESSES IN ELEMENTS OF VEHICLES' BRAKING SYSTEMS** **B1**
O. Grevtsev, N. Selivanova, P. Popovych, L. Poberezhny, Y. Rudyak, O. Shevchuk, L. Poberezhna, O. Skyba, V. Ostroverkhov, O. Shashkevych
- DYNAMIC MODELLING OF PISTON THE MOTION IN COMBUSTION ENGINES** **B9**
S. Narayan, S. Abubakar, M. U. Kaisan, H. Ndagi, Y. Tukur, I. Grujić, N. Stojanović
- SIMULATION OF A DUMMY CRASH TEST IN ADAMS** **B20**
M. Jaśkiewicz, D. Frej, M. Poliak
- CONSTRUCTION OF THE GEOMETRICAL MODELS OF A MULTIPLE-FACTOR OPTIMIZATION OF THE TECHNICAL AND OPERATING PARAMETERS OF THE TROLLEYBUSES WITH AN AUTONOMOUS MOVE MARGIN** **B29**
S. Pustiulha, V. Samchuk, V. Dembitsky, V. Samostian, V. Prydiuk
- PROPOSAL OF A METHOD FOR DETECTION OF A DAMAGED HYDRAULIC SHOCK ABSORBER IN A VEHICLE'S SUSPENSION SYSTEM** **B41**
M. Gorbunov, J. Dižo, M. Blatnický, K. Kravchenko, S. Semenov, E. Mikhailov
- ELECTRIC OR INTERNAL COMBUSTION ENGINES FOR PASSENGER CARS? - ENVIRONMENTAL AND ECONOMIC ASPECTS** **B49**
Z. Čekerevac, Z. Dvořák, L. Prigoda
- THE EFFECTS OF BIODIESEL ON NOX EMISSIONS FOR AUTOMOTIVE TRANSPORT** **B59**
R. Kolodnytska, O. Kravchenko, J. Gerlici, K. Kravchenko
- A CRITICAL REVIEW OF BIOFUELS AS AN ALTERNATIVE FUEL TO DIESEL IN GULF REGIONAL CORPORATION (GCC) REGION: CURRENT MARKET TRENDS AND FUTURE OPPORTUNITIE** **B67**
F. O. Mahroogi, S. Narayan, M. U. Kaisan, A. Aliyu, I. Yahuza, I. Grujić, N. Stojanović
- ANALYSIS OF THE POWERTRAIN COMPONENT SIZE OF ELECTRIFIED VEHICLES COMMERCIALY AVAILABLE ON THE MARKET** **B74**
R. Sanjarbek, J. Mavlonov, A. Mukhitdinov
- DEVELOPMENT OF A PROCEDURE FOR DETERMINING THE PRE-FAILURE CONDITION OF THE AXLE BOXES OF RAILWAY ROLLING STOCK** **B87**
I. Martynov, J. Gerlici, A. Trufanova, V. Petuhov, V. Shovkun, K. Kravchenko

VERIFICATION OF THE THERMAL EXPANSION EFFECT OF SILICONE MOLDS INTENDED FOR PRODUCTION OF THE PROTOTYPE COMPONENTS USING VACUUM CASTING TECHNOLOGY **B94**
P. Spišák, R. Sásik, J. Steininger, J. Jenis

C - ELECTRICAL ENGINEERING

REDUNDANT MULTI-OBJECT DETECTION FOR AUTONOMOUS VEHICLES IN STRUCTURED ENVIRONMENTS **C1**
S. Feraco, A. Bonfitto, N. Amati, A. Tonoli

ARTIFICIAL NEURAL NETWORK BASED MPPT ALGORITHM FOR MODERN HOUSEHOLD WITH ELECTRIC VEHICLE **C18**
J. Morgoš, P. Klčo, K. Hrudkay

D - CIVIL ENGINEERING IN TRANSPORT

TEMPERATURE CORRECTION OF DEFLECTIONS AND BACKCALCULATED ELASTICITY MODULI DETERMINED FROM FALLING WEIGHT DEFLECTOMETER MEASUREMENTS ON ASPHALT PAVEMENTS **D1**
I. Březina, O. Machel, T. Zavřel

THE STRESS-STRAIN STATE OF THE TUNNEL LINING THAT CROSSES THE FAULT ZONE OF SOIL BLOCKS DURING AN EARTHQUAKE **D9**
M. R. Miller, E. Y. Titov, S. S. Kharitonov, Y. Fang

ENSURING OPERATIONAL RELIABILITY OF OVERPASS ON "ALMATY-KAPSHAGAI" HIGHWAY SECTION IN KAZAKHSTAN **D23**
A. Jalairov, D. Kumar, K.-K. Kassymkanova, G. Murzalina, G. Jangulova

NAMIC RESPONSE OF A ROAD BRIDGE SUBJECTED TO PASSING A HEAVY VEHICLE OVER A STANDARD IRREGULARITY - NUMERICAL MODELLING AND EXPERIMENTAL TESTING **D37**
M. Moravčík

E - MANAGEMENT SCIENCE AND INFORMATICS

MEASURING THE SPEED OF DOCKING SHIP WITH TOTAL STATION **E1**
A. Felski

BATHYMETRIC MEASUREMENTS OF THE VISTULA SMIALA RIVER MOUTH WITH THE USE OF A HYDROGRAPHIC MANNED VESSEL **E11**
M. Skrzypek, B. Mach

BATHYMETRIC MEASUREMENTS OF A RETENTION RESERVOIR USING INTEGRATED HYDROGRAPHIC AND PHOTOGRAMMETRIC TECHNIQUES **E19**
B. Mach, M. Skrzypek

AIRCRAFT POSITION PREDICTION DURING THE CROSSWIND APPROACH **E28**
M. Grzegorzewski, J. Biały

PROCESSING OF THE RESULTS OF SATELLITE INLAND POSITIONING TRANSPORT USING MOBILE DEVICES AND THEIR VISUALIZATION **E36**
M. Kulas

THE COSTS OF CHARGING ELECTRIC VEHICLES IN POLAND

Ewelina Sendek-Matysiak, Hubert Rzędowski*

Department of Automotive Engineering and Transport, Kielce University of Technology, Kielce, Poland

*E-mail of corresponding author: hubertrz95@interia.pl

Resume

The very important factor that influences the decision of those interested in buying a vehicle is its operating costs. This paper determines the costs of driving 100km for various electric vehicles, charging service providers and chargers, which was then confronted with the costs of refueling. Based on the analysis carried out, it was determined that, at present, the lowest costs of fueling/charging of a vehicle in Poland are connected with use of an electric vehicle, but only when the charging is performed with use of public AC chargers. Moreover, it was determined that the savings that will result from charging electric vehicles at AC charging stations as compared to filling up internal combustion engine vehicles are small and do not compensate for the purchase price of an electric vehicle.

Article info

Received 8 January 2021

Accepted 8 April 2021

Online 25 September 2021

Keywords:

electromobility,
charging station,
electric vehicle

Available online: <https://doi.org/10.26552/com.C.2022.1.A1-A11>

ISSN 1335-4205 (print version)

ISSN 2585-7878 (online version)

1 Introduction

Nowadays, serious problems and threats to civilization are connected with emission of harmful components of fuel combustion to the atmosphere and gradual exhaustion of fossil fuels. Air pollution is largely attributed to transport, especially motorization. Operation of an internal combustion engine powered by diesel or gasoline causes emission into the atmosphere of such combustion components as carbon dioxide, carbon monoxide, sulfur compounds, nitrogen oxides, hydrocarbons, lead compounds, which contribute to destruction of the ecosystem and threaten human health on a global and local level. Moreover, their emissions cause global climate warming [1-5]. Nevertheless, an important problem associated with use of motorized transport is the noise level, which is harmful to human health, as well. In an ad hoc way, these problems may be minimized by improving the design of internal combustion engines to drastically reduce their specific fuel consumption, introducing fuels with very low or no carbon content (e.g. hydrogen) and using combustion-electric hybrid propulsion systems. Ideally, electric vehicles should be widely available, especially when electric energy is obtained from renewable sources [6-8]. The development of electromobility creates real prospects for improving the air quality and reducing transport related noise in cities, as well as in Poland [8-9]. On 20 September 2016. The Ministry of Energy in cooperation with the Ministry of Development presented the "Package for Clean Transport", a set of three

documents that define the strategy for electromobility development in Poland [10-13], i.e.:

- Electromobility Development Plan,
- National policy framework for development of alternative fuels infrastructure,
- Low Emission Transport Fund.

Complementing the cited regulations is the project adopted in September 2019 entitled: "Strategy for Sustainable Transport Development until 2030" in which, in particular, modern solutions are indicated to facilitate the functioning of the entire transport sector and reduce its negative impact on the environment and climate, so that it is possible to create a sustainable transport system of the country by 2030. The strategy envisages that the number of passenger cars from 2022 will remain at the level of 26 - 27 million units, but there will be changes in the structure, i.e. an increase in the fleet of electric and hybrid vehicles, the number of which in 2030 may reach over 600 thousand units [14].

2 The current BEV electric vehicles market in Poland

The process of electrification of road transport in Poland is currently at a relatively early stage of development, which is reflected, among other things, by a small share of electric vehicles in the automotive market. Despite the fact that the number of registrations of the new Battery Electric Vehicles (BEV) in Poland grew in 2011-2019 by 56% on average from year to year,

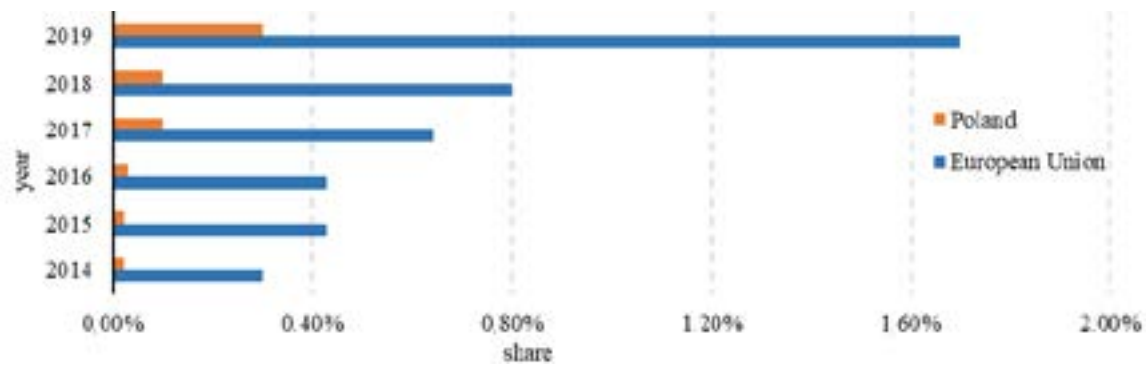


Figure 1 Share of the BEV vehicles in the automotive market in Poland in 2014-2019 (based on [15])

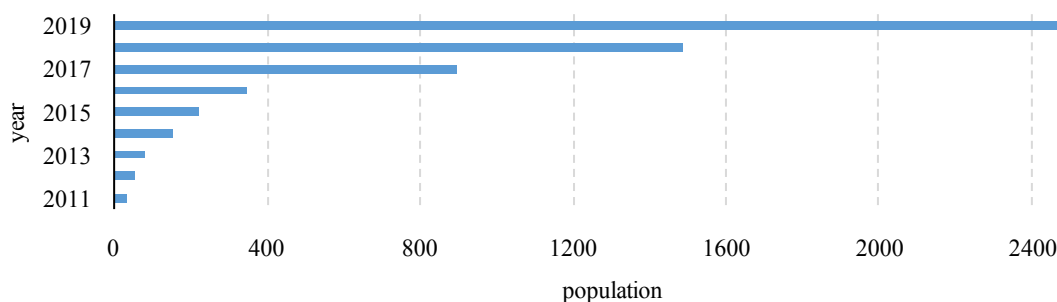


Figure 2 Total number of the BEV vehicles in Poland (based on [15])

Table 1 List of prices of selected new passenger vehicles with different engines in Poland [Euro] [21-23]

brand	model EV	price	model ZS*	price	model ZI**	price
Nissan	Leaf	568320 - 732600	Juke	319680 - 372960	Juke	319680 - 395160
Renault	Zoe	541236 - 634920	Clio	250860-279720	Twingo	204240 - 275280
Volkswagen	e-golf	723231	golf	381840 - 523920	golf	355200 - 417360
Volkswagen	e-Up!	511443	-	-	Up!	177600

ZS*- compression ignition

ZI**- spark ignition

the share of such vehicles in the automotive market in 2019 was 0.3% (2607 units) (Figure 1, 2).

According to [16-20] and the surveys carried out among Polish drivers, such a low interest in the purchase of electric vehicles is chiefly caused by their high price and technical limitations, such as the lack of generally accessible infrastructure for the charging of such vehicles, short driving range on a single charge (battery capacity), long charging time and great diversity of connectors.

Currently, even taking into account the proposed subsidies for the purchase of an electric vehicle, higher costs apply to the purchase of this type of vehicle compared to a combustion vehicle. A car whose size is sufficient for a family of 4 will cost from about Euro 444000. In general, a combustion engine car of a similar class can be bought for 50% of the price of an electric vehicle. Table 1 compares the prices of electric vehicles with combustion engine-powered cars available in Poland in 2019.

Moreover, potential EV users are concerned about the potential costs and location of vehicle servicing. At present, there are no independent service points for electric vehicles, which is a result of the lack of access to servicing procedures for this category of vehicles. This

situation may give rise to consumers' fears of higher prices of the BEV servicing. Not without significance for development of electromobility is the limited number of electric vehicle models that potential buyers have to choose from. In 2019 in Poland, consumers had only eighteen BEV models to choose from [24], which, in addition, can often not be seen in a vehicle showroom and after their purchase you have to reckon with a longer waiting time for pick-up. Moreover, not all the dealers sell such vehicles. For example, Volkswagen electric vehicles can be bought in Poland and then serviced in only four out of eighty-five Volkswagen dealerships [23]. Another very important impediment is the insufficient charging infrastructure for electric vehicles in Poland, which makes the electric vehicle essentially a city vehicle. According to estimates [15], there are currently over 945 publicly accessible electric vehicle charging points in Poland (Figure 3).

Although Poland has a very high ratio of charging stations to the number of vehicles of this type (one charger for every five vehicles), this is an effect of a very low number of electric vehicles registered in the country (Figure 4).

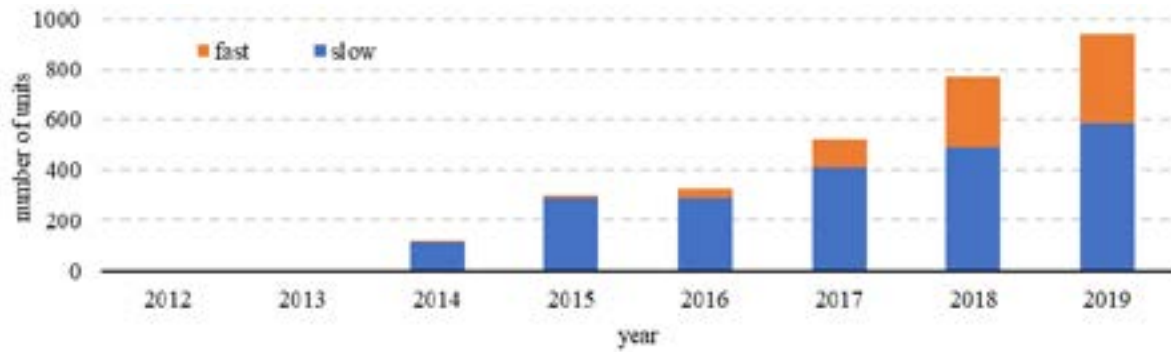


Figure 3 The number of publicly available electric vehicle charging points in Poland (based on [15])

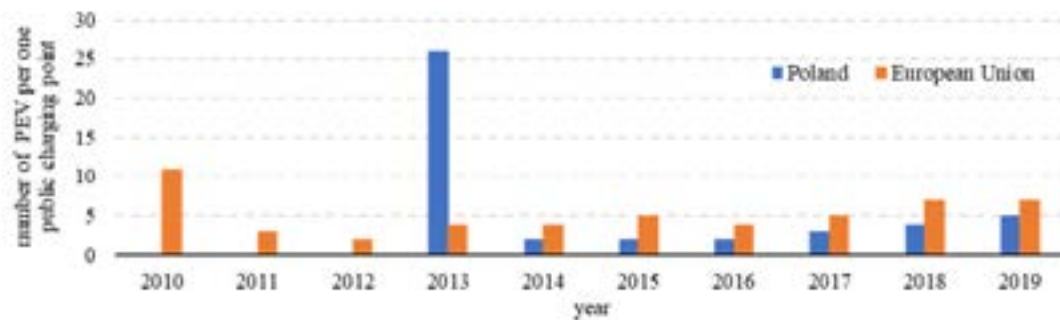


Figure 4 Number of electric cars per one public charging point (based on [15])



Figure 5 Distribution of EV charging stations in Poland, in 2020 (as of March 2020) [25]

The distribution of charging stations in Poland, as shown in Figure 5, indicates that they are chiefly located in large cities (48%) and along main transport routes. Lack of a sufficiently developed network of charging infrastructure, the current range of electric automotive vehicles and battery charging times make it necessary to plan longer trips in advance and spread them out in stages, which certainly limits the number of people interested in using electric vehicles.

Another, undoubtedly very important factor influencing the decision of those interested in buying

a vehicle, is the costs of refueling/charging. Until now, charging of electric vehicles on majority of charging stations available in Poland was free of charge. However, an increasing number of charging service providers operating in Poland have recently introduced and others are planning to introduce or increase, the currently binding charges for the of chargers provided by them. Therefore, the costs of driving 100 km for various electric vehicles, charging point operators and chargers has been determined below and then compared to the costs of refueling.

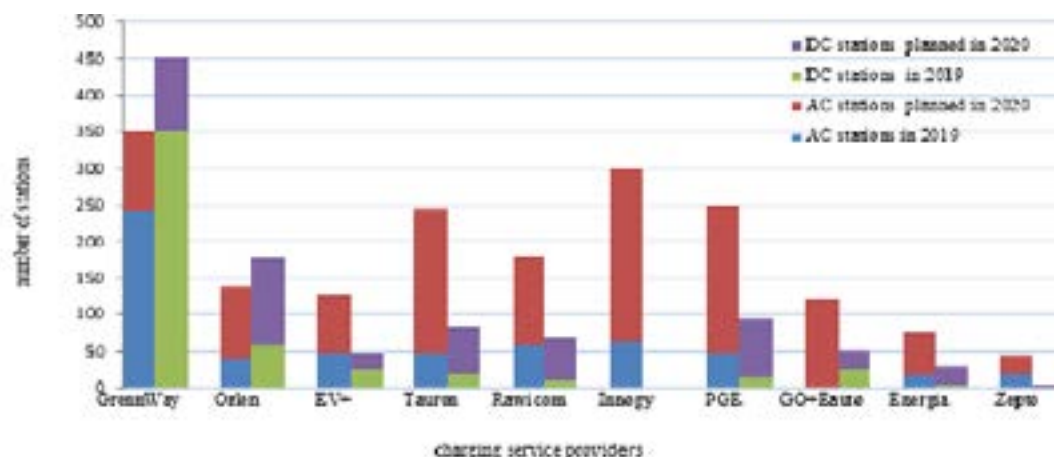


Figure 6 Ten largest electric vehicle charging networks in Poland [27-38]

Table 2 Costs of 1 kWh consumption at public charging stations in Poland in 2020 [27, 29-30, 34, 36-37] [Euro]

charging service provider	type of charging	
	AC	DC
GreenWay*	5.06	5.15
		5.72
		6.34
		6.61
		7.05
		8.74
		9.72
	11.49	
Tauron	7.10	9.81
EV+	5.32	7.99
GO+Eauto**	5.10	7.10
Elocity	4.44	-
Zepto **	3.99	-
	4.44	-
charging at home - G11 fare	2.44	-
charging at home - G12 tariff	1.11	-

*price depends on subscription

**price varies depending on location

3 Charging service providers in Poland

According to the Act of 11 January 2018 on electromobility and alternative fuels, at least one charging service provider should operate in a publicly available charging station. According to this Act, the charging service provider [26]:

- concludes with the electricity seller a contract for the sale of electricity, referred to in Article 5 (2) (1) of the Act of 10 April 1997. - Energy law;
- provides a charging service including charging and provides the opportunity to use the charging station infrastructure for charging purposes;
- provides, on its website, information about the price of the charging service and the conditions for its provision;
- provides the electric vehicle user with the option

of paying for electricity collected to charge the vehicle under the conditions specified in the sales contract.

In Poland, the largest suppliers of electric vehicle charging services are: GreenWay Polska Sp. z o.o., PGE Polish Energy Group, TAURON Polish Energy, Polish Oil Company Orlen, Innogy Stoen Operator Sp. z o.o., Rawicom, EVplus Sp. z o.o., GO + EAUTO Sp. z o.o., Energa, Zepto, EKOEN, IONITY, which jointly provide 86% of public charging points in the country, i.e. 1094 pieces, of which 55% are the fast chargers (DC).

According to the information obtained from the suppliers of the charging station, a total of another 17,469 charging points are to be launched by the end of 2020 [26-38]. Figure 6 shows the current and announced number of public charging points for major charging service providers in Poland.

3.1 Toll collection system in Poland

The price of the charging service is determined for a single charging point and may consist of three different charges:

- initial: fixed costs charged at the beginning of the charging session, regardless of duration and energy consumption;
- calculated based on energy consumption: costs proportional to the energy (kWh) used for charging;
- calculated based on charging time: hourly costs calculated from the beginning of the session to the end of the session.

In all the cases, the price of the charging service consists only of a charge based on energy consumption (kWh).

In Poland, the charge for electricity collected to charge a vehicle is binding at GreenWay Polska Sp. z o.o., TAURON Polish Energy, EVplus Sp. z o.o., GO + EAUTO Sp. z o.o., Elocity Sp z o.o., Zepto, Lotos Group S. A.

Currently, the costs of 1 kWh consumption at high-speed direct current stations at these suppliers' ranges from Euro 5.15 to Euro 11.49.

In turn, charging at slow or semi-fast stations involves an expenditure of Euro 3.99 to Euro 7.10 per 1 kWh, which makes it cheaper by 2-127% compared to using a higher power charger, comparing the offer of one operator (Table 2).

From 27 January 2020, Grupa Lotos S. A. also charges a fee of PLN 24 for using its charging stations regardless of the length of charging and the amount of

energy consumed [39].

On January 31, 2020, Ionity, the operator of the European network of ultra-fast charging stations, published a statement in which it stated that the expected price for each kWh collected at the station would be Euro 15.54 [40], while Innogy Polska would announce a rate for 1 kWh - Euros 4.44 and Ekoen, -7.05 Euros/kWh.

In addition, the PGE Polish Energy Group, Polish Oil Company Orlen, Energa intends to introduce a fee for electricity collected to charge the vehicle, the amount of which is not yet known.

3.1.1 Costs of driving 100 km

Below, Tables 3 and 4 show the costs of driving 100km for various electric cars and charging service providers currently in force in Poland, while Table 5 presents the costs per 1 kWh determined in accordance with the rates announced.

The costs determined refers to the charging itself and does not include e.g. fees and commissions connected with the electric vehicle charging service or costs connected with the battery pack consumption.

The drive train in electric vehicles consists of an electric motor, a battery pack and controllers (Figure 7).

This means fewer parts and therefore fewer components that could fail and lower operating costs, which are also omitted. The only maintenance tasks in their case are replacement of the battery coolant, oil in the transmission and replacement of worn out

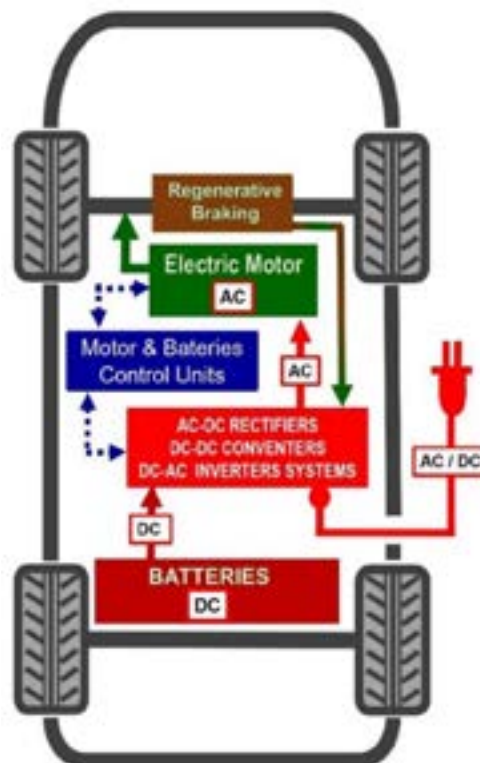


Figure 7 The BEV type car drive system [41]

Table 3 The costs of charging electricity per 100 km traveled in Poland [Euro]

brand	model	actual average electricity consumption per 100km, (kWh)	charging service provider							
			Tauron		EV+		GO+Eauto		Elocity	Zepto
			AC	DC	AC	DC	AC	DC	AC	AC
Hyundai	Ioniq electric	14.7	104.34	144.3	78.14	117.66	75.03	104.34	65.26	65.26
Volkswagen	e-golf	17.3	122.98	125.20	92.35	138.08	88.35	122.98	76.81	76.81
BMW	I3	17.4	123.43	170.94	92.79	131.08	88.8	123.43	77.25	77.25
Renault	Zoe	20.3	144.3	199.35	108.33	162.06	103.45	144.3	90.13	90.13
Nissan	Leaf	20.5	145.63	201.13	109.22	163.83	104.78	145.63	91.02	91.02
Tesla	SP90D	24.0	170.49	235.32	127.87	191.80	122.54	170.49	106.56	106.56
Tesla	100D	24.0	170.49	235.32	127.87	191.80	122.54	170.49	106.56	106.56

Table 4 The costs of charging electricity for 100 km travelled at GreenWay stations in Poland [Euro]

brand	model	package									
		AC	Energymax			Energyplus			Energystandard		
			DC			DC			DC		
			≤40 kW	40<x ≤150 kW	>150 kW	≤40 kW	40<x ≤150 kW	>150 kW	≤40 kW	40<x ≤150 kW	>150 kW
Hyundai	Ioniq electric	74.59	75.92	83.91	97.23	93.24	103.89	123.43	128.31	142.96	169.16
Volkswagen	e-golf	87.46	89.24	99.01	114.55	109.66	122.1	145.18	151.40	168.27	198.91
BMW	I3	87.91	89.68	99.45	114.99	110.55	122.98	146.07	152.73	169.16	200.24
Renault	Zoe	102.56	104.34	116.32	134.53	130.53	143.41	170.49	177.6	198.91	233.54
Nissan	Leaf	103.89	105.67	117.21	135.42	130.09	144.74	171.82	179.37	199.35	235.32
Tesla	S P90D	121.65	123.43	137.19	158.50	152.29	169.60	201.57	210.01	233.54	276.16
Tesla	100D	121.65	123.43	137.19	158.50	152.29	169.60	201.57	210.01	233.54	276.16

Table 5 Expected costs of charging electricity for 100 km traveled in Poland [Euro]

brand	model	charging service provider		
		Ionity	Innogy Polska	Ekoen
Hyundai	Ioniq electric	228.66	65.28	106.11
Volkswagen	e-golf	269.06	76.81	122.1
BMW	I3	270.39	77.25	122.98
Renault	Zoe	315.68	90.13	143.41
Nissan	Leaf	318.79	91.02	144.74
Tesla	S P90D	372.96	106.56	169.60
Tesla	100D	372.96	106.56	169.60

Table 6 Charging time for electric vehicles [42-45]

brand	model	type of charging	
		AC (7.2 kW) (h)	DC (50kW) (h)
Hyundai	Ioniq electric	6.25	0.5
Volkswagen	e-golf	1.5	0.5
BMW	I3	4.5	0.35
Renault	Zoe	6.5	1
Nissan	Leaf	6	1
Tesla	S P90D	11	2
Tesla	100D	11	2.

Table 7 Costs of charging electricity per 100km traveled from an electrical outlet[Euro]

brand	model	tariff	
		G11	G12
Hyundai	Ioniq electric	35.91	16.29
Volkswagen	e-golf	42.68	19.18
BMW	I3	42.49	19.31
Renault	Zoe	49.59	22.51
Nissan	Leaf	50.08	22.73
Tesla	S P90D	58.60	26.64
Tesla	100D	58.60	26.64

Table 8 Technical parameters of the analyzed vehicles [23, 29]

costs	Volkswagen Golf 5-door		
	Trendline 1.5 TSI ACT BlueMotion	Trendline 1.6 TDI	e-Golf
vehicle own weight (kg)	1 315	1 355	1 615
load capacity (kg)	418-575	402-574	408-480
overall length (m)	4.36	4.26	4.27
overall width (m)	1.79	1.79	1.78
fuel type	gasoline	diesel oil	electric current
average consumption of gasoline (l)/ diesel oil (l)/ electric energy (kWh) per 100 km	5	4.7	15.7
maximum power output (kW)	96	85	100
maximum torque (NM)	200	250	290
maximum speed (km/h)	210	198	150
acceleration to 100 km/h (s)	9.1	10.2	9.6
total driving range (combined) (km)	833.3	120.41	231
vehicle purchase costs (Euro)*	368342	392318	735663

Table 9 The costs of charging / refueling per 100km of analyzed vehicles

	Volkswagen Golf 5-door			
	Trendline 1.5 TSI ACT BlueMotion	Trendline 1.6 TDI	electric current	electric current
fuel type	gasoline	diesel oil	electric current	electric current
price for (1)/1kWh (Euro)*	20.64	20.60	4.88	17.13
average consumption of gasoline (l)/ diesel oil (l)/ electric energy (kWh) per 100 km	5.00	4.70	15.70	15.70
100 km journey costs (combined) (Euro)	103.23	96.79	76.81	269.06

*Prices valid on February 10, 2021

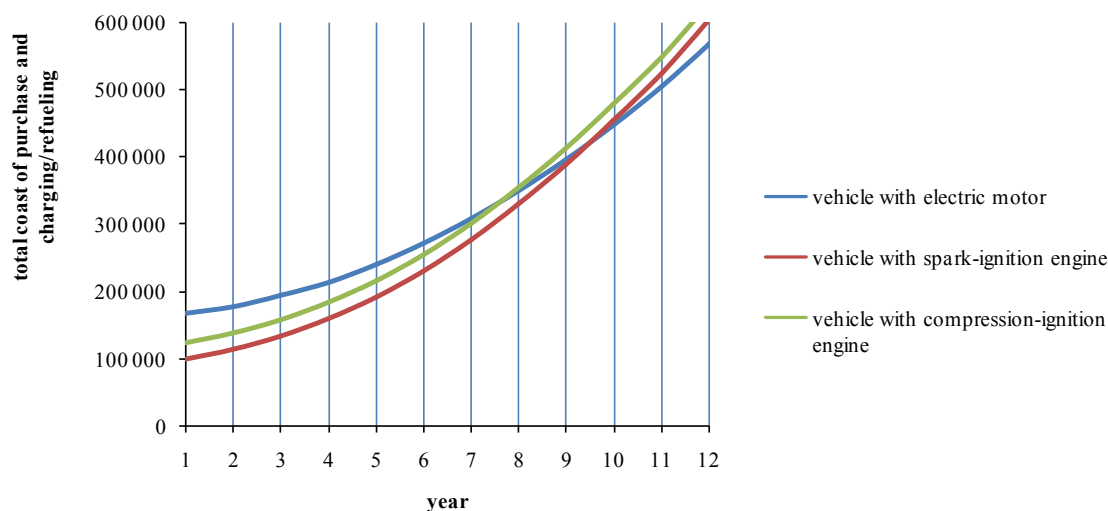
suspension and friction elements of the braking system, which also takes place in a vehicle with a conventional engine.

Analyzing the above costs, it should be noted that the electric vehicle will be more cheaply charged using the AC charging stations. However, the battery will take longer to recharge (up to 80% compared to DC), as demonstrated in Table 6.

The calculations show that among the cars under consideration, the Hyundai Ioniq electric is the cheapest in operation, taking into account only the costs of battery charging. In the case when the AC Zepto or Elocity Sp z o. o. charger is used to charge it, the costs of charging electricity for 100 km are 65.31 Euro. The highest costs of charging electricity per 100km for this type of charging are for TAURON Polish Energy and is 170.49 Euro.

Table 10 Total costs of fueling/charging vehicles with various types of propulsion [Euro] and the differences between them

	cumulative refuelling/charging cost				cumulative savings			
	electric vehicle		internal combustion engine vehicle		BEV vs PB95		BEV vs ON	
distance travelled	charging AC	charging DC	PB95	ON	charging AC	charging DC	charging AC	charging DC
30 000	23043.6	80719.2	29046	30969	6002.88	-51672.72	7925.4	-49750.2
60 000	46087.2	161438.4	58097.4	61938	12010.2	-103341	15850.8	-99500.4
90 000	69130.8	242157.6	87143.88	92907	18013.08	-155013.72	23776.2	-149250.6

**Figure 8** Total costs of purchasing and charging/refueling a vehicle in Poland [PLN]

In the case of the DC chargers, the lowest cost is 97.28 Euro, while the highest is 275.99 Euro. Even lower costs of charging an electric vehicle with electricity necessary to cover a distance of 100km are recorded in the case of charging from an electric socket available e.g. in a garage. Table 7 presents such costs for all the vehicles analyzed.

3.1.2 Comparison of the charging costs of an electric vehicle to the costs of refueling a car with an internal combustion engine

In Table 9 are presented the costs of fueling/charging per 100 km one model of vehicles of the same make, with different propulsion sources and systems, assigned to the same market segment (B). They have the same or comparable total power, the same body type, type of drive (front-wheel drive) and transmission (vehicles with conventional engines - manual, with electric motors - automatic). The fuel/electricity consumption in the mixed cycle as given by the vehicle manufacturer and the annual mileage: 30 000km were assumed. In the calculations are taken into account the lowest and the highest costs of electricity charging needed to drive per 100km at public charging stations.

Technical parameters and costs related to, among

others, the purchase of the considered vehicles contains Table 8.

The calculations show that currently the lowest costs, related to driving 100km in Poland, are related to use of an electric vehicle, but only when charging is done with public AC chargers (the lowest price for 1kWh - Euro 4.88). The highest, when charging is carried out with use of DC Ioney chargers (price for 1kWh - 17.13 Euro). Then the costs of charging would significantly exceed the costs of refueling vehicles with a conventional engine and would be higher by over 160%.

Table 10 gives the total costs of refueling/charging vehicles with different propulsion types and the differences between them that will be generated after three years.

The savings that would result from charging an electric vehicle at AC charging stations, as compared to refueling an IC engine vehicle after 3 years, are small and certainly do not make up for the purchase price of an electric vehicle, which is currently at least 40% higher than that of a conventional engine vehicle (Table 1). When comparing the total costs of purchasing and refueling/charging a vehicle, the total costs of purchasing and charging an electric vehicle would be equal to those of a compression ignition engine vehicle after a minimum of 7 years and of a spark ignition engine vehicle after a minimum of 9 years (Figure 8).

Meanwhile, after about 8 years or driving 160 000 km by the BEV, it is planned to replace the battery used in such a vehicle. Currently, battery replacement in Volkswagen e-Golf costs 382396.12 Euro. Thus, the battery costs converted per 100 km will amount to 239.67 Euro.

Taking into account the costs of electricity consumption (4.88 Euro per 100 km - the cheapest option) and the costs of depreciation of the battery - the costs of driving 100 km would then be 244.55 Euro. Assuming that the price of gasoline is 1/l, it corresponds to use of a combustion vehicle with an average fuel consumption of 11.97 l/100 km.

The advantage of electric vehicles is the simple structure of their drive system.

It is estimated that the driveline consists of around 4,000 components for a vehicle with a conventional engine and only 320 for the BEV.

The engine related devices are much simpler than in a combustion vehicle; for example, an electric motor does not require a cooling system. Its design itself is also much less complicated than that of an internal combustion unit. There are, for example, no intake or exhaust system, valves. Simple structure, relatively small dimensions and low weight allow to eliminate frequent maintenance and repairs connected with the necessary costs (fuel filter, air filter, oils, fluids, spark plugs, timing gears, adjustments, removal of leaks etc.).

However, all these do not compensate for the costs associated with buying an electric vehicle or a subsequent battery replacement.

4 Conclusions

Development of electromobility in Poland depends on overcoming a number of barriers, which are of different nature: technical, economic, social and organizational.

The most frequently cited obstacle is insufficient infrastructure for charging vehicles. Potential consumers are also discouraged by the significantly higher purchase costs of an electric vehicle, as compared to a combustion vehicle, even after taking into account the proposed subsidies. In addition, there are concerns about the possible costs and location of vehicle servicing, as well as future costs of battery replacement. Added to this is the inability to determine the value of an electric vehicle in the aftermarket in the future.

This paper shows that another significant barrier may also be the costs of charging such vehicles. Although the costs of charging from a socket with energy needed for 100 km is presently maximum Euro 57.72, it is connected with significant difficulties (long charging time, difficulties in connecting to an electric socket).

Currently, an electric vehicle can be charged for 100 km at public charging stations for the price from 62.16 Euro to 275.28 Euro. However, these amounts are not encouraging, considering the long charging time, short range of the vehicles ride, lack of a uniform charging standard and above all the costs of purchase of such a vehicle. The analysis shows that these costs will be compensated for after 7 years for a vehicle with a diesel engine and 9 years for a vehicle with a spark ignition engine. However, it should be noted that after 8 years or 160 000 km it is recommended to replace the battery in an electric vehicle, which generates a further costs of 381840 to 444000 Euro.

In 2020, Ionity charging stations were launched in Poland, where the average charging time was reduced to 15-25 minutes. However, the costs of charging at these stations turned out to be higher by up to 50% compared to refueling the IC vehicles. Therefore, it should be clearly stated that another very significant barrier to the development of electromobility in Poland are the costs of charging such vehicles.

References

- [1] POLAKOWSKI, K. Electric cars in the near future. Works of the Institute of Electrical Engineering. Warsaw, 2011.
- [2] BRODAKCI, D., POLASZCZYK, J. Emissivity of the operation of electric cars in the context of the strategic goals of the development of electromobility in Poland and the Netherlands. *Polityka Energetyczna - The Energy Policy Journal*. 2018, **21**(1), p. 99-115. ISSN 1429-6675.
- [3] PRADECKI K., GAJOS, E. Economic valuation of emission of selected substances into the air in Poland with particular emphasis on agriculture. Warsaw: Scientific Quarterly of the Vistula University, 2017. p. 189-207.
- [4] PRADECKI, K., SADOWSKI, M. International evolution of environmental protection. Warsaw: Academy of Finance, 2010.
- [5] SKRUCANY, T., KENDRA, M., STOPKA, O., MILOJEVIC, S., FIGLUS, T., CSISZAR, C. Impact of the electric mobility implementation on the greenhouse gases production in central European countries. *Sustainability [online]*. 2019, **11**(18), 4948. E ISSN 2071-1050. Available from: <https://doi.org/10.3390/su11184948>
- [6] Sustainable development of transport - an outline of the problem - Special vehicles / Zrownowazony rozwój transportu - zarys problem - Samochody Specjalne (in Polish) *[online]*. Available from: <https://samochody-specjalne.pl/2016/02/01/zrownowazony-rozwoj-transportu-zarys-problemu/>

- [7] MURAWSKI, J., SZCZEPANSKI, E. Perspectives for electromobility development in Poland. *Logistics*. 2014, **4**, p. 2249-2258. ISSN 1231-5478.
- [8] RADOVIC, U., The impact of electric cars on the Polish power system, CO2 emissions and other air pollutants. *Zeszyty Naukowe. Instytut Gospodarki Surowców Surowców Mineralnych i Energia Polskiej Akademii Nauk [online]*. 2018, **104**, p. 69-83. ISSN 2080-0819. Available from: <https://doi.org/10.24425/124366>
- [9] SENDEK-MATYSIAK, E. Analysis of the electromobility performance in Poland and proposed incentives for its development. In: 11th International Science-Technical Conference Automotive Safety 2018: proceedings [online]. IEEE, 2018. Available from: <https://doi.org/10.1109/AUTOSAFE.2018.8373338>
- [10] Ministry of Energy: Clean transport package - Renewable energy association / Ministerstwo energii: pakiet na rzecz czystego transportu – Stowarzyszenie Energii Odnawialnej (in Polish) [online]. Available from: <http://seo.org.pl/ministerstwo-energii-pakiet-na-rzecz-czystego-transportu/>
- [11] Plan for electromobility development in Poland - Ministry of Energy / Plan rozwoju elektromobilności w Polsce - Ministerstwo Energii (in Polish) [online]. Available from: <https://www.gov.pl/attachment/75d21d4a-fd28-400e-b480-a3bbc3f7db5e>
- [12] National Policy Framework for the Development of Alternative Fuel Infrastructure - Ministry of Energy / Krajowe ramy polityki rozwoju infrastruktury paliw alternatywnych - Ministerstwo Energii (in Polish) [online]. Available from: <http://www.subregioncentralny.pl/downloadnews/krajowe-ramy-polityki-rozwoju-infrastruktury-paliw-alternatywnych.pdf>
- [13] Service of the Republic of Poland / Serwis Rzeczypospolitej Polskiej (in Polish) [online]. Available from: <https://www.gov.pl/web/aktywa-panstwowe/fundusz-niskoemisyjnego-transportu>
- [14] Strategy of sustainable transport development until 2030 - Ministry of Infrastructure / Strategia zrównoważonego rozwoju transportu do 2030 roku - Ministerstwo Infrastruktury (in Polish) [online]. Available from: <https://www.gov.pl/web/infrastruktura/projekt-strategii-zrownowazonego-rozwoju-transportu-do-2030-roku2>
- [15] Alternative fuel station map - *European Alternative Fuels Observatory [online]*. Available from: <https://www.eafo.eu/>
- [16] ZANIEWSKA-ZIELINSKA, D. Problems of electromobility development in Poland. *Europa Regionum*. 2018, **35**, p. 63-78. ISSN 1428-278X, eISSN 2719-437X.
- [17] KRAWIEC, S., KRAWIEC, K. Development of electromobility in Poland. Conditions, objectives and barriers. *Scientific Papers of the University of Economics in Katowice*. 2017, **332**, p. 17-24. ISSN 2083-8611.
- [18] SENDEK-MATYSIAK, E., SZUMSKA, E. Infrastructure of charging as one of the elements of electromobility development in Poland. *Scientific Papers of Warsaw University of Technology*. 2018, **121**, p. 329-340. ISSN - 1230-9265.
- [19] TOMASZEWSKI, K. *Problems of electromobility development in Poland in the context of national energy policy*. Warsaw: Warsaw University, 2019. ISSN 1426-8876.
- [20] Electromobility. Electromobility development in Poland and the associated challenges for the electricity system [online]. Available from: <https://www.muratorplus.pl/technika/elektroenergetyka/elektromobilnosc-w-polsce-rozwoj-elektromobilnosc-i-wyzwania-dla-systemu-elektroenergetycznego-aa-t7oE-F5pC-pUTk.html>
- [21] Nissan (in Polish) [online]. Available from: <https://www.nissan.pl/>
- [22] Renault (in Polish) [online]. Available from: <https://www.renault.pl/>
- [23] Volkswagen ID.4 (in Polish) [online]. Available from: <https://www.volkswagen.pl/pl.html>
- [24] Electromobility / Elektromobilni (in Polish) [online]. Available from: <http://elektromobilni.pl>
- [25] Volkswagen (in Polish) [online]. Available from: <https://www.volkswagen.pl>
- [26] Pug share [online]. Available from: <https://www.plugshare.com/>
- [27] ISAP - Internet system of legal acts / ISAP - Internetowy system aktów prawnych (in Polish) [online]. Available from: <http://isap.sejm.gov.pl/isap.nsf/download.xsp/WDU20180000317/T/D20180317L.pdf>
- [28] Green way (in Polish) [online]. Available from: <https://greenwaypolska.pl/>
- [29] Orlen (in Polish) [online]. Available from: <https://www.ornel.pl/PL/Strony/default.aspx>
- [30] EVplus (in Polish) [online]. Available from: <http://evplus.com.pl/>
- [31] Tauron (in Polish) [online]. Available from: <https://www.tauron.pl/tauron/tauron-innowacje/emobility>
- [32] Rawicom (in Polish) [online]. Available from: <https://www.rawicom.pl/>
- [33] Innogy (in Polish) [online]. Available from: <https://www.innogy.pl/pl/dla-domu>
- [34] PGE (in Polish) [online]. Available from: <https://www.gkpge.pl/Oferta>
- [35] GO+EAUTO (in Polish) [online]. Available from: <https://gopluseauto.pl/>
- [36] Energa (in Polish) [online]. Available from: <https://www.energa.pl/dom>
- [37] Zepto (in Polish) [online]. Available from: <https://zepto.pl/>
- [38] Ranking of the biggest charging station networks in Poland / Ranking największych sieci stacji ładowania samochodów elektrycznych w Polsce (in Polish) [online]. Available from: <https://wysokienapiecie.pl/26820-ranking-najwiekszych-sieci-stacji-ladowania-samochodow-elektrycznych-w-polsce/>

- [39] Lotos (in Polish) *[online]*. Available from: <http://www.lotos.pl/>
- [40] Ionity *[online]*. Available from: <https://ionity.eu/>
- [41] SENDEK-MATYSIAK, E., LOSIEWICZ, Z. Analysis of the development of the electromobility market in Poland in the context of the implemented subsidies. *Energies [online]*. 2021, **14**(1), 222. eISSN 1996-1073. Available from: <https://doi.org/10.3390/en14010222>
- [42] Hyundai Ioniq Electric 2019 - Milivolt (in Polish) *[online]*. Available from: <https://www.milivolt.pl/hyundai-ioniq/>
- [43] Range, battery and charging / Zasieg, akumulator i ladowanie - Renault ZOE (in Polish) *[online]*. Available from: <https://www.renault.pl/samochody-elektryczne/zoe/akumulator-i-ladowanie.html>
- [44] Where, how and for how much will I charge my electric car? Volkswagen e-Golf in practice / Gdzie, jak i za ile naladuje swoje elektryczne auto? Volkswagen e-Golf w praktyce (in Polish) *[online]*. Available from: <https://antyweb.pl/gdzie-jak-i-za-ile-naladuje-elektryczne-auto-volkswagen-e-golf-w-praktyce/>
- [45] How much does an electric car charge depending on the power of the charging station? e-tron vs Model S vs i3 vs Leaf vs ipace / Ile laduje sie samochod elektryczny w zaleznosci od mocy stacji ladowania? e-tron vs Model S vs i3 vs Leaf vs ipace (in Polish) *[online]*. Available from: <https://elektrowoz.pl/ladowarki/ile-laduje-sie-samochod-elektryczny-w-zaleznosci-od-mocy-stacji-ladowania-e-tron-vs-model-s-vs-i3-vs-leaf-vs-i-pace/>

ANALYSIS OF THE TRAFFIC PARAMETERS ON A SECTION IN THE CITY OF THE NATIONAL ROAD DURING SEVERAL YEARS OF OPERATION

Andrzej Bąkowski*, Leszek Radziszewski

Faculty of Mechatronics and Mechanical Engineering, Kielce University of Technology, Kielce, Poland

*E-mail of corresponding author: abakowski@tu.kielce.pl

Resume

The study carried out an analysis of the vehicle traffic parameters on a national road in 2011-2016. The variability and uncertainty of results were evaluated. An analysis of traffic data recorded on the city's entry and exit lanes was carried out. The variations in traffic volume are of interest e.g. in dynamic traffic management systems and navigation services, examining the benefits of flexible work time and places and assessing the environmental effects of traffic congestion. Research has shown that the assumption that lanes perform equally is not always true. Traffic volume models should be periodically calibrated taking into account the shape of the daily profile, which may, for example, allow public transport timetables to be more responsive to the needs of travelers.

Article info

Received 17 September 2020

Accepted 5 May 2021

Online 6 October 2021

Keywords:

daily traffic volume profile on lanes, uncertainty of measurements, coefficient of variation

Available online: <https://doi.org/10.26552/com.C.2022.1.A12-A25>

ISSN 1335-4205 (print version)

ISSN 2585-7878 (online version)

1 Introduction

Studies on the nuisance of transport for people and nature are currently presented in numerous publications around the world [1-2]. The authors most often present their considerations either as a part of the idea and policy of "Sustainable transport development" or "Smart City" or as a part of the methodology associated with the "Intelligent Transport System" [3]. Air pollution, noise and vibration, as well as other phenomena that create environmental hazards, e.g. road accidents, depend to a large extent on traffic parameters: vehicle traffic intensity, vehicle speed, vehicle structure [4-5]. Therefore, the basis for all the research in this area must be the measurement and analysis of data, as a part of monitoring the road traffic [6-9]. For these reasons, the project "Expansion of Sciegiennego Str. along National Road No. 73 in Kielce" obtained funding from the European Regional Development Fund under the Operational Program Infrastructure and Environment 2007-2013 priority: VIII Transport safety and national networks transport action: 8.2. National roads outside the TEN-T network. The entire investment was located within the administrative boundaries of the city of Kielce on the section from Popieluszki Av. to the city limits along the national road No. 73, Figure 1.

Popieluszki Av. is a road with four lanes of traffic. The road is a part of the eastern bypass around Kielce

and part of the national road No. 73 (Warszawa/Lodz - Kielce - Tarnow - Krosno), which is directly connected with the Trans-European Transport Networks (TEN-T). As a part of the project, the widening and strengthening of the pavement was carried out by making a bituminous overlay of the existing western roadway, construction of the second eastern roadway. Over the extended road, 5km of pedestrian-bicycle paths and 3 bridge structures were created. A rainwater sewage system, acoustic screens, street lighting, traffic lights were built, the existing water supply system was rebuilt and secured. Implementation of such a large investment contributed to increase in safety but also caused a lot of acoustic nuisance for local residents and road users during the construction. This paper presents an analysis of results of the traffic volume measurements recorded by monitoring stations in period from 2011 up to 2016.

2 Related works

The overview of the traffic data collection systems were presented by Bennett at al. [11] and Gajda at al. [12]. Such systems can be divided into intrusive, e.g. inductive loop detectors, magnetic sensor, pneumatic tubes, weight-in-motion sensor, or non-intrusive sensors, e.g. microwave systems, cameras, GPS based systems. The recorded traffic volume data are the most often

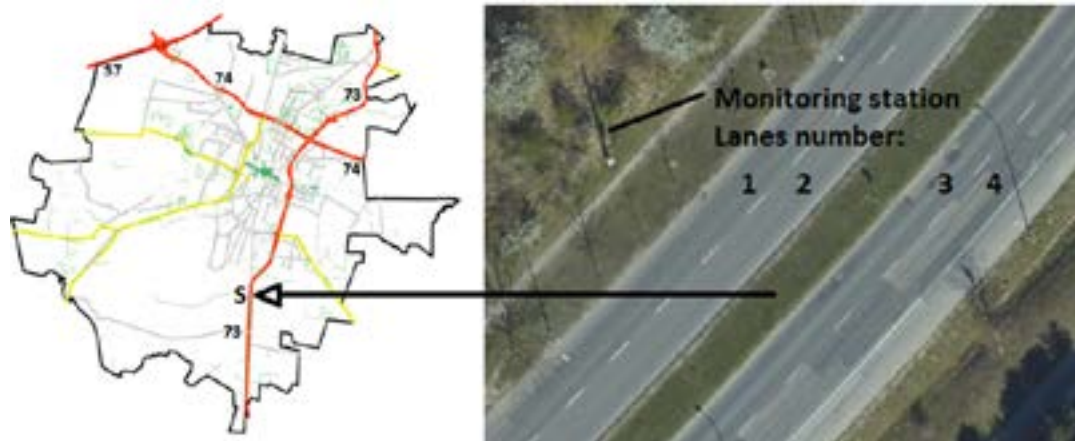


Figure 1 Layout of streets in Kielce [10]

analyzed using statistical or computational intelligence methods [13]. Analysis of the distribution of the traffic volume showed that in the case of uninterrupted traffic flows, e.g. on motorways, the normal distribution [14] occurs and in the case of interrupted traffic flows, e.g. in urban areas, it is usually non-normal [15]. Traffic in urbanized areas is characterized by high variability, which significantly hinders traffic management, e.g. route planning and vehicle travel time. The problem of variability can be analyzed depending on the adopted time interval and location of the road in the communication system of an urbanized area. In the period of one year, one can notice the so-called seasonality of vehicle traffic. Within one week, the traffic volume on weekdays differs significantly from the traffic on weekends and holidays. The period of one day can be divided into 24 hours. In each subsequent hour of the day, vehicle traffic parameters may be different [16]. It is also possible to increase the detail of measurements and divide the day into a larger number of sub-intervals [17], e.g. 48, 96 or even 1440, which however, makes analysis of results more complicated. Many studies in the literature are related to influence of the pre-determined parameters on changes in the traffic volume. One such parameter is the day of the week. Rakha and van Aerde [14] found that on Mondays and Fridays the traffic volume was different from the core weekdays (Tuesday-Thursday), but speeds and occupancy were not. They also examined the traffic flow, speed and occupancy histograms and showed that they have a normal distribution. Stathopoulos et al. [18] investigated the daily traffic volumes and found no significant differences between weekdays. However, the weekend days differed significantly from weekdays. The results indicate that the temporal distributions of traffic volumes are non-normal. The analyzed traffic volume data exhibit different patterns depending on the direction of movement (toward, in, or away from the central business district) and the periods of the day. Chrobok et al. [19] compared the patterns of the daily traffic volume based on the measurement error. They pointed to four distinctive groups: weekdays from Monday until Thursday, Friday and days before

holidays, Saturday and holidays and presented that the traffic volume pattern from Monday until Thursday has asymmetry due to the traffic tidal flow. Weijermars [20] showed differences in the traffic volume for each day of the week using the cluster analysis. The clustering based on the 15 minutes' traffic volumes resulted in a classification into five clusters (four clusters of weekdays were identified: Mondays, core weekdays, Fridays and days within holiday periods) that show distinct daily flow profiles and are representative for the days within the clusters. Besides the general shape of the daily flow profile, the shape of the peak periods is important for the traffic management, as well. Weijermars was the first to suggest the need to study the shape of the traffic volume profiles. The study concluded that shape of the daily volume profiles may differ between different type of days and motivates the need for such an analysis of the traffic patterns based on their inherent shape characteristics. Calafate et al. [16] detected the traffic volume patterns according to the day of the week, hour and type of street. To achieve this goal, he applied a clustering technique in order to automatically classify streets according to their daily traffic pattern. The problem of differences in the traffic shape and magnitude was continued by Guardiola et al. [21]. The method Functional Principal Component Analysis was used to identify the three Principal Components. The first appears to separate working from non-working days, the second may relate to the year and the third may be a seasonal factor. Crawford et al. [22] used the Functional Linear Regression Models for estimating the effect of the predictable variability, due to known explanatory factors, on the daily traffic flow profiles, for example the day of the week. The contribution of the research of Kayani [15] is use of the Mathematical Morphology tools to achieve proper classification of daily traffic profiles. Through the employment of such tools development of an analysis of shape is carried out in an effort to generate interpretable classification of historical daily traffic profiles. Use of the Partition Around Medoids (PAM) algorithm is employed to carry out the classification of daily profiles.

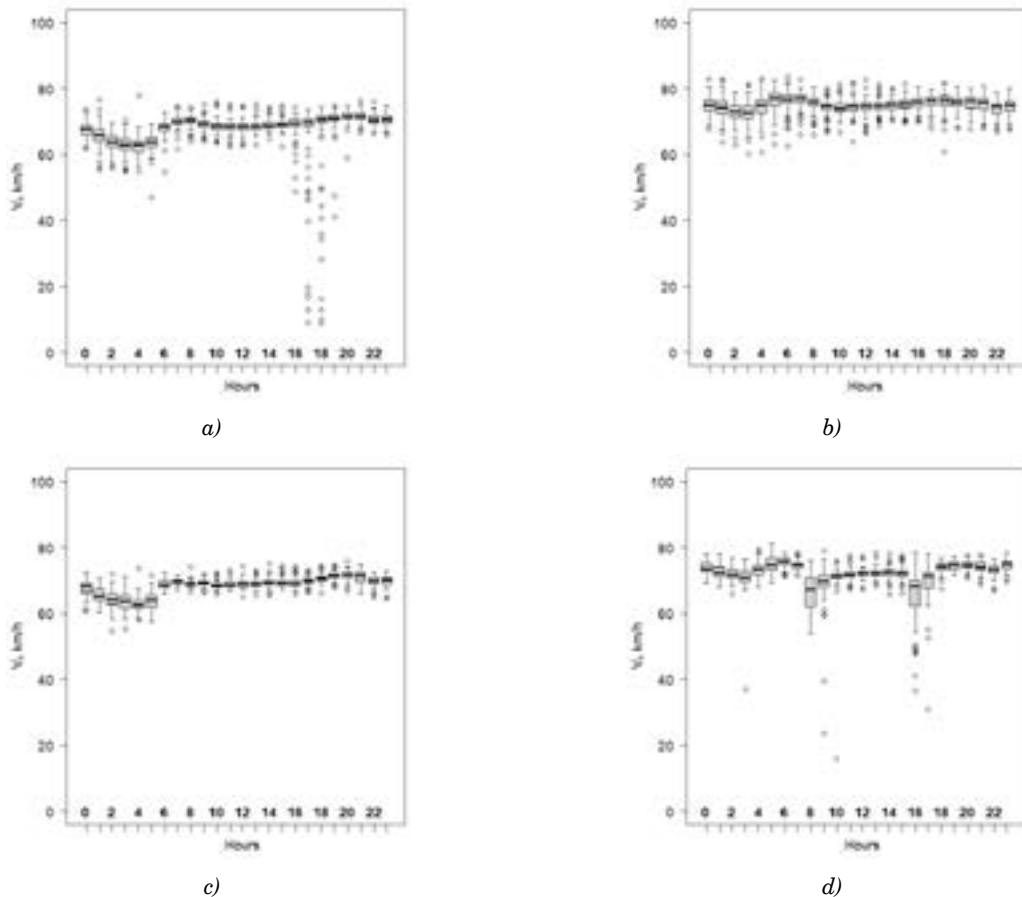


Figure 2 Box plots for weekdays of relation between the median average of annual hourly traffic speed and time for 24 h period a) in 2011 on lanes L_{12} , b) in 2011 on lanes L_{34} , c) in 2016 on lanes L_{12} , d) in 2016 on lanes L_{34}

The goal of this research was to obtain an insight into the traffic volume, measurement uncertainty, detecting traffic patterns according to the day of the week, hour and lanes and in particular on weekdays. For this purpose, the aggregated data for the period from 2011 to 2016 in the 24-hour interval have been divided into 4 sub-intervals of various lengths. To evaluate the results, a traffic volume model using the linear regression method was proposed.

3 Traffic volume measurements

The traffic volumes analyzed in this study were measured by the permanent station recording traffic volume and sound pressure levels, located in Popieluszka Av. in Kielce. The Popieluszka Av. is the main part of the outward route from the centre of Kielce towards Tarnow. The traffic monitoring station is located between the two intersections at a distance of about 500m. The station includes a road radar box, a sound level meter and a weather station. The traffic volume was measured by WAVETRONIX digital radar with an operating frequency of 245 MHz [23]. The measurements were carried out for 24 hours a day throughout the year 2011-2016. The traffic volume and speed data were recorded every minute (buffer) and the averaged results

were reported every hour. Owing to various technical problems, the monitoring station did not always correctly record traffic parameters and the database was incomplete. The counts were used to calculate the traffic volume (understood as the sum of the number of vehicles: passenger, heavy, medium heavy, two wheelers recorded within a time interval at all four lanes) and speed, split into seven days of the week, hours. As for some of the days no data were reported, only the days for which the traffic was recorded every hour for the whole 24-hour period were taken into account in the analysis. In this way, 803 days were selected for further analysis, i.e. 19,272 records, at various seasons of the year. Parameters such as: traffic volume, standard uncertainty of the measurement results (u_q), coefficient of positional variation of traffic volume (V_q), relative traffic volume, were determined in accordance with the procedure presented in [24]. The relative traffic volume was determined according to formula:

$$VOL_{rel}(d,L) = VOL(d,L)/VOL_{max}(d,L), \quad (1)$$

where:

$VOL(d,L)$ - median of the traffic volume,

$VOL_{max}(d,L)$ - the maximum median of the traffic volume of the vehicle set analysed on road lanes L_{12} and L_{34} ,

d - day of week.

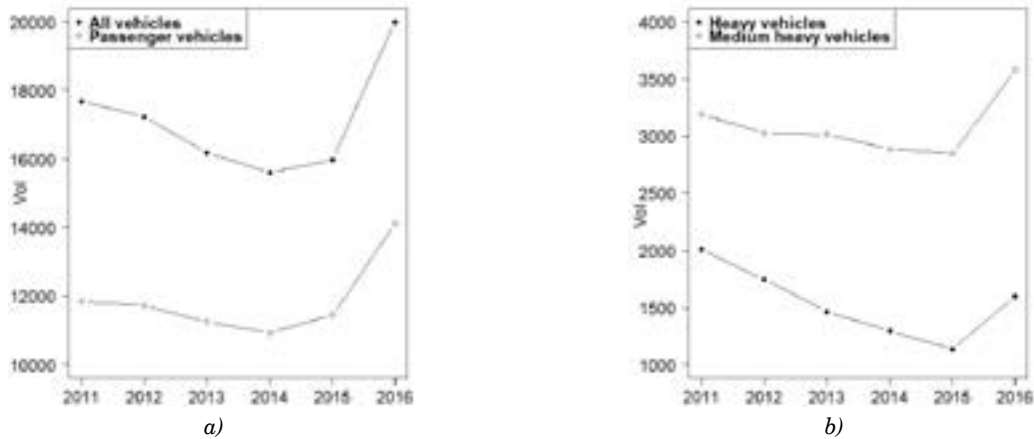


Figure 3 Median of annual daily traffic volume in the years 2011-2016

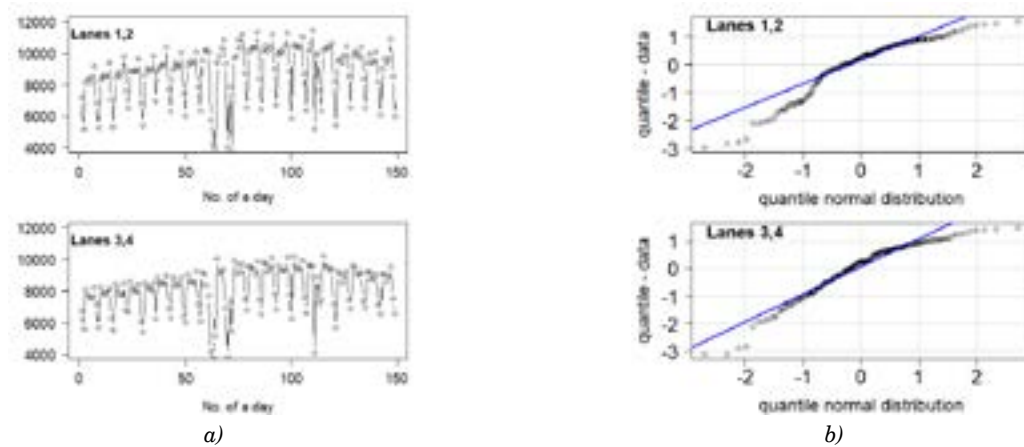


Figure 4 Traffic volume in 2011 a) values on individual days (data from 19.02. to 31.07.) for lanes L_{12} and L_{34} b) quantile graph for lanes L_{12} and lanes L_{34}

4 Measurements and calculations results

The median of average vehicle speed in the period studied from 2011 to 2016 slightly changed, which is shown in Figure 2. Nevertheless, the intersections of the road with traffic lights and speed cameras built as part of the renovation contributed to a decrease in its value, especially during the traffic rush hours. One can also see that the amount of outliers has decreased significantly. It is worth noting that the speed charts on entry lanes (L_{12}) and exit lanes (L_{34}) from the city and for different years have different courses, especially in 2016. In 2016, in lanes L_{12} from midnight, the median speed decreases to its minimum value at 4 AM and then increases to 7 AM. Then, in the subsequent hours, its value changes slightly and the highest occurs at 8 PM. On the other hand, for the lanes L_{34} , both the shape of the speed graph and values in individual hours, especially in traffic rush hours, are different.

The deteriorating condition of the road and the nuisance associated with its renovation contributed to a decrease in traffic in the years 2011 to 2016 by 9.7%. There was a 43.7% decrease for heavy vehicles, 10.7% for medium heavy vehicles and 3.3% for passenger vehicles.

However, in 2016 there was an increase in traffic (compared to 2011) of all vehicles by 13.1%, passenger vehicles by 19.3%, medium heavy vehicles by 12%, as shown in Figure 3.

Examples of traffic volume measurement results, after aggregation for 24-hour intervals, before and after the road renovation, are presented in Figure 4. In 2011, there is some increase in traffic volume in the middle of the year (the so-called seasonality known in the literature [25]). However, after the road renovation, such seasonal growth was not recorded in 2016. The Shapiro-Wilk statistical tests carried out, which are based on the positional statistics of the sample, allow to reject the H_0 hypothesis about compliance of the measurement data distribution with the normal distribution at the significance level of 0.05. In the cases raising doubts as to the normality of the tested distribution, the Jarque-Bera test was additionally carried out, which belongs to the group of tests based on the moments from the sample. For this purpose, measures of the shape of the distribution were calculated, such as skewness and kurtosis, whose values should be close to zero and three. The Jarque-Bera test results also allow to reject the H_0 hypothesis.

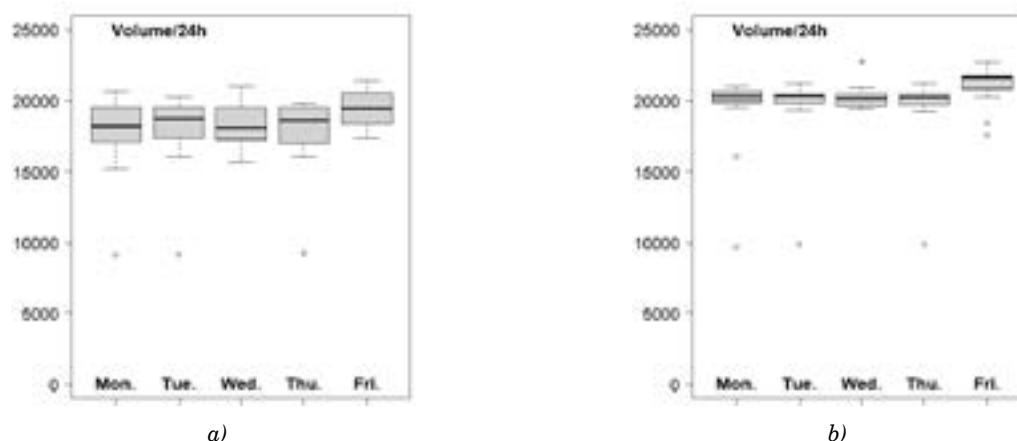


Figure 5 Box plots for traffic volume determined for weekdays a) in 2011, b) in 2016

The statistical calculations carried out showed that in 2011 on lanes L_{12} skewness was -0.99 and kurtosis 3.31, while on lanes L_{34} skewness was -0.94 and kurtosis 3.52, which confirms that distribution of the traffic values deviates from normal. The quantile charts, shown in Figure 4b confirm these conclusions. A deviation from the normal distribution may cause the calculated values of certain parameters, e.g. standard deviation, measurement uncertainty to be incorrect [26-27].

For this reason, the authors decided to split the results for the entire year into seven groups representing the measurement of the weekdays and weekends, as shown in Figure 5. The plots show that in 2011, from Monday to Thursday, the traffic volumes change slightly up and down, increase on Friday and decrease on weekend. The nature of these changes is consistent with the literature of the subject [20, 25]. In 2016, however, changes in traffic on weekdays and weekend, as well as the ranges between the C75 and C25 percentiles, were much smaller than in 2011. Statistical tests carried out showed that on some days of the week, e.g. Fridays in 2012, Saturdays and Sundays in 2013, Mondays in 2014, there were no grounds for rejection H_0 hypotheses. Values in 2011 of the daily traffic volume parameters for each day of the week are presented in Table 1. The

median traffic volume on lanes L_{12} in each day except Sundays is higher than on lanes L_{34} . These differences are less than 10% (taking into account the measurement uncertainty) and their value for each day is different, e.g. on Thursdays 3.6%, Fridays 9.8%. Values of the traffic volume measurement uncertainty was ranging from 133 to 312 veh/24 h on lanes L_{12} and 141 to 239 veh/24 h on lanes L_{34} . The coefficient of variation V_q was ranging from 4.4% to 8.5% on lanes L_{12} and from 4.9% to 7.9% on lanes L_{34} . Differences in values of the coefficient V_q in both directions and on individual days are about 1%, except for Saturdays when they are about 3.4%.

On Sundays, the median traffic volume of vehicles is lower than on Saturdays by approximately: 2000 veh. - on lanes L_{12} , 800 veh. - on lanes L_{34} .

In 2016, values of the median traffic volume on lanes L_{12} and L_{34} are similar, as shown in Table 2. There are only significant differences on Fridays and weekend. The coefficient V_q and the measurement uncertainty for both lanes are similar. Values of the traffic volume measurement uncertainty on lanes L_{34} was ranging from 91 to 422 veh/24 h. After the road renovation in 2016, the coefficient V_q was ranging from 1.0 to 4.4% and was much lower than in 2011.

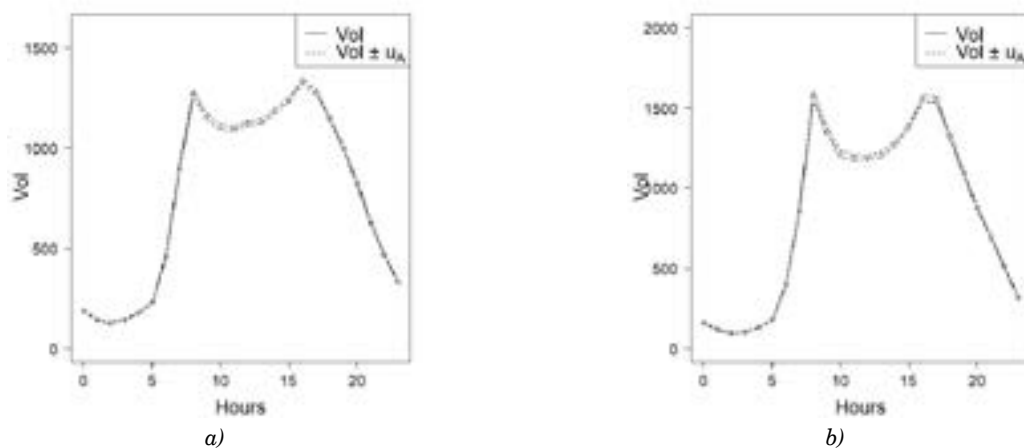
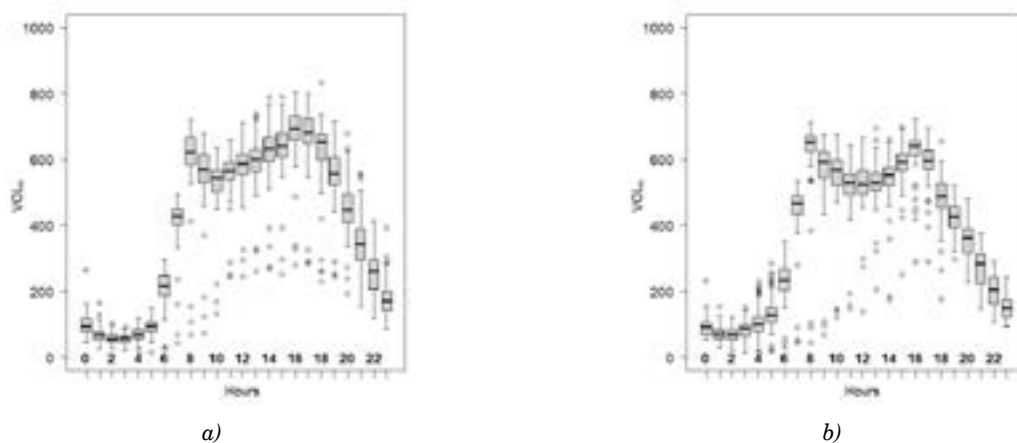
Knowledge of the statistical measures' values of the

Table 1 Values of statistical measures of traffic volumes on lanes- L_{12} and L_{34} determined for each average annual day of the 2011

Day	2011 lanes- L_{12}			2011 lanes- L_{34}		
	Median veh/24 h	V_q %	u_a veh/24 h	Median veh/24 h	V_q %	u_a veh/24 h
Weekday						
Monday	9188	7.1	293	9037	6.0	237
Tuesday	9612	5.9	312	9074	6.4	215
Wednesday	9419	5.0	170	8702	6.0	148
Thursday	9711	6.7	240	8911	5.6	239
Friday	10379	4.4	133	9199	5.7	141
Weekend						
Saturday	8019	8.3	183	7144	4.9	165
Sunday	6041	8.5	160	6302	7.9	202

Table 2 Values of statistical measures of traffic volumes on lanes L_{12} and L_{34} determined for each average annual day of the 2016

Day	2016 lanes- L_{12}			2016 lanes- L_{34}		
	Median veh/24 h	Vq %	u_a veh/24 h	Median veh/24 h	Vq %	u_a veh/24 h
Weekday						
Monday	9966	2.5	415	10333	1.5	370
Tuesday	10146	1.3	419	10155	1.0	309
Wednesday	10100	2.0	142	10040	2.2	91
Thursday	10132	1.2	356	10063	2.1	422
Friday	11055	2.4	164	10412	2.0	169
Weekend						
Saturday	8221	3.8	229	7557	3.8	240
Sunday	6660	3.6	151	7253	4.4	223

**Figure 6** Relation between the median (solid line) and median with standard uncertainty (dashed line) of annual hourly traffic volume and time for weekdays a) in 2011, b) in 2016**Figure 7** Box plots of relation between the annual hourly traffic volume and time for 24 h period in 2011 for weekdays: a) on lanes L_{12} , b) on lanes L_{34}

traffic volume, determined for each average annual day, is essential, e.g. for road design and public transport organization [28]. An additional complement to it is the knowledge of annual hourly traffic volume and time for 24 h period. Figure 6 shows the experimental relationships between the median of annual hourly traffic volume and time for weekdays before and after the road renovation.

The charts in Figure 6 show that the traffic peak hours are at 8 AM and 4 PM. In the morning hours from 5 AM to 10 AM, the increase in traffic volume and the decrease after 8 AM in 2016 is greater than in 2011. The decline in traffic volume after the afternoon peak is similar every year. The uncertainty of measurements is variable and the maximum values occurs during the

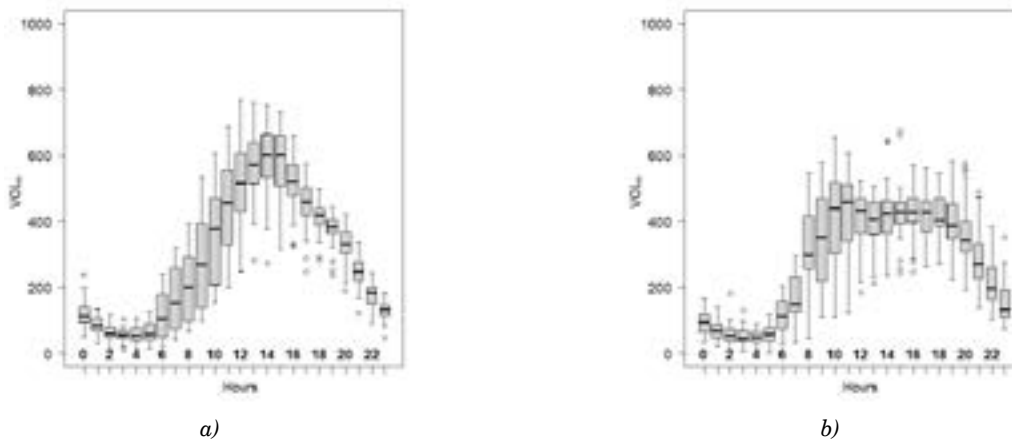


Figure 8 Box plots of relation between the annual hourly traffic volume and time in 2011 for weekends: a) on lanes L_{12} , b) on lanes L_{34}

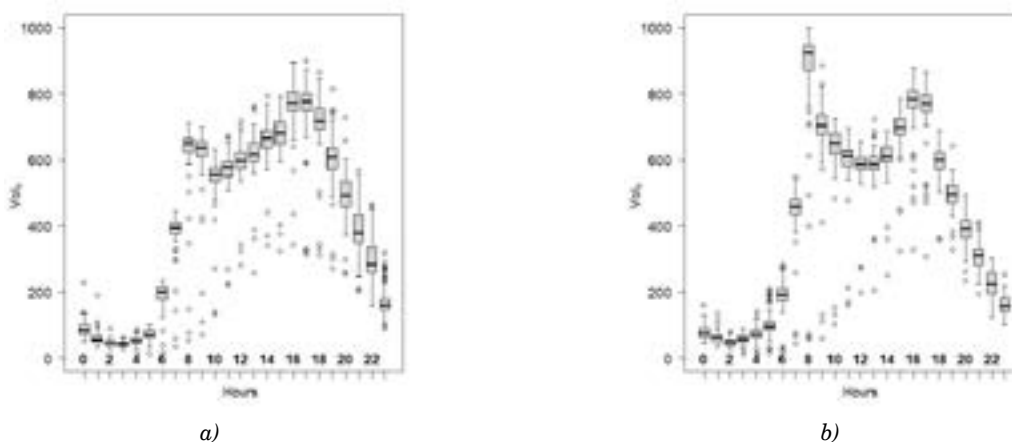


Figure 9 Box plots of relation between the annual hourly traffic volume and time in 2016 for weekdays: a) on lanes L_{12} , b) on lanes L_{34}

traffic peak hours. The box plots of relation between the annual hourly traffic volume and time for weekdays in 2011 are presented in Figure 7.

There are two local extreme points of traffic volumes on each lanes occurring at 8 AM and 4 PM. When comparing Figure 7a and Figure 7b, it can be noticed that during the morning traffic peak hours, until about 8 AM, the volume of vehicles on lanes L_{34} is higher than on lanes L_{12} . From 10 AM to 4 PM the volume of vehicles on lanes L_{12} (leaving Kielce) increases to a maximum value of approximately 660 veh/h. It seems that the assumption of symmetry between the time distribution of traffic volume entering and leaving the city is not always true. The relation between the annual hourly traffic volume and time in 2011 but only for weekends is presented in Figure 8.

On weekends, the traffic volume on lanes L_{12} increases from 5 AM to 2 PM (about 600 vehicles), there is only one peak of traffic at 14.00 but it lasts 2 hours, then the volume gradually decreases until 11 PM. On the other hand, on the lanes L_{34} the traffic volume increases from 5 AM to 1 AM (approx. 450 vehicles) and then decreases to approx. 420 vehicles at 2 PM and from 4 PM it decreases to 11 PM. It should be noted that the

graphs in Figures 8a and 8b differ not only in values but also in shape. In 2016, the traffic volume increased, which contributed to a change for weekdays in the shape and value of traffic volume in the charts shown in Figure 9. The traffic rush hours have not changed. There is also some similarity between the graphs in Figures 7 and 9. The qualitative changes in traffic volumes before the morning- and after the afternoon rush hour on individual lanes are similar. However, between the traffic rush hours, these changes vary, especially on lanes L_{34} .

On weekends in 2016, changes in the traffic volume on individual lanes are similar to 2011. Analysis of the box plots presented relation between the annual hourly traffic volume and time shows that some of the recorded data can be regarded as atypical. The authors of this paper did not remove the atypical data from the samples analysed. Figure 9 confirms the previously observed phenomenon of traffic asymmetry between vehicles entering and leaving the city (Figures 2, 7 and 8) [29]. The amount of outliers in Figures 7 (in 2011) is almost the same as in Figures 9 (in 2016). Both before and after the road renovation shape differences can be seen between the morning and afternoon peaks for each

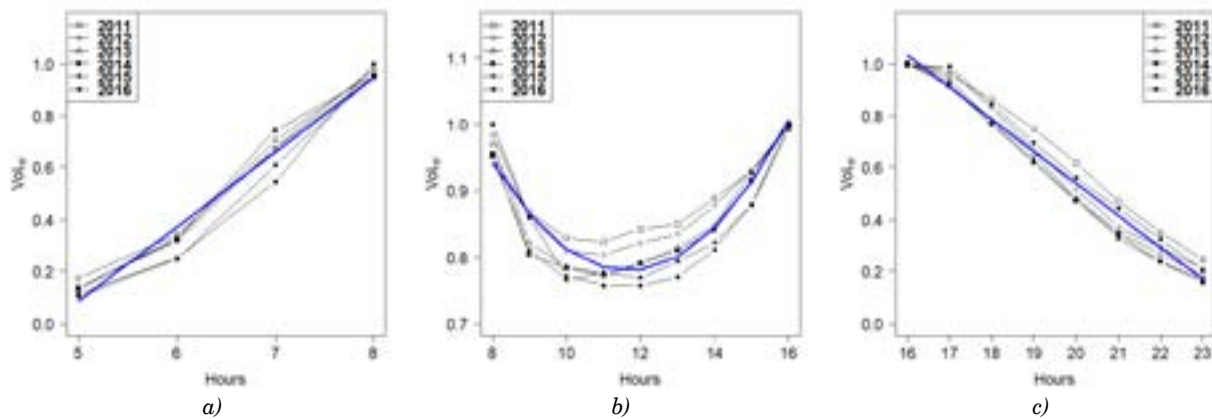


Figure 10 Relative annual hourly traffic volume and time for weekdays in 2011-2016, with the regression models marked (line marked in blue) a) sub-interval from 5 AM to 8 AM, b) sub-interval from 8 AM to 4 PM, c) sub-interval from 4 PM to 11 PM.

lanes and between the lanes (Figures 7 and 9). The morning peak is characterized by a rapid rise and fall and the afternoon peak is characterized by a slow rise and fall in traffic. On weekends, the graphs of changes in traffic volume versus time in each traffic direction differ in terms of both the values and shape. On the other hand, one can notice some similarity of shapes between the graphs shown in Figures 7a and 9a and in Figures 7b and 9b. The uncertainty of measurements in sub-interval from 8 AM up to 4 PM is in the range from 12 to 20 veh/h depending from time.

5 Discussion

Figure 6 shows relation between the relative annual hourly traffic volume versus time at weekdays in 2011 and in 2016. Such charts were made for each year from 2011 to 2016. The traffic volume diagrams in Figure 6 can be divided into four phases [18]. From 00 AM to 5 AM - the traffic volume is at least five times lower than in rush hours and does not create any serious logistical problems. From 5 AM to the morning peak at 8 AM a very high rate of the traffic volume increase can be described by a linear relationship. Between the morning and the afternoon peak at 4 PM it can be described by the second order polynomial. From the afternoon peak to 11 PM it can be described by a linear relationship. In order to compare these equations for different years, the data was normalized according to Equation (1) and for the further analysis this parameter, the so-called relative traffic volume, was used. These equations were then derived for each year. Values of the coefficients appearing in these equations depend on the year for which an analysis was performed and presented in [30]. The advantage of this model is that the coefficient of fitting the model curves to the experimental data is approximately $R^2 = 0.99$. The weakness, however, is the necessity to use different values of the coefficients in each year.

In this work, the authors decided to describe the relative traffic volume for particular time ranges by the

regression models. When determining the regression coefficients for each hourly range, data from 2011 to 2016 was used. The models presented in Figure 10 (blue line) describe the data obtained over several years.

The presented graphs for individual sub-intervals are described with the following equations:

- from 5 AM to 8 AM (model 1):

$$VOL_{rel} = 0.29x - 1.35, \quad (2)$$

- from 8 AM to 4 PM (model 2):

$$VOL_{rel} = 0.012x^2 - 0.28x + 2.42, \quad (3)$$

- from 4 PM to 11 PM (model 3):

$$VOL_{rel} = -0.12x + 3.01. \quad (4)$$

It is worth noting that the model curve describes changes in value of the VOL_{rel} in the analyzed period from 2011 to 2016. In all the sub-intervals, the satisfactory compliance of the model with the measurement data was obtained, which is confirmed by the high value of the R^2 coefficients, amounting to 0.97, 0.87 and 0.97, respectively. The calculations were performed using the R packet and the obtained coefficients can be considered statistically significant, which was indicated by the small value of the significance level (p-value). The advantage of such a modified model is the possibility of using it as a reference base for analysis of changes in the shape and value of experimental traffic volume graphs as a function of time for each day of the week. It is also less computationally intensive compared to clustering algorithms. The weakness, however, is the worse adjustment of the model to the experimental data. The discrepancies between the curves determined experimentally and according to the regression models were assessed based on the RMSE parameter value [28]:

$$RMSE = \sqrt{\frac{1}{N} \sum_{i=1}^N [VOL_{rel}(h) - VOL_{rel_model}(h)]^2}, \quad (5)$$

where:

N - number of hours in analysed period,

$VOL_{rel}(h)$ - experimental relative traffic volume for hour h ,

VOL_{rel_model} - relative traffic volume for hour h according to the regression model.

The ability to compare the experimental and model curves in the graphs makes it easier to see the differences between the relative number of vehicles at the same time in different years. Figure 11 shows the graphs of relative annual hourly traffic volume versus time at weekdays, with marked measurement uncertainty and curves according to the proposed regression model.

Comparing Figures 11a and 11b and the RMSE values, it is possible to see both the similarity, as well

as differences in the shapes of the graphs and different values of the relative median traffic volume at the same times of the day before and after the road renovation. For example, the traffic flow from 7 AM to 8 AM in 2016 is about 40% higher than in 2011. These observations are confirmed by different RMSE values for each sub-interval. In the range from 5 AM to 8 AM: in 2011 RMSE = 0.05 and in 2016 RMSE = 0.09. In the range from 8 AM to 4 PM in each of the examined years, RMSE = 0.03. In the range from 4 PM to 11 PM in 2011 RMSE = 0.07 and in 2016 RMSE = 0.04. The RMSE parameter indicates

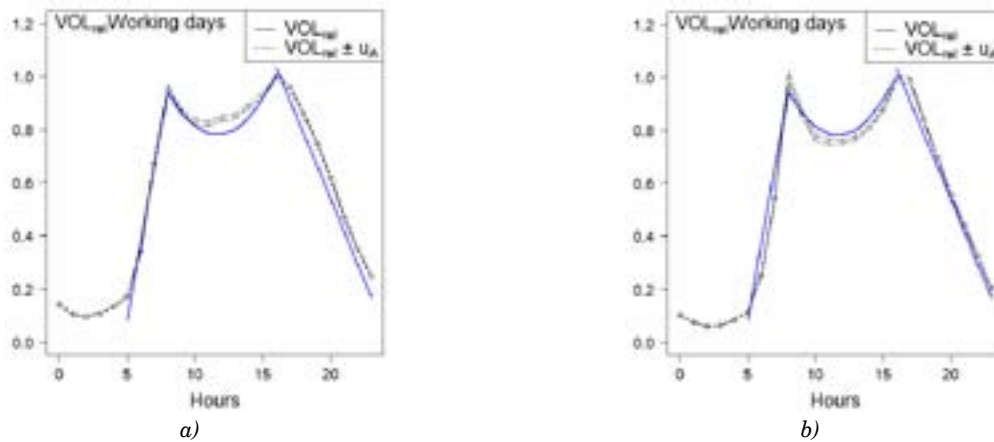


Figure 11 Relative annual hourly traffic volume versus time at weekdays: for median -solid line, for median with uncertainty $u_{a(rel)}$ - dashed line, for regression models - blue lines a) in 2011, b) in 2016

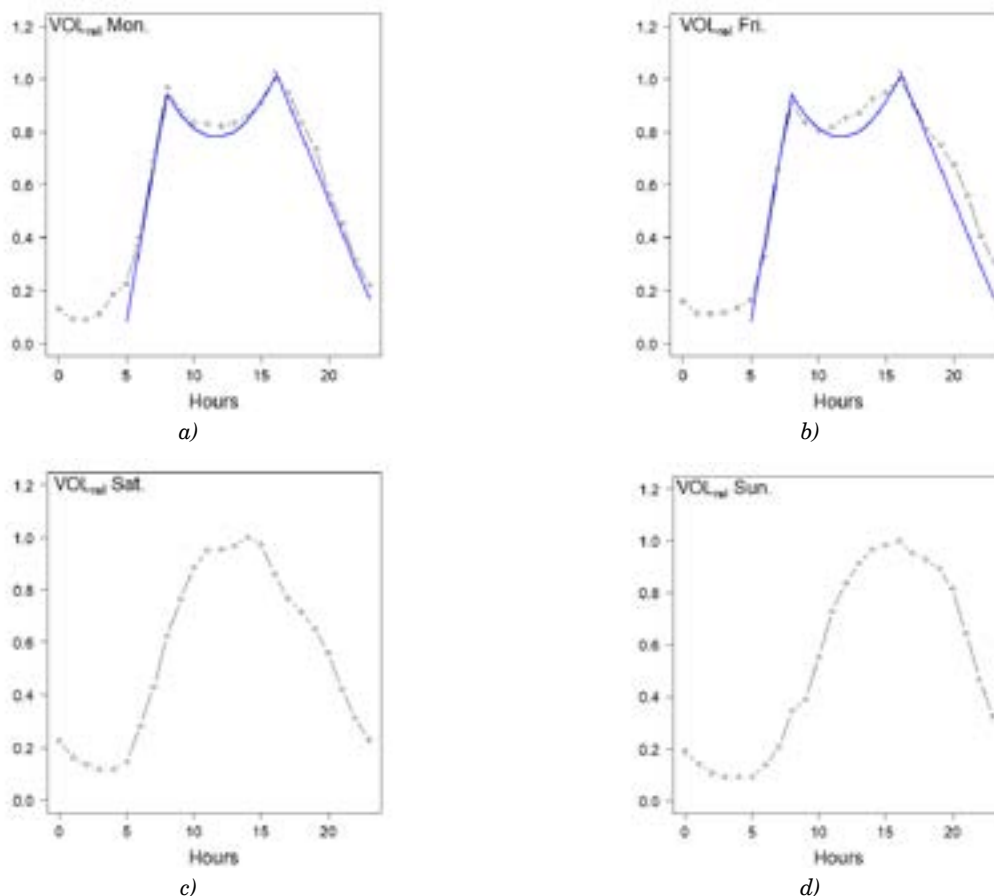


Figure 12 Relation between the relative median of annual hourly traffic volume and time in 2011 a) on Monday, b) on Friday, c) on Saturday, d) on Sunday

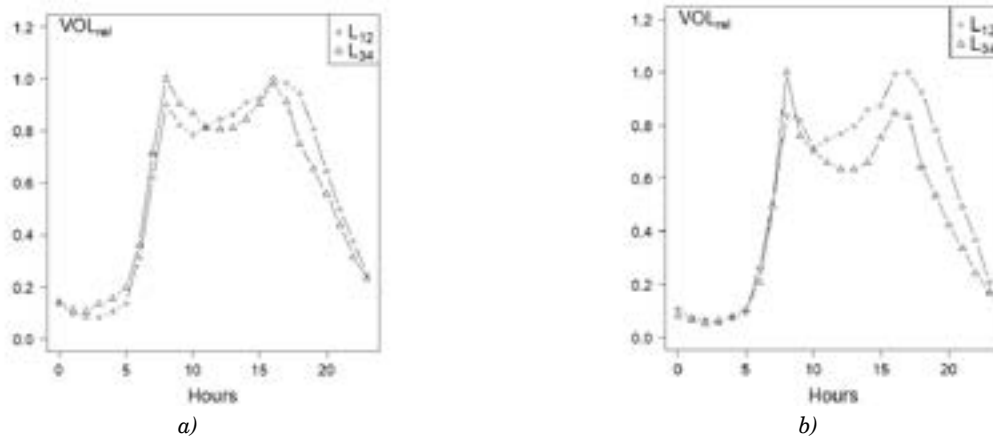


Figure 13 Relation between the relative annual hourly traffic volume and time for 24 h period at weekdays on entry lanes (L_{12}) and exit lanes (L_{34}) from the city a) in 2011, b) in 2016

the discrepancies between the experimental data and those determined based on the model. The weakness of this parameter is that it does not explain their causes. It facilitates the qualitative analysis but only slightly supports the quantitative one.

The use of intelligent transport systems, e.g. to optimize route planning and travel time, fuel consumption and exhaust pollutant, requires more detailed data than the annual average hourly values, even split into weekdays and weekends. It is required to know the values of traffic parameters for each day of the week and with time resolution e.g. every 5 min, or 15 min, or 60 min, [31]. This relatively new issue was analyzed in [5, 22, 29], but mainly for the entire road, i.e. without taking into account direction of the traffic. In this study, the analysis is carried out for both traffic directions. For this reason, in the further part of the work, analyses of the relative annual traffic volume registered every hour on individual days of the week were carried out, also taking into account both traffic directions, i.e. lanes L_{12} and L_{34} . For this purpose, the proposed regression model was also used.

Figure 12 shows the charts of relation between the relative median of annual hourly traffic volume and time for selected days of the week in 2011. Mondays and Fridays are characterized by the high value of traffic volume and large changes in the V_q coefficient. One can notice large differences in the time distribution of traffic on Monday and Friday in each of the sub-intervals. On Monday in the morning there are large deviations from the model values. On Friday, however, such deviations occur from 10 AM to 4 PM and then after 6 PM. In Figure 12b one can see an increase in the traffic volume after 6 PM, which may be due to the beginning of the weekend. On the weekend days, the traffic volume is much lower and there is only afternoon (at 2 PM or 4 PM) traffic volume peak. The shapes of the charts for Saturdays and Sundays differ significantly.

Figure 13 shows relation between the relative annual hourly traffic volume and time on entry lanes (L_{12}) and exit lanes (L_{34}) from the city in 2011 and in 2016.

The traffic volume analysis carried out shows differences in the traffic volume of vehicles entering and leaving the city. Asymmetry of traffic volume in 2016 is greater than in 2011. Figures 13a and 13b show a similarity of the curves until 8 AM. However, in 2016, after the morning peak - from 10 AM, there are significant differences in traffic volume between the directions of traffic.

Figure 14 shows a comparison of the model curves to the experimental ones on selected days of the week in 2011, taking into account the direction of traffic. These comparisons show that on each day of the week the traffic volume changes differently on lanes L_{12} than on lanes L_{34} . One can also see that on each of the lanes changes in the traffic volume are different every day. Particularly large differences are visible for Sundays - both the shape of the charts and the time of occurrence of the maximum values are different for each lane. The uncertainty value depends on the time of the measurement. In the morning rush hours, the uncertainty of VOL_{rel} on the lanes L_{12} is about 4% and is 1% lower than on the lanes L_{34} . On the other hand, in the afternoon rush hours, the uncertainty on the lanes L_{34} is about 3% and is 1% lower than on the lanes L_{12} . In the remaining hours of the day, the uncertainty is much smaller. Comparing the uncertainty calculated for weekdays (shown in Figure 11) to the uncertainty for Mondays on lanes L_{12} in 2011 (Figure 14a), differences in values can be seen. This is due to the fact that for Mondays there were statistically 5 times less data, so the uncertainty is increasing. The discrepancies between the curves, determined experimentally and according to the models, were assessed based on the RMSE parameter value. Table 3 summarizes values of this parameter for weekdays and each direction of traffic. Comparing the RMSE values in of the weekdays on the lanes L_{12} for individual models, it can be seen that they increase slightly from Monday and on Friday reach the highest values RMSE = 0.16. The greatest discrepancies in RMSE values occur for model 3, i.e. from 4 PM to 11 PM. In the case of the lanes L_{34} , almost all the RMSE values are between 0.03 and 0.15 and

change irregularly. Analyzing the RMSE in 2011, e.g. for Mondays and Tuesdays in the corresponding time periods from 8 AM to 11 PM, it can be seen that they have similar values. This does not mean, however, that the shapes of the VOL_{rel} diagrams are similar in the same time intervals, as shown in Figure 14. The RMSE values in 2016 are higher than in 2011, especially for the lanes L_{34} . This justifies validating traffic volume models every few years.

6 Conclusions

The deteriorating condition of the road and the nuisance associated with its renovation, contributed to a decrease in the traffic volume in the years 2011 to 2016 by 9.7%. It was only in 2016 that traffic volume increased (compared to 2011) of all the vehicles by 13%. Research on the share of vehicle groups in the traffic structure showed that passenger and medium

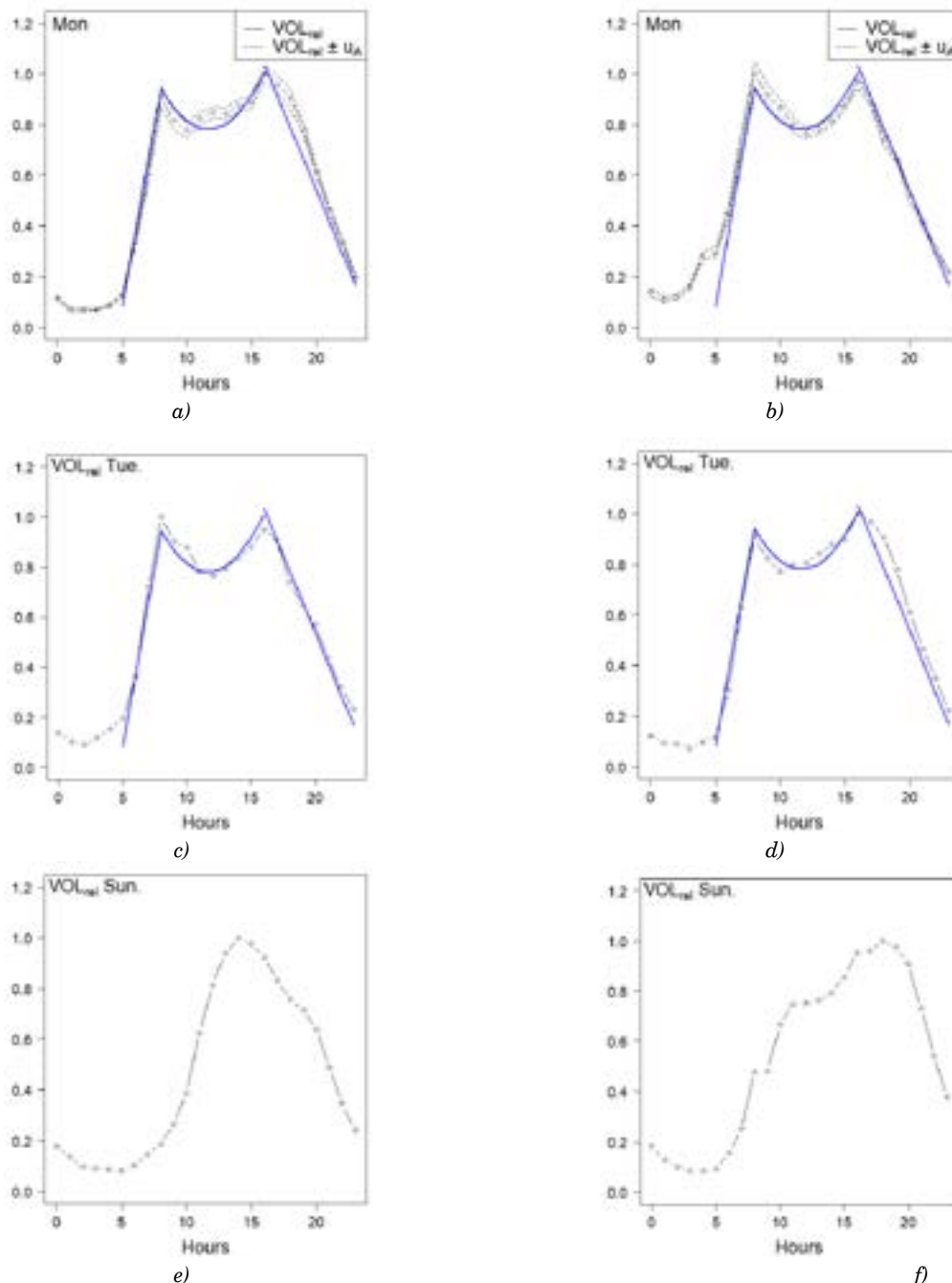


Figure 14 Relation between the relative median of annual hourly traffic volume and time in 2011 (for median - solid line, for median with uncertainty u_{rel} - dashed line, model - blue lines)
 a) on Monday on lanes L_{12} , b) on Monday on lanes L_{34} , c) on Tuesday on lanes L_{12} , d) on Tuesday on lanes L_{34} ,
 e) on Sunday on lanes L_{12} , f) on Sunday on lanes L_{34}

Table 3 Analysis of the RMSE values between the traffic volume models and experimental data for the relative median of annual hourly traffic volume and time in 2011 and 2016 on weekdays taking into account the direction of traffic

	RMSE for lanes L_{12}			RMSE for lanes L_{34}		
	Model 1	Model 2	Model 3	Model 1	Model 2	Model 3
2011						
Monday	0.04	0.04	0.07	0.12	0.04	0.04
Tuesday	0.04	0.03	0.08	0.07	0.04	0.05
Wednesday	0.04	0.04	0.09	0.06	0.03	0.03
Thursday	0.06	0.04	0.11	0.07	0.03	0.03
Friday	0.07	0.07	0.16	0.06	0.05	0.04
2016						
Monday	0.09	0.05	0.07	0.10	0.14	0.12
Tuesday	0.11	0.07	0.07	0.12	0.14	0.11
Wednesday	0.11	0.06	0.09	0.12	0.15	0.12
Thursday	0.11	0.06	0.09	0.13	0.15	0.12
Friday	0.14	0.08	0.16	0.13	0.12	0.09

heavy vehicles dominate and their share is about 90%. The statistical tests carried out allow to reject the H_0 hypothesis about the compatibility of the measurement data distribution with the normal distribution. The lack of normal distribution, the large amount of outliers results in the fact that the uncertainty of ADT in 2016 (after the road reconstruction) on lanes L_{34} ranges from 91 to 422 veh/24 h. The coefficient V_q in 2016 ranges from about 1% to 4% and is much lower than in 2011. The C95 ADT percentile value changes by 10% and depends on the group of vehicles analyzed and the day of the week. The median average speed during the period considered from 2011 to 2016 slightly changed. However, the speed charts on lanes L_{12} and L_{34} and for different years have different courses.

Research on the relationship between the annual hourly traffic volume and time in 2011-2016 showed that there is a lack of symmetry between the time distribution of the traffic flow of vehicles entering and leaving the city. The proposed regression model was

used as a reference base for the analysis of changes in the shape and value of experimental traffic volume graphs for each day of the week. From comparison of the model curves to experimental ones it results that on each day of the week the traffic volume changes differently on lanes L_{12} than on lanes L_{34} . On each of the lanes the changes in traffic volume are different every day. Particularly large differences are visible for Sundays - both the shape of the charts and the time of occurrence of the maximum values are different for each lane. The discrepancies between the curves determined experimentally and according to the regression models were assessed based on the RMSE parameter value. These analyses showed that the similar RMSE values do not mean, however, that the shapes of the VOL_{rel} plots are similar at the same time intervals. The RMSE values in 2016 are higher than in 2011, especially for the lanes L_{34} , which justifies the validation of the traffic volume models every few years.

References

- [1] DURCANSKA, D., DECKY, M., JANDACKA, D., REMISOVA, E. *Road transport and the environment*. Zilina: University of Zilina, 2019. ISBN 978-80-554-1590-1.
- [2] FU, M., KELLY, A., CLINCH, P. Estimating annual average daily traffic and transport emissions for a national road network: a bottom-up methodology for both nationally-aggregated and spatially-disaggregated results. *Journal of Transport Geography* [online]. 2017, **58**, p. 186-195. ISSN 0966-6923. Available from: <https://doi.org/10.1016/j.jtrangeo.2016.12.002>
- [3] SARKAN, B., GNAP, J., KIKTOVA, M. The importance of hybrid vehicles in urban traffic in terms of environmental impact. *Archiwum Motoryzacji* [online]. 2019, **85**(3), p. 115-122. eISSN 2084-476X. Available from: <https://doi.org/10.14669/AM.VOL85.ART8>
- [4] VAN KAMP, I., SIMON, S., NOTLEY, H., BALIATSAS, C., VAN KEMPEN, E. Evidence relating to environmental noise exposure and annoyance, sleep disturbance, cardio-vascular and metabolic health outcomes in the context of IGCB (N): a scoping review of new evidence. *International Journal of Environmental Research and Public Health* [online]. 2020, **17**, 3016. ISSN 1661-7827, eISSN 1660-4601. Available from: <https://doi.org/10.3390/ijerph17093016>

- [5] HARANTOVA, V., HAJNIK, A., KALASOVA, A. Comparison of the flow rate and speed of vehicles on a representative road section before and after the implementation of measures in connection with COVID-19. *Sustainability* [online]. 2020, **12**(17), 7216. eISSN 2071-1050. Available from: <https://doi.org/10.3390/su12177216>
- [6] RETALLACK, A. E., OSTENDORF, B. Current understanding of the effects of congestion on traffic accidents. *International Journal of Environmental Research and Public Health* [online]. 2019, **16**(18), p. 3400. ISSN 1661-7827, eISSN 1660-4601. Available from: <https://doi.org/10.3390/ijerph16183400>
- [7] JANDACKA, D., DECKY, M., DURCANSKA, D. Traffic related pollutants and noise emissions in the vicinity of different types of urban crossroads. *IOP Conference Series: Materials Science and Engineering* [online]. 2019, **661**, 012152. ISSN 1757-8981, eISSN 1757-899X. Available from: <https://doi.org/10.1088/1757-899X/661/1/012152>
- [8] PHILLIPS, G., REESON, D. *Representing the distribution of hourly flows through the year*. Supplementary report 804. Crowthorne: TRRL Environment Department of Transport, 1984. ISSN 0305-1315.
- [9] KURZHANSKIY, A. Estimation of hourly traffic flow profiles using speed data and annual average daily traffic data. US Patent Application Publication US 2015/0206428A1. USA: ITERIS, inc., California, 2015.
- [10] Geoportal Kielce [online]. Available from: <https://gis.kielce.eu/>
- [11] BENNETT, CH. R., DE SOLMINIHAC, H., CHAMORRO, A. Data collection technologies for road management [online]. Technical report. Washington: The World Bank, 2006. Available from: <https://openknowledge.worldbank.org/handle/10986/11776>
- [12] GAJDA, J. *Measurements of road traffic parameters* (in Polish). Warszawa: PWN, 2015. ISBN 978-83-01-18355.
- [13] BERNAS, M., PLACZEK, B., POROWIK, P., PAMULA, T. Segmentation of vehicle detector data for improved k-nearest neighbours-based traffic flow prediction. *IET Intelligent Transport Systems* [online]. 2015, **9**(3), p. 264-274. eISSN 1751-9578. Available from: <https://doi.org/10.1049/iet-its.2013.0164>
- [14] RAKHA, H., VAN AERDE, M. Statistical analysis of day-to-day variations in real-time traffic flow data. *Transportation Research Record*. 1995, **1510**, p. 26-34. ISSN 0361-1981.
- [15] KAYANI, W. Shape based classification and functional forecast of traffic flow profiles [online]. Doctoral dissertations 2409. Missouri: Missouri University of Science and Technology, 2015. Available from: https://scholarsmine.mst.edu/doctoral_dissertations/2409
- [16] CALAFATE, C., at al. Traffic management as a service: the traffic flow pattern classification problem. *Mathematical Problems in Engineering* [online]. 2015, **2015**, 716598. ISSN 1024-123X, eISSN 1563-5147. Available from: <https://doi.org/10.1155/2015/716598>
- [17] NOUSSAN, M., CARIONI, G., SANVITO F., COLOMBO, E. Urban mobility demand profiles: time series for cars and bike-sharing use as a resource for transport and energy modeling. *Data* [online]. 2019, **4**, 108. eISSN 2306-5729. Available from: <https://doi.org/10.3390/data4030108>
- [18] STATHOPOULOS, A., KARLAFTIS, M. Temporal and spatial variations of real - time traffic data in urban areas. *Transportation Research Record* [online]. 2001, **1768**, p. 135-140. ISSN 0361-1981. Available from: <https://doi.org/10.3141/1768-16>
- [19] CHROBOK, R., KAUMANN, O., WAHLE, J., SCHRECKENBERG, M. Different methods of traffic forecast based on real data. *European Journal of Operational Research* [online]. 2004, **155**(3), p. 558-568. ISSN 0377-2217. Available from: <https://doi.org/10.1016/j.ejor.2003.08.005>
- [20] WEIJERMARS, W. Analysis of urban traffic patterns using clustering. Ph.D. thesis. Enschede: University of Twente, 2007.
- [21] GUARDIOLA, I., LEON, T. MALLOR, F. A functional approach to monitor and recognize patterns of daily traffic profiles. *Transportation Research Part B: Methodological* [online]. 2014, **65**, p. 119-136. ISSN 0191-2615. Available from: <https://doi.org/10.1016/j.trb.2014.04.006>
- [22] CRAWFORD, F., WATLING, D., CONNORS, R. A statistical method for estimating predictable differences between daily traffic flow profile. *Transportation Research Part B: Methodological* [online]. 2017, **95**, p. 196-213. ISSN 0191-2615. Available from: <https://doi.org/10.1016/j.trb.2016.11.004>
- [23] CHANG, D., SAITO, M., SCHULTZ, G. G., EGGETT, D. L. Use of Hi-resolution data for evaluating accuracy of traffic volume counts collected by microwave sensors. *Journal of Traffic and Transportation Engineering (English Edition)* [online]. 2017, **4**(5), p. 423-435. ISSN 2095-7564. Available from: <https://doi.org/10.1016/j.jtte.2017.06.002>
- [24] BAKOWSKI, A., RADZISZEWSKI, L., SKROBACKI, Z., SWIETLIK, P., DEKYS, V. Analysis of urban traffic for various sets of vehicles. *IOP Conference Series: Materials Science and Engineering* [online]. 2019, **471**(6), 062024. ISSN 1757-8981, eISSN 1757-899X. Available from: <https://doi.org/10.1088/1757-899X/471/6/062024>
- [25] SPLAWINSKA, M. Models for determining annual average daily traffic on the national roads. *Archives of Civil Engineering*. 2015, **61**(2), p. 141-160. ISSN 1230-2945.
- [26] BAKOWSKI, A., DEKYS, V., RADZISZEWSKI, L., SKROBACKI, Z., SWIETLIK, P. Estimation of uncertainty and variability of urban traffic volume measurements in Kielce. In: 2018 XI International Science-Technical Conference Automotive Safety: proceedings. IEEE. 2018. ISBN 9781538645796, p. 1-8.

- [27] ROSSI, R., GASTALDI, M., GECHELE, G., KIKUCHI, S. Estimation of annual average daily truck traffic volume. Uncertainty treatment and data collection requirements. *Procedia-Social and Behavioral Sciences* [online]. 2012, **54**, p. 845-856. ISSN 1877-0428. Available from: <https://doi.org/10.1016/j.sbspro.2012.09.800>
- [28] SFYRIDIS, A., AGNOLUCCI, P. Annual average daily traffic estimation in England and Wales: an application of clustering and regression modelling. *Journal of Transport Geography* [online]. 2020, **83**, 102658. ISSN 0966-6923. Available from: <https://doi.org/10.1016/j.jtrangeo.2020.102658>
- [29] KILPI, J., NORROS, I., KUUSELA, P., MALIN, F., RATY, T. Robust methods and conditional expectations for vehicular traffic count analysis. *European Transport Research Review*. 2020, **12**, 10. ISSN 1866-8887. Available from: <https://doi.org/10.1186/s12544-020-0399-8>
- [30] BAKOWSKI, A., RADZISZEWSKI, L. Measurements of urban traffic parameters before and after road reconstruction. *Open Engineering*. 2021, **11**(1), p. 365-376. ISSN 2391-5439. Available from: <https://doi.org/10.1515/eng-2021-0035>
- [31] WANG, S., YU, D., MA, X., XING, X. Analyzing urban traffic demand distribution and the correlation between traffic flow and the built environment based on detector data and POIs. *European Transport Research Review*. 2018, **10**, 50. ISSN 1866-8887. Available from: <https://doi.org/10.1186/s12544-018-0325-5>

MIXED FUZZY-LOGIC AND GAME-THEORETICAL APPROACH TO JUSTIFY VEHICLE MODELS FOR SERVICING THE PUBLIC BUS LINE

Vitalii Naumov^{1,*}, Laura Bekmagambetova², Zukhra Bitileuova², Zhumazhan Zhanbirov³, Igor Taran⁴

¹Faculty of Civil Engineering, Cracow University of Technology, Cracow, Poland

²Faculty of Logistics and Transport Management, Kazakh Academy of Transport and Communications, Almaty, Kazakhstan

³Faculty of Fundamental Sciences, Central-Asian University, Almaty, Kazakhstan

⁴Department of Transport Management, Dnipro University of Technology, Dnipro, Ukraine

*E-mail of corresponding author: vnaumov@pk.edu.pl

Resume

One of the main problems to be solved by the transport operators is the substantiation of the vehicle models servicing the transport lines. A game-theoretical approach is proposed in this paper to justify the bus model choice based on the passengers' preferences and the structure of the passenger flows. To estimate the customers' preferences, the membership functions for fuzzy sets of the optimal vehicle models were defined. The simulation experiment aiming to estimate the city fleet structure in terms of the vehicles' capacity was conducted for the Talas city (Kazakhstan) based on the proposed approach with use of the corresponding software implementation of the developed mathematical models. As a result of the experimental studies, the impact of the passengers' flow structure and the number of carriers on the rational structure of the city bus fleet was studied in the paper.

Article info

Received 17 April 2021

Accepted 9 July 2021

Online 4 November 2021

Keywords:

public transport,
game theory,
fuzzy logic,
fleet optimization

Available online: <https://doi.org/10.26552/com.C.2022.1.A26-A34>

ISSN 1335-4205 (print version)

ISSN 2585-7878 (online version)

1 Introduction

Contemporary markets of the public transport services in the cities are highly stochastic environments where several servicing transport companies compete for the preferences of clients - the passengers who use the public transport lines.

The carrier's goal within the public transport system is the most complete coverage of the existing and potential market, for which it is necessary to attract passengers moving from and to the points that the transport line covers. If the fulfillment of the passenger's need for travel is possible in one way only - by using a single bus line available, then the carrier gets the maximum possible share of the market sector. However, if the need for movement can be realized in more than one way (the trip can be implemented by the means of more than one public transport line), the passenger has a choice. In that case, there will be a conflict situation between carriers who can potentially serve the same trip. Depending on the strategy chosen by the carrier, the passenger will give preference to the corresponding bus line.

This study aims to determine the optimal quality composition of the city bus fleet, considering the interests of passengers and carriers. The main objective of this

research is to determine the optimal carrier strategy (in terms of the choice of bus models) that guarantees the biggest possible market share.

2 Literature review

Buses are the most popular elements of public transport. Nowadays improvement of the passenger market takes place in main directions: promoting sustainable mobility solutions and usage of e-transport; timetabling and vehicle scheduling; solving vehicle routine problems; fleet size and fleet mix optimization.

The problem of choosing the optimal bus models for servicing the existing route network of a city, considering the specific preferences of passengers and existence of competing routes, is particularly relevant. Many publications have arisen recently that propose different approaches to solve that problem.

The simulation-based approach to justify the number of vehicles at the public bus routes in cities is proposed in [1]. The authors of research [2] provide a methodology to solve the problem of cost-optimized planning for the fleet of electric buses, whereas the study [3] presents a fleet replacement problem that allows

determining the bus replacement plans by considering total costs.

Various optimization techniques are used by researchers to solve the fleet optimization problem. The paper [4] provides a proper decision-making procedure regarding the process of replacing a diesel fleet with alternative-technology buses by using a deterministic mixed-integer programming model. The study [5] develops a framework to investigate the bus fleet operation risks by using probabilistic simulations. In the research [6], the problem of dispatching time control in rolling horizons is modeled, following a periodic optimization approach.

Timetabling and vehicle scheduling are the basis of security and efficiency for various bus enterprises. The paper [7] presents a model to optimize the bus schedule by considering bus stops and route segments as the integrated structure. The dynamic scheduling procedures that allow adapting timetables to demand and traffic conditions are considered by the authors of the study [8], as well. The article [9] deals with the flexible vehicle and crew scheduling problem to assign available resources to cover generated timetables. The study [10] also solves the bus and driver scheduling problems with mealtime windows for a single public transport bus route by using a self-adaptive search method. The authors of paper [11] propose an optimization model for designing the intervals and capacity of buses by minimizing the system's operating costs and users' personal costs.

The vehicle routing problem is about finding optimal routes for a fixed fleet of vehicles so that they can meet the demands of a set of given customers by traveling through those paths. This problem and its numerous expansions are one of the most important and most applicable transportation and city logistics problems [12]. Urban public transport operations in the peak periods, characterized by highly uneven demand distributions and scarcity of resources, are considered in the article [13]: the authors simultaneously reduce passenger waiting times and transport operational costs. Similar efficiency criteria are used by the author of the research [14] for solving the timetables synchronization problem at the public transport lines, whereas the authors of the paper [15] consider improvement of the passenger transportation process at the expense of the combined operating mode.

The next group of studies combines problems of routing, optimal vehicle-mix, fleet selection and transport demand within the city territory. The research [16] develops a framework to maximize service performance in a set of high-frequency bus routes, given their planned headways and a total fleet size constraint. The authors of the paper [17] introduce a fleet size and a mix dial-a-ride problem with multiple passenger types and a heterogeneous fleet. The study [18] introduces the solution to a strategic problem of fleet renewal to meet the future operational needs under uncertain conditions. The authors of the research [19] aim to

solve the fleet size and mix location-routing problem by considering a heterogeneous fleet and time windows. The paper [20] describes a probabilistic formulation that provides the global optimum selection and allocation of a bus fleet in the case when a third party is involved in transportation. The authors of the research [21] present a mathematical model aiming to minimize the total costs for the passengers and the transport operator by substantiating the number of buses and the dynamic holding time.

The completed review of the contemporary literature on the research topic shows that despite considering by the authors of numerous cases and efficiency criteria, there are no approaches that consider the competitive nature of the market of public transport services. In this paper, authors aimed to fill this gap by developing the game-theoretical approach to substantiate the carriers' strategies in terms of the bus fleet management.

3 Approach to substantiate the bus models for servicing passengers at public transport lines

The K origin-destination pairs (O-D pairs) that are served by n public transport lines are considered, assuming that any combination of m bus models can be chosen for passengers' servicing.

It is assumed that one line is served by one carrier. If one carrier serves several lines or one line is served by several carriers, the tuple "carrier-line" can be selected as a unit and further, be considered in the model as one carrier (one public transport line).

Let the vector Q be the total number of trips per O-D pair within the line, while the number of elements of the vector Q is equal to K :

$$Q = \{q_1, q_2, \dots, q_K\}, \quad (1)$$

where: q_j is the number of completed trips per j -th O-D pair [pax].

The matrix Ω for assigning the transport lines to O-D pairs is defined with elements of the matrix being $\omega_{ij} = 1$ if the i -th carrier can serve the j -th O-D pair (can satisfy the passengers need to travel from one city district to another - the bus line includes these stops in corresponding city districts) and the matrix elements are equal to 0 otherwise. Then the sum of the elements of this matrix along the j -th column will show the number of competitive lines potentially serving the j -th O-D pair and the sum of the elements along the i -th row $\sum_{j=1}^K \omega_{ij}$ - the number of O-D pairs that can potentially be served by i -th public transport line.

If $\omega_{ij} = 1$, then the j -th O-D pair is potentially served by the i -th carrier, however, if the used bus models or other conditions of the servicing process do not satisfy the passengers for the given O-D pair, they can refuse in whole or in part from the services of this

bus line (if there is an alternative available). The matrix Δ is defined, the elements of which δ_{ij} determine the share that the i -th carrier takes when servicing the j -th O-D pair. It's obvious that $\delta_{ij} = 0$ if $\omega_{ij} = 0$ and $\delta_{ij} \in [0, 1]$ if $\omega_{ij} = 1$.

If the number of trips per each O-D pair \mathbf{Q} and the distribution of trips between carriers Δ are known, then the vector \mathbf{P} of passenger traffic values on public transport lines is determined as follows:

$$\mathbf{P} = \Delta \cdot \mathbf{Q}^T. \quad (2)$$

In this case, values of elements for the vector \mathbf{P} can be calculated as

$$p_i = \sum_{j=1}^K \delta_{ij} \cdot q_j. \quad (3)$$

Given the values of p_i , it is possible to determine the required number of buses to operate on the lines and hence - the quantitative composition of the city bus fleet. Thus, the solution to the problem of determining the quantitative composition of the fleet can be obtained if the matrix Δ and the number of trips per O-D pair are known. However, the assignment of trips to public transport lines depends on preferences of passengers and the importance of the given O-D pair for a carrier (meaning that the carrier determines the strategy of behavior depending on the attractiveness of a particular O-D pair).

Passenger preferences, when choosing a public transport line, depend on three main indicators: delivery speed (travel time), comfort and service price. All of the above parameters are, to one degree or another, determined by the bus model. The delivery speed depends on the design features (however, in addition, the traffic speed is affected by the congestion of the road network and the used methods of traffic management). Comfortability directly depends on the passenger capacity of a vehicle and the design features of the cabin and suspension. The price of the service is determined based on the costs of the service, which depend on the performance characteristics of a particular bus model. Thus, one can say that the preferences of passengers when choosing a particular bus line depend on the bus models used by the given carrier. This assumption does not consider the timetables of public transport lines: that feature could be provided in the assessment of the passengers' preferences if the passengers' opinion on the service frequency would be studied (this characteristic was not covered in this study).

It is convenient to describe the preference by passengers of a particular bus model through a fuzzy subset of the given bus model belonging to the set of optimal models. In this case, the preference for different O-D pairs or for a given O-D pair at different times of the day (day of the week) will be different. So, for the O-D pairs associated with a sleeping area in the city, the significance of the delivery speed is different depending

on the time of day. In general, each O-D pair can be divided into subgroups of transport service consumers, based on the purpose of the trip, while the composition of O-D pairs will determine the type of the membership function.

If the preference by the criterion of the travel speed is described by the membership function μ_v , by the criterion of comfort - by the function μ_K and by the criterion of price - by the function μ_T , with $\mu_v \in [0; 1]$, $\mu_K \in [0; 1]$ and $\mu_T \in [0; 1]$, then the passenger's general preference can be expressed through a fuzzy subset μ , which is a combination of the subsets μ_v, μ_K and μ_T , as:

$$\mu = f(\mu_v, \mu_K, \mu_T). \quad (4)$$

The importance v_{ij} of the j -th O-D pair for the i -th carrier is determined based on the specific weight of the number of trips performed for the given O-D pair in the potential passenger traffic on the line (the bigger the number of trips for the O-D pair, the more attractive it is for the carrier):

$$v_{ij} = \frac{q_j}{\sum_{j=1}^K \omega_{ij} \cdot q_j}, \quad (5)$$

where: $\sum_{j=1}^K \omega_{ij} \cdot q_j$ is the maximum possible (potential) passenger traffic on a bus line (the passenger traffic that will be served by the line, if for all the covered O-D pairs $\delta_{ij} = \omega_{ij} = 1$) [pax].

A conflict situation between n_j carriers serving the j -th O-D pair is considered as a game of n_j persons [22]. Each of the carriers has at most m alternatives (bus models). Moreover, if the i -th carrier chooses the k -th model ($k_i = 1, 2, \dots, m$) and the $(i + 1)$ -th carrier chooses the same or another k_{i+1} -th model of the vehicle, then each of them, as a result, will win a certain share of trips for the j -th O-D pair. Or, using the terminology of the game theory, one can say that when choosing the k_i -th option, the i -th player's payoff will be the share δ_{ij} of trips for the j -th O-D pair.

Obviously, the ratio of the number of passengers who choose the i -th carrier to the number of passengers who choose the $(i + 1)$ -th carrier is equal to the ratio of the trips share for the i -th carrier to the trips share for the $(i + 1)$ -th carrier. In this case, the part of trips δ_{ij} is directly proportional to the importance for the i -th carrier of the j -th O-D pair and the preference by passengers from the j -th O-D pair of the k -th bus model:

$$\frac{\delta_{ij}}{\delta_{(i+1)j}} = \frac{v_{ij} \cdot \mu_{jk_i}}{v_{(i+1)j} \cdot \mu_{jk_{i+1}}}. \quad (6)$$

On the other hand, if one proceeds from the condition that the passengers' demand for travel is fully satisfied by carriers, then

$$\sum_{i=1}^{n_j} \delta_{ij} = 1. \quad (7)$$

Thus, to determine the payoffs of each of the n_j players, it is necessary to solve the system of Equations (6) and (7). It is easy to show that this system has the following solution:

$$\delta_{ij} = \frac{v_{ij} \cdot \mu_{jki}}{\sum_{i=1}^{n_j} v_{ij} \cdot \mu_{jki}}. \tag{8}$$

Knowing the payoffs of each of the players, it is possible to solve the described game and the solution will be the optimal strategies of each of the players (optimal bus models). The set of solutions will determine the optimal qualitative structure of the city bus fleet.

4 Game-theoretical approach to choose carriers' strategies at the market of public transport services

According to definition of the game [22], a conflict situation between n_j carriers serving the j -th O-D pair can be formally represented in the following way:

$$\Gamma = \langle R_D, \{r_\kappa\}_{\kappa \in R_D}, r, R_I, \{R_\kappa\}_{\kappa \in R_I} \rangle, \tag{9}$$

where: R_D is the set of all the decision-making parties; R_I is the set of all the subjects defending certain interests,

r_κ is the set of all the admissible decisions (strategies) of the game participants who make the decision; r is the set of all the situations (outcomes) of the game;

R_κ is the set of all interests of the parties concerned in the conflict.

Moreover, the set r is a subset of the Cartesian product for the sets of all the strategies of the participants involved in the game r :

$$r = \prod_{\kappa \in R_D} r_\kappa, \tag{10}$$

and the set of all interests R_κ is a binary relation on the set r :

$$R_\kappa \subset r \times r, \kappa \in R_I. \tag{11}$$

In accordance with the definition of the game in Equation (9), the set of all the decision-making subjects is the set of carriers (public transport lines). The carrier-line pair is a member of the R_D set. In the case when one carrier serves several lines, the set of elements of the set R_D for this carrier form a coalition.

The R_I set (the set of coalitions of interests) contains subsets such as carriers and passengers; city administrations can also be considered as an element of this set with further consideration of the influence of this element on the outcome of the game, however, in this study, when modeling a conflict situation r , such a participant is not taken into account.

The elements of the set r_κ are possible strategies of carriers with respect to the qualitative (in terms of the model range) and quantitative composition of the bus fleet. It is convenient to represent an element of the set of all the admissible strategies in the form of a vector $\Phi \subset r_\kappa$:

$$\Phi = \begin{pmatrix} \alpha_1 & \alpha_2 & \dots & \alpha_m \\ \varphi_1 & \varphi_2 & \dots & \varphi_m \end{pmatrix}, \tag{12}$$

where: $\alpha_1, \alpha_2, \dots, \alpha_m$ are the alternative bus models; $\varphi_1, \varphi_2, \dots, \varphi_m$ are the probabilities of using the corresponding bus models, $\sum_{k=1}^m \varphi_k = 1$.

In this case, the carrier's strategy is pure if one model of the bus α_{k^*} is used for operation on the route, i.e. $\varphi_{k^*} = 1$ and $\varphi_{k(k \neq k^*)} = 0$ for $k = 1, 2, \dots, m$. The carrier's strategy is mixed otherwise (several different bus models are used to work on the line when serving the given O-D pair), while the number of buses of the k -th model should be proportional to φ_k .

The set of all the outcomes of the game is presented by vectors, which elements δ_{ij} are values, for each i -th carrier for the considered j -th O-D pair. As elements of the set of interests R_κ of interested parties (passengers and carriers), we will consider the most complete coverage of target market segments (O-D pairs), considering the number of trips per O-D pair - for transport companies and the highest satisfaction of the existing needs for travel - for passengers.

Next, the following alternatives are considered, which arise when choosing the most rational bus models when servicing a given O-D pair:

- trips for the O-D pair can potentially be served by only one carrier;
- trips for the O-D pair can potentially be served by two carriers;
- trips for the O-D pair can potentially be served by more than two carriers.

Obviously, for the first option, the carrier needs to apply a pure strategy and choose the bus model for servicing the O-D pair trips that most satisfies the passengers:

$$\begin{cases} \varphi_{k^*} = 1, \varphi_{k(k \neq k^*)} = 0, \\ k^* = \operatorname{argmax} \mu_{jk}. \end{cases} \tag{13}$$

In the second version, the game r will be a game of two persons - Ψ_1 and Ψ_2 . Let's define the payment matrix for this variant of the game. If one assumes that each of the players has the same opportunities when choosing the vehicle models, then the payment matrix will be of size $m \times m$, where m is the number of alternative bus models. When some strategy is chosen by the player Ψ , the share of trips for the considered O-D pair is δ_{Ψ_1} , when a strategy is chosen by the player Ψ_2 , his share is δ_{Ψ_2} , where δ_{Ψ_1} and δ_{Ψ_2} are calculated according to Equation (8). The payment matrix for this game is defined as:

$$\Delta^* = \begin{matrix} & \alpha_1 & \alpha_2 & \dots & \alpha_m \\ \alpha_1 & \delta_{11}^* & \delta_{12}^* & \dots & \delta_{1m}^* \\ \alpha_2 & \delta_{21}^* & \delta_{22}^* & \dots & \delta_{2m}^* \\ \dots & \dots & \dots & \dots & \dots \\ \alpha_m & \delta_{m1}^* & \delta_{m2}^* & \dots & \delta_{mm}^* \end{matrix}, \quad (14)$$

where: $\delta^* = \delta_{\Psi_1} + \delta_{\Psi_2}$.

Based on the assumption that the needs of passengers in travels are fully satisfied, one can say that

$$\delta_{\Psi_1} + \delta_{\Psi_2} = 1. \quad (15)$$

Then the element of the payoff matrix can be defined in the following way:

$$\delta^* = 2 \cdot \delta_{\Psi_1} - 1. \quad (16)$$

Since according to the definition of the game in Equation (9), the element of the set of interests R_k is the most complete coverage of the O-D pair trips, one can say that the task for the player Ψ_1 is to win the biggest possible share of trips for the j -th O-D pair. From Equation (16) these conditions are satisfied when the value of δ^* is reached (the more δ^* , the bigger is the δ_{Ψ_1} value). The task for the player Ψ_2 is similar and the condition for a set of interests will be satisfied if the payoff of the player Ψ_1 is the smallest possible value.

One can see that, for the second variant in the

above setting, the game Γ takes the form of a matrix game with zero-sum. When solving such a game, the principle of obtaining the maximum guaranteed result under the worst conditions is used: the player Ψ_1 seeks to adopt a strategy that should ensure the maximum loss of the player Ψ_2 . Accordingly, the player Ψ_2 seeks to adopt a strategy that ensures the minimum payoff of the player Ψ_1 (as mentioned above, such a strategy will ensure the maximum payoff of the player Ψ_2). According to [22], if the lower value of the pure game price (maximin) matches the upper value of the pure game price (minimax), i.e.

$$\max_{k_{\Psi_1}} \min_{k_{\Psi_2}} \delta_{k_{\Psi_1}, k_{\Psi_2}}^* = \min_{k_{\Psi_2}} \max_{k_{\Psi_1}} \delta_{k_{\Psi_1}, k_{\Psi_2}}^*, \quad (17)$$

then the solution of such a game will be the pure optimal strategies $\alpha_{k_{\Psi_1}}$ and $\alpha_{k_{\Psi_2}}$ of the players Ψ_1 and Ψ_2 (in this case, the game Γ has a saddle point).

If the game Γ does not have a saddle point (that is, condition in Equation (17) is not satisfied), then the strategies of the players will be mixed: mixed strategies are applied if the game does not have a saddle point, the game is repeated many times under similar conditions and averaging of the game results allows the solution estimation. In this case, the solution of the game is found by the main theorem for arbitrary rectangular games [22], according to which every matrix game has a solution and a player in such a game always has an

optimal strategy. The price of the game in this case is determined as follows:

$$\delta_{opt}^* = \max_{\Phi_1} \min_{\Phi_2} \sum_{k_{\Psi_1}=1}^m \sum_{k_{\Psi_2}=1}^m \varphi_{k_{\Psi_1}} \varphi_{k_{\Psi_2}} \delta_{k_{\Psi_1}, k_{\Psi_2}}^*, \quad (18)$$

where: Φ_1 and Φ_2 are the strategies of the players Ψ_1 and Ψ_2 correspondingly.

The problem of finding the optimal strategies Φ_1 and Φ_2 can be solved by sequentially enumerating the probabilities $\Phi_1, \Phi_2, \dots, \Phi_m$ of choosing the bus models $\alpha_1, \alpha_2, \dots, \alpha_m$ with the given step $s, s \in (0, 1]$, whereby the optimality criterion is the condition in Equation (18). In this case, the total number of enumerations N_v may be estimated as

$$N_v \approx s^{-2 \cdot m}. \quad (19)$$

Since in practice more than 3 - 4 bus models are rarely used on one city transport line, the number of enumerations with the step of 10^{-1} will be about $10^6 \div 10^8$ per O-D pair, which is implementable by using contemporary computers in a reasonable time.

If the j -th O-D pair can be potentially served by more than two carriers, then the pairwise games of each of the players against the coalition of the remaining competitors should be considered to determine the optimal strategies. In this case, the i -th carrier is the player Ψ_1 and the player Ψ_2 is the coalition of the remaining transport companies potentially serving the given O-D pair. The element of the payment matrix for such a game is determined similarly by dependence in Equation (16).

As a result of solving a set of conflict situations for all the considered O-D pairs, optimal strategies Φ_{ij} of each of the competing transport companies can be obtained for the set of O-D pairs served by the i -th carrier:

$$\Phi_i^* = \begin{matrix} \varphi_{11} & \varphi_{12} & \dots & \varphi_{1m} \\ \varphi_{21} & \varphi_{22} & \dots & \varphi_{2m} \\ \dots & \dots & \dots & \dots \\ \varphi_{K1} & \varphi_{K1} & \dots & \varphi_{Km} \end{matrix}, \quad (20)$$

where: Φ_i^* is the matrix containing the set of optimal strategies of the i -th transport company.

It should be noted that if the i -th carrier cannot potentially serve the j -th O-D pair, then all the elements of the corresponding row of the matrix Φ_j^* are equal to 0.

Based on particular optimal strategies for the j -th O-D pair, the optimal qualitative structure of the bus fleet of the i -th carrier is defined as follows:

$$d_{ik} = \frac{\sum_{j=1}^K \varphi_{jk}}{\sum_{j=1}^K \omega_{ij}}, \quad (21)$$

where: d_{ik} is the part of vehicles of the k -th model at the i -th public transport line.

5 Case study and discussion

To calculate the optimal structure of the city's bus fleet using the developed models, it is necessary to determine the type of membership functions for a fuzzy subset of optimal bus models and standardize them for the main categories of passengers.

To define the dependencies for estimation of the membership functions, the methodology for analyzing the results of an expert survey was used. The passenger preference survey was conducted in October 2019 in the city of Talas (Kazakhstan). Within the survey, the preferences of the following social groups were identified: adults of working age, students and retirees. The survey was conducted at the bus stops of the Talas public transport system. First, the respondents answered the group of questions related to their social status (age, source of income, the average income, etc.). Afterwards, the respondents were asked to assess their preference related to the transport line choice for three basic features: the level of tariff, comfortability and travel speed. The detailed survey results are discussed in [23].

Based on the results of the conducted survey, the regression models for the membership functions were defined as the third-degree polynomial models. The results of calculating the coefficients of polynomial models to determine the dependence of the preference function on the value of the corresponding features are presented in [23].

The obtained polynomial models are used to determine the values of the function in Equation (4). The resulting membership function can be estimated as the weighted average for the partial membership functions:

$$\mu = a_v \cdot \mu_v + a_K \cdot \mu_K + a_T \cdot \mu_T, \quad (22)$$

where: a_v , a_K , a_T are the weighting factors for preference functions according to travel speed, comfort and tariff, respectively.

The weighting coefficients were evaluated as the arithmetic mean values for all the respondents participated in the survey: $a_v = 0.321$, $a_K = 0.322$, $a_T = 0.357$. As we can see, the selected features are evaluated by passengers in almost the same way.

The mathematical model for estimation of the transport companies' strategies related to the vehicle fleet was implemented in Python programming language. A detailed description of the basic software framework can be found presented in [24]. The developed software was used as the simulation tool to assess the bus fleet structure for all the transport companies servicing the public transport system of the Talas city (in total, 13 carriers are involved in the process of servicing 53 bus lines in the city).

To represent the structure of the city's bus fleet in the aggregated form, 4 groups of vehicles are distinguished according to the vehicles' capacity (up to 16 pax., from

17 to 24 pax., from 25 to 40 pax. and more than 40 pax.). Thus, the aggregated structure of the city bus fleet can be shown as a vector D :

$$D = |d_1 \ d_2 \ d_3 \ d_4|, \quad (23)$$

where: d_i is the share of buses of the i -th group.

It should be mentioned that the proposed model does not consider the fleet structure in terms of the age of vehicles, the type of fuel, etc. The capacity is distinguished as the main feature influencing the passengers' preferences.

Influence of characteristics of the existing public transport network on the optimal structure of the city bus fleet is now determined. For that purpose, the regression models are constructed of dependence of the buses' share on the structure of the passengers' flows and the number of carriers servicing the public transport lines. The following explanatory variables are considered in the regression models:

- share ε_a of adult passengers of working age;
- share ε_S of students;
- share ε_r of retirees;
- the number n of carriers.

The number of trips performed per each O-D pair is a highly stochastic variable since it is influenced by many factors that are difficult to enumerate and predict. Therefore, as a random factor characterized by the external environment, are considered: the number of O-D pairs, the place of their origin and destination (respectively, the possibility of servicing by a specific bus line) and the number of trips per O-D pair. Then, according to the proposed model for determining the optimal structure of the bus fleet, the total number of O-D pairs K , the vector representing the number of trips Q and the matrix of assigning O-D pairs to bus lines Ω will be random.

For the listed explanatory variables, the full-factor simulation experiment was conducted: the number of competing transport companies was considered in the range from 2 to 20, the shares of passengers were considered in the range from 0 to 1 assuming that the sum of shares for all the passenger groups is equal to 1. The number of model's runs in each of the experiment series was 300 that guarantees the probability of confidence in 95% for the obtained results.

To assess the influence of input factors on the system output (the structure of the city bus fleet), the linear functional dependence was used for the regression models:

$$d_i = b_{0i} + b_{1i} \cdot \varepsilon_a + b_{2i} \cdot \varepsilon_s + b_{3i} \cdot \varepsilon_r + b_{4i} \cdot n, \quad (24)$$

where b_{ji} are the regression coefficients, $i = 1 \dots 4$.

As a result of the regression analysis based on the conducted simulation experiment, the following linear models were obtained:

Table 1 Change in the rational structure of the city bus fleet with a 10% increase in indicators [%]

Indicator	Group of buses			
	1	2	3	4
part of adults	4.72	3.18	3.03	3.15
part of students	1.42	2.67	3.56	3.42
part of retirees	3.48	3.82	3.08	3.11
number of bus lines	-2.97	-2.38	-1.35	1.34

$$\begin{cases} d_1 = 0.10 \cdot \varepsilon_a + 0.03 \cdot \varepsilon_s + 0.07 \cdot \varepsilon_r + 1.0 \cdot 10^{-7} \cdot n \\ d_2 = 0.14 \cdot \varepsilon_a + 0.11 \cdot \varepsilon_s + 0.16 \cdot \varepsilon_r + 9.3 \cdot 10^{-9} \cdot n \\ d_3 = 0.23 \cdot \varepsilon_a + 0.27 \cdot \varepsilon_s + 0.23 \cdot \varepsilon_r + 5.0 \cdot 10^{-8} \cdot n \\ d_4 = 0.54 \cdot \varepsilon_a + 0.59 \cdot \varepsilon_s + 0.53 \cdot \varepsilon_r + 4.3 \cdot 10^{-8} \cdot n \end{cases} \quad (25)$$

Note that free coefficients b_{oi} are taken as zero values for the developed regression models (for such values, the adequacy of the models rises significantly). The obtained regression models are characterized by high adequacy: the determination coefficient is higher than 0.9 for each of the presented models. All the coefficients in the regression models in Equation (25) are statistically significant for the significance level of 0.05.

The next investigated is the influence of parameters on the required share of buses for all the possible options for the rational structure of the vehicle fleet. To do this, the change in the share of buses of each group was calculated, with a 10% increase in the parameters that determine the structure of the bus fleet. The increase in the share of buses Δd_j for the variant of the bus fleet structure for the j -th group is calculated by the formula

$$\Delta d_j = \frac{d_j(\bar{x} + \Delta x)}{d_j(\bar{x})} \cdot 100\%, \quad (26)$$

where \bar{x} is the average value of the indicator;

Δx is the indicator's increment, $\Delta x = 0.1 \cdot \bar{x}$.

The results of estimating the change in the share of buses with a 10% increase in the parameters that determine the structure of the city bus fleet are shown in Table 1.

According to Table 1, it can be noted that the change in the structure of transport service consumers has the greatest impact on the structure of the bus fleet. Moreover, an increase in the proportion of the working-age adult passengers leads to the greatest increase in the optimal proportion of buses with especially low passenger capacity characterized by the highest tariff and the highest delivery speed. With an increase in the share of passengers of retirement age, the biggest increase is in the share of buses with an average

passenger capacity and with an increase in the share of students, the optimal share of buses with a large passenger capacity grows.

With an increase in the number of routes, the share of buses in each of the first three groups decreases and the share of buses with a particularly large passenger capacity increases. This trend is positive in terms of reducing the traffic congestion and decreasing the environmental pollution by reducing the total number of buses.

6 Conclusions

The developed approach to determining the optimal qualitative and on its basis - the quantitative structure of the city bus fleet allows considering the preferences of consumers of transport services and the competitive nature of the transportation market. The use of the proposed method in practice allows transport engineers to assess the model range of the city's bus fleet.

The proposed methodology makes it possible to determine the optimal models of buses for transporting passengers and a rational quantitative ratio of buses of these models for each of the carriers for a city's existing public transport network. An obvious inconvenience of using this technique is the cumbersomeness of the calculations, which can be eliminated by creating a specialized software.

Analysis of influence of determining factors on the structure of the bus fleet allows to conclude that the change in the composition of consumers of transport services has the biggest impact on the fleet structure.

As the future research direction, it is planned to perform the studies with use of the developed approach based on other locations to confirm the obtained membership functions and the discovered influence of the passenger flows structure on the structure of the city bus fleet.

References

- [1] NAUMOV, V. Optimizing the number of vehicles for a public bus line on the grounds of computer simulations. In: 5th IEEE International Conference on Models and Technologies for Intelligent Transportation Systems 2017: proceedings [online]. 2017. ISBN 978-1-5090-6484-7, p. 176-181. Available from: <https://doi.org/10.1109/MTITS.2017.8005661>

- [2] ROGGE, M., VAN DER HURK, E., LARSEN, A., SAUER, D. U. Electric bus fleet size and mix problem with optimization of charging infrastructure. *Applied Energy* [online]. 2018, **211**, p. 282-295. ISSN 0306-2619. Available from: <https://doi.org/10.1016/j.apenergy.2017.11.051>
- [3] PELLETIER, S., JABALI, O., MENDOZA, J. E., LAPORTE, G. The electric bus fleet transition problem. *Transportation Research Part C: Emerging Technologies* [online]. 2019, **109**, p. 174-193. ISSN 0968-090X. Available from: <https://doi.org/10.1016/j.trc.2019.10.012>
- [4] ISLAM, A., LOWNES, N. When to go electric? A parallel bus fleet replacement study. *Transportation Research Part D: Transport and Environment* [online]. 2019, **72**, p. 299-311. ISSN 1361-9209. Available from: <https://doi.org/10.1016/j.trd.2019.05.007>
- [5] HARRIS, A., SOBAN, D., SMYTH, B. M., BEST, R. A probabilistic fleet analysis for energy consumption, life cycle cost and greenhouse gas emissions modelling of bus technologies. *Applied Energy* [online]. 2020, **261**, 114422. ISSN 0306-2619. Available from: <https://doi.org/10.1016/j.apenergy.2019.114422>
- [6] GKIOTSALITIS, K. A model for the periodic optimization of bus dispatching times. *Applied Mathematical Modelling* [online]. 2020, **82**, p. 785-801. ISSN 0307-904X. Available from: <https://doi.org/10.1016/j.apm.2020.02.003>
- [7] WAGALE, M., SINGH, A. P., SARKAR, A. K., ARKATKAR, S. Real-time optimal bus scheduling for a city using a DTR model. *Procedia - Social and Behavioral Sciences* [online]. 2013, **104**, p. 845-854. ISSN 1877-0428. Available from: <https://doi.org/10.1016/j.sbspro.2013.11.179>
- [8] KUMAR, B. A., PRASATH, G. H., VANAJAKSHI, L. Dynamic bus scheduling based on real-time demand and travel time. *International Journal of Civil Engineering* [online]. 2019, **17**, p. 1481-1489. ISSN 2383-3874. Available from: <https://doi.org/10.1007/s40999-019-00445-y>
- [9] BOYER, V., IBARRA-ROJAS, O. J., RIOS-SOLIS, Y. A. Vehicle and crew scheduling for flexible bus transportation systems. *Transportation Research Part B: Methodological* [online]. 2018, **112**, p. 216-229. ISSN 0191-2615. Available from: <https://doi.org/10.1016/j.trb.2018.04.008>
- [10] KANG, L., CHEN, S., MENG, Q. Bus and driver scheduling with mealtime windows for a single public bus route. *Transportation Research Part C: Emerging Technologies* [online]. 2019, **101**, p. 145-160. ISSN 0968-090X. Available from: <https://doi.org/10.1016/j.trc.2019.02.005>
- [11] IBEAS, A., ALONSO, B., DELL'OLIO, L., MOURA, J. L. Bus size and headways optimization model considering elastic demand. *Journal of Transportation Engineering* [online]. 2014, **140**(4), 04013021. ISSN 2473-2893. Available from: [https://doi.org/10.1061/\(asce\)te.1943-5436.0000641](https://doi.org/10.1061/(asce)te.1943-5436.0000641)
- [12] ALIZADEH FOROUTAN, R., REZAEIAN, J., MAHDAVI, I. Green vehicle routing and scheduling problem with heterogeneous fleet including reverse logistics in the form of collecting returned goods. *Applied Soft Computing* [online]. 2020, **94**, 106462. ISSN 1568-4946. Available from: <https://doi.org/10.1016/j.asoc.2020.106462>
- [13] GKIOTSALITIS, K., WU, Z., CATS, O. A cost-minimization model for bus fleet allocation featuring the tactical generation of short-turning and interlining options. *Transportation Research Part C: Emerging Technologies* [online]. 2019, **98**, p. 14-36. ISSN 0968-090X. Available from: <https://doi.org/10.1016/j.trc.2018.11.007>
- [14] NAUMOV, V. Synchronisation of timetables for public bus lines using genetic algorithms and computer simulations. *Lecture Notes in Networks and Systems* [online]. 2018, **36**, p. 44-53. ISSN 2367-3389. Available from: https://doi.org/10.1007/978-3-319-74454-4_4
- [15] TARAN, I., LITVIN, V. Determination of rational parameters for urban bus route with combined operating mode. *Transport Problems* [online]. 2018, **13**(4), p. 157-171. ISSN 2300-861X. Available from: <https://doi.org/10.20858/tp.2018.13.4.14>
- [16] SANCHEZ-MARTINEZ, G., KOUTSOPOULOS, H., WILSON, N. Optimal allocation of vehicles to bus routes using automatically collected data and simulation modelling. *Research in Transportation Economics* [online]. 2016, **59**, p. 268-276. ISSN 0739-8859. Available from: <https://doi.org/10.1016/j.retrec.2016.06.003>
- [17] TELLEZ, O., VERCRAENE, S., LEHUEDE, F., PETON, O., MONTEIRO, T. The fleet size and mix dial-a-ride problem with reconfigurable vehicle capacity. *Transportation Research Part C: Emerging Technologies* [online]. 2018, **91**, p. 99-123. ISSN 0968-090X. Available from: <https://doi.org/10.1016/j.trc.2018.03.020>
- [18] TURAN, H., ELSAWAH, S., RYAN, M. A long-term fleet renewal problem under uncertainty: A simulation-based optimization approach. *Expert Systems with Applications* [online]. 2020, **145**, 113158. ISSN 0957-4174. Available from: <https://doi.org/10.1016/j.eswa.2019.113158>
- [19] KOC, C., BEKTAS, T., JABALI, O., LAPORTE, G. The fleet size and mix location-routing problem with time windows: Formulations and a heuristic algorithm. *European Journal of Operational Research* [online]. 2016, **248**(1), p. 33-51. ISSN 0377-2217. Available from: <https://doi.org/10.1016/j.ejor.2015.06.082>
- [20] SAEED OSMAN, M. Uncertainty modeling for bus selection and allocation in a private transportation system. *Transportation Planning and Technology* [online]. 2019, **42**(7), p. 714-728. ISSN 1029-0354. Available from: <https://doi.org/10.1080/03081060.2019.1650435>

- [21] LIANG, S., MA, S., HE, S. Multi objective optimal formulations for bus fleet size of public transit under headway-based holding control. *Journal of Advanced Transportation* [online]. 2019, **2019**, 2452348. ISSN 2042-3195. Available from: <https://doi.org/10.1155/2019/2452348>
- [22] OWEN, G. *Game Theory*, 4. ed. Bingley: Emerald Group Publishing, 2013. ISBN 978-1781905074.
- [23] NAUMOV, V., ZHAMANBAYEV, B., AGABEKOVA, D., ZHANBIROV, Z., TARAN, I. Fuzzy-logic approach to estimate the passengers' preference when choosing a bus line within the public transport system. *Communications - Scientific Letters of the University of Zilina* [online]. 2021, **23**(3), p. A150-A157. ISSN 2585-7878, eISSN 2585-7878. Available from: <https://doi.org/10.26552/com.C.2021.3.A150-A157>
- [24] NAUMOV, V., SAMCHUK, G. Class library for simulations of passenger transfer nodes as elements of the public transport system. *Procedia Engineering* [online]. 2017, **187**, p. 77-81. Available from: <https://doi.org/10.1016/j.proeng.2017.04.352>

DETERMINATION OF THERMOMECHANICAL STRESSES IN ELEMENTS OF VEHICLES' BRAKING SYSTEMS

Oleksii Grevtsev¹, Ninel Selivanova¹, Pavlo Popovych², Liubomyr Poberezhny^{3,*}, Yurii Rudyak⁴, Oksana Shevchuk², Liubov Poberezhna³, Olena Skyba⁵, Viktor Ostroverkhov², Oleksandr Shashkevych²

¹National Transport University, Kyiv, Ukraine

²West Ukrainian National University, Ternopil, Ukraine

³Ivano-Frankivsk National Technical University of Oil and Gas, Ivano-Frankivsk, Ukraine

⁴I. Horbachevsky Ternopil National Medical University, Ternopil, Ukraine

⁵Ternopil Ivan Puluj National Technical University, Ternopil, Ukraine

*E-mail of corresponding author: lubomyrpoberezhny@gmail.com

Resume

The main objective of the study was to develop a model and analyze the thermomechanical behavior of the hub material of the vehicle brake disk. The simulation strategy was based on the solution of the three-dimensional problem of the theory of elasticity for the case of effect of external loads and temperature fields on the metal structure element of the vehicle brakes. To solve this type of task of the theory of elasticity, the differential equations of the second order were used for the first time. Adaptation of the proposed model, completed in the article, has proved the correctness of use of these equations in modeling the thermomechanical processes with determination of stresses and displacements in unevenly heated rotary cylinders of the final length. The proposed method can be applied with high efficiency in stress strain state simulation of individual parts of vehicles.

Article info

Received 8 February 2021

Accepted 25 May 2021

Online 30 September 2021

Keywords:

vehicles brakes,
temperature change,
metal structures of vehicles,
theory of elasticity,
brake defects and fracture,
thermomechanical stress

Available online: <https://doi.org/10.26552/com.C.2022.1.B1-B8>

ISSN 1335-4205 (print version)

ISSN 2585-7878 (online version)

1 Introduction

Frictional heat generation induces temperature gradients and thermal stresses in the contacting components of a brake. The complexity of a problem, incorporating a number of different phenomena, requires consideration at different scales. Among these scales, there are bulk, macro- and micro-levels [1-3].

Braking has a vital role in vehicle safety. In general, the braking system operates by the two main parts, the stator and the rotor. A braking system that is widely used is a friction brake, where the braking system uses the principle of friction. The rotor and the stator are creating a friction process. The brake system requires maintenance or replacement of components after a certain time. Increased life of brakes used under the large loads can be achieved by applying a layered braking system. Mechanical braking, supported with engine brakes, produces excellent braking and extends the life of the braking components [4-5].

2 Literature review

Based on the analysis of metal structures of vehicle elements, the dynamic loads, temperature, and

environment are found to be the main factors that cause malfunctions and defects of assembly units (Figure 1). All these factors promote formation of a scale or a film on surfaces with consideration of the surfaces condition, in particular coating, roughness, hardness, etc. [6-16]. The constant influence of these factors' combinations causes damages with subsequent destruction. The most typical damages are fatigue damage, thermomechanical damage, corrosion-mechanical wear, corrosion fatigue, corrosion cracking [17-21]. Fatigue fractures cause spontaneous failure of metal structures of vehicles' components and elements, lead to weight loss, intensify wear of joints, change the amount of surface roughness of parts, reduce fatigue strength and initiate cracks. Therefore, the reliability and durability of machines and their elements are reduced and the costs of repair and elimination of the consequences of failures are increased [16, 19].

The metal materials of nodes and parts of vehicles are a function of mechanical and thermal stresses considered in the spatial coordinate system. In the simulation of analytical models of stress - strain state in such materials, axisymmetric problems of elasticity theory are classified as spatial ones, which hardly could be solved from the standpoint of mathematics. The solution of the axisymmetric problem should strictly



Figure 1 Defects of the brake disk of a truck

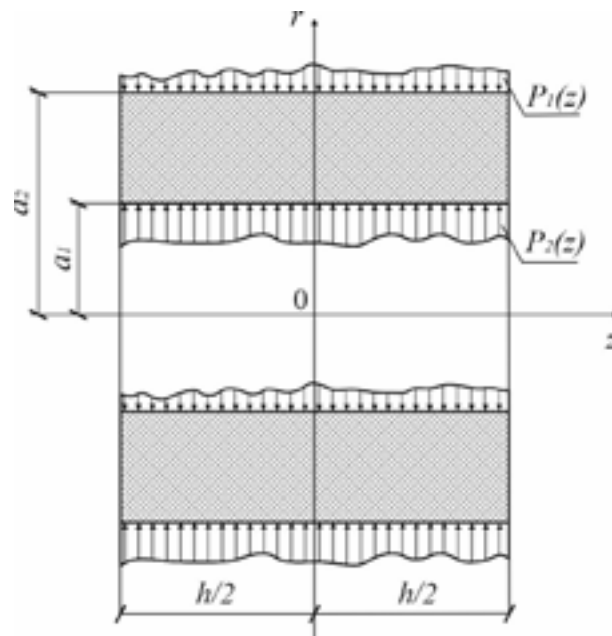


Figure 2 Analytical model of the cylinder under the action of centrifugal force

and completely satisfy all the boundary conditions on the side surfaces and ends of bodies of rotation [18]. Therefore, the decision-making of such a solution is problematic from the point of view of the elasticity theory. The problem of the stress-strain state of a cylinder of finite length can be solved by numerical methods, which leads to cumbersome constructions of many systems of linear algebraic equations, or to integral equations of the second kind [22-23]. In such equations, normal and tangential stresses are written in the form of series of special functions, which is inconvenient for practical application [24-25]. The ability to understand the processes occurring in the materials of the elements under study, without adequate recorded analytical dependencies, is limited; only the results of calculations can be analyzed. This is a disadvantage of

the stress strain state simulation of the metal structures elements by means of the 3D simulation technologies [21-22, 24-25]. When the force is applied on a brake pedal, it causes the brake pads to stick with disc brake, which creates artificial friction; due to this friction rusting of rotors and pads takes place, responsible for deformation and various thermal stresses due to large increase in temperature and friction takes place. Due to these unsuitable conditions, consequences appear, like the microscopic cracks, permanent failures, thermal deformation due to frictional heating and various elastic after-effect produces on the friction surfaces of disc [26].

The main objective of this study was to develop a model and to analyze the thermomechanical behavior of the vehicle brake disk material for ensuring the required operational reliability of disc brakes.

3 Methodology

To solve such problems with maximum accuracy, the provisions of the theory of elasticity should be applied; then, the adequate simulation of stresses and displacements under operating loads would be provided. It is advisable to improve the theoretical foundations for the better understanding of thermomechanical processes in rotating bodies, in particular cylindrical elements of metal structures of vehicles (brake disk hubs, etc.) that are under the simultaneous action of thermal and mechanical stresses.

A hollow cylinder of finite length z ($-h/2 \leq z \leq h/2$) (Figure 2), which rotates (without bending) under the action of centrifugal force F_r , is under study.

$F_r = \rho\omega^2 r$ in a temperature field $\theta = \theta(r, z)$ if ρ - material density; r - radial coordinate

In the cylindrical coordinate system (r, z) , for the considered body of rotation, the differential equations of equilibrium, written for displacements and stresses, are deduced [26-29]:

$$\Delta u_1 - \frac{u_1}{r^2} + \frac{e_1}{1-2\nu} - 2\frac{(1+\nu)}{(1-2\nu)}\alpha\theta_1 = 0, \tag{1}$$

$$\Delta u_3 + \frac{e_3}{1-2\nu} - 2\frac{(1+\nu)}{(1-2\nu)}\alpha\theta_3 = 0,$$

$$\sigma_{11,1} + \sigma_{13,1} + \frac{\sigma_{11} - \sigma_{22}}{r} = 0, \tag{2}$$

$$\sigma_{13,1} + \sigma_{33,3} + \frac{1}{r}\sigma_{13} = 0.$$

In Equations (1) and (2), the subscript written after the comma denotes the partial derivative by the corresponding coordinate: r or z .

Boundary conditions on the surface of the body of rotation (model of the brake disk hub) are developed [23-24]:

$$\begin{aligned} P_r &= \sigma_{11} \cos(r, n) + \sigma_{13} \cos(r, n), \\ P_z &= \sigma_{13} \cos(r, n) + \sigma_{33} \cos(r, n), \end{aligned} \tag{3}$$

if P_r and P_z - projections of surface forces to directions r and z , respectively; n - normal to the surface of the body of rotation.

Based on the Hooke's law for the spatial theory of elasticity, stress components are determined [28]:

$$\sigma_{ij} = 2G\left(e_{ij} + \frac{\nu}{1-2\nu}e\delta_{ij} - \frac{1+\nu}{1-\nu}\alpha\theta\delta_{ij}\right) \tag{4}$$

for $i, j = 1, 2, 3$,

where the known dependences between the displacements and deformations remain valid:

$$\begin{aligned} e_{11} &= u_{1,1}, \\ e_{22} &= \frac{1}{r}u_1, \\ e_{33} &= u_{3,1}, \\ 2e_{13} &= u_{1,3} + u_{3,1}. \end{aligned} \tag{5}$$

where δ_{ij} - Kronecker symbol; α and ν - respectively, coefficients of linear thermal expansion and Poisson's ratio; $e = e_{11} + e_{22} + e_{33}$ - volumetric expansion; $G = E/(1 + \nu)$ - shear module; E - modulus of elasticity; A - coefficient of linear thermal expansion.

The proposed method is based on successive approximations of solutions that satisfy the boundary conditions in Equation (3) on the side surfaces and ends of the investigated hollow cylinder of the finite length.

4 Results

In the first approximation the assumption is $e_{33} = u_{13} = \sigma_{33} = 0$. Since, according to the condition, the cylinder is not deformed by bending, then, based on the condition $e_{33} = u_{3,3} = 0$, the formula $u_3(r, z) = w(r) = 0$ is derived. Since $\sigma_{13} = 2G(u_{1,3} + u_{3,1}) = 0$, then $u_{1,3} = -u_{3,1}$. However, the deflection is $w(r) = 0$, then

$$u_1(r, z) = u(r). \tag{6}$$

Next, based on the condition $e_{33}=0$, the value of e_{33} is found, which was previously assumed to be zero:

$$e_{33} = -\frac{\nu}{1-\nu}(e_{11} - e_{22}) + \frac{1+\nu}{1+\nu}\alpha\theta, \tag{7}$$

for stresses:

$$\begin{aligned} \sigma_{11} &= \frac{2G}{1-\nu}\left[u_1 + \frac{\nu}{r}u - (1+\nu)\alpha\theta\right], \\ \sigma_{22} &= \frac{2G}{1-\nu}\left[\nu u_1 + \frac{1}{r}u - (1+\nu)\alpha\theta\right] \end{aligned} \tag{8}$$

The next assumption is $\sigma_{13} \neq 0$. The value σ_{13} is derived from the first equation of system in Equation (2) by integrating it by z in the interval from $-h/2$ to $h/2$, taking into account expression in Equation (8). Providing the condition of absence of tangential stresses at the ends of the cylinder under study is satisfied ($\sigma_{13} = 0$ for $z = -h/2; z = h/2$), then, for the temperature field of the form $\theta(r, z) = \theta_1(r) + f(z)$ after integration, the formula is deduced

$$\left[\frac{1}{r}(ru)_1\right] = (1+\nu)\alpha\theta_{1,1} - \frac{1-\nu}{2G}\rho\omega^2 r. \tag{9}$$

Based on Equation (9), the expression for displacement is:

$$\begin{aligned} u(r) &= \frac{1-\nu}{2G}\rho\omega^2 \frac{r^3}{8} + (1+\nu)\alpha \frac{1}{r} \int_{a_1}^r r\theta_1(r)ds + \\ &+ A_1 \frac{r}{2} + A_2 \frac{1}{r}, \end{aligned} \tag{10}$$

where a_1 - the radius of the central hole.

Moreover, if the cylinder is solid ($a_1 = 0$), then for the limited finite displacements $u(r)$, $A_2=0$ should be accepted.

In the second approximation, $\sigma_{13} \neq 0$, and a $\sigma_{13} = \sigma_{33} = 0$. Based on Equation (7), e_{33} is determined by

integrating by z in the range from 0 to z since according to Equation (6), $e_{33} = u_{33}$. Therefore,

$$u_3(r, z) = -\frac{vz}{1-v} \frac{1}{r} (ru)_1 + \frac{1+v}{1-v} \alpha \int_0^z \theta(r, z) dz. \quad (11)$$

From the condition $u_{1,3} = -u_{3,1}$, if $\sigma_{13} = 0$, based on Equation (9) and Equation (11), the resulting expression of the radial displacement $u_1(r, z)$ is derived:

$$u_1(r, z) = u(r) - \frac{z^2}{2} \left[(1-v) \alpha \theta_{1,1} + \frac{v}{2G} \rho \omega^2 r \right], \quad (12)$$

where $u(r)$ - radial displacement of the median plane points ($z = 0$). Then, after consideration of Equation (11) and Equation (7), the specified value of the axial movement $u_3(r, z)$ is defined taking into account Equation (12), that $e_{11} + e_{22}$:

$$u_3(r, z) = \frac{v}{1-v} \frac{z}{r} (ru)_1 + \frac{v}{1-v} \frac{z^3}{6} \times \left[(1+v) \alpha \Delta_1 \theta_1 + \frac{v}{G} \rho \omega^2 \right] + \frac{1+v}{1-v} \alpha \int_0^z \theta(r, z) dz, \quad (13)$$

if $\Delta_1 \theta_1 = \theta_{1,11} + \frac{1}{r} \theta_{1,1}$.

The displacements $u_1(r, z)$ and $u_3(r, z)$ are exact solutions of equilibrium equations in Equation (1) since they are identically satisfied after performing the substitution of Equations (12) and (13), taking into account expression in Equation (10). The temperature field $\theta_1 = \theta_1(r)$ is found based on the solution of the differential equation $(\Delta_1 \theta_1)_1 = 0$, which is integrated into the form:

$$\theta_1(r) = B_1 \frac{r^2}{4} + B_2 \ln(r) + B_3, \quad (14)$$

where B_1, B_2, B_3 - arbitrary integration constants.

5 Discussion

Based on the Hooke's law and the displacements found, taking into account Equation (14), in which the equation $B_2 = 0$ is accepted (i.e., the temperature is assumed to be distributed along the radius of the cylinder according to the quadratic law), stresses are determined. Moreover, the test proves that the voltage values σ_{13} and σ_{33} are zero (everywhere) and σ_{11} and σ_{22} are:

$$\sigma_{11} = \frac{2G}{1-v} \times \left\{ \begin{array}{l} -(1-v^2) \alpha B_1 \frac{r^2}{16} - \alpha B_3 - \frac{1-v}{2G} \\ \rho \omega^2 \frac{3+v}{8} r^2 + A_1 \frac{1+v}{2} - A_1 \frac{1+v}{2} \\ - \frac{z^2}{2} \left[\frac{(1+v)^2}{2} \alpha B_1 + \right. \\ \left. + \frac{v(1-v)}{2G} \rho \omega^2 \right] - (1+v) \alpha f(z) \end{array} \right\}, \quad (15)$$

$$\sigma_{12} = \frac{2G}{1-v} \times \left\{ \begin{array}{l} -(1-v^2) \alpha B_1 \frac{3r^2}{16} - (1+v) \alpha B_3 - \\ - \frac{v(1-v)}{2G} \rho \omega^2 \frac{3+v}{8} r^2 + A_1 \frac{1+v}{2} + \\ + A_2 \frac{1+v}{2} - \frac{z^2}{2} \left[\frac{(1+v)^2}{2} \alpha B_1 + \right. \\ \left. + \frac{v(1-v)}{2G} \rho \omega^2 \right] \\ - (1+v) \alpha f(z) \end{array} \right\}.$$

For an unevenly heated rotating hollow cylinder of the finite length loaded with a uniformly distributed load P_2 on the outer surface and a load P_1 on the inner surface, satisfying the boundary conditions in Equation (3), if $\sigma_{13} = \sigma_{33} = 0$, and excluding from Equation (15) the expression $(1+v) \alpha f(z)$, where $f(z)$ is an arbitrary function, the stresses σ_{13} and σ_{33} are defined:

$$\begin{aligned} \sigma_{11} &= \left(\frac{E \alpha B_r}{16} + \frac{3+v}{8} \rho \omega^2 \right) \left(a_2^2 + a_1^2 - \frac{a_1^2 a_2^2}{r^2} - r^2 \right) + \\ &+ \frac{P_2 a_2^2 (r^2 - a_1^2) - P_1 a_1^2 (a_2^2 - r^2)}{r^2 (a_2^2 - a_1^2)}, \\ \sigma_{22} &= \frac{E \alpha B_r}{16} \left(a_2^2 + a_1^2 - \frac{a_1^2 a_2^2}{r^2} - 3r^2 \right) + \frac{3+v}{8} \rho \omega^2 \times \\ &\times \left(a_2^2 + a_1^2 - \frac{a_1^2 a_2^2}{r^2} - \frac{1+3v}{3+v} r^2 + \right. \\ &\left. + \frac{P_2 a_2^2 (r^2 - a_1^2) - P_1 a_1^2 (a_2^2 - r^2)}{r^2 (a_2^2 - a_1^2)} \right), \end{aligned} \quad (16)$$

where a_2 and a_1 - respectively, the radii of the outer and inner surfaces of the cylinder.

In addition, if in a hollow cylinder the temperature field described by Equation (14) satisfies the equation of thermal conductivity and varies along the radius by the quadratic law ($B_2 = 0$), for its description the expression is written:

$$\theta_1(r) = T_1 + \frac{T_2 - T_1}{a_2^2 - a_1^2} (r^2 - a_1^2), \quad (17)$$

where T_1 and T_2 - respectively, the temperature on the inner a_1 and outer a_2 radii of the disk, then

$$\begin{aligned} B_1 &= \frac{4(T_2 - T_1)}{a_2^2 - a_1^2}, \\ B_2 &= T_1 - \frac{T_2 - T_1}{a_2^2 - a_1^2} a_1^2. \end{aligned} \quad (18)$$

substituting B_1 from Equation (18) into Equation (16), the final stress formulas σ_{11} and σ_{22} are deduced:

$$\begin{aligned} \sigma_{11} &= \left(\frac{E \alpha}{4} \frac{T_2 - T_1}{a_2^2 - a_1^2} + \frac{3+v}{8} \rho \omega^2 \right) \times \\ &\times \left(a_2^2 + a_1^2 - \frac{a_1^2 a_2^2}{r^2} - r^2 \right) + \\ &+ \frac{P_2 a_2^2 (r^2 - a_1^2) - P_1 a_1^2 (a_2^2 - r^2)}{r^2 (a_2^2 - a_1^2)}, \end{aligned} \quad (19)$$

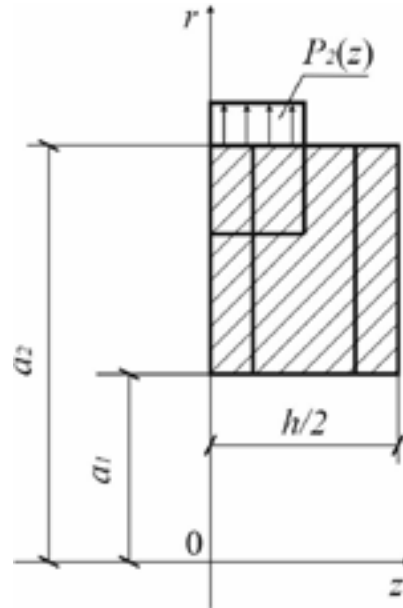


Figure 3 Analytical model of a site of the cylinder under study

$$\sigma_{22} = \frac{E\alpha}{4} \frac{T_2 - T_1}{a_2^2 - a_1^2} \left(a_2^2 + a_1^2 - \frac{a_1^2 a_2^2}{r^2} - 3r^2 \right) + \frac{3+v}{8} \rho \omega^2 \left(a_2^2 + a_1^2 - \frac{a_1^2 a_2^2}{r^2} - \frac{1+3v}{3+v} r^2 + \frac{P_2 a_2^2 (r^2 - a_1^2) - P_1 a_1^2 (a_2^2 - r^2)}{r^2 (a_2^2 - a_1^2)} \right).$$

Providing that ($P_1 = P_2 = 0$), Equation (19) is deduced:

$$\begin{aligned} \sigma_{11} &= \frac{E\alpha}{4} \frac{T_2 - T_1}{a_2^2 - a_1^2} \left(a_2^2 + a_1^2 - \frac{a_1^2 a_2^2}{r^2} - r^2 \right) + \frac{3+v}{8} \rho \omega^2 \left(a_2^2 + a_1^2 - \frac{a_1^2 a_2^2}{r^2} - r^2 \right), \\ \sigma_{22} &= \frac{E\alpha}{4} \frac{T_2 - T_1}{a_2^2 - a_1^2} \left(a_2^2 + a_1^2 - \frac{a_1^2 a_2^2}{r^2} - 3r^2 \right) + \frac{3+v}{8} \rho \omega^2 \left(a_2^2 + a_1^2 - \frac{a_1^2 a_2^2}{r^2} - \frac{1+3v}{3+v} r^2 \right). \end{aligned} \quad (20)$$

For a solid non-uniformly heated cylinder of the finite length, which is loaded on the outer surface by a uniformly distributed load P_2 ($a_1 = 0$), the formulas are developed:

$$\begin{aligned} \sigma_{11} &= \frac{E\alpha}{4} \frac{T_2 - T_1}{a_2^2} (a_2^2 - r^2) + \frac{3+v}{8} \rho \omega^2 \times (a_2^2 - r^2) + P_2, \\ \sigma_{22} &= \frac{E\alpha}{4} \frac{T_2 - T_1}{a_2^2 - a_1^2} (a_2^2 - 3r^2) + \frac{3+v}{8} \rho \omega^2 \times (a_2^2 - \frac{1+3v}{3+v} r^2) + P_2. \end{aligned} \quad (21)$$

Accordingly, based on the law in Equation (17), for a solid cylinder of the finite length, unevenly heated along the radius, in the absence of load, but in the presence of a temperature, the formulas are deduced:

$$\begin{aligned} \sigma_{11} &= \frac{E\alpha}{4} \frac{T_2 - T_1}{a_2^2} (a_2^2 - r^2) + \frac{3+v}{8} \rho \omega^2 (a_2^2 - r^2), \\ \sigma_{22} &= \frac{E\alpha}{4} \frac{T_2 - T_1}{a_2^2 - a_1^2} (a_2^2 - 3r^2) + \frac{3+v}{8} \rho \omega^2 \times (a_2^2 - \frac{1+3v}{3+v} r^2). \end{aligned} \quad (22)$$

Equations (19) - (22) are used in the courses of elasticity theory to determine the stresses in rotating disks of constant thickness under the quadratic law of temperature distribution along the radius. The authors have proved that these formulas are valid for cylinders of the finite length, as well.

As an example, the stress strain state of a hollow cylinder is calculated applying the proposed method, an approximate solution is given in [30]. The cylinder heated to a temperature of 500 °C is under the action of centrifugal forces and external uniformly distributed load, which is applied with a flat width $b = 0.1$ m along the ring of the cylinder. The inner a_1 and outer a_2 radii of the cylinder are equal to 0.1 m and 0.3 m, respectively; cylinder length is $h = 0.3$ m; material is steel 25 CrMo4 ($E = 179$ GPa, $\nu = 0.356$); material density is $\rho = 0.8 \cdot 10^4$ kg/m³; angular speed of rotation is $\omega = 400$ rad/s; intensity of the external load $P_2 = 64$ MPa.

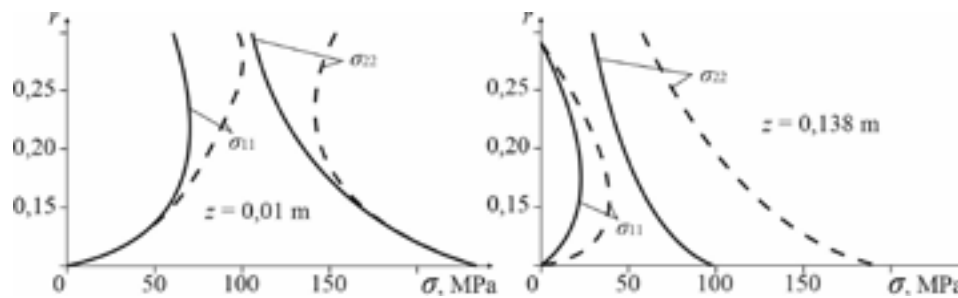
Therefore, for the reason of axial symmetry, to determine the stress strain state, one quarter of the meridional section of the cylinder should be calculated (Figure 3).

Stresses were determined in sections I-I ($z = 0.01$ m) and II-II ($z = 0.138$ m) at radii $r = 0.01$ m, 0.15 m, 0.20 m, 0.25 m and 0.30 m. The calculation results are shown in Table 1.

Based on Equation (19), the stresses were determined in the section I-I. Based on Equation (20), the load $P_1 = 0$ was determined in the section II-II.

Table 1 Stress-strain state of a metal cylinder

$z, \text{ m}; r, \text{ m}$	$\sigma_{11}, \text{ MPa}$		$\sigma_{22}, \text{ MPa}$	
	0.01	0.138	0.01	0.138
0.30	64	0	109	29
0.25	73	12	124	41
0.20	74	20	142	52
0.15	60	20	172	68
0.10	0	0	243	99

**Figure 4** Graphic representations of stress dependences on radial coordinates

According to the obtained results, the developed graphical dependences of the distribution of radial and circular stresses in the sections I-I and II-II (Figure 4) are shown by solid lines. The dashed lines show the stress distribution σ_{11} and σ_{22} according to results of the data calculations in [21].

The graphical images were developed based on the result of calculations performed by the proposed exact method; the graphs were developed based on the results of previous calculations [21]. The comparison of such images and graphs proves that the nature of stress distribution possesses good convergence. The correctness of the analytical dependences deduced by the authors were proved. However, the values of stresses, according to the written formulas, are lower compared to similar stresses calculated in [21]. Thus, for section I-I (Figure 4), stresses at radii $r = 0.10 \text{ m}$ and 0.15 m , which were found by the two methods, coincide; at a radius $r = 0.20 \text{ m}$, the differences are insignificant ($\sigma_{11} - 11\%$, $\sigma_{22} - 4\%$), but at a radius $r = 0.30 \text{ m}$, they are larger ($\sigma_{11} - 36\%$, $\sigma_{22} - 31\%$). In this case, to comply with the boundary conditions on the outer cylindrical surface, the value of the radial stress must be equal to the value of the external uniformly distributed load P_2 , i.e., $\sigma_{11} = P_2 = 64 \text{ MPa}$.

In the proposed method of calculation, the given condition is fulfilled exactly $\sigma_{11} = 64 \text{ MPa}$. In the calculation performed in [21], the accuracy is worse $\sigma_{11} = 100 \text{ MPa}$. This is the reason for the specified difference of stresses calculated on the radius $r = 0.30 \text{ m}$, which is insignificant. The possibility of correct analysis of the thermomechanical behavior of the material of the brake disk hub of the vehicle is proved.

6 Conclusions

The exact solution and the method for determining the stresses allow to conduct a correct analysis of the thermomechanical behavior of the material of the brake disk hub of the vehicle. The study is based on the solution of a three-dimensional problem of the elasticity theory for the case of action of external loads and temperature fields on a metal structure element. An analytical study of changes in the temperature field $\theta = \theta(r, z)$ and deformation of the metal cylinder under the action of the axisymmetric load is proved that effect of such load leads to a change in the temperature field in the material with the emergence of a heat flux.

References

- [1] TIROVIC, M., DAY, A. J. Disc brake interface pressure distributions. *Proceedings of the Institution of Mechanical Engineers, Part D: Journal of Automobile Engineering* [online]. 1991, **205**(2), p. 137-146. ISSN 0954-4070, eISSN 2041-2991. Available from: https://doi.org/10.1243/PIME_PROC_1991_205_162_02
- [2] DAY, A. J., TIROVIC, M., NEWCOMB, T. P. Thermal effects and pressure distributions in brakes. *Proceedings of the Institution of Mechanical Engineers, Part D: Journal of Automobile Engineering* [online]. 1991, **205**(3), p. 199-205. ISSN 0954-4070, eISSN 2041-2991. Available from: https://doi.org/10.1243/PIME_PROC_1991_205_171_02

- [3] TIROVIC, M. Development of a wheel mounted disc brake for a high-speed train. *Proceedings of the Institution of Mechanical Engineers Part F Journal of Rail and Rapid Transit* [online]. 1998, **212**(2), p. 113-121. ISSN 0954-4097, eISSN 2041-3017. Available from: <https://doi.org/10.1243/0954409981530724>
- [4] PUTRA, M. R. A., TJAHAJANA, D. D. D. P. Fractures on braking component and relations to land-based transportation accident. *Procedia Structural Integrity* [online]. 2020, **27**, p. 147-154. ISSN 2452-3216. Available from: <https://doi.org/10.1016/j.prostr.2020.07.020>
- [5] BONIARDI, M., D'ERRICO, F., TAGLIABUE, C., GOTTI, G., PERRICONE, G. Failure analysis of a motorcycle brake disc. *Engineering Failure Analysis* [online]. 2006, **13**(6), p. 933-945. ISSN 1350-6307. Available from: <https://doi.org/10.1016/j.engfailanal.2005.04.012>
- [6] BELHOCINE, A., ABDULLAH, O. I. Design and thermomechanical finite element analysis of frictional contact mechanism on automotive disc brake assembly. *Journal of Failure Analysis and Prevention* [online]. 2020, **20**, p. 270-301. ISSN 1547-7029. Available from: <https://doi.org/10.1007/s11668-020-00831-y>
- [7] MAHMOUDI, T., PARVIZI, A., POURSAEIDI, E., RAHI, A. Thermo-mechanical analysis of functionally graded wheel-mounted brake disk. *Journal of Mechanical Science and Technology* [online]. 2015, **29**, p. 4197-4204. ISSN 1738-494X, eISSN 1976-3824. Available from: <https://doi.org/10.1007/s12206-015-0914-3>
- [8] DOROSHENKO Y., ZAPUKHLIAK, V., GRUDZ, Y., POBEREZHZNY, L., HRYTSANCHUK, A., POPOVYCH, P., SHEVCHUK, O. Numerical simulation of the stress state of an erosion-worn tee of the main gas pipeline. *Archives of Materials Science and Engineering* [online]. 2020, **101**(2), p. 63-78. ISSN 1897-2764. Available from: <https://doi.org/10.5604/01.3001.0014.1192>
- [9] DOROSHENKO, Y., DOROSHENKO, J., ZAPUKHLIAK, V, et al. Modelling computational fluid dynamics of multiphase flows in elbow and T-junction of the main gas pipeline. *Transport* [online]. 2019, **34**(1), p. 19-29. ISSN 1648-4142, eISSN 1648-3480. Available from: <https://doi.org/10.3846/transport.2019.7441>
- [10] MARUSCHAK, P. O., OKIPNYI, I. B., POBEREZHZNYI, L. Y., MARUSCHAK, E. V. Study of heat-resistant steel strain hardening by indentation. *Metallurgist* [online]. 2013, **56**, p. 946-951. Available from: <https://doi.org/10.1007/s11015-013-9680-6>
- [11] POPOVYCH, P., LYASHUK, O., SHEVCHUK, O., TSON, O. P, POBEREZHZNA, L. Y., BORTNYK, I. M. Influence of organic operation environment on corrosion properties of metal structure materials of vehicles. *INMATEH Agricultural Engineering* [online]. 2017, **52**(2), p. 113-118. ISSN 2068-4215, eISSN 2068-2239. Available from: <https://inmateh.eu/volumes/old-volume/volume-52-no-2-2017/article/influence-of-organic-operation-environment-on-corrosion-properties-of-metal-structure-materials-of-vehicles>
- [12] POPOVYCH, P., LYASHUK, O., MUROVANYI, I., DZYURA, V. O., SHEVCHUK, O. S., MYNDYUK, V. D. The service life evaluation of fertilizer spreaders undercarriages. *INMATEH Agricultural Engineering* [online]. 2016, **50**(3), p. 39-46. ISSN 2068-4215, eISSN 2068-2239. Available from: <https://inmateh.eu/volumes/old-volume/volume-50-no-3-2016/article/the-service-life-evaluation-of-fertilizer-spreaders-undercarriages>
- [13] LYTVYNENKO, I. V., MARUSCHAK, P. O., LUPENKO, S. A., POPOVYCH, P. V. Modelling of the ordered surface topography of statically deformed aluminum alloy. *Materials Science* [online]. 2016, **52**, p. 113-122. ISSN 1068-820X, eISSN 1573-885X. Available from: <https://doi.org/10.1007/s11003-016-9933-1>
- [14] BARNA, R. A., POPOV CH, P. V. Influence of operating media on the fatigue fracture of steels for elements of agricultural machines. *Materials Science* [online]. 2014, **50**, p. 377-380. ISSN 1068-820X, eISSN 1573-885X. Available from: <https://doi.org/10.1007/s11003-014-9729-0>
- [15] HEVKO, B. M., DIACHUN, A. Y., LYASHUK, O. L., LIUBACHIVSKYI, R.O. The study of bulk material kinematics in a screw conveyor-mixer, *INMATEH Agricultural Engineering* [online]. 2015, **47**(3), p. 155-162. ISSN 2068-4215, eISSN 2068-2239. Available from: <https://inmateh.eu/volumes/old-volume/volume-47-no-3-2015/article/the-study-of-bulk-material-kinematics-in-a-screw-conveyor-mixer>
- [16] POPOVYCH, P., POBEREZHZNY, L., SHEVCHUK, O., MUROVANYI, I., T. DOVBUSH, T., KOVAL, Y., HRYTSULIAK, H. Evaluation of strength of carrying metal structures of trailers. *Journal of Achievements of Materials and Manufacturing Engineering* [online] 2020, **2**(100), p. 58-69. ISSN 1734-8412. Available from: <https://doi.org/10.5604/01.3001.0014.3345>
- [17] POPOVYCH, P., SHEVCHUK, O., DZYURA, V., POBEREZHZNA, L., DOZORSKYY, V., HRYTSANCHUK, A. Assessment of the influence of corrosive aggressive cargo transportation on vehicle reliability. *International Journal of Engineering Research in Africa* [online] 2018, **38**, p. 17-25. ISSN 1663-3571, eISSN 1663-4144. Available from: <https://doi.org/10.4028/www.scientific.net/JERA.38.17>
- [18] POPOVYCH, P. V., DZYURA, V., SHEVCHUK, O. S. Reliability estimation of transport means elements under the action of cyclic loads and corrosive environment. *International Journal of Automotive and Mechanical Engineering* [online] 2018, **15**(4), p. 5793 -5802. ISSN 2229-8649, eISSN 2180-1606. Available from: <https://doi.org/10.15282/ijame.15.4.2018.6.0443>

- [19] SOKIL, B., LYASHUK, O., SOKIL, M., POPOVICH, P., VOVK, Y., PERENCHUK, O. Dynamic effect of cushion part of wheeled vehicles on their steerability. *International Journal of Automotive and Mechanical Engineering* [online]. 2018, **15**(1), p. 4880-4892. ISSN 2229-8649, eISSN 2180-1606. Available from: <https://doi.org/10.15282/ijame.15.1.2018.1.0380>
- [20] POPOVYCH, P., POBEREZHZNY, L., SHEVCHUK, O., MUROVANYI, I., POBEREZHZNA, L., HRYTSANCHUK, A., KOVAL, Y. Corrosion-fatigue failure of tractor trailers metal materials in aggressive environments. *Koroze a Ochrana Materialu* [online]. 2020, **64**(2), p. 45-51. eISSN 1804-1213. Available from: <https://doi.org/10.2478/kom-2020-0007>
- [21] JIAN, Q., SHUI, Y. Numerical and experimental analysis of transient temperature field of ventilated disc brake under the condition of hard braking. *International Journal of Thermal Sciences* [online]. 2017, **122**, p. 115-123. ISSN 1290-0729. Available from: <https://doi.org/10.1016/j.ijthermalsci.2017.08.013>
- [22] HAN, M. J., LEE, C. H., PARK, T. W., LEE, S. P. Low and high cycle fatigue of automotive brake discs using coupled thermo-mechanical finite element analysis under thermal loading. *Journal of Mechanical Science and Technology* [online]. 2018, **32**(12), p. 5777-5784. ISSN 1738-494X, eISSN 1976-3824. Available from: <https://doi.org/10.1007/s12206-018-1125-5>
- [23] THOMSEN, J. J. *Vibrations and stability: advanced theory, analysis, and tools* [online]. Berlin, Heidelberg: Springer Science and Business Media, 2003. ISBN 978-3-662-10793-5. Available from: <https://doi.org/10.1007/978-3-662-10793-5>
- [24] HORGAN, C. O., CHAN, A. M. The pressurized hollow cylinder or disk problem for functionally graded isotropic linearly elastic materials. *Journal of Elasticity* [online]. 1999, **55**(1), p. 43-59. ISSN 0374-3535, eISSN 1573-2681. Available from: <https://doi.org/10.1023/A:1007625401963>
- [25] LEPIKHIN, P. P., ROMASHCHENKO, V. A., BEINER, STOROZHUK, V. N., BABICH, Y. N., BAKHTINA, E. V. A program for numerical calculation of dynamic stress-strain state and strength of hollow multilayer anisotropic cylinders and spheres. Part 1. Program description. *Strength of Materials* [online]. 2015, **47**(2), p. 249-256. ISSN 0039-2316, eISSN 1573-9325. Available from: <https://doi.org/10.1007/s11223-015-9655-x>
- [26] PARKUS, H. *Thermoelasticity* [online]. Vienna: Springer Science and Business Media, 2012. ISBN 978-3-7091-8447-9. Available from: <https://doi.org/10.1007/978-3-7091-8447-9>
- [27] KUMAR, R., NARWARIY, A. M. Failure analysis and design of disc in two wheeler. *International Journal for Research in Applied Science and Engineering Technology* [online]. **8**(II), p. 782-789. ISSN 2321-9653. Available from: <http://doi.org/10.22214/ijraset.2020.2120>
- [28] TYMOSHENKO, S. P., GOODIER, J. N. *Theory of elasticity*. New-York: McGraw - Hil, 1970. ISBN 978-0070701229.
- [29] TIMOSHENKO, S. P., GERE, J. M. *Theory of elastic stability*. Courier Corporation, 2009. ISBN 978-0070647206.
- [30] ATANACKOVIC, T. M., GURAN, A. *Theory of elasticity for scientists and engineers*. Boston, MA: Birkhauser, 2000. ISBN 978-1-4612-1330-7. Available from: <https://doi.org/10.1007/978-1-4612-1330-7>
- [31] KASSNER, M. E. *Fundamentals of creep in metals and alloys*. Butterworth-Heinemann, 2015. ISBN 978-0080994277.

DYNAMIC MODELLING OF PISTON THE MOTION IN COMBUSTION ENGINES

Sunny Narayan^{1,*}, Shitu Abubakar², Muhammad Usman Kaisan², Hauwa Ndagi², Yunusa Tukur³, Ivan Grujić⁴, Nadica Stojanović⁴

¹Mechanical Engineering Department, Qassim University, Burydah, Saudi Arabia

²Mechanical Engineering Department, Ahmadu Bello University, Zaria, Nigeria

³Department of Energy Planning and Analyses, Energy Commission of Nigeria, Abuja, Nigeria

⁴Department of Motor Vehicles and Motors, University of Kragujevac, Kragujevac, Serbia

*E-mail of corresponding author: rarekv@gmail.com

Resume

The presented work discusses a methodology for analysis of noise emissions from a diesel engine. A numerical model of the piston motion, analyzing its lateral, reciprocating and rotation motion, has been presented in order to investigate the lateral motion of the piston skirt assembly and resulting vibrations induced as a result of these motions in the engine block. Various parameters of modal analysis were obtained using the mobility analysis. The presented methodology was validated by data obtained from a diesel engine test set up. The predicted results matched well with those of measured data, hence validating the presented scheme.

Article info

Received 17 March 2021

Accepted 2 June 2021

Online 30 September 2021

Keywords:

acoustics,
vibrations,
noise,
piston motion

Available online: <https://doi.org/10.26552/com.C.2022.1.B9-B19>

ISSN 1335-4205 (print version)

ISSN 2585-7878 (online version)

1 Introduction

In combustion engines a lateral space is present between the skirt and a cylinder liner that gives a motion freedom in lateral direction during the engine operation [1]. The existence of this gap puts a limit on magnitude of piston motion [2]. The piston assembly contributes to about 30-40% of mechanical losses and hence its design is a major concern for automotive engineers [3-4]. The piston thrusts liner to other side due to changing in direction of side thrust force due to motion of a connecting rod [5-6].

A dynamic model of the crank slider mechanism has been presented by Flores et al. [2]. The existence of lateral gap makes the system nonlinear and chaotic in nature. The reaction force between the liner and a skirt also plays an important role in dynamics of motion. As the coefficient of restitution decreases, the motion transforms from bouncing to a periodic one [7-8].

McFadden and Turnbull analyzed effects of combustion gas pressure on primary motion of a piston [9]. A two degree of freedom system has been analyzed showing a correlation between the piston slap and resulting vibrations [10-16]. Various parameters affecting

piston motion has been considered, which includes location of a center of gravity [17], profile of a skirt [18-19], effects of inertial forces [20-21], frictional forces [22] and lubricating oil [23]. Mounted accelerometers on the block surface were used to simulate the piston's secondary motion [5].

2 Piston assembly model

The secondary motion of a skirt for the case of a 240 cc engine was modeled as depicted in Figure 1. The piston was considered as a point mass of 0.363 kg (m_p) and inertia (I_p) of 7.8540×10^{-9} kg·m² having two degree of freedom in motion (X_p, θ). The cylinder block was considered as a lumped mass of 48.5 kg (m_b) with a single degree of freedom X_b , as shown in equation (1).

The nominal clearance of 0.5 mm allows the piston assembly to move in the lateral direction, as well as to rotate about the piston pin. The clearance between the skirt and a liner X_c was modeled as a mechanical stop in lateral direction.

For condition of no impact, ($X_p - X_b = X_c$) the motion was governed by Equation (1).

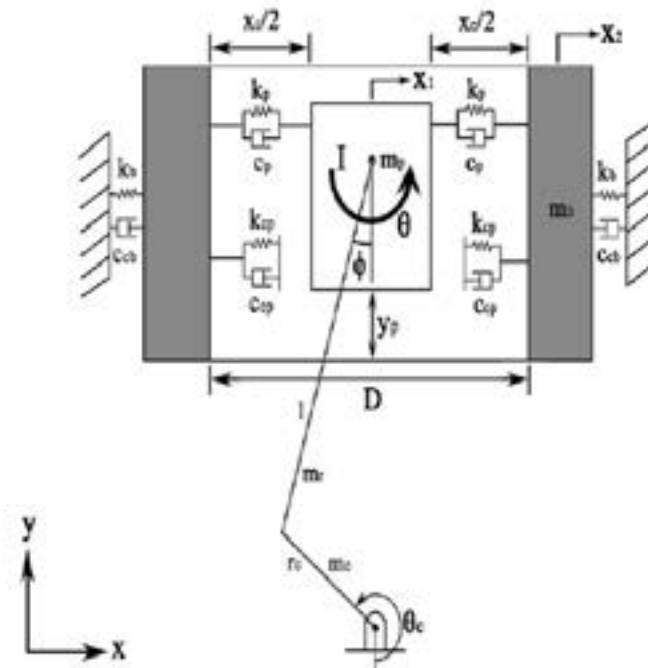


Figure 1 Numerical model of the piston motion

$$\begin{pmatrix} m_p & 0 & 0 \\ 0 & m_b & 0 \\ 0 & 0 & I_p \end{pmatrix} \begin{pmatrix} \ddot{X}_b^* \\ \ddot{X}_b^* \\ \ddot{\theta}^* \end{pmatrix} + \begin{pmatrix} C_p & -C_p & 0 \\ -C_p & C_p + C_b & 0 \\ 0 & 0 & C_\theta \end{pmatrix} \begin{pmatrix} \dot{X}_b^* \\ \dot{X}_b^* \\ \dot{\theta}^* \end{pmatrix} + \begin{pmatrix} k_p & -k_b & 0 \\ -k_p & k_p + k_b & 0 \\ 0 & 0 & k_\theta \end{pmatrix} \begin{pmatrix} X_b^* \\ X_b^* \\ \theta \end{pmatrix} = \begin{pmatrix} F_x \\ 0 \\ M_z \end{pmatrix} \quad (1)$$

3 Piston side thrust force

The major issue, affecting this lateral motion of a skirt, is the side thrust force (F_x) imparted to skirt by a connecting rod, as shown in Figure 2.

The frictional forces act between the piston skirt and a cylinder liner (F_f) as well as between the rings and a liner (F_{fr}). The force exerted by the connecting rod on piston pin was resolved along X (F_{rodX}), as well as Y axis (F_{rodY}). The side thrust force (F_x) takes into consideration both inertial forces as well as gas forces (F_g) [21-24].

$$F_x = [F_g - m_p r \omega^2 [\cos(\theta) + K \cos(2\theta)]] \lambda, \quad (2)$$

where: m_p - mass of piston,
 θ - crank angle,
 ω - angular speed,
 r - crank radius,
 K - crank radius-connecting rod length ratio,
 $\lambda = K \cos(\theta) / \sqrt{1 + \sin^2(\theta)}$.

4 Piston frictional force

Various friction forces play a predominant role in the total mechanical loss of an engine [25-26]. According to Zweiri et al. [27], frictional force between the rings

and a liner can be obtained from the product of elastic tension and the coefficient of frictional force. As the speed of engine increases, the coefficient of friction decreases gradually until reaching the minimum at the mid stroke. The frictional forces between the liner and a skirt (F_f) and piston rings and liner (F_{fr}) may be expressed in terms of the sliding velocity of a piston (V), nominal clearance (h), lubricating oil viscosity (μ), number of piston rings (n) and the shear area of a contact (A_s) as [27-57]:

$$F_f = \mu V A_{s1} / h, \quad (3)$$

$$F_{fr} = n \mu V A_{s2} / h, \quad (4)$$

where A_{s1} is the shear contact area between the liner and a skirt and A_{s2} is the shear contact area between the liner and rings.

5 Mobility parameter determination

The mobility may be defined as the ratio of velocity response $V(J\omega)$ of a structure to exciting force $F(J\omega)$ acting on a structure [5]:

$$M(J\omega) = V(J\omega) / F(J\omega), \quad (5)$$

$$M(J\omega) = -J\omega / (K - M\omega^2 + JC\omega) / M\omega^2 (K + JC\omega), \quad (6)$$

In the frequency range below the first anti resonance frequency value ($\omega_a = K/m$), the point mobility equation can be approximated as [5, 31-32]:

$$M(J\omega) = -J / m\omega_a. \quad (7)$$

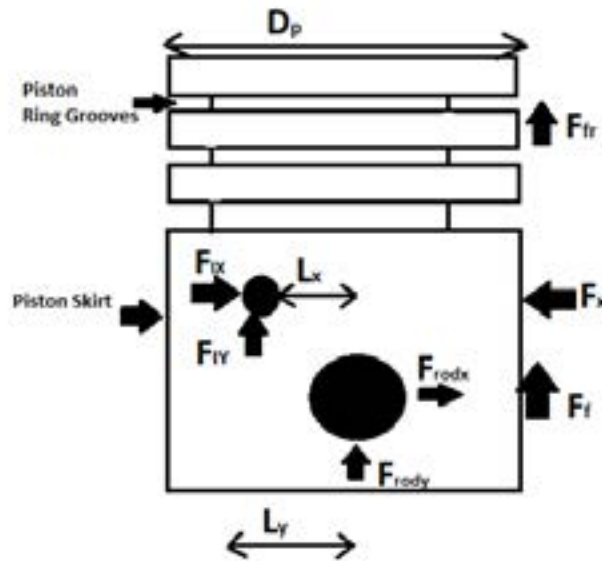


Figure 2 Force diagram of the piston skirt assembly

Above the anti resonance frequency, the point mobility can be written as :

$$M(j\omega) = -j\omega_s/K. \tag{8}$$

6 Experimental setup

Tests were done on a single cylinder HARTZ engine having specifications as presented in Table 1.

The in-cylinder pressure was monitored by an AVL transducer, having specifications shown in Table 2. Block vibrations were measured by means of an Endveco7240C type Mono axial accelerometer, having features accelerometer are presented in Table 3.

Various engine testing speeds in rpm (Revolutions

per minute)-(2000 rpm and 3000 rpm) and load values (80% and 100%) were chosen with an aim to cover complete engine operational conditions. The data recorded during each test was under steady state conditions as seen in Table 4.

Figure 3 shows the general layout of the test rig with placement of various sensors.

7 Results and discussions

Figures 4 and 5 depict variations of the piston side thrust force. This force changes its direction five times in a complete engine cycle indicating five possible instances of lateral contact of the skirt with a liner.

COMSOL 7 multi physics software was used to

Table 1 Engine specifications

Type	Diesel Engine
Make	HARTZ
Number of cylinders	1
Bore	69 mm
Stroke	65 mm
Displacement	0.243 liter
Compression	22:1
Maximum power	3.5kW @ 4400 rpm
Maximum torque	10N-m @ 2000 rpm

Table 2 Pressure transducer specifications

Range	0-250 Bar
Sensitivity	20 pC/Bar
Resonance Frequency	160 kHz

Table 3 Accelerometer specifications

Range	1000 g
Sensitivity	3 pC/g
Resonance Frequency	90 kHz

Table 4 Testing specifications

Case	rpm	Load	P _{injection} (Bar)
1	2000	80%	716
2	2000	100%	692
3	3000	80%	814
4	3000	100%	612
5	3000	-	512

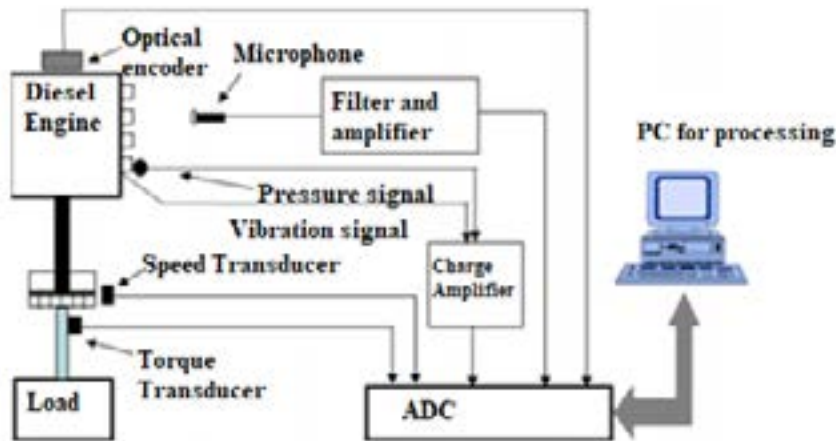


Figure 3 Experimental setup

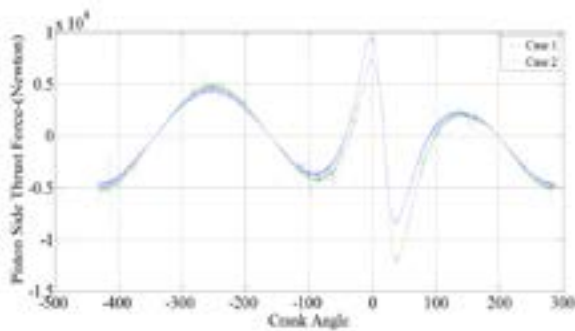


Figure 4 Variations of the piston side thrust force (2000 rpm)

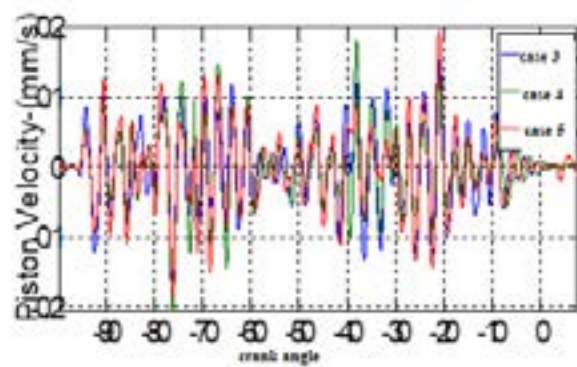


Figure 7 Variations of the piston velocity (3000 rpm)

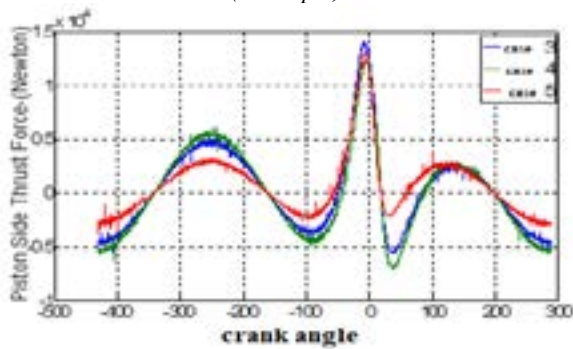


Figure 5 Variations of the piston side thrust force (3000 rpm)

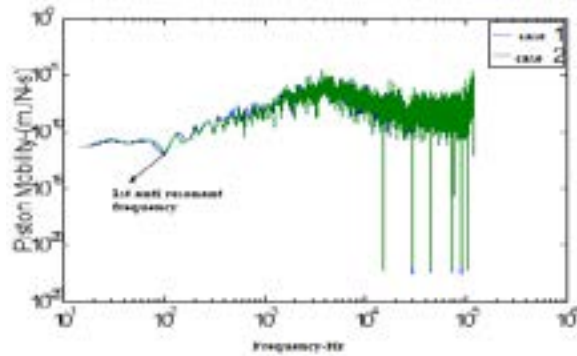


Figure 8 Variations of the piston mobility (2000 rpm)

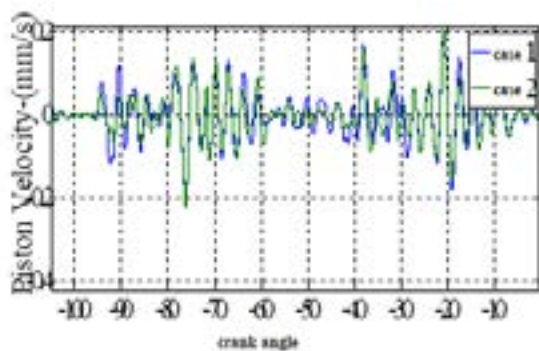


Figure 6 Variations of the piston velocity (2000 rpm)

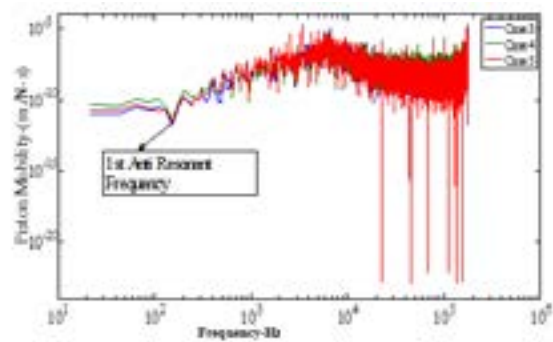


Figure 9 Variations of the piston mobility (3000 rpm)

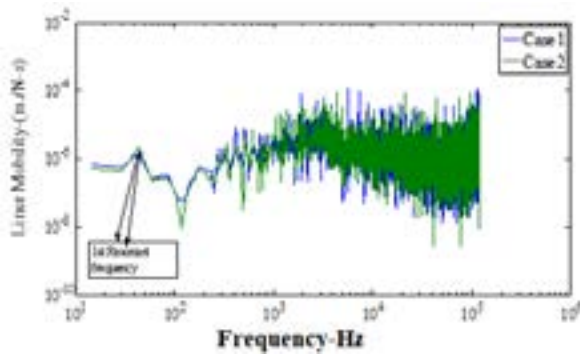


Figure 10 Variations of the piston mobility (2000 rpm)

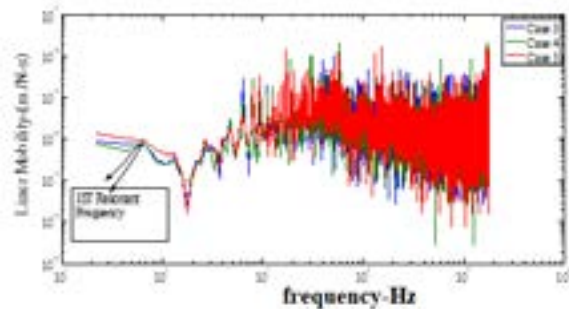


Figure 11 Variations of the piston mobility (3000 rpm)

Table 5 Dynamic features of a system

Test case	Piston parameter	Liner parameter
1	ω_a 100 Hz	ω_a 39 Hz
	C_p 109330 (kg/s)	C_b 42884 (kg/s)
	K_p 174 (kg/s ²)	K_b 175 (kg/s ²)
	m_p 174 (kg)	m_b 175 (kg)
	ω_a 100 Hz	ω_a 39 Hz
2	C_p 109330 (kg/s)	C_b 109330 (kg/s)
	K_p 174 (kg/s ²)	K_b 174 (kg/s ²)
	m_p 174 (kg)	m_b 174 (kg)
	ω_a 158 Hz	ω_a 63 Hz
	C_p 172750 (kg/s)	C_b 69669 (kg/s)
3	K_p 174 (kg/s ²)	K_b 175 (kg/s ²)
	m_p 174 (kg)	m_b 176 (kg)
	ω_a 158 Hz	ω_a 63 Hz
	C_p 109330 (kg/s)	C_b 109330 (kg/s)
	K_p 174 (kg/s ²)	K_b 174 (kg/s ²)
4	m_p 174 (kg)	m_b 174 (kg)
	ω_a 158 Hz	ω_a 63 Hz
	C_p 172750 (kg/s)	C_b 69669 (kg/s)
	K_p 174 (kg/s ²)	K_b 175 (kg/s ²)
	m_p 174 (kg)	m_b 176 (kg)
5	ω_a 158 Hz	ω_a 63 Hz
	C_p 172750 (kg/s)	C_b 69669 (kg/s)
	K_p 174 (kg/s ²)	K_b 175 (kg/s ²)
	m_p 174 (kg)	m_b 176 (kg)

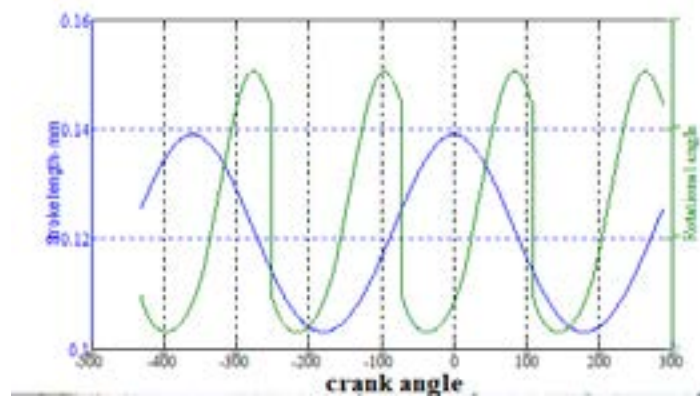


Figure 12 Variations of the rotation motion of a skirt (Case 1)

simulate the piston velocity for given testing conditions, as shown in Figures 6 and 7.

Using Equation (6), the mobility was computed, e as seen in Figures 8 and 9.

Similarly, the Mobility of a r cylinder block was computed using integration of accelerometer data as shown in Figures 10 and ,11.

Using the concept of anti-resonant frequency(ω_a), as discussed in previous section, various dynamic parameters of the liner-piston were computed for the given test conditions (Table 4), as seen in Table 5.

During the motion simulation, the bottom dead center positions (BDC) was taken as a reference point. The initial location of a piston is set at 0mm as the bottom boundary of liner and the upper boundary of the cylinder liner is set at 0.5mm, which is a clearance between the skirt and a liner.

As seen from Figure 12, the piston tilting angle

changes its direction at both dead centers. In order to visualize the pistons secondary motion during the reciprocating motion, the piston secondary motion is represented in a graphical form and the piston lateral motion and rotating motion are normalized to the piston stroke position, based on the reciprocating motion of a piston, as shown in Figure 13.

It is evident from the plot that the piston remains at the lower boundary cylinder liner for a longer time, as compared to the upper boundary of a cylinder wall. In addition, the piston is predicted to slide for a crank angle of 100 ° before the TDC along the cylinder liner (Figure 13).

Figure 14 shows the measured vibratory response of the cylinder block in the vibration amplitudes, as captured by accelerometer. The vibration of the cylinder decays after the first impact of the piston on the upper boundary of a liner. The vibration is induced once

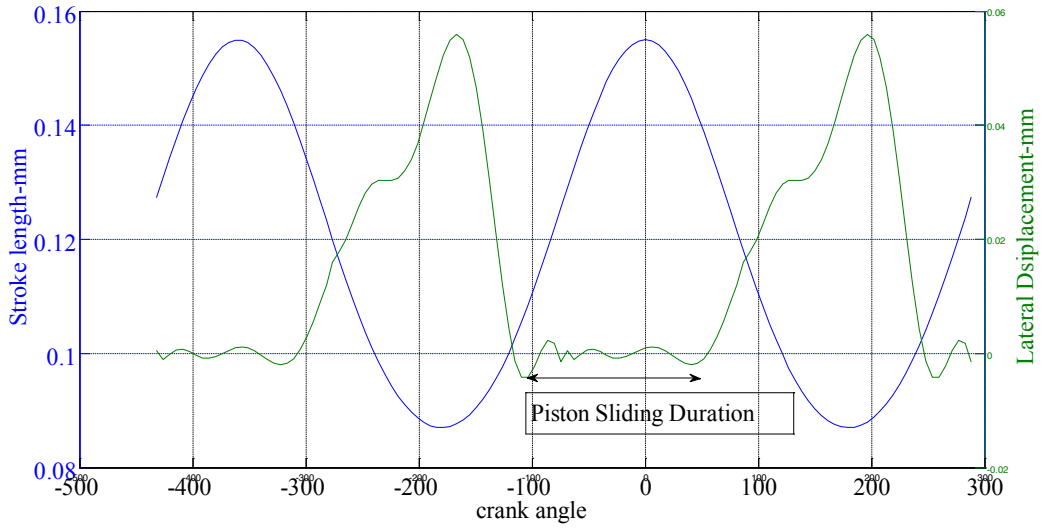


Figure 13 The piston's secondary motion (Case 1)

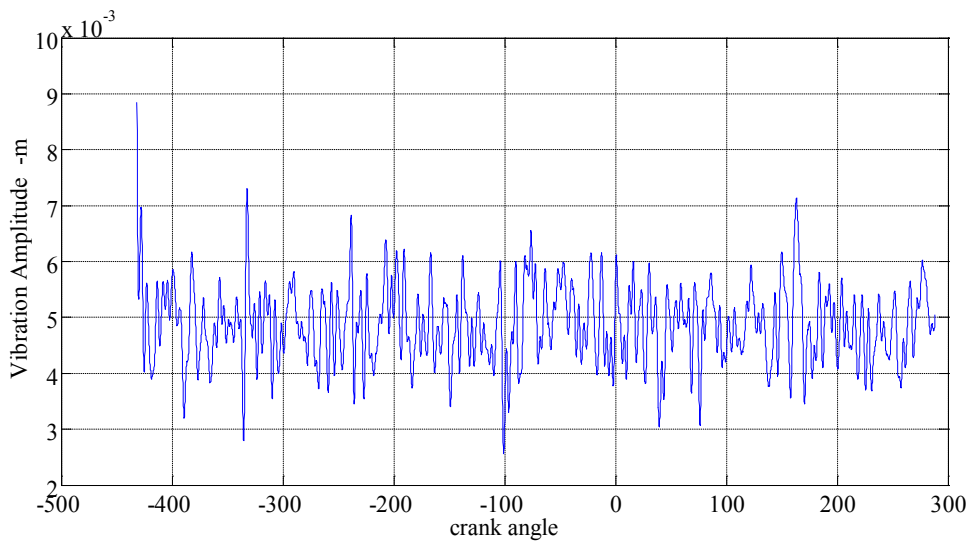


Figure 14 Vibration response of the engine block (Case 1)

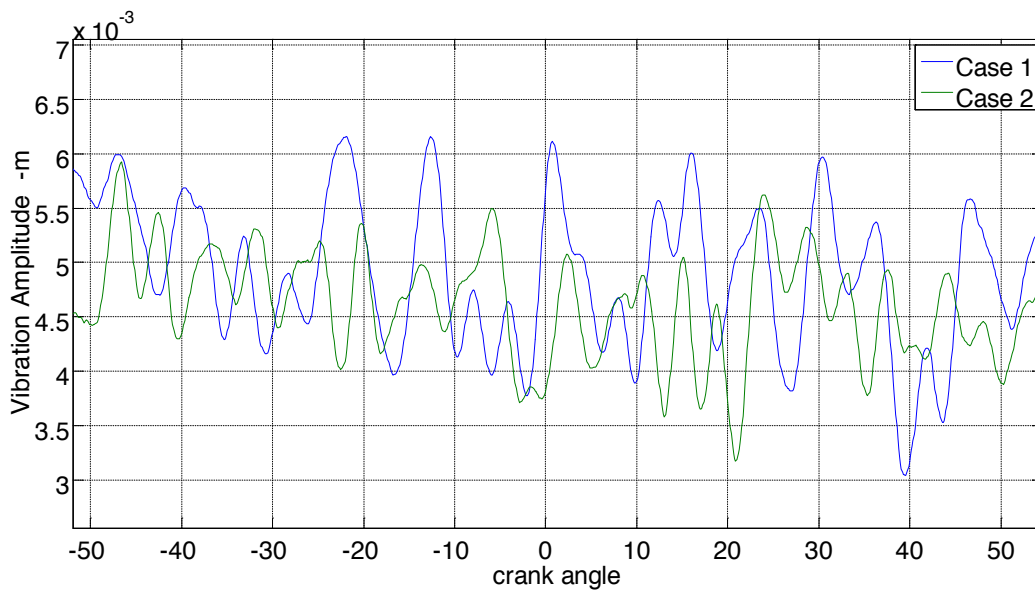


Figure 15 Effects of variations of the engine speed on engine block vibrations (2000 rpm)

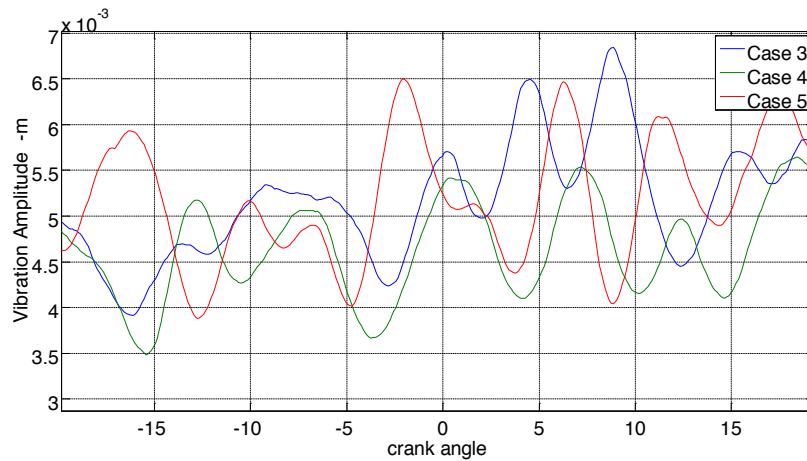


Figure 16 Effects of variations of the engine speed on block vibrations (3000 rpm)

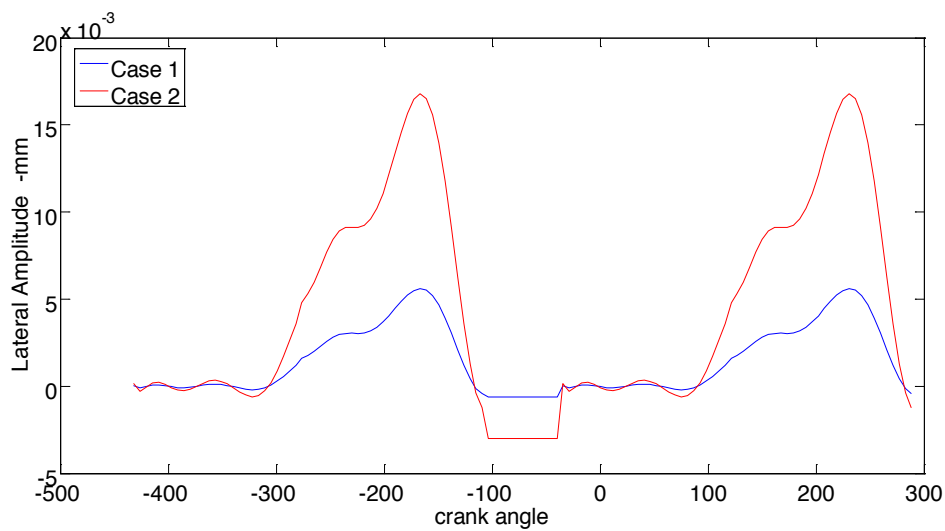


Figure 17 Effects of variations of the engine speed on the secondary motion of a skirt (2000 rpm)

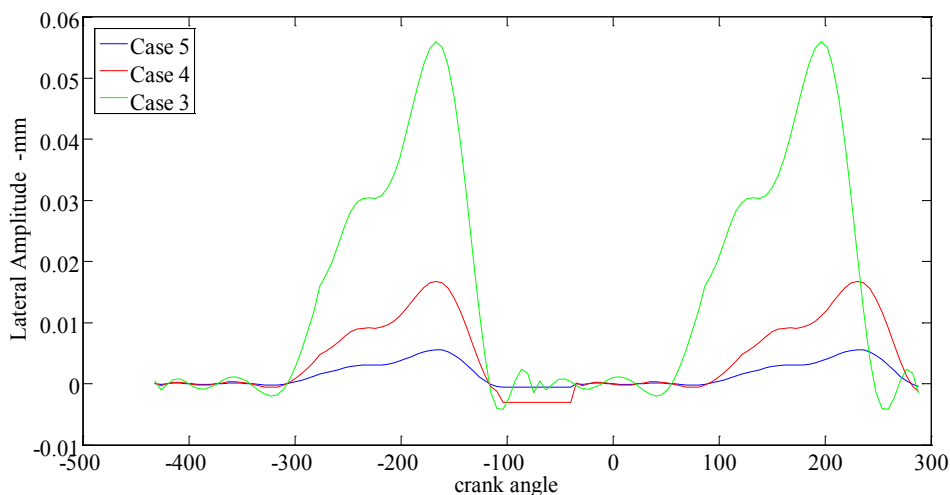


Figure 18 Effects of variations of the engine speed on the secondary motion of a skirt (3000 rpm)

again when the piston impacts lower cylinder liner. The induced vibrations had an amplitude of order of 7×10^{-3} m. As the engine operating speed increases, the piston side thrust force, which is a function of the engine rotating speed, increases. An increase in the side thrust

force, acting on the piston, results in the piston bouncing off the cylinder liner more frequently at higher speeds, as seen from Figures 15 and 16.

The induced vibrations of a block also increase with engine speed. The sliding duration also falls with

an increase in velocity as shown in Figures 17 and 18. This is due to the higher impact force and acceleration generated during the piston slap and the reaction impact force from a liner acting on the skirt increases. At the lower engine speeds, the vibration response of the cylinder block induced by the first slap of a piston has a longer duration to decay before the second slap occurs. However, with the speed increase, the vibration response of a block has the shorter duration of decay and response from the second slap is combined with the first one.

8 Conclusions

A lumped system model was discussed in the present paper. Various dynamic parameters of a system were calculated, using the concept of mobility, which were later used to simulate the lateral motion of a piston, as well as the resulting engine block vibrations.

Values of the first resonance frequencies of both the skirt and a liner were found to be in 100 Hz-160 Hz range and it remains unaffected by variations in the engine operational conditions. Several peaks were found in the simulated block vibrations, which were related to impacts of a skirt with liner. The COMSOL-7 software was then used to analyze the tilting motion of a piston, which showed a good match with that simulated by solving dynamic equations of motion. Effects of load and speed on lateral motion of piston skirt were also investigated. The piston skirt was also found to slide along a liner a few crank angle degrees before the TDC position. This sliding motion was less dominant during the power stroke as the bouncing motion dominates the dynamic motion of a skirt. The duration of sliding motion of a piston along the liner was observed to decrease with increase in load and speed conditions, which is in agreement with previous available literature.

References

- [1] WANNATONG, K., CHANCHAONA, S., SANITJAI, S. Simulation algorithm for piston ring dynamics. *Simulation Modelling Practice and Theory* [online]. 2008, **16**(1), p. 127-146. ISSN 1569-190X. Available from: <https://doi.org/10.1016/j.simpat.2007.11.004>
- [2] FLORES, P., AMBROSIO, A., CLARO, J., LANKARANI, H. Translational joints with clearance in rigid multibody systems. *Journal of Computational and Nonlinear Dynamics* [online]. 2008, **3**(1), 011007. ISSN 1555-1415, eISSN 1555-1423. Available from: <https://doi.org/10.1115/1.2802113>
- [3] HAN, D.-CH., LEE, J.-S. Analysis of the piston ring lubrication with a new boundary condition. *Tribology International* [online]. 1998, **31**, p. 753-760. ISSN 0301-679X. Available from: [https://doi.org/10.1016/S0301-679X\(98\)00096-6](https://doi.org/10.1016/S0301-679X(98)00096-6)
- [4] RAHNEJAT, H., BALAKRISHNAN, S., KING, P., HOWELL-SMITH, S. In-cylinder friction reduction using a surface finish optimization technique. *Proceedings of the Institution of Mechanical Engineers, Part D: Journal of Automobile Engineering* [online]. 2006, **220**(9), p. 1309-1318. ISSN 0954-4070, eISSN 2041-2991. Available from: <https://doi.org/10.1243/09544070JAUTO282>
- [5] CHO, S. H., AHN, S. T., KIM, Y. H. A simple model to estimate the impact force induced by piston slap. *Journal of Sound and Vibration* [online]. 2002, **255**(2), p. 229-242. ISSN 0022-460X. Available from: <https://doi.org/10.1006/jsvi.2001.4152>
- [6] ZHANG, Z., XIE, Y., ZHANG, X., MENG, X. Analysis of piston secondary motion considering the variation in the system inertia. *Proceedings of the Institution of Mechanical Engineers, Part D: Journal of Automobile Engineering* [online]. 2009, **223**(4), p. 549-563. ISSN 0954-4070, eISSN 2041-2991. Available from: <https://doi.org/10.1243/09544070JAUTO1078>
- [7] FLORES, P., LEINE, R., GLOCKER, C. Modeling and analysis of planar rigid multibody systems with translational clearance joints based on the non-smooth dynamics approach. *Multibody System Dynamics* [online]. 2010, **23**, p. 165-190. ISSN 1384-5640, eISSN 1573-272X. Available from: <https://doi.org/10.1007/s11044-009-9178-y>
- [8] FARAHANCHI, F., SHAW, S. W. Chaotic and periodic dynamics of a slider-crank mechanism with slider clearance. *Journal of Sound and Vibration* [online]. 1994, **177**(3), p. 307-324. ISSN 0022-460X. Available from: <https://doi.org/10.1006/jsvi.1994.1436>
- [9] MCFADDEN, P., TURNBULL, S. Dynamic analysis of piston secondary motion in an internal combustion engine under non-lubricated and fully flooded lubricated conditions. *Proceedings of the Institution of Mechanical Engineers, Part C: Journal of Mechanical Engineering Science* [online]. 2011, **225**(11), p. 2575-2585. ISSN 0954-4062, eISSN 2041-2983. Available from: <https://doi.org/10.1177/0954406211408674>
- [10] GENG, Z., CHEN, J. Investigation into piston-slap-induced vibration for engine condition simulation and monitoring. *Journal of Sound and Vibration* [online]. 2005, **282**(3-5), p. 735-751. ISSN 0022-460X. Available from: <https://doi.org/10.1016/j.jsv.2004.03.057>
- [11] OFFNER, G., HERBST, H. M., PRIEBSCHE, H. H. A methodology to simulate piston secondary movement under lubricated contact conditions. In: SAE 2001 World Congress: proceedings [online]. USA: SAE International, 2001.

- ISSN 0148-7191, eISSN 2688-3627, technical paper 2001-01-0565. Available from: <https://doi.org/10.4271/2001-01-0565>
- [12] LIU, K., XIE, Y., GUI, C. A comprehensive study of the friction and dynamic motion of the piston assembly. *Proceedings of the Institution of Mechanical Engineers, Part J: Journal of Engineering Tribology* [online]. 1998, **212**(3), p. 221-226. ISSN 1350-6501, eISSN 2041-305X. Available from: <https://doi.org/10.1243/1350650981542038>
- [13] KIM, T. J. Numerical analysis of the piston secondary dynamics in reciprocating compressors. *Journal of Mechanical Science and Technology*. 2003, **17**(3), p. 350-356. ISSN 1738-494X, eISSN 1976-3824.
- [14] RUGGIERO, A., SENATORE, A. Computer model for the prediction of the impact force induced by piston slap in internal combustion engines, *The Annals of the University Dunarea de Jos of Galati, Fascicle VIII: Tribology* [online]. 2003, **2003**, p. 129-134. ISSN 1221-4590.
- [15] DESAI, H. Computer aided kinematic and dynamic analysis of a horizontal slider crank mechanism used for single-cylinder four stroke internal combustion engine. In: World Congress on Engineering WCE 2009: proceedings [online]. Vol. II. 2009. ISBN 978-988-18210-1-0, p. 1-3.
- [16] WILSON, R., FAWCETT, J. N. Dynamics of the slider-crank mechanism with clearance in the sliding bearing. *Mechanism and Machine Theory* [online]. 1974, **9**(1), p. 61-80. ISSN 0094-114X. Available from: [https://doi.org/10.1016/0094-114X\(74\)90008-1](https://doi.org/10.1016/0094-114X(74)90008-1)
- [17] HADDAD, S. D., TJAN, K. T. An analytical study of offset piston and crankshaft designs and the effect of oil film on piston slap excitation in a diesel engine. *Mechanism and Machine Theory* [online]. 1995, **30**(2), p. 271-284. ISSN 0094-114X. Available from: [https://doi.org/10.1016/0094-114X\(94\)00035-J](https://doi.org/10.1016/0094-114X(94)00035-J)
- [18] KOIZUMI, T., TSUJIUCHI, N., OKAMURA, M., TSUKIJIMA, H., KUBOMOTO, I., ISHIDA, E. Reduction of piston slap excitation by optimizing piston profiles. In: SPIE 2002: proceedings [online]. 2002. p. 107-113.
- [19] JANG, S., CHO, J. Effects of skirt profiles on the piston secondary movements by the lubrication behaviors. *International Journal of Automotive Technology*. 2004, **5**(1), p. 23-31. ISSN 1229-9138, eISSN 1976-3832.
- [20] NARAYAN, S. Effects of various parameters on piston secondary motion. In: 18th Asia Pacific Automotive Engineering Conference: proceedings [online]. USA: SAE International, 2015. ISSN 0148-7191, eISSN 2688-3627, technical paper 2015-01-0079. Available from: <https://doi.org/10.4271/2015-01-0079>.
- [21] GUZZOMI, A., HESTERMAN, D., STONE, B. Variable inertia effects of an engine including piston friction and a crank or gudgeon pin offset. *Proceedings of the Institution of Mechanical Engineers, Part D: Journal of Automobile Engineering* [online]. 2008, **222**(3), p. 397-414. ISSN 0954-4070, eISSN 2041-2991. Available from: <https://doi.org/10.1243/09544070JAUTO590>
- [22] GUZZOMI, A., HESTERMAN, D., STONE, B. The effect of piston friction on engine block dynamics. *Proceedings of the Institution of Mechanical Engineers, Part K: Journal of Multi-body Dynamics* [online]. 2007, **221**(2), p. 277-289. ISSN 1464-4193, eISSN 2041-3068. Available from: <https://doi.org/10.1243/14644193JMBD66>
- [23] GERGES, S. N. Y., DE LUCA, J. C., LALOR, N. The influence of cylinder lubrication on piston slap. *Journal of Sound and Vibration* [online]. 2002, **257**(3), p. 527-557. ISSN 0022-460X. Available from: <https://doi.org/10.1006/jsvi.2002.5051>
- [24] TAN, Y. C., RIPIN, Z. Technique of measuring piston secondary motion using laser displacement sensors. *Experimental Mechanics* [online]. 2012, **52**, p. 1447-1459. ISSN 0014-4851. Available from: <https://doi.org/10.1007/s11340-012-9600-x>
- [25] COMFORT, A. An introduction to heavy-duty diesel engine frictional losses and lubricant properties affecting fuel economy - Part I. SAE International [online]. 2003, 2003-01-3225. ISSN 0148-7191, eISSN 2688-3627. Available from: <https://doi.org/10.4271/2003-01-3225>
- [26] TAYLOR, R., COY, R. Improved fuel efficiency by lubricant design: A review. *Proceedings of the Institution of Mechanical Engineers: Part J: Journal of Engineering Tribology* [online]. 2000, **214**(1), p. 1-15. ISSN 1350-6501, eISSN 2041-305X. Available from: <https://doi.org/10.1177/135065010021400101>
- [27] ZWEIRI, Y., WHIDBORNE, J., SENEVIRATNE, L. Instantaneous friction components model for transient engine operation. *Proceedings of the Institution of Mechanical Engineers: Part D: Journal of Automobile Engineering* [online]. 2002, **214**, p. 809-824. ISSN 0954-4070, eISSN 2041-2991. Available from: <https://doi.org/10.1243/0954407001527664>
- [28] TAN, Y. C., RIPIN, Z. M. Frictional behavior of piston rings of small utility two-stroke engine under secondary motion of piston. *Tribology International* [online]. 2011, **44**(5), p. 592-602. ISSN 0301-679X. Available from: <https://doi.org/10.1016/j.triboint.2010.12.009>
- [29] SHI, X., POLYCARPOU, A. A. Measurement and modeling of normal contact stiffness and contact damping at the meso scale. *Journal of Vibration and Acoustics* [online]. 2005, **127**(1), p. 52-60. ISSN 1048-9002, eISSN 1528-8927. Available from: <https://doi.org/10.1115/1.1857920>
- [30] CAWLEY, P., CLAYTON, D. A vibration technique for the measurement of contact stiffness. *Mechanical Systems and Signal Processing* [online]. 1987, **1**(3), p. 273-283. ISSN 0888-3270. Available from: [https://doi.org/10.1016/0888-3270\(87\)90104-X](https://doi.org/10.1016/0888-3270(87)90104-X)

- [31] HIXSON, E. L. Mechanical impedance. In: *Harris' shock and vibration handbook*. HARRS, C. M., PIERSOL, A. G. (eds). New York: McGraw-Hill, 1988. ISBN 0-07-137081-1.
- [32] HYNNA, P. *Mechanical mobility technique* [online]. Research report no. BVAL37-021228. Espoo: VTT Technical Research Centre of Finland, 2002. Available from: <http://www.vtt.fi/inf/julkaisut/muut/2002/BVAL37-021228.pdf>
- [33] MITTLER, R., MIERBACH, A., RICHARDSON, D. Understanding the fundamentals of piston ring axial motion and twist and the effects on blow-by. In: ASME 2009 Internal Combustion Engine Division Spring Technical Conference: proceedings [online]. 2009, ICES2009:76080. ISBN 978-0-7918-4340-6, p. 721-735. Available from: <https://doi.org/10.1115/ICES2009-76080>
- [34] TAKIGUCHI, M., ANDO, H., TAKIMOTO, T., URATSUKA, A. Characteristics of friction and lubrication of two-ring piston. *JSAE Review* [online]. 1996, **17**(1), p. 11-16. ISSN 0389-4304. Available from: [https://doi.org/10.1016/0389-4304\(95\)00050-X](https://doi.org/10.1016/0389-4304(95)00050-X)
- [35] XIAO, S., YAN, F., LU, CH., LU, Z. Optimization design of piston structure for abnormal noise control in a single-cylinder gasoline engine. *Advances in Mechanical Engineering* [online]. 2018, **10**, p. 1-16. ISSN 1687-8140, eISSN 1687-8140. Available from: <https://doi.org/10.1177/1687814018769407>
- [36] NARAYAN, S., GUPTA, V. Numerical analysis of secondary motion of piston skirt in engines. *International Journal of Acoustics and Vibrations*. 2018, **23**(4), p. 557-565. ISSN 1027-5851, eISSN 2415-1408.
- [37] NARAYAN, S. Analysis of piston slap motion. *International Journal of Applied Mechanics and Engineering* [online]. 2015, **20**(2), p. 445-450. eISSN 2353-9003. Available from: <https://doi.org/10.1515/ijame-2015-0030>
- [38] NARAYAN, S. Piston slap noise in engines. *International Journal of Applied Engineering Research*. 2015, **8**(14), p. 1695-1700. ISSN 0973-4562, eISSN 0973-9769.
- [39] MAHROOGI, F., NARAYAN, S. Dynamic-analysis-of-piston-secondary-motion-using FEM method. In: 26th International Congress on Sound and Vibration: proceedings. 2019. ISSN 2329-3675, ISBN 978-1-9991810-0-0.
- [40] KAISAN, M. U., YUSUF, L. O., IBRAHIM, I. U., ABUBAKAR, S., NARAYAN, S. Effects of propanol and camphor blends on emissions and performance of a spark ignition engine. *American Chemical Society (ACS) Omega* [online]. 2020, **5**(41), p. 26454-26462. ISSN 2470-1343. Available from: <https://doi.org/10.1021/acsomega.0c02953>
- [41] GRUJIC, I., STOJANOVIC, N., PESIC, R., DAVINIC, A., NARAYAN, S. Numerical analysis of IC engine operation with high pressure hydrogen injections. *Transactions of FAMENA* [online]. 2020, **44**(1), p. 55-56. ISSN 1333-1124, ISSN 1849-1391. Available from: <https://doi.org/10.21278/TOF.44105>
- [42] MAHROOGI, F. O., NARAYAN, S. A recent review of hybrid automotive systems in GCC region. *Proceedings of Institute of Mechanical Engineers Part D: Journal of Automotive Engineering* [online]. 2019, **233**(14), p. 1393-1402. ISSN 0954-4070, eISSN 2041-2991. Available from: <https://doi.org/10.1177/0954407019836055>
- [43] ABUBAKAR, S., ANAFI, F. O., KAISAN, M. U., NARAYAN, S., UMAR, S., UMAR, U. A. Comparative analysis of experimental and simulated performance of a mixed mode solar dryer. *Proceedings of Institute of Mechanical Engineers Part C: Journal of Mechanical Engineering* [online]. 2019, **234**(7), p. ISSN 0954-4062, eISSN 2041-2983. Available from: <https://doi.org/10.1177/0954406219893394>
- [44] KAISAN, M. U., ABUBAKAR, S., ASHOK, B., BALASUBRAMANIAN, D., NARAYAN, S., GRUJIC, I., STOJANOVIC, N. Comparative analyses of biodiesel produced from Jatropha and neem seed oil using a gas chromatography mass spectroscopy technique. *Biofuels* [online]. 2018, latest articles. ISSN 1759-7269, eISSN 1759-7277. Available from: <https://doi.org/10.1080/17597269.2018.1537206>
- [45] NARAYAN, S. A review of diesel engine acoustics. *FME Transactions* [online]. 2014, **42**(2), p. 150-154. ISSN 1451-2092, eISSN 2406-128X. Available from: <https://doi.org/10.5937/fmet1402150N>
- [46] NARAYAN, S., MILOJEVIC, S., GUPTA, V. Combustion monitoring in engines using accelerometer signals. *Journal of Vibroengineering* [online]. 2019, **21**(6), p. 1552-1563. ISSN 1392-8716, eISSN 2538-8460. Available from: <https://doi.org/10.21595/jve.2019.20516>
- [47] MAHROOGI, F. O., NARAYAN, S., GUPTA, V. Acoustic transfer function in gasoline engines. *International Journal of Vehicle Noise and Vibration (IJVNV)* [online]. 2018, **13**(3), p. 270-280. ISSN 1479-1471, eISSN 1479-148X. Available from: <https://doi.org/10.1504/IJVNV.2018.097212>
- [48] NARAYAN, S. Wavelet analysis of diesel engine noise. *Journal of Engineering and Applied Sciences* [online]. 2013, **8**(8), p. 255-259. ISSN 1816-949x, eISSN 1818-7803. Available from: <https://doi.org/10.36478/jeasci.2013.255.259>
- [49] NARAYAN, S. Effect of dwell time on noise radiated from diesel engine. *International Journal of Applied Engineering Research*. 2013, **8**(11), p. 1339-1347. ISSN 0973-4562, eISSN 0973-9769.
- [50] MUHAMMED, M. M., KAISAN, M. U., ABUBAKAR, S., NARAYAN, S. Determination of wear metals debris concentration in aircraft engines. *International Journal of Innovative Technology and Exploring and Engineering (IJITEE)*. 2019, **8**(11), p. 1289-1292 eISSN 2278-3075.
- [51] NARAYAN, S., ALSAGRI, A. S., GUPTA, V. Design and analysis of hybrid automotive suspension system. *International Journal of Mechanical and Production Engineering Research and Development (IJMPERD)* [online]. 2019, **9**(4), p. 637-642. ISSN 2249-6890, eISSN 2249-8001. Available from: <https://doi.org/10.24247/ijmperd201963>

- [52] MAHROOGI, F. O., NARAYAN, S. Design and analysis of double wishbone suspension systems for automotive applications. *International Journal of Mechanical and Production Engineering Research and Development (IJMPERD)* [online]. 2019, **9**(4), p. 1433-1442. ISSN 2249-6890, eISSN 2249-8001. Available from: <https://doi.org/10.24247/ijmperdaug2019148>
- [53] STOJANOVIC, N., GLISOVIC, J., GRUJIC, I., NARAYAN, S. Influence of size of ventilated brake disc ribs on air flow velocity. *International Journal of Advanced Science and Technology(IJAST)* [online]. 2020, **29**(1), p. 637-647. ISSN 2005-4238, eISSN 2207-6360. Available from: <http://serc.org/journals/index.php/IJAST/article/view/3285>
- [54] MAHROOGI, F. O., NARAYAN, S. Effects of dampers on piston slapping motion. *International Journal of Vehicle Noise and Vibration (IJVNV)* [online]. 2020, **16**(1/2), p. 46-57. ISSN 1479-1471, eISSN 1479-148X. Available from: <https://doi.org/10.1504/IJNVV.2020.112432>
- [55] NARAYAN, S., GUPTA, V. Frequency characteristics of in cylinder pressure of a gasoline engine. *Journal of Applied Engineering Science* [online]. 2021, **19**(1), p. 92-97. ISSN 1451-4117, eISSN 1821-3197. Available from: <https://doi.org/10.5937/jaes0-27156>
- [56] NARAYAN, S. Modelling of noise radiated from engines. In: The 11th International Conference on Automotive Engineering: proceedings [online]. 2015. 2015-01-0107. ISSN0148-7191, eISSN 2688-3627. Available from: <https://doi.org/10.4271/2015-01-0107>
- [57] NARAYAN, S. Analysis of noise emitted from diesel engines. *Journal of Physics: Conference Series* [online]. 2015, **662**, 012018. ISSN 1742-6588, eISSN 1742-6596. Available from: <https://doi.org/10.1088/1742-6596/662/1/012018>

SIMULATION OF A DUMMY CRASH TEST IN ADAMS

Marek Jaśkiewicz^{1,*}, Damian Frej¹, Miloš Poliak²

¹Department of Automotive Engineering and Transport, University of the Kielce University of Technology, Kielce, Poland

²Department of Road and Urban Transport, University of Zilina, Zilina, Slovakia

*E-mail of corresponding author: m.jaskiewicz@tu.kielce.pl

Resume

The article presents a model designed dummy for crash test in ADAMS. The simulated model dummy has dimensions, shapes and mass corresponding to a 50-percentile man. The simulation program allows modification of the dummy parameters. It allows to study the dynamics of motion, distribution of forces and loads of individual parts of the body of the simulated model. The article describes the design process and how to select the appropriate stiffness and damping joints for the simulated dummy. The article contains the results of simulation crash tests performed in the ADAMS program, which were compared to results of the Hybrid III dummy physical crash test. The simulation is designed to reflect the greatest compliance of the movements of individual parts of the human body during the low speed collision.

Article info

Received 7 April 2021

Accepted 8 June 2021

Online 5 October 2021

Keywords:

computer simulation,
dummy,
crash test

Available online: <https://doi.org/10.26552/com.C.2022.1.B20-B28>

ISSN 1335-4205 (print version)

ISSN 2585-7878 (online version)

1 Introduction

Currently, more attention is paid to safety of people and motor vehicles. Automotive threats are becoming more and more apparent due to increase in the number of vehicles traveling on the roads and capabilities achieved by the high-speed cars [1-3]. The classic division of passenger cars in Europe, as well as in Poland, is based on the size of vehicles. There are 10 categories of passenger cars, each category has a different letter of the alphabet. The lower the letter of the alphabet, the lower the vehicle class. Cars from category A and some of B are designed for city driving, which is why one is increasingly seeing versions of these cars with electric motors. On the other hand, category C and D cars are designed to cover greater extra-urban distances [2, 4-6]. The intended use of the car plays an important role in terms of safety; usually the city cars have a smaller power unit, which makes them unsuitable for developing high speeds on the road. In contrast, cars designed for longer routes are usually designed to achieve high speeds while driving. The increase in the level of technology favors development of the automotive industry, each car is equipped with several to several dozens of different security systems [6-8].

The issue of choosing the right equipment is more dependent on what the car is intended for. The active safety of a vehicle is affected by its design and equipment, which aims to reduce the risk of a collision or road accident [8-9].

Most car equipment packages include systems such as ABS (Antilock Brake System), ASR (Anti Skid Regulation), ESC (Electronic Stability Control), EBD (Electronic Brake Distributor). There are many other systems that can increase vehicle safety, such as automatic parking systems, Traffic Sign Recognition, side collision threat detection (Side Detect System), rear collision detection (Rear Detect System) or automatic braking vehicle system [1, 8-11].

Each of these systems increases the safety of people in the car and other road users. Before such a system could be introduced to the market, it has to undergo a number of tests and trials, including the crash tests. Tests are usually carried out at a request of the car manufacturers, consumer organizations and insurance companies. Simulation tests of road accidents are conducted worldwide by various institutes and organizations. In Europe, tests are systematically carried out by Euro-NCAP, i.e. the European New Car Assessment Program [8-9, 11]. The following programs carry out similar activities, independently of the Euro-NCAP: Global NCAP, Japan NCAP, Korean NCAP, Latin NCAP, ASEAN NCAP, IIHS, NHTSA in the USA, NASVA in Japan and ANCAP in Australia. Ratings issued after the crash tests help consumers to choose the safest vehicles. In addition, they motivate the car manufacturers to improve vehicle design and increase driver and passenger safety. The increase in safety systems in motor vehicles is conducive to the decreasing number of road accidents [4, 9, 12].

Over the past ten years, there has been a downward trend in frontal and side collisions in Poland, while rear collisions remain at the same level (Figure 1). The comparison of the number of injured in road accidents looks similar in Poland per year, there are 6,000 injured as a result of a rear collision (Figure 2). The number of

fatalities in the road accidents has a visible downward trend for fatalities in the side and frontal collisions. Fatalities during the rear impact have remained at the same level for 10 years (Figure 3). The rear collisions are becoming more common. This is due to the development of infrastructure. It means that the increase in highways

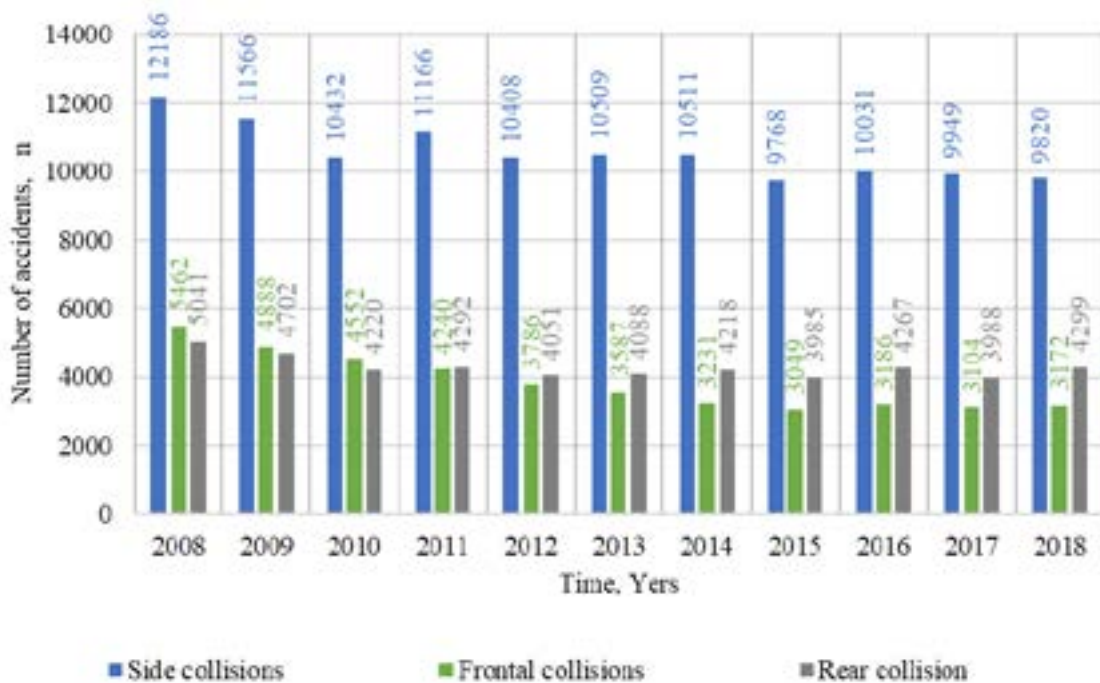


Figure 1 Comparison of the number of car accidents in Poland in the years 2008 -2018 [13]

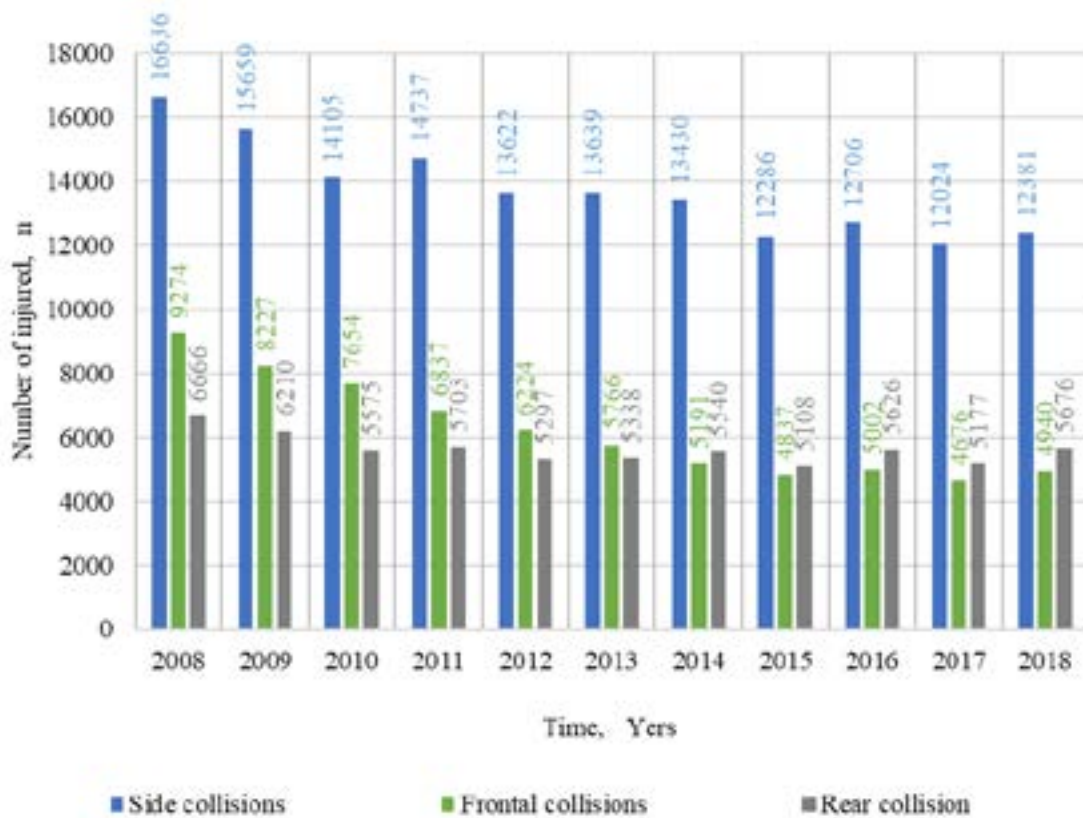


Figure 2 Number of injured in car accidents in Poland in the years 2008 -2018 [13]

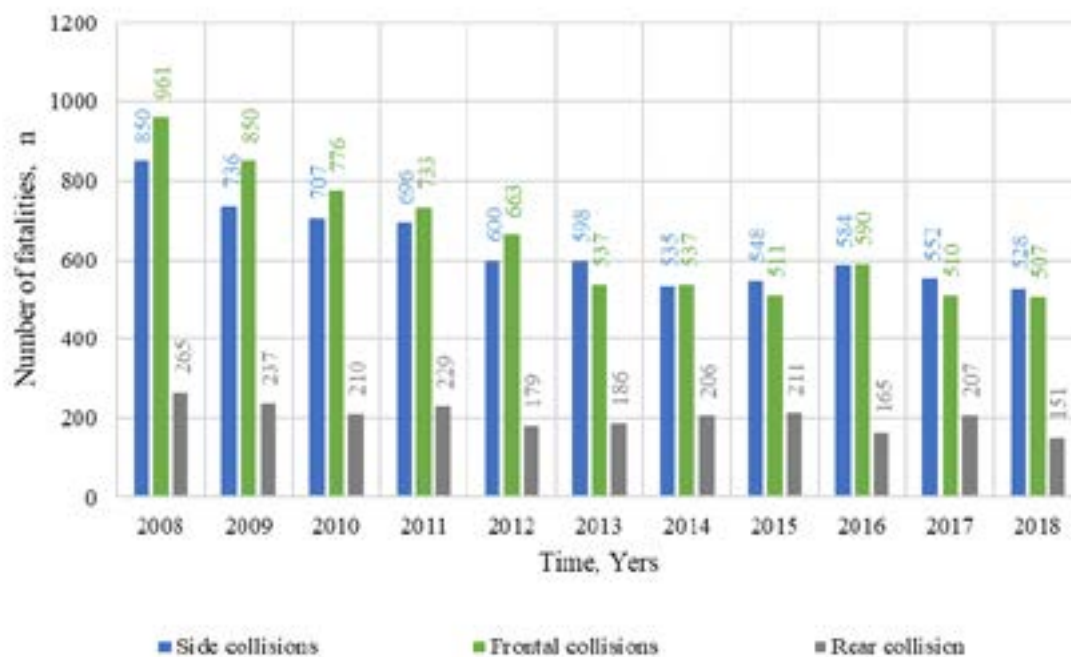


Figure 3 Number of fatalities in car accidents in Poland in the years 2008 -2018 [13]

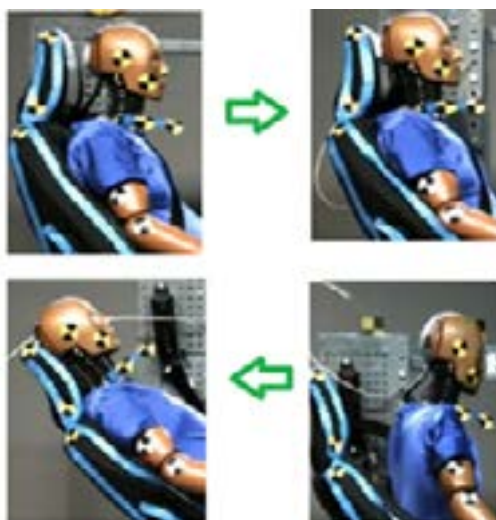


Figure 4 Phases of the head displacement of the rear impact case [18]

and expressways prevents head-on collisions, because the vehicles move in one direction. These conditions favor the occurrence of rear collisions by hitting the rear of the car or not braking the vehicle [10, 13].

The rear collisions occur most often in the speed range from 10 to 30 km/h. Even at such low speeds, one can experience a serious spinal injury, since during the rear collision, the cervical spine becomes the most vulnerable [7, 11, 16]. The injury may affect muscles, tendons, intervertebral discs and nerves of the head and neck. The spinal injuries can be divided according to the mechanism [12, 16]:

- bending- consisting of fracture of the vertebral body and damage to the intercostal and longitudinal posterior ligaments,
- straightened - consisting in damage to the anterior

longitudinal ligament and fracture of the first and second cervical vertebra (C1 and C2),

- compression fracture - where the vertebral bodies fracture,
- rotational (rotation of the chin to the shoulder) - involving the fracture of the lateral vertebra,
- hyperextension.

Cervical spine injuries associated with rapid and excessive deformity of the spine can be difficult to diagnose and treat for a long time. They are also commonly found in rear impacts at low speed. While such accidents rarely result in fatalities, the consequences of the cervical spine injuries have a huge impact on society, with an estimated annual cost in Europe of around EUR 10 billion [12, 17].

In the event of the rear impact, there are four

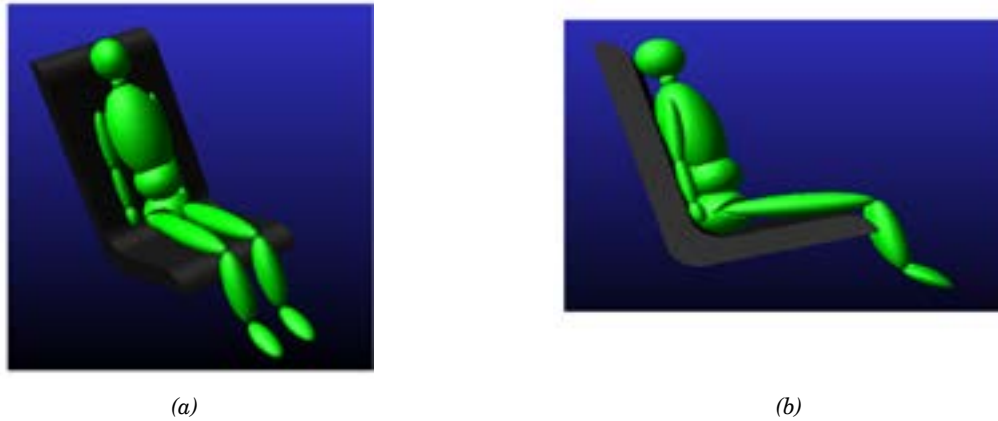


Figure 5 Anthropometric dummy for the crash tests made in ADAMS program, (a) isometric view, (b) side view

Table 1 The masses of individual body parts of the simulation dummy

No.	Simulation dummy	
	The name of the block	Mass, kg
1	forearm	3.60
2	arm	0.50
3	hand	4.60
4	foot	9.4
5	shank	0.60
6	thigh	13.80
7	neck	0.95
8	head	3.70
9	hips	20.40
10	chest	9.80
11	stomach	10.00
()		78.7kg

head displacement stages (Figure 4). In the first phase, the head is moved to the headrest of the chair. Then, in the second phase, the head is pressed against the headrest as a result of the inertial force after the rear impact. In the third phase, the head begins to move forward at a speed increased by the energy of the headrest's elastic force. In the last phase, the head begins to move backwards again relative to the headrest [12, 14, 18].

Currently, in the frontal impact tests of a car, anthropometric dummies from the Hybrid III family and dummy THOR, representing a 50th percentile man, are used. Anthropometric dummies through the elastic-damping materials used correspond to the structure and behavior of a person during a vehicle collision [14-15].

In the event of rear impacts, the BioRID (50th Male) dummy is used [1, 9-10, 19]. The distinguishing feature of BioRID-II is the spine, which consists of 24 separate vertebrae: 5 lumbar, 12 thoracic and 7 cervical. The other components of the dummy are identical to those of the Hybrid III dummy representing the 50th percentile male. The BioRID dummies only reflect a 50th percentile male, while there is no crash test dummy representing

the female centile population and the 5th and 95th percentile men [1, 20].

Crash tests and tests testing various types of security systems require considerable financial and time expenditure. The simulation programs of anthropometric dummies, include such programs as: Madymo, Dytran, Dassault Systemes SIMULIA, ANSYS Engineering Simulation, SIMPACT Caterham Super 7, MSC Software ADAMS. These programs allow to perform simulated crash tests with minimal financial burdens. Only after collecting the appropriate amount of data confirming the effectiveness of simulation tests are the crash tests carried out. The demand for simulation programs and performing computer simulations prior to experimentation affects the development of specialized program networks [18-22].

2 Research object

The human model from a physical point is a set of interrelated solids that are characterized by appropriate damping and rigidity. Each block has the right shape



Figure 6 Mass settings and stiffness of elements in ADAMS

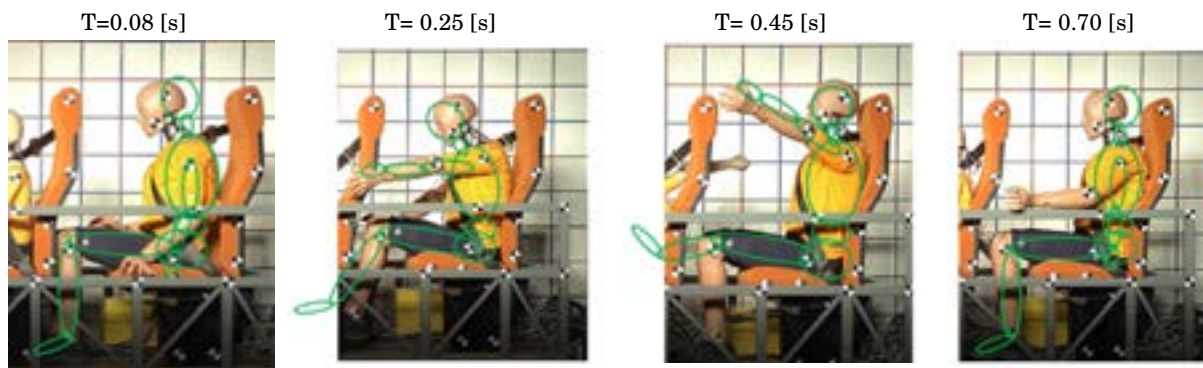


Figure 7 Identification of the basic parameters of the model based on recorded real collisions with dummies

and mass. The designed crash test dummy (Figure 5) at low speed was made in the MSC Adams program. The program can examine the dynamics of movement of individual parts of the dummy's body. It is also possible to determine the distribution of loads and forces acting on individual joints of the dummy. The program enables the transformation of a rigid body into a flexible model for finite element analysis. It allows to modify data and get detailed information about the exact movement of individual parts of the model, presenting them in a graphic way.

The designed dummy model consists of 17 block of a certain mass and size. The dummy was designed in the image of the Hybrid III dummy. Table 1 presents the masses of individual body parts of the designed dummy. The dummy was placed on a car seat consisting of one block, having properly selected stiffness and damping characteristics. The seat belts in the model under construction are a system of parallel springs and vibration dampers mounted in a horizontal plane parallel to the horizontal axis X. The only force on the system is the initial speed.

Creating a model in ADAMS focuses on connecting individual elements with special joints. The program environment makes it easy to make corrections related to mass or stiffness and damping of individual parts. In addition, ADAMS allows to introduce restrictions related to the displacement of individual elements, choose the appropriate articulation and the number of degrees of freedom. Figure 6 presents categories of mass modification and stiffness of elements in ADAMS.

3 Results of simulation tests

The simulation dummy was compared with the hybrid III dummy. The experiment was carried out at a speed of 20 km/h. In order to verify and validate the dummy parameters, the computer simulation crash test was compared to the experimental crash test. An experimental crash test was carried out at a speed of 20 km/h, using the Hybrid III dummy. The crash test stand is located at the Automotive Industry Institute in Warsaw. The stand for experimental research consists of a trolley to which a car seat with a dummy is attached.

The test element is accelerated by means of the rubber ropes of a total length of 25 meters, five on each side.

The desired speed is obtained by pulling the ropes with the trolley to a certain length. After stretching the trolley ropes for a certain length, the stretched ropes are released and the trolley then gains speed. The desired speed of the trolley is measured in the non-driven section where the trolley moves inertly. Then the trolley is braked with 600 mm polyurethane bushes. The test run of the experimental event test, carried out at the Automotive Industry Institute in Warsaw, was recorded with a high speed NAC camera at 2500 frames/second [17].

The terms of the trial event experimental test have been reproduced in the MSC Adams program. In the computer simulation, a built-in software camera using 2500 frames per second was used. The simulation time was 5s. The car seat and the dummy were accelerated

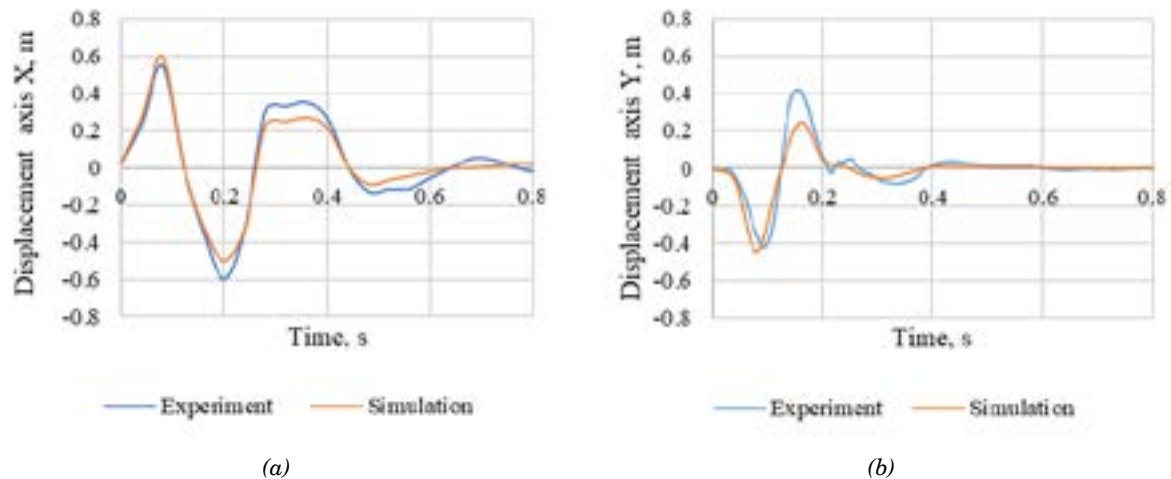


Figure 8 Displacement of the dummy head (a) relative to the X axis, (b) relative to the Y axis

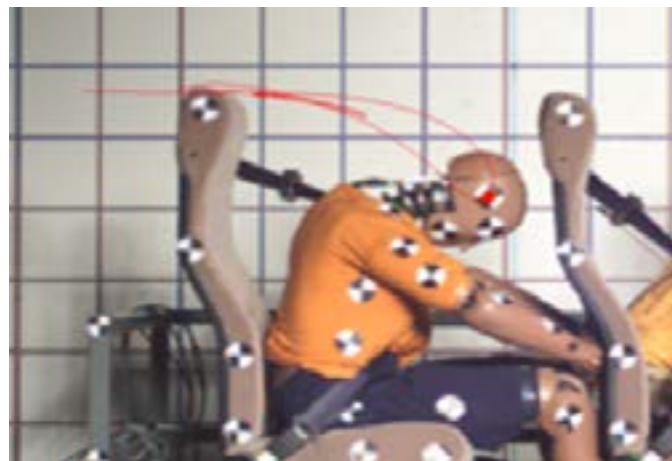


Figure 9 Hybrid III dummy head trajectory during the experiment

from zero to the assumed speed. At this stage, the car seat moved for 2 seconds, after which it was braked to zero. The braking of the car seat is designed to simulate the collision of a vehicle with a stationary obstacle. Computer simulation of the crash test was superimposed to the recorded image of the Hybrid III dummy experimental crash test. Comparison of the simulation to the crash test is shown in Figure 7.

Most often, during the collisions at a low speed, the trauma occurs to the cervical spine – 33%, head including wounds and concussion – 23%, lower limbs – 21%, chest – 8%, other organs – 15%. The most liable parts of the body to damage at low speeds are the neck and head. Figure 8 compares the displacement of the simulation dummy head and the Hybrid III dummy [10, 20-21].

The head displacements in both the X and Y axes can be divided into two stages, in the first of them the head moves forward due to the inertia force associated with the rapid braking. Then the head moves towards the headrest of the car seat, hitting it. The second stage of displacement begins when the head hits the car seat headrest, then the head together with the additional force coming from the elasticity of the car seat headrest

begins to move forward again.

In the first phase of the head movement, the computer simulation of the crash test obtained the compliance of the movement with the experiment at the level of 95%, while the second phase of the movement achieved the compliance of about 80%. The second phase is closely related to the stiffness and damping of the car seat.

In the TEMA Automotive program, the trajectory of the head of the Hybrid III dummy was determined during the experiment (Figure 9). The superimposed trajectories of the first phase of the head movement of the Hybrid III dummy during the experiment and the anthropometric dummy during the simulation are shown in Figure 10. Considered compatibility of the trajectory of the computer simulation motion with the experiment is at the level of 95%.

In addition, for the purposes of further verification of the compatibility of the computer simulation (the built-in dummy) with the experimental (Dummy Hybrid III), the resultant of the dummy head was determined based on the data from the ADAMS program environment. The resultant head of the simulated dummy was compared to result of the Hybrid III dummy head (Figure 11).

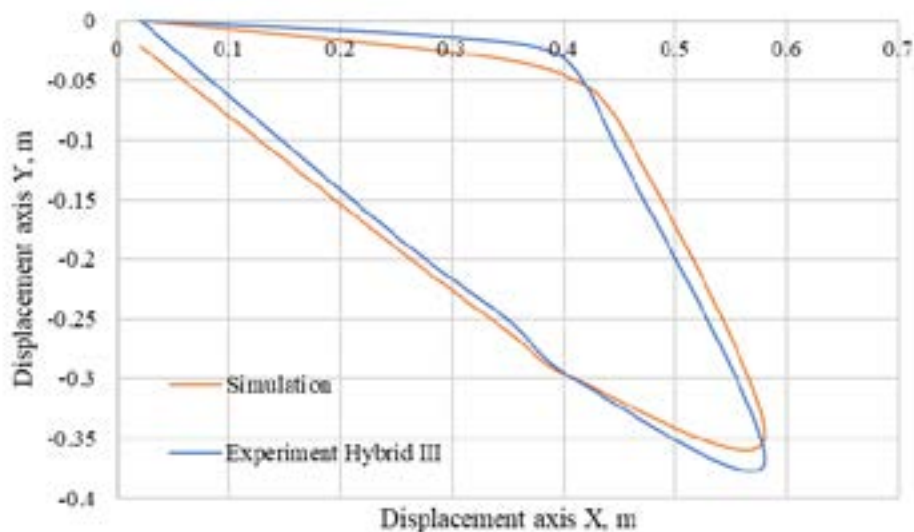


Figure 10 Comparison of trajectories of dummies head

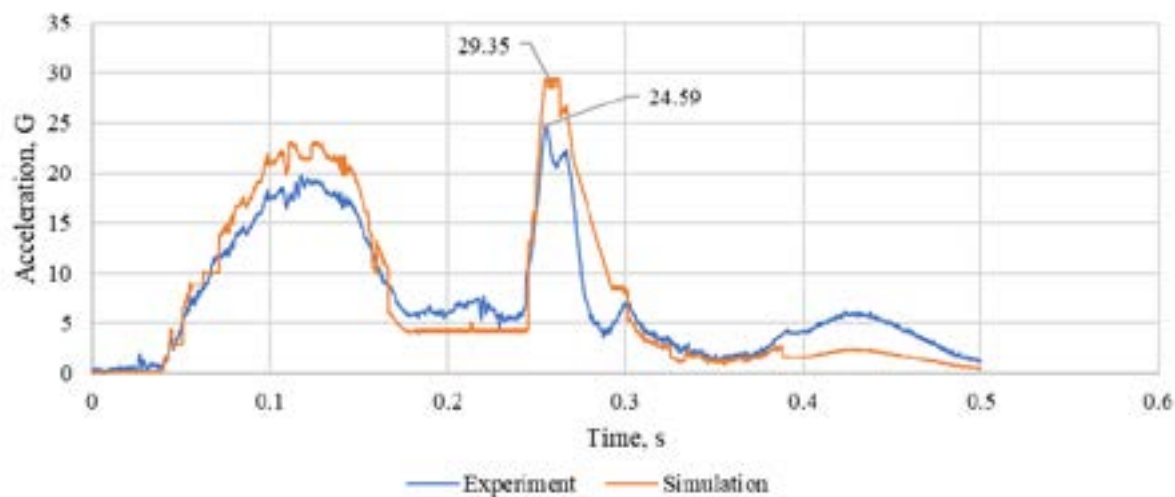


Figure 11 Accidental displacement characteristics of the simulated and experimental dummy head

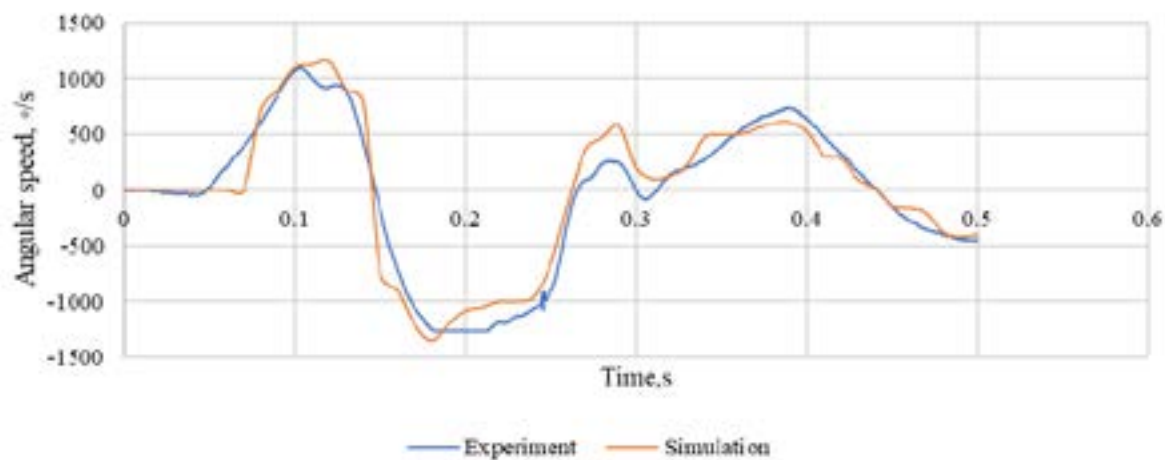


Figure 12 Angle speed characteristics of the simulated and experimental dummy head

The difference between the results was up to 19%. On the other hand, Figure 12 shows the angular velocity of the head of the dummies. It can be noticed that the difference between values of the angular velocity of the simulated dummy and the dummy hybrid III overlap in 80%.

4 Conclusions

Car accidents in Poland from 2008 to 2018 have a downward trend in the case of frontal and side collisions, whereas rear collisions are maintained at the same level and reach an average of 4,000 per year. The neck spine is the most liable during the rear collision and symptoms often appear several hours after the accident. Only one BioRid II dummy is used for the rear impacts, which is an improved version of the BioRid I from 1989. It represents a 50 percentile man. In the case of the rear collisions, there are no dummies representing the percentile population of women, children and the 5th and 95th percentile men.

The Adams program allows modifications of the dummy's structure and adopted model parameters. The built in dummy in the program had stiffness and attenuation parameters in accordance with the Hybrid III dummy parameters. Comparison of computer simulation

to the experiment at 20 km/h showed that the data from the computer simulation differ from the experiment data by 20%. By modifying the parameters of stiffness and damping, as well as the mass of individual parts of the dummy's body, data corresponding to the crash test can be obtained, taking into account individual percentiles of the human population.

It should be emphasized that simulation programs significantly facilitate a number of operations related to improving the safety of motor vehicles. More than 70 years have passed since the creation of the first dummy (Sierra Sam Dummy). There is still a need to design new joints and the construction of individual body parts of the anthropometric dummy to be similar to the human body. Contemporary simulation programs, such as Dytran or ADAMS, are geared towards the crash test simulations and data validation with experimental tests. This is due to the fact that nowadays they are an irreplaceable element of the structure, which must first successfully pass the simulation tests to be able to be physically performed.

Work on the physical structure of a simulation dummy involves use of elements corresponding to the shape, mass and dimensions of individual parts of the human body and also involves use of the special joints reflecting the range of motion of individual human joints.

References

- [1] JASKIEWICZ, M., JURECKI, R., WITASZEK, K., WIECKOWSKI, D. Overview and analysis of dummies used for crash tests. *Scientific Journals Maritime University of Szczecin*. 2013, **35**(107), p. 22-31. ISSN 1733-8670.
- [2] LUO, X., DU, W., ZHANG, J. Safety benefits of belt pre-tensioning in conjunction with precrash braking in a frontal crash. In: 2015 IEEE Intelligent Vehicles Symposium (IV): proceedings [online]. IEEE. 2015. ISSN 1931-0587, p. 871-876. Available from: <https://doi.org/10.1109/IVS.2015.7225794>
- [3] FREJ, D., GRABSKI, P. The impact of the unbalanced rear wheel on the vibrating comfort of the child seat. *Transportation Research Procedia* [online]. 2019, **40**, p. 678-685. ISSN 2352-1465. Available from: <https://doi.org/10.1016/j.trpro.2019.07.096>
- [4] GUPTE, S., MASOUD, O., MARTIN, R. F. K., PAPANIKOLOPOULOS, N. P. Detection and classification of vehicles. *IEEE Transactions on Intelligent Transportation Systems* [online]. 2002, **3**(1), p. 37-47. ISSN 1524-9050, eISSN 1558-0016. Available from: <https://doi.org/10.1109/6979.994794>
- [5] CHEN, Z., ELLIS, T. Multi-shape descriptor vehicle classification for urban traffic. In: 2011 International Conference on Digital Image Computing: Techniques and Applications: proceedings [online]. IEEE. 2011. p. 456-461. Available from: <https://doi.org/10.1109/DICTA.2011.83>
- [6] European classification for vehicle category, based in UNECE standards - European Alternative Fuels Observatory [online] [accessed 2020-10-15]. Available from: <https://www.eafo.eu/knowledge-center/european-vehicle-categories>
- [7] BURCZEWSKI, P., JACKOWSKI, J. Modelling the human body in low speed collisions. *Logistyka*. 2014, **3**, p. 915-921. ISSN 1231-5478.
- [8] LIU, W., WEN, X., DUAN, B., YUAN, H., WANG, N. Rear vehicle detection and tracking for lane change assist. In: 2007 IEEE Intelligent Vehicles Symposium: proceedings [online]. IEEE. 2007. ISSN 1931-0587, p. 252-257. Available from: <https://doi.org/10.1109/IVS.2007.4290123>
- [9] KIM, S. Y., OH, S.-Y., KANG, J. K., RYU, Y. W., KIM, K., PARK, S.-CH., PARK, K. H. Front and rear vehicle detection and tracking in the day and night times using vision and sonar sensor fusion. In: 2005 IEEE/RSJ International Conference on Intelligent Robots and Systems: proceedings [online]. IEEE. 2005. ISBN 0-7803-8912-3, p. 2173-2178. Available from: <https://doi.org/10.1109/IROS.2005.1545321>

- [10] STANCZYK, T. L., ZUSKA, A. Review of anthropo-dynamic dummies used to evaluate the effect of vibrations on sitting human (vehicle driver). *The Archives of Automotive Engineering - Archiwum Motoryzacji*. 2014, **65**(3), p. 65-74. eISSN 2084-476X.
- [11] FOSTER, J., KORTGE, J., WOLANIN, M. Hybrid III-A biomechanically-based crash test dummy. *SAE Technical Paper* [online]. 1977, 770938. ISSN 0148-7191, e-ISSN 2688-3627. Available from: <https://doi.org/10.4271/770938>
- [12] SPITZER, W. O., SKOVRON, M. L., SALMI, L. R., CASSIDY, J. D., DURANCEAU, J., SUISSA, S., ZEISS, E. Scientific monograph of the Quebec Task Force on Whiplash-Associated Disorders: redefining “whiplash” and its management. *Spine*. 1995, **20**(8 Suppl), p. 1S-73S. ISSN 0362-2436, eISSN 1528-1159.
- [13] Wypadki drogowe - raporty roczne - Policja (Road accidents - annual reports – Police) [online] [accessed 2020-04-01]. Available from: <http://statystyka.policja.pl/st/ruch-drogowy/76562,Wypadki-drogowe-raporty-roczne.html>
- [14] ONO, K., KANECKA, K., WITTEK, A., KAJZER, J. Cervical injury mechanism based on the analysis of human cervical vertebral motion and head-neck-torso kinematics during low speed rear impacts. *SAE Transactions* [online]. 1997, **106**(6), p. 3859-3876. ISSN 0096-736X. Available from: www.jstor.org/stable/44720153
- [15] HAN, Y., TANG, H., TIAN, F., HUANG, H., MIZUNO, K. Analysis of the equation of motion on the chest of hybrid III 3YO dummy in dynamic loads. In: 2018 International Conference on Robots & Intelligent System (ICRIS): proceedings [online]. IEEE. 2018. p. 529-533, Available from: <https://doi.org/10.1109/ICRIS.2018.00137>
- [16] PEARSON, A. M., IVANCIC, P. C., ITO, S., PANJABI, M. M. Facet joint kinematics and injury mechanisms during simulated whiplash. *Spine* [online]. 2004, **29**(4), p. 390-397. ISSN 0362-2436, eISSN 1528-1159. Available from: <https://doi.org/10.1097/01.brs.0000090836.50508.f7>
- [17] Impact of pain on society costs the EU up to 441 billion euros annually - SIP Platform [online] [accessed 2020-10-15]. Available from: <https://www.sip-platform.eu/press-area/article/impact-of-pain-on-society-costs-the-eu-up-to-441-billion-euros-annually>
- [18] Driving advice - The Automobile Association [online] [accessed 2020-10-15]. Available from: http://www.theaa.com/motoring_advice/safety/whiplash.html
- [19] NOUREDDINE, A., ESKANDARIAN, A., DIGGES, K. Computer modelling and validation of a hybrid III dummy for crashworthiness simulation. *Mathematical and Computer Modeling*. 2002, **35**, p. 885-893. ISSN 0895-7177
- [20] Humanetics [online] [accessed 2020-10-18]. Available from: <https://www.humaneticsatd.com>
- [21] XU, T., SHENG, X., ZHANG, T., LIU, H., LIANG, X., DING, A. Development and validation of dummies and human models used in crash test. *Applied Bionics and Biomechanics* [online]. 2018, **2018**, 3832850. ISSN 1176-2322, eISSN 1754-2103. Available from: <https://doi.org/10.1155/2018/3832850>
- [22] JASKIEWICZ, M. Simulation tests of active headrest / Symulacyjne badania działania zagłowka aktywnego (in Polish). Doctoral dissertation. Kielce: Politechnika Świętokrzyska, 2007.

CONSTRUCTION OF THE GEOMETRICAL MODELS OF A MULTIPLE-FACTOR OPTIMIZATION OF THE TECHNICAL AND OPERATING PARAMETERS OF THE TROLLEYBUSES WITH AN AUTONOMOUS MOVE MARGIN

Serhii Pustiulha¹, Volodymyr Samchuk², Valerii Dembitsky^{3,*}, Viktor Samostian³, Valentyn Prydiuk³

¹Department of Architecture and Design, Lutsk National Technical University, Lutsk, Ukraine

²Department of Building and Civil Engineering, Lutsk National Technical University, Lutsk, Ukraine

³Department of Automobiles and Transport Technologies, Lutsk National Technical University, Lutsk, Ukraine

*E-mail of corresponding author: dvm2@meta.ua

Resume

While introducing into a system of passenger traffic the ecologically clean vehicles, namely the electric buses, a task of providing them with a rational move margin is actual. This problem is especially acute while using the trolleybuses with an autonomous move at urban and suburban routes.

A constructed multiple-factor model and a proposed algorithm of finding the main parameters allow forming the offers concerning a constructive providing of an additional equipment process with the means of autonomous move. Based on a visual presentation of the multidimensional spaces at Radishchev drawing an effective way is offered of a geometrical interpretation of mutual influence of the optimization factors set on the operating characteristics of the additionally equipped vehicles.

Article info

Received 6 May 2021

Accepted 29 June 2021

Online 20 October 2021

Keywords:

trolleybus,
autonomous move,
multidimensional space,
multiple-factor optimization model,
passenger capacity,
electrical energy store

Available online: <https://doi.org/10.26552/com.C.2022.1.B29-B40>

ISSN 1335-4205 (print version)

ISSN 2585-7878 (online version)

1 Introduction

The world-wide tendencies in an automobile field look more and more towards a development of ecologically clean technologies, the main direction of which is using of an electric power on the vehicles. Almost all the car manufacturers concentrate their great efforts on creation and development of the electric cars and electric buses. Along with that, many countries in Europe declare or even, on a legislative level, determine the restrictions about using cars in cities or some parts of them. All these factors also need an application of corresponding effective decisions of local authorities, in order to optimally organize traffic on a territory of communes and to assure a necessary level of transport availability.

In Ukraine, in spite of existing economic problems, there are actively introduced the technologies that reduce an ecological burden on environment, including transport. According to National transport strategy of Ukraine, for a period up to 2030, it is possible to distinguish the next tasks concerning a development of ecologically clean transport:

- assuring a priority of the ecological safety requirements, obligation of respecting the ecological

standards, norms and limits of using the natural resources when making an economic, administrative and other activity;

- realization of preventive measures concerning the environmental protection in automotive field and creating a mechanism of compensation for damages;
- introducing of mechanism of economic stimulation of changing the freight and passenger traffic to more ecologically clean types of transport;
- implementation of economic and other measures of stimulation for using the ecologically more effective types of transport in cities, namely the electric cars, city electric transport - underground, trams, trolleybuses, electric buses and bicycle transport (system of public bicycle hire);
- introducing a mechanism of economic stimulation of the carriers to reduce the pollutant emissions and the greenhouse gases, to lower the level of the vehicles noise;
- stimulation of using the alternative energy sources and the ecological types of vehicles and specialized transport;
- realization of a complex of regulatory and fiscal measures, namely implementation of the international ecological norms for vehicles,

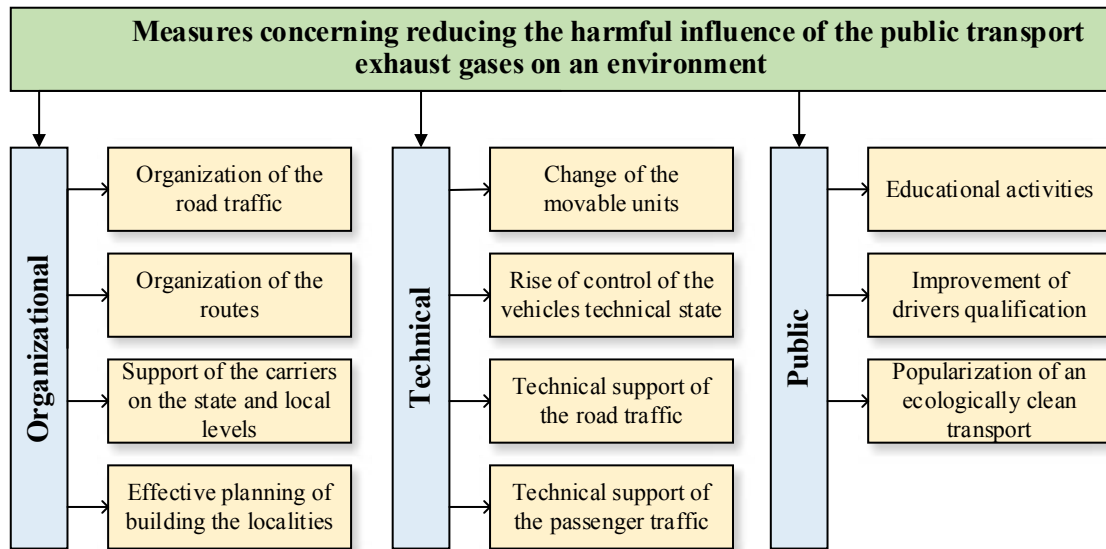


Figure 1 Measures concerning reducing the harmful influence of the public transport exhaust gases on environment

Table 1 The most common types of the city passenger transport and their advantages and disadvantages

Type of a movable unit	Advantages	Disadvantages
bus	high mobility; big move margin; comparatively low costs of a vehicle;	harmful emissions; considerable level of noise; high value of the traffic costs;
hybrid bus	high mobility; big move margin; ecological compatibility;	high costs of a vehicle; high value of the traffic costs; harmful emissions; considerable level of noise;
trolleybus	ecological compatibility; low level of noise; low cost value of traffic; time-proof in operating;	high costs of a vehicle; low mobility; needs for an arrangement of additional infrastructure;
electric bus	ecological compatibility; low level of noise; low cost value of traffic; high mobility;	high costs of a vehicle; long-lasting charging;

improvement of mechanism of using the alternative engine fuels, introducing of economic stimulus, while putting into operation the vehicles of higher ecological level.

The named tasks will contribute to development of ecological transport, namely to a wide introduction of the electric vehicles. Taking into consideration all the aforementioned, a question of ecological influence on environment by passenger traffic is the most prevalent in Ukraine that is caused by a row of reasons, the main of which are:

- dense bus traffic schedule;
- duplication of bus routes, especially in central parts of the cities;
- low passenger flow on a trolleybus transport;
- absence of a complex approach to the cities transport net planning.

At the same time, an influence of automobile

transport on environmental pollution of the localities is rather significant. The researches results show this [1-2].

2 Literature review

In modern phase of development of the ecological safety knowledge, there are some ways to solve the questions of reducing the harmful influence of the public transport exhaust gases on environment that are shown at Figure 1.

The list of measures, shown in Figure 1, is not exhausted and can be extended, depending on the concrete circumstances. Certainly, the most effective would be a complex implementation of the offered measures. Along with that, to evaluate their effectiveness in complex, it is possible to exam an influence of each

measure separately and the most perspective is, in authors' point of view, a substitution of the movable units by the ecologically clean ones.

In Table 1 there are given the most common types of city passenger transport and there are defined their advantages and disadvantages.

When analyzing Table 1, one can see that the disadvantages of some vehicles are the advantages of the others and vice versa. That is why one of the optimal variants, from the point of view of operation, is using trolleybuses with an autonomous move that will join the ecological features of the electrical buses, the mobility of the buses and the low value of costs and durability of the ordinary trolleybuses.

The present question was examined and clarified in the research works [3-4]. The trolleybuses with an autonomous move are effectively operated today all over the world [5], namely in Poland [6], Greece [7], Sweden [8], Italy [9]. In addition, a question of the electric buses operation in small and average communes by size was investigated in a research work [10] that is actual for Ukraine, especially in today's phase of decentralization. Here is mentioned only a small part of the countries where the trolleybuses with an autonomous move are used, their number is extremely big and investigation of researchers testifies of the interest of scientists to solving the questions of the localities' ecology improvement.

In Ukraine, the trolleybuses with an autonomous move are used in Kryvyi Rih, Lviv, and in Lutsk the electric buses are operated. Along with that, while buying the trolleybuses by the electric transport enterprises of Ukraine, in tender requirements for purchase one of the requirements stands for a presence of an autonomous move not less than 10...20km. But the declared distance of an autonomous move is not proved by anything, the calculations are not made and the optimal opportunities of a vehicle with an autonomous move are not used.

While analyzing the publications and researches on a given question, it was found that rather often a trolleybus that can use a trolley line and move from a power supply of on-board system, is called an autonomous electrical bus, a trolleybus, a hybrid trolleybus, an electric bus, a hybrid electric bus. In present research work such a vehicle is called a trolleybus with an autonomous move.

On the other hand, an analysis of publications testifies about a great interest of scientists to research the influence of the vehicle's weight on its technical and operating indices. In a research work [11] is investigated an influence of increasing of a trolleybus weight on the power consumption by a drive and the lack of energy during its transmission. According to the researches results, given in [12], the authors affirm that an effectiveness of passenger traffic by buses equipped by the internal combustion engines and by electrical buses, is almost equal, taking into account that 1kg of modern tractive storage battery has got 0.25 kW-h of energy. That is, to ensure a margin of a bus move by

50l of fuel, one can use, as an alternative, a battery of 562kg weight.

It is necessary to notice a research concerning the use of different combinations of the storage batteries and super capacitors for vehicles with a definition of the smallest electricity consumption [13]. Such researches are presented in a work [14]. The analysis of technical characteristics of the electrical buses in real operating conditions is given in [15]. In a work [16] is shown an entire methodology of taking the system decisions to ensure an effective operation of the electric buses in concrete operating conditions.

In a publication [17], the authors has made a research and estimated a possibility of choosing the corresponding types of the storage batteries for concrete routes and operating conditions of the electric vehicles.

Besides that, in many publications there is a rather interested multiple-criteria approach in choosing the effective parameters of electric buses [18-19], the main of which were: margin (range) of move and passenger capacity.

The analysis of the mentioned literature sources testifies that a multiple-criteria approach, in choosing the effective parameters of the vehicles, can be an effective instrument when taking an optimal decision.

On the other hand, based on the research in [12], it is necessary to say that namely an operation of trolleybuses with an autonomous move on the city routes is the most effective while comparing to the other types of the electric wheeled vehicles.

While summing up all the aforementioned, one can make the conclusions:

- for today, a solution of questions of rising the technical-operating and technical-economical parameters of the electric buses and trolleybuses with an autonomous move is actual;
- a passenger capacity and a move margin - are the ones of key factors while choosing the electric vehicles;
- the trolleybuses with an autonomous move are the most effective types of the vehicles for passenger traffic in cities that have a developed contact trolley line.

3 Research methods

The most important factor, from the point of view of the technical and operating characteristics of the trolleybuses with an autonomous move, is an autonomous move margin that directly depends on a number and characteristics of the tractive storage batteries. However, an increasing of the storage batteries number would certainly lead to an increase of the vehicle's weight. Along with that, a part of a weight that falls on a trolleybus axle would be a restrictive parameter.

It is evident that in order to eliminate an overload on the axles, it is necessary to decrease a passenger capacity

of a vehicle, that, in turn, according to the requirements of Regulations № 107 would be defined by a compartment area destined for passenger transportation.

All these things stipulate taking into account a whole row of the technological, constructive, compositional, economical parameters and factors for the vehicles that make a decision algorithm of optimal choice of their quantity dependences, proceeding from the operating conditions, namely - a trolleybus autonomous move margin.

A modeling of the multiple-factor problems always includes the elements of optimization. It allows to operate the technical and operating characteristics of the examined objects more effectively, to determine the parameters of their common stable operation, to organize a lookup of conditions to obtain the best results. At the same time, using of classical methods of solving such problems, is often low effective for an optimization of many real multiple-factor processes, due to the necessity to take into account their specific features, for finding out the regularities concerned with influence of a great number of the parameters and for setting the quantity interconnections between them that determine, as a result, a quality of optimization. Besides that, the offered mathematical models are characterized by a great volume of calculating operations and by an absence of a complex visual idea about the research objects.

Recently, in science, while modeling and optimizing the multiple-factor processes, the methods of applied geometry of multidimensional spaces are used more effectively. Firstly, it is due to the fact that the tasks, appearing in practice, are rather difficult to solve by the traditional analytical methods of mathematical modeling, as though a number of the variables and parameters, which reflect the corresponding multiple-space functional dependences, exceeds the dimensions of space where these processes are examined.

At the same time, a multiple-space applied geometry allows investigating the multidimensional objects as the geometrical models with many variables what gives a possibility to represent them visually and clearly, that, with a help of modern computer technique, allows determining promptly the optimal modes, to assort the effective parameters and characteristics of the examined multiple-factors processes.

A literature review showed that there exists a great number of different ways of visual presentation of a multidimensional space and of making the graphic models of multidimensional configurations, based on a projective device of hyper-coordinate planes. A disadvantage of most of them is that, with an increasing of dimensionality of objects or spaces, such models become bulky, there happens an imposition of coordinate planes, narrowing at the same time the possibilities of visual presentation of the multiple-factor optimization problems.

In a research work [20] was offered to represent the discrete or continuous geometric objects in spaces of

arbitrary number of spaces in two ways.

The first presentation was related to a coordinate hyper-net where there were fixed the values n of independent reasons and each value of function with this, for example:

$$Z = f(k, l, m, \dots, s, t). \quad (1)$$

The second presentation is related to a coordinate axis set, where each value of function was determined depending on one argument. For example, a manifold of Equation (1) can be presented as a system of functions:

$$\begin{cases} Z = \varphi_1(k) \\ Z = \varphi_2(l) \\ Z = \varphi_3(m) \\ \dots\dots\dots \\ Z = \varphi_{n-1}(s) \\ Z = \varphi_n(t) \end{cases}. \quad (2)$$

If a number of independent arguments (k, l, m, \dots, s, t) is equal to p , Equations (1) and (2) would be the models of a manifold in $p + 1$ dimensional space. Along with that, the most convenient to solve different practical tasks is a presentation of a manifold of Equation (2) at Radishchev drawing [20]. Its feature consists of a fact that a set of improper axes of manifold of Equation (2) constitutes an improper plane of hyper-plane (k, l, m, \dots, s, t) . Any hyper-plane that crosses this improper plane would be parallel to a hyper-plane (k, l, m, \dots, s, t) and that is why it is perpendicular to the Z axis. It means that n projections of any point at Radishchev drawing would be situated on one connection line, perpendicular to the Z axis. All the aforementioned would be right and in the case when instead of the Z axis any other axis would be chosen.

According to an aforementioned model, a multiple-factor problem of finding the optimal technical and operating parameters for trolleybuses with an autonomous move margin, can be presented by a function:

$$L_p = f(M_{batt}, M_{\mu 1}, M_{\mu 2}, P, k_s, R, E_{batt} \dots), \quad (3)$$

where:

$M_{\mu 1}, M_{\mu 2}$ - load on the axles of a vehicle, kg;
 M_{batt} - weight of the tractive storage batteries;
 k_s - parameter of using a compartment area designated for standing and/or sitting passengers;
 P - passenger capacity of a vehicle, persons;
 E_{batt} - electric capacity of the batteries;
 R - indices of recuperation accounting;
 and other technical and operating parameters of a vehicle.

Thereafter, the aim of the present research work is to reach the optimal technical and operating indices of the trolleybuses, with an autonomous move margin, by the way of determining the rational dependencies between an autonomous move margin, a vehicle

Table 2 Models of the vehicles that are manufactured nowadays or were manufactured during the last ten years

Brand of trolleybus (electric bus)	Overall dimensions, mm		Weight, kg		Passenger capacity, persons		Producing country
			curb weight	total weight	general	sitting passengers	
	length	width					
Skoda 28Tr Solaris	14590	2550	12700...15500	24000	160...170	41...49	Czech Republic
Skoda 32Tr SOR	12000	2550	10180	17000	100	32	Czech Republic
SOR NB 18	18750	2550	14500	22500	117	44	Czech Republic
Skoda 24Tr Irisbus	11990	2500	11500	18300	99	30	Czech Republic
Skoda 33Tr SOR	18750	2550	16000	24200	120	47	Czech Republic
Oreos 2X	7243	2170	4100	6100	22	13	France
Oreos 4X	9312	2350	9100	13500	49	25	France
Protterra EcoRide	10900	2580	12700	19300	97	60	USA
Solaris Trollino 15	14590	2550	12700...15500	24000	130...150	36...47	Poland
Solaris Trollino 18	18000	2550	15500...18500	28000	160...170	41...49	Poland
Solaris Trollino 24	24000	2550	19100	34000	190...220	60...70	Poland
AKSM-E433	19000	2500	17720	28000	153	38	Belorussia
BKM-42003	11790	2500	13500	18000	115	35	Belorussia
AKSM-321	11755	2500	11100	18000	115	26	Belorussia
BKM-43303	18750	2500	17720	28000	153	38	Belorussia
AKSM-333	17805	2500	16400	28000	164	49	Belorussia
KAMAZ-6282	18725	2550	17800	28000	135	48	Russia
LiAZ3-6274	11990	2500	10720	18200	110	25	Russia
VMZ-5298.01-50 «Avangard»	12950	2530	11300	18600	107	30	Russia
PTS-6281	12920	2550	10100	18600	125	25	Russia
Trolza-5265.0 «Megapolis»	12660	2550	10700	18000	100	36	Russia
T70110	11960	2550	11870	19000	105	34	Ukraine
T70115	11960	2550	11760	18900	105	34	Ukraine
T80110	15000	2550	14200	24000	150	38	Ukraine
T90110	18950	2550	17980	30500	184	50	Ukraine
Dnipro T203	12200	2500	11200	18000	107	31	Ukraine
E183	12000	2550	11200	18000	100	30	Ukraine
E301A2	18750	2550	17750	30000	180	56	Ukraine

passenger capacity, the indices of effective use of its areas, observing the norms of extreme loading on the vehicle axles, the economical indices, a choice of optimal storage batteries and so on.

Given researches are especially actual at solving the tasks of additional equipment of a trolleybus park that are already operated by the electric transport enterprises, by the means of autonomous move. Such formulation of a problem is related to introduction on minimum number of constructive changes in the project requirements with observing the layout schemes of trolleybuses compartments, assuring a control of extreme loadings on the axles and other.

Analysis of open sources has showed that in the countries of Eastern Europe and former Soviet Union the most extended brands of trolleybuses that are

operating on urban and suburban routes, are the vehicles manufactured in Germany, France, Czech Republic, USA, Poland, Russia, Belorussia and Ukraine. In Table 2 are shown the weight and overall dimensions indices of the most popular trolleybuses and electric buses manufactured in the aforementioned countries.

The analysis of the weight and dimensions indices of the examined vehicles has showed that for almost all the brands of trolleybuses, from 30 to 40% of their total weight falls on a front axle and the maximum load on the rear axle does not exceed 11500kg. That is why in this task definition a passenger capacity and an autonomous move margin of an electric vehicle are the interconnected parameters. An increasing of one of these indices automatically leads to a necessity of decreasing the other one; that is why a definition of

Table 3 Calculation of passenger capacity and weight indices of the passenger transport

Bus (trolleybus) class	Part of an area that falls on 1 standing passenger, m ²	Mass of 1 passenger, m ²
I	0.15	68
II	0.125	71

Table 4 Weight and dimensions indices for calculating the passenger capacity of trolleybuses for sitting and standing passengers

Bus (trolleybus) class	Mass of a sitting passenger, including a mass of seat with a support, kg	Area that falls on a sitting passenger, m ²		Specific weight that falls on 1 m ² of area designed for sitting passengers, kg/ m ²	
		Individual seat	Double seat	Individual seat	Double seat
I	83.7...91.5	0.325	0.2925	257.5...281.5	286.2...312.8
II	98...103	0.34	0.306	288.2...302.9	320.3...336.6
Number of standing passengers that falls on 1 m ² , persons/m ²		Mass of standing passengers that falls on 1 m ² , kg/m ²			
I	6.67			453.6	
II	8			568.0	

Table 5 Comparison of different types of tractive storage batteries

Battery type	Rated voltage, V	Specific power W/kg	Specific power intensity, Wh/kg
Pb-acid	2	100...300	20...40
NiCd	1.2	150	40...60
NiMH	1.2	250...1000	30...80
LiCoO ₂	3.6	800...3000	150...190
LiMnO ₂	3.8	800...3000	110...135
LiFePO ₄	3.3	800...3000	90...120
Li-pol	3.6	800...900	N/A
LT	2.4	3000...7000	30...110
Double-layer capacitors for reserve copying of memory (DLC);	1.2...3.3	2000...10000	1.5...3.9
Ultra-capacitors for power applications	2.2...3.3	3000...10000	4...9
Pseudo- and hybrid capacitors	2.2...3.8	3000...14000	10...15

rational relations of the aforementioned and other technical and operating parameters of the vehicles to assure both a necessary autonomous move margin and maximum permissible passenger capacity, is an actual practical task.

According to the Regulations № 107 in a vehicle there should be predicted some seats that correspond to requirements of a point 7.7.8 of the Regulations № 107. In the case of a vehicle of classes I and II, a number of seats should at least correspond to a number of square meters of a floor destined for passengers and (if necessary) for crew, rounded to the closest less integral number; in the vehicles of class I this number can be reduced by 10%. The standard indices, according to the Regulations, of a calculation of passenger capacity and weight indices of the passenger transport, are given in Table 3.

In Table 4 there are given the weight and dimensions indices for calculating the passenger capacity of trolleybuses for sitting and standing passengers.

When analyzing the data of Table 4, it was found out that a relation between the values of specific weight indices, which fall on a unity of area for sitting and standing passengers, fluctuates in a range from 1.45 to 1.97, depending on a vehicle class.

The next phase of the research is a definition of relation between an autonomous move margin of additionally equipped trolleybus and a type of tractive storage batteries and its passenger capacity.

Based on the research materials [21], where a comparison was made of different types of tractive storage batteries, in Table 5 are given values of their principal specific characteristics.

Next is presented a check of effectiveness of the aforementioned multiple-factor model of research of rational relations between the technical and operating parameters and additional equipment of trolleybuses by means of assuring an autonomous move at an example of trolleybus T70110 (Ukraine).

Table 6 Tests results of trolleybus T70110

No.	Definable indices	Actual values of indices	
		Equipped trolleybus, $M_a = 11800$ kg	Trolleybus with technically permissible maximum weight, $M_a = 11940$ kg
1	Electricity consumption at trolleybus acceleration up to 40 km/h, W.h	380	550
2	Electricity consumption by a trolleybus at control strip ($L_{route} = 10.2$ km), kWh	- total: 12.5 - taking into account a recuperation: 10.5	- total: 19.0 - taking into account a recuperation: 17.0
3	Specific electricity consumption by a trolleybus at a given control strip, W.h/t.km	- total: 103.9 - taking into account a recuperation: 87.2	- total: 98.3 - taking into account a recuperation: 88.0

Table 7 Results of calculating the weight of different types of tractive accumulator batteries to assure an autonomous move of 5, 10 and 30 km

Battery type	Weight of accumulator batteries without operation of energy recuperation system, kg			Weight of accumulator batteries with operation of energy recuperation system, kg			Influence of recuperation system on a weight of accumulator batteries, kg		
	5 km	10 km	30 km	5 km	10 km	30 km	5 km	10 km	30 km
Pb-acid	498.7	997.4	2992.2	446.45	892.9	2678.7	52.25	104.5	313.5
NiCd	277.05	554.1	1662.3	248	496.0	1488	29.05	58.1	174.3
NiMH	304.75	609.5	1828.5	272.85	545.7	1637.1	31.9	63.8	191.4
LiCoO2	79.3	158.6	475.8	71	142.0	426	8.3	16.6	49.8
LiMnO2	109.7	219.4	658.2	98.2	196.4	589.2	11.5	23.0	69
LiFePO4	129.3	258.6	775.8	115.75	231.5	694.5	13.55	27.1	81.3
LT	282.1	564.2	1692.6	252.55	505.1	1515.3	29.55	59.1	177.3
Double-layer capacitors for reserve copying of memory (DLC)	6137.8	12275.6	36826.8	5494.7	10989.4	32968.2	643.1	1286.2	3858.6
Ultra-capacitors for power applications (UCP)	2401.15	4802.3	14406.9	2149.55	4299.1	12897.3	251.6	503.2	1509.6
Pseudo- and hybrid capacitors (PHC)	1108.2	2216.4	6649.2	992.1	1984.2	5952.6	116.1	232.2	696.6

According to the tests results of a given trolleybus type, made by scientific and testing centre «Urban electric transport» of state enterprise «Scientific-experimental and construction-technological institute of urban economy», the data of its electricity consumption, obtained experimentally are shown in Table 6.

To assure a run of a trolleybus for the defined distance, taking into account a coefficient of efficiency of elements and systems of a vehicle, including a storage battery, a tractive electric engine and a transmission, a necessary number of energy would be found as:

$$E_p = E_{Sp} \cdot L_p / \eta, \quad (4)$$

where:

E_{Sp} - a specific electricity consumption by a vehicle, kW·h/km;

η - a coefficient of efficiency of elements and systems of a vehicle, including a storage battery, a tractive electric engine and a transmission.

In the general case, taking into account the loading of a vehicle, a relation of Equation (4) would look like:

$$E_p = E_{Sp}^{t,km} \cdot M_a \cdot L_p / \eta, \quad (5)$$

where:

$E_{Sp}^{t,km}$ - a specific electricity consumption by a vehicle per unit of mass, kW·h/t.km;

M_a - weight of a vehicle, t.

To provide a vehicle with electricity, a set of tractive storage batteries is necessary, whose weight can be calculated by a relation:

$$M_{batt} = E_p / E_{Sp.batt.}, \quad (6)$$

where:

$E_{Sp.batt.}$ - specific power intensity of a battery, W.h/kg.

Thus, based on Equations (4) - (6), a length of a trolleybus autonomous move L_p taking into account given mode of movement and some type of tractive

storage batteries, can be calculated by a formula:

$$L_p = \frac{E_{Sp,batt} \cdot M_{batt}}{E_{Sp}^{t,km} \cdot M_a} \quad (7)$$

In Table 7 are given results of the weight calculations of different types of tractive accumulator batteries to assure an autonomous move of 5, 10 and 30km in an additionally equipped trolleybus T70110 when loading it up to its full loaded mass.

As it is shown in Table 7, it is the most effectively, by the weight indices, to use lithium-ionic accumulator batteries. Besides that, using a system of recuperative braking allows reducing a batteries weight for 10%. For further research, an application of the LiFePO4 tractive accumulator batteries on a trolleybus is accepted.

A problem of finding a trolleybus optimal passenger capacity and of planning a passenger compartment can be presented in the following way. Let, for a trolleybus T70110 be necessary to assure an autonomous move for a distance L_p . At the same time the following restrictions are imposed:

- maximum permissible loading on a supporting surface of one axle is not more than 11500 kg;
- a change of maximum permissible technical weight of a trolleybus is not allowed;
- a change of weight distribution by axles and a displacement of weight center: by axes x and y is not allowed, by the z axis - displacement is only downward;
- dimensions of passenger compartment can be only reduced;
- it is allowed to change of trolleybus class, under the condition of respecting the requirements of the Regulations No. 107.

A multiple-factor problem of finding the optimal technical and operating characteristics for an additionally equipped trolleybus, with a presented number of restrictions, can be visually realized at Radishchev drawing, as multiple-parameters dependence of many values in a multidimensional space (Figure 2), the main of which are:

$$\left\{ \begin{array}{l} m_{AB} = \varphi_1(L_{an}) \text{ -- mass of accumulator battery} \\ \text{ -- autonomous move} \\ P_{st} = \varphi_2(L_{an}) \text{ -- number of standing passengers} \\ \text{ -- autonomous move} \\ P_{sitt} = \varphi_3(L_{an}) \text{ -- number of sitting passengers} \\ \text{ -- autonomous move} \\ P = \varphi_4(L_{an}) \text{ -- total passenger number} \\ E_{AB} = \varphi_5(L_{an}) \text{ -- specific capacity of accumulator} \\ \text{ -- battery -- autonomous move} \\ R_{AB} = \varphi_6(L_{an}) \text{ -- recuperation parameter} \\ \text{ -- autonomous move} \\ k_S = \varphi_7(L_{an}) \text{ -- parameter of used vehicle area} \\ \text{ -- autonomous move} \end{array} \right. \quad (8)$$

A dimensionality of space for such a formulation of a problem - 8. The functions $\varphi_1 - \varphi_7$ are found from the standardized sources and number values, according to calculations, - are given in Tables 3-7.

A dimensionality of a manifold of Equation (8) can be increased by the way of application of other parameters, interesting for a client.

Taking into consideration that in such multiple-factor problems an improvement of one indices automatically leads to a deterioration of the others, a research of rational relations between the basic values of a model is offered to make in two ways.

The first one consists of a determination of the critical boarders of changing the model base parameter, for example the needs in providing an additionally equipped trolleybus with an autonomous move margin from 10 to 22km (Figure 2). After that, at Radishchev drawing the marginal values of all the other parameters are determined to assure the basic requirement. An analysis of these values and a choice of optimal ones from the conditions of assuring of technical and operating characteristics of a vehicle gives an information concerning the correction of a model basic parameter to its improvement.

Another approach is based on an optimization of some set or of all the parameters that are presented by functions in a model. An influence of each parameter on all the others is determined; that is why a zone in multidimensional coordinate system of a rational relation of given rating values of a model is found.

Both the first and the second approaches are rather effective when solving the multiple-factor problems of such kind. However, it is just the second one that gives a possibility to take into account not only the optimal relations between the rating parameters, but to form the precise offers concerning an effective technological and operating assuring of them, as well.

For example, for the trolleybus T70110, in the considered problem, the brands and the marginal weights of accumulator batteries from 320 to 640kg are determined, a number of sitting passengers in a compartment can vary from 27 to 32, a number of standing passengers - from 60 to 64, a power capacity of transport accumulator batteries can be taken in a range from 20 to 52 kWh, as though to restore their charge at final stops of a route, the vehicle has a limited time. A coefficient of using a compartment area should be within the framework from 0.90 to 0.93.

An effectiveness of energy recuperation system significantly depends on a vehicle movement tachogram, which is why a power capacity of batteries taking it into account, in general non-linearly depends on an autonomous move length.

After have reflected on every graph the given conditions and restrictions, an interval of rational value of a trolleybus autonomous move distance was obtained.

A common zone in a given multidimensional system of coordinates allows to receive a rational relation between all the rating parameters of a multiple-factor model (in Figure 2 - a common zone is shaded - the green common zone) and to determine the ways of taking them into account while operating an additionally equipped vehicle.

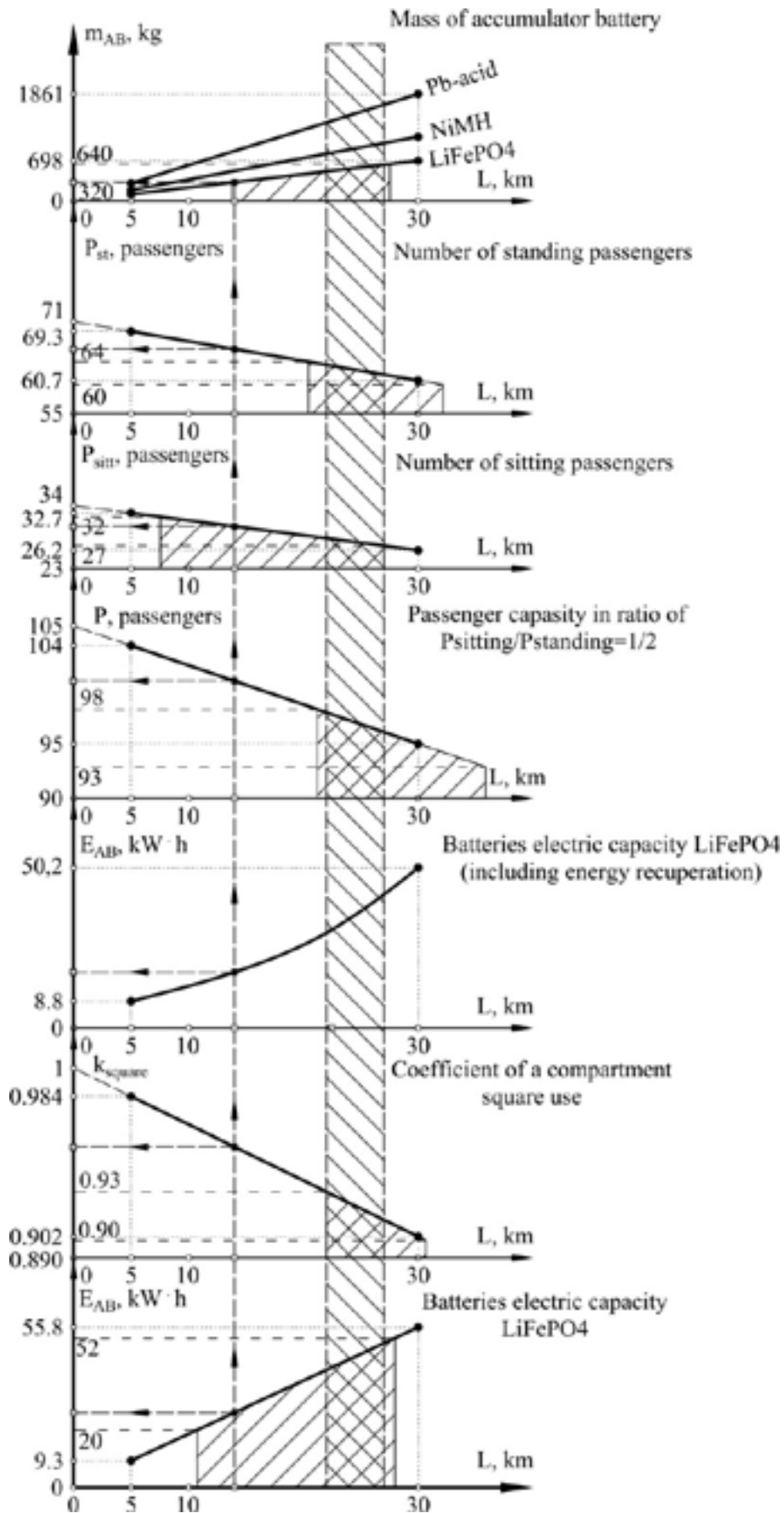


Figure 2 Radishchev drawing

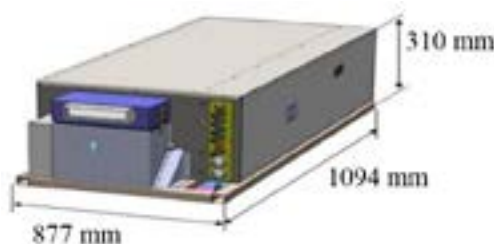


Figure 3 Blocks of accumulator batteries

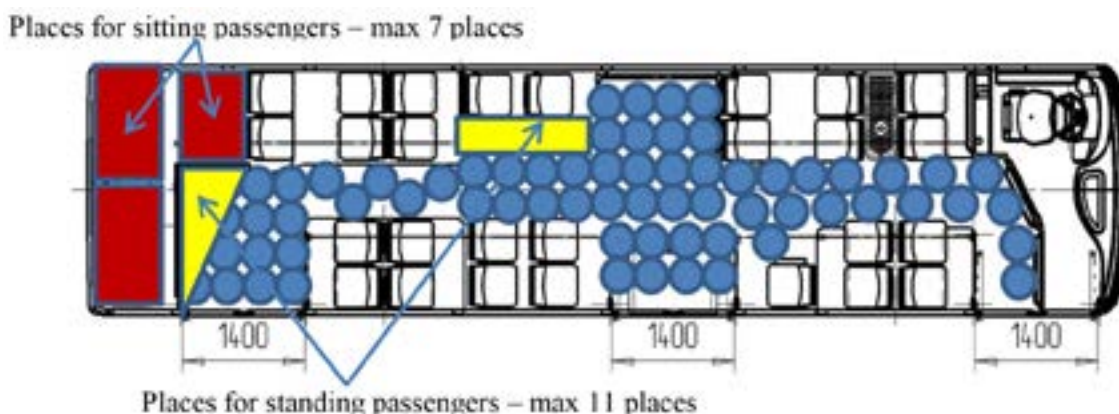


Figure 4 Trolleybus salon planning

4 Research results

A construction of a multiple-factor model and offered algorithm of determining the main parameters allows forming the offers concerning a constructive assuring of an additional equipment process of such a type of trolleybus. Thus, without a significant interruption in a vehicle construction of brand T70110, in rear part of a compartment there is a place for two blocks of accumulator batteries of the necessary type (Figure 3).

The next variants to assure the loading restriction conditions on the axles of chosen vehicle are possible: to reduce a number of standing passengers (maximum number is 11), while restricting along with that, an operating area of passenger compartment; to reduce a number of places for sitting passengers (maximum number is 7); to update an arrangement drawing, after having partially changed the areas for standing passengers by the passenger seats (Figure 4).

In Figure 4 are shown the possible variants of changing a number of sitting places in a compartment of T70110 by the red zones and by yellow - those of a number of standing places, to assure in a multiple-factor model the conditions of the maximum permissible loading on a rear axle 11500 kg. A satisfaction of given restriction is assured by a way of installation in a trolleybus of special hand-rail - restrictors, with the possibilities to quickly transform their construction to correct an arrangement drawing.

The chosen rating parameters of assuring a trolleybus autonomous move will be situated in the most rational relations at its operation on the accumulator batteries in a range from 21 to 27 km (Figure 2), that is completely

enough for a majority of cities that have a developed infrastructure of trolleybus routes.

As though a given multiple-factor model is not attached to any particular brand of a trolleybus that have to be additionally equipped and is not restricted by a number and a list of optimization factors, it can be used as a universal one, to calculate the necessary parameters of the random brand vehicles.

5 Conclusions

The presented research work is devoted to an actual problem of additional equipment of the trolleybuses by the means of assuring an autonomous move in the conditions of their practical operation by the electric transport enterprises. In this work is offered a multiple-factor optimization model for finding the rational relations between the determinative technical and operating parameters, while making an additional equipment of the ordinary trolleybuses.

Based on a visual presentation of multidimensional spaces at Radishchev drawing, an effective way is offered for geometrical interpretation of mutual influence of an optimization factors' manifold on the operating characteristics of the reequipped vehicles. It allows to quickly and effectively assort the restrictions of multiple-criteria problem, to range by significance and by meaning the chosen optimization factors for an enterprise, to quickly correct an influence of each technical and operating parameter on a final result that is an assuring of a vehicle by the means of an autonomous move.

References

- [1] GASSNER, A., LEDERER, J., KANITSCHAR, G., OSSBERGER, M., FELLNER, J. Extended ecological footprint for different modes of urban public transport: the case of Vienna, Austria. *Land Use Policy* [online]. 2018, **72**, p. 85-99. ISSN 0264-8377. Available from: <https://doi.org/10.1016/j.landusepol.2017.12.012>
- [2] PUSTIULHA, S., PRYDIUK, V., HOLOVACHUK, I. A method of fractal estimation of index of imposition of rout charts is for optimization of municipal passenger transportations. *Advances in Mechanical Engineering and Transport*. 2020, **1**(14), p. 124-136. ISSN 2313-5425.
- [3] BARBOSA, F. Modern trolleybus systems as a technological option for greening bus corridors - a technical economical assessment. *SAE Technical Paper* [online]. 2016, 2016-36-0177. ISSN 0148-7191, eISSN 2688-3627. Available from: <https://doi.org/10.4271/2016-36-0177>
- [4] ZHANG, D., JIANG, J., WANG AND, L. Y., ZHANG, W. Robust and scalable management of power networks in dual-source trolleybus systems: a consensus control framework. *IEEE Transactions on Intelligent Transportation Systems* [online]. 2016, **17**(4), p. 1029-1038. ISSN 1524-9050, eISSN 1558-0016. Available from: <https://doi.org/10.1109/TITS.2015.2492564>
- [5] LI, X., CASTELLANOS, S., MAASSEN, A. Emerging trends and innovations for electric bus adoption - a comparative case study of contracting and financing of 22 cities in the Americas, Asia-Pacific and Europe. *Research in Transportation Economics* [online]. 2018, **69**, p. 470-481. ISSN 0739-8859. Available from: <https://doi.org/10.1016/j.retrec.2018.06.016>
- [6] BOROWIK, L., CYWINSKI, A. Modernization of a trolleybus line system in Tychy as an example of eco-efficient initiative towards a sustainable transport system. *Journal of Cleaner Production* [online]. 2016, **117**, p. 188-198. ISSN 0959-6526. Available from: <https://doi.org/10.1016/j.jclepro.2015.11.072>
- [7] MATZOROS, A. Electric trolley buses or thermal buses? The case of Athens. 2002.
- [8] BJORKLUND, S., SOOP, CH., ROSENQVIST, K., YDSTEDT, A. *New concepts for trolley buses in Sweden* [online]. KFB-Rapport 2000:70. Malmo: Swedish Transport and Communication Research Board, 2000. ISSN 1104-2621, ISBN 91-89511-25-5. Available from: <http://www.tbus.org.uk/R-00-70.pdf>
- [9] BUZZONI, L., PEDE, G. New prospects for public transport electrification. In: 2012 Electrical Systems for Aircraft, Railway and Ship Propulsion ESARS 2012: proceedings. IEEE. 2012.
- [10] WANG, X. C., GONZALEZ, J. A. Assessing feasibility of electric buses in small and medium-sized communities. *International Journal of Sustainable Transportation* [online], 2013, **7**(6), p. 431-448. ISSN 1556-8318, eISSN 1556-8334. Available from: <https://doi.org/10.1080/15568318.2012.667864>
- [11] STANA, G., BRAZIS, V. Trolleybus with ESS motion simulation considering common mass increase and transmission losses. In: 2017 IEEE 58th International Scientific Conference on Power and Electrical Engineering of Riga Technical University RTUCON: proceedings [online]. IEEE. 2017. p. 1-6. Available from: <https://doi.org/10.1109/RTUCON.2017.8124769>
- [12] GARCIA-OLIVARES, A., SOLE, J., OSYCHENKO, O. Transportation in a 100% renewable energy system. *Energy Conversion and Management* [online]. 2018, **158**, p. 266-285. ISSN 0196-8904. Available from: <https://doi.org/10.1016/j.enconman.2017.12.053>
- [13] LEBKOWSKI, A. Studies of energy consumption by a city bus powered by a hybrid energy storage system in variable road conditions. *Energies* [online]. 2019, **12**(5), 951. eISSN 1996-1073. Available from: <https://doi.org/10.3390/en12050951>
- [14] MIN, H., LAI, C., YU, Y., ZHU, T., ZHANG, C. Comparison study of two semi-active hybrid energy storage systems for hybrid electric vehicle applications and their experimental validation. *Energies* [online]. 2017, **10**(3), 279. eISSN 1996-1073. Available from: <https://doi.org/10.3390/en10030279>
- [15] PERROTTA, D., MACEDO, J. L., ROSSETTI, R. J. F., DE SOUSA, J. F., KOKKINOGENIS, Z., RIBEIRO, B., AFONSO, J. L. Route planning for electric buses: a case study in Oporto. *Procedia - Social and Behavioral Sciences* [online]. 2014, **111**, p. 1004-1014. ISSN 1877-0428. Available from: <https://doi.org/10.1016/j.sbspro.2014.01.135>
- [16] GOHLICH, D., FAY, T., JEFFERIES, D., LAUTH, E., KUNITH, A., ZHANG, X. Design of urban electric bus systems. *Design Science* [online]. 2018, **4**, E15. eISSN 2053-4701. Available from: <https://doi.org/10.1017/dsj.2018.10>
- [17] SINHUBER, P., ROHLFS, W., SAUER, D. U. Study on power and energy demand for sizing the energy storage systems for electrified local public transport buses. In: 2012 IEEE Vehicle Power and Propulsion Conference: proceedings [online]. IEEE. 2012. ISSN 1938-8756, p. 315-320. Available from: <https://doi.org/10.1109/VPPC.2012.6422680>
- [18] HAMURCU, M., EREN, T. Electric bus selection with multicriteria decision analysis for green transportation. *Sustainability* [online]. 2020, **12**(7), 2777. eISSN 2071-1050. Available from: <https://doi.org/10.3390/su12072777>

-
- [19] AYDIN, S., KAHRAMAN, C. Vehicle selection for public transportation using an integrated multi criteria decision making approach: a case of Ankara. *Journal of Intelligent and Fuzzy Systems* [online]. 2014, **26**(5), p. 2467-2481. ISSN 1064-1246, eISSN 1875-8967. Available from: <https://doi.org/10.3233/IFS-130917>
- [20] PUSTYULGA, S. I. Discrete definition of geometric objects by numerical sequences. Dis. Dr. tech. Science. 05.01.01. Kiev: KNUCA, 2006.
- [21] ARHUN, S. Determination of the most effective traction current sources for electric cars. *Automobile Transport*. 2017, **41**, p. 11-22. ISSN 2219-8342, eISSN 2309-981X.

PROPOSAL OF A METHOD FOR DETECTION OF A DAMAGED HYDRAULIC SHOCK ABSORBER IN A VEHICLE'S SUSPENSION SYSTEM

Mykola Gorbunov^{†1}, Ján Dizo^{2,*}, Miroslav Blatnický², Kateryna Kravchenko², Stanislav Semenov¹, Evgeny Mikhailov¹

¹Volodymyr Dahl East Ukrainian National University, Severodonetsk, Ukraine

²University of Zilina, Zilina, Slovak Republic

*E-mail of corresponding author: jan.dizo@fstroj.uniza.sk

Resume

In principle, every vehicle is equipped by a suspension system, which usually consists of springs and shock absorbers. The main purpose of the suspension system is to eliminate vibration of sprung and unsprung masses. Therefore, the proper operation conditions of the shock absorbers affect in a fundamental way total running properties of vehicles. However, during operation, shock absorbers are being worn out or they can even be damaged. Then, such a situation is unwanted and it has to be detected as soon as possible. The content of this article is focused on analysis of vehicles' shock absorbers defects. Methods for detection of possible shock absorbers faults are presented. Further, a proposal of the method for detection of a state of a hydraulic shock absorber during its operation is presented. The method uses identification of the temperature change of a hydraulic shock absorber during operation.

Article info

Received 13 May 2021

Accepted 27 June 2021

Online 26 October 2021

Keywords:

new method,
hydraulic shock absorber,
vehicle,
damage detection

Available online: <https://doi.org/10.26552/com.C.2022.1.B41-B48>

ISSN 1335-4205 (print version)

ISSN 2585-7878 (online version)

1 Introduction

Diagnostics and control of the technical conditions of transport facilities is an essential attribute of their operation, because due to comprehensive monitoring, the necessary level of reliability, safety and stability of freight and passengers transport can be achieved [1-2]. An important parameter of technical conditions of vehicles, which determines the comfortable performance and affects the safety of transport, is efficiency of the shock absorbers, which are used to improve the dynamic qualities of vehicles through use of damping properties of their structural elements [3-5].

The shock absorbers are designed to compensate forces that cause oscillations of a body of a vehicle during its movement. The damping of the body oscillations energy must be performed simultaneously in three directions with respect to the straight-line movement of a vehicle itself. A locomotive can be equipped by as many as 32 shock absorbers. In the case of defective conditions of shock absorbers, a spring suspension does not ensure the operation of railway vehicles within the defined running smoothness and may endanger the transport safety. The presence of a defective shock absorber increases wear on elements of vehicles, adversely affecting a track and leads to a need for a speed reduction. Regarding the absence of the needed methodology for determining the failure of shock absorbers during operation in practice,

there are such situations, when 50% of defective shock absorbers per locomotive exist. The change of their temperature or the gradient of the heating rate of any particular object during the vehicle running is one of the important characteristics of the working shock absorbers [6-9].

2 Vehicles' suspension system

Vehicles suspension system absorbs shocks and vibrations, which are generated during the vehicle movement on an uneven track. Track unevenness causes quite rough and fast shocks, which are transmitted to the suspension system and transformed to soft and damped deviations of individual vehicle's body [10-11].

The suspension system of a vehicle affects the running safety, ride comfort for passengers and loading of a track [12-15]. If the suspension system works properly, it ensures the constant contact of wheels with a track. It means, that all the forces in the wheel/track contact can be transmitted to the track [16-18], i.e. driving forces, guiding forces and braking forces [19-20]. Thus, the proper function of all the components of a vehicle suspension system is one of the most important factors for safety and comfort operation of vehicles [21].

As it was mentioned above, the track unevenness causes movements of a vehicle. Profiles of unevenness

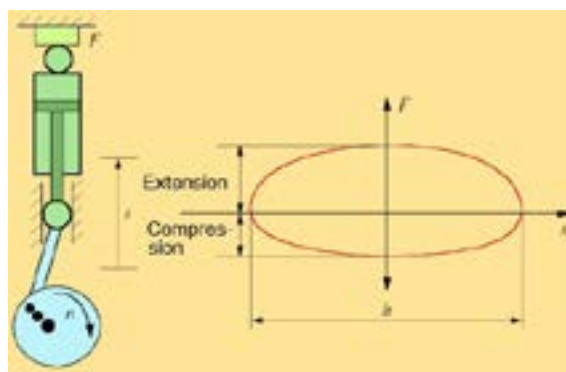


Figure 1 Operating characteristics of a shock absorber:
F - force; *s* - piston movement; *h* - full stroke

of roadway surfaces or railway tracks are irregular and in the point of view of the statistic dynamics, unevenness are stochastic [22-25]. When the vibration properties of vehicles are investigated, sometimes a single unevenness or impact is considered [26]. Based on numerous research, such unevenness can lead to significantly worse running properties of vehicles and even to an accident [27-28].

Generally, the suspension system of a vehicle consists of springs and shock absorbers. While spring ensures the required positions of individual components of a vehicle with respect to each other and allow their mutual movements in determined directions, the main functionality of the shock absorbers is to reduce amplitudes and frequencies of generated vibrations.

Based on described above, the proper operation of the shock absorbers is extremely important in terms of running properties of vehicles. In the opposite case, the insufficiently effective shocks absorbers or even damaged shock absorbers can cause a number of deficiencies [29-31], among others the following:

- Time extension of vibration of individual bodies of a vehicle while running on track unevenness,
- Excessive vibration of a vehicle body, when it runs on successive track unevenness,
- Large deviations of a vehicle body at the improper frequencies generate excessive values of accelerations, which deteriorate the ride comfort for passengers [15, 32],
- Due to high amplitudes of vibrations, a wheel can lose the contact with a track, which means really dangerous situation in terms of the running safety,
- It leads to the worsen effectiveness of braking and directional stability of a vehicle (a normal force is lower) and causes a danger of a skid mainly during running in curves [33].

3 Methods for identification of a damaged shock absorber

Hydraulic shock absorbers undergo maintenance as a part of the system of the preventive maintenance [34-35]. Their premature failures are detected during

the scheduled inspections, while, as a rule, attention is paid to traces of oil and external damage. Methods for testing the shock absorbers directly on a vehicle are being researched, which would make possibility of repairing according to their technical conditions.

The attention is focused on development of a fundamental database of shock absorbers damages, since only incomplete information was available about their type and numbers. A database of damage types and characteristics is created. It is used in modelling the characteristics of shock absorbers of wagon oscillations. The simulation is carried out based on characteristics of the real shock absorbers, which are then prepared for experiments on a roller stand, as well as by a measuring wagon.

Objective monitoring of the performance of hydraulic shock absorbers is carried out on specialized stands using the harmonic oscillation method with diagram recording. A diagram determines parameters of the resistance and then it compares them to the standard values, resistance forces, their symmetry on the extension-compression strokes and maximum values in the valve mode, possible defects in a shock absorber.

Currently, studies of the damping ability in the most studies are performed only according to the performance characteristics (Figure 1) in compliance with the secondary data, in the construction of which, both in working diagrams and experimentally, substantial inaccuracies are allowed, do not provide a sufficiently adequate idea for the real view of the absorbed and scattered energy by the shock absorbers for the cycle of oscillatory motion of a vehicle [36-38].

The working diagram is recorded in these coordinates: *y* - axis is the piston movement; *x* - axis is the resistance force. In the case of a working hydraulic shock absorber in the throttle mode, the diagram has the form of a closed ellipse and in the valve mode it comes closer to a rectangle (Figure 2), where *F* is the damping force, *h* is a piston stroke in a damper, *L_e* is value of a damper expansion and *L_c* is a damper compression.

The area of the ellipse reflects the work of the forces of the shock absorber resistance:

$$W = \pi \cdot a \cdot F(\alpha, \omega), \quad (1)$$

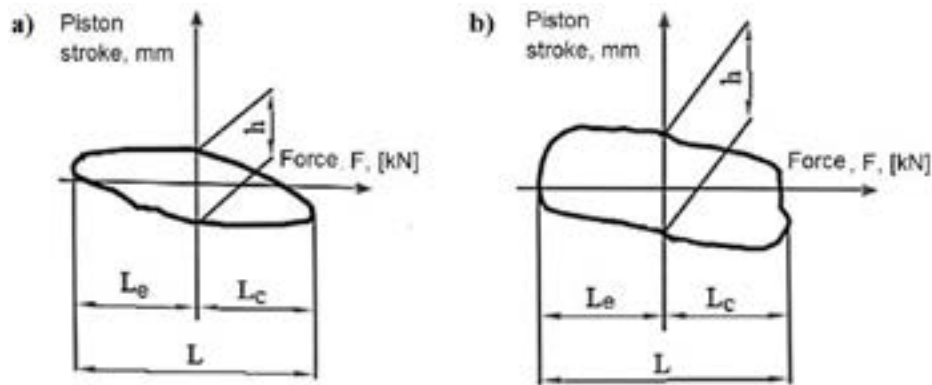


Figure 2 Working diagrams of the hydraulic shock absorbers: a - throttle mode, b - valve mode

Table 1 Analysis of diagrams of hydraulic shock absorbers on a stand at various working modes

Form of a diagram, when:				Analysis of the resistance forces	Failure
$v_{e1} = 0.04 - 0.06 \text{ m}\cdot\text{s}^{-1}$		$v_{e2} = 0.08 - 0.10 \text{ m}\cdot\text{s}^{-1}$			
Expansion	Compression	Expansion	Compression		
				A damper works properly, it is in good conditions. Resistance forces are approximately the same under extension and compression.	
				The small force in the compression	Few oil, contamination, leakage of safety and intake valves in the bottom



Figure 3 Examples of damaged hydraulic shock absorbers: a) leakage of absorber's oil, b) a broken piston rod

i.e. the energy efficiency rating of the shock absorber (α - oscillation amplitude, $\omega = 2 \cdot \pi \cdot f$ - angular frequency, f - oscillation frequency from 1 to 4 Hz) [39]. The length of the diagram, at a given scale along the y-axis, represents the maximum resistance - the total resistance from the extension and compression stroke $2 \cdot F(\alpha, \omega) = 2 \cdot F_m$ - the force indicates the inelastic shock absorber resistance.

The most advanced method for determining faults of the shock absorbers is use of the bench equipment. To do this, the shock absorbers have to be removed from a vehicle, installed and mounted on the test bench. Next, the shock absorber loads are applied and the working diagrams of its operation are recorded. The obtained data are compared to the sample diagrams of

properly working shock absorbers. As a result, the state of the shock absorber and/or internal and external shock absorber defects are determined. Outer defects are also determined by observation a shock absorber during the testing process on the test stand. An infringement of required form indicates the presence and the form of a defect (Table 1, Figure 3).

Stand "ENGA" type SIL-02-01 is designed for testing the hydraulic shock absorbers of locomotives, passenger wagons, metro wagons, etc. Tests are carried out by harmonic oscillations at an installation angle of the shock absorber from 0° to 90° , by constructing the working diagram of the hydraulic shock absorber in a test.

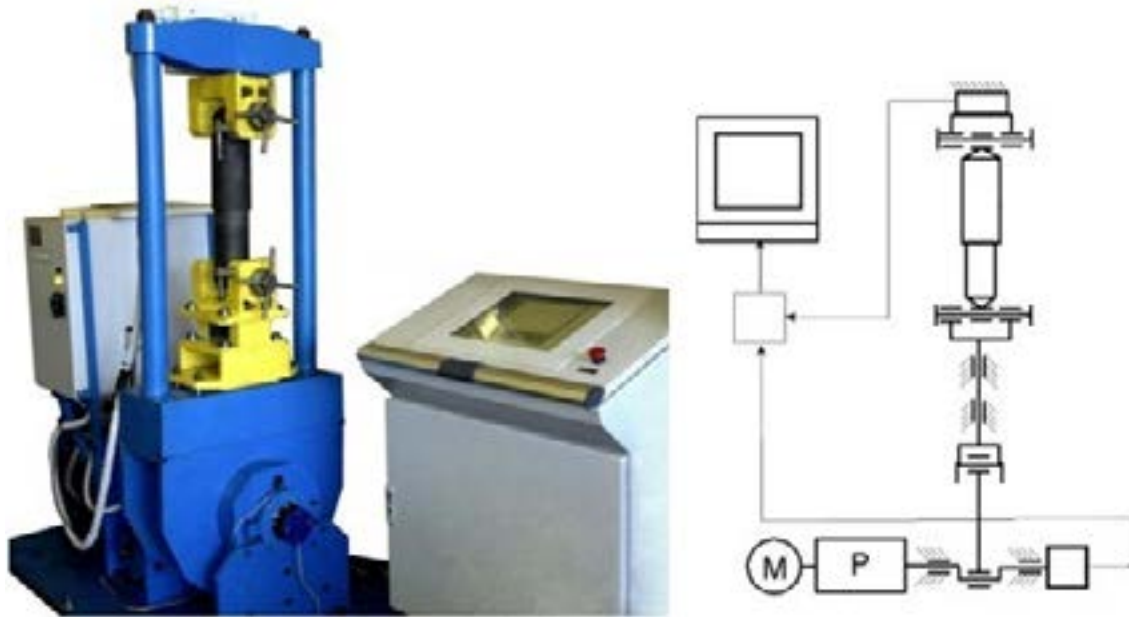


Figure 4 An example of a test stand for the damage detection of a hydraulic shock absorber

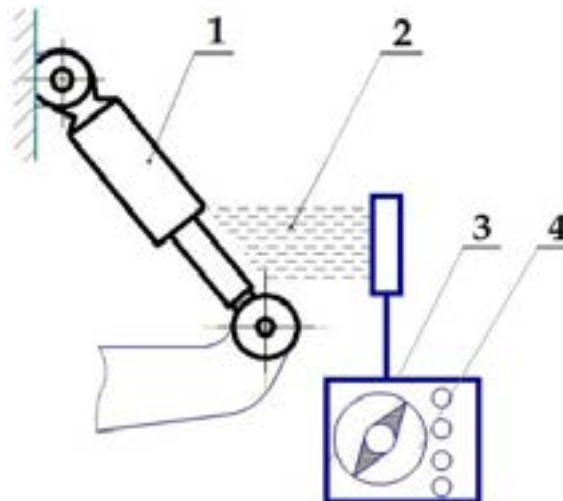


Figure 5 The device for temperature measuring of a shock absorber:
1 - shock absorber; 2 - emitted infrared rays; 3 - radiometer; 4 - receiver

Figure 4 shows the ENGA test stand [40]. The test bench consists of a test module, control module and registration module. The test module consists of the base and a frame of a portal type. In the lower part of the frame, a gearbox of the power drive, the crank mechanism, the fixing mechanism of the lower eye of the tested hydraulic shock absorber, the gearbox for changing the angle inclination, a brake mechanism, a position sensor, sensors of the vertical position and counting of the angle of the stand and the power module, are located. In the upper part of the test module, the fixing mechanism of the upper eye of the tested hydraulic shock absorber, a force-measuring device and a micro-controller module, are located. The control and registration module form a special rack with a system unit, a monitor, a keyboard and a printer.

The study [41] discloses a method for evaluating the damping capacity of the hydraulic shock absorbers.

The method consists of statistical processing of measurements of experimental diagrams. The diagrams are created in the process of experimental tests with different scale and speeds of the piston. Herewith, the number of measurements should be sufficient to ensure the statistical reliability of results. For data processing, the method of regression analysis is used.

Monitoring of technical conditions of the shock absorber can also be performed according to the values of accelerations of the unsprung mass of a vehicle oscillatory motion during its running on track unevenness [42-43]. This method involves comparing information on one hand from sensors, which measure accelerations of the oscillatory motion of the unsprung mass of a vehicle when running on unevenness and, on the other hand, from sensors mounted on the body. The microcontroller processes the results using the mathematical method of the spectral analysis [44-45]. If a disagreement arises

between the theoretical and experimental power spectral density of the vertical accelerations of the sprung mass, the microcontroller sends a signal to an information board and it shows which shock absorber is failed.

Diagnostics of the shock absorbers is obtained with help of reliable information on their technical condition, based on the fact, that their failures are detected and prevented in a timely manner. Especially important are the diagnostic methods for monitoring the performance of hydraulic shock absorbers without removing them from bogies and without disassembling.

Diagnostic parameters that characterize the technical state of the shock absorbers, are the required amount of working fluid, the intensity of infrared radiation from heating and the background noise of fluid throttling. Measurement of these parameters is carried out on diagnostic devices. Moreover, a radiometer is used for determining the shock absorbers' heating.

The working principle is shown in Figure 5. During operation, the shock absorber (1) heats up and emits infrared rays (2), which are absorbed by the receiver (3). After amplification and transformation of a signal in the radiometer (4), they are registered by the indicator arrow. According to the level of temperature, the indicator determines the operation capability of the shock absorber.

5 Development of a method for detection of the damaged shock absorber

The main problem with using the methods presented above for determination of a properly working shock absorber is the inability to detect a faulty shock absorber during the operation. As it is known, one of the extended defects of vibration shock absorbers is the leakage of the working fluid. As a result, the vehicle runs with idle shock absorbers until the vehicle's maintenance [42]. Accordingly, the dynamics, smoothness, comfort and effects related with them are deteriorated [46-48].

The research is based on the task of reducing costs, labor-intensive maintenance, improving the quality of maintenance, reducing the time to restore the operational condition of vehicles with timely detection of the idle shock absorbers and their subsequent replacement during operation, improving the economic efficiency of operation, transportation and help to carriers to secure themselves against accidents on tracks and breakdowns during operation [49-51].

The method is proposed for determining a defective shock absorber, which is as follows:

- Determination of a failure of a shock absorber in operation; the mounted shock absorber is painted with a heat-sensitive color, activity of which depends on temperature. The heat-sensitive colors change their crystal lattice when heated and, as a result, change color (based on the change in the absorption spectrum due to a phase transition). One form of

production of the thermal indicator inks are the wax pencils.

- The sensors for detecting the ambient temperature; the temperature of the shock absorber and the color change of the vibration shock absorber are installed and connected to a data processing unit (DPU). The DPU software calculates the permissible heat of the working shock absorber depending on the ambient temperature.
- For verification of a relevant results of the method is used a sensor, which reacts to colors of the shock absorber. The software processes information from this sensor and compares it to the temperature sensor.
- After processing information in the DPU, information about the operational capability of the shock absorber is shown on the control display of a mobile unit.
- To further check the operation of the shock absorber, the operator performs an external inspection of it immediately after the vehicle stops and by its color confirms the state of the shock absorber and records that in a fault book.

6 Conclusion

According to results of the study, it was determined, that a large number of shock absorbers do not work properly. This phenomenon worsens the running characteristics of a vehicle and impairs its running dynamics. There are many methods for eliminating the non-working shock absorbers, but the main ones are based on using the bench equipment. In this case, it is necessary to remove a shock absorber from a vehicle. This complicates the procedure for identifying a defective shock absorber. A method is proposed for diagnostics of the shock absorbers on vehicles, based on an assessment of the shock absorber's temperature. This method allows:

- Reducing costs,
- Reducing maintenance effort,
- Improving the maintenance quality,
- Reducing time for restoring the operation capability condition of vehicles with timely detection of non-working shock absorbers and their subsequent replacement during operation and
- Increase the economic efficiency of the operation of vehicles and helps to carriers to secure themselves against accidents on tracks and breakdowns during operation.

Acknowledgement

The authors of the article express their deep gratitude for the joint work with the outstanding professor Mykola Gorbunov. The technical ideas of the article have

originated as the results of scientific discussion with him. His irreplaceable contribution to development of modern science is expressed by the non-standard and creative nature of the proposed technical solutions, some of which are also presented in this article.

This research was supported by the Cultural and Educational Grant Agency of the Ministry of Education of the Slovak Republic in the project No. KEGA 023ŽU-4/2020: "Development of advanced virtual models for studying and investigation of transport means operation

characteristics".

This research was also supported by the Slovak Research and Development Agency of the Ministry of Education, Science, Research and Sport of the Slovak Republic in Educational Grant Agency of the Ministry of Education of the Slovak Republic in the project No. VEGA 1/0558/18: "Research of the interaction of a braked railway wheelset and track in simulated operational conditions of a vehicle running in a track on the test bench".

References

- [1] GERLICI, J., SAKHNO, V., YEFYMENKO, A., VERBITSKII, V., KRAVCHENKO, A., KRAVCHENKO, K. The stability analysis of two-wheeled vehicle model. In: 22nd Slovak-Polish Scientific Conference on Machine Modelling and Simulations MMS 2017: proceedings. 2017.
- [2] SAKHNO, V., POLIAKOV, V., TIMKOV, O., KRAVCHENKO, O. Lorry convoy stability taking into account the skew of semitrailer axes. *Transport Problems* [online]. 2016, **11**(3), p. 69-76. eISSN 2300-861X. Available from: <https://doi.org/10.20858/tp.2016.11.3.7>
- [3] LOVSKA, A., FOMIN, O., PISTEK, V., KUCERA, P. Dynamic load modelling within combined transport trains during transportation on a railway ferry. *Applied Sciences* [online]. 2020, **10**(16), 5710. eISSN 2076-3417. Available from: <https://doi.org/10.3390/app10165710>
- [4] LOVKSA, A., FOMIN, O., PISTEK, V., KUCERA, P. Dynamic load and strength determination of carrying structure of wagons transported by ferries. *Journal of Marine Science and Engineering* [online]. 2020, **8**(11), 902. eISSN 2077-1312. Available from: <https://doi.org/10.3390/jmse8110902>
- [5] STASTNIAK, P., MORAVCIK, M. Development of two types of freight wagons with bogies for non-standard wheelbase or track wheelset, complying with the criteria for interoperability, environmental issues, safety and reliability. In: 23rd International Conference on Current Problems in Rail Vehicles: proceedings. 2017. p. 401-408.
- [6] ALEGRE, D. M., KOROISHI, E. H., MELO, G. P. Experimental fault diagnosis in systems containing finite elements of plate of Kirchhoff by using state observers methodology. *Journal of Physics: Conference Series* [online]. 2015, **628**(1), 012022. ISSN 1742-6588, eISSN 1742-6596. Available from: <https://doi.org/10.1088/1742-6596/628/1/012022>
- [7] VAICIUNAS, G., BUREIKA, G., STEISUNAS, S. Rail vehicle axle-box bearing damage detection considering the intensity of heating alteration. *Eksplatacja i Niezawodnosc-Maintenance and Reliability* [online]. 2020, **22**(4), p. 724-729. ISSN 1507-2711. Available from: <http://dx.doi.org/10.17531/ein.2020.4.16>
- [8] ZHAO, Z., WU, B., ZHOU, T. Feature analysis of degradation signal of rolling stock lateral damper. *Information* [online]. 2020, **11**(6), 298. eISSN 2078-2489. Available from: <https://doi.org/10.3390/info11060298>
- [9] SUCHANEK, A., HARUSINEC, J., LOULOVA, M., STRAZOVEC, P. Analysis of the distribution of temperature fields in the braked railway wheel. *MATEC Web of Conferences* [online]. 2018, **157**, 02048. eISSN 2261-236X. Available from: <https://doi.org/10.1051/mateconf/201815702048>
- [10] SAGA, M., VASKO, M., HANDRIK, M., KOPAS, P. Contribution to random vibration numerical simulation and optimisation of nonlinear mechanical systems. *Scientific Journal of Silesian University of Technology-Series Transport* [online]. 2019, **103**, p. 143-154. ISSN 0209-3324, eISSN 2450-1549. Available from: <https://doi.org/10.20858/sjsutst.2019.103.11>
- [11] REZAZADEH, A., MORADI, H. Design of optimum vibration absorbers for a bus vehicle to suppress unwanted vibrations against harmonic and random road excitations. *Scientia Iranica* [online]. 2021, **28**(1), p. 241-254. ISSN 1026-3098. Available from: <https://doi.org/10.24200/SCI.2020.50911.1911>
- [12] PAVELCIK, V., BARTA, D., SAPIETA, M. Proposal of a mechanism for car seat movement. *Advances in Science and Technology-Research Journal* [online]. 2020, **14**(1), p. 50-57. ISSN 2299-8624. Available from: <https://doi.org/10.12913/22998624/113286>
- [13] ZEHELEIN, T., HEMMERT-POTTMANN, T., LIENKAMP, M. Diagnosing automotive damper defects using convolutional neural networks and electronic stability control sensor signals. *Journal of Sensor and Actuator Networks* [online]. 2020, **9**(1), 8. eISSN 2224-2708. Available from: <https://doi.org/10.3390/jsan9010008>
- [14] GARDYNSKI, L., CABAN, J., BARTA, D. Research of composite materials used in the construction of vehicle bodywork. *Advances in Science and Technology-Research Journal* [online]. 2018, **12**(3), p. 181-187. ISSN 2299-8624. Available from: <https://doi.org/10.12913/22998624/92096>

- [15] SUCHANEK, A., HARUSINEC, J., LOULOVA, M. Evaluation of passenger riding comfort of a rail vehicle by means dynamic simulations. In: 23rd Polish-Slovak Scientific Conference on Machine Modelling and Simulations MMS: proceedings. 2018.
- [16] KORZEB, J., CHUDZIKIEWICZ, A. Evaluation of the vibration impacts in the transport infrastructure environment. *Archive of Applied Mechanics* [online]. 2015, **85**(9-10), p. 1331-1342. ISSN 0939-1533, eISSN 1432-0681. Available from: <https://doi.org/10.1007/s00419-015-1029-0>
- [17] SAVARESI, D., FAVALLI, F., FORMENTIN, S., SAVARESI, S. M. On-line damping estimation in road vehicle semi-active suspension systems. In: 9th IFAC Symposium on Advances in Automotive Control AAC 2019: proceedings. 2019.
- [18] KOJIMA, T., SUGAHARA, Y. Fault detection of vertical dampers of railway vehicle based on phase difference of vibrations. *Quarterly Report of RTRI (Railway Technical Research Institute)* [online]. 2013, **54**(3), p. 139-144. ISSN 0033-9008, eISSN 1880-1765. Available from: <https://doi.org/10.2219/rtrqr.54.139>
- [19] GERLICI, J., TKACHENKO, V., SAPRONOVA, S., LACK, T. Steerability research of railway vehicles. In: 24th International Conference on Current Problems in Rail Vehicles: proceedings. p. 145-152. 2019.
- [20] TKACHENKO, V., SAPRONOVA, S. Steerability of railway vehicles. *Transport Problems*. 2007, **2**(4), p. 9-16. ISSN 1896-0596, eISSN 2300-861X.
- [21] SAPRONOVA, S., TKACHENKO, V., KRAMAR, N., VORONKO, A. Regularities of shaping of a wheel profile as a result of deterioration of the rolling surface in exploitation. *Transport Problems*. 2008, **3**(4), p. 47-54. ISSN 1896-0596, eISSN 2300-861X.
- [22] LEITNER, B., DECKY, M., KOVAC, M. Road pavement longitudinal evenness quantification as stationary stochastic process. *Transport* [online]. 2019, **34**(2), 195-203. ISSN 1648-4142, eISSN 1648-3480. Available from: <https://doi.org/10.3846/transport.2019.8577>
- [23] LEITNER, B., FIGULI, L. Fatigue life prediction of mechanical structures under stochastic loading. In: 22nd Slovak-Polish Scientific Conference on Machine Modelling and Simulations MMS: proceedings. 2017.
- [24] HERNANDEZ-ALCANTARA, D., MORALES-MENENDEZ, R., AMEZQUITA-BROOKS, L., SENAME, O., DUGARD, L. Fault estimation methods for semi-active suspension systems. In: 17th IEEE International Autumn Meeting on Power, Electronics and Computing ROPEC 2015: proceedings. IEEE. 2015. ISBN 978-1-4673-7121-6.
- [25] SAGA, M., JAKUBOVICOVA, L. Simulation of vertical vehicle non-stationary random vibrations considering various speeds. *Scientific Journal of Silesian University of Technology-Series Transport*. 2014, **84**, p. 113-118. ISSN 0209-3324, eISSN 2450-1549.
- [26] HAUSER, V., NOZHENKO, O., KRAVCHENKO, K., LOULOVA, M., GERLICI, J., LACK, T. Impact of three axle boxes bogie to the tram behavior when passing curved track. In: 12th International Scientific Conference of Young Scientists on Sustainable, Modern and Safe Transport TRANSCOM 2017: proceedings. 2017. ISBN 9781510843349, p. 295-300.
- [27] STASTNIAK, P., MORAVCIK, M. Stability investigation of a new balance beam system solution for a 3-axle railway bogie. In: 24th International Conference on Current Problems in Rail Vehicles PRORAIL 2019: proceedings. 2019. p. 309-318.
- [28] SMETANKA, L., HRCEK, S., STASTNIAK, P. Investigation of railway wheelset profile wear by using computer simulation. In: 23rd Polish-Slovak Scientific Conference on Machine Modelling and Simulations MMS: proceedings. 2018.
- [29] WEYSSENHOFF, A., OPALA, M., KOZIAK, S., MELNIK, R. Characteristics and investigation of selected manufacturing defects of passenger car tires. In: 13th International Scientific Conference on Sustainable, Modern and Safe Transport TRANSCOM 2019: proceedings. 2019. p. 119-126.
- [30] KRAVCHENKO, K., SAKNO, O., LUKICHOV, A. Research of dynamics of tire wear of trucks and prognostication of their service life. *Transport Problems*. 2012, **7**(4), p. 85-94. eISSN 2300-861X.
- [31] KOSTRZEWSKI, M. Analysis of selected acceleration signals measurements obtained during supervised service conditions - study of hitherto approach. *Journal of Vibroengineering* [online]. 2018, **20**(4), p. 1850-1866. ISSN 1392-8716, eISSN 2538-8460. Available from: <https://doi.org/10.21595/jve.2018.19367>
- [32] HARUSINEC, J., SUCHANEK, A., LOULOVA, M., KURCIK, P. Design of a prototype frame of an electrically driven three-wheel vehicle. In: 23rd Polish-Slovak Scientific Conference on Machine Modelling and Simulations MMS: proceedings. 2018.
- [33] HAUSER, V., NOZHENKO, O., KRAVCHENKO, K., LOULOVA, M., GERLICI, J., LACK, T. Proposal of a steering mechanism for tram bogie with three axle boxes. In: 12th International Scientific Conference of Young Scientists on Sustainable, Modern and Safe Transport TRANSCOM 2017: proceedings. 2017. p. 289-294.
- [34] DROZDZIEL, P., KOMSTA, H., KRZYWONOS, L. Repair costs and the intensity of vehicle use. *Transport Problems*. 2013, **8**(3), p. 131-138. eISSN 2300-861X.
- [35] CABAN, J., DROZDZIEL, P., KRZYWONOS, L., RYBICKA, I., SARKAN, B., VRABEL, J. Statistical analyses of selected maintenance parameters of vehicles of road transport companies. *Advances in*

- Science and Technology-Research Journal [online]. 2019, **13**(1), p. 1-13. ISSN 2299-8624. Available from: <https://doi.org/10.12913/22998624/92106>
- [36] JEREMENKO, V.S., SHEGEDIN, P.A., PEREJODENKO, A.V. Development of a diagnostic system for damping characteristics of rolling stock vibration shock absorbers (In Russian). *East European Advanced Technology Journal* [online]. 2014, **5/7**(71), p. 10-15. ISSN 1729-3774, eISSN 1729-4061. Available from: <http://journals.uran.ua/ejet/article/view/27818/25377>
- [37] PARK, C H., KIM, S., LEE, J., LEE, D.-K., NA, K., SONG, J., YOUN, B. D. Hybridizing data-driven and model-based approaches for fault diagnosis of rail vehicle suspensions. In: 9th Annual Conference of the Prognostics and Health Management Society PHM 2017: proceedings. 2017. P. 612-620.
- [38] BORJAK, K. F., MANZARUK, M. A. Different approaches to the evaluation of technical condition of the hydraulic shock absorbers. In: 4th International Partner Conference Innovative Solutions for Railway Rolling Stock: Practice, Results of Implementation EUROTRAIN 2013: proceedings. 2013.
- [39] WANG, Y.-X., CHEN, E.-L., QI, Z., LIU, P.-F., ZHANG, L. Analysis of dynamic behaviour of high-speed railway vehicle with faulty anti-hunting shock absorber. *Journal of Advances in Vehicle Engineering*. 2017, **3**(3). ISSN 2423-7345.
- [40] Passport STR 02-01.00.000. PS: Stand for testing dampers hydraulic railway rolling stock. Limited Liability Company "Diesel-Test-Kit".
- [41] RYKOV, S. P., TARASJUK, V. N., KOVALS, V. S., KUPRIJANOV, A. P. Modeling and evaluation of the damping capacity of hydraulic shock absorbers (In Russian). *Systems. Methods. Technologies* [online]. 2013, **20**(3), p. 27-32. ISSN 2077-5415. Available from: https://brstu.ru/static/unit/journal_smt/docs/number_20/27-32.pdf
- [42] DOBROWOLSKI, D., DROZDZIEL, P., MADLENAK, R., SILUCH, D., RYBICKA, I. Daily kilometrage analysis for selected vehicle groups. *Advances in Science and Technology-Research Journal* [online]. 2018, **12**(3), p. 39-46. ISSN 2299-8624. Available from: <https://doi.org/10.12913/22998624/92109>
- [43] KOZIAK, S., CHUDZIKIEWICZ, A., OPALA, M., MELNIK, R. Virtual software testing and certification of railway vehicle from the point of view of their dynamics. In: 13th International Scientific Conference on Sustainable, Modern and Safe Transport TRANSCOM 2019: proceedings. 2019. p. 729-736.
- [44] SAPIETOVA, A., SAGA, M., STANCEKOVA, D., SAPIETA, M. Contribution to numerical study of vehicle vertical stochastic vibration. In: 22nd Slovak-Polish Scientific Conference on Machine Modelling and Simulations MMS 2017: proceedings. 2017.
- [45] MORATO, M. M., SENAME, O., DUGARD, L. LPV-MPC fault tolerant control of automotive suspension dampers. *IFAC - PapersOnLine* [online]. 2018, **51**(26), p. 31-36. ISSN 2405-8963. Available from: <https://doi.org/10.1016/j.ifacol.2018.11.172>
- [46] LACK, T., GERLICI, J. Integration methods for rail vehicle ride dynamics solution assessment. In: 23rd International Conference on Current Problems in Rail Vehicles: proceedings. 2017. p. 217-234.
- [47] LOVSKA, A., GERLICI, J., FOMIN, O., KRAVCHENKO, K., FOMINA, Y., LACK, T. Special aspects of determining the dynamic load of the tank container during its transportation in an integrated train set by a railway ferry. In: 11th Transbaltica International Scientific Conference Transbaltica 2019: proceedings. 2019, p. 581-590.
- [48] MELNIK, R., KOSTRZEWSKI, M. Rail vehicle's suspension monitoring system - analysis of results obtained in tests of the prototype. In: 2nd International Conference on Smart Diagnostics of Structures: proceedings. 2012, p. 281-288.
- [49] LEITNER, B., MOCOVA, L., HROMADA, M. A new approach to identification of critical elements in railway infrastructure. In: 10th International Scientific Conference on Transportation Science and Technology Transbaltica 2017: proceedings. 2017. p. 143-149.
- [50] BUREIKA, G., GAIDAMAUSKAS, E., KUPINAS, J., BOGDEVICIUS, M., STEISUNAS, S. Modelling the assessment of traffic risk at level crossing of Lithuanian Railways. *Transport* [online]. 2017, **32**(3), p. 282-290. ISSN 0209-3324, eISSN 2450-1549. Available from: <https://doi.org/10.3846/16484142.2016.1244114>
- [51] STEISUNAS, S., BUREIKA, G. Study of freight wagon running dynamic stability taking into account the track stiffness variation. *Transport Problems*. 2014, **9**(4), p. 131-143. eISSN 2300-861X.

ELECTRIC OR INTERNAL COMBUSTION ENGINES FOR PASSENGER CARS? - ENVIRONMENTAL AND ECONOMIC ASPECTS

Zoran Čekerevac¹, Zdeněk Dvořák^{2,*}, Lyudmila Prigoda³

¹Faculty of Business and Law, „MB“ University in Belgrade, Belgrade, Serbia

²Faculty of Security Engineering, University of Žilina, Žilina, Slovakia

³FSBEI HE "Maikop State Technological University", Maykop, Russia

*E-mail of corresponding author: zdenek.dvorak@fbi.uniza.sk

Resume

The paper is focused on fuels, their users - engines and the end-user, the vehicles, from an environmental and economic point of view. The basic characteristics of potential fuels for internal combustion engines, as well as possible sources of electricity, are analysed. A comparative analysis of characteristics of vehicle propulsion with gasoline, diesel fuel, compressed natural gas, liquefied petroleum gas and electricity was performed. The research has shown that the application of vehicles with an electric motor is ecologically justified only in cases of obtaining electricity in an environmentally friendly way and that in other cases there is no profit in an ecological sense. From an economic point of view, if there were no subsidies to manufacturers and buyers of electric cars, they would not be competitive with internal combustion engines now. Within the research, potential solutions for reducing air pollution and improving the quality of life in cities have been proposed.

Article info

Received 3 June 2021

Accepted 24 June 2021

Online 4 November 2021

Keywords:

oline,
diesel,
LPG,
CNG,
methanol,
ethanol,
fuel consumption

Available online: <https://doi.org/10.26552/com.C.2022.1.B49-B58>

ISSN 1335-4205 (print version)

ISSN 2585-7878 (online version)

1 Introduction

The modern world is taking more and more seriously the impact of environmental pollution on the life and survival of living people, as well as that pollution is transmitted through the atmosphere and occurs where it is not expected, in uninhabited and industrially underdeveloped areas.

Depending on current problems and technological possibilities, the focus of efforts to reduce the harmful effects of air pollution changes. In the developed world until the second half of the 20th century, the main pollutants were sulfur dioxide and soot, due to use of the low-quality fossil fuels, primarily low-quality coal and fuel oil. It is unfortunate, but even now a significant part of air pollution in many cities is a consequence of the same energy sources. The use of cleaner fuels and flue gas filters has greatly reduced the problem. In the sixties of the twentieth century, there was an increase in the number of motor vehicles, which gave rise to new risk factors. Imperfect technology of Diesel engines and carburetors of gasoline engines, with low-quality gasoline, have led to appearance of danger of pollution by lead, nitrogen oxides and unburned hydrocarbons. With improvement of technology at the leading engine manufacturers, the conditions were created for appearance of restrictions in the allowed emission of

harmful gases, so even the smaller manufacturers were forced to change their technologies and products. The norms became stricter over time. For that reason, many producers began to unite or fail. The new standards have contributed to application of better-quality fuel injection systems, controlled injection and removal of carburetors from use, improved production of parts and engines and more uniform quality, as well as to a significant improvement in fuel quality. All this has led to a reduction in fuel consumption per kilometer traveled and even to the fact that the harmful emissions of one vehicle have been reduced many times over in relation to the vehicles from the 1970s. Increase in the number of people on Earth, with the increase in the purchasing power of the population, has led to accelerated growth in the number of motor vehicles. World trends in the growth of the number of vehicles are shown in Figure 1. If one looks at the trends of vehicle registration by year, one can see that in fifty years the total number of registered vehicles has increased more than 11 times. The number of passenger motor vehicles increased 10.6 times and the number of trucks 13.6 times. It is estimated that there were 1.4 billion vehicles in the world in 2019, which means that in relation to the total number of inhabitants (7.674 billion), there were 182 vehicles per 1000 inhabitants. Given number of vehicles, it is logical to expect that over time there will

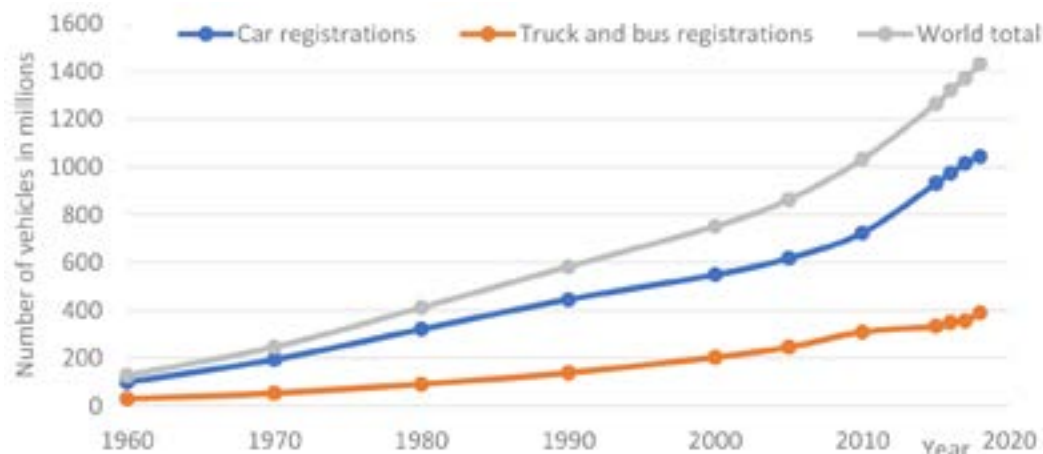


Figure 1 World vehicle registration trends [1]

Table 1 C/H ratio and minimum required amount of air for full fuel combustion (A/F) [2, p. 813]

Fuel	C	H	O	C/H	A/F
	% (m/m _{fuel})			-	$\frac{\text{kg}_{\text{air}}}{\text{kg}_{\text{fuel}}}$
Methane	~ 74.9	~ 25.1	-	~ 3.0	~ 17.4
Propane	~ 81.8	~ 18.2	-	~ 4.5	~ 15.8
Butane	~ 82.8	~ 17.2	-	~ 4.8	~ 15.6
Gasoline	~ 85.5	~ 14.5	-	~ 5.9	~ 14.9
Super gasoline	~ 85.1	~ 13.9	~ 1	~ 6.1	~ 14.6
SuperPlus	~ 84.7	~ 13.3	~ 2	~ 6.5	~ 14.4
Diesel fuel	~ 86.3	~ 13.7	-	~ 6.3	~ 14.8
Methanol	~ 37.5	~ 12.6	~ 49.9	~ 3.0	~ 6.5
Ethanol	~ 52.1	~ 13.2	~ 34.7	~ 4.0	~ 9.0

be increasing of air pollution, which at some point could become critical for human survival. If the impact of air traffic (which is not the topic of this paper) is added to this, it is clear what the challenge is.

At the beginning of the 21st century, the focus shifted from lead, which has been removed from gasoline and ceased to be a critical element, to nitrogen oxides and unburned hydrocarbons, which have been reduced by exhaust catalysts and fuel injection technology, to carbon dioxide. With Diesel engines, the use of carbon black catchers significantly reduced harmful emissions, but the problem of carbon dioxide remained.

The aim of this paper was to consider the justification of tendency to replace the internal combustion engines by electric motors. In this sense, the null hypotheses are set:

H_{01} : Internal combustion engines are always more environmentally unfavorable than the use of electric motors to drive passenger cars.

H_{02} : The use of internal combustion engines is always economically less favorable than the use of electric motors to drive the passenger motor vehicles.

Alternative hypotheses have also been set:

H_{a1} : Internal combustion engines are in some situations more environmentally friendly than the use of

electric motors to power passenger motor vehicles.

H_{a2} : The use of internal combustion engines is, in some situations, more favorable than the use of electric motors to drive passenger motor vehicles, from an economic point of view.

2 Fuels

Nowadays, hydrocarbon-based fuels, primarily gasoline and diesel, are still used the most to power vehicle engines. Not predominantly because of awareness of the air pollution but because of occasional oil shortages or fears and forecasts that oil deposits will be depleted, alternative fuels occasionally come into focus. Some of the most intensive such research were conducted in the 1970s when the possibilities of using various alternative fuels were investigated, primarily liquefied petroleum gas (LPG), methane (CNG), methanol, ethanol and hydrogen, as well as their mixtures. Each of the fuels had its advantages and disadvantages, which over time, with the change of technology, had a different weight. Today, the emphasis is on the impact of a fuel on environment and therefore on fuel consumption. Before analyzing the behavior of vehicles depending on the type

of propellant, some basic characteristics of possible fuels for the propulsion of vehicle engines are considered, see Table 1.

2.1 Fuels for Diesel (compression ignition) engines

From the environmental aspect, the most important for diesel fuel are the lowest density, the lowest final boiling point and the lowest sulfur content. Petroleum naturally contains sulfur which, when burned with more than 95%, is converted into sulfur dioxide (SO_2). The rest passes into the particle mass of the exhaust that contains sulfurous acids and sulfates. Sulfur compounds cause increased corrosion and increased air pollution. The residue is mixed with soot, which contains many compounds that are considered carcinogenic. Thanks to improved fuel processing processes, the SO_2 emissions of diesel engines are no longer a risk to the environment. Since the particles cannot be completely removed by limiting the sulfur content, it is necessary to further treat the exhaust gases with appropriate filters, particle traps. To improve the fuel quality, detergents and dispersant additives, corrosion inhibitors, lubricant additives, antifoaming agents and regeneration aids for particle filters are added to diesel fuels.

As an alternative to classic diesel fuel, biodiesel appears. The idea is to emit as much CO_2 into the atmosphere as plants take from the air for their growth. In this way, no additional amount of CO_2 would be emitted into the atmosphere. However, biodiesel brings with it new problems in the form of a small increase in NO_x emissions, the appearance of "fritting" odor from the exhaust and polycyclic aromatic hydrocarbons, insufficient stability, substantial deposits on the nozzles and in the combustion chambers [2, p. 821].

Methanol and ethanol are bad fuels for Diesel engines if used alone and could eventually be used in dual-fuel propulsion. However, it is economically unprofitable.

The use of diesel and water emulsions brings lower concentrations of NO_x emissions and black smoke, however, it increases hydrocarbon (HC) and carbon monoxide (CO) emissions, as well as fuel stratification, endangering the injection system and potential freezing of water at low temperatures, so when all this is considered, these solutions are not a good choice to apply to vehicle engines.

The use of LPG and CNG in Diesel engines requires an additional classic fuel injection system for the mixture to ignite in the cylinder. Such solutions exist with some city buses, but users more often decide to rework the engines by replacing the injectors with spark plugs and the injection pumps with an electric ignition system. All this must be followed by reducing the compression ratio to the level of the SI engine, 11: 1. However, this is not widespread either.

2.2 Fuels for vehicle spark-ignition engines (SI)

The most common fuel for spark-ignition engines¹ is gasoline, which is a fuel that consists of many hydrocarbons found in basic gasoline that is obtained in refineries by various processing methods from petroleum from a wide range of origins. It is a mixture of reformates, crack gasolines (olefins), pyrolysis gasolines, isoparaffins, butane, alkylates, the so-called replacement components such as alcohols and ethers and slight amounts of additives [2, p. 824]. It has been used for a long time with the use of carburetors, but due to the better control of the fuel-air mixture, today's new engines work with fuel injection.

As an alternative to gasoline in Otto engines as fuel, appear [2, p. 836]:

- LPG - Liquefied Petroleum Gas. Pressurized, liquefied auto gas based on propane and butane.
- CNG - Compressed natural gas based on methane.
- LNG - Liquefied Natural Gas. Gas liquefied at low temperatures based on methane.
- MEOH - Methanol. Alcohol, usually from natural gas (methane), also termed wood spirit.
- ETOH - Ethanol. Alcohol from sugar-containing plants.
- GH_2 - Gaseous Hydrogen. Can be made from water and all the hydrogen-containing energy carriers.
- LH_2 - Liquefied Hydrogen. Hydrogen that is liquid at low temperature.

Use of the liquefied gases in spark-ignition engines brings a few advantages in terms of fuel consumption and emission, but only in engines designed for this. When adapting the engine, dual-fuel propulsion, more favorable exhaust emissions will be obtained due to a more favorable C/H ratio, however, the high resistance to detonation cannot be exploited. In addition, the storage of the other fuel requires an additional tank that significantly reduces the usable space of the trunk.

2.2.1 Gasoline

Gasoline is a fuel that is exposed to a certain risk of explosion while stored in a tank. An explosion can occur in the zone where the volumetric ratio of fuel and air is at the level of 1-8%. Under normal circumstances, the concentration of gasoline in the fuel tank is significantly above the upper limit of 8%. Critical situations can occur in the case of low volatility and low environmental temperature, but in addition to the appropriate concentration, there must exist the source of ignition to ignite the mixture, so these risks are at an acceptable level.

An important characteristic of gasoline is the octane value, which provides it with resistance to detonating

¹Spark-ignition engines (SI) - Otto engines known as "gasoline engines" in the USA and "petrol engines" in the UK.

combustion. With the elimination of lead from use, ethers appeared as components to increase the octane number of fuels in addition to the further developed high-octane, classic components and alcohols. There is no uniform standard for gasoline quality in the world. For example, three types of gasoline are sold in Serbia:

- Euro Premijum BMB 95 (Euro 95 Regular unleaded motor gasoline).
- Euro BMB 98 (Euro 98 Unleaded Motor Gasoline).
- Euro BMB 100 (Euro 100 Unleaded Motor Gasoline).

where the numerical values correspond to the minimum RON² value that the fuel must have.

Application of the modern fuel injection systems has brought the need to bring the fuel density to a narrow range to enable computer systems to work properly and reduce the fuel consumption and emissions.

To reduce CO and unburned HC, oxygen-rich compounds such as MTBE (Methyl tertiary-butyl ether), ETBE (Ethyl tertiary-butyl ether), butanol, or ethanol are added to gasoline in controlled amounts. In addition to this, various other additives are added to gasoline to improve the characteristics, as well as the color to differentiate gasoline by types and to identify gasoline manufacturer.

Sulfur appears as a regular component of oil, so it should be removed to avoid SO₂ emissions. In addition, some catalytic converters in uncontrolled conditions tend to convert sulfur into hydrogen sulfide (H₂S) that smells. As the sulfur content increases, efficiency of the catalytic converters decreases. Consequently, emissions of CO, HC and NO_x occur are increased, which can have serious consequences.

2.2.2 LPG (Liquid Petroleum Gas)

LPG (Liquid Petroleum Gas) is a blend of propane and butane compressed between 5 and 7 bars. Propane and butane mixture is liquefied by cooling to a low temperature or by compressing. When being liquefied, the mixture's volume is reduced 260 times in comparison to the gaseous phase. The LPG is a fuel like gasoline. Its density is 550 kg/m³. In its gaseous form, the LPG is heavier than air. When bearing in mind its effects on human health, the LPG is not toxic, however, it is unbreathable with slightly toxic effects [3].

The LPG has higher flame propagation speed compared to gasoline at the range of lean-to stoichiometric equivalence ratios. At the rich mixtures range, gasoline flame speed is superior. Compared to gasoline the energy content of the LPG is slightly higher, 45.7 MJ/kgK to 44 MJ/kgK of gasoline [4]. In addition, the LPG has an advantage in terms of octane number, which allows it to work at higher compression ratios.

Use of the LPG in Diesel engines is difficult to pay

²RON - Research Octane Number

off, due to the cost of investment in the adaptation of Diesel engines and research on the use of the LPG as a fuel in spark-ignition engines has shown [5] that:

- By a small increase in the pre-ignition angle, relative to the factory setting for the gasoline drive, the coefficient of variation of the indicated mean effective pressure (COVIMEP) can be reduced. At the same time, CO and HC emissions are decreasing, but NO_x emission is increasing. On the other hand, later ignition has the opposite effect followed by a reduction in engine power.
- The engine efficiency is lower at low speeds when running on gasoline and at higher speeds, the advantage is on the LPG side.
- The LPG combustion achieves significantly more favorable CO and HC emissions, five and seven times respectively, as well as twice as high NO_x emissions at higher engine speeds.

The LPG can be injected into the engine cylinders in the gaseous state, as well as by directly injecting fuel into the cylinder. This is described in detail in [6].

2.2.3 CNG (Compressed Natural Gas)

CNG (Compressed Natural Gas), is the same as the gas used to heat houses. Natural gas is a resource that is very widely available in the world. Because of its chemical composition, it is less polluting than gasoline or diesel. It consists mainly of methane and is compressed between 200 and 300 bars. It can be stored as a gas at ambient temperatures.

Compared to gasoline, natural gas has a lower burning rate, higher quenching distance and narrow flammability range. In addition, it requires a higher ignition energy [7].

The main advantages of the CNG are [8]:

- 77% less particle emission than a diesel.
- 11% reduction in CO₂ emissions (without taking the extraction method into account).
- 90% less nitrogen oxides.
- much cheaper than diesel or gasoline.

From the environmental and economic aspect, the disadvantage of the CNG application is that if it is not obtained by fermentation of plant waste, the ecologically positive impact of its application is significantly degraded, since during the extraction one part of methane always leaks and methane is a gas that has the more negative greenhouse effect impact of CO₂.

2.2.4 Hydrogen

Hydrogen could be an ideal fuel because it exists in nature in unlimited quantities. When burned hydrogen does not emit CO₂, but only water vapor and the air that remains after the combustion. Big obstacles are the price to produce hydrogen in a form suitable for use,

increased NO_x emission due to the high temperature of hydrogen combustion and the fact that hydrogen burns with a colorless flame. In the case of fire, the flame will not be visible to firefighters that can endanger their safety. High storage pressure of 350 bar (up to 700 bar) can affect the mood of users who need to drive such a vehicle. Metal hydride storage tanks provide a more cost-effective solution but can store less hydrogen. Due to the high pressure, very massive tanks are needed, which is difficult to accept for the passenger vehicles. Storing hydrogen in a liquid state requires exceptionally low temperatures (20 K), which requires a cryotank³ with efficient insulation. With all this in mind, it is hard to believe that hydrogen would emerge as a fuel for vehicle engines soon, although tests have been performed as early as the 1970s.

2.2.5 Alcohols

Alcohol contains the OH group in its molecules that is a suitable fuel component for spark-ignition engines. Producing of alcohol has been known since ancient times and is well developed. Alcohol can be transported in the same way as gasoline. Its characteristics in terms of resistance to detonation combustion are at the level of RON = 114.4, which is higher than the level that exists with gasoline, so engines powered by alcohol (primarily methanol and ethanol) can work with a higher compression ratio. Alcohols burn faster than gasoline, which means that their fuel pre-ignition map must be adjusted. Significantly higher heat of vaporization of alcohol, compared to gasoline, provides greater internal cooling of the fuel mixture and thus the degree of filling of the engine cylinder. Consequently, alcohols give a higher thermodynamic efficiency and even better performance. Due to the OH group, the calorific value of alcohol is significantly lower than the calorific value of gasoline, which implies significantly higher fuel consumption. In addition to that, an increased risk of corrosion must be considered. In the case of use of pure alcohol, there may be a need to preheat the intake air in winter conditions.

Alcohols can be used in their pure form or in combination with gasoline. In the case of mixing with gasoline, it should be borne in mind that fuel stratification can occur. Low concentrations of alcohol, of 5 to 10% Vol, in the mixture, in principle, do not represent any special problem, but the profit is small. Concentrations greater than 15% Vol. can stratify depending on external conditions, e.g., in cold weather and prolonged vehicle standstill. In the case of occasional mixing of fuel and hot weather, even the concentration of 30% Vol. of the methanol in the mixture will not stratify [11]. In the

³A cryotank or cryogenic tank is a tank that is used to store material at very low temperatures [9]. An insulated tank used for the storage of cryogenic liquids [10].

case of pure methanol, it is necessary to add a small amount of HC in the phase of cold start and engine warm-up, but also for the safety reasons. Alcohol burns with a colorless flame, which could endanger rescuers in the event of a vehicle fire. Engine lubricating oil must contain additives that will prevent formation of a sticky mass in the case of contact of the oil with alcohol, as well as anti-corrosion additives.

2.3 Vehicles powered by alternative fuels

2.3.1 LPG

If one compares the fuel supply systems, it can be seen that the LPG supply systems are generally at a much lower technological level than the corresponding gasoline systems, except when the engine was designed to use the LPG as fuel. When the LPG is an alternative fuel in the gasoline engine, this influences the combustion process and there appear additional problems with power regulation and exhaust composition. The owner can choose between power and money.

From the environmental aspect, the major attractions of the LPG, compared to the conventional gasoline, lie in its relatively low carbon content. The LPG burns cleanly with lower emissions of CO, CO₂ and HC. It provides better thermal efficiency and improved fuel economy [5]. Whether the use of the LPG drives will increase depends on several factors. One of the factors is the price of fuel. The price is significantly lower in the case of LPG compared to gasoline. It is the main stimulating factor for users because the state does not provide subsidies and tax relief for this fuel as it does for electric vehicles. If the LPG use increases, the price of fuel would also increase. Application of the LPG also has one essential drawback. Due to the fuel characteristics, drivers are forbidden to park the LPG vehicles in closed garages due to the risk of explosion.

2.3.2 CNG (Compressed Natural Gas)

The CNG-powered vehicles are usually vehicles with a dual-fuel drive and a two-part tank. Those allow them to switch to gasoline when they run out of CNG. Depending on the vehicle model, the CNG operation also implies a higher purchase price of a vehicle. The difference in prices of a new CNG vehicle and new diesel or gasoline vehicles usually ranges from EUR 500 to EUR 8000. It is possible to upgrade the CNG equipment to existing vehicles with gasoline engines, but it is a question of cost-effectiveness because the upgrade can cost 4-6000 EUR. Upgrading a Diesel engine is even more problematic and expensive, over 10,000 EUR. In all this, one should keep in mind the significant reduction of available luggage space. There are currently more than 20 million vehicles in the world running on natural gas [8]. The number of

such vehicles is increasing and it has been accelerated by increasing the number of the CNG pumping stations. The main advantages of the CNG are [8]:

- a CNG vehicle tank can be filled up as quickly as with conventional fuels, much faster than recharge batteries in electric vehicles.
- The CNG lessens the wear and tear on engines since it produces less combustion residue.
- a CNG vehicle can also run on biogas, which increases the environmental benefit.
- City buses and taxis running on the CNG offer a solution for the low-emission zones in big cities.
- Natural gas is transported via the underground transport and distribution network, which could significantly reduce the number of trucks on the roads.
- The CNG is lighter than air and vehicles that use this gas are not subjected to the ban of access to underground car parks.

Disadvantages of the CNG application in motor vehicles are [8]:

- Insufficient number of the CNG pumping stations and very rarely these stations sell biomethane.
- Vehicles with the CNG drive are not allowed access to the Eurotunnel and some ferry lines.

2.4 DiesOtto engine

One of the possible alternative solutions to improve the characteristics of internal combustion engines is a combination of Diesel and Otto engines, DiesOtto engine (Mercedes Benz) and Skyactiv-X (Mazda). Mazda was the first to introduce such a solution into series production. This solution uses Mazda's patented technology in which an extremely poor mixture ($A/F = 40$) is compressed to high pressure and burns as in Diesel engines. The spark plug ignites a small part of the rich mixture around. The rich mixture burns and heats the remaining compressed lean mixture. A pressure and temperature increase are creating conditions for the remaining mixture to ignite as with a Diesel engine. The fuel burns faster and more completely, which has a positive effect on performance and exhaust emissions. This engine does not have a turbocharger and it uses only a small compressor. Therefore, there is no delay in responding to a change in the position of the accelerator pedal [12].

The main advantages of the Skyactiv-X engine are shown in Figure 2. More detailed information about the Skyactiv-X engine is available in [13].

Another such attempt is taking place at Mercedes Benz. The DiesOtto engine combines many technologies and combines variable compression, turbocharging and direct injection. The spark plugs fire when compression is low. They do not fire when compression is high enough to self-ignite the air-fuel mixture. The compression ratio varies with engine load [14]. This technology is more

complex than Mazda's and is still in the experimental phase for now. Due to the complicated construction, it is to expect a higher price of such engines. Such a solution can be accepted mainly by large and expensive vehicles, so it is not surprising why Mercedes chose the S class to promote this technology.

2.5 Electric vehicles

Instead of internal combustion engines, electric vehicles use one or more electric motors for propulsion. A high-capacity rechargeable battery is required to ensure a sufficient action radius. While Diesel engines without problems provide vehicle mobility of more than 1000 km, modern batteries parred with electric motors cannot offer that. Aware of these shortcomings, manufacturers of electric vehicles are constantly trying to improve the quality of used electric motors. They must pay even more attention to development and quality of batteries. Now, manufacturers encounter the need for constant compromises. By improving one feature, they endanger others. For example, to improve a vehicle journey range, the battery's charging speed, or storage capacity, a compromise may need to be made in its durability or life expectancy [15]. Lithium-ion batteries currently are considered the best technical solution, but their production is expensive and the method of obtaining lithium significantly endangers the environment.

Some companies, producers of lithium-metal batteries, claim that they have found a way to prevent fires⁴ and dendrites⁵ while still allowing ions to easily pass without degrading the battery performance. The batteries will become significantly cheaper and electric vehicles will be able to compete with gasoline-powered vehicles [16].

One of the advantages of the electric motor drive is a significantly smaller number of moving parts and parts in general, which facilitates vehicle maintenance and reduces operating costs.

Efficient recovery/regeneration of braking energy is easily achievable with electric motors, with the same machine - the drive motor, which instantly becomes a generator.

Vehicles use different variants of electric motors for their drive. For example, the Tesla Roadster uses a 214 kW asynchronous motor with a 90% efficiency.

⁴Physical damage to battery cells, pollution in the electrolyte or the poor quality of the separator may cause a fire in li-ion batteries⁴, [17].

⁵Lithium dendrites are metallic microstructures that form on the negative electrode during the charging process. Lithium dendrites are formed when extra lithium ions accumulate on the anode surface and cannot be absorbed into the anode in time. They can cause short circuits and lead to catastrophic failures and even fires⁵, [18].

	Otto engine	Skyactiv-X	Diesel engine
Small fuel consumption	○	✓	✓
High torque	○	✓	✓
Quick response	○	✓	✓
High power output	✓	✓	○
Low heat emission	✓	✓	○
Cleaner exhaust gases	✓	✓	○

Figure 2 What Skyactiv took from Otto - and what from the Diesel engine, [12]

Table 2 Comparison of the number of kilometers traveled and the price of ZOE and Clio vehicles from 2016

	Renault ZOE Experience R110 Z.E. 50		Renault Clio (gasoline) Experience TCe 100		Clio V Experience (diesel) 1.5 BLUE dCi 85 EU6d-T	
	km	EUR	km	EUR	km	EUR
Average	42837	7267	46707	7586	57206	6213
Median	40337	7000	45707	7500	70100	7990
New_2021	0	20490	0	15789	0	16590

Source: [19]

The Rimac Concept one uses four water-cooled synchronous motors with permanent magnets with a total power of 913 kW and an efficiency of 97%. One of Nissan LEAF's best-selling electric cars uses a synchronous power motor like its competitor Renault ZOE.

3 A comparative analysis

The propulsion by internal combustion engines is complex. In addition to mechanical, it also involves many thermal processes. Converting fuel energy into mechanical energy involves combustion and providing optimal conditions for fuel combustion. There are also many moving parts. Therefore, the maximum degree of fuel energy utilization of vehicle engines is about 0.4 for Diesel engines and about 0.35 for Otto engines. With electric motor drive, the efficiency is up to 0.97, depending on the type of motor, power and energy efficiency class. When adding appropriate power transmissions (differentials, gearboxes and reducers) to the drive units, the efficiency is further reduced, with the situation being more favorable with electric drives. That would mean that the electric drive is more energy-efficient and even more environmentally friendly. But is it true? All this refers to the period from bringing energy or fuel into the vehicle up to the road on that the wheel moves. The situation becomes more complicated and unclear when we observe the complete cycle from the beginning of mining raw materials for the vehicle production and operation, including the method of obtaining electricity, up to the movement of vehicles on the road. There is a big difference whether the electricity is produced in the coal-fired power plants or some other, more environmentally friendly way. The situation is different in this respect in different countries. When

one take the time factor into account and that the technologies are improved daily, it is easy to understand that it is impossible to give an unambiguous general conclusion.

In addition, when the analysis talks about the environmental aspect of the electric cars application, one should keep in mind the annual number of kilometers traveled by one vehicle. Due to the current limitations regarding the battery life, those electric vehicles that exceed many kilometers are more environmentally friendly. If one compares electric propulsion with gasoline and diesel propulsions, on the example of Renault car models ZOE and Clio, as shown in Table 2, one can notice that owners of ZOE cars had covered, on average, fewer kilometers than Clio owners with gasoline propulsion about 9.03% (or, comparing medians 13.3%). The difference is much bigger when comparing electro to diesel. Average the ZOE driver passed 33.5% (or comparing medians 73.7%) less than the owner of the diesel-powered Clio. The mileage of the average and median of offered ZOE vehicles were taken as a reference value, respectively. The analysis we performed on the first 30 vehicles from 2016 from the category used cars "Top Angebot" on May 7, 2021.

On average, the owners of ZOE vehicles lost the most in the value of their cars, which after less than five years were worth only 35% of the current purchase price of a new vehicle. In the case of the gasoline- and diesel-powered Clios, the corresponding values were 48% or 37.4%. Although it looks similar numerically, the difference between prices of electric- and diesel-driven cars is significantly unfavorable, because analyzed diesel cars have covered much more mileage and they are notably cheaper. If one looks at the median values of used vehicles, it can be seen that the vehicle values after less than five years are 34% for ZOE, 47.5% for Clio

Table 3 Fuel consumption or kWh for different types of vehicle propulsion Renault Clio (2021)

Drive type		Electro*	CNG	LPG	Gasoline	Diesel
Liter of fuel or kWh		6575 kWh	1371	2299	1977	1573
kg CO ₂ for 40337km	Coal	0.94 kg/kWh	6180 ^I			
	Fuel oil	0.8 kg/kWh	5260 ^{II}			
	Natural gas	0.5 kg/kWh	3287 ^{II}	3751	3792	4840
	Solar, wind, hydro, nuclear	0.05 kg/kWh	328 ^{II}			3792
	USA average	0.709 kg/kWh	4662 ^{III}			

Sources: ^I [20], ^{II} [21], ^{III} [22]

gasoline and 48.2% for Clio diesel.

Today's automotive industry is shifting to electric-driven cars without a globally conducted, comprehensive analysis that would cover all the critical points, from the start of vehicle production to vehicle destruction. No one can say with certainty that electric cars are the best environmentally friendly solution. Next are compared the vehicles from Table 2 and an additional electric vehicle of similar power and the fuel consumption and CO₂ emissions were calculated, for the median kilometers covered by analyzed electric cars. One can see that when electricity is obtained by burning coal, one would get significantly higher CO₂ emissions from electric-driven cars. Such a comparison is shown in Table 3. For the calculation results shown in Table 3, the reference value is the mileage corresponding to the median mileage achieved by the offered electric vehicles, as determined in Table 2. In the second table row are shown the energy consumption in the case of an electric vehicle and fuel consumption in liters for the reference mileage and different engine types. In the third row, CO₂ emissions for the observed vehicles are shown, with more detailed results being given in the case of electric vehicles, where they depend on the method of obtaining electricity. Thus, e.g. 1 kWh of electricity, when produced from a coal-burning power plant, will generate 0.94 kg of CO₂ emissions to the atmosphere according to CNCF.

In the case of obtaining electricity using the natural gas, electric vehicles become more competitive in terms of CO₂ emissions, but only using nuclear, solar, hydro and wind energy significant reduction in CO₂ emissions come to the fore. However, even in this case, other parameters of pollution caused by the construction of power plants and the production of electric vehicle batteries should not be neglected. If we analyze data on CO₂ emission for electricity production in the United States, we can see no practical benefit from producing and using electric vehicles. one can expect benefits only there where it is possible to produce electricity without fossil fuels.

The analysis performed in this research showed that the expectations were not justified in all the cases and refuted the set null hypotheses at the expense of alternative ones:

H_{a1}: Internal combustion engines are in some situations

more environmentally friendly than the use of electric motors to power passenger motor vehicles.

H_{a2}: The use of internal combustion engines is, in some situations, more favorable than the use of electric motors to drive passenger motor vehicles, from an economic point of view.

4 Conclusions

Otto and Diesel engines are used to power vehicles for more than a century and were constantly improved. The enormous progress of technology, primarily information technology, has enabled a significant increase in the quality of engines and vehicles. The technology also helped the rise of the fuels' quality level and the management of engine work processes. Regardless of the type of engine and the fuel used, modern engines have a long service life. They are economical and environmentally more acceptable than engines from the last century. Given the ever-growing number of vehicles and people and the limited resources of the Earth's atmosphere, development continues exploring new ways to avoid the negative impact of motorization. One of the old ideas that went into focus again over the past decade and are still receiving the most attention with financial incentives from vehicle manufacturers and car buyers is electric propulsion in passenger vehicles and much less in buses.

To promote the production and sale of electric vehicles, the governments of many countries provide subsidies to both manufacturers and buyers of these vehicles. That cannot go on indefinitely because it is logical that it must stop once. After all, the countries will lose the significant revenues they now generate from every liter of fuel sold.

In addition to continuous improvements of powertrains that could reduce the negative impact of vehicles on the environment, it is necessary to take much more radical measures than these. It is to reduce the number of cars moving around the globe and even the total number of vehicles. No matter how small the impact of an individual vehicle is, they all together have a crushing influence on the climate change. Any energy used to power vehicles causes an increased thermal load on the atmosphere, especially in large cities. No matter

how the raw materials for the vehicle production were obtained, they will affect the amount of waste needed to be dealt with.

Authors believe that one of the best solutions that would protect the environment and would not lower the level of quality of human life, is the replacement of ownership of vehicles by shared use of cars, car-sharing, on the principle of subscription. Car-sharing enables the same as classic car rental, but in a more flexible way [23]. That would significantly reduce the number of cars on the streets and the required number of vehicles in general, the number of necessary garage spaces, the required asphalted area intended for motor vehicles and

the required production of materials for car production. That is the win-win solution in every way. Applying the ride-sharing model in the intercity traffic can obtain an additional improvement [24].

In addition to this solution, it is necessary to improve the mass transportation. Massive use of the environmentally friendly metro, tram and trolleybus will reduce air pollution to acceptable limits.

One of the positive solutions in terms of pollution could be to limit the growth of cities, or, better said, to improve the dispersion of the population of the territory. Several smaller cities are in every respect more favorable than one large city.

References

- [1] DAVIS, S. C., BOUNDY, R. G. *Transportation energy data book* [online]. 39. ed. United States: Oak Ridge National Laboratory, 2021. Available from: <https://doi.org/10.2172/1767864>
- [2] VAN BASSHUYSEN, R., SHAEFER, F. (eds.). *Internal combustion engine handbook*. 2. ed. Warrendale, PA: SAE International, 2016. ISBN 978-0-7680-8024-7.
- [3] JEMNI, M., KASSEM, S., DRISS, Z., ABID, M. Effects of hydrogen enrichment and injection location on in-cylinder flow characteristics, performance and emissions of gaseous LPG engine. *Energy* [online] [accessed 2021-05-09]. 2018, **150**, p. 92-108. ISSN 0360-5442. Available from: <https://doi.org/10.1016/j.energy.2018.02.120>
- [4] LOGANATHAN, M., RAMESH, A. Study on manifold injection of LPG in two stroke SI engine. *Journal of the Energy Institute* [online]. 2007, **80**(3), p. 168-174. ISSN 1743-9671, eISSN 1746-0220. Available from: <https://doi.org/10.1179/174602207X216255>
- [5] SHANKAR, K. S., MOHANAN, P. MPFI gasoline engine combustion, performance and emission characteristics with LPG injection. *International Journal of Energy and Environment*. 2011, **2**(4), p. 761-770. ISSN 2076-2895, eISSN 2076-2909.
- [6] SYNAK, F., CULIK, K., RIEVAJ, V., GANA, J. Liquefied petroleum gas as an alternative fuel. *Transportation Research Procedia* [online]. 2019, **40**, p. 527-534. ISSN 2352-1465. Available from: <https://doi.org/10.1016/j.trpro.2019.07.076>
- [7] MELAIKA, M., HERBILLON, G., DAHLANDER, P. Spark ignition engine performance, standard emissions and particulates using GDI, PFI-CNG and DI-CNG systems. *Fuel* [online]. 2021, **293**, 120454. ISSN 0016-2361. Available from: <https://doi.org/10.1016/j.fuel.2021.120454>
- [8] Are natural gas cars a real alternative? - energuide.be [online] [accessed 2021-05-09]. Available from: <https://www.energuide.be/en/questions-answers/are-natural-gas-cars-a-real-alternative/198/>
- [9] Cryotank - WordSense Online Dictionary [online] [accessed 2021-06-27]. Available from: <https://www.wordsense.eu/cryotank>
- [10] Cryotank, Google Arts and Culture - Wikipedia [online] [accessed 2021-05-27] Available from: <https://artsandculture.google.com/entity/cryotank/m0r8ldn2?hl=en>
- [11] CEKEREVAC, Z. *The effects of the application of methanol to the driving and ecological characteristics of SI-engines*. Belgrade: Faculty of Mechanical Engineering, 1977.
- [12] Skyactiv-X - Mazda [online] [accessed 2020-04-27]. Available from: <https://www.mazda.rs/zasto-mazda/skyactiv-x>
- [13] PATRASCU, D. 2020 Mazda3 gets revolutionary Skyactiv-X engine, full details released [online] [accessed 2019-06-05]. Available from: <https://www.autoevolution.com/news/2020-mazda3-gets-revolutionary-skyactiv-x-engine-full-details-released-134984.html>
- [14] IRESON, N. Mercedes-Benz continues DiesOtto work, S-class still slated to be first [online] [accessed 2020-07-10] Available from: https://www.motorauthority.com/news/1050228_mercedes-benz-continues-diesotto-work-s-class-still-slated-to-be-first
- [15] BANDYOPADHYAY, K. R. *Electric vehicles*. New York: Salem Press Encyclopedia [online] [accessed 2021-08-17]. 2021. Available from: https://searchworks.stanford.edu/articles/ers__89475083
- [16] TEMPLE, J. Lithium-metal batteries. *MIT Technology Review*. 2021, February, p. 38-41. ISSN 0040-1692.
- [17] ELLINGBO, A. R. Li-ion batteries - a fire hazard, if... [online] [accessed 2021-06-27]. Available from: <https://www.if-insurance.com/large-enterprises/insight/risk-consulting-magazine/risk-consulting-2019-1/li-ion-batteries-a-fire-hazard>

- [18] KONG, L., PECHT, M. A look inside your battery: watching the dendrites grow - Battery Power 2020 [online] [accessed 2021-06-27]. Available from: <https://www.batterypoweronline.com/news/a-look-inside-your-battery-watching-the-dendrites-grow>
- [19] Autoscout24.de [online] [accessed 2021-05-07]. Available from: <https://www.autoscout24.de/>
- [20] MCLEAN, R. How much CO2 emissions per kWh of electricity? [online] [accessed 2018-01-06]. Available from: <https://slightlyunconventional.com/co2-per-kwh-of-electricity/>
- [21] WILSON, L. Graph of the day: how green is your electricity? [online] [accessed 2021-05-09]. Available from: <https://reneweconomy.com.au/graph-of-the-day-how-green-is-your-electricity-12278/>
- [22] Greenhouse gases equivalencies calculator - calculations and references - EPA [online] [accessed 2021-05-09]. 2020. Available from: <https://www.epa.gov/energy/greenhouse-gases-equivalencies-calculator-calculations-and-references>
- [23] BOGAVAC, M., PRIGODA, L., CEKEREVAC, Z. SMEs digitalization and the sharing economy. *MEST Journal*. 2020, **8**(1), p. 36-47. ISSN 2334-7058. Available from: <https://doi.org/10.12709/mest.08.08.01.05>
- [24] CEKEREVAC, Z., PRIGODA, L., BOGAVAC, M. IoT application in smart cities with an accent on traffic and transportation. In: International Scientific-Practical Conference Economic Security in the Context of Sustainable Development: proceedings [online] [accessed 2021-05-09]. ASEM. 2021. ISBN 978-9975-155-01-4, p. 226-235. Available from: <http://irek.ase.md:80/xmlui/handle/1234567890/1121>

THE EFFECTS OF BIODIESEL ON NO_x EMISSIONS FOR AUTOMOTIVE TRANSPORT

Ruslana Kolodnytska¹, Oleksandr Kravchenko¹, Juraj Gerlici², Kateryna Kravchenko²

¹Zhytomyr Polytechnic State, Zhytomyr, Ukraine

²University of Zilina, Zilina, Slovak Republic

*E-mail of corresponding author: kateryna.kravchenko@fstroj.uniza.sk

Resume

Automobiles with internal combustion engine using diesel fuel have large harmful emissions of nitrogen oxides and soot, which affect the health of the population and especially children and carbon dioxide, which is dangerous for the planet as a whole. Biodiesel is used in Europe as an additive to diesel fuel to reduce soot emissions (including carcinogens), as well as to improve the balance of carbon dioxide on the planet. Using the biodiesel in internal combustion engines tends to show higher nitrogen oxides emissions compared to diesel. In this paper, the impact of flame temperature, ignition delay and density on NO_x formation of biodiesel and its component for both stationary engine and automotive engine were analysed. Emissions of nitrogen oxides increase with increasing load. In no-load modes, biodiesel shows lower emissions of nitrogen oxides than diesel.

Article info

Received 17 June 2021

Accepted 8 July 2021

Online 4 November 2021

Keywords:

automotive transport,
nitrogen oxides,
biodiesel,
ignition delay,
flame temperature

Available online: <https://doi.org/10.26552/com.C.2022.1.B59-B66>

ISSN 1335-4205 (print version)

ISSN 2585-7878 (online version)

1 Introduction

Developing promising methods to reduce the environmental impact of the road transport on environment [1-7], scientists are making great efforts to ensure that transport is “green”. Automobiles using diesel fuel have large harmful emissions of nitrogen oxides and soot, which affect the health of the population and especially children and carbon dioxide, which is dangerous for the planet as a whole.

The ban on diesel engines in some European countries leads to the fact that automobiles with these engines are more sold and used in Ukraine. At the moment, in Ukraine most of the buses with diesel engines are more than 10 years old.

Biodiesel is used in Europe as an additive to diesel fuel in order to reduce soot emissions as well as carcinogens. Biofuels made from used vegetable oil and animal fat residues are used in London; there are 9,500 buses in the UK. The UK has begun using biodiesel made from coffee residues as fuel for city buses. To operate one bus on biofuel (B20) mixed with diesel fuel, only 2,550,000 cups of coffee are needed per year. Biofuels consumption for transport in Slovakia peaked at 175.4 kilotons of oil equivalent in 2017 [8]. By 2019, it decreased by 30 kilotons of oil equivalent. At that time, the country’s biodiesel consumption was at 127.9 kilotons of oil equivalent [8]. The amount of bioethanol consumed was significantly smaller compared to biodiesel.

Since biodiesel has higher nitrogen oxide emissions, modeling nitrogen oxide emissions from road transport is a very important task. It is impossible to solve this problem without understanding the processes occurring in internal combustion engines.

2 Analysis of previous research

The theoretical and experimental study of nitrogen oxide emissions from use of the diesel fuel and biodiesel in diesel engine was considered by scientists in [9-19]. Analysis of influence of factors on nitrogen oxide emissions when using fuels containing oxygen, made in [9]. In [10], the influence of individual molecules, from which biodiesel is composed, on emissions of nitrogen oxides is considered. Some aspects of spraying, evaporation and combustion of biodiesel are shown in [11-17].

Emissions of nitrogen oxides are highly dependent on the temperature in the combustion chamber, as well as on the concentration of oxygen that is present in the combustion products [18]. Higher emissions of nitrogen oxides from biodiesel are mainly because this fuel usually has a slightly lower ignition delay than diesel fuel. This shorter ignition delay increases the maximum cylinder temperatures and pressures. All this is due to the higher cetane number of fuel, which usually biodiesel has, compared to diesel.

Table 1 Emissions of nitrogen oxides for diesel fuel (D2) and its mixture with biodiesel fuel (B35) for various cycles (DDC series 60)

WVU truck cycle			WVU 5-mi route cycle		
B35	D2	%	B35	D2	%
16.597	16.957	2.123017	16.631	17.986	7.533637

Studies [18] carried out with Cummins engines for the B35 mixture show that nitrogen oxides when using biodiesel fuel increase only for relatively old engine models (for example, Cummins 855). For the newer engine models (DDC series 60), nitrogen oxide emissions were slightly lower for biodiesel than for diesel. Nitrogen oxide emissions were different for different test cycles of trucks with engines, shown in Table 1.

It was shown in [10] that at the same injection time, molecules with long chains of fatty acids had higher emissions of nitrogen oxides than molecules with short chains. Some molecules tend to form large emissions of particulate and nitrogen oxides. For example, this was observed in the case of unsaturated molecules (with double bonds), when both NO_x and particle emissions increased with an increase in the degree of unsaturation [10, 16]. Experiments [16] have shown that polyunsaturated methyl ester (C18:3) produces the largest amount of nitrogen oxides, which once again confirms the fact that molecules with a longer ignition delay produce more nitrogen oxides. Thus, experiments show that nitrogen oxide emissions increase with the number of double bonds unless the ignition delay is deliberately changed.

As known, for a constant load (whether it is a fixed start of injection or the start of combustion), the ignition delay is correlated with NO_x emissions. However, the mechanism of this influence is not yet fully understood. Optical diagnostics [10] showed that nitrogen oxides are formed not at the early fast stages of combustion (premixed combustion phase), but at a later stage of diffusion combustion. Some researchers believe that the rapid combustion of enriched fuels at low temperatures results in significant emissions of nitrogen oxides. It has also been shown that when a large proportion of the fuel is burned during a fast initial combustion mode, it can lead to an increase in the global temperature of the gas in the cylinder, leading to more formation of nitrogen oxides.

Fuel viscosity has a significant impact on NO_x emissions. Analysis of scientific works, where NO_x emissions were analyzed as a function of viscosity and an increase in NO_x with increasing viscosity at low temperatures was revealed in [16]. Since the kinematic viscosity of biodiesel is greater than that of diesel fuel, this reduces fuel leaks during the injection and results in higher pressure, as well as advanced injection times. Advancement of the injection time increases the mass of fuel injected, which, in turn, leads to an increase in NO_x emissions. Thus, it is possible to achieve a reduction in NO_x emissions by about 3.52% at a reduced viscosity of

soy methyl ester to the level of petroleum diesel fuel [16].

Although the number of publications on diesel fuel has grown exponentially over the past 15 years, little attention has yet been paid to study of influence of various factors on the nitrogen oxide emissions from fuel combustion.

3 Formulation of the problem

To reduce harmful emissions from motor vehicles with internal combustion engines, a deep understanding of the spontaneous combustion processes and combustion of fuel is required. Fuel self-ignition is characterized by the two main parameters: the initial temperature (the minimum temperature at which the fuel can self-ignite) and the ignition delay (the time between the fuel injection and ignition). Those parameters depend on the pressure in the combustion chamber, the type and chemical composition of the fuel, etc. The chemical kinetics of spontaneous combustion includes about 1000 chemical reactions and about a hundred fuel components. An additional difficulty is that the rate coefficients of all the reactions are not known and the solution to this problem requires a lot of time and finance since it is often associated with use of a powerful computer. Researchers are working to reduce the number of equations describing the combustion of diesel fuel in internal combustion engines.

In order to tackle the problem of reducing the NO_x emissions from biodiesel for road transport, it is important to have a deep understanding of factors that influence these emissions and the ability to manage them.

The purpose of this work was to analyze influence of various factors on formation of the nitrogen oxides in the internal combustion engine of motor vehicles when using biodiesel. The objective of this work was to determine correlations between the nitrogen oxide emissions, fuel density, flame temperature and fuel ignition delay.

4 Influence of various factors on formation of nitrogen oxides

The NO emissions from the combustion of fuel in an internal combustion engine can be calculated using the following equation [9]:

$$\frac{d[NO]}{dt} = 2k[O][N_2], \quad (1)$$

Table 2 Temperatures of adiabatic flame T_{ad} for fuels and their components

Fuels	(C/H) _{eff}	T _{ad} , K
C16:0	0.463	2660
C18:0	0.467	2665
C18:1	0.492	2670
C18:2	0.493	2680
C18:3	0.522	2700
B100	0.522	-
D2	0.552	2700

where:

[NO] is the nitric oxide concentration,

[O] is the atomic oxygen concentration,

[N₂] is the molecule nitrogen concentration,

k is the reaction rate coefficient.

The reaction rate coefficient can be described using the Arrhenius equation as

$$k = AT^\beta \exp[-E/(R_o T)], \quad (2)$$

where:

E is the activation energy,

R_o is the universal gas constant,

$R_o = 8 - 314 [J \cdot mol^{-1} \cdot K^{-1}]$

T is the temperature,

A and β are constants.

Due to its strong temperature dependence, the thermal NO emissions are largely ignored at temperatures less than 1800 K. Müller et al. [9] note that the thermal NO_x emissions tend to increase with increasing the in-cylinder temperature, residence time of the mixture in the cylinder at high temperature, the concentration of oxygen atoms O₂ and nitrogen N₂.

This paper analyzes influence of the flame temperature, fuel density and fuel ignition delay on the thermal formation of NO_x in an internal combustion engine.

4.1 Influence of the flame temperature

As a rule, the gases temperature in the engine cylinder is estimated using the ideal gas equation, for example, in [9]:

$$T = \frac{pV}{nR_o}, \quad (3)$$

where:

p is the ambient pressure,

V is the cylinder volume,

n is the number of moles,

R_o is the universal gas constant.

Inflame adiabatic temperature is understood as the temperature of a mixture during combustion at constant

pressure without converting heat and without changing the kinetic or potential energy. This temperature for hydrocarbon fuels is closely related to the C/H ratio. If this ratio increases, then the flame temperature also increases. The CO₂ formation requires more energy than H₂O formation. Thus, the C/H ratio can be used to describe the influence of hydrocarbon composition (including double bonds) on flame temperature. However, for biodiesel fuels, this ratio may be less accurate. Müller et al. [9] recommended using the following ratio for fuels containing oxygen:

$$\frac{C}{H_{eff}} = \frac{C - \frac{1}{4}O_+ - \frac{1}{2}O_-}{H}, \quad (4)$$

where O₊ and O₋ is the number of oxygen atoms with single and double bonds, respectively.

Using Equation (4), (C/H)_{eff} is 0.552 and 0.522 for diesel and biodiesel, respectively.

For the conditions of experimental studies in a single-cylinder engine [8] (gas pressure 63 bars, fuel temperature 95 °C, initial air temperature 910 K), the adiabatic flame temperatures for various fuels and constituent components (molecules) of biodiesel fuel are shown in Table 2.

Consequently, the adiabatic flame temperature for components (molecules) of biodiesel is lower than for diesel fuel. Hence, one can expect lower flame temperatures for biodiesel (B100) than for diesel.

It was assumed [12] that the average temperature of gases in the cylinder during the fuel combustion will be 80 °K higher than the temperature obtained for an ideal cycle. This assumption leads to the following calculation formula for the adiabatic flame temperature T_f:

$$T_f = 298.15 \cdot r^{0.3} + 80, \quad (5)$$

where r is the compression factor.

The adiabatic flame temperature obtained as a result of calculations by Equation (5) during the combustion of diesel fuel, which is 783.6 K (when using the compression factor $r = 17.5$), seems to be too low comparing to adiabatic flame temperature T_{ad} (see Table 2).

4.2 Influence of the fuel density

The biodiesel density is greater than that diesel. Modelling the density of biodiesel, as well as the molecules, from which this fuel is composed, are described in [13]. Vaporization of biodiesel fuel is discussed in detail in [14]. Influence of the fuel density on nitrogen oxide emissions is considered in [13]. Atomization of the high density fuels is inferior to low density fuels, resulting in an increase of the diameter of the fuel droplets. This increases the physical delay in ignition of the fuel, which is the time from the start of fuel injection until the chemical reaction conditions are reached. During that period, the fuel is atomized, evaporated, mixed with air and the temperature rises to the autoignition temperature. A large physical delay increases the maximum pressure during the initial part of the combustion process; therefore, the maximum temperature also increases, which, in turn, increases the NOx concentration.

In this work, the technique described in [13-14] is used for calculation of the diesel fuel components (molecules) density.

4.3 Influence of the fuel ignition delay

Modeling the ignition delay for a molecule of biodiesel fuel with the number of carbon atoms equal to 10, without double bonds (C10: 0) at a pressure of 20 atm, which is a part of biodiesel fuel, was performed in [17]. It was concluded that the ignition delay depends on the cetane number only at low and medium temperatures and at high temperatures the ignition delay is independent of the cetane number.

The following general trend has been observed, which is that fuels with better ignition properties (higher cetane number) have lower NOx emissions, since they have a short lift off length (LOL), which means a richer mixture and less heat released during the fuel ignition [9]. Fuels with a higher cetane number tend to be more saturated, that is, they have a lower C/H ratio and lower adiabatic temperatures flame, which means less nitrogen oxide emissions.

The ignition delay of biodiesel fuel molecules was estimated from the dependences given in [17].

5 Modelling of nitrogen oxide emissions for stationary engines and automobile engines

In [12], the modelling of nitrogen oxides for a stationary engine and an automobile engine are considered separately. Calculation of nitrogen oxide emissions (ppm) for automobile engines can be performed using the following correlation [12]:

$$NEI = 20956.69 \cdot p_f \left[1 + C \left(\frac{-9.91/1000L^2 +}{1.608L - 18.431} \right) \right] \cdot \exp(2.9 \cdot ID - 19.627) \cdot \exp(4626.44/T_f), \quad (6)$$

where:

p_f is the fuel density, [kg/m³],

L is the load, [%],

ID is the ignition delay, [ms],

T_f is the flame temperature, [K],

$C = 1$ for load conditions, [%] ($C = 0$ – without load).

Calculation of the nitrogen oxide emissions (ppm) for a stationary engine:

$$NEI = 20956.69 \cdot p_f \left[1 + C \left(\frac{-5.740/1000L^2 +}{0.0995L - 0.603} \right) \right] \cdot \exp(0.948 \cdot ID - 18.83) \cdot \exp(4626.44/T_f). \quad (7)$$

Without considering the load, formulas are simplified.

For a stationary engine, Equation (6) takes the form:

$$NEI = 20956.69 \cdot p_f \cdot \exp(0.948 \cdot ID - 18.83) \cdot \exp(4626.44/T_f). \quad (8)$$

For an automobile engine, Equation (7) takes the form:

$$NEI = 20956.69 \cdot p_f \cdot \exp(2.9 \cdot ID - 19.627) \cdot \exp(4626.44/T_f). \quad (9)$$

As can be seen from the comparison of Equations (6), (8) and (7), (9), the difference is contained in the ignition delay of the fuel. Researchers [12] believed that the ignition delay of the same fuel should be different in the conditions of stationary engines and automobile engines. They made such a conclusion by comparing the emissions of nitrogen oxides of these engines. The ignition delay in [12] was found based on the NOx emissions, as well as on the assumption that the activation energy of NOx formation is constant for all fuels and is equal to 38465.61 J/mol.

Tables 3 and 4 show the ignition delays and NOx emissions at various loads when using a stationary engine and an automobile engine, respectively. Tables contain data that was obtained in [12]. The comparison of NOx emissions for diesel and biodiesel (crude rice bran oil methyl ester - CRBME) is shown in Figure 1.

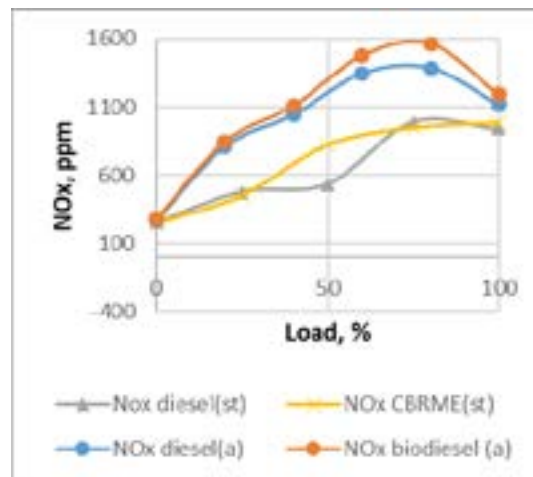
As can be seen from Figure 1, NOx emissions increase with increasing load for both diesel and biodiesel. The maximum emissions for the two fuels are observed in the load range of 60-80%. In no-load mode, as shown in a study [12], biodiesel has lower NOx emissions than diesel.

Table 3 Ignition delay (ID) and NO_x emissions (stationary engine)

Load, %	Diesel, ID [ms]	NO _x (ppm)	Biodiesel (CRBME)	NO _x (ppm)
0	1.74	252	1.68	246
25	1.72	478	1.64	453
50	1.67	534	1.59	825
75	1.63	993	1.55	952
100	1.59	940	1.52	986

Table 4 Ignition delay (ID) and NO_x emissions (automobile engine)

Load, %	Diesel, ID [ms]	NO _x (ppm)	Biodiesel	NO _x (ppm)
0	0.96	273	0.92	281
20	0.52	811	0.501	847
40	0.317	1041	0.304	1106
60	0.207	1343	0.198	1475
80	0.143	1384	0.137	1565
100	0.104	1116	0.099	1192

**Figure 1** Comparison of the NO_x emissions for diesel and biodiesel (CRBME) for the stationary engine (st) and car engine (a)

6 Modelling of nitrogen emissions for the composed biodiesel components.

Of great interest for modelling are not only the emissions of nitrogen oxides from biodiesel, but the components from which this fuel is composed, as well. Most often, biodiesel is made from vegetable oils with addition of the methyl alcohol. Therefore, methyl esters of fatty acids are the most common constituents of biodiesel, the names, formulas and cetane number (CN) of which are shown in Table 5. The presence of oxygen in biodiesel (about 11%) is also considered to be one of the reasons for the increase in NO_x emissions [19].

The third column of Table 5 shows the designation of methyl esters, where the numbers of carbons in fatty acids and numbers of double bonds are shown by numbers to the left and the right of “:”, respectively. The biodiesel ignition delay can be calculated based on the DCN (Derived Cetane Number) obtained from the IQT (Ignition Quality Tester) test. In [20], the DCN

was calculated based on the ID value according to the following formula: $DCN = 4.460 + 186.6/ID$.

From here one gets the ID value: $ID = 186.6/(DCN - 4.460)$.

The latter formula was used to calculate the ID of the biodiesel components.

Verification of Equation (8), as applied to components of biodiesel fuel with the values of activation temperature and flame temperatures, given in [12], showed unrealistically large NO_x emissions. Therefore, for the calculations, the flame temperatures (T_{ad}) were chosen, which are given in Table 2.

The activation energy of biodiesel fuel (38.465 kJ/mol), which is adopted in [12], also needs to be clarified. In work [13], the activation energies of biodiesel and its components were analyzed. The activation energies for C18:1M, C10:0M and C12:0M molecules are 67, 151 and 193 kJ/mol, respectively. The activation energy of 67 kJ/mol was taken for calculations, which gives an activation temperature of 8058.38 K in comparison to 4626.44 K,

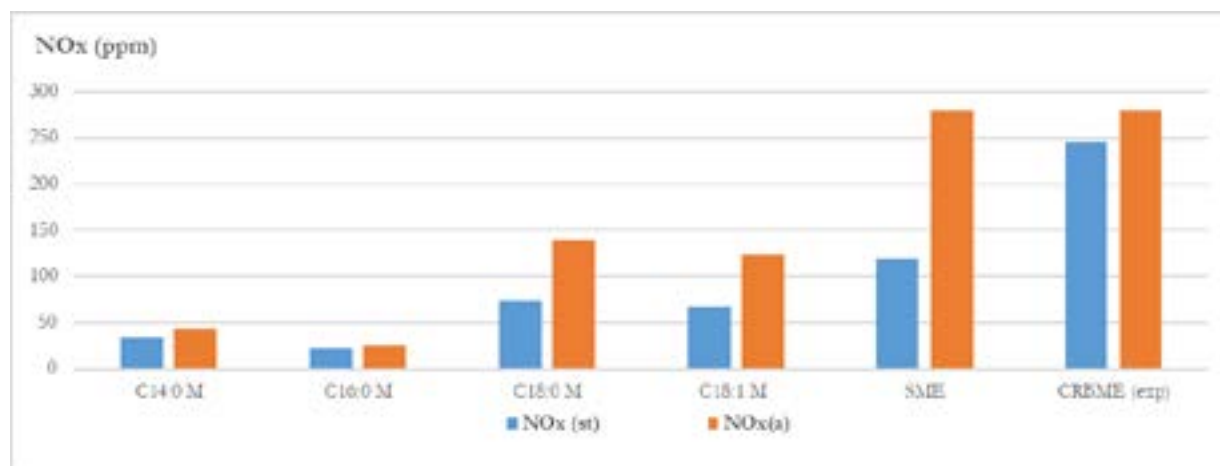
Table 5 Values of cetane numbers of biodiesel fuel components obtained by different methods

Biodiesel components	Formula	Notation	CN (experiment) [20]	DCN (experiment IQT) [20]	CN (modelling) [13]
methyl laurate	C13H26O2	(C12:0M)	66.7; 66.3; 66.7	-	61.1
methyl myristate	C15H30O2	(C14:0M)	73.5; 66.2	75.8	69.9
methyl palmitate	C17H34O2	(C16:0M)	74.5;74.3;74.3	85.9	74.4
methyl stearate	C19H38O2	(C18:0M)	86.9;75.6	95.6	76.3
methyl palmitoleate	C17H32O2	(C16:1M)	-	56.6	51
methyl oleate	C19H36O2	(C18:1M)	56.0	59.8;56.6;59.3	57.2
methyl linoleate	C19H34O2	(C18:2M)	41.7	43.9; 38.2	36.8
methyl linolenate	C19H32O2	(C18:3M)	45.9; 23	37.0	21.6
methyl α -linolenate	C19H32O2	-	-	22.7	-
methyl γ -linolenate	C19H32O2	-	-	29.2	-

Table 6 Calculated NO_x emissions (NEI) of different biodiesel component for automotive engine and stationary engine

Component	Density	DCN	ID	T _{ad} , K	NEI (ppm) stationary engine Equation (10)	NEI (ppm) - automotive engine Equation (11)
C14:0M	865.0363	75.8	2.62	2555	33.67	43.73
C16:0M	863.2509	85.9	2.29	2660	21.81	24.87
C18:0M	861.8251	56.6	3.58	2665	73.39	140.40
C18:1M	874.2283	58.1	3.48	2670	67.32	123.72
C18:2M	886.6315	41.05	5.10	2680	313.90	1106.73
C18:3M	899.0347	37	5.73	2700	568.16	2585.49
SME	877*	49.9*	4.10	2700	118.43	280.09

* The cetane number and density values for soybean biodiesel fuel (SME) are taken from [9].

**Figure 2** Comparison of calculated NO_x of biodiesel components and SME with experimental NO_x of CBRME for the stationary engine (st) and automobile engine (a)

which was adopted in [12]. To simulate NO_x emissions in an automotive engine, the multiplier containing the ID has also been changed to better match the experimental data. Given the above changes, emissions of nitrogen oxides (ppm) of biodiesel components (no-load mode) can be modelled using the following formulas:

- in a stationary engine:

$$NEI = 20956.69 \cdot p_f \cdot \exp(0.948 \cdot ID - 18.83) \cdot \exp(8058.38/T_f) \quad (10)$$

- for automotive engine:

$$NEI = 20956.69 \cdot p_f \cdot \exp(1.35 \cdot ID - 19.62) \cdot \exp(8058.38/T_f) \quad (11)$$

Results of calculating the nitrogen oxides of biodiesel components, as well as SME (soybean oil methyl ester) according to Equations (10) and (11), are shown in Table 6.

The methyl ester density, shown in Table, 6 was estimated based on the following formulas [21]:

$$\begin{aligned}\rho_i &= \rho_{i0} - \alpha_T(T - 288.15), \\ \rho_{i0} &= 851.471 + \frac{250.718DB + 280.899}{1.214 + n_{acid}}, \\ \alpha_T &= \frac{7.536}{\ln(n_{acid}) + 3.584} - 0.446,\end{aligned}\quad (12)$$

where DB is numbers of double bonds, n_{acid} is the number of carbons in fatty acids.

Figure 2 shows values of the nitrogen oxides of components and SME, calculated by Equations (10) and (11) in comparison to experimental data [12] for CBRME.

7 Conclusions

1. Flame temperature, ignition delay and fuel density are important factors influencing the formation of nitrogen oxides in the internal combustion engine of motor vehicles.

2. Emissions of nitrogen oxides increase with increasing load. In the no-load mode, biodiesel has lower NO_x emissions than diesel.
3. Since biodiesel fuels have the lower ignition delay values than diesel fuel, this is the factor that reduces the nitrogen oxide emissions.
4. An increase in the flame temperature contributes to formation of more nitrogen oxide emissions. Calculation of the flame temperature of diesel biofuels and their components requires additional research.
5. Approximations were proposed and nitrogen oxide emissions for the components (methyl esters of fatty acids) of biodiesel are calculated based on the DCN value for these of the components.
6. The approximations for modelling of NO_x emission for biodiesel components (methyl esters of fatty acids) were proposed and values of NO_x for both the stationary engine and automotive engine were calculated based on the DCN value of the components.

References

- [1] PUKALSKAS, S., KRIAUCIUNAS, D., RIMKUS, A., PRZYBYLA, G., DROZDZIEL, P., BARTA, D. Effect of hydrogen addition on the energetic and ecologic parameters of an SI engine fuelled by biogas. *Applied Sciences* [online]. 2021, **11**(2), 742. ISSN: 2076-3417. Available from: <https://doi.org/10.3390/app11020742>
- [2] PUNOV, P., GECHEV, T., MIHALKOV, S., PODEVIN, P., BARTA, D. Experimental study of multiple pilot injection strategy in an automotive direct injection diesel engine. *MATEC Web of Conferences* [online]. 2018, **234**, 03007. ISSN 2261-236X. Available from: <https://doi.org/10.1051/mateconf/2018234007>
- [3] HONIG, V. Specifications of wear of oils in two-fuel systems. *Manufacturing Technology* [online]. 2018, **18**(4), p. 567-571. ISSN 1213-2489. Available from: <https://doi.org/10.21062/ujep/139.2018/a/1213-2489/MT/18/4/567>
- [4] HOLUBEK, M., PEXA, M., PAVLU, J., CEDIK, J., VESELA, K., KUCHAR, P. Analysis of the influence of fuel on oil charge and engine wear. *Manufacturing Technology* [online]. 2019, **19**(1), p. 64-70. ISSN 1213-2489. Available from: <https://doi.org/10.21062/ujep/245.2019/a/1213-2489/MT/19/1/64>
- [5] FOMIN, O., AKIMOVA, A., AKIMOVA, J., MASTEPAN, A. The criteria choice of evaluating the effectiveness of the process and automatic control systems. *Procedia Computer Science* [online]. 2019, **149**, p. 246-251. ISSN 1877-0509. Available from: <https://doi.org/10.1016/j.procs.2019.01.130>
- [6] FOMIN, O., MASTEPAN, A., BONDARENKO, A., LUTAI, S. Electromagnetic compatibility of systems autonomous voltage inverter - induction motor with a power source. *Procedia Computer Science* [online]. 2019, **149**, p. 278-281. ISSN 1877-0509. Available from: <https://doi.org/10.1016/j.procs.2019.01.135>
- [7] DIZO, J., BLATNICKY, M. Use of multibody system dynamics as a tool for rail vehicle behaviour diagnostics. *Diagnostyka*. 2016, **17**(2), p. 9-16. ISSN 1641-6414.
- [8] Biofuels consumption for transport in Slovakia in 2015-2019 - Statista [online]. Available from: <https://www.statista.com/statistics/613307/biofuels-consumption-transport-slovakia/>
- [9] MUELLER, C. J., BOEHMAN, A. L., MARTIN G. S. An experimental investigation on the origin of increasing NO_x emissions when fuelling a heavy-duty compression engine with soy biodiesel. *SAE International Journal of Fuels and Lubricants* [online]. 2009, **2**(1), p. 789-816. ISSN 1946-3952. Available from: <https://doi.org/10.4271/2009-01-1792>
- [10] SCHONBORN, A., LADOMMATOS, N., WILLIAM, S. J., ALLAN, R., ROGERSON, J. The influence of molecular structure of fatty acid monoalkyl esters on diesel combustion. *Combustion and Flame* [online]. 2009, **156**(7), p. 1396-1412. ISSN 0010-2180. Available from: <https://doi.org/10.1016/j.combustflame.2009.03.011>
- [11] KAYA, T., KUTLAR, O. A., TASKIRAN, O. O. Evaluation of the partially premixed compression ignition combustion with diesel and biodiesel blended diesel at part load condition. *Engineering Science and Technology, an International Journal* [online]. 2021, **24**(2), p. 458-468. ISSN 2215-0986. Available from: <https://doi.org/10.1016/j.jestch.2020.07.011>

- [12] SARAVANAN, S., NAGARAJAN, G., ANAND, S., SAMPATH, S. Correlation for thermal NO_x formation in compression ignition (CI) engine fuelled with diesel and biodiesel. *Energy* [online]. 2012, **42**(1), p. 401-410. ISSN 0360-5442. Available from: <https://doi.org/10.1016/j.energy.2012.03.028>
- [13] KOLODNYTSKA, R. V. *Evaporation and combustion processes of diesel biofuel in internal combustion engines* (in Ukrainian). Zhytomyr: Zhytomyr State Technological University, 2018. ISBN 978-966-683-499-0.
- [14] KOLODNYTSKA, R. V. *Spraying of diesel fuel and biofuel in internal combustion engines*. (in Ukrainian). Zhytomyr: Zhytomyr State Technological University, 2017. ISBN 978-966-683-489-1.
- [15] GUTAREVICH, Y. F., KAREV, S. V. Calculations effect of exhaust gas recirculation on formation of nitrogen oxides in the application of the combined method of power control of modern gasoline engine (in Ukrainian). *Visnyk NTU*. 2012, **26**, p. 133-138. ISSN 2413-4295.
- [16] KOLODNYTSKA, R. V. Calculations effect of exhaust gas recirculation on formation of nitrogen oxides in the application of the combined method of power control of modern gasoline engine (in Ukrainian). *Visnyk of Zhytomyr Polytechnic State University, Technical Sciences*. 2018, **2**(82), p. 63-68. ISSN 1728-4260.
- [17] KOLODNYTSKA, R. V., KRAVCHENKO, A. P. Modelling the ignition delay of diesel biofuel in the internal combustion engine of road transport (in Ukrainian). In: International Scientific and Practical Conference dedicated to the 90th anniversary of the Kharkiv Automobile and Highway University and the 90th anniversary of the Automobile Faculty "Modern trends in the Development of Road Transport and Industrial Engineering": proceedings. 2020. p. 239-241.
- [18] WANG, W. G., LYONS, D. W., CLARK, N. N., GAUTAM, M., NORTON, P. M. Emissions from nine heavy trucks fueled by diesel and biodiesel blend without modification. *Environmental Science and Technology* [online]. 2000, **34**(6), p. 933-939. ISSN 0013-936X. Available from: <https://doi.org/10.1021/es981329b>
- [19] KUMAR, A., KIM, D.-S., OMIDVARBORNA, H., YARLAGADDA, M., KUPPILI, S. K., SAWTARIE, N. M. Experimental modelling of NO_x and PM generation from combustion of various biodiesel blends for urban transport buses. MNTRC project 1245. Toledo: The University of Toledo, 2016.
- [20] YANOWITZ, J., RATCLIFF, M. A., MCCORMICK, R. L., TAYLOR, J. D., MURPHY, M. J. Compendium of experimental cetane numbers. Technical report NREL/TP-5400-67585. Golden: National Renewable Energy Laboratory, 2017.
- [21] SAZHIN, S. S., AL QUBEISSI, M., KOLODNYTSKA, R., ELWARDANY, A. E., NASIRI, R., HEIKAL, M. R. Modelling of biodiesel fuel droplet heating and evaporation. *Fuel* [online]. 2014, **115**, p. 559 - 572. ISSN 0016-2361. Available from: <https://doi.org/10.1016/j.fuel.2013.07.031>

A CRITICAL REVIEW OF BIOFUELS AS AN ALTERNATIVE FUEL TO DIESEL IN GULF REGIONAL CORPORATION (GCC) REGION: CURRENT MARKET TRENDS AND FUTURE OPPORTUNITIES

Faisal O. Mahroogi¹, Sunny Narayan^{2*}, Muhammad Usman Kaisan³, Abdulkabir Aliyu⁴, Ibrahim Yahuza⁵, Ivan Grujić⁶, Nadica Stojanović⁶

¹Mechanical Engineering Department, Islamic University of Madinah, Saudi Arabia

²Mechanical Engineering Department, Qassim University, Burydah, Saudi Arabia

³Mechanical Engineering Department, Ahmadu Bello University, Zaria, Nigeria

⁴School of Water Energy and Environment, Cranfield University, Bedfordshire, United Kingdom

⁵Department of Automotive Engineering, Airforce Institute of Technology, Kaduna, Nigeria

⁶Department of Motor Vehicles and Motors, University of Kragujevac, Kragujevac, Serbia

*E-mail of corresponding author: rarekv@gmail.com

Resume

Bio Fuels are considered as good alternatives for conventional fossil fuels. By the year 2020, in the GCC region these fuels are able to meet around 0.5 - 1% of total transportation fuel demand. This industry grew at rate of 3.4% over the period of 2015-2020 with a strong projected growth in the Kingdom of Saudi Arabia (KSA). Bio fuels are used to operate automotive for mining and construction industries. Critical barriers in foreign investments pose a major challenge for growth of this sector in the GCC region. The presented work discusses situation and growth predictions of Bio-Fuel industry in the GCC region. It also discusses about current growth, trends, opportunities and challenges being faced by major companies operating in the GCC region.

Article info

Received 1 April 2021

Accepted 16 May 2021

Online 4 November 2021

Keywords:

energy,
alternative fuels,
biofuels

Available online: <https://doi.org/10.26552/com.C.2022.1.B67-B73>

ISSN 1335-4205 (print version)

ISSN 2585-7878 (online version)

1 Introduction

Use of biofuels has played a vital role in transformation of global economy towards sustainable and renewable resources [1-23]. Along with electric vehicles, these fuels can help to move away from using traditional oil resources [23-35]. Liquid biofuels provide bright future scope for the road, shipping and aviation-based industries. These fuels face challenges on fields of technological innovations, supply chain, market and policy making. The costs of production for biofuels have been estimated to about USD 0.60-1.10 per litre by the year 2045. However, various innovations may reduce this by up to a third over coming period. These fuels have a potential to reduce greenhouse gas (GHG) emissions by 60 - 95% [36]. Figure 1 shows economic comparisons of biofuels with fossil fuels over the period of 2015-2045. Diesel and gasoline substitute fuels have highest costs.

2 Background

The most well-known first-generation biofuel additive is ethanol, that is produced from fermentation

of sugar extracted from starch. Global production of bio-ethanol in the year 2006 was about 51 billion litres [37]. China and India contributed about 11% to it. Various raw materials for ethanol, include feedstock like cane, corn, starch and other sugars. Table 1 compares various merits and demerits of first-generation biofuels.

The second-generation biofuels are produced from lignocellulosic biomass, enabling the use of lower-cost, non-edible feedstocks. These biofuels can be further classified as: biochemical or thermochemical. Ethanol or butanol-based fuels are made via biochemical processing, while all the other are made by thermochemical processing. The second-generation includes methanol, Fischer-Tropsch liquids (FTL), dimethyl ether (DME), green diesel and pyrolysis oils. Table 2 presents a summary of the secondary biofuels, their applications and properties.

Ethanol based biofuels have a higher latent heat of evaporation and thus a poorer cold start ability in winter [38]. Damage and driveability issues occur for vehicles operating on ethanol blends. Use of biodiesel needs much lesser engine modifications as compared to use of bio gasoline blends [38]. For some vehicles, rubber seals in the fuel lines may require replacement with

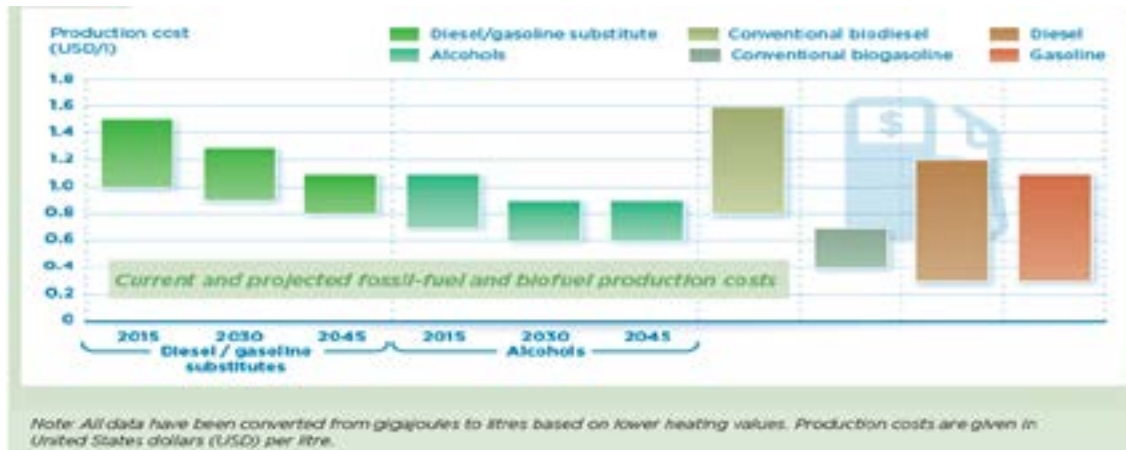


Figure 1 Current and projected production charges of fossil fuel and biofuels [36]

Table 1 Summary of comparisons of primary biofuels [37]

Merits	Disadvantages
Easily available feed stocks.	Feed stocks compete with food stocks.
Simpler production methods.	Higher costs of feedstock.
Variable production capacities.	Modest reductions in greenhouse emissions.

Table 2 Summary of applications of secondary biofuels products

Product	Description	Application and product replacement	Blending limits
Methanol	Single carbon atom alcohol with energy density 50% lower as compared to gasoline	May be used with gasoline as methyl tert-butyl ether as a Transportation fuel	May be converted to dimethyl ether (DME) as replacement.
Fischer-Tropsch fuels	Paraffinic hydrocarbons similar to diesel.	May be mixed with gasoline, diesel or jet fuels	Fischer-Tropsch kerosene is mixed for maximum ratio of 50% with jet fuel.
FAME biodiesel	Fatty acid methyl ester (FAME)	May be mixed with diesel for use in transportation.	Up to 7% FAME mixed with diesel as per euro EN 590.
Butanol	Four carbon alcohol having density similar to gasoline.	May be mixed with gasoline or diesel as transportation.	Up to 16% butanol mixed with gasoline as per US standard -ASDMD 4814.
Synthetic aromatic fuel	Hydrocarbon fuel containing aromatic compounds.	Mixed with jet fuel for aviation use.	ASTM certification needed

non-rubber products. Biodiesel becomes thick during the cold weather. It may cause issues during starting. Fuel heating system or using biodegradable additives may be a good alternative. The use of multiple injections with an increased pressure reduces the NOx emissions [38-39].

The heating of biodiesel decreases viscosity making them suitable for diesel engines [39-41]. There is a decrease in unburned hydrocarbon, carbon monoxide and BSFC and an increase in thermal efficiency.

Engine wear by using the biodiesel has been found to be lesser than that of the petroleum diesel. Deposits and clogging are due to oxidization of low-quality biofuels.

Pollution in engine exhaust is much lesser due to its higher oxygen content.

Depending on the type of engine, the components of engine coming in contact with biodiesel can be made from compatible materials. Oil leakage to crankcase has an impact on engine durability and longevity. Impacts on injectors, filters and other system components can deteriorate engine performance. Emission after treatment systems, like catalysts and particulate filters, can be affected by biodiesel fuels.

3 Biofuels as an alternative for GCC region [42]

Results from the biomass resource and bioenergy potential modelling for each GCC country are presented in Table 3 [42].

Table 3 Biomass potential in GCC region

	Biomass resource potential (Mtpa)				Bioenergy potential (PJ ^{elec}) ^a	Proportion of overall electricity consumption (%) ^b
	Animal wastes	Crop Residue	Sewage	MSW		
Bahrain	0.27	0.01	0.02	0.68	6.59	6.3
Kuwait	1.71	0.64	0.06	1.17	23.10	10.1
Oman	3.57	0.07	0.07	0.85	27.59	22.5
Qatar	1.39	0.47	0.04	0.68	16.40	9.9
Saudi Arabia	14.35	0.20	0.51	12.50	179.45	14.4
UAE	4.24	0.30	0.15	3.46	50.71	11.0
Total	25.52	1.68	0.87	19.35	303.84	13.0

^abased on assumption of thermal conversion efficiency of 36% used by IEA bioenergy

^bbased on national electricity consumption levels for 2019

Saudi Arabia had the largest overall potential, followed by UAE and Oman. For each region the dominant categories of biomass potentially available for bioenergy are waste resources generated by animals and organic MSW materials. Agricultural residue and sewage wastes have lesser opportunities.

According to the International Energy Agency (IEA), the share of biofuels in the Middle East reached 5% by 2020 [42]. With more and more biofuel companies coming into the picture in the Middle East, there is an acute increase in the market share of biofuels.

The demand for fossil fuels is ever increasing against a tight economic environment. Consumption of oil and gas in Saudi Arabia has shown a rise of 5.9% over the past five years. The demand for electricity has seen an annual growth rate of 8%. Although the GCC countries are the world's leading producers of energy, many clean technology projects have been launched recently indicating the region's need to exploiting renewable sources of energy. Found in the Middle Eastern arid region, algae are available significantly. It can withstand hot temperatures, as well as grow in higher salinity ranges making the prospects of algae-based biofuels production for the Middle East region as appealing. The region is suitable for the mass production of algae due to following factors:

- Presence of non-arable lands and extensive coastal area.
- Presence of oil refineries and power plants to capture CO₂.
- Highest annual solar radiations.
- Presence of a number of sewage and wastewater treatment plants.

Algae Research Laboratory at Abu Dhabi and Microbial Environmental Chemical Engineering Laboratory (MECEL) of the Masdar Institute of Science and Technology, are currently taking up projects to analyze the algae-based fuel production for use as aviation and jet fuel. Lootah Biofuels based in Dubai has made an agreement to develop raw materials for production of algae oil. Photo bioreactors (PBR) and solar-

powered, open pond constructions for algae production are becoming an attractive choice for producing algae in the Middle East region.

The King Abdul Aziz City for Science and Technology (KACST) is working on a project to screen lipid hyper-producer algae species in Saudi Arabian coastal waters for biofuel production. The aim of this project is to increase research in algae-based biofuel production for use in bio refinery within the next ten years.

With Etihad Airways commercial flight operation powered by fuel produced from plant matter, the UAE has demonstrated importance of biofuel development [13]. To help in further development, the Sustainable Bioenergy Research Consortium (SBRC) located is working to implement Bio jet Abu Dhabi, a project being that brings together various sectors of fuel development, energy, aviation, refining, environmentalists as well as financial/investors and legal fraternity.

Investing in the UAE's sector could also provide an annual revenue of US\$7.6 billion by the year 2023, with \$69 billion being invested in new production capacity worldwide over the next 10 years.

4 Economic scenario

This section deals with study of economic potential of biofuels, that also needs analysis of production and refining methods. The costs of production of biofuels depends on available feedstock, conversion process and production scale. Among all the parameters, the costs of raw feedstock play a major role in overall costs. One of the factors that have limited use of biofuels is perception of higher costs. However, this is just a myth as the biodiesel provided by Lootah Biofuels in UAE is cheaper than the conventional diesel.

Amongst all the fuels Ethanol has the lowest costs, higher octane fuel additive available to gasoline operated systems. During year of 2011, The National Renewable Energy Laboratory (NREL) projected a minimum support value of 0.57 US\$/L. Some of the major contributors to production cost of ethanol includes

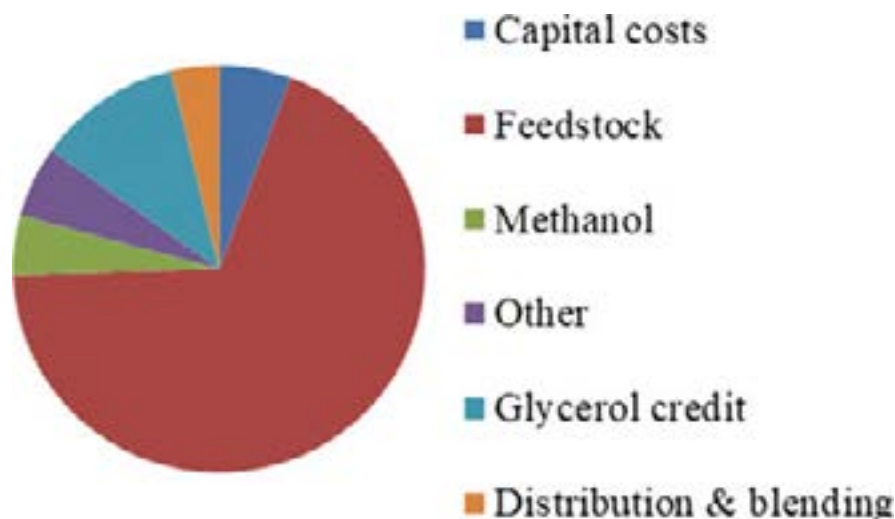


Figure 2 Production costs of the palm oil based biodiesel

Factors	Conventional Vehicles	Electric Vehicles	Methanol vehicles
Resources	Excellent	Poor	Good
Energy Density	Good	Poor	Excellent
Emissions	Good	Good	Excellent
Fueling Infrastructure	Good	Poor	Excellent
Price	Good	Poor	Excellent
Status	 Excellent Good Poor		

Figure 3 Comparison of vehicles operated on various fuels

feedstock costs (23 - 28 %), costs of capital (40 - 49 %), yield and enzymes costs [15].

Zhang et al. [39], Marchetti et al. [40] and Apostolakou et al. [41] have done analysis of economic requirement for production of biodiesel fuels. The production costs of biodiesel were higher as compared to diesel. Graboski and McCormick studied benefits of using glycerol in order to reduce the production costs in KSA [42]. An approximate distribution of production costs of palm oil based biodiesel is shown in Figure 2. Explicitly, the feedstock costs are predominant and with an economic return on glycerol, the choice of larger plant has lowered the price.

Figure 3 presents a rough comparisons of automotive vehicles operated on conventional fuel, electric and methanol based biofuels.

Methanol based biofuel vehicles performed best in terms of emissions, fuel infrastructure, price and resources.

Microalgae is a good choice for the sustainable production of biofuels. Algae produce lipids that have the potential for aviation fuel and cultivation of microalgae could mitigate carbon dioxide and other greenhouse gases Oman has a good potential to cultivate algae being richer in water resources as compared to rest of region. The government is looking for ways to use

biofuels for transportation and power generation. Qatar is also investing in algae biofuels industry. In 2019, Total company and Qatar University initiated two projects to investigate microalgae. In 2018, the country had a biomass installed capacity of 38 Megawatt.

The GCC algae biofuel prospects market is consolidated. Some of the key players in this market include Total SA, Royal Dutch Shell PLC, Chevron Corporation, Exxon Mobil Corporation, Qeshm Microalgae Biorefinery Co.

5 Future trends

The global biofuels market alone was projected to grow to \$139 billion by 2021. Commercial use of various biofuel is still in the phase of being implemented in the GCC region. In the Middle East region growing market demand provides an opportunity in transportation fuels and petrochemical derivatives. Algae producers have established pilot and demonstration scale projects that are able to produce fuels from microalgae, cyanobacteria and other microbes. These factors make it imperative on GCC nations to develop a robust research, development and market deployment plan for a comprehensive approach for bio product synthesis.

6 Conclusions

This paper presents a comprehensive review of production and adoption of biodiesel as an alternative source of fuel for the GCC region. Based on the findings, as well as data gathered from available literatures on this subject, the following conclusions can be made:

1. The high demand for various fossil fuels has increased the need to explore alternative
2. An increasing trend has been seen in the use of biodiesel from production rates and usage as various new jobs are created to meet up with labour requirements for expansion of industry.
3. Reduction in greenhouse gas emissions can be achieved through increase in production of biodiesel.

resources of renewables like biodiesel that are derived from cheap sources giving rise to improvements in exhaust emissions and engine performances.

References

- [1] REICHE, D. Energy policies of Gulf Cooperation council (GCC) countries - possibilities and limitations of ecological modernization in rentier states. *Energy Policy* [online]. 2010, **38**(5), p. 2395-2403. ISSN 0301-4215. Available from: <https://doi.org/10.1016/j.enpol.2009.12.031>
- [2] REYNOLDS, R. M. Physical oceanography of the Gulf, Strait of Hormuz, and the Gulf of Oman - Results from the Mt. Mitchell expedition. *Marine Pollution Bull* [online]. 1993, **27**, p. 35-59. ISSN 0025-326X. Available from: [https://doi.org/10.1016/0025-326X\(93\)90007-7](https://doi.org/10.1016/0025-326X(93)90007-7)
- [3] SALE, P., FEARY, D., BURT, J., BAUMAN, A., CAVALCANTE, G., DROUILLARD, K., KJERFVE, B., MARQUIS, E. TRICK, C., USSEGLIO, P., VAN LAVIEREN, H. The growing need for sustainable ecological management of marine communities of the Persian Gulf. *AMBIO* [online]. 2011, **40**(1), p. 4-17. ISSN 0044-7447, eISSN 1654-7209. Available from: <https://doi.org/10.1007/s13280-010-0092-6>
- [4] AL-BADI, A. H., MALIK, A., GASTLI, A. Assessment of renewable energy resources potential in Oman and identification of barrier to their significant utilization. *Renewable and Sustainable Energy Reviews*. 2009, **13**(9), p. 2734-2739. ISSN 1364-0321.
- [5] CHEDID, R., CHAABAN, F. Renewable-energy developments in Arab countries: a regional perspective. *Applied Energy*. 2003, **74**(1-2), p. 211-220. ISSN 0306-2619.
- [6] DOUKAS, H., PATLITZIANAS, K. D., KAGIANNAS, A. G., PSARRAS, J. Renewable energy sources and rationale use of energy development in the countries of GCC: myth or reality? *Renewable Energy* [online]. 2006, **31**(6), p. 755-770. ISSN 0960-1481. Available from: <https://doi.org/10.1016/j.renene.2005.05.010>
- [7] HAMZEH, Y., ASHORI, A., MIRZAEI, B. ABDULKHANI, A., MOLAEI, M. Current and potential capabilities of biomass for green energy in Iran. *Renewable and Sustainable Energy Reviews* [online]. 2011, **15**(9), p. 4934-4938. ISSN 1364-0321. Available from: <https://doi.org/10.1016/j.rser.2011.07.060>
- [8] KAZEM, H. A., CHAICHAN, M. T. Status and future prospects of renewable energy in Iraq. *Renewable and Sustainable Energy Reviews* [online]. 2012, **16**(8), p. 6007-6012. ISSN 1364-0321. Available from: <https://doi.org/10.1016/j.rser.2012.03.058>
- [9] Kim, S., Dale, B. Global potential bioethanol production from wasted crops and crop residues. *Biomass Bioenergy* [online]. 2004, **26**(4), p. 361-75. ISSN 0961-9534. Available from: <https://doi.org/10.1016/j.biombioe.2003.08.002>
- [10] ALAMDARI, P., NEMATOLLAHI, O., ALEMRAJABI, A. A. Solar energy potentials in Iran: a review. *Renewable and Sustainable Energy Reviews* [online]. 2013, **21**, p. 778-788. ISSN 1364-0321. Available from: <https://doi.org/10.1016/j.rser.2012.12.052>
- [11] GHOBADIAN, B., NAJAFI, G., RAHIMI, H., YUSAF, T. F. Future of renewable energies in Iran. *Renewable and Sustainable Energy Reviews* [online]. 2009, **13**(3), p. 689-95. ISSN 1364-0321. Available from: <https://doi.org/10.1016/j.rser.2007.11.010>
- [12] BAGHERI, N., MOGHADDAM, S., MOUSAVI, M., NASIRI, M., MOALLEMI, E. A., YOUSEFDEHI, H. Wind energy status of Iran: evaluating Iran's technological capability in manufacturing wind turbines. *Renewable and Sustainable Energy Reviews* [online]. 2011, **15**(8), p. 4200-4211. ISSN 1364-0321. Available from: <https://doi.org/10.1016/j.rser.2011.07.029>
- [13] NARAYAN, S., ALSAGRI, A. S., GUPTA, V. Design and analysis of hybrid automotive suspension system. *International Journal of Mechanical and Production Engineering Research and Development (IJMPERD)* [online]. 2019, **9**(4), p. 637-642. ISSN 2249-6890, eISSN 2249-8001. Available from: <https://doi.org/10.24247/ijmperd201963>
- [14] MAHROOGI FAISAL, O., NARAYAN, S. Design and analysis of double wishbone suspension systems for automotive applications. *International Journal of Mechanical and Production Engineering Research and Development (IJMPERD)* [online]. 2019, **9**(4), p. 1433-1442. ISSN 2249-6890, eISSN 2249-8001. Available from: <https://doi.org/10.24247/ijmperd2019148>

- [15] STOJANOVIC, N., GLISOVIC, J., GRUJIC, I., NARAYAN, S. Influence of size of ventilated brake disc ribs on air flow velocity. *International Journal of Advanced Science and Technology (IJAST)* [online]. 2020, **29**(1), p. 637-647. ISSN 2005-4238, eISSN 2207-6360. Available from: <http://sersec.org/journals/index.php/IJAST/article/view/3285>
- [16] MAHROOGI, F. O., NARAYAN, S. Effects of dampers on piston slapping motion. *International Journal of Vehicle Noise and Vibration (IJVNV)* [online]. 2020, **16**(1/2), p. 46-57. ISSN 1479-1471, eISSN 1479-148X. Available from: <https://doi.org/10.1504/IJVNV.2020.112432>
- [17] MAHROOGI, F., NARAYAN, S. Dynamic-analysis-of-piston-secondary-motion-using FEM method. In: 26th International Congress on Sound and Vibration: proceedings. 2019. ISSN 2329-3675, ISBN 978-1-9991810-0-0.
- [18] SHERIFF, S.A., KUMAR, I. K., MANDHATHA, P. S., JAMBAL, S. S., SELLAPPAN, R., ASHOK, B., NATHAGOPAL, K. Emission reduction in CI engine using biofuel reformulation strategies through nano additives for atmospheric air quality improvement. *Renewable Energy* [online]. 2020, **147**(1), p. 2295-2308. ISSN 0960-1481. Available from: <https://doi.org/10.1016/j.renene.2019.10.041>
- [19] KUMAR, A. N., KISHORE, P. S., RAJU, K. B., NANTHAGOPAL, K., ASHOK, B. Experimental study on engine parameters variation in CRDI engine fuelled with palm biodiesel. *Fuel* [online]. 2020, **276**, 118076. ISSN 0016-2361. Available from: <https://doi.org/10.1016/j.fuel.2020.118076>
- [26] THIYAGARAJAN, S., SONTHALIA, A. V., GEO, V. E., PRAKASH, T., KARTHICKEYAN, V., ASHOK, B., NANTHAGOPAL, K., DHINESH, B. Effect of manifold injection of methanol/n-pentanol in safflower biodiesel fuelled CI engine. *Fuel* [online]. 2020, 261, 116378. ISSN 0016-2361. Available from: <https://doi.org/10.1016/j.fuel.2019.116378>
- [20] BALASUBRAMANIAN, D., KAMARAJ, S., KRISHNAMOORTHY, R. Synthesis of biodiesel from waste cooking oil by alkali doped calcinated waste egg shell powder catalyst and optimization of process parameters to improve biodiesel conversion [online]. SAE Technical Paper 2020-01-0341. 2020. ISSN 0148-7191, eISSN 2688-3627. Available from: <https://doi.org/10.4271/2020-01-0341>
- [21] KARTHICKEYAN, V., ASHOK, B., THIYAGARAJAN, S., NANTHAGOPAL, K., GEO, V. E., DHINESH, B. Comparative analysis on the influence of antioxidants role with Pistacia khinjuk oil biodiesel to reduce emission in diesel engine. *Heat and Mass Transfer / Waerme- und Stoffuebertragung* [online]. 2020, **56**(4), p. 1275-1292. ISSN 1432-1181, eISSN 0947-7411. Available from: <https://doi.org/10.1007/s00231-019-02797-6>
- [22] SAKTHIVEL, R., RAMESH, K., PURNACHANDRAN, R., SHAMEER, M. P. A review on the properties, performance and emission aspects of the third generation biodiesels. *Renewable and Sustainable Energy Reviews* [online]. 2018, **82**(3), p. 2970-2992. ISSN 1364-0321. Available from: <https://doi.org/10.1016/j.rser.2017.10.037>
- [23] SAKTHIVEL, R., RAMESH, K., SHAMEER, P. M., PURNACHANDRAN, R. Experimental investigation on improvement of storage stability of bio oil derived from intermediate pyrolysis of calophyllum inophyllum seed cake. *Journal of the Energy Institute* [online]. 2019, **92**(3), p. 768-782. ISSN 1743-9671. Available from: <https://doi.org/10.1016/j.joei.2018.02.006>
- [24] SAKTHIVEL, R., RAMESH, K., MARSHAL, J. J., SADASIVUNI, S., KUMAR, K. Prediction of performance and emission characteristics of diesel engine fueled with waste biomass pyrolysis oil using response surface methodology. *Renewable Energy* [online]. 2018, **136**, p. 91-103. ISSN 0960-1481. Available from: <https://doi.org/10.1016/j.renene.2018.12.109>
- [25] SHAMEER, P. M., RAMESH, K., SAKTIVEL, R., PURNACHANDRAN, R. Effects of fuel injection parameters on emission characteristics of diesel engines operating on various biodiesel: a review. *Renewable and Sustainable Energy Reviews* [online]. 2017, **67**, p. 1267-1281. ISSN 1364-0321. Available from: <https://doi.org/10.1016/j.rser.2016.09.117>
- [26] ANNAMALAI, M., DHINESH, B., NATHAGOPAL, K., SIVARAMAKRISHNAN, P., J. RAMESHLALWANI, J. I. J., PARTHASARTHY, M., ANNAMALAI, K. An assessment on performance, combustion and emission behavior of a diesel engine powered by ceria nanoparticle blended emulsified biofuel. *Energy Conversion and Management* [online]. 2016, **123**, p. 372-380. ISSN 0196-8904. Available from: <https://doi.org/10.1016/j.enconman.2016.06.062>
- [27] Innovation Outlook: Advanced Liquid Biofuels - IRENA [online]. 2016. Available from: <https://www.irena.org/publications/2016/Oct/Innovation-Outlook-Advanced-Liquid-Biofuels>
- [28] Biofuel production technologies: status, prospects and implications for trade and development - United Nations Conference on Trade and Development [online]. Available from: https://unctad.org/en/Docs/ditcted200710_en.pdf
- [29] KHAN, I. Bolstering a biofuels market in the Middle East - Renewable Energy World [online]. 2015. Available from: <https://www.renewableenergyworld.com/2015/03/05/bolstering-a-biofuels-market-in-the-middle-east/#gref>
- [30] RIOS, A. UAE's home-grown biofuel is important milestone in aviation - Khalifa University [online]. 2014. Available from: <https://www.ku.ac.ae/uae-s-home-grown-biofuel-is-important-milestone-in-aviation/>

- [31] Engine modification [online]. Available from: http://www.esru.strath.ac.uk/EandE/Web_sites/02-03/biofuels/perf_mods.htm
- [32] KHAN, T. M. Y. A Review of performance - enhancing innovative modifications in biodiesel engines. *Energies*. 2020, **13**, 4395. eISSN 1996-1073. Available from: <https://doi.org/10.3390/en13174395>
- [33] Using biodiesel fuel in your engine - Penn State Extension [online]. 2016. Available from: <https://extension.psu.edu/using-biodiesel-fuel-in-your-engine>
- [34] JAASKELAINEN, H., MAJEWSKI, W. A. Compatibility of biodiesel with petroleum diesel engines - DieselNet Technology Guide [online]. Available from: https://dieselnet.com/tech/fuel_biodiesel_comp.php
- [35] PEREIRA, F. M., VELASQUEZ, J. A., RIECHI, J. L., TEIXEIRA, J., RONCONI, L., RIOLFI, S., KARAS, E. L., ABREU, R. A., TRAVAIN, J. C. Impact of pure biodiesel fuel on the service life of engine-lubricant: a case study. *Fuel* [online]. 2020, **261**, 116418. ISSN 0016-2361. Available from: <https://doi.org/10.1016/j.fuel.2019.116418>
- [36] WELFLE, A., ALAWADHI, A. Bioenergy opportunities, barriers and challenges in the Arabian Peninsula - resource modelling, surveys and interviews. *Biomass and Bioenergy* [online]. 2021, **150**, 106083. ISSN 0961-9534. Available from: <https://doi.org/10.1016/j.biombioe.2021.106083>
- [37] WRITER, S. Biofuels gain traction in the GCC - Oil and Gas [online]. 2015. Available from: <https://www.oilandgasmiddleeast.com/article-14769-biofuels-gain-traction-in-the-gcc>
- [38] CHENG, C. H., CHEUNG, C. S., CHAN, T. L., LEE, S. C., YAO, C. D., TSANG, K. S. Comparison of emissions of a direct injection diesel engine operating on biodiesel with emulsified and fumigated methanol. *Fuel* [online]. 2008, **87**, p. 1870-1879. ISSN 0016-2361. Available from: <https://doi.org/10.1016/j.fuel.2008.01.002>
- [39] ZHANG, Y., DUBE, M., MCLEAN, D., KATES, M. Biodiesel production from waste cooking oil: 2. Economic assessment and sensitivity analysis. *Bioresour Technology* [online]. 2003, **90**(3), p. 229-240. ISSN 0960-8524. Available from: [https://doi.org/10.1016/S0960-8524\(03\)00150-0](https://doi.org/10.1016/S0960-8524(03)00150-0)
- [40] MARCHETTI, J. M., MIGUEL, V. U., ERRAZU, A. F. Techno-economic study of different alternatives for biodiesel production. *Fuel Process Technology* [online]. 2008, **89**(8), p. 740-748. ISSN 0378-3820. Available from: <https://doi.org/10.1016/j.fuproc.2008.01.007>
- [41] APOSTOLAKOU, A. A., KOOKOS, I. K., MARAZIOTI, C., ANGELOPOULOS, K. Techno-economic analysis of a biodiesel production process from vegetable oils. *Fuel Process Technology* [online]. 2009, **90**(7-8), p. 1023-1031. ISSN 0378-3820. Available from: <https://doi.org/10.1016/j.fuproc.2009.04.017>
- [42] GRABOSKI, M. S., MCCORMICK, R. L. Combustion of fat and vegetable oil derived fuels in diesel engines. *Progress in Energy and Combustion Science* [online]. 1998, **24**(2), p. 125-164. ISSN 0360-1285. Available from: [https://doi.org/10.1016/S0360-1285\(97\)00034-8](https://doi.org/10.1016/S0360-1285(97)00034-8)

ANALYSIS OF THE POWERTRAIN COMPONENT SIZE OF ELECTRIFIED VEHICLES COMMERCIALY AVAILABLE ON THE MARKET

Ruzimov Sanjarbek^{1,*}, Jamshid Mavlonov¹, Akmal Mukhitdinov²

¹Turin Polytechnic University in Tashkent, Tashkent, Uzbekistan

²Tashkent State Transport University, Tashkent, Uzbekistan

*E-mail of corresponding author: sanjar.ruzimov@polito.uz

Resume

The paper aims to present an analysis of the component sizes of commercially available vehicles with electrified powertrains. The paper provides insight into how the powertrain components (an internal combustion engine, an electric motor and a battery) of mass production electrified vehicles are sized. The data of wide range of mass production electrified vehicles are collected and analyzed. Firstly, the main requirements to performance of a vehicle are described. The power values to meet the main performance requirements are calculated and compared to the real vehicle data. Based on the calculated values of the power requirements the minimum sizes of the powertrain components are derived. The paper highlights how the sizing methodologies, described in the research literature, are implemented in sizing the powertrain of the commercially available electrified vehicles.

Article info

Received 18 June 2021

Accepted 13 July 2021

Online 12 November 2021

Keywords:

electrified powertrain,
hybrid electric vehicle,
battery electric vehicle,
component sizing,
power requirement,
drive cycle

Available online: <https://doi.org/10.26552/com.C.2022.1.B74-B86>

ISSN 1335-4205 (print version)

ISSN 2585-7878 (online version)

1 Introduction

The current trend to reduce vehicle emissions by means of the powertrain electrification results in increased number and models of hybrid electric vehicles (HEV). Some countries are planning to ban partially or fully vehicles with conventional Internal Combustion Engine (ICE) by 2025 and onwards [1-2]. The powertrain hybridization is mainly driven by the fact that it allows substantial fuel consumption reduction [3] and could position as an intermediate step in passing to a fully clean vehicle [4-5]. Therefore, the HEVs will not yet fall into category of vehicles banned in the future, even though they utilize ICE as the main source of motion [2]. The main benefits from hybridization of the conventional ICE powered vehicles are: Stop&Start feature to avoid engine idling, engine downsizing, operation of the engine at high efficiency region and regeneration of braking energy [3].

Hybrid electric vehicles are classified based on the architecture, on electric motor position and on hybridization ratio [6-7]. Mainly the three HEV architectures are widely used, such as: Series, Parallel and Combined (can be Power-Split or Series-Parallel). Based on the position of the Electric Motor (EM), the HEVs are classified as P0 to P5 as shown in Figure 1 [7].

Some of the peculiarities of P0-P5 HEVs can be summarized as follows [6-9]:

P0 -The EM is installed on the accessory belt drive of the engine;

P1 -the EM motor is installed on the output of the engine, before the main clutch;

P2 -the EM is located on the input shaft of the gearbox, after the main clutch (this configuration is considered as pre-transmission [6, 8]);

P3 - the EM is mounted on the output of the gearbox (this configuration is considered as post-transmission [6, 8]);

P4 -the engine and the EM are connected “through the road” [8-9], as they are mounted in different axles;

P5 - in this configuration wheel motors are used [8].

The Plugin HEV (PHEV) is a type of hybrid vehicle that can be recharged from external grid, therefore should have larger battery capacity compared to the HEV [9].

Each of the above mentioned configurations has advantages and disadvantages that must be considered in choosing the either one for implementation on a specific vehicle to be designed.

The selection of configurations depends on number of factors as vehicle class, specific requirements, driving conditions where the vehicle is to be used and others.

Another important step in designing the HEVs is to properly select the powertrain component sizes. The main powertrain components of the HEV are ICE, EM and traction battery pack.

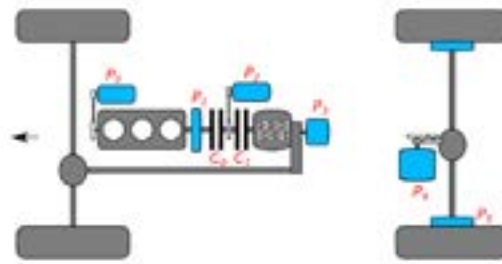


Figure 1 Classification of HEVs based on motor position. P0-P5 positions of the motors and C0, C1 are positions of the friction clutches

The ICE is the main power source of the conventional vehicles and its size is derived from the vehicle minimum dynamic requirements, while, in HEV the ICE can be used in different modes, but still functions as the main power source. Since the first appearance of HEV at the market, vast variety of the literature has been devoted to sizing of the HEV powertrain components.

In the work of Rahman et al. [10] the engine is sized to produce an average load power, which allows the engine to work at constant loads, avoiding transient operations where it consumes more fuel. In that case, the transient loads during the acceleration or deceleration modes are provided by the electric motor. Size of the electric battery is defined from a consideration to deliver the electric motor peak power and to guarantee a certain electric driving range while staying within the allowed SOC (State of Charge) range of the battery. A Lead Acid battery and the charge sustaining control strategy are considered in the analysis [10].

In further evolution of the work [11], the authors suggest to size the engine and the electric motor power such that they together are able to accelerate the vehicle to 96 km.h⁻¹ in 10 s. Moreover, the power sources are verified to deliver enough power to drive at a constant speed of 55 mph (~89 km.h⁻¹) on a 6.5% grade and at a maximum speed of 100 mph (~161 km.h⁻¹) on a flat road. Both pre- (this terminology is used [11] to describe the P1 and P2 configurations) and post-transmission (is used to describe the P3 configuration) HEV configurations are considered [11]. The battery capacity is defined as a ratio of the maximum electric motor power to 3 kW power [11]. This might be due to the fact that the single battery module under the consideration supplies 3 kW and the previous ratio defines the number of parallel battery modules.

The P1 and P2 configurations are studied by Sundstrom et al. in [12-13]. A constant ratio of the total power to vehicle mass equal to 67 W/kg is obtained by scaling the engine and electric motor powers, thus varying the hybridization ratio. The constant power to mass ratio allowed to keep the vehicle performance (time to accelerate to 100 km.h⁻¹ in 11.3 s, maximum speed of 120 km.h⁻¹ and gradeability) within a similar range in all the considered cases. The Nickel Metal Hydride (NiMH) battery with the maximum power corresponding to the maximum power requirement of the electric motor (accounting all the losses) is considered [13].

Carignano et al. [14] defines the total power of the ICE and the electric motor to meet the required acceleration levels. However, the minimum size of the ICE is limited by constraint that the latter alone should be able to run the vehicle at 120 km.h⁻¹. Maximum rated power of the electric motor is considered in defining the size of the electric battery [14].

Recently, different companies started to offer hybrid powertrain modules, as one presented by [15], a standalone P4 hybrid powertrain module, which uses 70 kW continuous (90 kW peak) power motor supplied by 400 V battery pack. Another solution for the P2 configuration HEVs with 50 kW continuous power (100 kW peak power for 30 s) and for input torque range of 150-350 Nm from the ICE is declared [15]. These standalone modules require further readjustment of the control strategies while integrated with different engines.

While the above-mentioned literature mainly focuses on the HEVs, Gao and Ehsani [16] discussed a design methodology of the electric motor and the battery size for PHEV. The electric motor is sized to provide the maximum required power in urban driving condition considering the transmission efficiency. The battery capacity is defined to have 40 miles (around 64km) of pure electric traction in urban driving conditions (urban driving part of the FTP75 cycle is used). The battery power is sized to be able to provide the electric motor maximum power. As the latter is defined by the maximum discharge current limitations of the battery, it is expected that this limitation does not take part in the PHEVs, as the battery capacity is large enough.

Murgovski et al. [17] dealt with sizing of a battery for the PHEV bus. Dynamic Programming based optimization method is used to minimize the total costs of ownership that also includes the battery replacement costs due to its degradation. The simulation is performed in a representative driving cycle considering the battery capacity degradation by 20%.

The size of the powertrain components of the PHEV with a hybrid energy storage system (HESS - i.e. combination of super-capacitor and Lithium Polymer battery) are defined by Song et. al [18]. Battery capacity degradation as a function of its temperature and the discharging rate is introduced in this work. The battery pack and super-capacitor capacities are optimized summing the fuel, the electricity and the

battery degradation costs, using the Pontryagin's minimum principle. The lower bound for the battery size, used in the optimization problem, is selected to satisfy 50km of pure electric range at constant speed of 40 km.h⁻¹.

The analysis of the broad literature on the subject, mainly based on research papers, highlights that the size of the electric motor and the battery largely depend on the performance requirements, the configuration of the hybrid vehicle, the features and the used control strategy. It can be observed, that the size of the ICE and the electric motor are mainly derived from requirements of the vehicle acceleration and the maximum speed performance, while the battery capacity is derived either from the maximum power required from the traction electric motor or from the desired electric drive range.

There are about 200 HEV and PHEV models available on the market, including the ones available only at local markets [19]. Jung [19] analysed 65 models of the HEVs and PHEVs available on the market to find the correlation between the fuel economy, the driving range and the vehicle mass. Zhang et al. [20] attempted to analyse the market development of the PHEVs in United States and China. By analysing the PHEV models available on two markets, they defined the most widespread powertrain architecture, configuration and vehicle categories for each market [20]. However, these works did not consider the powertrain component sizing issues of currently available hybrid powertrains on the market.

Published studies show that there is no study on how the powertrain components of HEVs and PHEVs available on the market are sized. Therefore, this paper attempts to reveal the sizing methodologies of powertrain components of various HEVs and PHEVs by comparing power values and the battery capacities with necessary values to meet the performance requirements. Furthermore, the performance of commercially available Conventional (CONV) and Battery Electric Vehicles (BEVs) and the size of their powertrain components are compared to those of the HEVs and PHEVs. Thus, all the vehicle types with different electrification level, ranging from conventional to pure electric vehicle, can be critically reviewed and compared.

To fulfil that aim, this paper is organized as follows:

The first (previous) section analysed the sizing methodologies of the hybrid powertrain components available in the research literature. The following second section is devoted to description of the theoretical fundamentals of the power and capacity values calculation to meet the main performance requirements. The third section illustrates the data collection, analysis of various powertrain component data and comparison between the computed results of a desired performance. The discussion and conclusions include interpretation of results in terms of the powertrain components' sizing.

2 Theoretical calculation of vehicle performance

In this section the main requirements to vehicle performance, the theoretical basis of calculation of the required traction power and the desired battery capacity are presented.

2.1 Vehicle performance requirements

The performance requirements that vehicle must meet define the size of the powertrain components. The companies have to follow international, national or internal regulations and goals. Most widely recognized performance goals are listed in Partnership for a New Generation of Vehicles (PNGV), the initiative by United States Government [21-22], which specifies the lower thresholds of vehicle performances. The requirements by PNGV can be summarized as follows [21-22]:

- Minimum acceleration requirement from 0-60 mph (0-96 km.h⁻¹) in less than 12 s;
- Overtaking manoeuvre 40-60 mph (65-96 km.h⁻¹) in less than 5.3 s;
- Maximum speed, not less than 85 mph (137 km.h⁻¹);
- Driving at a constant speed of 55 mph (89 km.h⁻¹) on a 6.5% slope;
- Maximum gradeability (required for climbing in parking places).

2.2 The theory of required power computation

The power and energy needed to fulfil the above-mentioned requirements can be obtained using the quasi-static approach with a backward model [3, 22-24]. The approach can be used for different classes of vehicles by varying their mass.

Below, the theoretical basis of defining the required power in different modes are discussed.

The power P_g required to drive the vehicle on a grade with a slope α_s at a certain speed v_s is calculated as:

$$P_g = m_v \cdot g \cdot v_v \cdot \sin \alpha_g + m_v \cdot g \cdot f_r \cdot v_v + \frac{1}{2} \cdot \rho_a \cdot c_x \cdot A_f \cdot v_v^3, \quad (1)$$

where m_v - vehicle mass, kg, f_r - tyre rolling resistance coefficient, ρ_a - air density, kg.m⁻³, c_x - aerodynamic drag coefficient, and A_f - vehicle frontal area, m².

The power $P_{V_{max}}$ required to drive at maximum speed v_{max} on a flat road, can be calculated as:

$$P_{V_{max}} = m_v \cdot g \cdot f_r \cdot v_{max} + \rho_a \cdot c_x \cdot A_f \cdot v_{max}^3, \quad (2)$$

where, v_{max} is the vehicle maximum speed, m.s⁻¹.

The power P_{acc} required to accelerate the vehicle from a standstill to 60 mph, can be calculated using the

Table 1 Main vehicle parameters used in the required power and energy calculations

#	Parameter	Nomenclature	Units	Value
1.	Vehicle mass	m_v	kg	var
2.	Aerodynamic drag coefficient	c_x	–	0.3
3.	Tyre rolling coefficient	f_r	–	0.01
4.	Road grade	α_g	%	6.5
5.	Driving speed on a grade α_g	v_g	km.h ⁻¹	89
6.	Frontal area	A_f	m ²	2

approach proposed by Plotkin et al. [22]:

$$P_{acc} = m_v \cdot \frac{v_f^2}{0.1} \left(\left(\frac{t_f + 0.1}{t_f} \right)^x - 1 \right) + m_v \cdot g \cdot f_r \cdot v_f + \frac{1}{2} \cdot \rho_a \cdot c_x \cdot A \cdot v_f^3, \quad (3)$$

where v_f is the vehicle final speed during the acceleration, m.s⁻¹; x is the exponent, which was selected to be equal to 0.66 (is selected in the range 0.5-0.66 [22]).

To calculate the energy and power requirements in a homologation driving cycle, the backward simulation approach [3, 24] can be considered, which requires the calculation of traction forces on the driving wheel. In general, the power P_{wheel} required on the wheels to accelerate and overcome the aerodynamic and road resistances at each time instant is calculated as:

$$P_{wheel} = m_v \cdot a_x \cdot v_v + m_v \cdot g \cdot f_r \cdot v_v + \frac{1}{2} \cdot \rho_a \cdot c_x \cdot A \cdot v_v^3, \quad (4)$$

where a_x is the vehicle longitudinal acceleration, m.s⁻². It is calculated using the speed profile of the driving cycle.

The required power values are calculated using the data shown in Table 1 and carrying the vehicle mass. Obviously, the variation of the vehicle mass leads to change of many vehicle parameters (geometry, aerodynamics, tyre type, etc). However, in the calculation procedure following assumptions are made:

- The aerodynamic drag coefficient is constant regardless the vehicle class and the mass;
- The tyre rolling resistance coefficient is constant and does not depend on vehicle class, the mass and the vehicle speed;
- The vehicle frontal area is constant for all the considered vehicle mass;
- For above parameters the average values of different vehicle class were used.

The size of the battery can be derived from the energy required for motion to perform a certain driving cycle. Based on such a derived value of the energy and the distance traveled during the cycle, the battery size can be calculated knowing the desired electric driving range with one complete charge.

The energy required for motion E_{wheel} can be obtained by integrating the power needed for traction at wheel level over a time T :

$$E_{wheel} = \int_0^T P_{wheel} \cdot dt. \quad (5)$$

Depending on the operation mode, the energy at wheel level can be divided to traction ($E_{trac.wheel}$) and braking ($E_{brake.wheel}$) energy:

$$E_{wheel} = \begin{cases} E_{trac.wheel} & \text{if } P_{wheel} \geq 0 \\ E_{brake.wheel} & \text{else } P_{wheel} < 0 \end{cases}. \quad (6)$$

The traction energy required at the battery level $E_{trac.bat}$ can be computed using the average efficiency of the path (battery→electric motor→transmission→wheels), which consists of the transmission η_{trans} , electric motor η_{em} and battery discharging η_{bat} efficiencies.

$$E_{trac.bat} = E_{trac.wheel} / (\eta_{trans} \cdot \eta_{em} \cdot \eta_{bat}). \quad (7)$$

In the braking phase, the regenerative braking energy $E_{brake.bat}$ reaches the battery with losses, which again can be accounted with efficiency of the path in the battery charging:

$$E_{brake.bat} = E_{brake.wheel} \cdot \eta_{trans} \cdot \eta_{em} \cdot \eta_{bat}. \quad (8)$$

It is assumed that the efficiencies of the charging and discharging phases are equal. Obviously, the above-considered efficiencies are function of the load and speed. However, for simplification reasons, the calculations carried out here are performed with the average values of efficiencies.

The equivalent energy at the end of the driving cycle $E_{eq.cycle}$ is the sum of the consumed energy during the traction and one returned to the battery:

$$E_{eq.cycle} = E_{trac.bat} + E_{brake.bat}, \quad (9)$$

where the energy values are in J ($E_{eq.cycle,J}$) and can be converted to kWh ($E_{eq.cycle,kWh}$) as:

$$E_{eq.cycle,kWh} = \frac{E_{eq.cycle,J}}{3.6e6}. \quad (10)$$

Once the energy $E_{eq.cycle,kWh}$ over given cycle with distance S_{cycle} is defined, the energy $E_{eq,kWh}$ required to drive a certain range S_{range} can be calculated as follows:

$$E_{eq,kWh} = E_{eq.cycle-kWh} \cdot \frac{S_{range}}{S_{cycle}}. \quad (11)$$

For HEVs, the battery size Q_{kWh} (in kWh) is derived

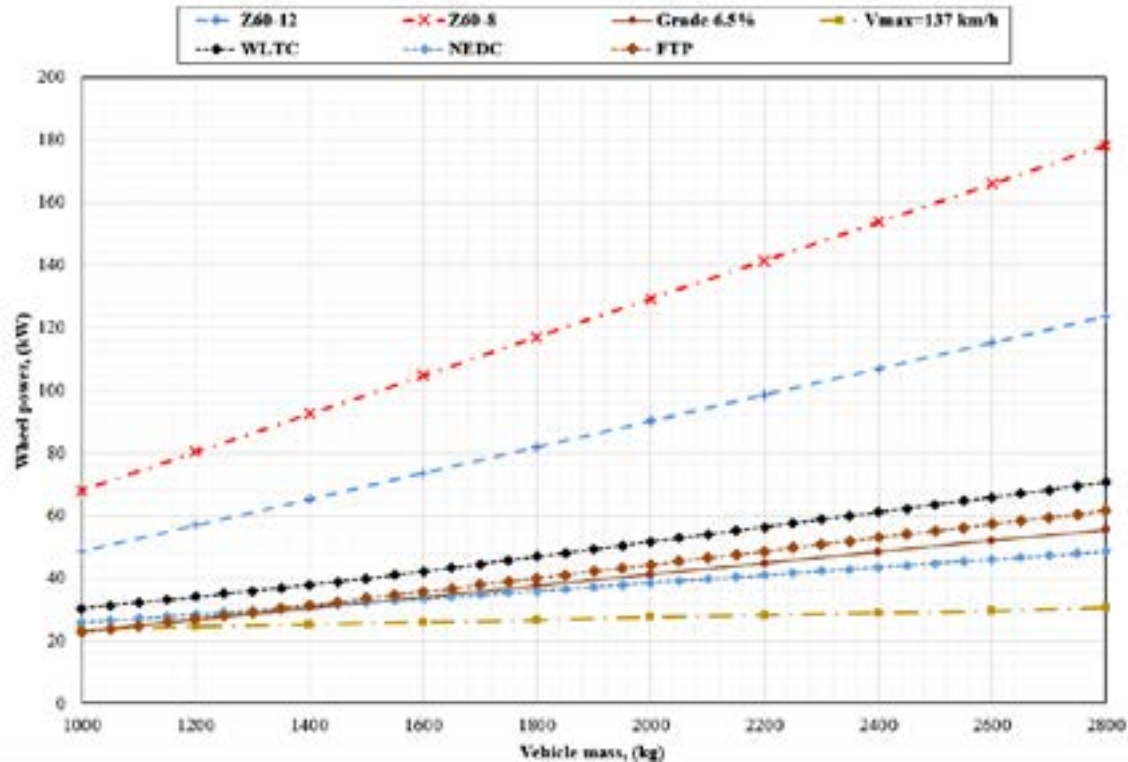


Figure 2 Different power requirements calculated at the wheel level

from the maximum power requirement in traction considering the efficiency of the path and the maximum discharge rate of the battery C_{rate} , as:

$$Q_{kWh} = \frac{P_{em,max}}{C_{rate} \cdot \eta_{em} \cdot \eta_{bat}} \quad (12)$$

For many lithium based batteries maximum value of C_{rate} is about 40 for peak currents (10 s) and 20 for continues current operations [25].

For the PHEVs and the BEVs the battery size can be derived as a ratio of the energy required over the desired driving range to the difference of State of Charge ΔSOC at the beginning and the end of the travel.

$$Q_{kWh} = E_{eq,kWh} / \Delta SOC \quad (13)$$

In general, to avoid overcharging and overheating the upper and lower limits of the lithium based batteries are set to 90% and 10%, respectively [6, 25]. Then the useful range of the battery State of Charge ΔSOC is equal to 80%.

3 Numerical simulation analysis of the powertrain components sizing

In this analysis, the specifications of mass production hybrid and electric vehicles are collected from the references [19, 20, 26-29]. The missing data was completed from the manufacturers' websites. The data of the most widespread 41 HEV, 73 PHEV and 85

BEV models were considered from 21 manufacturers. The list of the manufacturers and the models used in the paper is summarized in [29]. For some of the HEVs and PHEVs, the modifications of the model and different manufacturing year were considered as different data point. Due to lack of the complete data, some of the models were not included. The data for conventional ICE powered vehicles include specifications of around 900 different passenger vehicle models. The models with basic P0 hybrid configuration was not considered, as there are few vehicle models available with complete set of data required in the present analysis.

3.1 Power requirements

Based on Equations (1) to (4) the power at wheels needed to satisfy different requirements can be calculated. Figure 2 depicts all the power requirements listed above as a function of the vehicle mass. It is evident that the maximum power requirement corresponds to the one related to acceleration performance, which corresponds to lines Z60-8 and Z60-12. These lines describe the power requirement to accelerate from standstill to 60 mph in 8 and 12 s, respectively. The minimum power requirement corresponds to maximum speed performance (line $V_{max}=137 \text{ km}\cdot\text{h}^{-1}$). The results of a maximum power required on the vehicle driving wheels on three different driving cycles (NEDC, WLTC and FTP with corresponding lines) show that the WLTC power requirements are the highest. Therefore, for the

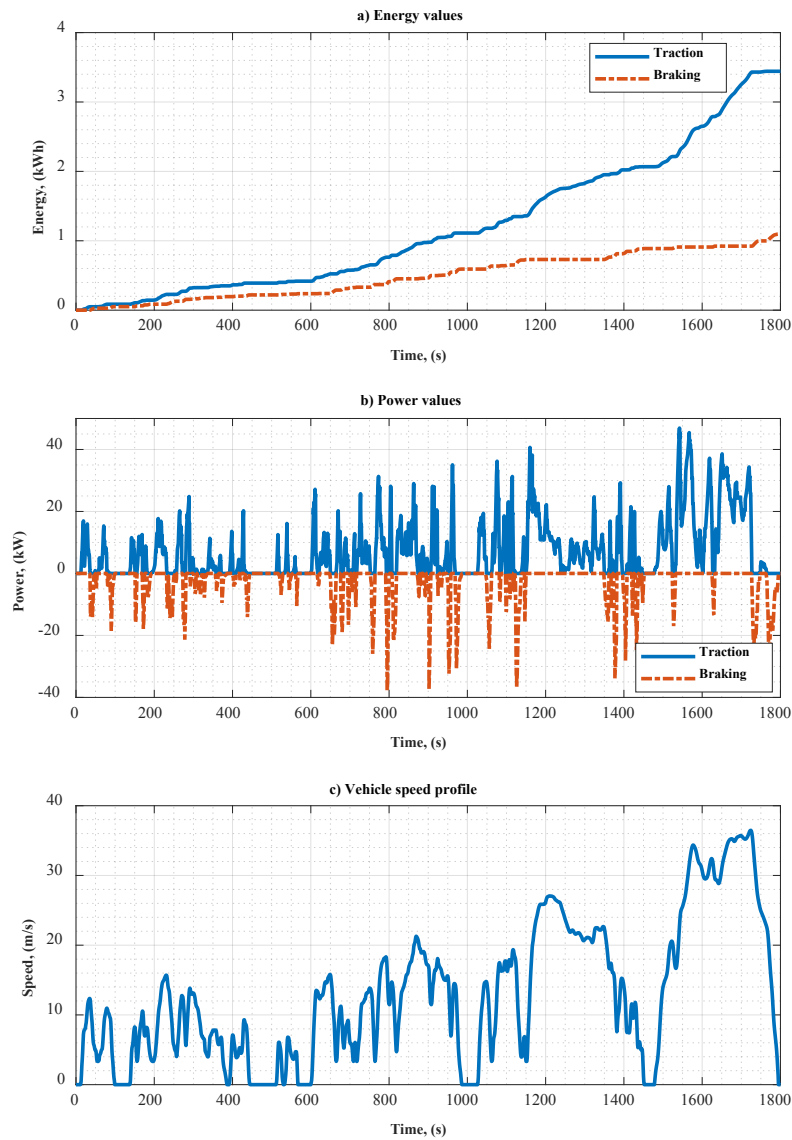


Figure 3 Energy, power values and speed profile at the wheel level on a WLTC

further analysis this line is considered as a maximum power required for motion on a driving cycle. The power required to drive on a grade of 6.5% slope at a constant speed of 55 mph is in between the power requirements Z60-12 and Vmax. It is nearly equivalent to the power requirement on NEDC driving cycle.

Figure 3 shows the energy, power and speed on the wheel level on the WLTC driving cycle for a vehicle with 1800 kg mass. Energy required for traction and braking (absolute values are given for latter in Figure 3a) can be used to define the required battery size, while the maximum power values (Figure 3b) are used to plot Figure 2 by varying the vehicle mass. As can be seen from the Figure 3b, the maximum power over cycle corresponds to the extra-urban part (at time 1543 s) of the cycle. This power is higher than the maximum required power needed in urban part of the cycle by 30-50% (higher value corresponds to lower mass). The Figure 3c shows the vehicle speed profile on a complete

WLTP cycle. The maximum speed of the cycle is about 131 km.h⁻¹.

3.2 Internal combustion engine size

In the conventional vehicle, ICE is solely responsible for traction of the vehicle and therefore must ensure its proper performance. Figure 4 shows the dependence of the 0-100 km.h⁻¹ acceleration time on the specific power (maximum power to mass ratio) of the traction source. The data points of available HEVs, PHEVs and BEVs are depicted in Figure 4. The dashed line (CALC) represents values of the acceleration time as a function of specific power calculated using Equation (3). The line can be expressed as a power regression function with R-square close to 1. This equation does not take into account the power requirements of the auxiliaries, therefore it shows the upper bound of the performance at a given specific

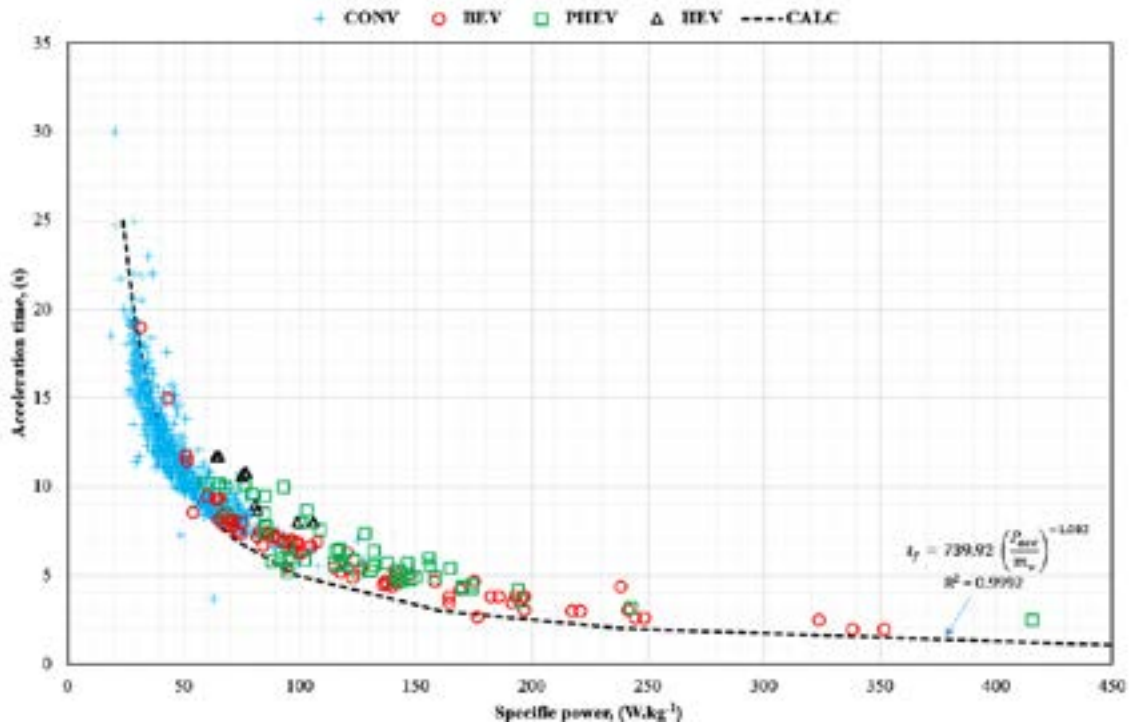


Figure 4 Acceleration time as a function of the traction source specific power for different vehicle types and models

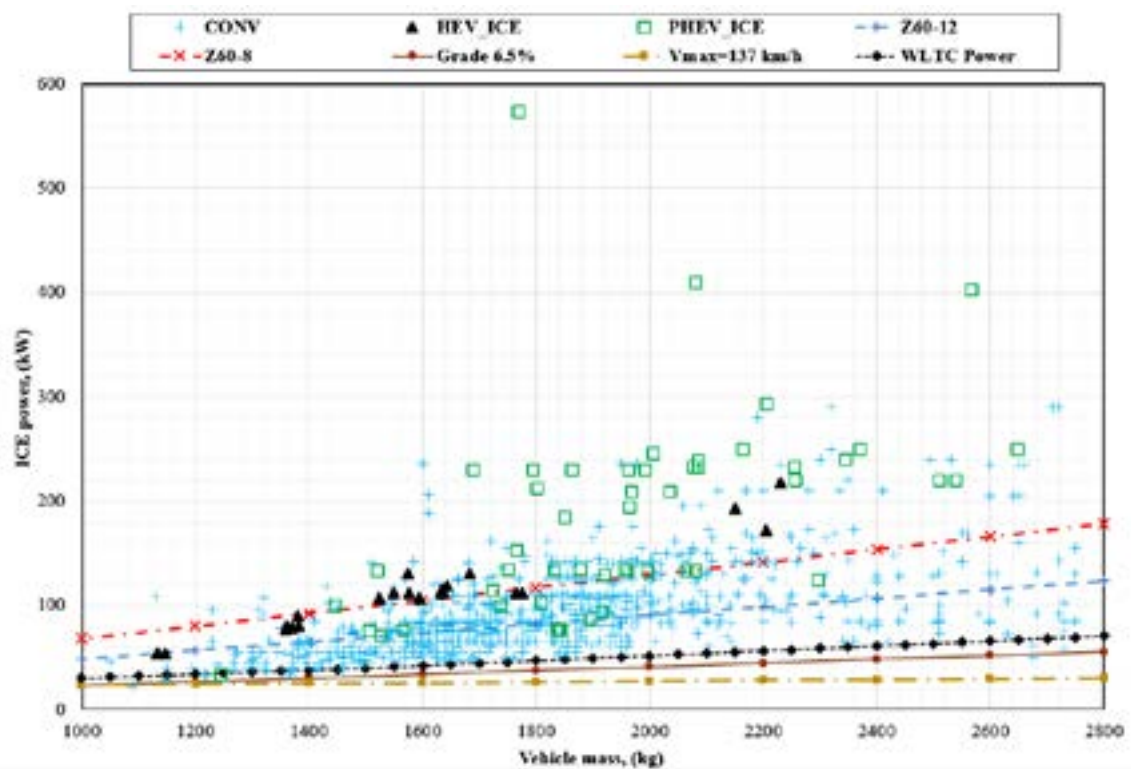


Figure 5 ICE power of Conventional vehicle, HEVs and PHEVs

power. It is evident that for the same specific power, the BEVs provide the highest acceleration performance. Furthermore, Figure 4 shows that the latter equation can be used with good confidence to estimate the power required to accelerate the vehicle.

Figure 5 shows the maximum ICE power points for various vehicle configurations (Conventional, HEV and

PHEV). The power required at the wheel level to fulfill various performance requirements discussed in Figure 2 are also superimposed.

Figure 5 evidences that the ICE maximum power in conventional vehicle is mainly chosen based on a minimum acceleration performance represented by line Z60-12. However, not all the conventional vehicles

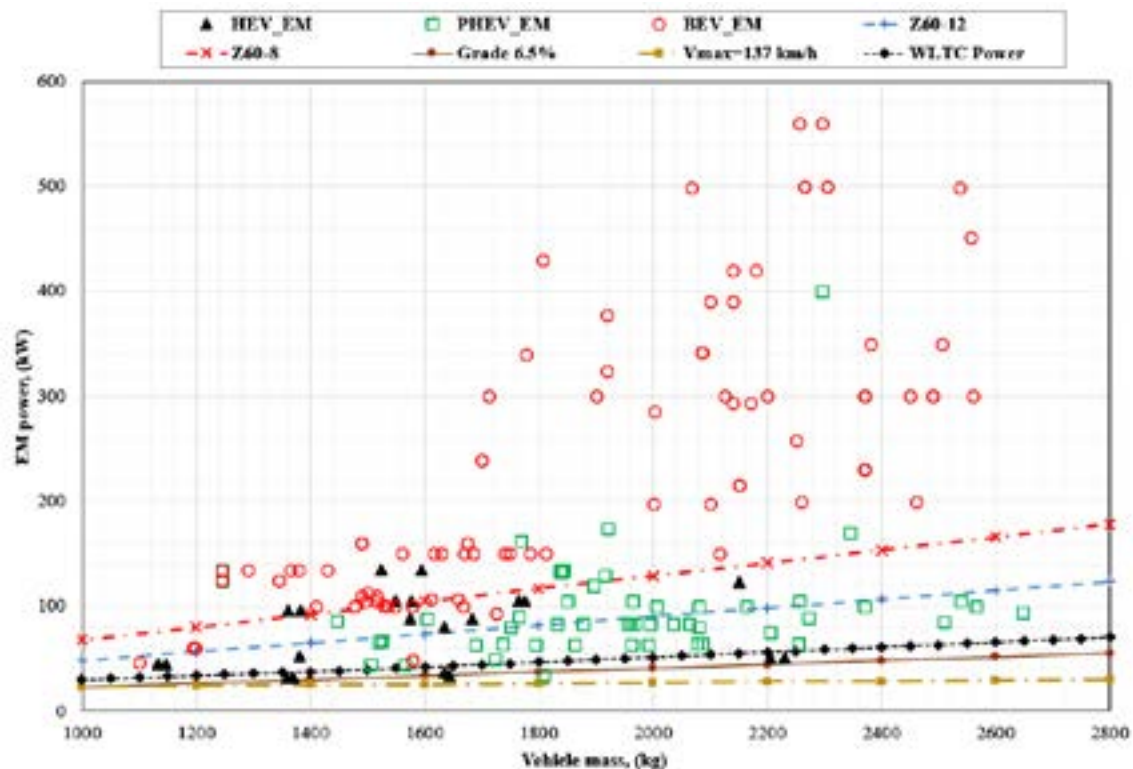


Figure 6. Electric motor peak power for the HEVs, PHEVs and BEVs

can fulfill this requirement. The ICE of the conventional vehicle is at least able to fulfill the maximum power requirement of mild driving cycles as NEDC, which is sufficient for moving in the traffic without causing any potential issues for other participants. This can be seen from the fact that the minimum power of the ICE for all the conventional vehicle models is higher than the power required to drive at 55 mph at 6.5% grade (Grade 6.5% line with circle marker).

For the majority of the analyzed HEV and PHEV models, the ICE alone is able to provide minimum acceleration performance. This could be useful in the case when the battery charge is near its lower limits and electric motor cannot provide an assist to the ICE. Furthermore, the higher power of the ICE for hybridized powertrain vehicles can be required to drive the vehicle while charging the battery when latter is depleted. The high power demanding cycle as WLTC can be performed without any limitations using only the ICE.

The ICE of hybrid vehicles can deal with higher power demands compared to the conventional counterparts. The fact highlights that even though downsizing an engine is listed as a potential benefit of the powertrain hybridization that appears rarely practiced in the hybridized vehicles available on the market.

3.3 Electric motor size

Figure 6 shows the peak power data points for the electric motor of HEVs, PHEVs and BEVs under

consideration. In the electric motors the peak power is usually used for a short time (around 10-60 s) to avoid thermal issues of mainly the batteries [25]. The electric motor continuous power is less than the peak power by around 30-40% [30]. As it was stated in previous section, the drive cycles have the high power demand in extra-urban when compared to urban portion (by 30-50% for the WLTC). This means that the peak and continuous powers can be used in the analysis for the extra-urban and the urban portions, respectively.

The HEVs (triangle marker) in Figure 6 have the electric motor size that is enough to accomplish the low power demand cycle as NEDC. Furthermore, the urban part of the WLTC can be performed only in the electric mode for a short period, as the thermal issues may arise due to continuous work at peak power.

The electric motor of the majority of the PHEVs (Figure 6, square marker) can accomplish at least the WLTC maximum power demand. That means the urban part of the WLTC can be certainly covered with the electric motor using it in the continuous operation mode. This highlights that the size of electric motors of the PHEVs allow the pure electric vehicle operation if limitation does not come from the batteries. However, not all the PHEV models can fulfill the minimum acceleration performance (line Z60-12) with an electric motor alone.

Obviously, for the BEVs the electric motor is the only traction source. Therefore, as Figure 6 shows, these vehicles with only electric motor are more performant than other vehicle types. The electric motors of the

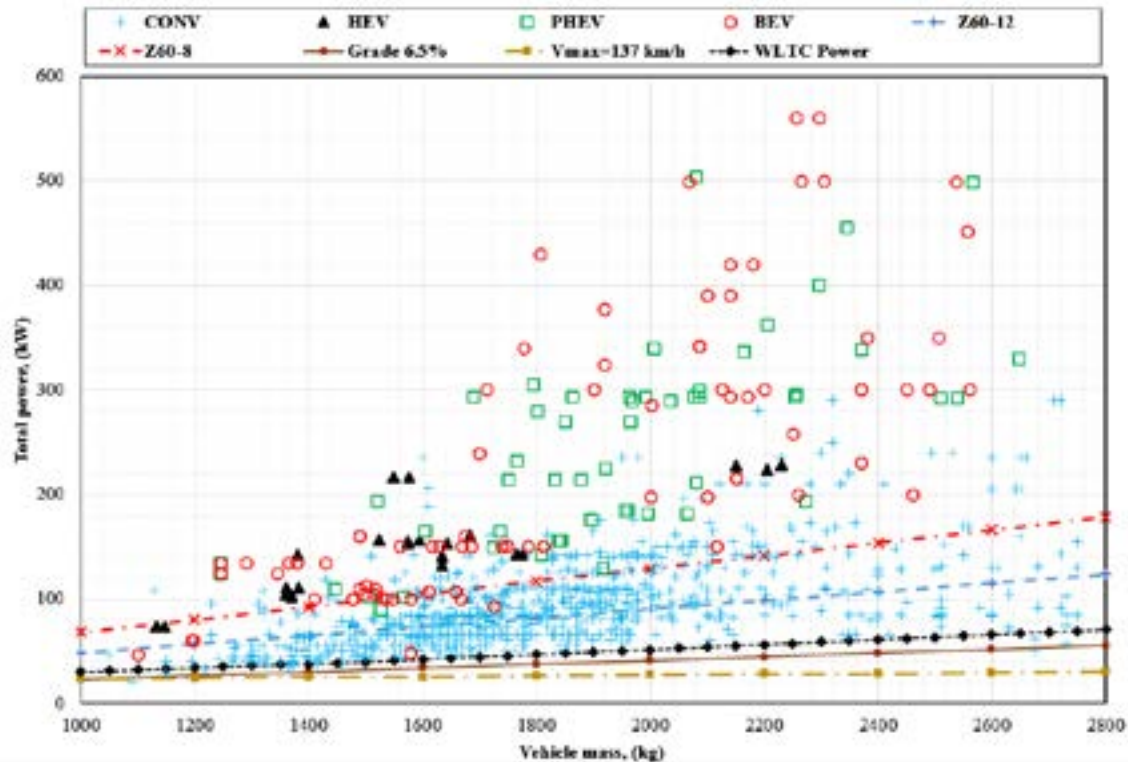


Figure 7 Combined maximum power for the Conventional vehicle, HEVs, PHEVs and BEVs

majority of BEVs on the market can at least provide Z60-12 acceleration performance or better. Figure 4 indicates the performance of the BEVs in terms of shorter acceleration time.

3.4 Total powertrain size

Figure 7 shows the combined (ICE+EM) total power for the Conventional vehicles, HEVs, PHEVs and BEVs. As it can be noticed, the power values for the Conventional vehicles and BEVs do not change, as they have one traction source. Instead, for the HEVs and PHEVs the combined power represents the sum of powers available traction sources and can affect substantially the vehicle performance.

The HEVs with total power can have Z60-12 acceleration performance, at minimum, for all the considered models, but mostly fulfills the Z60-8 or higher acceleration performance.

The PHEVs fulfills the aggressive acceleration performance with combined power of ICE and EM. The acceleration levels are equivalent to those of the BEVs. This fact is also evidenced in Figure 4. In addition, it can be noticed that PHEV powertrains are implemented on the vehicle class with curb mass more than 1400 kg.

3.5 Electric battery size

The battery capacity for all the considered vehicle configurations and the capacity of the battery required

to fulfill a certain pure electric driving range are shown in Figure 8. The energy balance at the end of the driving cycle (WLTC is used) is computed using the average efficiency values for transmission $\eta_{trans} = 0.95$, electric motor $\eta_{em} = 0.9$ and battery discharge $\eta_{bat} = 0.95$.

As it can be noticed, the battery capacity of the HEVs can allow the travel of around 10km, which corresponds to line “WLTC 10km” representing the energy equilibrium in that cycle. The line “Max C-rate” is derived using Equation (12). It shows that nearly all the vehicle categories have the battery size able to deliver the maximum required power on a WLTC cycle. However, the battery thermal limitation might limit the continuous electric traction.

The battery capacities of the PHEVs are able to provide 50km electric driving range on a WLTC. The corresponding line “WLTC 50km” is calculated using Equations (11) and (13).

As for the BEVs, the only source of traction is the battery, the size of which directly affects the vehicle total driving range. Therefore, the battery size in the BEVs is mainly derived from the desired driving range and obviously the costs of a vehicle. Models of the BEVs considered in the paper can mainly run more than 200km on a single charge on a WLTC representative cycle.

The share of the battery capacity used in various vehicle configurations is presented in Figure 9, where the ranges of the battery capacity have different step size. Between 0 and 5 kWh capacity the step size is equal to 1 kWh to better highlight the region for the

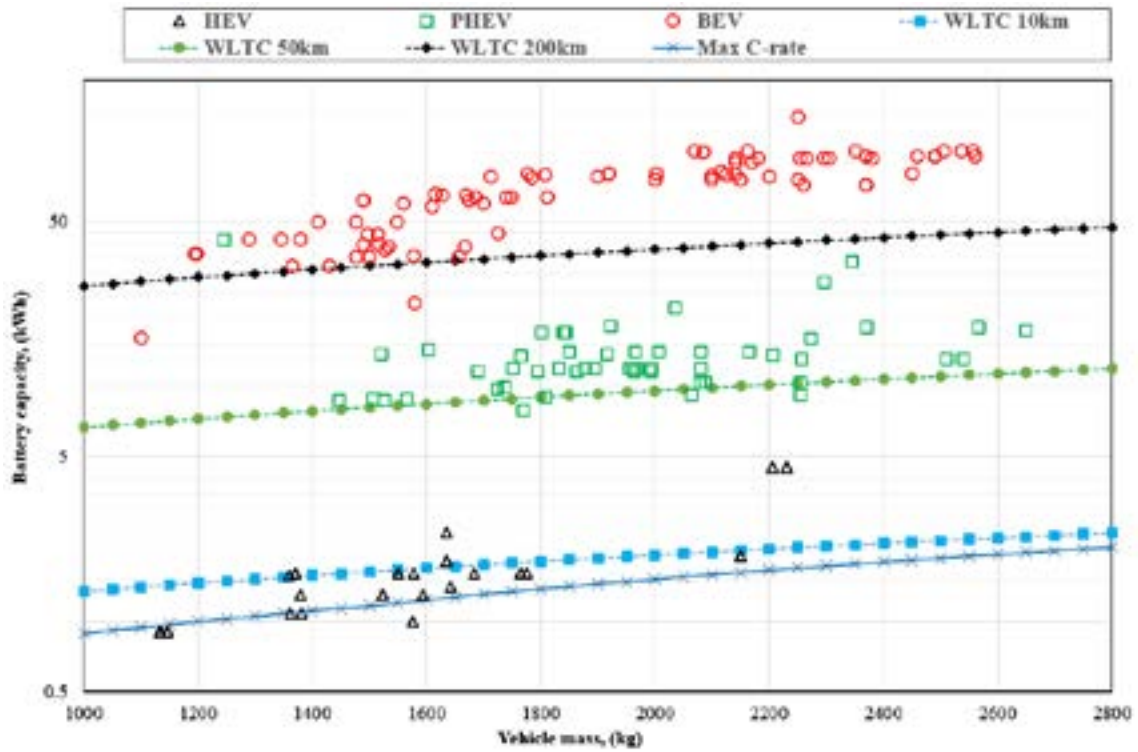


Figure 8 Battery capacity for the HEVs, PHEVs and BEVs

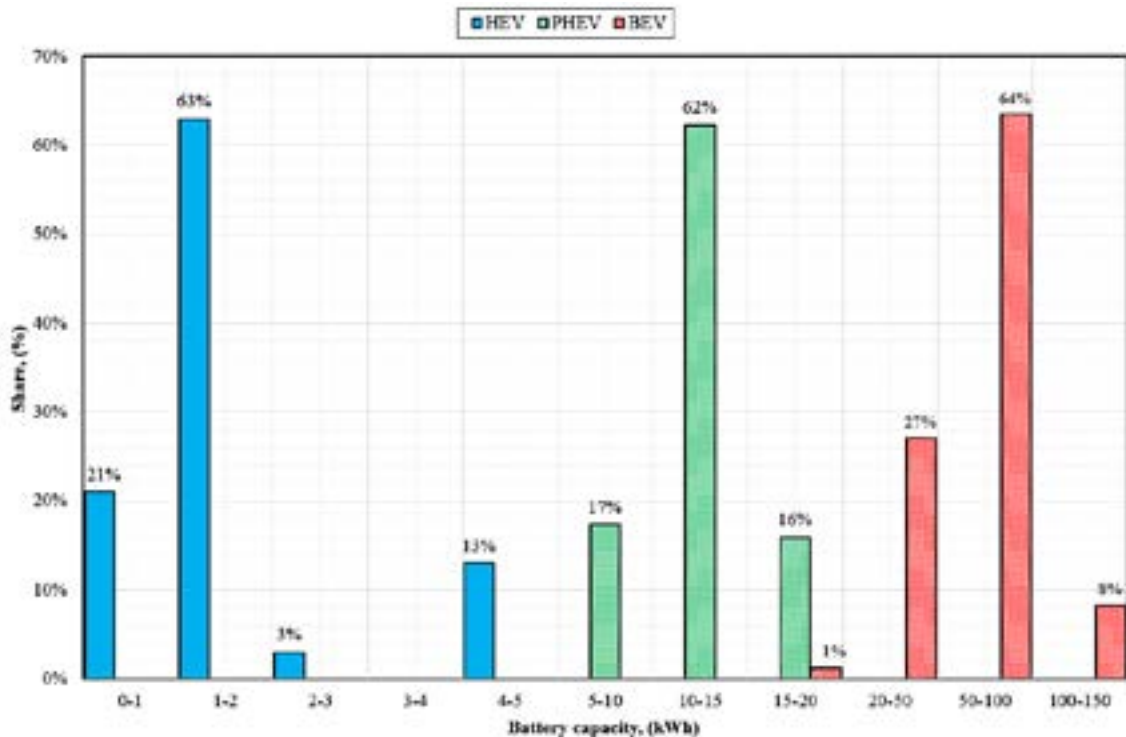


Figure 9 Battery capacity share for the HEVs, PHEVs and BEVs

HEV battery capacities. The range between 5 and 20 kWh represents mainly the PHEV configurations and the step size for this range is given as 5 kWh. For the range above 50 kWh capacity, the step size is also 50 kWh. It can be noticed that the majority of the HEVs in mass production (around 63%) have battery capacity in the range of 1-2 kWh. Referring to Figure 3, this capacity should be enough to regenerate completely the

braking energy over the WLTC cycle. As for the PHEVs the battery capacity is mainly derived from the electric drive range of around 50km, the majority (62%) of considered vehicle battery capacities are in the range of 10-15 kWh.

Around 64% of the BEVs' models have the battery capacity in the range of 50-100 kWh. It is almost 5 to 7 times of one installed on the PHEVs.

4 Discussion and conclusions

The paper provides insight into how the powertrain components of the mass production electrified vehicles are sized. Data of a wide range of mass produced electrified vehicles is collected and sorted. The main PNGV vehicle performance requirements are used to calculate the power values and to compare to the real vehicle data. The results show that the acceleration levels of the PHEVs are equivalent to those of the BEVs. Based on the calculated values of power requirements the minimum sizes of the powertrain components to satisfy such requirements are derived.

The results of this analysis showed that the ICE of hybrid vehicles could deal with higher power demands compared to the conventional counterparts. It emphasizes that the engine downsizing is rarely implemented in hybridized vehicles available on the market.

The electric motors used in the HEVs have a size that is sufficient to accomplish the low power demand cycle or urban part of more power demanding cycles like the WLTC.

The electric motor of the majority of the PHEVs under consideration can fulfill the maximum power demand on the WLTC, which comes from extra-urban part of the cycle. This indicates that the urban part of the WLTC can certainly be driven in pure electric mode if limitation does not come from the batteries.

It is important to note that the considered vehicles have powertrains with excessive power (when total power is considered) with respect to one required to accomplish the real driving requirements.

The battery capacity of the HEVs can allow the travel of about 10km. The battery capacities of the PHEVs are able to provide 50km electric driving range on a WLTC. The BEVs' models considered can drive more than 200km on a single charge. The HEVs in mass production (around 63%) have battery capacity in the range of 1-2 kWh, while the PHEVs mostly use the battery capacities in the range of 10-15 kWh. Around 64% of the BEVs' models have the battery capacity in the range of 50-100 kWh, i.e. almost 5 to 7 times of one installed on the PHEVs.

References

- [1] EU plotting ban on internal combustion engine as of 2025: industry - European Council for an Energy Efficient Economy [online] [accessed 2021-06-14]. 2021. Available from: <https://www.eceee.org/all-news/news/eu-plotting-ban-on-internal-combustion-engine-as-of-2025-industry/>
- [2] WAPPELHORST, S. The end of the road? An overview of combustion - engine car phase - out announcements across Europe - International Council on Clean Transportation [online] [accessed 2021-06-14]. 2020: Available from: <https://theicct.org/sites/default/files/publications/Combustion-engine-phase-out-briefing-may11.2020.pdf>
- [3] ONORI, S, LORENZO SERRAO, L., RIZZONI, G. *Hybrid electric vehicles: energy management strategies*. London: Springer, 2016. ISBN: 978-1-4471-6781-5.
- [4] Clean Vehicles Directive - European Commission, Mobility and Transport [online] [accessed 2021-06-14]. Available from: https://ec.europa.eu/transport/themes/urban/clean-vehicles-directive_en
- [5] SMOKERS, R. T., VERBEEK, M. M., OBDEIJN, C., HILL, N., NORRIS, J., VAN ESSEN, H., KAMPMAN, B., WRIGLEY, S., O'BRIEN, S., TROMPETELER, P. Consideration of alternative approaches to regulating CO2 emissions from light duty road vehicles for the period after 2020 [online] [accessed 2021-06-14]. 2013. Available from: https://ec.europa.eu/clima/sites/clima/files/transport/vehicles/docs/alternatives_en.pdf
- [6] EHSANI, M., GAO, Y., LONGO, S., EBRAHIMI, K. *Modern electric, hybrid electric, and fuel cell vehicles* [online]. 3. ed. Boca Raton: CRC Press, 2018. eISBN 9780429504884. Available from: <https://doi.org/10.1201/9780429504884>
- [7] RAHMEH, H., BONFITTO, A., RUZIMOV, S. Fuzzy logic vs equivalent consumption minimization strategy for energy management in P2 hybrid electric vehicles. In: International Design Engineering Technical Conferences and Computers and Information in Engineering Conference ASME 2020: proceedings. 2020. Available from: <https://doi.org/10.1115/DETC2020-22431>
- [8] eMobility is our future - MAGNA [online] [accessed 2021-05-15]. Available from: <http://electrification.magna.com/powertrain-electrification/>
- [9] CHEN, M. Y., YANG, K., SUN, Y. Z., CHENG, J. H. An energy management strategy for through-the-road type plug-in hybrid electric vehicles. *SAE International Journal of Alternative Powertrains* [online]. 2019, 8(1), p. 61-75. ISSN 2167-4191, eISSN 2167-4205. Available from: <https://doi.org/10.4271/08-08-01-0004>
- [10] RAHMAN, Z., BUTLER, K., EHSANI, M. A study of design issues on electrically peaking hybrid electric vehicle for diverse urban driving patterns. *SAE Technical Paper* [online]. 1999, 1999-01-1151. ISSN 0148-7191, eISSN 2688-3627. Available from: <https://doi.org/10.4271/1999-01-1151>
- [11] RAHMAN, Z., BUTLER, K., EHSANI, M. A comparison study between two parallel hybrid control concepts. *SAE Technical Paper* [online]. 2000, 2000-01-0994. ISSN 0148-7191, eISSN 2688-3627. Available from: <https://doi.org/10.4271/2000-01-0994>

- [12] SUNDSTROM, O., GUZZELLA, L., SOLTIC, P. Optimal hybridization in two parallel hybrid electric vehicles using dynamic programming. *IFAC Proceedings Volumes* [online]. 2008, **41**(2), p. 4642-4647. ISSN 1474-6670. Available from: <https://doi.org/10.3182/20080706-5-KR-1001.00781>
- [13] SUNDSTROM, O., GUZZELLA, L., SOLTIC, P. Torque-assist hybrid electric powertrain sizing: from optimal control towards a sizing law. *IEEE Transactions on Control Systems Technology* [online]. 2009, **18**(4), p. 837-849. ISSN 1063-6536, eISSN 1558-0865. Available from: <https://doi.org/10.1109/TCST.2009.2030173>
- [14] CARIGNANO, M. G., NIGRO, N. M., JUNCO, S. Hybridization effect on fuel consumption and optimal sizing of components for hybrid electric vehicles. In: *Integrated Modeling and Analysis in Applied Control and Automation IMAACA-I3M: proceedings*. 2015.
- [15] Optimized electromotive transmission solutions for various applications by FEV - FEV Group GmbH [online] [accessed 2021-06-15]. Available from: <http://magazine.fev.com/en/electronic-drive-unit/>
- [16] GAO, Y., EHSANI, M. Design and control methodology of plug-in hybrid electric vehicles. *IEEE Transactions on Industrial Electronics* [online]. 2009, **57**(2), p. 633-640. ISSN 0278-0046. Available from: <https://doi.org/10.1109/TIE.2009.2027918>
- [17] MURGOVSKI, N., JOHANNESSEN, L. M., EGARDT, B. Optimal battery dimensioning and control of a CVT PHEV powertrain. *IEEE Transactions on Vehicular Technology* [online]. 2013, **63**(5), p. 2151-2161. ISSN 0018-9545, eISSN 1939-9359. Available from: <https://doi.org/10.1109/TVT.2013.2290601>
- [18] SONG, Z., ZHANG, X., LI, J., HOFMANN, H., OUYANG, M., DU, J. Component sizing optimization of plug-in hybrid electric vehicles with the hybrid energy storage system. *Energy* [online]. 2018, **144**, p. 393-403. ISSN 0360-5442. Available from: <https://doi.org/10.1016/j.energy.2017.12.009>
- [19] JUNG, H. Fuel economy of plug-in hybrid electric and hybrid electric vehicles: effects of vehicle weight hybridization ratio and ambient temperature. *World Electric Vehicle Journal* [online]. 2020, **11**(2), 31. eISSN 2032-6653. Available from: <https://doi.org/10.3390/wevj11020031>
- [20] ZHANG, B., YANG, F., TENG, L., OUYANG, M., GUO, K., LI, W., DU, J. Comparative analysis of technical route and market development for light-duty PHEV in China and the US. *Energies* [online]. 2019, **12**(19), 3753. eISSN 1996-1073. Available from: <https://doi.org/10.3390/en12193753>
- [21] CHALK, S. G., PATIL, P. G., VENKATESWARAN, S. R. The new generation of vehicles: market opportunities for fuel cells. *Journal of Power Sources* [online]. 1996, **61**(1-2), p. 7-13. ISSN 0378-7753. Available from: [https://doi.org/10.1016/S0378-7753\(96\)02332-4](https://doi.org/10.1016/S0378-7753(96)02332-4)
- [22] PLOTKIN, S., SANTINI, D., VYAS, A., ANDERSON, J., WANG, M., BHARATHAN, D., HE, J. Hybrid electric vehicle technology assessment: methodology, analytical issues, and interim results - U.S. Department of Energy Office of Scientific and Technical Information [online]. 2002. Available from: <https://doi.org/10.2172/807353>
- [23] GENTA, G. *Motor vehicle dynamics: modeling and simulation*. Singapore: World Scientific, 1997. ISBN: 978-981-02-2911-5.
- [24] GUZZELLA, L., SCIARRETTA, S. *Vehicle propulsion systems: introduction to modeling and optimization*. Berlin: Springer-Verlag Berlin Heidelberg, 2007. ISBN 978-3-642-35913-2.
- [25] 48V lithium-ion battery - 8Ah - A123 Systems [online] [accessed 2021-06-16]. Available from: http://www.a123systems.com/wp-content/uploads/48V-Battery-Flier_2016.pdf
- [26] U.S. Department of Energy - Energy Efficiency and Renewable Energy [online] [accessed 2021-06-16]. Available from: <https://www.fueleconomy.gov/>
- [27] Fuel consumption guide, CO2 emissions and electricity consumption of new passenger car models in German market / Leitfaden uber den Kraftstoffverbrauch, die CO2-Emissionen und den Stromverbrauch aller neuen Personenkraftwagenmodelle, die in Deutschland zum erkauf angeboten werden (in German) [online] [accessed 2021-06-16]. Available from: <https://www.datgroup.com/leitfaden/LeitfadenCO2.pdf>
- [28] Availability of hybrid and plug-in electric vehicles - U.S. Department of Energy - Energy Efficiency and Renewable Energy [online] [accessed 2021-06-16]. Available from: https://afdc.energy.gov/vehicles/electric_availability.html
- [29] KANE, M. Compare electric cars: EV range, specs, pricing and more – INSIDEEVs [online] [accessed 2021-06-16]. Available from: <https://insideevs.com/reviews/344001/compare-evs/>
- [30] CAI, W. Comparison and review of electric machines for integrated starter alternator applications. In: *IEEE 39th IAS Annual Meeting Industry Applications Conference: proceedings* [online]. 2004. ISSN 0197-2618, ISBN 0-7803-8486-5. Available from: <https://doi.org/10.1109/IAS.2004.1348437>

List of abbreviations

Abbreviation	Meaning/phrase
BEV	Battery Electric Vehicle
CONV	Conventional Vehicle
EM	Electric Motor
FTP	Federal Test Procedure
HESS	Hybrid Energy Storage System
HEV	Hybrid Electric Vehicle
ICE	Internal Combustion Engine
NEDC	New European Driving Cycle
NiMH	Nickel Metal Hydride
PHEV	Plugin Hybrid Electric Vehicle
PNGV	Partnership for a New Generation of Vehicles
SOC	State of Charge
WLTC	The Worldwide harmonized Light vehicles Test Cycles
Z60-8	Time to accelerate to a specific speed (60 mph in 8 s)
Z60-12	Time to accelerate to a specific speed (60 mph in 12 s)

DEVELOPMENT OF A PROCEDURE FOR DETERMINING THE PRE-FAILURE CONDITION OF THE AXLE BOXES OF RAILWAY ROLLING STOCK

Igor Martynov¹, Juraj Gerlici², Alyona Trufanova¹, Vadim Petuhov¹, Vadim Shovkun¹, Kateryna Kravchenko^{2,*}

¹Ukrainian State University of Railway Transport, Kharkiv, Ukraine

²University of Zilina, Zilina, Slovakia

*E-mail of corresponding author: kateryna.kravchenko@fstroj.uniza.sk

Resume

It has been determined that the greatest risk of an error in determining the technical condition of the axle box unit in the so-called "zone of uncertainty" is in the impossibility of unambiguously assessing its technical condition. To solve this problem, a model is proposed in the form of an n-dimensional radius vector, which has a direction towards an increase in the probability of failure and a deterioration in its parameters' values. Such a model for determining the axle box unit's pre-failure condition will reduce the risk of errors in decision-making.

Article info

Received 26 May 2021

Accepted 8 June 2021

Online 16 November 2021

Keywords:

axle box unit,
control of technical condition,
built-in control,
ambiguity area,
pre-failure condition,
radius vector

Available online: <https://doi.org/10.26552/com.C.2022.1.B87-B93>

ISSN 1335-4205 (print version)

ISSN 2585-7878 (online version)

1 Introduction

One of the main requirements for the railway rolling stock is to ensure transportation of goods and passengers [1-4]. One of the elements that directly affect the safety of cars' movement are the axle boxes with rolling bearings [4]. Failure of the axle box during the train's movement along the haul requires an immediate stop of the train and uncoupling of the faulty car. Untimely detection of the axle box unit's malfunction can lead to a fracture of the wheelset axle neck and then to the derailment of the car and an accident.

Control of the technical condition of axle boxes of cars on the railways is carried out in two ways: by car inspectors visually and tactilely and using the remote thermal control devices.

The appearance on the railways of a new generation of rolling stock [5] with various types of bearing assemblies led to difficulties in monitoring axle boxes' technical conditions.

Control of existing remote (non-contact) devices often leads to false alarms, which account for about 13% of all the train stops associated with the axle boxes' heating. There is a tendency towards increasing the number of such false alarms due to the increased number of cars equipped with various types of axle box housings, bearings and grease. As a result, this can cause unreasonable delays in trains' movement,

disruptions to stability and rhythm of transportation, irrational expenditures of labor and material resources.

A qualitatively new development level of the axle box unit control system in operation has appeared by the built-in control means. Such control systems are used by leading manufacturers of bearing assemblies (SKF (Sweden), FAG (Germany), Timken (USA), etc.). The sensors' placement on the axle boxes is carried out promptly and officially and the technical condition is monitored. The data are obtained using wireless networks for making operational management decisions [6-9]. Similar studies are being conducted in Ukraine [10].

2 Analysis of recent research

The analysis of works devoted to studying, and axle box units' technical conditions shows that the problem of monitoring and diagnostics of the running gears of cars is very acute [11]. At the same time, a significant part of the problem is devoted to increasing the reliability of assessing the technical condition of the axle boxes [12-13]. Article [14] is devoted to studying the operating temperature regimes of axle boxes. Changes in design of the axle box units led to several questions. So, in the study [15], the testability of axle boxes of a new type is considered. Methods for early detection of malfunctions of axle boxes of cars are analyzed in the article [16].

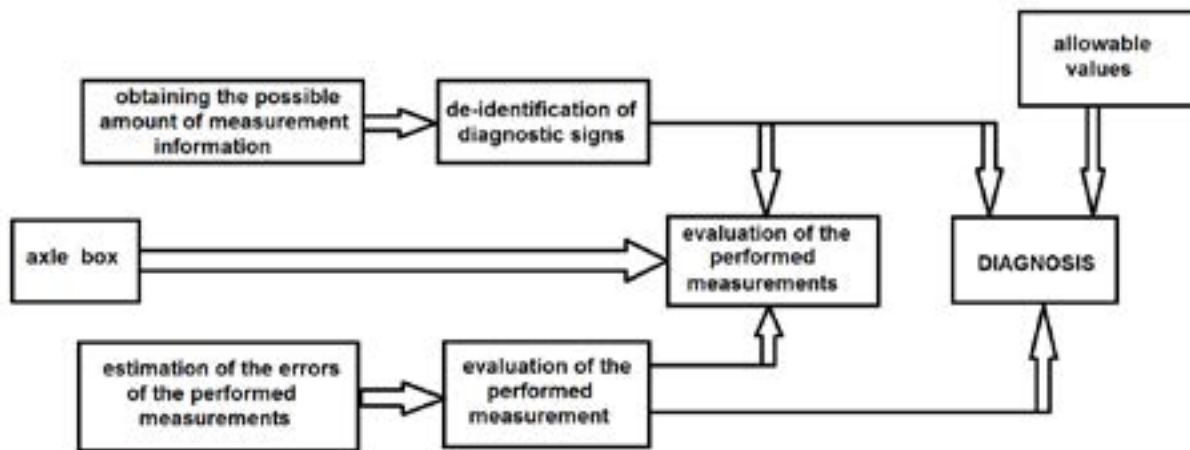


Figure 1 Diagram of the diagnostic procedure

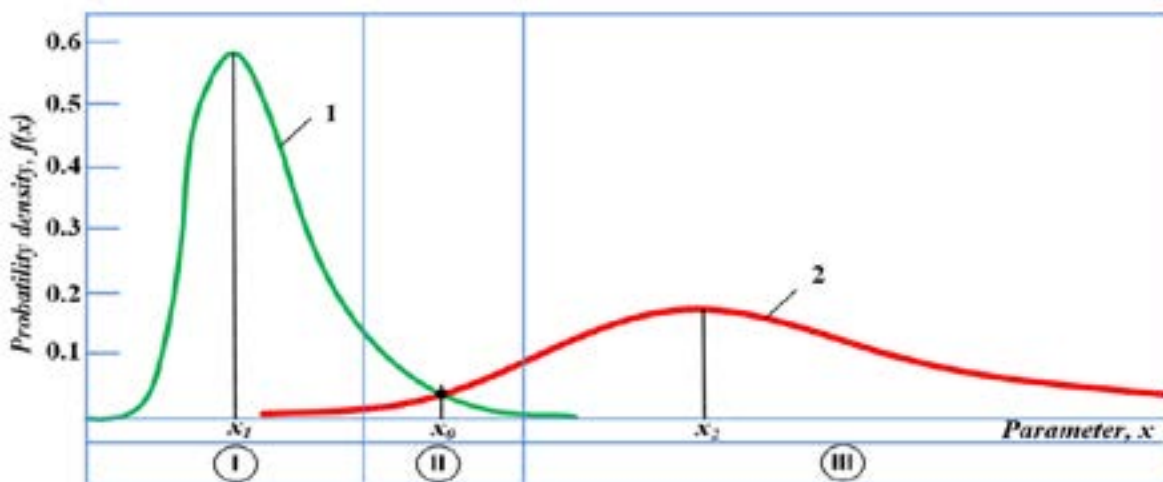


Figure 2 Graphic illustration of the “zone of uncertainty” when assessing the technical condition of the axle box unit

Obviously, the problem associated with the axle box unit failures’ timely detection while the train is moving remains extremely urgent. Out of the field of vision of scientists are definitions of such concepts as “pre-failure state of the axle box”, “the zone of the uncertainty of the technical state of the axle box”, as well as the construction of a diagnostic model of the axle box.

3 Material and methods

According to the current regulatory documents [17-18], the means of thermal control of the rolling stock give the operator three levels of alarm signals. The signal of the pre-emergency level “Alarm-0” does not require stopping the train. At the signal of the emergency level “Alarm-1,” the train must be stopped for inspection at the nearest station. At the critical level “Alarm-2,” an immediate stop and inspection of the specified car’s axle boxes are required. Moreover, these critical levels may be different, depending on the operating conditions on different routes.

However, the axle boxes’ technical condition (classification as serviceable or faulty) is always

associated with the risk of a false alarm or a failure to detect a failure [19].

The diagnostic procedure for axle boxes consists of assessing their technical condition. The result of the work is to obtain a conclusion about the location of the object in one of the possible technical conditions. To do this, the following needs to be done:

1. Get the possible amount of information on directly measured values,
2. Estimate the errors of experimental information,
3. Perform the identification of the diagnostic features of the object using the diagnostic model,
4. Estimate the obtained identification errors for a given set of permissible parameters.
5. To assess the information content for a given set of directly measured values,
6. Make a diagnosis about the controlled object’s technical condition at the time of this stage.

Figure 1 shows a schematic diagram of the diagnostic procedure.

In some cases, the diagnostic system is not able to unambiguously assess the technical condition of the axle boxes. In such cases, the diagnosis provides for such a concept as “zone of uncertainty”. The “zone

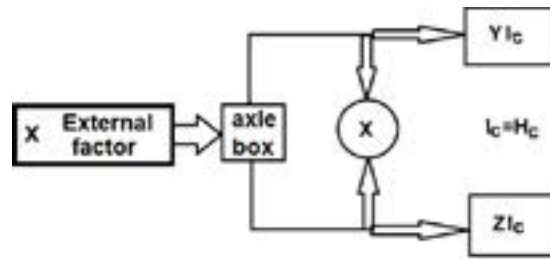


Figure 3 Diagnostic control method

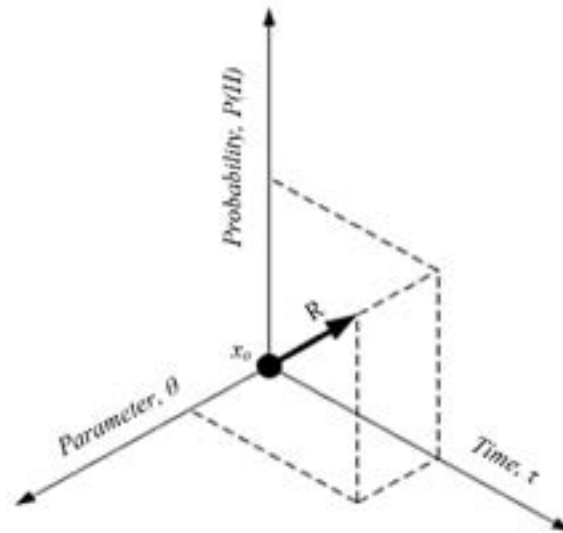


Figure 4 Radius vector of the technical condition of the axle box unit

of uncertainty” is clearly shown in Figure 2 - the distribution function of the probability density of the parameter: 1 - serviceable axle boxes; 2 - faulty axle boxes; I - zone of good condition; II - zone of uncertainty; III - fault zone.

This condition of the axle box occurs under the following conditions:

- $X_1 - I_c = 1$ - good condition,
- $X_0 - I_c = H_c$ - zone of uncertainty,
- $X_2 - H_c > I_c$ - faulty state,

where I_c - good condition, H_c - faulty condition.

The axle box’s technical condition for control systems can be described by the following diagram (Figure 3).

Among the many operational states of the axle box, a pre-failure state can be distinguished, leading to a limit state and then to a transition to an inoperative state. The destruction of the bearing of the axle box is irreversible and, with the further operation, inevitably leads to a fracture of the journal of the wheelset axle.

It is necessary to determine at what technical condition of the axle box unit its further operation would lead to failure, i.e., when the failure has not yet occurred. Still, the likelihood of its occurrence is high.

Suppose that the axle assembly is operable at some arbitrary moment in time, but one of the diagnostic signs tends to approach the limiting (dangerous) value. That is, further operation of the axle box unit will lead to its failure. This state of the axle box unit is classified as the pre-failure.

A condition for detecting the pre-failure state is a change in the axle boxes’ parameters (for example, heating temperature). The absence of an increase in the axle box units’ heating temperature indicates that the pre-failure state has not occurred. If the probability of being in a faulty state H_c is greater than the probability of I_c being in a good state, the tendency for the parameters to deteriorate remains.

To identify the pre-failure state of the axle box unit, the following conditions must be met:

$$\begin{aligned} X_1 &= [Y - YI_c] = 1, \\ X_0 &= [Y - (YI_c = H_c)] \neq 1, \\ X_2 &= [Y - (YI_c = H_c)] > ZI_c. \end{aligned} \tag{1}$$

The choice of methods and means of diagnostics, development of algorithms for finding a defect in the diagnostic object, presupposes a diagnostic model of the object. The diagnostic model is usually called a formal description of a given object, which characterizes it both in good working order and in a faulty state. The object description form can be any (analytical, tabular, vector, etc.).

To determine the axle box’s pre-failure state, a diagnostic model is proposed in the form of an n -dimensional radius vector of the technical state of the axle box, which has a direction towards an increase in the probability of failure and a deterioration in the values of diagnostic parameters.

Table 1 Temperature values of axle boxes on one side of the car

Axle box No.	Axle box temperature T [°C] at the moment of time τ [min]			
	τ_1	τ_2	τ_3	τ_4
2	15	17.2	20.8	23.9
4	15	17.4	23.9	29.9
6	15	17.1	22.5	23.2
8	15	17.3	21.4	23.2
T_{av}^*	15	17.2	21.57	23.43

For a more accurate determination of the pre-failure condition as a vector value, it is advisable to use the “dynamic” recognition signs that reflect changes in parameters over time. In a particular case, the model for determining a pre-failure state has the form of a three-dimensional radius vector, where the abscissa corresponds to the value of time τ , the ordinate is the diagnostic parameter - the temperature θ , the applicate is the probability that the axle unit is in a faulty state $P(H)$ (Figure 4). The value of the parameter at which $P(I)=P(H)$, is taken as the origin of coordinates, in Figure 4 that is the point x_0 .

To create an algorithm for detecting the axle box's pre-failure state, it is required to determine the diagnostic signs (recognition signs) that characterize the technical condition of the axle box. When diagnosing an object, the area of possible values of the measured parameter (diagnostic sign) is in most cases divided into intervals and the presence of the parameter value in this interval is characteristic. In this regard, the quantitative determination of the measured parameter can be considered as a sign that takes several possible states [20].

During the movement, numerous external factors act on the axle unit, located in a certain conditional space of external influences U , which can take on values ($U_1, U_2, \dots, U_i; i = 1 \dots \infty$). As a result of U_i impact, the axle box unit of the car will be in the technical state A_i from the space of possible technical states A ($A_1, A_2, \dots, A_i; i = 1 \dots \infty$). Moreover, each technical state A_i will correspond to a set of some diagnostic parameters S , which, in turn, will be characterized by a set of diagnostic features K . Feature K_j has m possible states: $k_{j1}, k_{j2}, \dots, k_{jm}$. If, as a result of diagnostics, it is revealed that for a given state of the axle box, the sign K_j has the value k_{jp} , this value is the implementation of the sign.

The diagnostic value of a feature is determined by the information entered by the feature into the system of states of the object being diagnosed. As the diagnostic weight of the implementation of the K_j feature for the state A_i of the object, take

$$D_{A_i}(k_{jL}) = \log_2 \frac{P(A_i/k_{jL})}{P(A_i)} = \log_2 \frac{P(k_{jL}/A_i)}{P(k_{jL})} \quad (2)$$

where:

$P(A_i/k_{jL})$ is the probability of determining the state A_i , provided that the sign K_j received the value k_{jL} ;

$P(A_i)$ - the prior probability of the diagnosis;

$P(k_{jL}/A_i)$ is the probability of the K_j feature hitting the L interval for an object with the A_i state;

$P(k_{jL})$ - the probability of this interval's appearance for all the investigated control objects with different technical conditions.

The generally accepted indicator for monitoring the technical condition of axle boxes is their heating temperature. Moreover, the most informative sign for detecting the overheated axle boxes is the reduced temperature of the axle boxes on one side of the car to the average temperature of the axle boxes on the same side of the car $\theta_i = T_i/T_{av}^*$, determined without the maximum temperature of one of the axle boxes [21].

4 Results

In 2015, operational tests of the built-in control system were carried out in Ukraine [8]. The purpose of the tests was to confirm the possibility of continuous monitoring of the axle boxes' technical condition by built-in means, as well as the wireless transmission of diagnostic information from the axle box to the ground modules of the control point when the train is moving.

An open-top car with axle boxes was used for the tests, having end fastening with an M110 nut. An onboard module was mounted in each axle box of the car on the end of the PY1 axle. The thermal sensor was fixed on the axle end face, which ensured the axle neck temperature control's maximum reliability.

The methodology program provided for the movement of an experimental gondola car at speeds of 20, 30, 40 km/h with the receipt of diagnostic information from the axle box and real data comparison.

The results obtained made it possible to simulate the heating level of the axle box units. Table 1 shows the axle boxes' temperatures on one side of the car, obtained from temperature measurements at the moments $\tau_1, \tau_2, \tau_3, \tau_4$.

The absolute temperature values of heating of all the axle boxes did not exceed the threshold values. Therefore, as mentioned earlier, to identify a faulty axle box unit, the sign “reduced temperature θ ” was used.

If the axle boxes are in good working order, then when the car is moving, the ratio between the axle boxes' heating temperatures will be constant. An increase in

Table 2 Sequence of differences in the reduced temperatures of the axle boxes

Axle box №	θ_1	θ_2	θ_3	θ_4	$\Delta\theta_{2,1}$	$\Delta\theta_{3,2}$	$\Delta\theta_{4,3}$
2	1.00	1.000	0.964	1.020	0.00	-0.036	0.055
4	1.00	1.012	1.108	1.276	0.012	0.097	0.168
6	1.00	0.994	1.043	0.990	-0.006	0.049	-0.053
8	1.00	1.006	0.992	0.990	0.006	-0.014	0.002
	3σ				0.014	0.108	0.133

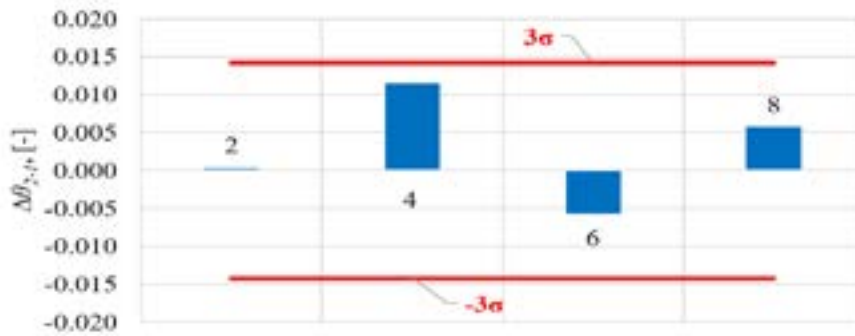


Figure 5 Sequence of differences in the reduced values of the temperatures of the axle boxes $\Delta\theta_{2,1}$

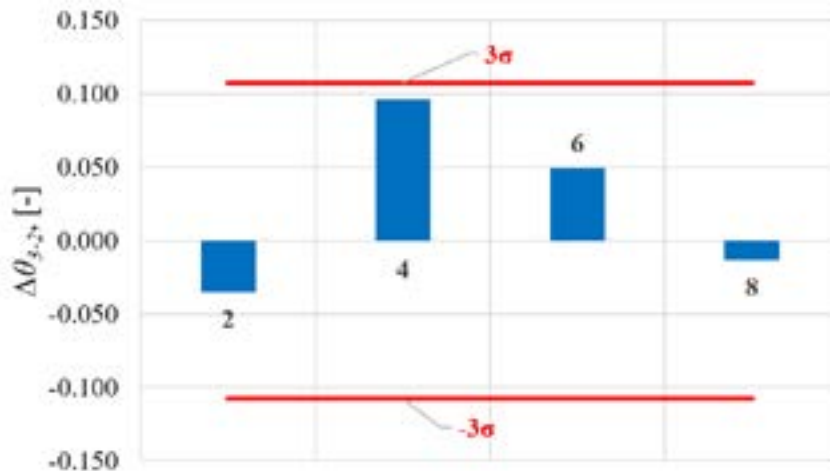


Figure 6 Sequence of differences in the reduced values of the temperatures of the axle boxes $\Delta\theta_{3,2}$

one of the axle boxes' reduced temperatures indicates development of an axle box defect.

Table 2 shows the sequence of differences in the reduced values of the temperatures of the axle boxes $\Delta\theta_i = \theta_{i,j+1} - \theta_{i,j}$ at times $\tau_1, \tau_2, \tau_3, \tau_4$.

To detect a pre-failure axle box, a threshold of significance of the reduced temperature increment is set, the excess of which indicates a malfunction. Assuming the normal distribution of increments as the threshold of significance, the boundaries of the confidence interval of values corresponding to a probability of 0.997 (the "3σ" rule) were taken.

$$3\sigma = 3 \cdot \left(\sqrt{\frac{\sum_{i=1}^n (\theta_{i,j+1} - \theta_{i,j})^2}{n-1}} \right). \quad (3)$$

These boundaries of the increment component equal to $\pm 3\sigma$ are calculated according to Equation (3). The results are listed in Table 2 and shown in Figures 5-7 by solid lines.

In addition, Figures 5-7 show the sequence of differences in the reduced values of the axle boxes' temperatures at the moments of time τ_2, τ_3, τ_4 .

As shown in Figures 5-7, the temperature increment of the 4th axle box in the direction of travel tends to increase the difference in the reduced temperature compared to other axle boxes. It then goes beyond the confidence interval at time τ_4 , which indicates its pre-failure state.

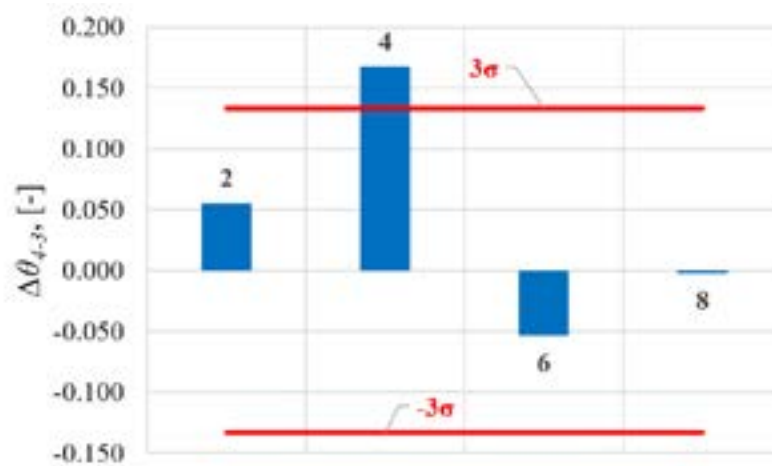


Figure 7 Sequence of differences in the reduced values of the temperatures of the axle boxes $\Delta\theta_{4,3}$

5 Conclusions

The task of modern diagnostic systems is early detection of faults and prevention of operation of the rolling stock with developing defects of critical units. Moreover, only the identification of the emergency axle box during the movement of the train no longer meets modern requirements.

The technical policy pursued by various railway administrations is aimed at the development and operation of the modern rolling stock with increased reliability. In operation, it leads to appearance of a variety of undercarriage designs with different types of bearings and grease. Therefore, it is not possible to unify the control algorithms, threshold values and accident rate criteria with existing thermal control systems for all the rolling stock units. Thus, the problem of control of axle boxes is already becoming urgent, which leading manufacturers solve, in particular, with help of the built-in control facilities, modernization of methods and algorithms for detecting faults. The greatest risk of an error in determining the technical condition of the axle box unit arises in the so-called “zone of uncertainty”

due to the impossibility of unambiguously assessing its technical condition.

The built-in condition monitoring the technical condition of the axle boxes at this stage makes it possible to record not only the temperature, but also other parameters characterizing the condition of the axle box unit and the wheelset. In addition, taking into account the centralization of rolling stock control systems, the presence of powerful data processing centers and high-speed computer networks, it is possible to create an expert system to analyze the technical state of the unit and predict its resource.

However, the theoretical basis of such a control method is still under development and requires further work on its creation and development.

A procedure for detecting the pre-failure axle box unit, when its actual controlled parameters did not go beyond the permissible values, is proposed. The developed model for determining the pre-failure state and the procedure for identifying the pre-failure axle box unit would help to reduce the likelihood of making erroneous decisions about the train movement mode.

References

- [1] DIZO, J., BLATNICKY, M., STEISUNAS, S., SKOCILASOVA, B. Assessment of a rail vehicle running with the damaged wheel on a ride comfort for passengers. *MATEC Web of Conferences* [online]. 2018, **157**, 03004. ISSN 2261-236X. Available from: <https://doi.org/10.1051/mateconf/201815703004>
- [2] DIZO, J., HARUSINEC, J., BLATNICKY, M. Computation of modal properties of two types of freight wagon bogie frames using the finite element method. *Manufacturing Technology* [online]. 2018, **18**(2), p. 208-214. ISSN 1213-2489. Available from: <https://doi.org/10.21062/ujep/79.2018/a/1213-2489/MT/18/2/208>
- [3] DIZO, J., BLATNICKY, M., HARUSINEC, J., FALENDYSH, A. Modification and analyses of structural properties of a goods wagon bogie frame. *Diagnostyka* [online]. 2019, **20**(1), p. 41-48. ISSN 1641-6414. Available from: <https://doi.org/10.29354/diag/99853>
- [4] STASTNIAK, P., KOHAR, R., SMETANKA, L. Dynamic analysis of force interactions in rolling bearings components. *AIP Conference Proceedings* [online]. 2019, **2198**, 020018. ISSN 0094-243X. Available from: <https://doi.org/10.1063/1.5140879>

- [5] MARTINOV, I. E. The results of temperature tests of the research axle boxes of freight wagon. *Eastern-European Journal of Enterprise Technologies*. 2004, **7**(1), p. 66-69. ISSN 1729-3774.
- [6] HODGE, V. J., O'KEEFE, S., WEEKS, M., MOULDS, A. Wireless sensor networks for condition monitoring in the railway industry: a survey. *IEEE Transactions on Intelligent Transportation Systems* [online]. 2015, **16**(3/06), p. 1088-1106. ISSN 1524-9050. Available from: <https://doi.org/10.1109/TITS.2014.2366512>
- [7] NAN, W., QINGFENG, M., BIN, Z., TONG, L., QINGHAI, M. Research on linear wireless sensor networks used for online monitoring of rolling bearing in freight train. *Journal of Physics: Conference Series* [online]. 2011, **305**(1), 012024. ISSN 1742-6588. Available from: <https://doi.org/10.1088/1742-6596/305/1/012024>
- [8] SCHOBEL, A., KARNER, J. Optimization potential in the positioning of hotbox detectors (in German). *ETR. Eisenbahntechnische Rundschau*. 2005, **12**, p. 805-808. ISSN 0013-2845
- [9] REASON, J. M., CHEN, H., CREPALDI, R., DURÌ, S. Intelligent telemetry for freight trains. *Lecture Notes of the Institute for Computer Sciences, Social-Informatics and Telecommunications Engineering* [online]. 2010, **35**, p. 72-91. ISSN 1867-8211. Available from: https://doi.org/10.1007/978-3-642-12607-9_6
- [10] MARTYNOV, I. E., PETUHOV, V. M. Full-scale testing of axle box troubleshooting station (in Russian). *World of Transport and Transportation*. 2013, **2**, p. 180-182. ISSN 1992-3252.
- [11] DIZO, J., BLATNICKY, M. Use of multibody system dynamics as a tool for rail vehicle behaviour diagnostics. *Diagnostyka*. 2016, **17**(2), p. 9-16. ISSN 1641-6414.
- [12] AI, S., WANG, W., WANG, Y., ZHAO, Z. Temperature rise of double-row tapered roller bearings analyzed with the thermal network method. *Tribology International* [online]. 2015, **87**, p. 11-22. ISSN 0301-679X. Available from: <https://doi.org/10.1016/j.triboint.2015.02.011>
- [13] TRESTMAN, E. E., LOZINSKIJ, S. N., OBRAZCOV, V. L. *Automation of axle boxes control in trains* (in Russian). Moscow: Transport, 1983.
- [14] YAN, K., WANG, N., ZHAI, Q., ZHU, Y., ZHANG, J., NIU, Q. Theoretical and experimental investigation on the thermal characteristics of double-row tapered roller bearings of high speed locomotive. *International Journal of Heat and Mass Transfer* [online]. 2015, **84**(May 2015), p. 1119-1130. ISSN 0017-9310. Available from: <https://doi.org/10.1016/j.ijheatmasstransfer.2014.11.057>
- [15] MIRONOV, A. A., OBRAZTSOV, V. L., PAVLYUKOV, A. E., Traceability of rolling stock for thermal contactless diagnostics (in Russian). *Journal Automation, Communication, Informatics*. 2006, **11**, p. 54-57. ISSN 0005-2329.
- [16] PANKRATOV, L. V., CHISTYAKOV S. N. Monitoring of axle boxes heating (in Russian). *Journal Automation, Communication, Informatics*. 2008, **6**, p. 23-24. ISSN 0005-2329.
- [17] Instructions for the placement, installation and operation of automatic monitoring means of the technical condition of rolling stock during train movement (in Ukrainian) - TsV-TsSh-0053. Normative document of the State Administrative Administration of Railway Transport of Ukraine. Kyiv: Ukrzaliznytsya, 2003.
- [18] Basic subsystem ASDK-B of automatic diagnostic control system ASDK (Automated dispatch control systems). Service technology (in Ukrainian). - TsSh-0037. Normative document of the State Administrative Administration of Railway Transport of Ukraine. Kyiv: Ukrzaliznytsya, 2005.
- [19] BIRGER, I. A. *Technical diagnostics* (in Russian). 2 ed. URSS, 2019. ISBN 978-5-9710-6012-3.
- [20] ALEKSEEVA, T. V., BABANSKAYA V. D., BASHTA T. M., ZAGREBELSKIJ, V. I., ZAJONCHKOVSKIJ, G. I., KOLOSOV S. V. *Technical diagnostics of hydraulic drives* (in Russian). Moskow: Mashinostroenie, 1989. ISBN 5-217-00489-4.
- [21] PETUHOV, V. M. Analysis of temperature signs of identifying faulty axle boxes. *Collection of Science Works of UkrDAZT*. 2009, **107**, p. 128-132. ISSN 1994-7852.

VERIFICATION OF THE THERMAL EXPANSION EFFECT OF SILICONE MOLDS INTENDED FOR PRODUCTION OF THE PROTOTYPE COMPONENTS USING VACUUM CASTING TECHNOLOGY

Peter Spišák^{1,*}, Róbert Sásik¹, Ján Steininger¹, Jozef Jenis²

¹Institute of Competitiveness and Innovations, University of Zilina, Zilina, Slovak Republic

²Department of Design and Mechanical Elements, Faculty of Mechanical Engineering, University of Zilina, Zilina, Slovak Republic

*E-mail of corresponding author: peter.spisak@fstroj.uniza.sk

Resume

The article deals with vacuum casting technology and especially with the assessment of the influence of the tempering temperature of silicone molds on the dimensions of future castings. The aim was to evaluate the actual size of the castings, using different tempering temperatures of the molds and different casting materials. After examining the resulting dimensions of the individual castings, a procedure was established by which these effects could be minimized. In the end, a test of the proposed procedure is performed, which confirmed its correctness.

Article info

Received 14 June 2021

Accepted 12 September 2021

Online 23 November 2021

Keywords:

tempering,
vacuum casting,
thermal expansion,
silicone mold

Available online: <https://doi.org/10.26552/com.C.2022.1.B94-B98>

ISSN 1335-4205 (print version)

ISSN 2585-7878 (online version)

1 Introduction

The high demand for the new products at the market forces manufacturers to constantly improve and accelerate their production process. Everyone tries to shorten the time from product development to its launch, as much as possible. Rapid response to changes in demand is one of the most important factors of competitiveness. With this in mind, companies try to involve as many modern technologies as possible in the process prototypes development, including use of simulations and analyses [1-3].

They compete who will develop the best and cheapest product in the shortest time possible. One of the technologies that can significantly reduce the time required for the product development and production is the Rapid Prototyping technology. Its development dates back to 1986 and its practical use was the most widespread after 1996 in the automotive industry and now in development of electric cars, as well, [4-6].

This method utilises the latest knowledge about materials and laser technologies and is able to produce even very complex models in a short period of time. The basis is a process, in which the model is created by gradually adding materials to a computer-controlled machine.

The Vacuum Casting technology is one of the frequently used technologies in component development. The essence of the technology lies in the casting of various types of material (rubber, plastic, wax) in a vacuum into the most common silicone moulds. This technology is the most efficient in small verification batches of 10-20 pieces, being far more advantageous either in terms of the time required for production or financially compared to conventional methods of production [7].

2 Vacuum casting

The method of vacuum casting into silicone moulds is used for production of functional plastic prototypes or wax meltable models. Models used on the 3D printers or 3D production systems are mainly used as master models.

The main advantages of vacuum casting into a silicone mould include the ability to cast very complex models, thin-walled models, models with a negative bevel, high-precision copying of the master model surface, as well as the low cost of the prototype, compared to the plastic injection. Vacuum casting is one of the Rapid Prototyping technologies, which allows to quickly obtain a functional prototype and thus speed up



Figure 1 Vacuum chamber MK Technology System 1



Figure 2 Master model - Glass cylinder

the new product development process. Vacuum casting can also be used to produce the wax models for melt casting [8].

The production of the mould and consequently the components themselves is very fast. For simple shaped parts it is possible to have the first copy made after 5-6 hours, which is much faster than with production in a conventional way (aluminium moulds, injection moulding machine). Vacuum chamber that was used to make the molds and castings is shown in Figure 1.

Materials intended for vacuum casting are the most often two-component polyurethanes with different properties, which allows to achieve properties similar to rubber, polypropylene, ABS plastic, or polycarbonate. If one uses the plastics with good sliding properties, it is also possible to produce complicated components of small dimensions, such as gears [7, 9].

The casting production process can be divided into two main groups:

Production of mould, which includes the following operations:

- preparation of the master model,
- preparation for mould production,
- mould production,
- demoulding of the master model,
- preparation of the mould for the casting process.

Casting production:

- preparation of material for casting,
- vacuuming and casting,
- tempering,

- removing the casting from the mould,
- finalisation of the casting.

3 Verification of the thermal expansion effect of silicone moulds

From the practical experience with the VC technology, it was observed that there is a certain dimensional instability, especially with larger castings, such as bearing cages or gear prototypes [10-11]. This is due to the thermal expansion of the silicone during the tempering in the furnace (oven/kiln).

SP ICON A40 Protoform silicone was used to make the mold. Its main features are:

- high chemical resistance to plasticizers and aggressive components of some resins,
- high tensile strength, tear resistance, abrasion resistance: guarantees long mold life,
- high accuracy in reproducing small details,
- high dimensional and shape stability,
- high temperature resistance,
- excellent self-separating effect.

The expansion confirmed by the manufacturer at 70 °C is 0.7%.

To verify the thermal expansion, a glass cylinder with a diameter of 13mm and a length of 300.05mm was used as the master model. Master model is shown in Figure 2.

Then, a silicone mould was produced, into which

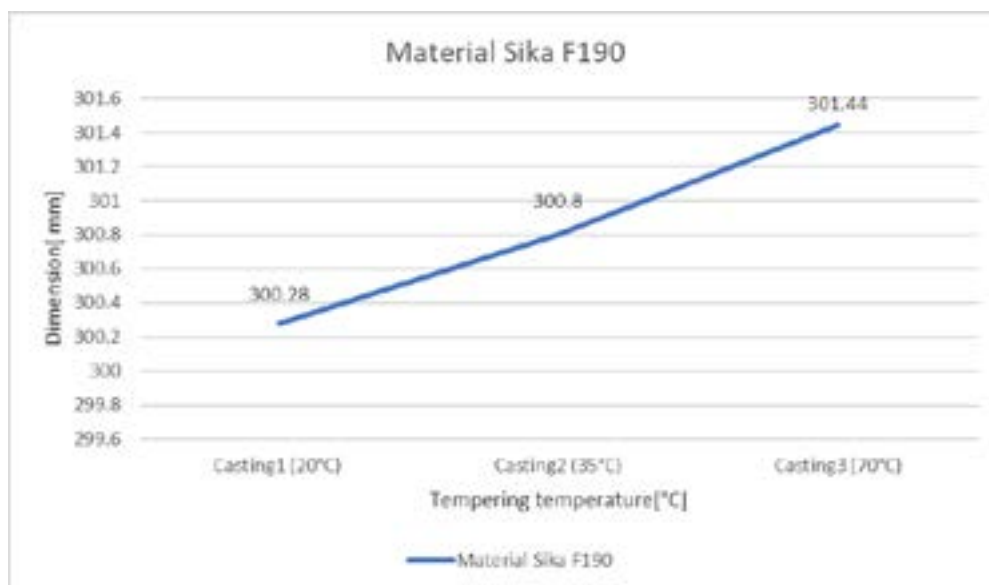


Figure 3 Dependence of thermal expansion on tempering temperature 1

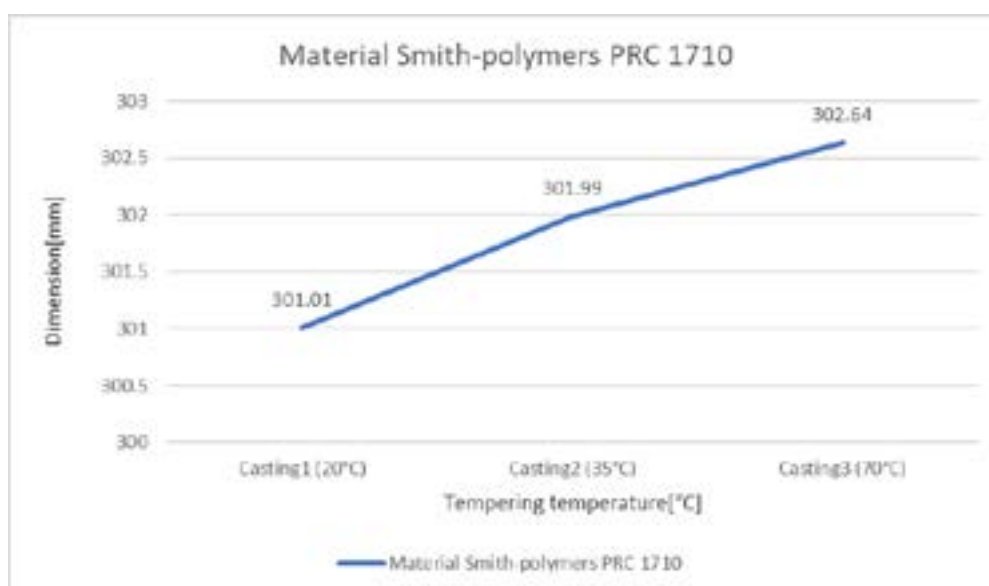


Figure 4 Dependence of thermal expansion on tempering temperature 2

several types of casting materials were then cast at different temperatures. As the number of castings increases, the silicone mold degrades, resulting in deterioration of the surface quality and roughness of the casting. Therefore, it is necessary to produce a new mold after about ten castings. This degradation depends on the following factors: shape and surface quality of the master model, type of casting material used, type of silicone catalyst used, frequency of use of the mold, tempering temperature, [12-13].

- The first casting of each material was cast in a mould tempered to 20 °C.
- A second casting of each material was cast into a mould tempered at 35 °C.
- A third casting of each material was cast in a mould tempered to 70 °C.

4 Material 1 - Sika F190

The advantage of this material is low viscosity, ease of use, it is especially suitable for larger castings. The final colour of the casting is beige. Dependence of thermal expansion on tempering temperature for material F190 is shown in Figure 3 [14].

5 Material 2 - Smith - polymers PRC1710

It is a transparent UV stable material which is mainly used in the automotive industry. Its advantages are the high mechanical properties, UV resistance, high transparency. Dependence of thermal expansion on tempering temperature for material PRC1710 is shown in Figure 4 [15].

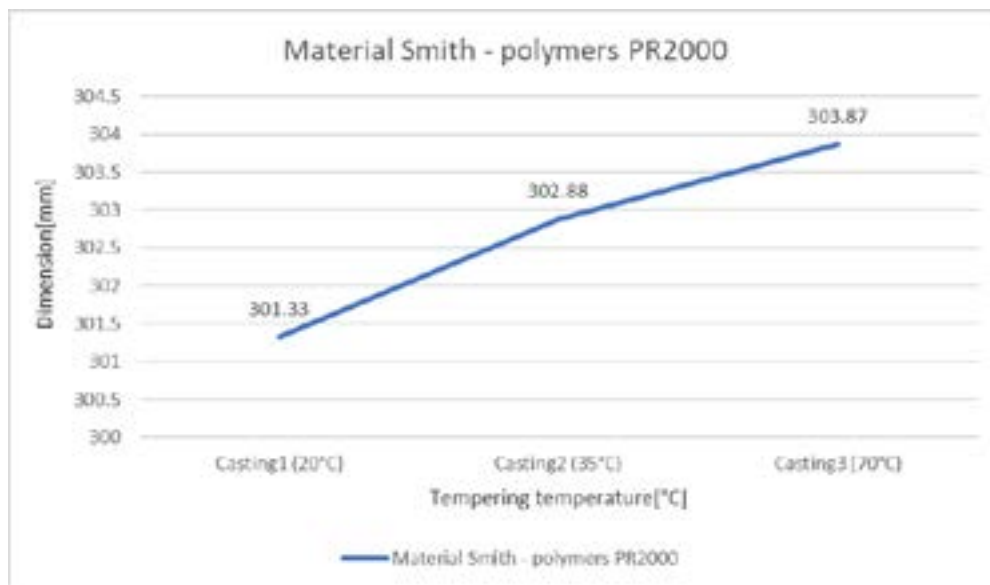


Figure 5 Dependence of thermal expansion on tempering temperature 3

Table 1 Summary of Moulds thermal expansion results

Material	F190	PRC1710	PR2000
Master model [mm]	300.05	300.05	300.05
Casting 1 [mm]	300.28	301.01	301.33
Casting 2 [mm]	300.8	301.99	302.88
Casting 3 [mm]	301.44	302.64	303.87



Figure 6 Silicone mould with casting from the PRC1710 material

6 Material 3 - Smith - polymers PR2000

The advantage of this material is low viscosity, short demoulding time, high toughness. The resulting colour is white. It is not UV stable. Dependence of thermal expansion on tempering temperature for material PR2000 is shown in Figure 5 [15].

Summary of Moulds thermal expansion results is shown in Table 1.

To verify the correctness of the previous findings, the PR2000 material and the tempering temperature of 70 °C were chosen, where the length increase was the largest. The original master model had a size of 300.05 mm, the casting had a size of 303.87 mm, which is an increase of 1.27%. Thus, if one wants the resulting casting to have a size of 300.00 mm, one should adjust the master model to 296.19 mm. After

modifying the master model to the size of 296.19 mm, a new silicone mould was produced. Subsequently, the mould warmed up to 70 °C and the mould cavity was filled with PR2000. After the time specified by the manufacturer for tempering the material, the casting was removed and we checked its size. It was 300.03 mm, which confirmed the correctness of the master model modification to minimize the effect of thermal expansion of the silicone mould. Silicone mould and casting from the PRC1710 material is shown in Figure 6.

7 Conclusion

The result shows that the thermal expansion of silicone moulds is affected not only by the tempering

itself, but by the type of casting material used, as well. Due to the fact that the used material was two-component polyurethane resins, when mixed it caused a chemical reaction, which generates additional heat and thus further impacts the extensibility of the mould.

Therefore, when designing the master model, it is necessary to take into account the material from which

will the casting be produced and adjust the dimensions accordingly, if possible. (3D printing, milling ...).

Acknowledgment

This work was supported by Grant System of University of Zilina No. 1/2020 (8085).

References

- [1] TOMASIKOVA, M., TROPP, M., GAJDOSIK, T., KRZYWONOS, L., BRUMERCIK, F. Analysis of transport mechatronic system properties. *Procedia Engineering* [online]. 2017, 192, p. 881-886. ISSN 1877-7058. Available from: <https://doi.org/10.1016/j.proeng.2017.06.152>
- [2] BRUMERCIK, F., BASTOVANSKY, R., LUKAC, M., GLOWACZ, A. Molybdenum strip test experiments and simulations at various temperatures to determine friction coefficients. *Measurement* [online]. 2021, **172**, 108859. ISSN 0263-2241. Available from: <https://doi.org/10.1016/j.measurement.2020.108859>
- [3] CACO M., KOHAR R., HRCEK S., TRIBULA R., SCERBA P. Use the method of TRIZ in optimizing automated machine for ultrasonic welding. *Procedia Engineering* [online]. 2017, **192**, p. 80-85. ISSN 1877-7058. Available from: <https://doi.org/10.1016/j.proeng.2017.06.014>
- [4] BISTAK, M.; BRUMERCIK, F.; LUKAC, M. Weighing systems in traffic. *Scientific journal of Silesian University of Technology - Series Transport* [online]. 2017, **97**, p. 5 -15. Published: 2017. ISSN 0209-3324, eISSN 2450-1549. Available from: <https://doi.org/10.20858/sjsutst.2017.97.1>
- [5] BISTAK, M., MEDVECKY, S., HRCEK, S. The above-ground weighbridge. *Procedia Engineering* [online]. 2017, **192**, p. 52-57. ISSN 1877-7058. Available from: <https://doi.org/10.1016/j.proeng.2017.06.009>
- [6] MITKA, M., BASTOVANSKY, R., BRUMERCIK, F., IGNACIUK, P. Local resistance of heating molybdenum sheet in a test device. *Advances in Science and Technology - Research Journal* [online]. 2017, **11**(3), p. 87-93. ISSN 2299-8624. Available from: <https://doi.org/10.12913/22998624/74182>
- [7] SPISAK, P., MADAJ, R. The process of preparation prototypes bearing cages for the durability testing. In: 55th International Conference of Machine Design Departments ICMD 2014: proceedings. 2014. ISBN 978-80-01-05542-7, p. 271-276.
- [8] Wayken rapid manufacturing limited [online] [accessed 2021-05-28]. Available from: <https://waykenrm.com/technologies/urethane-vacuum-casting/>
- [9] BRUMERCIK, F., LUKAC, M., CABAN, J., KRZYSIAK, Z., GLOWACZ, A. Comparison of selected parameters of a planetary gearbox with involute and convex-concave teeth. *Applied Sciences* [online]. 2020, **10**(4), 1417. eISSN 2076-3417. Available from: <https://doi.org/10.3390/app10041417>
- [10] MEDVECKY, S., KOHAR, R., HRCEK, S. Dynamic analysis of cage behavior in a tapered roller bearing. In: 7th international Symposium Machine and Industrial Design in Mechanical Engineering KOD 2012 = Konstruisanje - Oblikovanje - Dizajn: proceedings. 2012. ISBN 978-86-7892-399-9, p. 45-50.
- [11] KUCERA, L., GAJDOSIK, T. The vibrodiagnostics of gears [online]. In: *Modern methods of construction design. lecture notes in mechanical engineering*. SEVCIK, L., LEPSIK, P., PETRU, M., MASIN, I., MARTONKA, R. (Eds.). Cham: Springer, 2014. ISBN 978-3-319-05202-1, eISBN 978-3-319-05203-8, p. 3118. Available from: https://doi.org/10.1007/978-3-319-05203-8_16
- [12] BRUMERCIK, F., BASTOVANSKY, R., LUKAC, M., GLOWACZ, A. Molybdenum strip test experiments and simulations at various temperatures to determine friction coefficients. *Measurement* [online]. 2021, **172**, 108859. ISSN 0263-2241. Available from: <https://doi.org/10.1016/j.measurement.2020.108859>
- [13] DRBUL, M., MARTIKAN, P., BRONCEK, J., LITVAJ, I., SVOBODOVA, J. Analysis of roughness profile on curved surfaces. In: Innovative Technologies in Engineering Production ITEP'18: proceedings [online]. Vol. 244. 2018. Available from: <https://doi.org/10.1051/mateconf/201824401024>
- [14] Modico (in Slovak) [online] [accessed 2021-03-23]. Available from: <http://www.modiko.sk/>
- [15] Smith - Polymers - Smith & Partner s.r.o. (in Slovak) [online]. Available from: <https://www.smith-polymers.com/polyuretanove-zivice/rapid-prototyping/synthese/>

REDUNDANT MULTI-OBJECT DETECTION FOR AUTONOMOUS VEHICLES IN STRUCTURED ENVIRONMENTS

Stefano Feraco*, Angelo Bonfitto, Nicola Amati, Andrea Tonoli

Politecnico di Torino, Torino, Italy

*E-mail of corresponding author: stefano.feraco@polito.it

Resume

This paper presents a redundant multi-object detection method for autonomous driving, exploiting a combination of Light Detection and Ranging (LiDAR) and stereocamera sensors to detect different obstacles. These sensors are used for distinct perception pipelines considering a custom hardware/software architecture deployed on a self-driving electric racing vehicle. Consequently, the creation of a local map with respect to the vehicle position enables development of further local trajectory planning algorithms. The LiDAR-based algorithm exploits segmentation of point clouds for the ground filtering and obstacle detection. The stereocamera-based perception pipeline is based on a Single Shot Detector using a deep learning neural network. The presented algorithm is experimentally validated on the instrumented vehicle during different driving maneuvers.

Article info

Received 29 April 2021

Accepted 4 June 2021

Online 30 September 2021

Keywords:

perception,
autonomous driving,
obstacle detection,
point-cloud segmentation,
single shot detector,
LiDAR (Light Detection
and Ranging)

Available online: <https://doi.org/10.26552/com.C.2022.1.C1-C17>

ISSN 1335-4205 (print version)

ISSN 2585-7878 (online version)

1 Introduction

Self-driving vehicles are experiencing a steadily increasing interest all over the world thanks to the most recent technological development, as witnessed in [1] and [2]. Although many Advanced Driving Assistance Systems (ADAS) are already present in the majority of vehicles of the recent mass production [3], fully autonomous vehicles are still considered as a disruptive force that could eruptively change the traffic environment and the whole mobility in the next years, thanks to the contribution of Artificial Intelligence, as stated in [4-6]. Recently, immense research efforts have been dedicated to autonomous systems and the DARPA Grand Challenge is one of the great results that the global mobile robotics community has achieved in the last decades [7-8], allowing to reach the high level of autonomy in nowadays commercial cars [9]. Moreover, about 94% of the road accidents are caused by human errors, according to a recent survey [10]. Therefore, these efforts have been motivated not only by the promise of preventing accidents, but also of reducing emissions and reducing driving-related stress [11]. Nevertheless, a consistent burden to adoption of driverless vehicles is the lack of public trust, since significant concerns, including but not limited to privacy and cybersecurity, have arisen [4]. Considering this framework, environment perception is a fundamental task for autonomous vehicles, which provides the vehicle a crucial assessment about the driving scenario, including an accurate information about the surrounding obstacles positions [12].

A vast variety of sensors is currently exploited for the purpose of environment perception with peculiar characteristics [13]. Cameras can offer a wide range of configurations in resolution, frame rate, size and optics parameters. Moreover, stereocameras are effective sensors in the self-driving vehicles since they can also be used to estimate depth map from images, enabling further obstacle detection and trajectory planning algorithms [14-15]. Nevertheless, camera-based sensors have some drawbacks for autonomous driving tasks under varying light and visibility conditions and with scenes with a high dynamic range, such as in entering or exiting a tunnel [13]. Furthermore, stereo vision is characterized by depth inaccuracies in the case of low-textured patterns [13] and the computed depth map has typically a limited range, which could be useless for automated driving at high speed. Therefore, the LiDAR (Light Detection and Ranging) sensors represent a recent technology that accurately computes distance to objects by measuring the flight-time of multiple laser light pulses [13]. Although the LiDAR sensors are mostly indicated devoted to the creation of accurate 3D maps in a huge horizontal Field-Of-View (FOV) [13, 16], they have also some important drawbacks in the environment perception. They typically have a limited vertical resolution and they are not suitable for detecting small objects placed at great distances since they compute a sparse map [13]. Moreover, the LiDAR measurement could be strongly affected by light and weather conditions, suggesting the usage of the redundant camera sensors in self-driving vehicles [17-18]. In addition, the Radar

sensors are used in the automotive perception tasks, being characterized by a strong measurement robustness with respect to the light and weather conditions. However, the high sensibility to target reflectivity and the low resolution of the radar technology strongly discourage the application of the technology for certain kinds of driving scenario, such as environments with small or far obstacles, which are detected with a low accuracy [13]. Therefore, the Radar sensors are not considered for the proposed sensing architecture.

This paper proposes a combined sensor architecture with both stereocamera and LiDAR sensors to enhance the perception pipeline robustness in terms of redundancy of the system. The redundancy in the proposed perception algorithm is of pivotal importance to avoid misclassification in the object detection process and poor environment sensing, as witnessed in the recent literature [19-21]. The investigated method does not implement a sensor fusion technique between the stereocamera and LiDAR, since it is intended to build a local map from the sensors, even in the case of a failure on one of the two sensors. This task is crucial to enable any further trajectory planning and control algorithm for autonomous driving [22-25].

Specifically, the proposed perception method is devoted to a driverless electric racing vehicle, thus requiring redundancy and robustness in the environment sensing process. The LiDAR-based perception pipeline relies on data coming from a Velodyne VLP-16 sensor that is placed onto the vehicle's front wing. The sensor can provide a full 360° view of the surrounding environment at 10 Hz to obtain an accurate real-time 3D data reconstruction, recorded by 16 light channels. It ranges up to 100m with 30° vertical field-of-view (FOV) and an angular resolution up to 0.1° in the horizontal plane. The stereocamera-based perception algorithm exploits a Stereolabs ZED dual camera that is mounted on the top of the vehicle's roll bar. The stereocamera can perform a long-range 3D sensing up to 20m distance with an increased accuracy in the short range (less than 10 m). The vehicle also features an NVIDIA Jetson AGX Xavier high-performance computing platform with embedded GPUs to process data coming from these sensors in a dedicated Robotic Operating System (ROS) software environment. The vehicle is autonomously driven on a racetrack at a varying speed without any prior knowledge of the path. The racetrack is properly structured with traffic cones, which are peculiar in terms of shape and colors (blue, yellow and orange). Since the ROS is not a hard-real-time system, a proprietary model-based software interface called RTMaps is used in the hardware that manages the vehicle dynamics control. In detail, RTMaps is a component-based software development and execution environment, which enables the synchronization and hard-real-time requirements for further control strategies that are implemented on target hardware machines.

The three-dimensional raw point cloud recorded by the LiDAR sensor is processed with a segmentation algorithm

that is properly designed for the ground plane filtering. This filtering task is a common practice that is necessary to avoid considering ground points in the obstacles detection stage [26-27]. Therefore, an algorithm for point-cloud clustering is applied to detect clusters of point. Each cluster represents a detected object delimiting the structured track, as witnessed by other methods for clusters detection discussed in the recent literature [28]. The proposed LiDAR-based perception pipeline can estimate the distance and the position of the clusters representing the obstacles in the driving environment. In the autonomous driving framework, alternative methods for the object detection in 3D point clouds are voxel-based Artificial Neural Networks (ANNs) [29] and other architectures of deep convolutional ANNs [30-32]. The vision-based perception pipeline is based on an SSD (Single Shot Detector) architecture based on MobileNetV1 using a single deep learning neural network to perform the object detection task in each frame. The SSD-based perception algorithms are proven to be very fast and robust in the recent literature [33-35]. The proposed perception algorithm can accurately estimate the distance of the detected objects by means of matching the depth map generated from the ZED stereocamera with the bounding boxes identified in the image by the SSD. The information deriving from the LiDAR and stereocamera pipelines is fused and synchronized to compute a detailed local map with the sensed obstacles up to 20m in front of the vehicle. Nevertheless, each of the two pipelines is redundant with respect to the other one in order to prevent inaccuracies in the obstacle detection process. Creation of a resulting local map enables further trajectory planning algorithms.

Therefore, the main contribution of this manuscript is to provide a redundant combined method for the multi-object perception in a structured environment for an autonomous electric racing vehicle. Moreover, the peculiar design and integration of the perception pipeline is tested during the extensive experimental validation on a real vehicle. The reported results include a set of different outdoor driving situations at a varying vehicle's speed. The redundancy in the perception pipeline is not novel at a system level in the context of driverless racing competitions, since it has been already proposed in [19] and [36]. Nevertheless, the investigated scheme is novel with respect to the existing literature, since it is based on an SSD and a clustering algorithm for point clouds that work in parallel, thus allowing to have a fully independent throughput from the perception pipeline. This configuration has not been reported in the literature so far.

The paper is structured as follows: section 2 illustrates the design of the proposed obstacle detection method for the LiDAR-based and stereocamera-based algorithms, along with the considered vehicle setup and the retained hardware and software architecture; section 3 presents the obtained results for both the perception pipelines and the creation of the local map during different maneuvers.

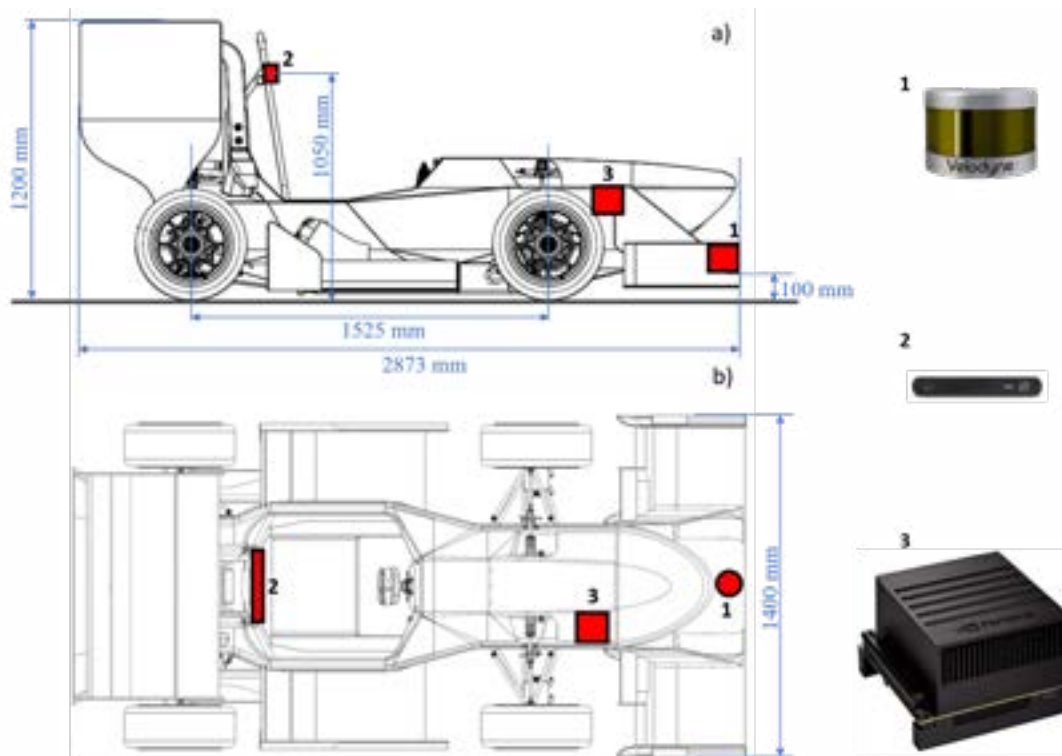


Figure 1 Vehicle and considered hardware positions: a) side view; b) top view. 1: Velodyne VLP-16 LiDAR sensor; 2: Stereolabs ZED stereocamera; 3: NVIDIA Jetson AGX Xavier high-performance computing platform

2 Method

In this section, the retained vehicle setup is presented first. Furthermore, the complete hardware and software architecture, deployed on a vehicle, is illustrated. Eventually, the designed LiDAR-based and stereocamera-based perception methods are described in devoted subsections, respectively, providing pseudo-code of the implemented algorithms.

2.1 Vehicle layout and hardware/software setup

The considered all-wheel drive electric vehicle is represented in Figure 1. A high-performance racing vehicle is considered due to reasons of prototyping, however, the outcomes of the research paper can be easily adapted to a commercial vehicle. The vehicle has an integral carbon fiber chassis built with honeycomb panels, double wishbone push-rod suspensions, an on-wheel planetary transmission system and a custom aerodynamic package. The vehicle can reach a maximum speed equal to 120 km/h with longitudinal acceleration peaks reaching up to 1.6g. The Velodyne VLP-16 LiDAR sensor is mounted on the front wing of the vehicle. The sensor is fixed at a height equal to 0.1m from the ground. The Stereolabs ZED stereocamera sensor is mounted at a height of 1.05m from the ground and it is fixed to the vehicle's rollbar, as represented in Figure 1. The NVIDIA Jetson Xavier high-performance computing platform is placed inside the vehicle's monocoque, fixed to

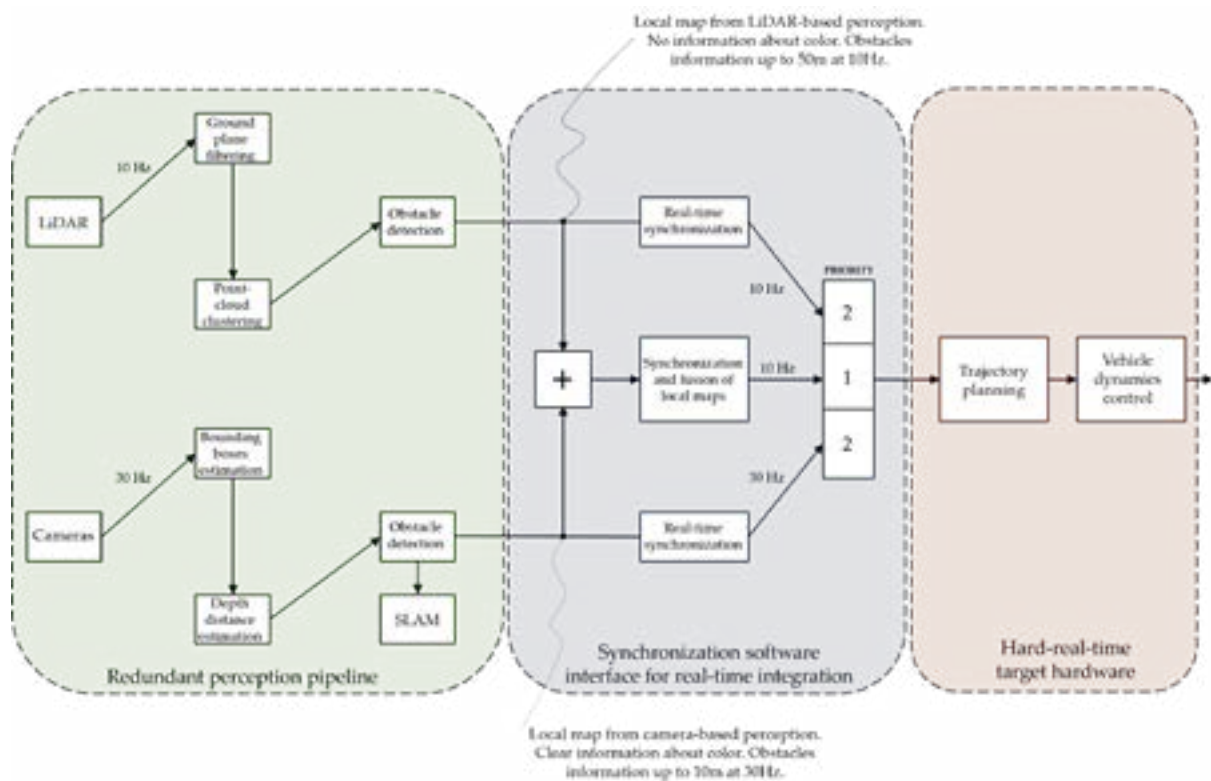
its right side. The main vehicle's parameters are listed in Table 1. A proper wiring system has been set up to correctly interface and supply the sensors to the computing platform, using a 12 V 10 Ah rechargeable Lithium battery as the devoted power source along with properly connected DC-DC power converter for the computing platform.

The Velodyne VLP-16 LiDAR sensor provides a full 360-degree point-cloud of the surrounding environment at 10 Hz to obtain an accurate real-time data reconstruction recorded by 16 light channels. It ranges up to 100m with 30° vertical field-of-view (FOV) and an angular resolution up to 0.1° in the horizontal plane [37]. The LiDAR sensor is connected to the computing platform with embedded GPUs through an Ethernet connection. Specifically, the computing platform creates a ROS network, which allows to process the information streaming from the LIDAR-based sensor. The ROS Melodic (2018) is used for the arm64 architecture of the computing platform that features Ubuntu 18.04 release.

The Stereolabs ZED stereocamera is connected via 3.0 USB port to the computing platform. The considered stereocamera features stereo 2K cameras with dual 4MP RGB sensors. It has a field of view of 110° and can stream uncompressed video at a rate up to 100 FPS. Left and right video frames are synchronized and streamed as a single uncompressed video frame format. Several configurations parameters, as resolution, brightness, contrast, saturation, can be tuned properly [38]. In the investigated algorithm, default parameters have been set both for the LiDAR and stereocamera sensors. The camera is used in the high-

Table 1 Main parameters of the considered all-wheel drive electric vehicle

Parameter	Symbol	Value	Unit
Mass	m	190	kg
Vehicle wheelbase	l	1.525	m
Overall length	L	2.873	m
Front axle distance to CG	a	0.839	m
Rear axle distance to CG	b	0.686	m
Vehicle track width	t	1.4	m
Overall width	W	1.38	m
Wheel radius	R_w	0.241	m
Maximum power	P_{max}	80	kW
Motors peak torque	T_{max}	84	Nm

**Figure 2** Redundant perception pipeline and global software architecture

definition 1080 mode (HD1080) at 30 Frame Per Second (FPS). ZED stereocamera is used since it is capable of accurately recording dense depth map information using triangulation from the geometric model of non-distorted rectified cameras up to 10m [38].

The NVIDIA Jetson AGX Xavier is an embedded Linux high-performance computing platform with embedded GPUs with 32 TOPS of peak computational power and 750 Gbps of high-speed input/output capability in less than 50 W of needed power. The retained high-performance computing platform enables intelligent vehicles with end-to-end autonomous capabilities since it is based on the most complex System-on-Chip (SoC) ever created up to 2018 [39]. The platform comprises an integrated 512-core NVIDIA Volta GPU including 64 Tensor Cores, 8-core NVIDIA Carmel ARMv8.2 64-bit CPU, 16GB 256-bit LPDDR4x,

dual NVIDIA Deep Learning Accelerator (DLA) engines, NVIDIA Vision Accelerator engine, HD video codecs, 128 Gbps of dedicated camera ingest and 16 lanes of PCIe Gen 4 expansion. Memory bandwidth over the 256-bit interface weighs in at 137 GB/s, while the DLA inference accelerator engines offload inferencing of Deep Neural Networks (DNNs). The NVIDIA's JetPack Software Development Kit 4.1.1 deployed for Jetson AGX Xavier includes CUDA 10.0, cuDNN 7.3 and TensorRT 5.0 libraries, thus providing a complete artificial intelligence software stack [39].

In order to validate the proposed method, the driving environment is properly structured with traffic cones according to the rules listed in [40]. In fact, each traffic cone has a height equal to 0.325 m and a square base, with a side length equal to 0.228 m. The cones of the right lane boundary are yellow with a black stripe, while the right

lane boundary is built with blue cones with a white stripe. Bigger orange cones indicate the starting and the ending points of the track.

The sensor fusion is a renowned solution to increase obstacle estimation accuracy [36, 41], thus it could be also used as an alternative approach for the investigated application. Nevertheless, the sensor fusion is always constrained by the sensor with lower throughput frequency, i.e. 10 Hz in this case and is strongly dependent on both used sensors. On the contrary, as represented in Figure 2, the proposed redundant perception pipeline can provide consistent results even in the case of failure of a single sensor. Moreover, the information at 30 Hz from camera-based pipeline is used for the mapping purposes, at the same time. Furthermore, a fused local map with higher priority for trajectory planning is created in the real-time synchronizing interfaced (RTMaps) at 10 Hz rate. This approach is quite different from the sensor fusion at a sensor level, that is performed in [41], because the information is fused and synchronized in the local map building process via over-imposition and synchronization of the detected obstacles. Indeed, avoiding the sensor fusion at a sensor level can save computational costs, as no additional algorithms are deployed on the devoted control unit. In fact, fusing information on the created local map only involves an easy operation of two-dimensional points over-imposition and time synchronization. The obtained local map is thus used with the higher priority for the local trajectory planning algorithms.

2.2 LiDAR-based perception algorithm

The LiDAR sensor records point clouds at a frequency equal to 10 Hz consisting of thousands of 3D points in a 360° range on the horizontal plane, while the vertical FOV is $\pm 15^\circ$. Each point-cloud contains the distance of each point in the 3D space along with the intensity of the reflected light in that point. Then, the raw point cloud is filtered by removing all the points out of the region-of-interest (ROI). Therefore $ROI(x, y, z)$ is defined as:

$$ROI(x, y, z) = \left\{ \begin{array}{l} 0 < x < 50 \\ -15 < y < 15 \\ -0.5 < z < 1.5 \end{array} \right\}, [m]. \quad (1)$$

A ground plane filtering segmentation algorithm is then applied to the raw point-cloud in $ROI(x, y, z)$ in order to remove all the points belonging to the ground, which can badly affect the proposed object detection method. Therefore, a clustering algorithm is applied the filtered point-cloud and the distance to the detected obstacles is finally estimated.

2.2.1 Ground-plane filtering segmentation

Efficient segmentation algorithms often try to reduce

dimensionality from LiDAR 3D point-clouds to 2D grid fixed to the ground. Firstly, this approach was proposed by many teams participating at DARPA Urban Challenge robot competition in past years [42-44], although it is heavily affected by under-segmentation issues and merging of different objects in the same segments [26]. Recently, other algorithms can process the point-cloud in full 3D [26, 45-49]. However, most of them could not be implementable in real-time because of the large amount of points they take into account resulting into a high computational costs, which can be solved only by means of treating the point cloud in cylindrical coordinates and fitting the line segments to the point-cloud [26]. Considering a LiDAR 3D point-cloud, the points belonging to the ground surface are often the majority of the recorded points. Therefore, the removal of the ground points can reduce the computational efforts required by further algorithms and ease the object detection task. In the proposed algorithm, an iterative multiple plane fitting technique for the ground-plane filtering is applied to the LiDAR 3D point-cloud in the considered $ROI(x, y, z)$. A single plane model is often inaccurate in the segmentation of the actual ground surface, since the ground points are not uniquely defined and the LiDAR measurements are often affected by huge noise, especially in the case of long distances [27].

The investigated algorithm divides the point-cloud into multiple segments along the direction of travel of a vehicle, namely the x-axis and iteratively applies the ground plane filtering algorithm in each of these segments. In each point-cloud, the retained LiDAR sensor can measure 16 segments according to the 16 sensing channels. The proposed ground plane filtering algorithm extracts a set of points with low height values (seeds), which are used to estimate the plane model of the ground surface in each of the considered point-cloud segments. The initial seed points are defined using the lowest point representative (LPR) approach, using an average value of the lowest height values of points in the point-cloud [27]. Therefore, noisy measurements do not affect the plane estimation. Once the LPR is computed, it is assumed as the point with the lowest height in the point cloud, thus all the points inside the seed height threshold are used to build the initial seeds set. The seed height threshold is heuristically set to 0.35m in the proposed algorithm. Then, each point in the segment is evaluated with respect to the estimated plane model by computing the distance from the orthogonal projection of the point onto the identified plane to the point itself. The resulting distance is then compared to a threshold distance, which is heuristically defined to decide if the point belongs to the ground surface or not. The points belonging to the ground plane are used as new seed points to estimate a new plane model and the process repeats for the defined number of iterations. Eventually, all the identified ground points in each of the segments are concatenated to define the ground plane. The number of iterations is heuristically set to 80, the threshold distance is set to 0.1m and the number of LPR initial seeds is set to 14. At each iteration, the ground plane is estimated by a simple linear model that is defined

as follows:

$$ax + by + cz + d = 0, \quad (2)$$

$$\tau^T x = -d, \quad (3)$$

where $\tau^T = [abc]^T$ and $x = [xyz]^T$ and solved for τ by using the covariance matrix $C \in R^{3 \times 3}$ that is computed considering the set of seed points $S \in R^3$ as in:

$$C = \sum_{i=1:|S|} (s_i - \hat{s})(s_i - \hat{s})^T, \quad (4)$$

with $\hat{s} \in R^3$ that is the mean of all the seeds $s_i \in R^3$.

The covariance matrix C should be decomposed in three singular vectors describing the directions of the seed dispersion by applying the singular value decomposition. Then, considering the ground plane, the normal τ indicates the direction with the least variance. Therefore, d can be computed using Equation (2) by substitution of x by \hat{s} . A complete theoretical background of the proposed method can be found in [27]. Once the ground plane has been identified, it can be filtered out of the point-cloud in order to consider only the remaining points for further processing algorithms. The pseudocode of the proposed approach is illustrated in Algorithm 1, that is represented in Figure 3.

Algorithm 1: Ground plane filtering for one segment of the point-cloud.

INITIALIZATION

- 1 π_{gnd} : ground points
- 2 π_{NOTgnd} : non-ground points
- 3 Π : input point-cloud
- 4 $\Pi_{sortedH}$: input point-cloud sorted on height
- 5 μ_{IT} : number of iterations
- 6 μ_{LPR} : number of points used in the LPR estimation
- 7 Δ_{seeds} : initial seeds threshold
- 8 Δ_{dist} : plane distance threshold

MAIN

- 9 $\pi_{gnd} = \text{InitialSeedsExtraction}(\Pi, \mu_{LPR}, \Delta_{seeds})$
- 10 **for** $i=1:\mu_{IT}$ **do**
- 11 plane = **EstPlane**(π_{gnd})
- 12 **clear**(π_{gnd}, π_{NOTgnd})
- 13 **for** $j = 1: |\Pi|$ **do**
- 14 **if** plane (p_k) < Δ_{dist} **then**
- 15 $\pi_{gnd} \leftarrow p_k$
- 16 **else**
- 17 $\pi_{NOTgnd} \leftarrow p_k$
- 18 **end**
- 19 **end**
- 20 **end**
- 21 **InitialSeedsExtraction:**
- 22 LPR = **Average**($\Pi_{sortedH}(1:\mu_{LPR})$)
- 23 **for** $i = 1: \Pi$ **do**
- 24 **if** p_k .height < LPR.height + Δ_{seeds} **then**
- 25 seeds_set $\leftarrow p_k$
- 26 **end**
- 27 **return** (seeds_set)

Figure 3 Algorithm 1 - ground plane filtering for one segment of the point-cloud

2.2.2 Point-cloud clustering and obstacles distance estimation

At each iteration, the point-cloud, obtained after the ground-plane filtering process, is further segmented in order to detect significant clusters of points representing the objects in the structured environment. Positions of the clusters are then estimated in real-time.

The input of the cluster detector is the filtered point-cloud Π_{filt} that includes all the non-ground points π_{NOTgnd} defined in Algorithm 1. Non-overlapping clusters of adjacent points are then extracted considering their relative Euclidean distance in the three-dimensional space as commonly intended in [50] and [51]. However, considering the vertical angular resolution γ of the Velodyne VLP-16 LiDAR sensor equal to 2° , the resulting distance in the z-axis (vertical) can be huge for far objects. Although fast and effective, distance-based clustering could be inaccurate, especially in the case of distant objects. If the threshold distance is not properly set in the clusters definition, there is a risk of splitting single objects into multiple adjacent clusters or merging different objects into a single cluster [16]. Therefore, considering the two generic clusters Γ_α and Γ_β both included in Π_{filt} , the non-overlapping condition can be written as:

$$\Gamma_\alpha \cap \Gamma_\beta = \emptyset \Rightarrow \min \|\pi_{NOTgnd\alpha} - \pi_{NOTgnd\beta}\| \geq \delta, \quad (5)$$

where $\alpha \neq \beta$ (i.e. the clusters are different), $\pi_{NOTgnd\alpha} \in \Gamma_\alpha$, $\pi_{NOTgnd\beta} \in \Gamma_\beta$ and δ is the threshold distance to define the cluster that is defined as follows:

$$\delta = 2 \cdot \rho \cdot \tan \frac{\gamma}{2}. \quad (6)$$

By considering the non-ground points π_{NOTgnd} only in the defined $ROI(x, y, z)$, the risk of considering too many 3D points in the clustering is limited, avoiding to increase the computational effort. To further reduce the data complexity, the horizontal space in the xy-plane is divided into multiple nested regions at a fixed constant distance threshold within each of them, as proposed in [52]. Therefore, a set of threshold distance values δ_i is retained at multiple fixed intervals d_δ where $\delta_{i+1} = \delta_i + d_\delta$. In each of the defined intervals, the maximum cluster detection range ρ_i is computed using Equation (6). Therefore, the corresponding radius \mathcal{R}_i is determined straightforward. The width of the i i -th region w_i is simply computed as:

$$w_i = \mathcal{R}_i - \mathcal{R}_{i-1}. \quad (7)$$

To define the circular region, a width w equal to 1.5 m is set heuristically in the proposed algorithm and d_δ is set to 0.1 m, after a necessary trial and error stage to find the best parameters for detecting traffic cones used in the retained structured environments. Therefore, clusters that are too large or too small are neglected.

Once the number of clusters k in Π_{filt} is computed, a straightforward implementation of the proposed

clustering method can be obtained with the renowned k -d tree algorithm in order to group the points in the correct cluster [52-53]. An efficient alternative method can be k -means clustering [16, 54]. An analysis on the robustness and stability of a k -d tree implementation of the proposed method, dedicated to detection of humans in point-clouds, is given by [52].

For each of the detected clusters, representing the obstacles in the structured environment, the centroid of the cluster is considered as the position of a cone in the defined $ROI(x, y, z)$, by means of collapsing all the clustered points onto the horizontal plane. This operation is performed by means of setting a null z-coordinate to the clustered points. Thus, the centroid of each cluster is computed as the geometric center of all the points in the cluster. Therefore, if a generic cluster Γ includes a certain number π_Γ of sparse points, its centroid $\omega(x_\omega, y_\omega)$ will be computed as:

$$\omega(x_\omega, y_\omega) = \begin{pmatrix} \frac{x_1 + x_2 + \dots + x_{\pi_\Gamma}}{\pi_\Gamma} \\ \frac{y_1 + y_2 + \dots + y_{\pi_\Gamma}}{\pi_\Gamma} \end{pmatrix}. \quad (8)$$

Eventually, a two-dimensional local map can be created considering the identified centroids. which represents the detected obstacles with respect to the LiDAR sensor position in the xy-plane.

2.3 Stereocamera-based perception algorithm

The stereocamera-based perception algorithm is designed to detect cones and extract the color features from the detected obstacles, namely blue, yellow and orange cones. The distance with respect to the sensor is then computed by matching the detected bounding boxes representing the obstacles with the recorded depth map from the ZED stereocamera. This algorithm is redundant to the LiDAR-based one. Nevertheless, it performs a peculiar task since it can estimate not only the position of the detected obstacles but also the color of the detected cones if nearer than 10m from the sensor, i.e. the maximum distance in which the generated depth map is reliable. In this section, the proposed SSD design and architecture are presented. Then, the image and depth map matching method for distance estimation is discussed.

2.3.1 Single Shot Detector design and architecture

The proposed perception stereocamera-based algorithm exploits an SSD algorithm based on the renowned MobileNetV1 structure to detect the objects [55]. This Convolutional Neural Network (CNN) structure is used since it is proven to be accurate and very fast in the object detection task in the recent literature [56], thus being compliant with the proposed real-time application of autonomous driving. As a matter of fact, the proposed

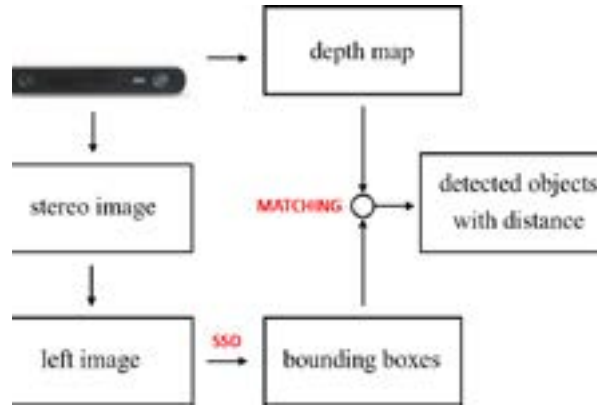


Figure 5 Block-scheme of the proposed stereocamera-based perception algorithm

blue cone (class 1), yellow cone (class 2) and orange cone (class 3). This is a standard procedure to apply a known CNN structure to a specific target domain of images, as widely discussed in [57].

MobileNetV1 is an efficient CNN architecture that use the depthwise separable convolutions, which factorize a standard convolution into a depthwise convolution and a pointwise convolution, in order to efficiently build lighter models with respect to earlier architectures [55]. Moreover, MobileNetV1 introduces two global hyper-parameters, which allow to perform a trade-off between latency and accuracy, namely the width multiplier and resolution multiplier. Therefore, the MobileNetV1 is built with multiple depthwise separable convolution layers and each depthwise separable convolution layer consists of a depthwise convolution and a pointwise convolution. The MobileNetV1 has 28 layers by counting depthwise and pointwise convolution as separate layers [55]. The size of the input images is $224 \times 224 \times 3$ pixels, thus the streaming images from the ZED left camera are properly resized before feeding them into the proposed CNN. The detailed architecture of the MobileNetV1 is given in Table 2 [55]. A complete theoretical background about the CNN MobileNetV1 can be found in [55].

Figure 4 illustrates the layout of the retained CNN MobileNetV1 with reference to Table 2 and [55].

2.3.2 Stereo image and depth map matching for distance estimation

After a preliminary camera calibration stage performed with the provided ZED Software Development Kit (SDK), the ZED stereocamera is ready to provide a reliable depth information in real-time up to 10m distance, thanks to its embedded algorithms. The ZED stereocamera already provides rectified images, facilitating the stereo disparity estimation, which is a fundamental process prior to the estimation of the depth map [38]. The ZED camera can compute depth map using triangulation from the geometric model of non-distorted rectified cameras. The depth D of each point p is computed as:

$$D = \frac{fb}{xi^L - xi^R}, \quad (9)$$

where f is the focal length, b is the baseline distance of the stereocamera and $xi^L - xi^R$ is the disparity value [38, 58]. The focal length f is assumed equal for the two cameras retaining that they are co-planar with parallel optical axes. The left camera is assumed as the origin frame for the resulting depth map. Disparity map is inversely proportional to the two-dimensional depth map, since the high disparity means that the point is closer to the stereocamera baseline and vice versa.

The 3D reconstruction phase uses the depth information in the disparity map along with camera calibration parameters by matching the RGB pixels with the two-dimensional coordinates, related to the disparity map created with respect to the optical center of the left camera. The result of this process is a dense map of the RGB points in 3D coordinates [59], which is accurately obtained for distances lower than 10m. Therefore, the obtained 3D reconstruction can be finally exploited for estimating the distance of the objects, corresponding to the identified bounding boxes. This task is commonly performed by computing the center point in each of the bounding boxes and projecting it into the disparity map. The distance from the left camera frame to each of the point is computed straightforward, as in [59] and [60]. Therefore, a two-dimensional local map can be computed by knowing the position and distance of the detected obstacles.

A block scheme of the proposed stereocamera-based perception algorithm is provided in Figure 5.

3 Results and discussion

In this section, the results of the proposed LiDAR-based and stereocamera-based object detection algorithms are presented, considering multiple dataset recorded on the instrumented vehicle in the structured environment. Specifically, the acquisitions are performed in Italy (Piedmont region) in 2020, in two different racetracks under different light and weather conditions. The proposed redundant method accurately detects the obstacles at fast refresh rates: up to 10 Hz for the LiDAR-based algorithm and up to 30 Hz for the stereocamera-based method, when running at the same time in the NVIDIA Jetson

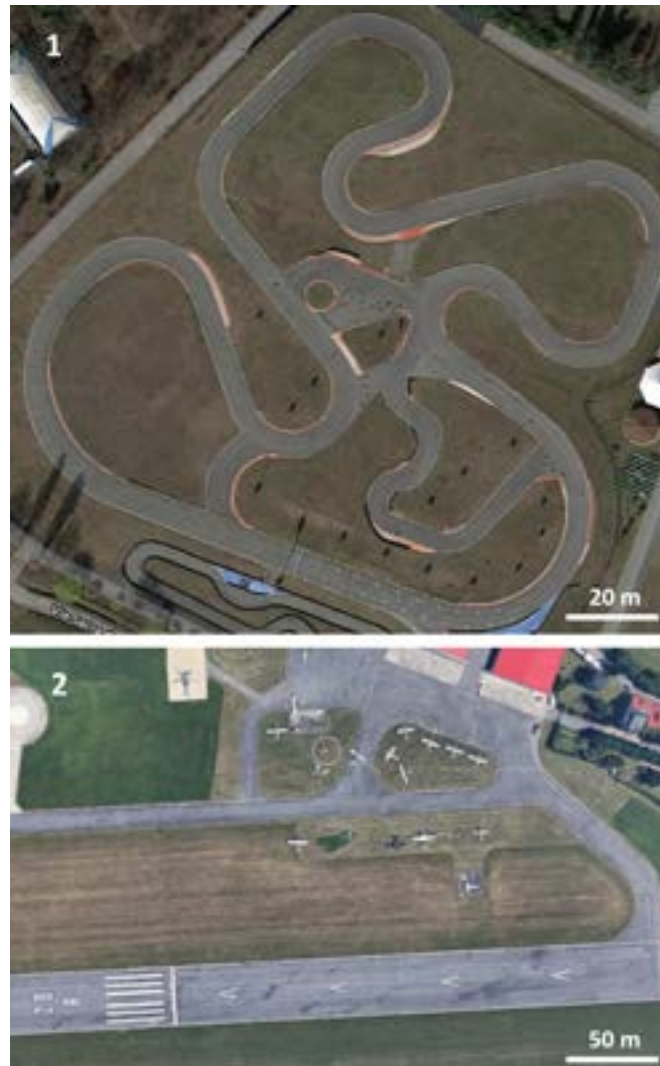


Figure 6 Aerial views of a racetrack 1 and a racetrack 2 (data from Google Maps, 2020)

AGX Xavier platform. The 10 Hz frequency of the LiDAR detections could not be feasible for the real-time assessment of environment perception during the vehicle motion at high speed. However, it is important to notice that the proposed perception method is particularly devoted to an accurate assessment of the obstacles position during the first lap of the racing track, that is driven at low speed (up to 15 km/h). Once the first lap is concluded, a global map can be generated via Simultaneous Localization and Mapping (SLAM) algorithms. Then, global trajectory planning algorithms can be implemented, neglecting the streaming data from the perception pipeline.

Figure 6 shows aerial images of the retained racetracks where the cones are properly placed to define the structured environment. The image data are taken from Google Maps service (2020).

Figure 7 illustrates an example of a single frame while moving in the racetrack 1. The LiDAR raw point-cloud is represented in Subfigure 7a and the ground-filtered point-cloud is shown in Subfigure 7b. LiDAR points have the color of the reflected light intensity parameters (from 0 to 255). In the figure, each square box has a side length equal

to 1m. The zoomed portions show how the unnecessary ground points are filtered out of the point-cloud without loss of information with respect to the points representing the obstacles.

Figure 8 represents the LiDAR-based detection results obtained at standstill in racetrack 1, at the starting point of the track. Clusters centroids are indicated with red arrows in Subfigure 8b and the LiDAR sensor position is indicated by a black dot. The resulting two-dimensional local map is shown in Subfigure 8b with grey dots representing the centroids of the detected obstacles.

Similarly, Figure 9 illustrates the LiDAR-based detection results obtained at standstill in racetrack 1, at the end of the track. Clusters centroids are indicated with red arrows in Subfigure 9b and the two-dimensional local map is shown in Subfigure 9b.

Figure 10 represents the detection results obtained with the LiDAR-based algorithm in poor weather and light conditions in racetrack 2, with the vehicle moving in a left curve. The vehicle speed is not constant during this maneuvers and can reach up to 80 km/h. Clusters centroids are indicated with red arrows in Subfigure 10b and the two-

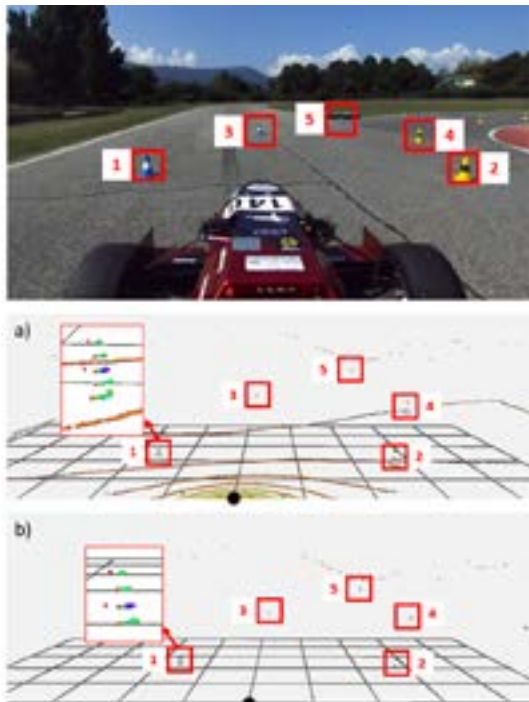


Figure 7 Example of a single LiDAR frame while moving in the driving scenario (racetrack 1): a) raw point-cloud; b) filtered point-cloud

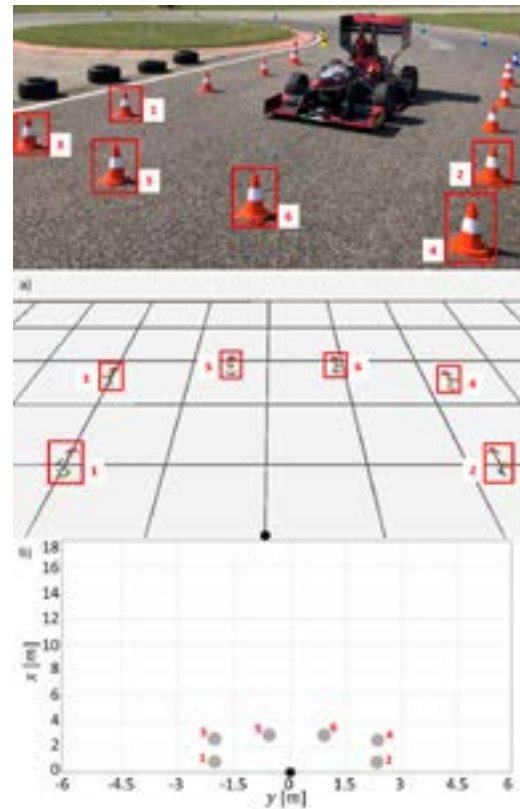


Figure 9 LiDAR-based detection results (racetrack 1) at standstill (end of the track): a) filtered ground-points and cluster centroids; b) resulting 2D local map

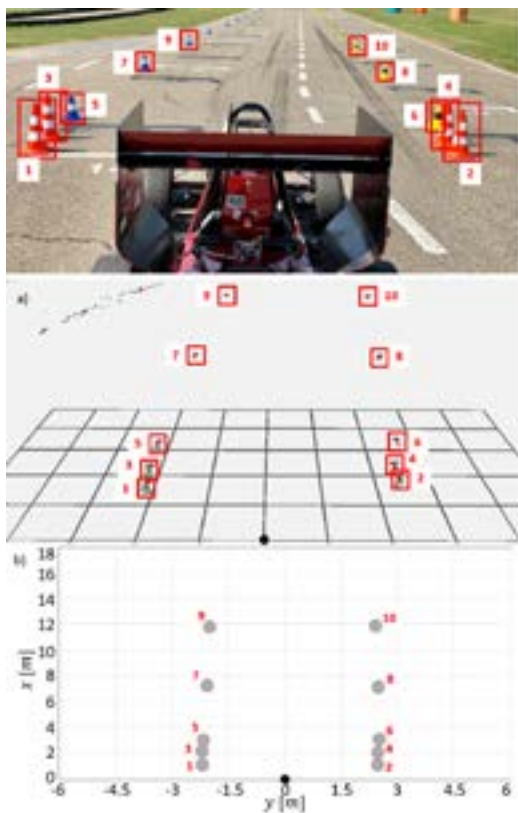


Figure 8 LiDAR-based detection results (racetrack 1) at standstill (start of the track): a) filtered ground-points and cluster centroids; b) resulting 2D local map

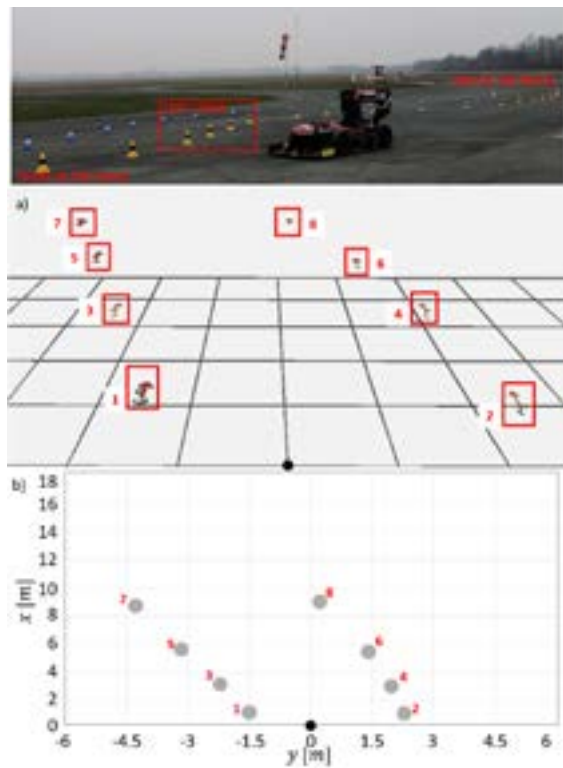


Figure 10 LiDAR-based detection results (racetrack 2) during the cornering (left curve): a) filtered ground-points and cluster centroids; b) resulting 2D local map

dimensional local map is shown in Subfigure 10b. Similarly, Figure 11 illustrates the results obtained in the same poor light and weather conditions (racetrack 2), while the vehicle is moving in a right curve.

Figures 12-14 illustrate the results obtained with the stereocamera-based algorithm along with the resulting two-dimensional local map in the following maneuvers: at standstill at the start of the racetrack (Figure 10); approaching the end of the racetrack 2 (Figure 13); during the cornering left or right in racetrack 1 (Figures 14 and 15, respectively). The sensor position in the map is represented by a black dot, while the other dots represent the estimated

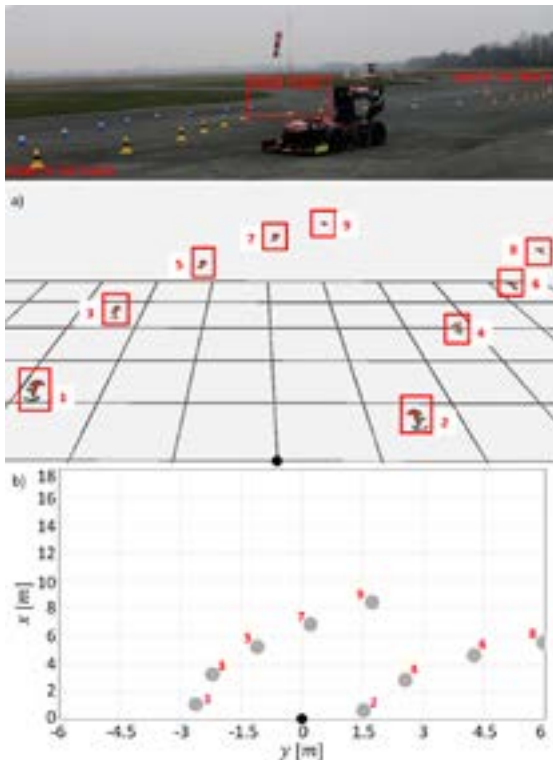


Figure 11 LiDAR-based detection results (racetrack 2) during the cornering (right curve): a) filtered ground-points and cluster centroids; b) resulting 2D local map

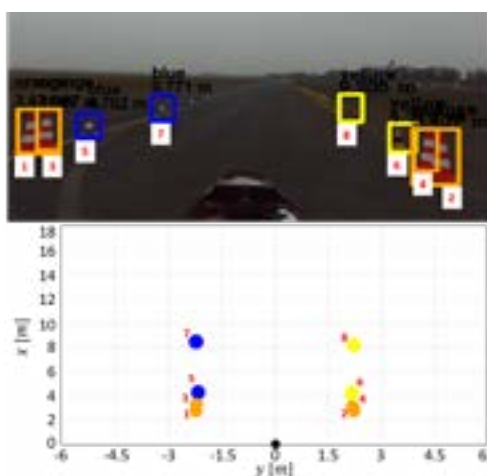


Figure 12 Stereocamera-based detection results and resulting 2D local map (racetrack 2) at standstill (start of the track)

position and color for each of the detected obstacles. The computed bounding boxes and the estimated obstacles distances are reported in each of Figures 12-15 onto the recorded raw left image of the stereocamera.

The proposed redundant perception method is not affected by ambient and light conditions since it is proven in different racetracks and weather circumstances. The ground points are correctly filtered out of the raw point-cloud and the information related to the obstacles points is robustly preserved from being filtered. The refresh map of the two-dimensional local map is always high when deployed on the NVIDIA Jetson AGX Xavier platform, thus

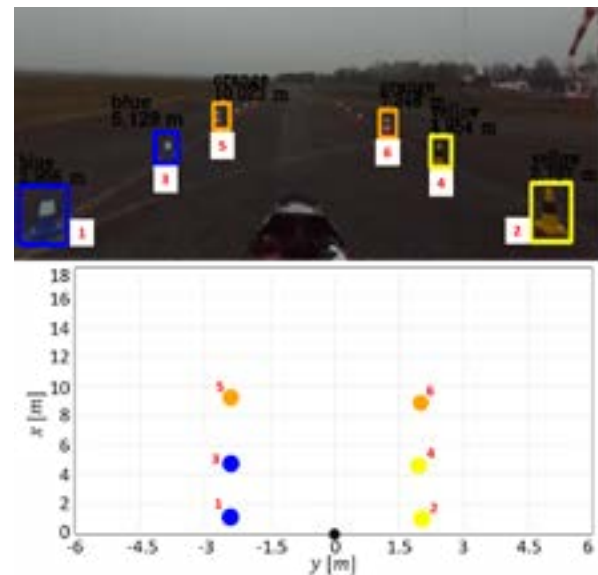


Figure 13 Stereocamera-based detection results and resulting 2D local map (racetrack 2) while approaching the end of the track

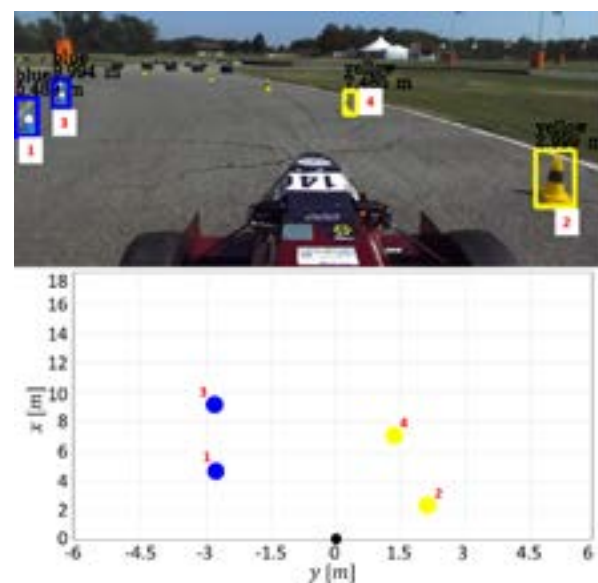


Figure 14 Stereocamera-based detection results and resulting 2D local map during the cornering (racetrack 1, left curve)

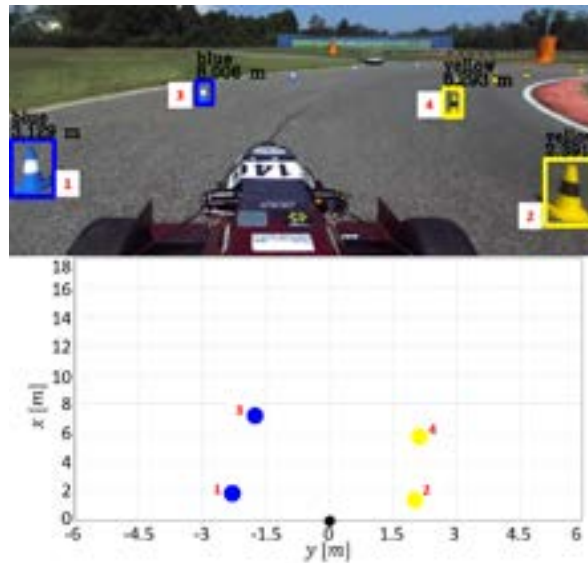


Figure 15 Stereocamera-based detection results and resulting 2D local map during the cornering (racetrack 1, right curve)

enabling its usage for autonomous driving purposes. The local map is actually created up to 20m in the case of the LiDAR-based algorithm and up to 10m using the stereocamera based method. The method is also robust with respect to possible outliers, being proven in a challenging environment, i.e. stripes on the ground and other types of objects in the environment that can affect the accuracy.

The distance estimation has been validated with respect to the ground truth provided by a roll-meter with a negligible error that is equal to few centimeters, as well as in the case of stereocamera-based algorithm.

The proposed method could also be implemented for any other kind of obstacles by means of properly changing the clustering parameters and by applying a proper transfer learning procedure for the SSD image classifier. This process is beyond the purpose of this paper since it is addressed to a peculiarly structured environment.

The algorithm is sufficiently redundant in the case of a failure in one of the sensors, thus avoiding common issues in the LiDAR-camera sensor fusion, when both measurements must always be provided to build a local map. Therefore, the local map can enable any further trajectory planning technique for autonomous driving.

4 Conclusion

Considering the recent innovations in the framework of the self-driving vehicles, a redundant multi-object detection algorithm has been presented. The proposed method exploits the combination of the LiDAR and stereocamera sensors, both to detect different obstacles and to create a local map by estimating the obstacles distance.

The method can accurately filter out of the point-cloud the unnecessary points with a segmentation algorithm and identify the clusters relative to each obstacle in the structured environment. Moreover, it is very robust with respect to outliers in the vision-based perception algorithm, that is performed with an SSD architecture. The solution is presented as a reliable alternative to existing methods to guarantee redundancy on the local map, which is successfully created, frame by frame, up to 20m in front of the vehicle. The performance of the method was evaluated experimentally during the real driving maneuvers, which have been performed by an all-wheel drive electric racing vehicle in a properly structured racetrack. The proposed approach is different from the sensor fusion at a sensor level, because the information is fused and synchronized in the local map building process via the two-dimensional over-imposition and synchronization of the detected obstacles. In fact, avoiding the sensor fusion at a sensor level can save computational costs, as no additional algorithms are deployed on the devoted control unit. According to the proposed perception method, creation of a local map, with respect to the vehicle position, is enabled for the deployment of further local trajectory planning algorithms. Consequently, an extensive validation stage of the method, considering several obstacles, is required before its deployment on commercial vehicles.

Acknowledgements

This research work was developed in the framework of the activities of the Interdepartmental Center for Automotive Research and Sustainable Mobility (CARS) at Politecnico di Torino (www.cars.polito.it).

References

- [1] SILBERG, G., MANASSA, M., EVERHART, K., SUBRAMANIAN, D., CORLEY, M., FRASER, H., SINHA, V. *Self-driving cars: are we ready?* [online]. Netherlands: KPMG LLP, 2013. Available from: <https://assets.kpmg/content/dam/kpmg/pdf/2013/10/self-driving-cars-are-we-ready.pdf>
- [2] FRAEDRICH, E., LENZ, B. Automated driving: individual and societal aspects. *Transportation Research Record: Journal of the Transportation Research Board* [online]. 2014, **2416**(1), p. 64-72. ISSN 0361-1981, eISSN 2169-4052. Available from: <https://doi.org/10.3141/2416-08>
- [3] ZIEBINSKI, A., CUPEK, R., GRZECHCA, D., CHRUSZCZYK, L. Review of advanced driver assistance systems (ADAS). *AIP Conference Proceedings* [online]. 2017, **1906**(1), 120002. ISSN 0094-243X, eISSN 1551-7616. Available from: <https://doi.org/10.1063/1.5012394>
- [4] KAUR, K., RAMPERSAD, G. Trust in driverless cars: Investigating key factors influencing the adoption of driverless cars. *Journal of Engineering and Technology Management* [online]. 2018, **48**, p. 87-96. ISSN 0923-4748. Available from: <https://doi.org/10.1016/j.jengtecman.2018.04.006>
- [5] HORL, S., CIARI, F., AXHAUSEN, K. W. *Recent perspectives on the impact of autonomous vehicles* [online]. Working paper 10XX. Zurich: Institute for Transport Planning and Systems, 2016. Available from: <https://doi.org/10.3929/ethz-b-000121359>
- [6] BONFITTO, A., FERACO, S., TONOLI, A., AMATI, N. Combined regression and classification artificial neural networks for sideslip angle estimation and road condition identification. *Vehicle System Dynamics* [online]. 2020, **58**(11), p. 1766-1787. ISSN 0042-3114, eISSN 1744-5159. Available from: <https://doi.org/10.1080/00423114.2019.1645860>
- [7] BUEHLER, M., IAGNEMMA, K., SINGH, S. *The 2005 DARPA grand challenge: the great robot race* [online]. Vol. 36. Berlin Heidelberg: Springer, 2007. ISBN 978-3-540-73429-1, eISBN 978-3-540-73429-1. Available from: <https://doi.org/10.1007/978-3-540-73429-1>
- [8] THRUN, S., MONTEMERLO, M., DAHLKAMP, H., STAVENS, D., ARON, A., DIEBEL, J., FONG, P., GALE, J., HALPENNY, M., HOFFMANN, G., LAU, K., OAKLEY, C., PALATUCCI, M., PRATT, V., STANG, P., STROHBAND, S., DUPONT, C., JENDROSSEK, L. - E., KOELEN, CH., MARKEY, CH., RUMMEL, C., VAN NIEKERK, J., JENSEN, E., ALESSANDRINI, P., BRADSKI, G., DAVIES, B., ETTINGER, S., KAEHLER, A., NEFIAN, A., MAHONEY, P. Stanley: The robot that won the DARPA Grand Challenge [online]. *Journal of Field Robotics*. 2006, **23**(9), p. 661-692. eISSN 1556-4967. Available from: <https://doi.org/10.1002/rob.20147>
- [9] LITMAN, T. Autonomous vehicle implementation predictions: implications for transport planning. In: *Transportation Research Board 94th Annual Meeting: proceedings*. 2015. No. 15-3326.
- [10] SINGH, S. *Critical reasons for crashes investigated in the national motor vehicle crash causation survey*. Washington, DC: National Center for Statistics and Analysis, 2015. No. DOT HS 812 115.
- [11] YURTSEVER, E., LAMBERT, J., CARBALLO, A., TAKEDA, K. A survey of autonomous driving: common practices and emerging technologies. *IEEE Access* [online]. 2020, **8**, p. 58443-58469. eISSN 2169-3536. Available from: <https://doi.org/10.1109/ACCESS.2020.2983149>
- [12] PENDLETON, S. D., ANDERSEN, H., DU, X., SHEN, X., MEGHJANI, M., ENG, Y. H., RUS, D., ANG, M. H. Perception, planning, control and coordination for autonomous vehicles. *Machines* [online]. 2017, **5**(1), 6. eISSN 2075-1702. Available from: <https://doi.org/10.3390/machines5010006>
- [13] MARTI, E., DE MIGUEL, M. A., GARCIA, F., PEREZ, J. A review of sensor technologies for perception in automated driving. *IEEE Intelligent Transportation Systems Magazine* [online]. 2019, **11**(4), p. 94-108. ISSN 1939-1390, eISSN 1941-1197. Available from: <https://doi.org/10.1109/MITS.2019.2907630>
- [14] KEMSARAM, N., DAS, A., DUBBELMAN, G. A stereo perception framework for autonomous vehicles. In: *2020 IEEE 91st Vehicular Technology Conference VTC2020-Spring: proceedings* [online]. IEEE. 2020. eISBN 978-1-7281-5207-3, p. 1-6. Available from: <https://doi.org/10.1109/VTC2020-Spring48590.2020.9128899>
- [15] FERACO, S., BONFITTO, A., KHAN, I., AMATI, N., TONOLI, A. Optimal trajectory generation using an improved probabilistic road map algorithm for autonomous driving. In: *22nd International Design Engineering Technical Conferences and Computers and Information in Engineering Conference: proceedings* [online]. American Society of Mechanical Engineers. Vol. 83938. 2020. ISBN 978-0-7918-8393-8, V004T04A006. Available from: <https://doi.org/10.1115/DETC2020-22311>
- [16] FERACO, S., BONFITTO, A., AMATI, N., & TONOLI, A. A LIDAR-based clustering technique for obstacles and lane boundaries detection in assisted and autonomous driving. In: *22nd International Design Engineering Technical Conferences and Computers and Information in Engineering Conference: proceedings* [online]. American Society of Mechanical Engineers. Vol. 83938. 2020. ISBN 978-0-7918-8393-8, V004T04A007. Available from: <https://doi.org/10.1115/DETC2020-22339>

- [17] WANG, M., LIU, W. - Q., LU, Y. - H., ZHAO, X. - S., SONG, B. - CH., ZHANG, Y. - J., WANG, Y. - P., LIAN, C. - H., CHEN, J., CHENG, Y., LIU, J. - G., WEI, Q. - N. Study on the measurement of the atmospheric extinction of fog and rain by forward-scattering near infrared spectroscopy. *Spectroscopy and Spectral Analysis*. 2008, **28**(8), p. 1776-1780.
- [18] PHILLIPS, T. G., GUENTHER, N., MCAREE, P. R. When the dust settles: the four behaviors of LIDAR in the presence of fine airborne particulates. *Journal of Field Robotics* [online]. 2017, **34**(5), p. 985-1009. eISSN 1556-4967. Available from: <https://doi.org/10.1002/rob.21701>
- [19] GOSALA, N., BUHLER, A., PRAJAPAT, M., EHMKE, C., GUPTA, M., SIVANESAN, R., GAWEL, A., PFEIFFER, M., BURKI, M., SA, I., DUBE, R., SIEGWART, R. Redundant perception and state estimation for reliable autonomous racing. In: 2019 International Conference on Robotics and Automation ICRA 2019: proceedings [online]. IEEE. 2019. Available from: <https://doi.org/10.1109/ICRA.2019.8794155>
- [20] KUMAR, G. A., LEE, J. H., HWANG, J., PARK, J., YOUN, S. H., KWON, S. LiDAR and camera fusion approach for object distance estimation in self-driving vehicles. *Symmetry* [online]. 2020, **12**(2), 324. eISSN 2073-8994. Available from: <https://doi.org/10.3390/sym12020324>
- [21] ROSIQUE, F., NAVARRO, P. J., FERNANDEZ, C., PADILLA, A. A systematic review of perception system and simulators for autonomous vehicles research. *Sensors* [online]. 2019, **19**(3), 648. eISSN 1424-8220. Available from: <https://doi.org/10.3390/s19030648>
- [22] LEE, K. B., HAN, M. H. Lane-following method for high speed autonomous vehicles. *International Journal of Automotive Technology* [online]. 2008, **9**(5), p. 607-613. ISSN 1229-9138. eISSN 1976-3832. Available from: <https://doi.org/10.1007/s12239-008-0072-z>
- [23] CHU, K., KIM, J., JO, K., SUNWOO, M. Real-time path planning of autonomous vehicles for unstructured road navigation. *International Journal of Automotive Technology* [online]. 2015, **16**(4), p. 653-668. ISSN 1229-9138. eISSN 1976-3832. Available from: <https://doi.org/10.1007/s12239-015-0067-5>
- [24] HU, J., XIONG, S., ZHA, J., FU, C. Lane detection and trajectory tracking control of autonomous vehicle based on model predictive control. *International Journal of Automotive Technology* [online]. 2020, **21**(2), p. 285-295. ISSN 1229-9138. eISSN 1976-3832. Available from: <https://doi.org/10.1007/s12239-020-0027-6>
- [25] KHAN, I., FERACO, S., BONFITTO, A., AMATI, N. A model predictive control strategy for lateral and longitudinal dynamics in autonomous driving. In: International Design Engineering Technical Conferences and Computers and Information in Engineering Conference ASME 2020: proceedings. American Society of Mechanical Engineers Digital Collection. 2020.
- [26] HIMMELSBACH, M., HUNDELSHAUSEN, F. V., WUENSCH, H. J. Fast segmentation of 3D point clouds for ground vehicles. In: 2010 IEEE Intelligent Vehicles Symposium: proceedings. IEEE. 2010. ISBN 978-1-4244-7866-8, p. 560-565.
- [27] ZERMAS, D., IZZAT I., PAPANIKOLOPOULOS, N. Fast segmentation of 3D point clouds: a paradigm on LiDAR data for autonomous vehicle applications. In: 2017 IEEE International Conference on Robotics and Automation ICRA 2017: proceedings [online]. IEEE, 2017. eISBN 9781509046331, ISSN 1050-4729. Available from: <https://doi.org/10.1109/ICRA.2017.7989591>
- [28] NYGREN, P., JASINSKI, M. *A comparative study of segmentation and classification methods for 3D point clouds* [online]. MS thesis. Gothenburg, Sweden: Chalmers University of Technology, University of Gothenburg, 2016. Available from: <https://hdl.handle.net/20.500.12380/238602>
- [29] ZHOU, Y., TUZEL, O. Voxelnet: End-to-end learning for point cloud based 3D object detection. In: IEEE Conference on Computer Vision and Pattern Recognition CVPR 2018: proceedings [online]. 2018. p. 4490-4499. Available from: <https://doi.org/10.1109/CVPR.2018.00472>
- [30] LIU, W., SUN, J., LI, W., HU, T., WANG, P. Deep learning on point clouds and its application: a survey. *Sensors* [online], 2019, **19**(19), 4188. eISSN 1424-8220. Available from: <https://doi.org/10.3390/s19194188>
- [31] GRILLI, E., MENNA, F., REMONDINO, F. A review of point clouds segmentation and classification algorithms. *The International Archives of the Photogrammetry, Remote Sensing and Spatial Information Sciences* [online]. 2017, **XLII**, p. 339-344. eISSN 2194-9034. Available from: <https://doi.org/10.5194/isprs-archives-XLII-2-W3-339-2017>
- [32] GUO, Y., WANG, H., HU, Q., LIU, H., LIU, L., BENNAMOUN, M. Deep learning for 3D point clouds: a survey. *IEEE Transactions on Pattern Analysis and Machine Intelligence* [online]. 2020, early access. ISSN 0162-8828, eISSN 1939-3539. Available from: <https://doi.org/10.1109/TPAMI.2020.3005434>
- [33] LIU, W., ANGUELOV, D., ERHAN, D., SZEGEDY, C., REED, S., FU, C. Y., BERG, A. C. SSD: Single shot multibox detector. In: European Conference on Computer Vision: proceedings [online]. Springer, Cham. 2016. ISBN 978-3-319-46447-3, eISBN 978-3-319-46448-0, p. 21-37. Available from: https://doi.org/10.1007/978-3-319-46448-0_2

- [34] ZHAO, Z. Q., ZHENG, P., XU, S. T., WU, X. Object detection with deep learning: A review. *IEEE Transactions on Neural Networks and Learning Systems* [online]. 2019, **30**(11), p. 3212-3232. ISSN 2162-237X, eISSN 2162-2388. Available from: <https://doi.org/10.1109/TNNLS.2018.2876865>
- [35] JIAO, L., ZHANG, F., LIU, F., YANG, S., LI, L., FENG, Z., QU, R. A survey of deep learning-based object detection. *IEEE Access* [online]. 2019, **7**, p. 128837-128868. eISSN 2169-3536. Available from: <https://doi.org/10.1109/ACCESS.2019.2939201>
- [36] KABZAN, J., VALLS, M. I., REIJGWART, V. J., HENDRIKX, H. F., EHMKE, C., PRAJAPAT, M., BUHLER, A., GOSALA, N., GUPTA, M., SIVANESAN, R., DHALL, A., CHISARI, E., KARNCHANACHARI, N., BRITS, S., DANGEL, M., SA, I., DUBE, R., GAWEL, A., PFEIFFER, M., LINIGER, A., LYGEROS, J., SIEGWART, R. AMZ driverless: The full autonomous racing system. *Journal of Field Robotics* [online]. 2020, **37**(7), p. 1267-1294. eISSN 1556-4967. Available from: <https://doi.org/10.1002/rob.21977>
- [37] GLENNIE, C. L., KUSARI, A., FACCHIN, A. Calibration and stability analysis of the VLP-16 laser scanner. *The International Archives of the Photogrammetry, Remote Sensing and Spatial Information Sciences* [online]. 2016, **XL**, p. 55-60. eISSN 2194-9034. Available from: <https://doi.org/10.5194/isprs-archives-XL-3-W4-55-2016>
- [38] ORTIZ, L. E., CABRERA, E. V., GONÇALVES, L. M. Depth data error modeling of the ZED 3D vision sensor from stereolabs. *ELCVIA: Electronic Letters on Computer Vision And Image Analysis* [online]. 2018, **17**(1), p. 1-15. eISSN 1577-5097. Available from: <https://doi.org/10.5565/rev/elcvia.1084>
- [39] DITTY, M., KARANDIKAR, A., REED, D. Nvidia's xavier SoC. I: Hot Chips: A Symposium on High Performance Chips: proceedings. 2018.
- [40] FSG competition handbook 2019 - Formula Student Germany [online]. 2019. Available from: https://www.formulastudent.de/fileadmin/user_upload/all/2019/rules/FSG19_Compensation_Handbook_v1.0.pdf
- [41] WANG, S., WU, T., VOROBAYCHIK, Y. Towards robust sensor fusion in visual perception [online]. 2020. Available from: arXiv:2006.13192
- [42] URMSON, C., ANHALT, J., BAGNELL, D., BAKER, C., BITTNER, R., CLARK, M. N., DOLAN, J., DUGGINS, D., GALATALI, T., GEYER, CH., GITTLEMAN, M., HARBAUGH, S., HEBERT, M., HOWARD, T. M., KOLSKI, S., KELLY, A., LIKHACHEV, M., MCNAUGHTON, M., MILLER, N., PETERSON, K., PILNICK, B., RAJKUMAR, R., RYBSKI, P., SALESKY, B., SEO, Y. - W., SINGH, S., SNIDER, J., STENTZ, A., WHITTAKER, W. "R.", WOLKOWICKI, Z., ZIGLAR, J., BAE, H., BROWN, T., DEMITRISH, D., LITKOUHI, B., NICKOLAOU, J., SADEKAR, V., ZHANG, W., STRUBLE, J., TAYLOR, M., DARMS, M., FERGUSON, D. Autonomous driving in urban environments: boss and the urban challenge. *Journal of Field Robotics* [online]. 2008, **25**(8), p. 425-466. eISSN 1556-4967. Available from: <https://doi.org/10.1002/rob.20255>
- [43] KAMMEL, S., ZIEGLER, J., PITZER, B., WERLING, M., GINDELE, T., JAGZENT, D., SCHRODER, J., THUY, M., GOEBL, M., VON HUNDELSHAUSEN, F., PINK, O., FRESE, CH., STILLER, CH. Team AnnieWAY's autonomous system for the 2007 DARPA urban challenge. *Journal of Field Robotics* [online]. 2008, **25**(9), p. 615-639. eISSN 1556-4967. Available from: <https://doi.org/10.1002/rob.20252>
- [44] MONTEMERLO, M., BECKER, J., BHAT, S., DAHLKAMP, H., DOLGOV, D., ETTINGER, S., HAEHNEL, D., HILDEN, T., HOFFMANN, G., HUHNKE, B., JOHNSTON, D., KLUMPP, S., LANGER, D., LEVANDOWSKI, A., LEVINSON, J., MARCIL, J., ORENSTEIN, D., PAEFGEN, J., PENNY, I., PETROVSKAYA, A., PFLUEGER, M., STANEK, G., STAVENS, D., VOGT, A., THRUN, S. Junior: the Stanford entry in the urban challenge. *Journal of Field Robotics* [online]. 2008, **25**(9), p. 569-597. eISSN 1556-4967. Available from: <https://doi.org/10.1002/rob.20258>
- [45] MOOSMANN, F., PINK, O., STILLER, C. Segmentation of 3D LiDAR data in non-flat urban environments using a local convexity criterion. In: IEEE Intelligent Vehicles Symposium IV 09: proceedings [online]. 2009. ISSN 1931-0587. Available from: <https://doi.org/10.1109/IVS.2009.5164280>
- [46] KLASING, K., WOLLHERR, D., BUSS, M. Realtime segmentation of range data using continuous nearest neighbors. In: 2009 IEEE International Conference on Robotics and Automation ICRA: proceedings 2009.
- [47] KLASING, K., WOLLHERR, D., BUSS, M. A clustering method for efficient segmentation of 3D laser data. In: IEEE International Conference on Robotics and Automation ICRA 2008: proceedings. 2008. p. 4043-4048.
- [48] STEINHAUSER, D., RUEPP, O., BURSCHKA, D. Motion segmentation and scene classification from 3D LiDAR data. In: IEEE Intelligent Vehicles Symposium: proceedings. 2008. p. 398-403.
- [49] ANGUELOV, D., TASKAR, B., CHATALBASHEV, V., KOLLER, D., GUPTA, D., HEITZ, G., NG, A. Discriminative learning of Markov random fields for segmentation of 3D scan data. In: 2005 IEEE Computer Society Conference on Computer Vision and Pattern Recognition CVPR'05: proceedings. Vol. 2. 2005. p. 169-176.
- [50] RUSU, R. B. Semantic 3D object maps for everyday manipulation in human living environments. *KI-Kunstliche Intelligenz* [online]. 2010, **24**(4), p. 345-348. ISSN 0933-1875, eISSN 1610-1987. Available from: <https://doi.org/10.1007/s13218-010-0059-6>
- [51] RUSU, R. B., COUSINS, S. 3D is here: Point cloud library (PCL). In: 2011 IEEE International Conference on Robotics and Automation: proceedings. 2011. p. 1-4.

- [52] YAN, Z., DUCKETT, T., BELLOTTO, N. Online learning for 3D LiDAR-based human detection: experimental analysis of point cloud clustering and classification methods. *Autonomous Robots* [online]. 2020, **44**(2), p. 147-164. ISSN 0929-5593, eISSN 1573-7527. Available from: <https://doi.org/10.1007/s10514-019-09883-y>
- [53] BENTLEY, J. L. Multidimensional binary search trees used for associative searching. *Communications of the ACM* [online]. 1975, **18**(9), p. 509-517. ISSN 0001-0782, eISSN 1557-7317. Available from: <https://doi.org/10.1145/361002.361007>
- [54] MACQUEEN, J. B. Some methods for classification and analysis of multivariate observations. In: 5-th Berkeley Symposium on Mathematical Statistics and Probability: proceedings. Berkeley, University of California Press. Vol. 1. 1967. p. 281- 297.
- [55] HOWARD, A. G., ZHU, M., CHEN, B., KALENICHENKO, D., WANG, W., WEYAND, T., ANDREETTO, M., ADAM, H. Mobile nets: efficient convolutional neural networks for mobile vision applications [online]. 2017. Available from: <http://arxiv.org/abs/1704.04861>
- [56] GALVEZ, R. L., BANDALA, A. A., DADIOS, E. P., VICERRA, R. R. P., MANINGO, J. M. Z. Object detection using convolutional neural networks. In: IEEE Region 10 Conference TENCON 2018: proceedings. 2018. p. 2023-2027.
- [57] ZHUANG, F., QI, Z., DUAN, K., XI, D., ZHU, Y., ZHU, H., XIONG, H., HE, Q. A comprehensive survey on transfer learning. *Proceedings of the IEEE* [online]. 2020, **109**(1), p. 43-76. Available from: <https://doi.org/10.1109/JPROC.2020.3004555>
- [58] R. SZELISKY, Computer vision: algorithms and applications [online]. London: Springer Link, 2012. ISBN 978-1-84882-934-3, eISBN 978-1-84882-935-0. Available from: <https://doi.org/10.1007/978-1-84882-935-0>
- [59] ADI, K., WIDODO, C. E. Distance measurement with a stereo camera. *International Journal of Innovative Research in Advanced Engineering* [online]. 2017, **4**(11), p. 24-27. ISSN 2349-2163. Available from: <https://doi.org/10.26562/IJIRAE.2017.NVAE10087>
- [60] ZAARANE, A., SLIMANI, I., AL OKAISHI, W., ATOUF, I., HAMDOUN, A. Distance measurement system for autonomous vehicles using stereo camera. *Array* [online]. 2020, **5**, 100016. ISSN 2590-0056. Available from: <https://doi.org/10.1016/j.array.2020.100016>

ARTIFICIAL NEURAL NETWORK BASED MPPT ALGORITHM FOR MODERN HOUSEHOLD WITH ELECTRIC VEHICLE

Ján Morgoš*, Peter Klčo, Karol Hrudkay

University Scientific Park, University of Zilina, Zilina, Slovakia

*E-mail of corresponding author: jan.morgos@uniza.sk

Resume

This paper deals with implementation of artificial neural network in the maximum power point tracking (MPPT) controller algorithm for modern household where electric vehicle (EV) was purchased. The proposed MPPT algorithm was designed to achieve the best possible efficiency of the MPP (maximum power point) tracking and the best possible energy harvesting to charge the EV's battery. The artificial neural networks have strong advantage in fast input to output response of signals and the finding of MPP is faster than in commonly used algorithms. In this article, the optimised simulation model based on artificial neural network will be introduced. The proposed artificial neural network algorithm was designed for non-shielded photovoltaic panels.

Article info

Received 24 May 2021

Accepted 23 August 2021

Online 24 November 2021

Keywords:

artificial neural network,
MPPT algorithm,
electric vehicle,
battery,
photovoltaic,
(photo-voltaic) PV panel,
high efficiency

Available online: <https://doi.org/10.26552/com.C.2022.1.C18-C26>

ISSN 1335-4205 (print version)

ISSN 2585-7878 (online version)

1 Introduction

In recent years there has been growing interest in producing electricity from solar energy and other renewable energy sources (RES). Since it is truly renewable energy source, it is a valuable non-polluting alternative to fossil fuel energy sources in industrial, household or transport applications. Main disadvantages of the solar energy are relatively high costs, lower efficiency of photovoltaic (PV) systems (37 - 40%) and dependence on weather conditions, as well as difficulties of storing this kind of energy [1]. In addition, the maintenance and cleaning of solar panels is not easy in some cases, i.e. on high-rise buildings. With assistance of the PV panels, or other renewable energy sources, the electric grid energy consumption and electricity bills can be easily reduced. The whole PV panel industry has been growing market creating new job opportunities and new opportunities for research. The effort of many research teams is aimed at efficiency maximization of the solar energy conversion. In addition, the smart control methods can increase the efficiency significantly. New materials with higher efficiency are researched and new algorithms for the PV systems power control, as well [1-4].

2 Theoretical background

The electrical power of the PV cells can vary significantly during the day, therefore maximum power

point tracking method is strongly required to maximize generated power. The PV panel used is modelled as a single-diode circuit with current source and serial and parallel resistances [4]. Principal schematic of one PV cell is illustrated in Figure 1. The mathematic relation between the PV cell's output current and output voltage can be described as:

$$I_{CELL} = I_{PV} - I_s \left[\exp\left(\frac{V + IR_s}{V_T}\right) - 1 \right] - \frac{V + IR_s}{R_p}, \quad (1)$$

where:

I_{CELL} output current of PV module,
 V_{PV} output voltage,
 I_{PV} photocurrent,
 I_s diode saturation current,
 V_T the thermal voltage,
 R_p equivalent serial resistance,
 R_s equivalent serial resistance.

The thermal voltage is expressed as:

$$V_T = \frac{n * k * T * N_s}{q}, \quad (2)$$

where:

n ideality factor,
 k Boltzmann constant [1.381 x 10⁻²³ J/K],
 T temperature of the cell,
 N_s number of solar cells in the PV module connected in series,
 q elementary electron charge [4-6].

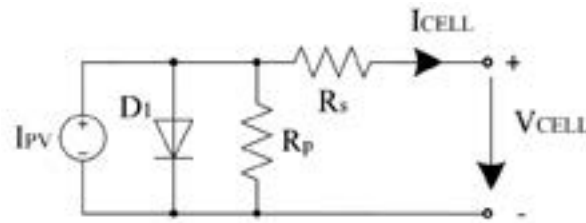


Figure 1 Principal schematic of diode model of PV panel

Artificial neural networks (ANN) are considered as mathematical-computational models inspired by biological neural networks. Neural networks were used in various areas, like robotics, function approximation, regression analysis, time series prediction, classification, modelling or data processing [7]. The ANN have become a standard tool in computer science for the function approximation of various digital patterns and data inputs. and are also considered to be one of the most successful computer classification models.

According to the universal approximation theorem, the ANN with just 1 hidden layer can approximate any continuous function. ANNs can be therefore considered as efficient function approximators. These statements deal predominately with existence of solution in the form of unique weight coefficients, they do not say anything about exact method how to find the most optimal parameters of a neural network. It is not always easy to find solution that represents global minimum of the cost function instead of locally minimum [8]. Figure 2 shows principal diagram of the feed-forward neural network.

3 MPPT controller based on ANN

System consists of PV panels, isolated switching converter, household battery and the EV's battery. In this system, only the unidirectional energy flow is realized from the PV panel to the electric vehicle battery

back. Due to cloud shielding, the solar energy flow is not continuous; it is necessary for the system to use the household battery to supply energy during disturbances caused by the clouding of the PV panels.

The trained ANN implemented to the control system (microcontroller) controls the switching converter with the requested current I^* to create the optimal load for the PV panels to achieve maximum charging performance. Reference current signal is internally converted into the pulse width modulation (PWM) signals used to switching MOSFET transistors in switching converter [9-10]. The ANN controls the converter with using of PV panel voltage, PV panel current and PV panel temperature signals. For the safety reasons, the battery voltage and current are connected to control block and the system is switched off if any error occurs. Big advantage of this setup with household battery is supplying the EV charger without interruptions and energy flow fluctuations during the clouding. Principal block diagram of used model is shown in Figure 3.

The solar irradiance and the PV panel temperature are usually chosen as input data for neural network in MPPT control. The advantage is possibility to simulate photovoltaic panel in simulation software MATLAB. However, the sensors for measurement of solar irradiance are much more expensive and the whole solution is therefore less cost-effective. Random electrical current, voltage of PV panels and real temperature of photovoltaic panels are also used as input data (input neurons) for the trained neural network [10-15].

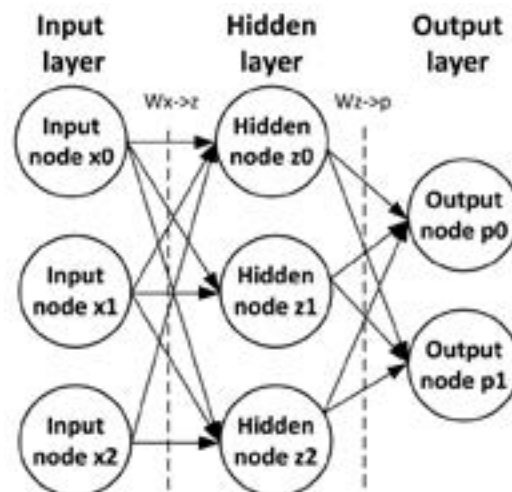


Figure 2 Principal diagram of neural network

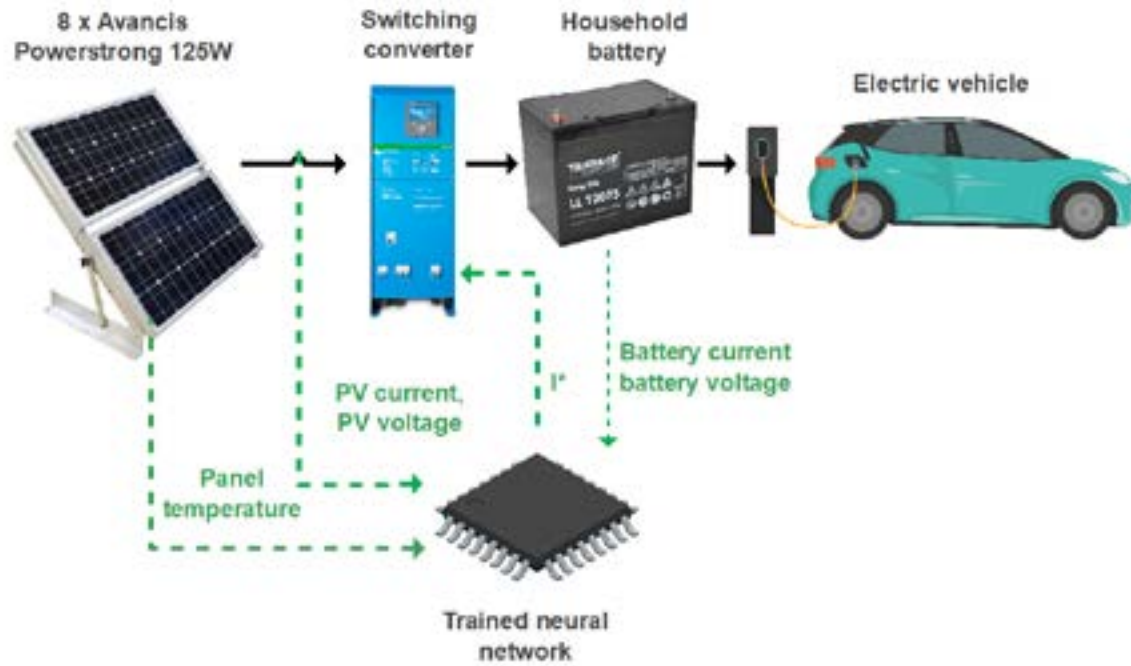


Figure 3 Principal schematics of the MPPT system based on ANN

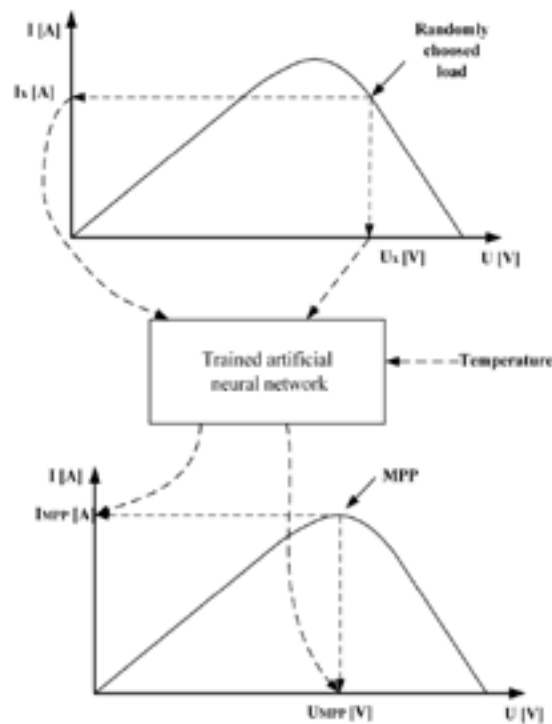


Figure 4 Principal working diagram of proposed MPPT algorithm based on ANN

The MPP searching algorithm, due to trained values, estimates the PV current, PV voltage and the PV power at the maximal power point (3 output neurons). Then in the MPPT algorithm the estimated MPP current by the ANN is requested by the switching converter interpreted by the change of duty of the PWM signal. This cycle periodically in the infinite loop. The graphical interpretation of the proposed MPPT algorithm is shown in Figure 4 [16].

4 Methods

The real PV installation contained 8 x (2 in series, 4 in parallel) amorphous CSI (copper-selenium-indium) Avancis Powermax 125W panels. The installation of PV panels is shown in Figure 5. Electrical parameters of the PV panel are described in Table 1.

The neural network's input data were obtained from the simulation of P-V and I-V characteristics of the PV



Figure 5 The PV string installation on the University Science Park's roof in Zilina, Slovakia

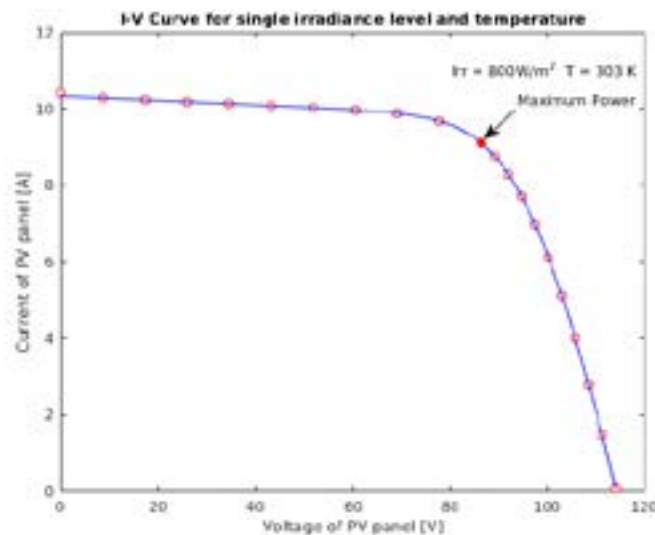


Figure 6 I-V curve of the PV panel

Table 1 The specification of single Avancis PowerMax 125 PV

Maximum power	125 W
Voltage at maximum power	44 V
Current at maximum power	2.84 A
Open circuit voltage	59.3 V
Short circuit voltage	3.22 A
Nominal operating voltage	52.6 V

panels in MATLAB Simulink There were 96 different temperature levels (min -20 °C; max 75 °C; step 1 °C) and 100 irradiance levels (min 10 W/m²; max 1000 W/m²; step 10 W/m²). During the PV panels simulation more than 200 000 unique combinations of mentioned parameters were created. The temperature, electrical current and voltage of the PV panel were chosen as input data of the neural network for MPPT control. Since MATLAB Simulink model of PV panel uses temperature and solar irradiance as input data, the reference values of electrical voltage and current of PV panels had to be

obtained for the neural network training. These electrical parameters were depended on temperature and solar irradiance level and were obtained in simulation. Figure 6 describes the process of gathering electrical parameters from I-V characteristics of the PV panels. The 10 points were chosen from point of maximum power (red circle) towards the zero current and 10 points towards the maximum current of photovoltaic panel characteristics. The intervals were linearly spaced along the x axis; therefore, one solar irradiance value corresponded to 21 current and voltage values.

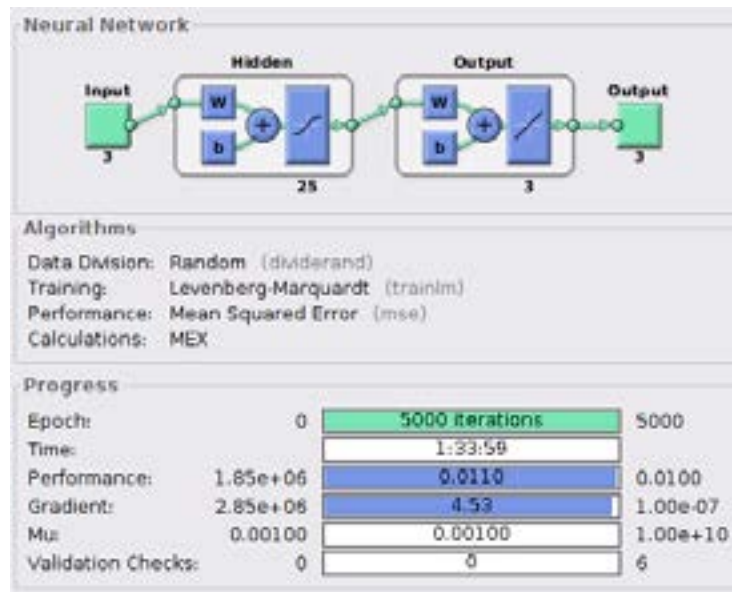


Figure 7 The proposed architecture of the ANN for MPPT controller

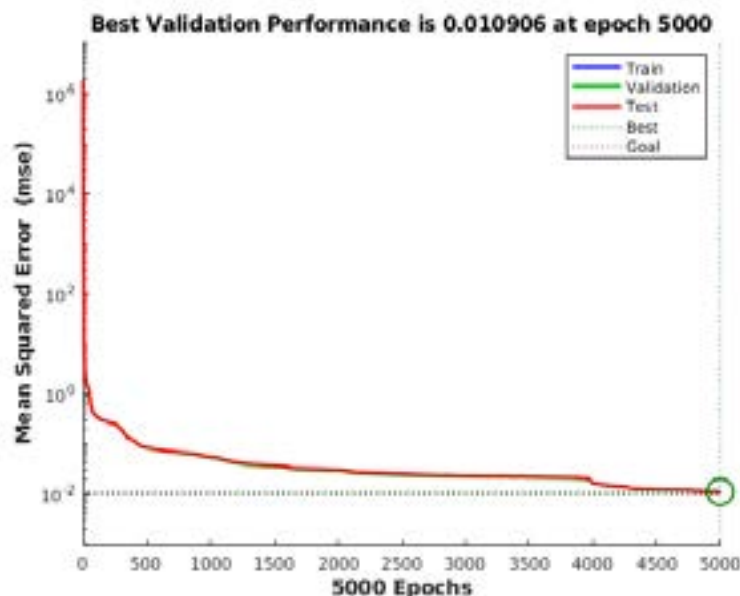


Figure 8 The ANN's training performance vs. epochs

The neural network contains 3 input neurons - input current, input voltage and input temperature. Hidden layer contains 25 neurons and output layer contains 3 neurons. These 3 neurons (outputs) interpret the PV current (1st neuron), PV voltage (2nd neuron) that occurs at the maximum output power (3rd neuron) for specified input temperature of PV panels. The sigmoidal activation function was used in the hidden layer and the linear activation function in the output layer. The network was trained with Levenberg-Marquardt optimization algorithm [7]. Number of neurons in the hidden layer was obtained experimentally as a number with the best network's MSE (mean squared error) in an interval (5; 50). Due to improving the training time, the conjugate gradient optimization method was chosen and every ANN architecture was trained 10 times by

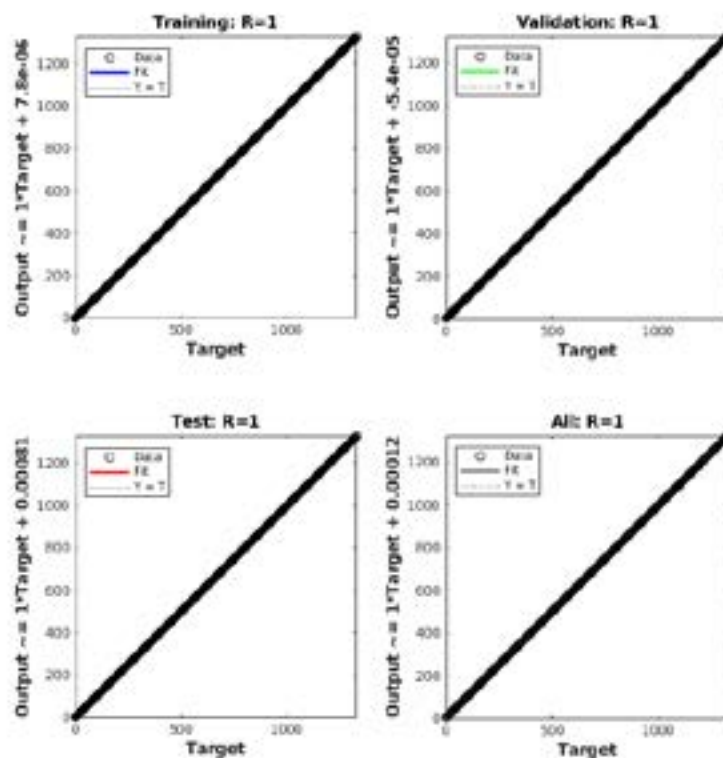
resetting state of random number generator at each trial. In order to potentially implement the neural network in a microcontroller, the basic type of the feed-forward 2-layer neural network (FFNN) was chosen. The ANN was implemented with MATLAB and its architecture is shown in Figure 7.

5 Simulation results

The dataset was divided to training (70 %), validation (15%) and testing (15%) set. The effort to prevent the ANN from overfitting was important, therefore the division of data to individual sets was random and training was stopped after increasing of network's error in validation set. Several optimization

Table 2 The ANN performance in individual cases (R^* is rounded to 7 decimal places)

Case	MSE	Corr. coef. R^*
1	0.0251	1.0
2	0.0524	1.0
3	0.1011	1.0
4	0.0249	1.0
5	0.0536	1.0
6	0.0801	1.0
7	0.0251	1.0
8	0.0524	1.0
9	0.0199	1.0
10	0.0149	1.0

**Figure 9** Regression plots across training, validation and test set

methods for the neural network training have been compared. Finally, the Levenberg-Marquardt algorithm was chosen, since the best network's performance and speed of convergence were achieved. The training's stop criterium was met at finishing 5000 iteration cycles or MSE (mean-square error) lower than 0.0001. Figure 8 shows the dependence of the neural network MSE on iteration cycles. The convergence speed is very high and MSE decreased more than 1000 times during the initial iterations. This result is consistent over validation and testing set, as well as in the whole spectrum of tested values.

Table 2 shows neural network's mean square error after 1000 training iteration cycles and regression coefficients in 10 random training cases. No significant

increasing of MSE parameter in validation set was observed. The correlation coefficient R is related to linear correlation between target and predicted values of neural network model. R is considered as indicator of goodness of neural network's fit for the observation data and is expressed as:

$$R = \frac{\sum_{i=1}^n (x_i - \bar{x})(y_i - \bar{y})}{\sqrt{\sum_{i=1}^n (x_i - \bar{x})^2} \sqrt{\sum_{i=1}^n (y_i - \bar{y})^2}} \quad (3)$$

where:

- x_i predicted value of sample i
- \bar{x} mean of predicted values
- y_i target value of sample i
- \bar{y} mean of target values
- n sample size (number of patterns)

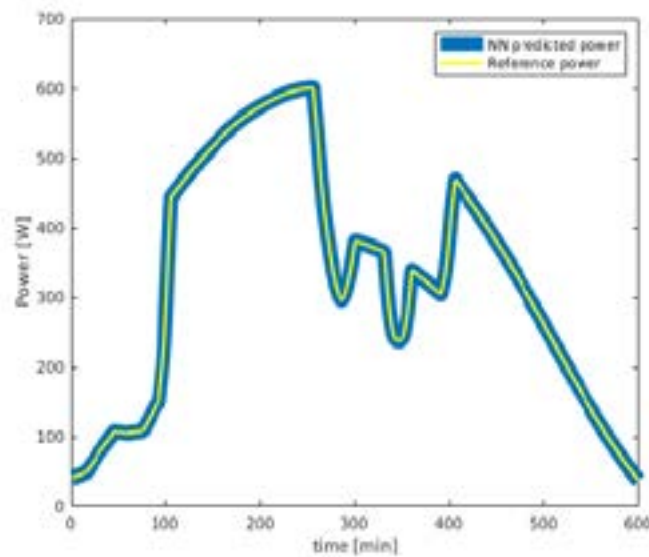


Figure 10 The comparison of ANN's predicted power versus the reference power

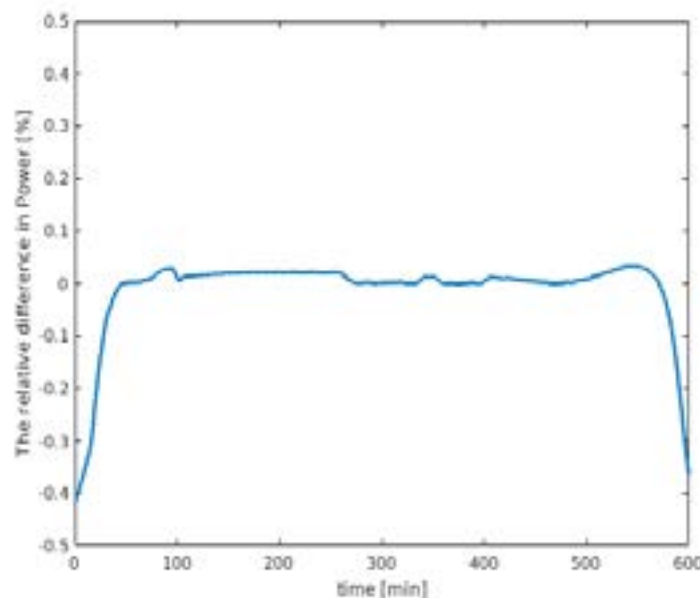


Figure 11 The relative difference in ANN predicted power versus the reference power

Figure 9 shows regression plots of training, validation and test sets. The regression coefficient in all sets is close to 1. These results successfully confirmed the ANN ability to track maximum power with high accuracy.

In order to verify capability of the trained neural network to track the maximum power of the PV panel, the numerical simulation was performed. The simulation input data were collected from Copernicus Atmosphere Monitoring Service (CAMS) after registration on the SoDa web service [17]. The time series of temperature and beam irradiation for the actual geographical location and weather condition were obtained for year 2020. These data were analysed with respect to cumulative absolute difference in solar irradiance during the day.

The September 12, 2020 was chosen as an example for graphic presentation of NN performance since the solar irradiance was changing significantly during the day. The irradiance and temperature were used for computing the reference values of maximum power (blue curve in Figure 10) of the PV panels simulated in MATLAB Simulink. The ANN simulated maximum power corresponds to yellow curve. Since the curves were completely overlapped, different widths of lines were chosen. These results confirmed neural network's potential to quickly respond to sudden changes of solar irradiance, since the network error did not increase in predicted maximum power.

Figure 10 shows the relative difference in predicted power of used neural network model versus the reference

power obtained from the atmospheric data. The same irradiance and temperature obtained from online CAMS service on September 12, 2020 were used for computation of power reference values [18]. The relative difference in predicted and real power, as shown in Figure 11, was obtained below 0.1% during the most of the day and did not exceed 0.5% at sunrise and sunset periods.

6 Conclusions

In this article, the MPPT algorithm, based on artificial neural network, for modern household with an electric vehicle, was presented. All the parameters of the PV system and MPPT controller were designed to achieve the best maximum power point tracking efficiency and maximum charging performance of the EV's battery. The final architecture of neural network, layers and activation functions were described. The main advantage of the proposed model is simplicity of obtaining the neural network input data such as voltage, current or temperature. The solar irradiance sensors are not needed. The electrical current, voltage and temperature of PV panels are easily measurable variables with affordable sensors. The neural network model's input data were obtained from computer simulations of the PV panels at wide range of solar irradiance and temperature values. The exact method of generating electrical current and voltage values for

neural network input was introduced. This method requires I-V curves of a particular PV panel under various solar irradiance values. The needed I-V curves of that PV panel can be generated in MATLAB Simulink, the solar irradiance and temperature are only required parameters. The neural network's performance was tested in computer simulation based on satellite-derived solar irradiance data. The presented neural network MPPT model can quickly respond to sudden changing of solar irradiance values. The response time depends mainly on speed of input data acquisition since the neural network model contains only 150 weight connections. Partial shading conditions of the PV systems were not the object of this research. Additional sensors, measuring the shielded area of a PV system, could provide important information for neural network in order to deal with partial PV panels shading conditions. These conditions will be a part of the authors' future research.

Acknowledgement

This publication was realized with support of Operational Program Integrated Infrastructure 2014 - 2020 of the project: Innovative Solutions for Propulsion, Power and Safety Components of Transport Vehicles, code ITMS 313011V334, co-financed by the European Regional Development Fund.

References

- [1] CAMERON, L., VAN DER ZWAAN, B. Employment factors for wind and solar energy technologies: a literature review. *Renewable and Sustainable Energy Reviews* [online]. 2015, **45**, p. 160-172. ISSN 1364-0321. Available from: <https://doi.org/10.1016/j.rser.2015.01.001>
- [2] LEWIS, N. S. Toward cost - effective solar energy use. *Science* [online]. 2007, **315**(5813), p. 798-801. ISSN 1095-9203. Available from: <https://doi.org/10.1126/science.1137014>
- [3] POLMAN, A., KNIGHT, M., GARNETT, E. C., EHRLER, B., SINKE, W. C. Photovoltaic materials: present efficiencies and future challenges. *Science* [online]. 2016, **352**(6283), aad4424. ISSN 1095-9203. Available from: <https://doi.org/10.1126/science.aad4424>
- [4] RASHID, M. H. *Power electronics handbook* [online]. 4.ed. Oxford: Butterworth-Heinemann, 2018. ISBN 9780128114070, eISBN 9780128114087. Available from: <https://doi.org/10.1016/C2016-0-00847-1>
- [5] LAUDANI, A., MANCILLA-DAVID F., RIGANTI-FULGINEI F., SALVINI A., Reduced-form of the photovoltaic five-parameter model for efficient computation of parameters. *Solar Energy* [online]. 2013, **97**, p. 122-127. ISSN 0038-092X. Available from: <https://doi.org/10.1016/j.solener.2013.07.031>
- [6] MANCILLA-DAVID F., RIGANTI-FULGINEI F., LAUDANI A., SALVINI A., A neural network-based low-cost solar irradiance sensor. *IEEE Transactions on Instrumentation and Measurement* [online]. 2014, **63**(3), p. 583-591. ISSN 0018-9456, eISSN 1557-9662. Available from: <https://doi.org/10.1109/TIM.2013.2282005>
- [7] SIRAT, J. A., NADAL, J. P. Neural trees: a new tool for classification. *Network: Computation in Neural Systems* [online]. 1990, **1**(4), p. 423-438. ISSN 0954-898X, eISSN 1361-6536. Available from: https://doi.org/10.1088/0954-898X_1_4_003
- [8] HAYKIN, S. *Neural networks: a comprehensive foundation*. Vol. 2. Hoboken, New Jersey, USA: Prentice Hall, 1998. ISBN 0-13-273350-1.
- [9] KELLNER, J.; PRAZENICA, M. Design of charging system with the elimination of electric arc during switching off. In: 13th International Conference ELEKTRO 2020: proceedings. 2020. CFP2048S-USB. ISBN 978-1-7281-7541-6.

- [10] KELLNER, J., PRAZENICA, M. Example of inrush current elimination after connection of high input DC voltage. *Przegląd Elektrotechniczny* [online]. 2020, **96**(8), p. 102-105. ISSN 0033-2098. Available from: <https://doi.org/10.15199/48.2020.08.20>
- [11] SHERIFF, I. M., SESHADARI, S. Artificial neural network based MPPT of solar photovoltaic cells. *International Journal of Innovative Research in Science, Engineering and Technology* [online]. 2018, **7**(5), p. 5972-5982. ISSN 2347-6710, eISSN 2319-8753. Available from: <https://doi.org/10.15680/IJIRSET.2018.0705175>
- [12] LAUDANI, A., FULGINEI, F. R., SALVINI, A., LOZITO, G. M., MANCILLA-DAVID, F. Implementation of a neural MPPT algorithm on a low-cost 8-bit microcontroller. In: 2014 International Symposium on Power Electronics, Electrical Drives, Automation and Motion: proceedings [online]. IEEE. 2014. eISBN 978-1-4799-4749-2, p. 977-981. Available from: <https://doi.org/10.1109/SPEEDAM.2014.6872101>
- [13] CHORFI, J., ZAZI, M., MANSORI, M. A new intelligent MPPT based on ANN algorithm for photovoltaic system. In: 2018 6th International Renewable and Sustainable Energy Conference IRSEC 2018: proceedings [online]. IEEE. 2018. p. 1-6. Available from: <https://doi.org/10.1109/IRSEC.2018.8702858>
- [14] DI VINCENZO, M. E.; INFELD, D. Artificial neural network for real time modelling of photovoltaic system under partial shading. In: International Conference on Sustainable Energy Technologies ICSET: proceedings [online]. IEEE. 2010. ISBN 9781424471928, p. I-5. Available from: <https://doi.org/10.1109/ICSET.2010.5684464>
- [15] YILMAZ, U., TURKSOY, O., IBRIKICI, T., TEKE, A. Estimation of electrical characteristics and maximum power point of photovoltaic panel. *Journal of Electrical Systems* [online]. 2017, **13**(2), p. 255-265. ISSN 1112-5209. Available from: https://journal.esrgroups.org/jes/papers/13_2_4.pdf
- [16] LOUKIL, J., DERBEL, N. Control strategy for a photovoltaic/lead-acid batteries energy production system. *Journal of Electrical Systems* [online]. 2019, **15**(3), p. 459-479. ISSN 1112-5209. Available from: https://journal.esrgroups.org/jes/papers/15_3_9.pdf
- [17] FARANDA, R., LEVA, S., MAUGERI, V. MPPT techniques for PV systems: energetic and cost comparison. In: IEEE Power and Energy Society General Meeting: proceedings [online]. IEEE. 2008. ISSN 1932-5517. Available from: <https://doi.org/10.1109/PES.2008.4596156>
- [18] CAMS Radiation Service - Atmosphere Monitoring Service [online] [accessed 2021-02-03]. Available from: <http://www.soda-pro.com/web-services/radiation/cams-radiation-service>

TEMPERATURE CORRECTION OF DEFLECTIONS AND BACKCALCULATED ELASTICITY MODULI DETERMINED FROM FALLING WEIGHT DEFLECTOMETER MEASUREMENTS ON ASPHALT PAVEMENTS

Ilja Březina*, Ondřej Machel, Tomáš Zavřel

Transport Research Centre (CDV), Brno, Czech Republic

*E-mail of corresponding author: ilja.brezina@cdv.cz

Resume

The evaluation of the bearing capacity of asphalt pavements is usually performed by analysing the deflections measured by a Falling Weight Deflectometer (FWD). The deflection changes with the pavement temperature. In evaluation is necessary to consider the thermal gradient of pavement and perform the temperature correction. The article contains an analysis of effects of the pavement temperature on FWD results on the long-term monitored sections. The temperature correction was performed on measured deflections or back-calculated elasticity moduli. The moduli recalculated to the temperature of 20 °C according to both procedures were similar. Comparison of moduli determined by recalculation to moduli back-calculated from the deflection bowls measured at the temperature of 20 °C, has proven smaller differences for the moduli determined from the deflection bowl corrected to the temperature of 20 °C.

Article info

Received 3 March 2021

Accepted 13 May 2021

Online 18 October 2021

Keywords:

asphalt pavement,
elasticity modulus,
deflection,
deflectometer (FWD),
temperature correction

Available online: <https://doi.org/10.26552/com.C.2022.1.D1-D8>

ISSN 1335-4205 (print version)

ISSN 2585-7878 (online version)

1 Introduction

Asphalt layers of flexible pavements contain a bituminous binder that is sensitive to temperature changes occurring in a pavement due to air temperature changes. In [1] it is stated that the temperature of asphalt layers not only changes within the year, but within a single day, as well, when changes of temperature gradients occur in asphalt layers. A change in the stiffness of a bituminous binder used in asphalt mixtures causes a change in their stiffness. Therefore, a deflection measured in one place in a different time will have different values. This has to be considered in diagnostics and evaluation of asphalt pavement bearing capacity. The necessity of temperature correction has already been clearly proven in numerous scientific publications, e. g. [2-11].

Due to the fact that the temperature gradient in a pavement can be high (particularly during the sunny summer days), some requirements, limiting measurements in relation to pavement temperature, can be found. According to [12], the temperature of pavement during the measurement has to be in the range of 0 - 30 °C. The temperature of pavement is characterized by the average temperature of asphalt layers, which is considered as the temperature in a certain depth under the pavement surface, e. g. 40 mm [1-12] or 50 mm [10].

As the average temperature of asphalt layers should be determined at every diagnostic point, a non-destructive method, based on the surface temperature of pavement and temperature gradients during the day, is optimum for its determination. According to [13], the average temperature of asphalt layers can be determined from the surface temperature of asphalt pavement and the temperature difference between the surface temperature and the average temperature of asphalt layers. Other ways of predicting temperature in asphalt pavement, based on the pavement surface temperature, can be found e. g. in [14] or [15].

Two approaches of temperature correction can be used in the evaluation process of data from an FWD device. The first is the temperature corrections of deflections, which are subsequently used for back-calculation of elasticity moduli. Possible approaches, used for the temperature correction of deflections, are presented e. g. in [6, 10]. An important finding, regarding the temperature correction of deflections, is that the effect of temperature decreases with growing distance from the load axis and can be neglected at a certain distance. According to [10], the effect of temperature on deflections can be neglected at a distance longer than 600 mm from the load axis d . Different impact of temperature on deflections at various distances from the load axis was also proven in [6].

Table 1 Composition of tested pavements

Section	Thickness of layer (mm)			Total
	Asphalt	Base	Subbase	
1	190	200	200	590
2	100	400	0	500
3	110	200	200	510
4	350	450	0	800
5	70	450	0	520
6	180	400	0	580
7	250	200	400	850
8	140	400	0	540
9	120	300	0	420
10	90	300	0	390

The other option is the back-calculation of elasticity moduli for a specific temperature occurring during the measurement and temperature correction of the back-calculated moduli. Various reference temperatures are used worldwide depending on the next use (calculation of residual life, design of overlay thickness, etc.) and relates to used method. The value of 20 °C [4], or potentially 25 °C [5], is frequently used as a reference temperature. Equation published in [6] allows to select own reference temperature (e. g. 20 °C, 25 °C). The method of the elasticity moduli temperature correction is described in numerous publications, e. g. [4, 7-8, 11]. An extensive overview of models for the temperature correction of the asphalt layers elasticity moduli by different authors is shown in [2].

As the two mentioned approaches can lead to different outputs, the aim of the presented study was to investigate differences in the back-calculated moduli recalculated to the reference temperature of 20 °C using both approaches.

2 Experimental sections and methodology

The effect of temperature on measured deflections and back-calculated elasticity moduli was investigated on 10 testing sections with different composition of asphalt pavement structures (Table 1). Three points with the interval of 1m were selected for repeated testing in each section.

Deflections were generated and registered by the deflectometer FWD RODOS. Twenty cycles were performed at each testing point. Each cycle was executed at different temperature and consisted of three drops with the load force of 50 kN.

Temperature of air and pavement on surface, in the depth of 30 - 40 mm and 70 - 90 mm was registered during the measurements in the vicinity of the tested point. The total temperature range was 1-35 °C.

The modulus of elasticity of individual pavement layers was determined by back-calculation using the computer program PADAL.

3 Temperature correction of backcalculated elasticity moduli

This approach uses the elasticity moduli calculated for a specific temperature occurring during the measurements. These are corrected (recalculated) to a “reference” temperature.

The plot of temperature against elasticity moduli back-calculated directly from a measured deflection bowl and determination of the regression curve was the first step in determination of the temperature effect on asphalt layers elasticity moduli. The example in Figure 1 shows the back-calculated elasticity moduli derived from all the repeated measurements at three points of the section 5 that were performed at different times and temperatures. The coefficient of determination is high and the temperature effect on back-calculated modulus is evident.

The temperature correction coefficients of each section, intended for the recalculation of the back-calculated elasticity moduli to the reference temperature of 20 °C, were derived from the regression curve using the formula:

$$c_E = E_{20}/E_T, \quad (1)$$

where:

c_E = temperature correction coefficient for modulus of elasticity [-],

E_{20} = elasticity modulus of asphalt layers at the temperature of 20 °C calculated from the regression curve [MPa],

E_T = elasticity modulus of asphalt layers at the temperature T calculated from the regression curve [MPa].

The set of curves, representing the calculated temperature correction coefficients (Figure 2) was used for determination of a general formula:

$$c_E = e^{-0,0387(20-T)}. \quad (2)$$

Using this, the recalculation of elasticity modulus to the reference temperature of 20 °C was determined in the form:

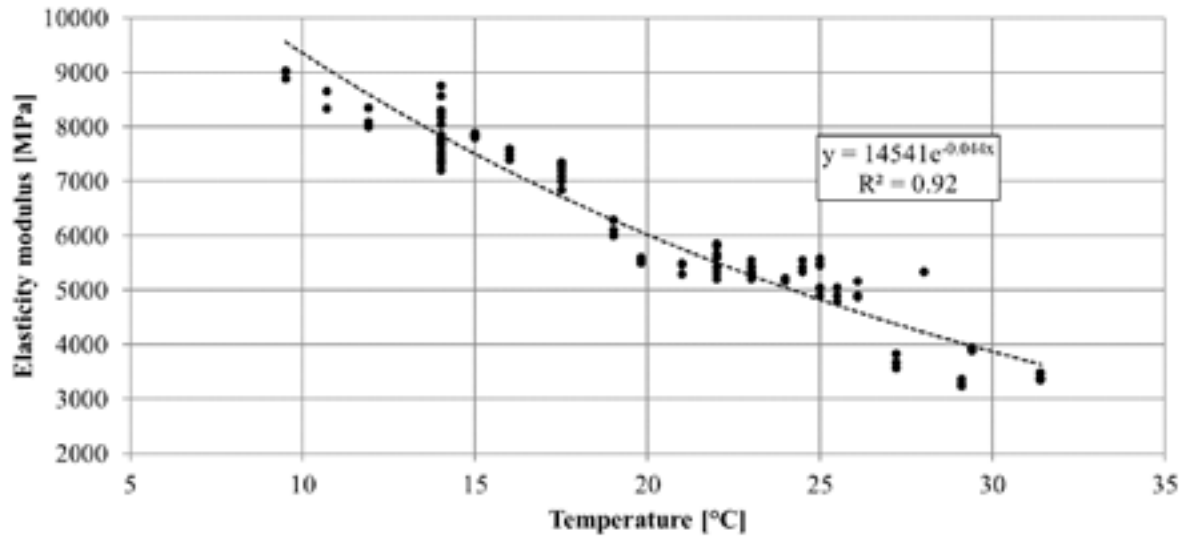


Figure 1 Variation of the asphalt layers elasticity moduli with temperature (section 5)

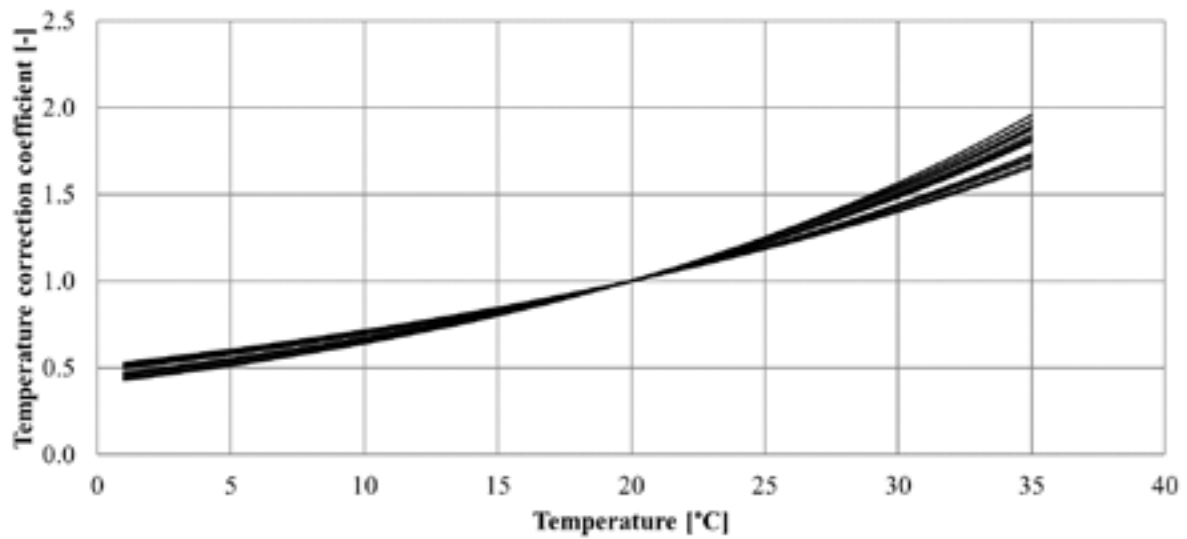


Figure 2 Calculated temperature correction coefficients

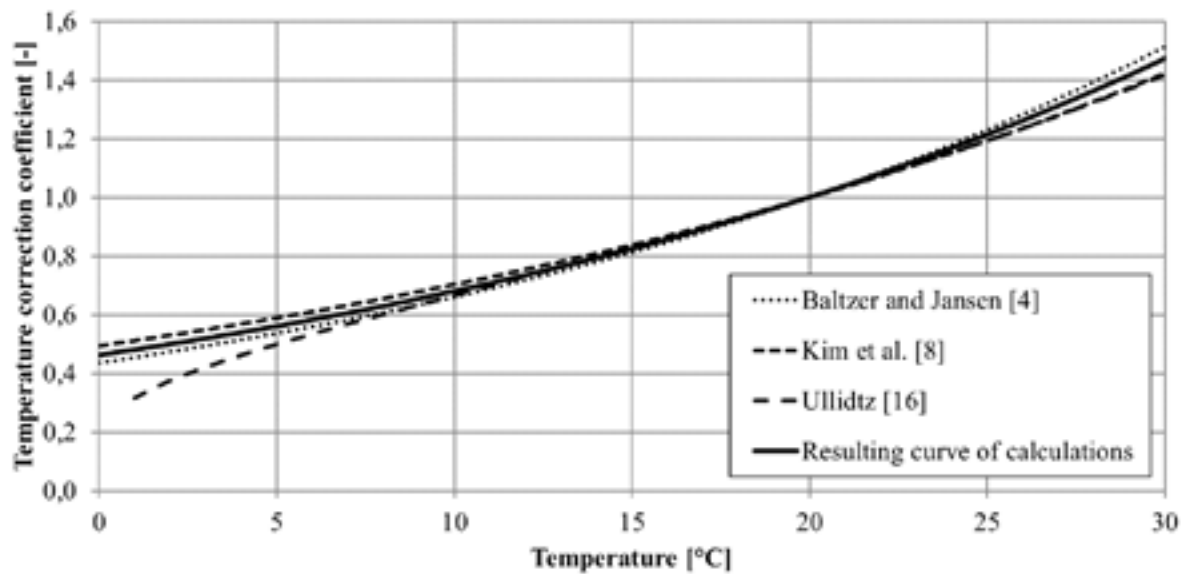


Figure 3 Comparison of determined correction to results of other authors

$$E_{20,cor} = E_T \cdot e^{-0.0387 \cdot (20 - T)}, \quad (3)$$

where:

$E_{20,cor}$ = elasticity modulus of asphalt layers corrected to the reference temperature of 20 °C [MPa],

E_T = back-calculated elasticity modulus of asphalt layers for the test temperature T [MPa],

T = test temperature of asphalt layers in the depth of 40 mm [°C].

The determined temperature correction coefficients of elasticity modulus of asphalt layers are similar to previously published results [4, 8, 16] (see Figure 3).

4 Temperature correction of measured deflections

The direct correction of deflections is another option how to consider the effect of temperature. To do this,

correction coefficients must be known. Therefore, the deflections measured at the position of sensors were plotted against the test temperature and a regression curve was derived (Figure 4). The example in Figure 4 that shows deflections from repeated measurements at the same point(s) at different times and temperature conditions, confirms the linear dependency for all the distances of sensors and variability of the temperature effect. The change in deflection due to the temperature variation is the most significant in the case of the central deflection (the distance of 0 mm from the load axis) and gradually decrease for the more distant sensors.

The temperature correction coefficients for each sensor to the reference temperature of 20 °C were derived from the regression curve using the formula:

$$c_d = d_{20}/d_T, \quad (4)$$

where:

c_d = temperature correction coefficient for deflections [-],

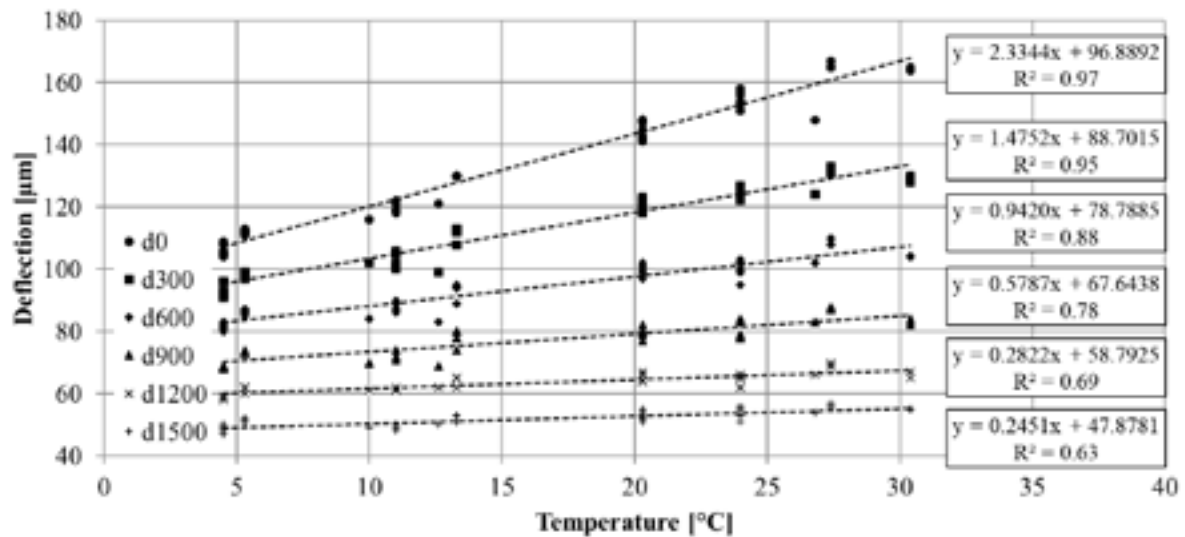


Figure 4 Change of deflections with temperature (section 5)

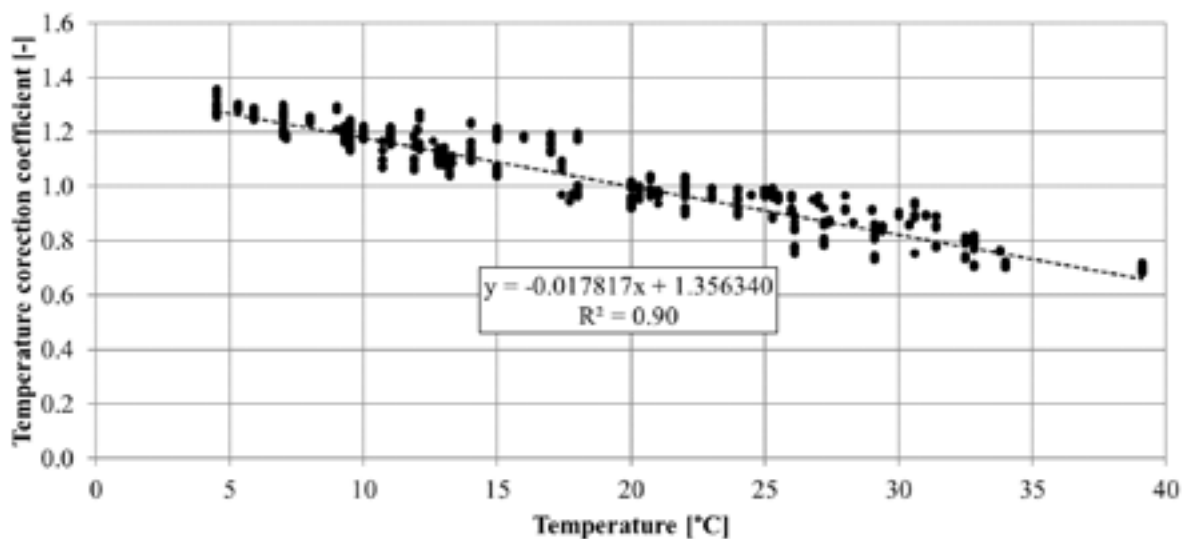


Figure 5 Regression curve of the temperature correction coefficient deflection d_0 (in the load axis)

d_{20} = deflection at the temperature of 20 °C calculated from the regression curve [μm],

d_T = deflection at the temperature T calculated from the regression curve [μm].

Subsequently, all of correction coefficients, calculated for a given sensor from the measurements on all of test sections, were grouped together and the final regression curve was derived (Figure 5). This procedure was applied for all the sensors and the regression curves according to distance of a sensor from the load axis given by Equations (5) - (10).

$$c_{d,0} = -0.017817 \cdot T + 1.35634 (R^2 = 0.90), \quad (5)$$

$$c_{d,300} = -0.012116 \cdot T + 1.24232 (R^2 = 0.82), \quad (6)$$

$$c_{d,600} = -0.007555 \cdot T + 1.15110 (R^2 = 0.64), \quad (7)$$

$$c_{d,900} = -0.0003958 \cdot T + 1.07916 (R^2 = 0.36), \quad (8)$$

$$c_{d,1200} = -0.002838 \cdot T + 1.05676 (R^2 = 0.24), \quad (9)$$

$$c_{d,1500} = -0.000631 \cdot T + 1.01262 (R^2 = 0.03), \quad (10)$$

where:

$c_{d,i}$ = deflection correction coefficient to the reference temperature of 20 °C at a distance i from loading axis [-].

As it was found out, the correction of deflections at sensors with spacing more than 900 mm from the load axis has marginal effect, the final equations for correction of deflections to the reference temperature of 20 °C were derived only for e deflections $d_0 - d_{900}$. They were set in the form:

$$d_{0,20,cor} = d_{0,T} \cdot (1 + 0.017817 \cdot (20 - T)), \quad (11)$$

$$d_{300,20,cor} = d_{300,T} \cdot (1 + 0.012116 \cdot (20 - T)), \quad (12)$$

$$d_{600,20,cor} = d_{600,T} \cdot (1 + 0.007555 \cdot (20 - T)), \quad (13)$$

$$d_{900,20,cor} = d_{900,T} \cdot (1 + 0.0003958 \cdot (20 - T)), \quad (14)$$

where:

$d_{i,20,cor}$ = deflection at a distance i from the load axis

corrected to the reference temperature of 20 °C [μm],

$d_{i,T}$ = deflection measured at temperature T at a distance i from the load axis [μm],

T = average temperature of asphalt layers in the depth of 40 mm [°C].

All the measured deflection bowls were subsequently corrected according to the derived equations. Then, example of the temperature correction of the deflection bowls to the reference temperature of 20 °C, is shown in Figure 6.

The corrected deflection bowls were used in the next step as an input for the back-calculation of elasticity modulus of pavement layers.

5 Comparison of the back-calculated moduli resulting from different approaches

This stage included statistical processing of moduli of elasticity determined by the back-calculation from the original (non-corrected) deflection bowls and subsequently corrected to the temperature of 20 °C and moduli of elasticity determined by the back-calculation from deflection bowls corrected to the temperature of 20 °C before performing the back-calculation. In the ideal case the elasticity moduli determined by both approaches should reach the same values.

The average elasticity moduli of asphalt layers, determined according to the presented approaches on all the tested sections, are shown in Figure 7. Three groups of moduli can be observed, which are located around the moduli of elasticity of 4500, 5500 and 7000 MPa. The elasticity moduli in each of the groups, determined by both approaches (Figure 8), differ slightly at the sections 1 - 7 and for these sections can be concluded that the used approach does not significantly affect the value of elasticity modulus recalculated to the reference temperature of 20 °C. More significant deviations can be observed for sections 8-10 with the higher moduli determined by recalculation of the modulus determined from an original deflection bowl.

The previous findings regarding the differences between the elasticity moduli of asphalt layers that are resulting from two used approaches, lead to a question,

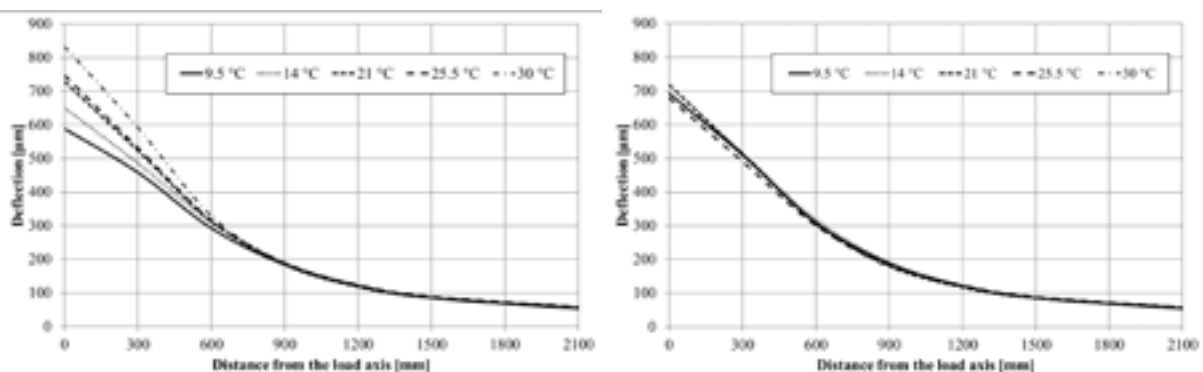


Figure 6 Deflection bowls measured at different temperatures (left) and corrected to the reference temperature of 20 °C; (right) section 5, point 1

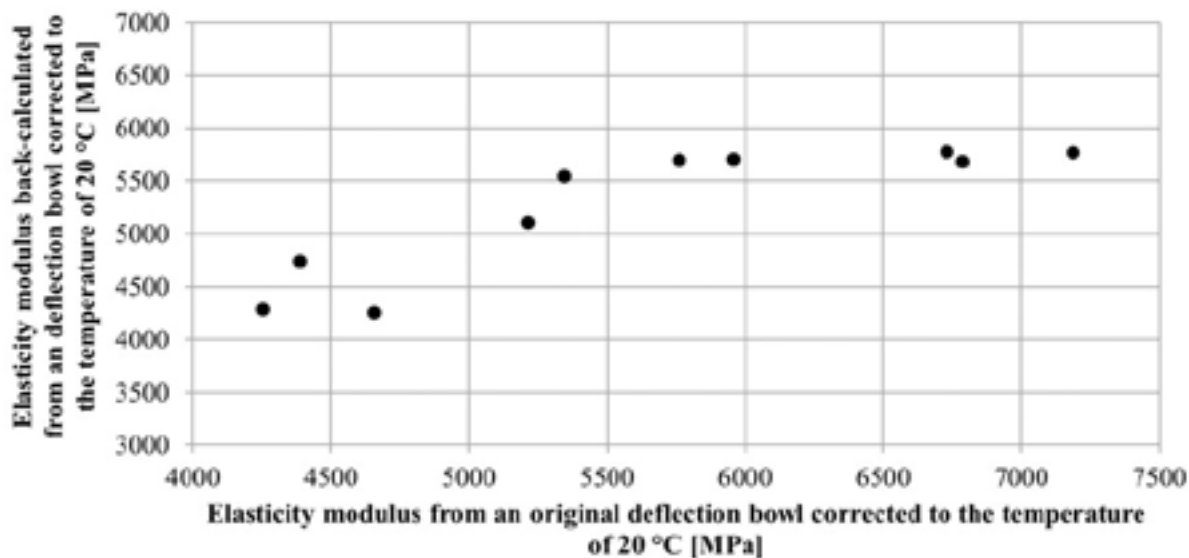


Figure 7 Average elasticity moduli of asphalt layers on tested sections

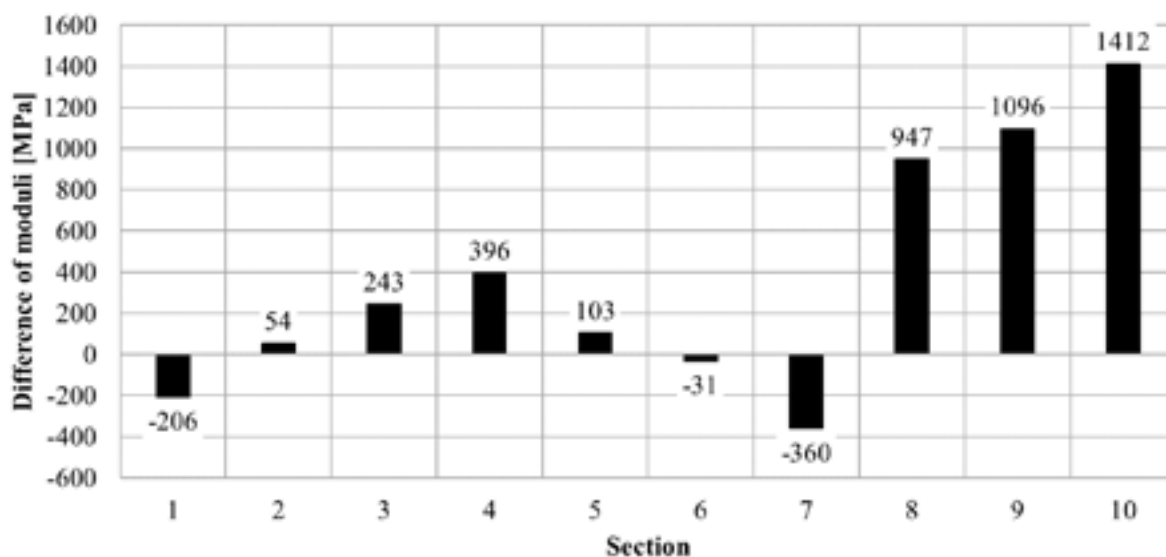


Figure 8 Differences in elasticity moduli of asphalt layers due to different approaches used for their determination

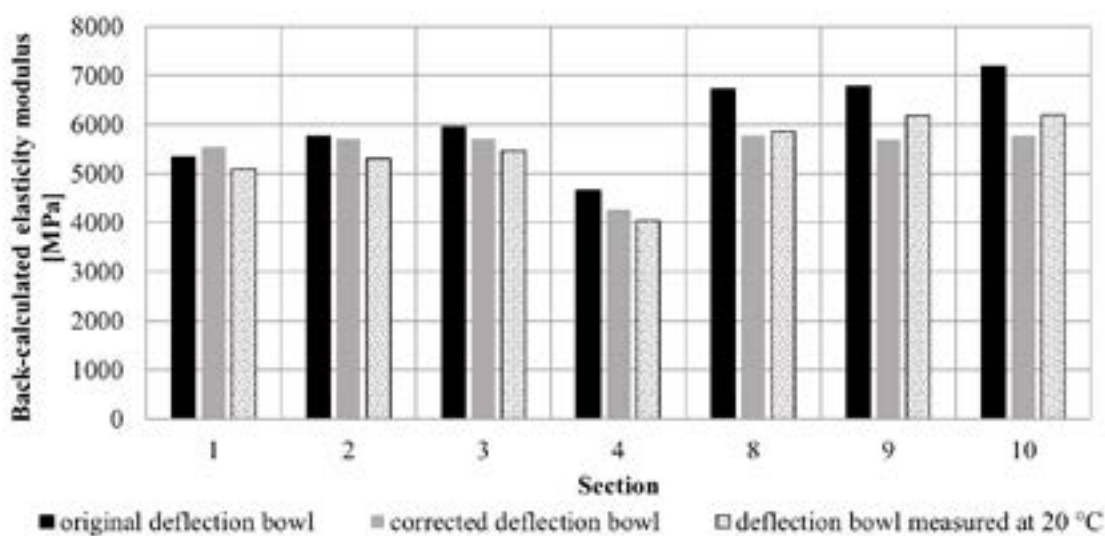


Figure 9 Elasticity moduli of asphalt layers recalculated to temperature of 20 °C and determined from measurements at temperature of 20 °C

which of approaches is more accurate. As both approaches recalculate moduli of deflection from a test temperature T to the reference temperature of 20 °C, the comparison of average recalculated moduli to values back-calculated from the deflection bowl measured exactly at 20 °C can be a useful information. Unfortunately, measurements at 20 °C were performed only on some of the test sections. Nevertheless, it is clear from Figure 9 that in most cases the moduli back-calculated from the corrected deflection bowl are closer to the values calculated directly for the test temperature of 20 °C.

6 Conclusions

The presented research confirmed known effect of temperature of asphalt pavement on measured deflections and back-calculated elasticity moduli.

Temperature correction of back-calculated moduli or measured deflections to the reference temperature of 20 °C was performed using temperature correction coefficient derived from regression curves.

Temperature correction coefficients applied on a measured deflection bowl were determined only for the sensors with spacing up to 900 mm from the load axis, since it was found out that the temperature

has marginal effect on deflections measured by more distanced sensors.

The comparison of elasticity moduli of asphalt layers determined for the reference temperature of 20 °C according to two applied approaches (the correction of moduli back-calculated from an original (non-corrected) deflection bowl vs the correction of measured deflection bowl to the reference temperature of 20 °C and the subsequent back-calculation of moduli) has proven similarity of moduli for majority of the tested sections. On the remaining sections, the moduli back-calculated from an original deflection bowl were higher. When the corrected moduli, or those determined from the corrected deflection bowl, were compared to moduli back-calculated from the deflection bowls measured at the temperature of 20 °C smaller differences were recorded for the moduli determined from the deflection bowl corrected to the reference temperature of 20 °C.

Acknowledgement

The research presented in this article was realized with the financial support of the Ministry of Transport of Czech Republic within the programme of long-term conceptual development of research institutions.

References

- [1] KOMACKA, J., KORENKO, M., PIALA, J. Relation of temperature changes in asphalt pavements to pavement bearing capacity evaluation. *Communications - Scientific Letters of the University of Zilina*. 2007, **9**(3), p. 33-36. ISSN 1335-4205, eISSN 2585-7878. Available from: <http://komunikacie.uniza.sk/index.php/communications/article/view/1139>
- [2] AKBARZADEH, H., BAYAT, A., SOLEYMANI, H., R. Analytical review of the HMA temperature correction factors from laboratory and falling weight deflectometer tests. *International Journal of Pavement Research and Technology* [online]. 2012, **5**(1), p. 30-39. ISSN 1997-1400. Available from: <http://www.ijprt.org.tw/files/sample/V5N1%2830-39%29.pdf>
- [3] APPEA, A. K. Validation of FWD testing results at the Virginia smart road: theoretically and by instrument responses [online]. Ph.D. Thesis. Blacksburg, Virginia: Faculty of the Virginia Polytechnic Institute and State University, 2003. p. 293. Available from: <http://hdl.handle.net/10919/26715>
- [4] BALTZER, S., JANSEN, J. M. Temperature correction of asphalt-moduli for FWD measurements. In: 4th International Conference Bearing Capacity of Roads and Airfields: proceedings. 1994. ISBN 9788790145149, p. 753-768.
- [5] CHANG, J.-R., LIN, J.-D., CHUNG, W.-CH., CHEN, D.-H. Evaluating the structural strength of flexible pavements in Taiwan using the falling weight deflectometer. *International Journal of Pavement Engineering* [online]. 2002, **3**(3), p. 131-141. ISSN 1029-8436. Available from: <https://doi:10.1080/1029843021000067854>
- [6] CHEN, D.-H., BILYEU, J., LIN, H.-H., MURPHY, M. Temperature correction on falling weight deflectometer measurements. *Transportation Research Record: Journal of the Transportation Research Board* [online]. 2000, **1716**(1), p. 30-39. ISSN 0361-1981. Available from: <https://doi:10.3141/1716-04>
- [7] JOHNSON, A. M., BAUS, R. L. Alternative method for temperature correction of backcalculated equivalent pavement moduli. *Transportation Research Record: Journal of the Transportation Research Board*. 1992, **1355**, p. 75-81. ISSN 0361-1981. Available from: <http://onlinepubs.trb.org/Onlinepubs/trr/1992/1355/1355-009.pdf>
- [8] KIM, Y. R., HIBBS, B. O., LEE, Y. CH. Temperature correction of deflections and backcalculated asphalt concrete moduli. *Transportation Research Record: Journal of the Transportation Research Board*. 1995, **1473**, p. 55 - 62. ISSN 0361-1981. Available from: <http://onlinepubs.trb.org/Onlinepubs/trr/1995/1473/1473-007.pdf>

- [9] PARK, H. M., KIM, Y. R., PARK, S. Temperature correction of multiloading-level falling weight deflectometer deflections. *Transportation Research Record: Journal of the Transportation Research Board* [online]. 2002, **1806**(1), p. 3-8. ISSN 0361-1981. Available from: <https://doi:10.3141/1806-01>
- [10] STRAUBE, E., JANSEN, D. Temperature correction of falling weight deflectometer measurements. In: 8th International Conference Bearing Capacity of Roads, Railways and Airfields BCR2A'09: proceedings. 2009. ISBN 9780415871990, p. 789-798.
- [11] STUBSTAD, R. N., BALTZER, S., LUKANEN, E. O., ERTMAN-LARSEN, H. J. Prediction of AC Mat temperatures for routine load/deflection measurements. In: 4th International Conference Bearing Capacity of Roads and Airfields: proceedings. Minneapolis, 1994. ISBN 9788790145149, p. 401 - 412.
- [12] European Commission. COST 336 Use of falling weight deflectometers in pavement evaluation. Final report of the action. 2. ed. Luxembourg: Office for Official Publications of the European Communities, 2005. p. 392.
- [13] KOMACKA, J. Change of bearing capacity characteristics of asphalt pavement. *Communications - Scientific Letters of the University of Zilina*. 2011, **13**(3), p. 52-55. ISSN 1335-4205, eISSN 2585-7878. Available from: <http://komunikacie.uniza.sk/index.php/communications/article/view/863>
- [14] ASTM D7228-06a Standard test method for prediction of asphalt-bound pavement layer temperatures. West Conshohocken: ASTM International, 2020.
- [15] PARK, D.-Y., BUCH, N., CHATTI, K. Effective layer temperature prediction model and temperature correction via falling weight deflectometer deflections. *Transportation Research Record: Journal of the Transportation Research Board* [online]. 2001, **1764**(1), p. 97-111. ISSN 0361-1981. Available from: <https://doi:10.3141/1764-11>
- [16] ULLIDTZ, P. *Pavement analysis. Developments in civil engineering*. Amsterdam: Elsevier Science Publishers B. V., 1987. ISBN 0-444-42817-8, p. 318.

THE STRESS-STRAIN STATE OF THE TUNNEL LINING THAT CROSSES THE FAULT ZONE OF SOIL BLOCKS DURING AN EARTHQUAKE

Mark R. Miller¹, Evgeniy Y. Titov², Sergey S. Kharitonov^{2*}, Yong Fang¹

¹Department of Civil Engineering, Southwest Jiaotong University, Chengdu, Sichuan, China

²Department of Bridges and Tunnels, Russian University of Transport (MIIT), Moscow, Russia

*E-mail of corresponding author: mr.kharitonov.94@mail.ru

Resume

The study examines the question of the tunnel behavior under seismic or geophysical load in the zone of changes in the hardness of the surrounding soil mass. In the course of the study, the internal forces and displacements arising in the structure of a tunnel in the zone of intersection of the boundaries of soil layers with different properties, in the case when these layers move relative to each other, were determined by analytical and numerical solutions. The data obtained by the analytical method was compared to numerical models using practical examples.

Article info

Received 17 January 2021

Accepted 31 March 2021

Online 22 October 2021

Keywords:

transport tunnels,
beam on an elastic foundation,
finite elements,
tunnel damage,
earthquake

Available online: <https://doi.org/10.26552/com.C.2022.1.D9-D22>

ISSN 1335-4205 (print version)

ISSN 2585-7878 (online version)

1 Introduction

During an earthquake, soil layers with different properties often move in different ways. Tunnels that cross such borders may be damaged [1-2]. Tunnels located in soft ground can be considered as beams in an elastic medium (or considered as beams on an elastic foundation), Figure 1. As a rule, faults are usually the boundaries of soil layers with different engineering and geological characteristics. This study examines the stress-strain state of the tunnel lining that crosses the fault zone of two soil blocks [3]. At this stage of calculation, the goal is to obtain analytical and numerical solutions and then compare them. The initial data are parameters of the lining cross-section, characteristics of the soil and value of the relative displacement of the soil layers [5].

2 The fault is perpendicular to the tunnel axis

2.1 Analytical method

Differential equation of the bending beam, (Figure 2) [7-8], is:

$$EI_x \frac{d^4 y}{dx^4} + kby = q. \quad (1)$$

The well-known solution of Equation (1) has the form:

$$y = e^{-\beta x} (C_1 \cos \beta x + C_2 \sin \beta x) + e^{\beta x} (C_3 \cos \beta x + C_4 \sin \beta x) + v_0(q), \quad (2)$$

where $\beta = \sqrt{\frac{kb}{4EI_x}}$, here k is a coefficient of the subgrade reaction, b is the width of a beam, E is Young modulus, I_x is a moment of inertia.

In this case, the deformed view is as in Figure 3.

For simplifying the solution, the model of the semi-infinite beam on an elastic foundation is used (Figure 4), when $0 \leq x \leq \infty$. In this case, if $x \rightarrow \infty, e^x \rightarrow \infty$, there is no physical meaning, so $C_3 - C_4 = 0$. In addition, from initial data follows that $q = 0$.

In view of the above, Equation (2) will take a form:

$$y = e^{-\beta x} (C_1 \cos \beta x + C_2 \sin \beta x). \quad (3)$$

To define the integration constants C_1 and C_2 , one has to twice take the derivative of a function in Equation (3). Below is the sequence of actions for this operation.

$$\begin{aligned} y &= C_1 e^{-\beta x} \cos \beta x + C_2 e^{-\beta x} \sin \beta x \\ y' &= C_1 (e^{-\beta x} \cos \beta x)' + C_2 (e^{-\beta x} \sin \beta x)' \\ 1. (e^{-\beta x} \cos \beta x)' &= -\beta e^{-\beta x} \cos \beta x + \\ &+ \beta e^{-\beta x} (-\sin \beta x) = \beta e^{-\beta x} (-\cos \beta x - \sin \beta x) \end{aligned} \quad (4)$$

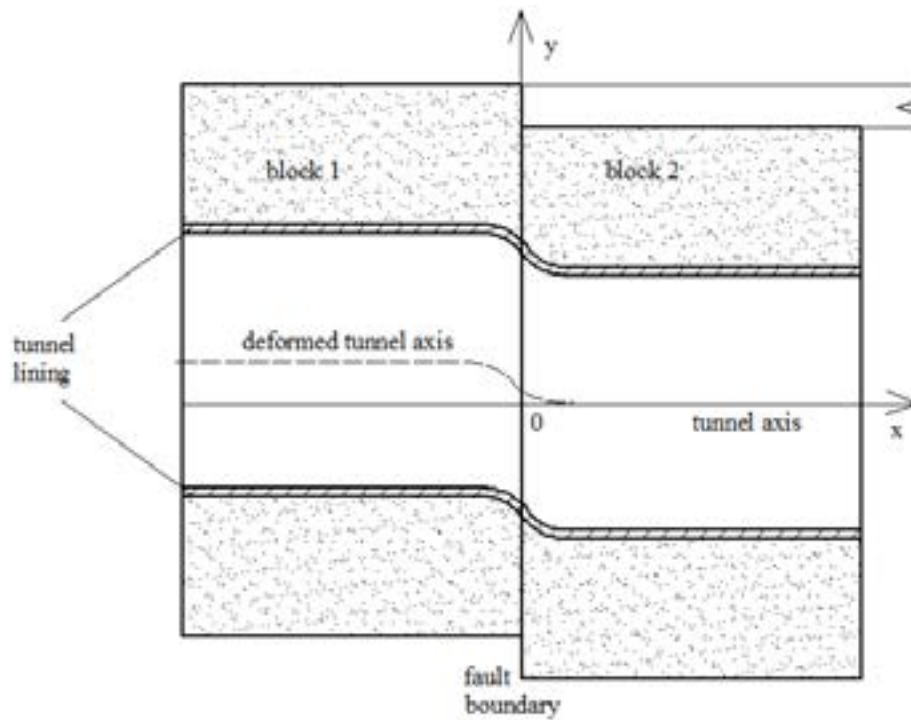


Figure 1 Scheme of a tunnel through fault fracture zone

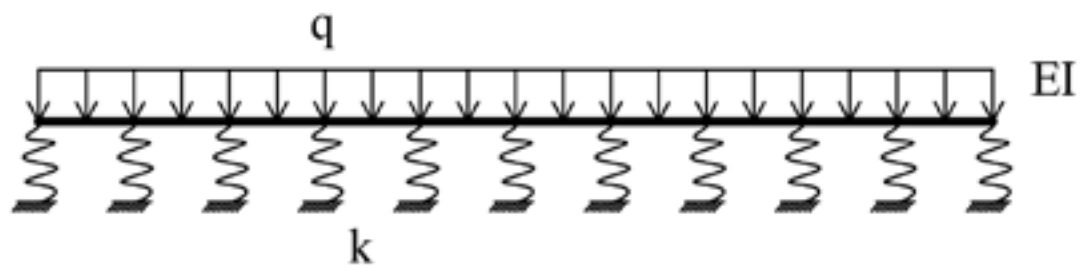


Figure 2 Classical beam on elastic foundation using the Winkler assumption

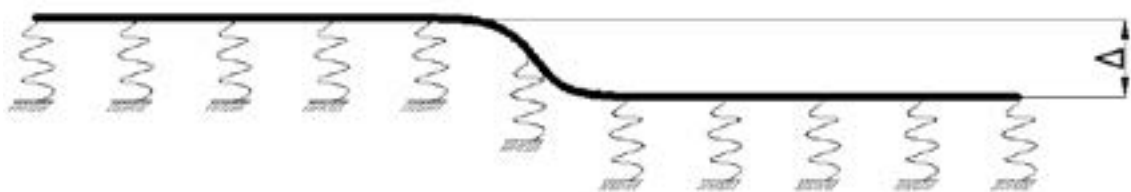


Figure 3 Deformed view of the calculation scheme

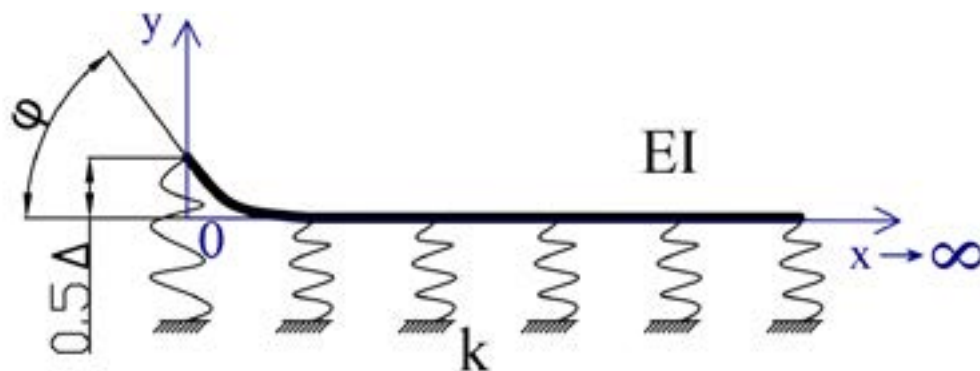


Figure 4 Accepted calculation scheme

$$\begin{aligned}
 2. (e^{-\beta x} \sin \beta x)' &= -\beta e^{-\beta x} \sin \beta x + \\
 &+ \beta e^{-\beta x} \cos \beta x = \beta e^{-\beta x} (-\sin \beta x + \cos \beta x) \\
 y' &= C_1 [\beta e^{-\beta x} (-\cos \beta x - \sin \beta x)] + \\
 &+ C_2 [\beta e^{-\beta x} (-\sin \beta x + \cos \beta x)].
 \end{aligned}
 \tag{4}$$

$$\begin{aligned}
 y'' &= C_1 \beta [-e^{-\beta x} \cos \beta x - e^{-\beta x} \sin \beta x]' + \\
 &+ C_2 \beta [e^{-\beta x} \cos \beta x - e^{-\beta x} \sin \beta x]' \\
 y'' &= C_1 \beta \left[-\beta e^{-\beta x} (-\cos \beta x - \sin \beta x) - \right. \\
 &\left. -\beta e^{-\beta x} (-\sin \beta x + \cos \beta x) \right] + \\
 &+ C_2 \beta \left[\beta e^{-\beta x} (-\cos \beta x - \sin \beta x) - \right. \\
 &\left. -\beta e^{-\beta x} (-\sin \beta x + \cos \beta x) \right] \\
 y'' &= C_1 \beta^2 e^{-\beta x} \left[(\cos \beta x + \sin \beta x) - \right. \\
 &\left. -(\sin \beta x + \cos \beta x) \right] + \\
 &+ C_2 \beta^2 e^{-\beta x} \left[(-\cos \beta x - \sin \beta x) - \right. \\
 &\left. -(-\sin \beta x + \cos \beta x) \right] \\
 y'' &= C_1 \beta^2 e^{-\beta x} \left[\cos \beta x + \sin \beta x + \right. \\
 &\left. + \sin \beta x - \cos \beta x \right] + \\
 &+ C_2 \beta^2 e^{-\beta x} \left[-\cos \beta x + \sin \beta x + \right. \\
 &\left. + \sin \beta x - \cos \beta x \right] \\
 y'' &= C_1 \beta^2 e^{-\beta x} * 2 \sin \beta x - C_2 \beta^2 e^{-\beta x} * 2 \cos \beta x \\
 y'' &= 2\beta^2 e^{-\beta x} (C_1 \sin \beta x - C_2 \cos \beta x).
 \end{aligned}
 \tag{5}$$

If the properties of the neighboring ground-blocks and bending stiffness of the tunnel lining are constant, for right-hand part of an infinite beam the following boundary conditions can be used [9]:

$$\begin{cases} y(0) = \frac{\Delta}{2} \\ \frac{d^2 y(0)}{dx^2} = 0 \Rightarrow y''(0) = 0 \end{cases}
 \tag{6}$$

When $x = 0$, the tangent angle takes the extreme value, the second derivative should be equal to zero, whence follows $y''(0) = 0 > M(0) = 0$.

Substituting the boundary conditions in Equations (6), (3) and (5) gives:

$$\begin{aligned}
 1. y''(0) &= \frac{\Delta}{2}: \frac{\Delta}{2} = e^{-\beta \cdot 0} (C_1 \cos \beta * 0 + \\
 &+ C_2 \sin \beta * 0) = \\
 \Rightarrow C_1 &= \frac{\Delta}{2}, \\
 2. y''(0) &= 0: 0 = 2\beta^2 e^{-\beta \cdot 0} (C_1 \sin \beta * 0 - \\
 &- C_2 \cos \beta * 0) = \\
 \Rightarrow C_2 &= 0.
 \end{aligned}
 \tag{7}$$

Taking into the constants found, Equation (3) takes the form:

$$y = \frac{\Delta}{2} e^{-\beta x} \cos \beta x.
 \tag{8}$$

Using the well-known dependencies between the internal force factors (bending moment M and shear force Q) and a deflection function, one can get equations:

$$\begin{aligned}
 \frac{M}{EI} &= -y'' = -2\beta^2 e^{-\beta x} \frac{\Delta}{2} \sin \beta x; \\
 M &= -EI \Delta \beta^2 e^{-\beta x} \sin \beta x,
 \end{aligned}
 \tag{9}$$

$$\begin{aligned}
 \frac{Q}{EI} &= -y''' = -\Delta \beta^3 (e^{-\beta x} \sin \beta x)' = \\
 &= -\Delta \beta^3 [\beta e^{-\beta x} (-\sin \beta x + \cos \beta x)]; \\
 Q &= EI \Delta \beta^3 e^{-\beta x} (\cos \beta x - \sin \beta x).
 \end{aligned}
 \tag{10}$$

The presence of $e^{-\beta x}$ multiplier in equations indicates that all these functions decrease with increasing distance from the block border ($x \rightarrow \infty, e^{-\beta x} \rightarrow 0$). One

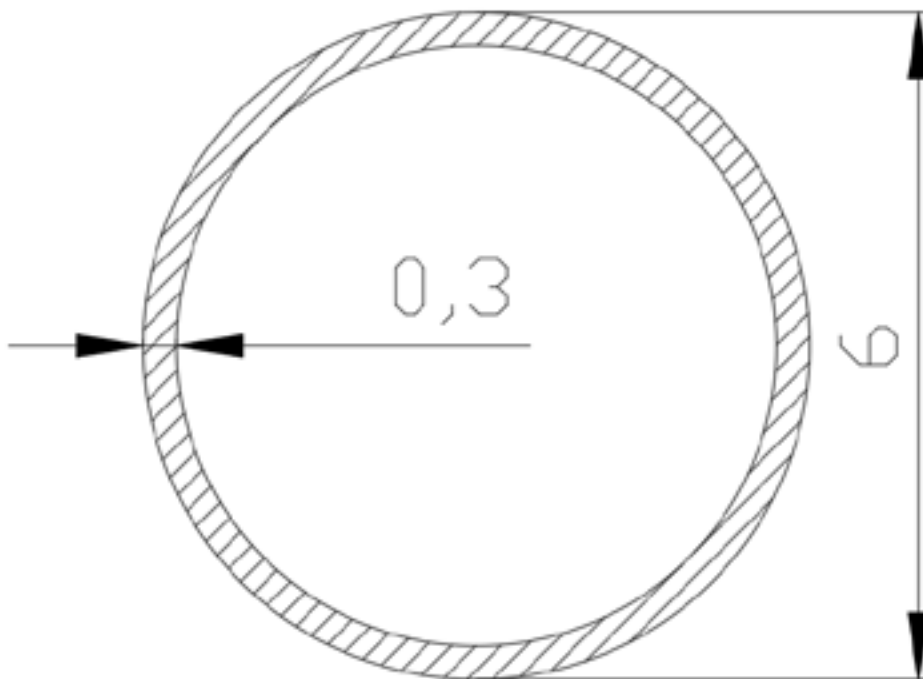


Figure 5 Cross-section area of the tunnel lining

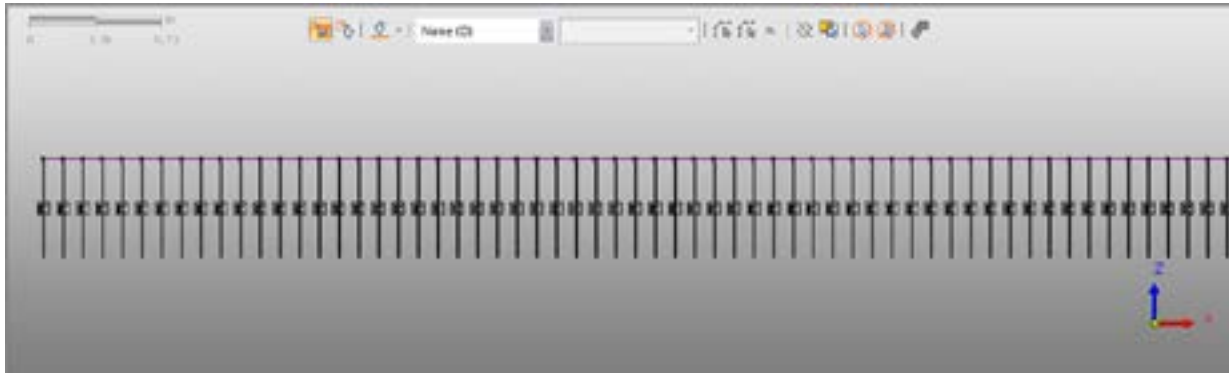


Figure 6 Part of the finite-element model of a beam on elastic foundation

can assess the zone of influence by function $e^{-\beta x}$. If $x = 0, e^{-\beta \cdot 0} = 1$.

If $\beta x = \pi, e^{-\pi} = 0.043$ and with an accuracy of 5% one can say that it equals to zero. In this case, from $\beta l_{\text{inf}} = \pi$ follows:

$$l_{\text{inf}} = \frac{\pi}{\beta}. \quad (11)$$

2.2 Example

As an example, the stress-strain state of the tunnel lining (Figure 5) is considered for the beam element. Parameters of concrete are: Young modulus $E = 35500 \text{ Mpa}$, Poisson ratio $\nu = 0.2$.

The vertical deflection of left-hand part is $\Delta = 0.01 \text{ m}$. The results were obtained by Excel and presented below (comparing the analytical solution to the numerical simulation's one).

2.3 Numerical simulation

2.3.1 Model of a Winkler's beam on elastic foundation

An analytical solution, using a mathematical model of a beam on elastic foundation, allows to quickly and easily assess the inertial forces factors in the tunnel lining from the displacement of blocks along the fault boundary; however that is not a universal solution. Numerical modeling helps to solve this problem. First, the numerical finite element model was created in the MIDAS GTS NX software, based on the calculation scheme of a Winkler beam on an elastic foundation (Figure 2). The beam nodes are connected to the ground by elastic springs with a step of 1m, the spring stiffness corresponds to the stiffness of the ground foundation. The length of the simulated tunnel section is 200 meters. The external impact is set as a 0.01m upward shift of the left block. The model is shown in Figure 6.

2.3.2 Model with the 2D plane strain elements.

The next step in verifying the proposed calculation method is to create a 2D model.

The tunnel lining is modeled by beam finite elements, a concrete is considered as the isotropic elastic material, using parameters like for a model of beam on an elastic foundation. The area of analysis is 200 x 40m. The surrounding ground mass is modeled by the 2D plane strain elements, using Mohr-Coulomb model with parameters: silty clay, Young modulus $E = 3700 \text{ kPa}$, Poisson ratio $\nu = 0.3$, friction angle $\varphi = 18.4^\circ$, cohesion $c = 33.8 \text{ kPa}$. A friction was modeled like an interface elements with strength reduction factor $R_c = 0.5$. This model is shown in Figure 7.

For the integrity of the analysis, the model of a beam on an elastic foundation was used, as well. In this case, one needs to use the coefficient of a subgrade reaction k .

Based on an elastic theory, Scott [6] derived the relation between the coefficient of subgrade reaction and a Young modulus, as follow:

$$k = \frac{E}{d(1 - \nu^2)}, \quad (12)$$

where d is a diameter of a pile.

For the presented method, it is acceptable to take d as the tunnel diameter. In this case, for the silty clay the coefficient is $k = 6777 \text{ kN/m}^2$.

For the convenience of estimating the stress-strain state in each model, the graphs for each case are presented in Figure 8.

2.4 Practical application

2.4.1 The 1D scheme

Using the numerical simulation model, a study of the changing inertial forces factors was carried with different stiffness of mountain blocks (Figure 9). Getting analytical results is a difficult procedure in solving

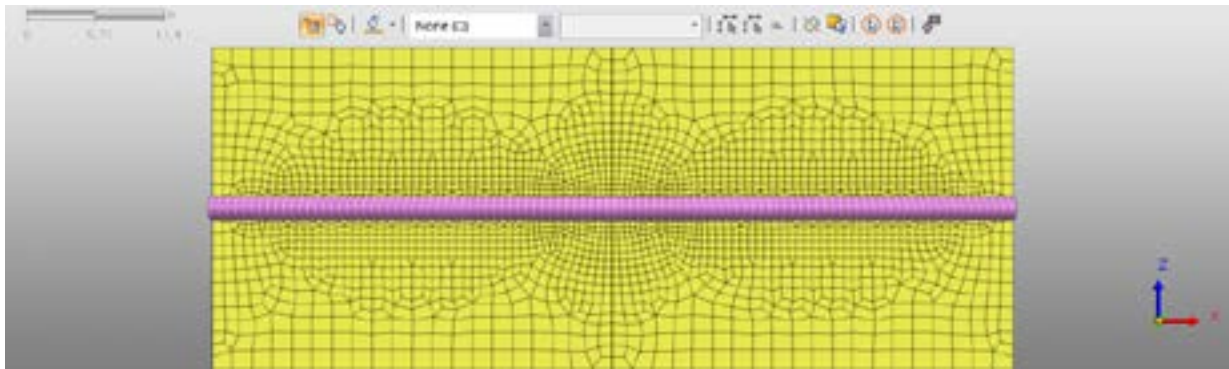


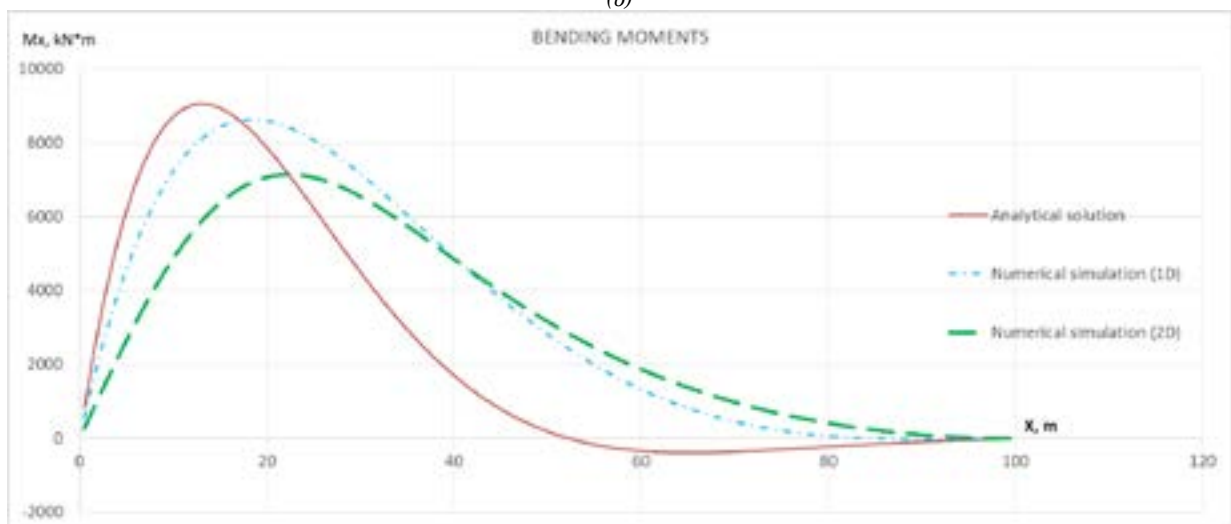
Figure 7 Model with the 2D plane strain elements



(a)



(b)



(c)

Figure 8 Results for the silty clay subgrade. Diagram of displacement (a), shear forces (b) and the bending moments (c)

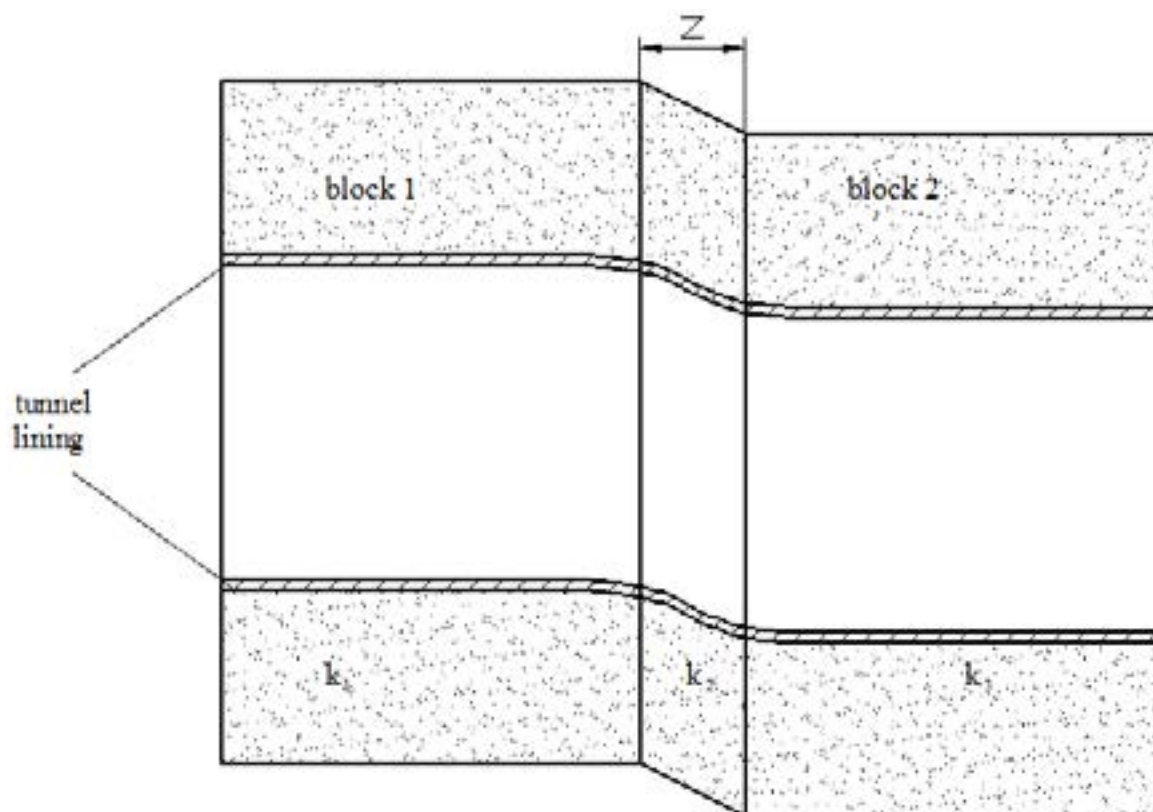


Figure 9 Using different coefficients subgrade reaction

such problems, because due to different stiffness of the rock blocks, the deformation and stress plots are not symmetrical.

The stiffness of the first block is characterized by a coefficient of subgrade reaction k_1 , the stiffness of the second block by k_3 and the filling space “z” between blocks by k_2 [9-10].

- a) An effect of the distance z on internal forces in the tunnel lining

Consider the following additional initial data:

$$k_1 = 40000 \text{ kN/m}^2, k_2 = 0.2k_1 = 8000 \text{ kN/m}^2, \\ k_3 = k_1 = 40000 \text{ kN/m}^2$$

The distance z varies from 10 to 100 meters. The results are presented in Figure 10.

- b) An effect of the value k_2 on internal forces in the tunnel lining

In this case consider the following additional initial data:

$$k_1 = 8000 \text{ kN/m}^2, k_2 = 10k_1 = 80000 \text{ kN/m}^2, z = 40 \text{ m.}$$

The coefficient k_2 takes values from 8000 to 80000 kN/m^2 . The results are presented in Figure 11. The most interesting is that with increase in the subgrade reaction coefficient, internal force factors increase too and the displacement diagram has t changed slightly.

2.4.2 The 2D scheme

Using this approach, similar operations were performed with the 2D scheme. For connection of the soil

models of the 1D and 2D schemes, the Scott Equation (12) is used.

- a) An effect of the distance z on internal forces in the tunnel lining

Consider the following additional initial data:

$$E_1 = 218400 \text{ kN/m}^2, E_2 = 0.2E_1 = 43680 \text{ kN/m}^2, \\ E_3 = E_1 = 218400 \text{ kN/m}^2$$

The distance z varies from 10 to 100 meters. The results are presented in Figure 12.

- b) An effect of the value k_2 on internal forces in the tunnel lining

In this case consider the following additional initial data:

$$E_1 = 43680 \text{ kN/m}^2, E_3 = 10E_1 = 436800 \text{ kN/m}^2, z = 40 \text{ m.}$$

E_2 takes values from 43680 to 436800 kN/m^2 . The results are presented in Figure 13.

3 The fault is along to the tunnel axis

3.1 Analytical method

Consider a tunnel with length $2L$, external diameter d , and with compressive (or tensile) stiffness EA . Using the Winkler model to describe the interaction of the surrounding soil mass and the tunnel structure, the coefficient of elastic resistance at the shift k_s is introduced (Figure 14).

The movement of the tunnel cross-sections w along the x axis is described by the following differential

equation [5]:

$$EA \frac{d^2 w}{dx^2} - \pi d k_s w = 0. \tag{13}$$

3.2 Example

For example, a tunnel lining with the above

characteristics was adopted: $A = 5.372 \text{ m}^2$, $d = 6 \text{ m}$. Coefficient k_s is adopted as a quarter of the normal coefficient of subgrade reaction. For silty clay: $k_s = 2000 \text{ kN/m}^2$.

For the ease of calculation, consider the right-hand cut-off part in accordance with the methods of strength of materials (Figure 15).

The well-known differential relationship between

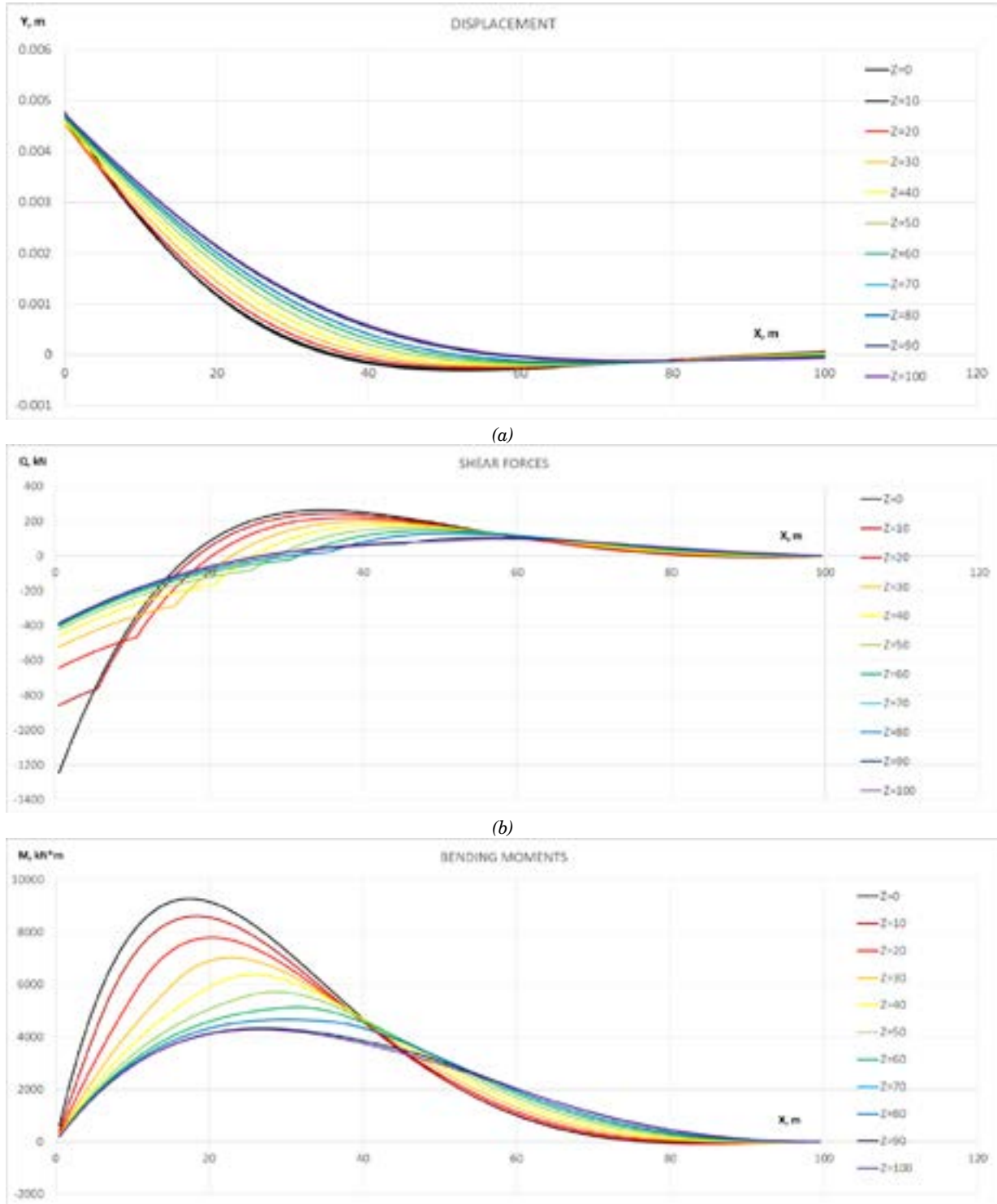


Figure 10 Diagram of displacement (a), shear forces(b) and bending moments(c) in terms of z (1D scheme)

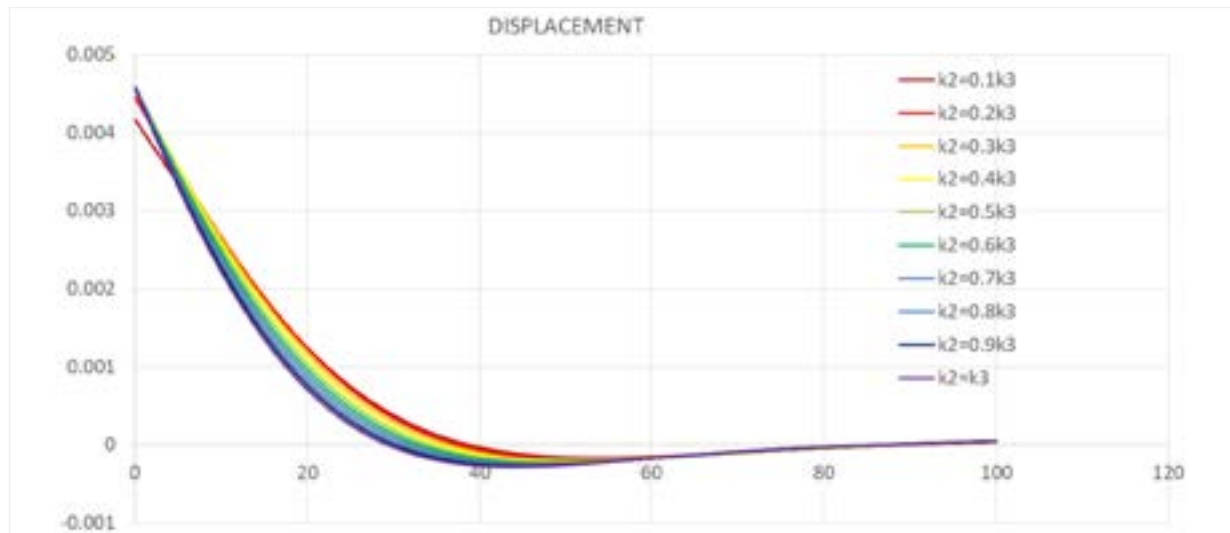
the force and the deflection is:

$$EA \frac{d^2 w}{dx^2} = N_z \tag{14}$$

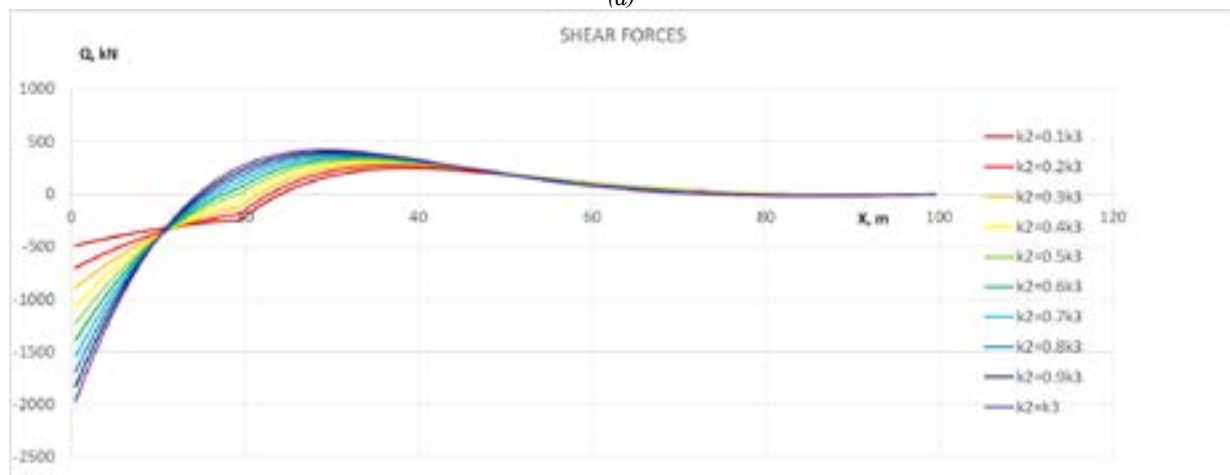
$$N_z = \pi d k_s w = 1687 \text{ kN} . \tag{15}$$

Given Equation (13) and the equilibrium equation for the right-hand cut-off part, one gets:

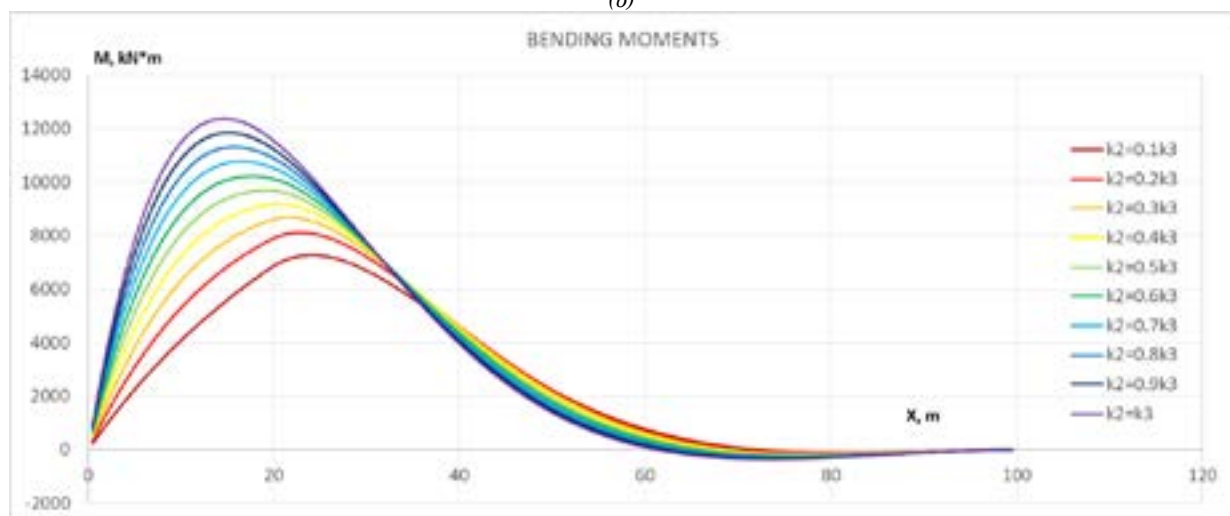
Obviously, the force at the ends of the tunnel is equal to zero. Then, one can plot the diagram internal forces N_z .



(a)



(b)



(c)

Figure 11 Diagram of displacement (a), shear forces(b) and bending moments (c) in terms of k_2 (1D scheme)

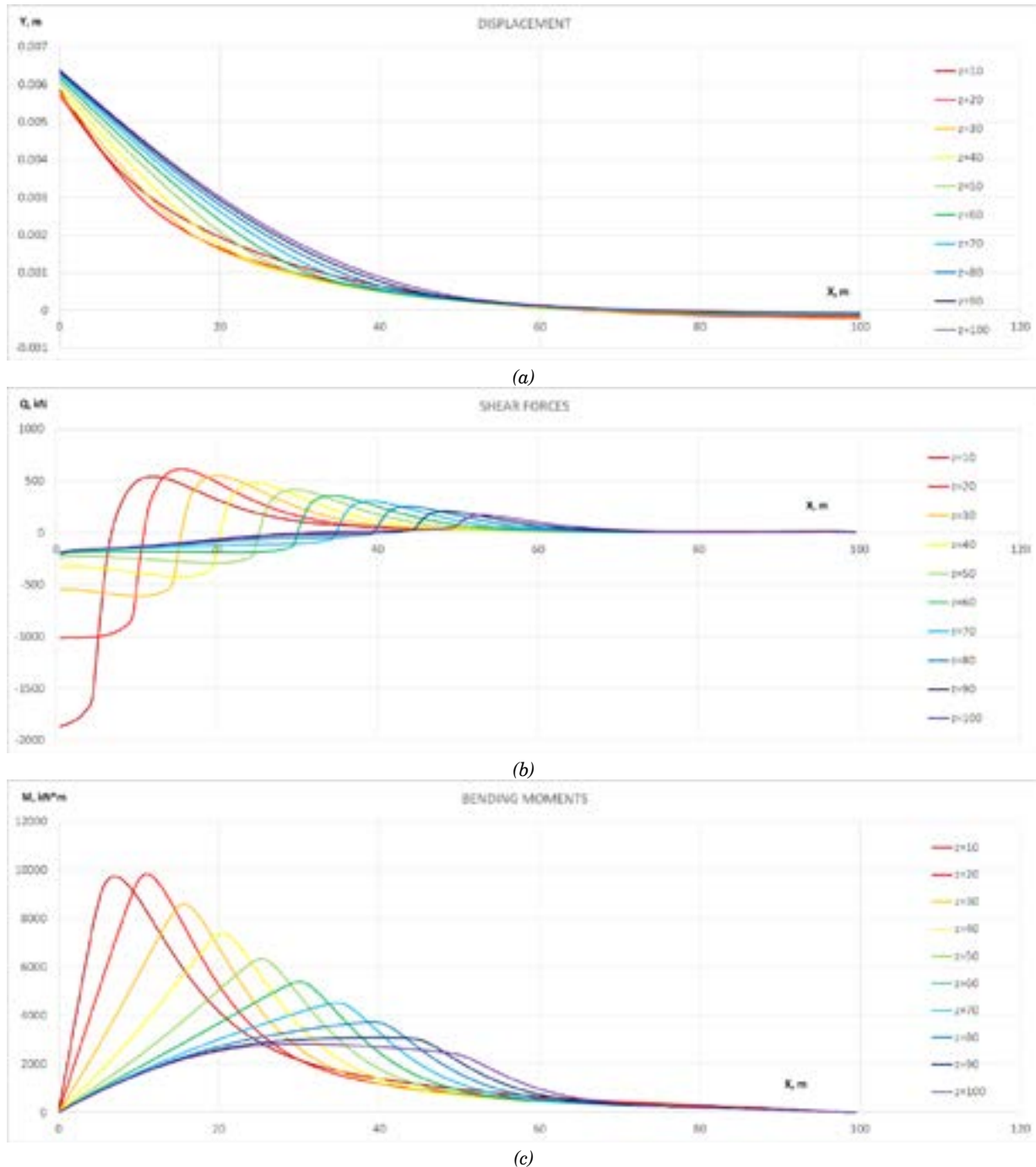


Figure 12 Diagram of displacement (a), shear forces (b) and bending moments (c) in terms of z (2D scheme)

3.3 Numerical simulation

For comparing the results, the previously presented models of the tunnel as beams on an elastic base with springs (1D) and model with ground given as plane strain elements (2D) are used.

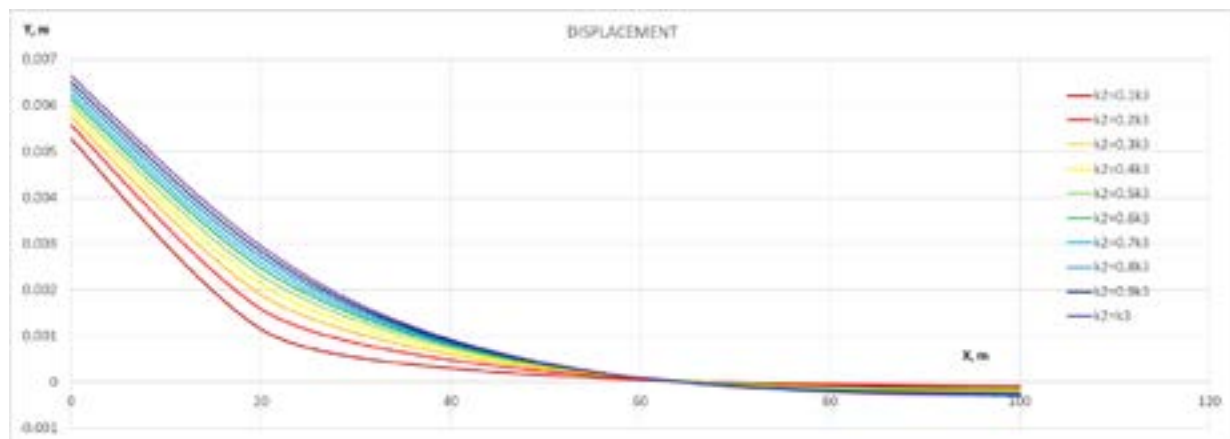
Using these models, with a difference only in the direction of the applied load (the horizontal direction instead of the vertical one). Friction was modeled like an interface elements with strength reduction factor $R_c = 0.5$. The results are presented in Figure 16.

4 Simultaneous action of the fault perpendicular and along the tunnel axis

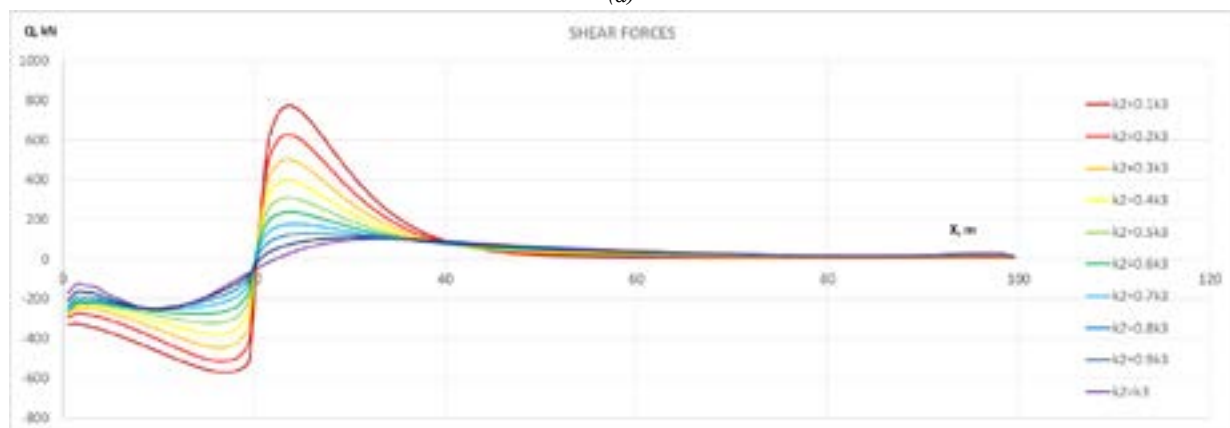
Using the introduced calculation schemes, it is possible to consider the problem combine stress-strain state of the tunnel lining (Figure 17). For clarity the 1D and 2D schemes were compare, the obtained results are presented in Figure 18.

Initial data:

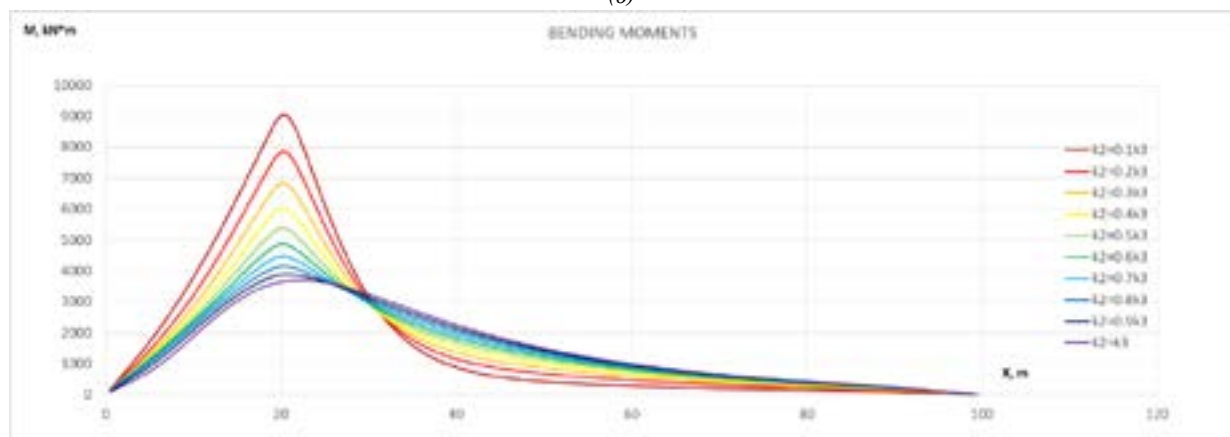
- For the 1D scheme:
 $k_1 = 40000 \text{ kN/m}^2$, $k_2 = 0.2k_1 = 8000 \text{ kN/m}^2$,
 $k_3 = k_1 = 40000 \text{ kN/m}^2$



(a)



(b)



(c)

Figure 13 Diagram of displacement (a), shear forces (b) and bending moments (c) in terms of E_2 (2D scheme)

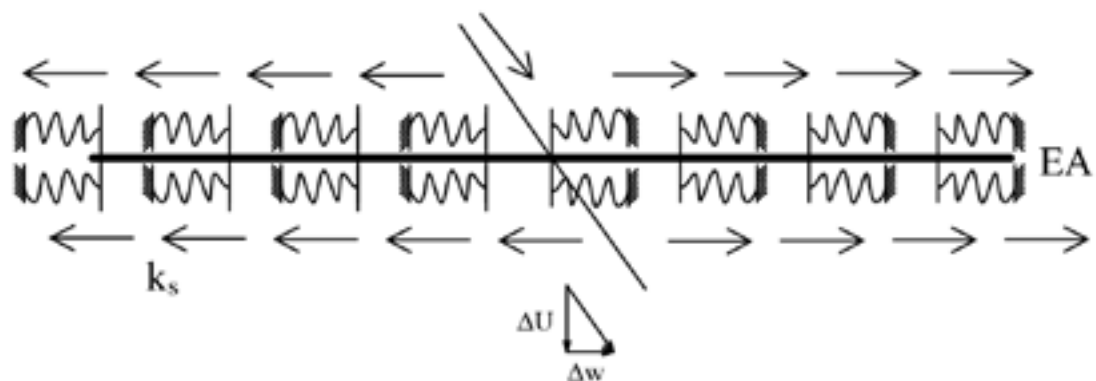


Figure 14 Calculation scheme for the case when fault is along the tunnel cross sections axis

- For the 2D scheme to transition to another soil model, the Scott's Equation (12) was used to obtain the Young modulus for the ground blocks.
- Value of the displacement in each direction equals to 0.005 m.
- Same tunnel lining geometrical and physical parameters.
- $k_1 = 40000 \text{ kN/m}^2$, $k_2 = 0.2k_1 = 8000 \text{ kN/m}^2$,

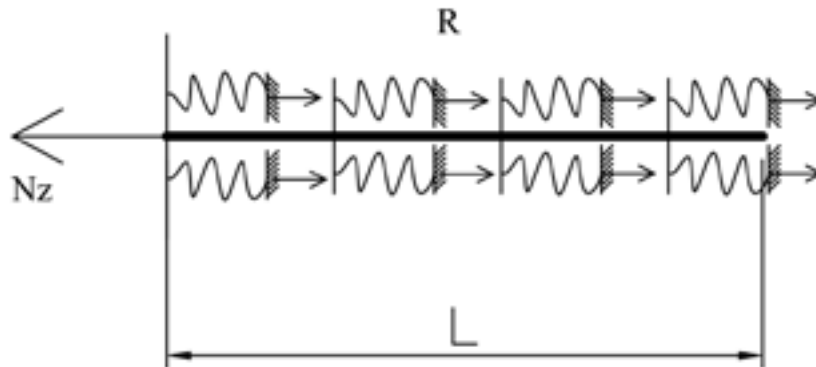


Figure 15 The right-hand cut-off part

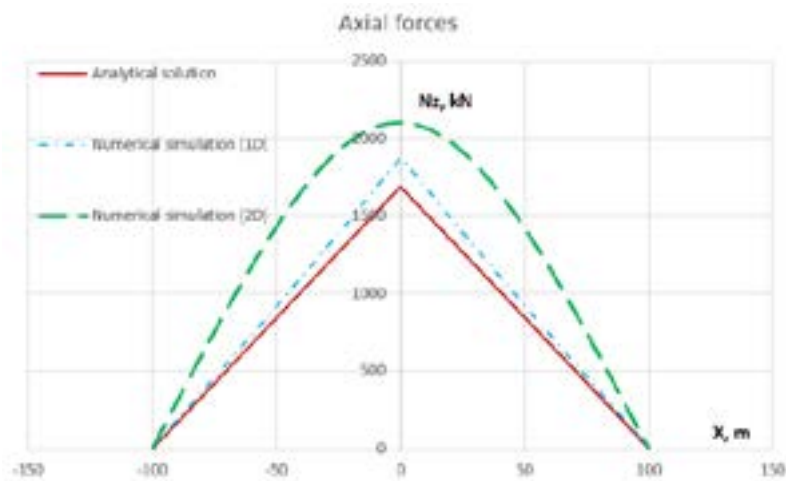


Figure 16 Results of axial forces for the silty clay subgrade

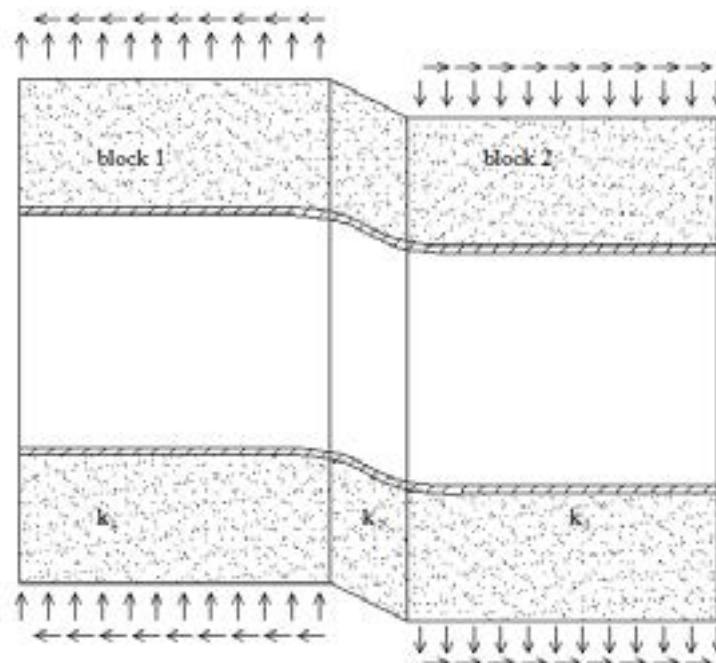


Figure 17 The combined load set

$k_3 = k_1 = 40000 \text{ kN/m}^2 \cdot 0.005 \text{ m}$ The diagrams of shear forces and bending moments have a good match, so it is acceptable to use these schemes to consider the bending and shear effects. The diagrams of axial forces have error rate of about 20%, so it means that this approach allows to estimate previous assessment of stress-strain state under the combined load set. However, the displacement diagrams have a big divergence, as well.

In the 1D scheme it is impossible to consider mass of the ground above the tunnel, moreover, to transit to the 2D scheme, an approach given by Scott (1981) was used. Obviously, these models have different stiffness of the whole system “ground-structure”.

The main hypothesis is that the coefficient of the subgrade reaction for the tension-compression is a quarter of a normal coefficient of the subgrade reaction for bending and shearing actions $k_s = \frac{1}{4}k$. This investigation was completed for piles and for tunnels it is necessary to continue this research.

5 Equivalent stiffness

In all the tasks discussed above, the tunnel lining is assumed to be made of monolithic concrete with a constant cross-section. However, in engineering practice, the precast structures, made of reinforced concrete or cast iron, are also used. In this case, one needs to take into account the bending stiffness and tensile-compression stiffness, which differ depending on the geometry, type of cast iron, type of bars in the reinforced concrete, location of joints of the segmental linings, number of bolts in a specific cross-section.

5.1 Equivalent stiffness in tension and compression

Stiffness of the transverse joint in tension is:

$$K_j = \frac{nE_j A_j}{l_j}, \quad (16)$$

where n is the number of bolts in the cross-section area, $E_j A_j$ - the stiffness of a bolt in tension, l_j - length of a bolt.

In compression, bolts do not carry load, so in this case equivalent stiffness is determined by the lining stiffness; however in tension the lining ring and the transverse joint link work together, so equivalent stiffness can be presented:

$$\frac{l_s}{(EA)_{eq}^T} = \frac{1}{K_j} + \frac{l_s}{E_s A_s} \text{ or } (EA)_{eq}^T = \frac{K_j E_s A_s / l_s}{K_j + E_s A_s / l_s}. \quad (17)$$

5.2 Equivalent stiffness in bending of the segment lining

Consider the equilibrium of a part of structure, consisting of the two halves of a ring and the transverse joint (Figures 19 and 20) with assumptions:

- 1) the width of a ring is much smaller than the tunnel length, so changes in the stress along the axis can be neglected,
- 2) the thickness of a ring is much smaller than the radius.

Equivalent stiffness of the transverse joint [4] is:

$$(EI)_j = \frac{E_s I_s l_j}{l_s} \frac{\cos^3 \theta}{\cos \theta + \left(\frac{\pi}{2} + \theta\right) \sin \theta}, \quad (18)$$

where $I_s = \pi R^3 t$ is an axial moment of inertia of ring's cross-section area.

The rotation angle of equivalent ring's cross-section area is a sum of rotation angles of the ring and a joint, i.e.

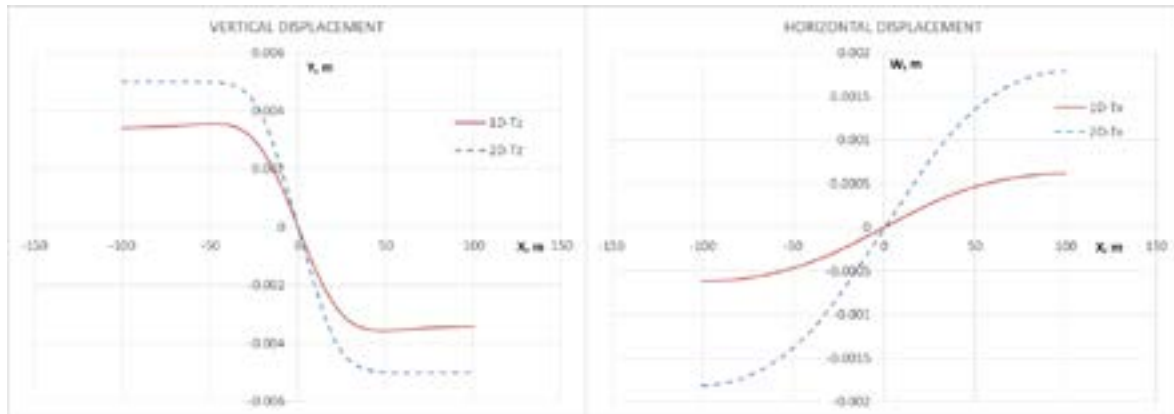
$$\frac{l_s}{(EI)_{eq}} = \frac{l_s}{E_s I_s} + \frac{l_j}{(EI)_j} \quad (19)$$

Combining Equations (18) and (19), one obtains the equivalent stiffness of the cross-section tunnel lining in bending as:

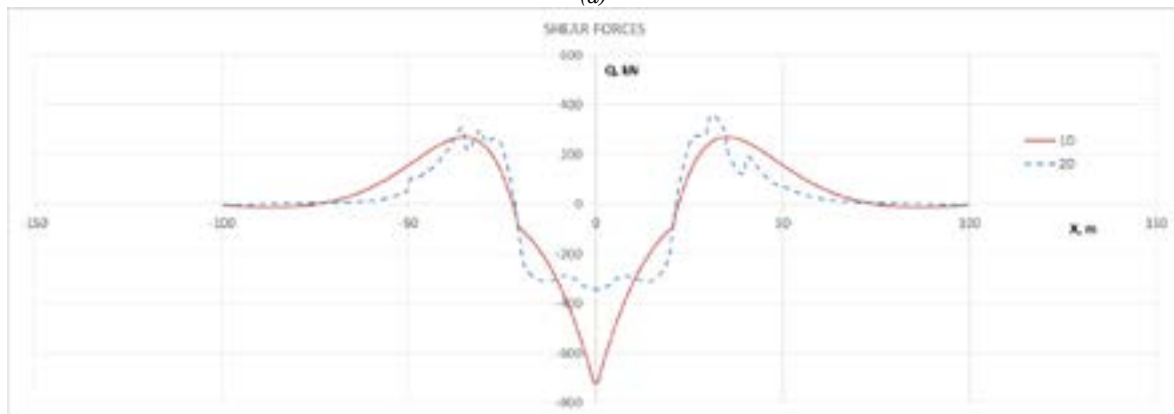
$$(EI)_{eq} = E_s I_s \frac{\cos^3 \theta}{\cos^3 \theta + \cos \theta + \left(\frac{\pi}{2} + \theta\right) \sin \theta}. \quad (20)$$

6 Conclusions

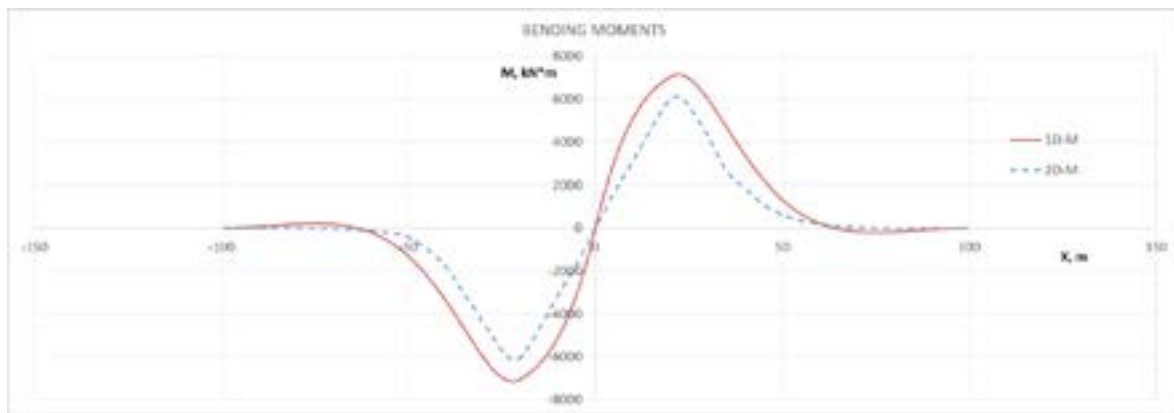
- Classical model of a beam on an elastic foundation is adopted for solving the problem of seismic and geophysics impact on the tunnel in fracture zone;
- The 1D and 2D numerical simulation models for solving the mentioned problem are introduced and verified by analytical solutions;
- Those models in complex combined loading case are tested;
- The case with equivalent stiffness of the tunnel lining is presented.



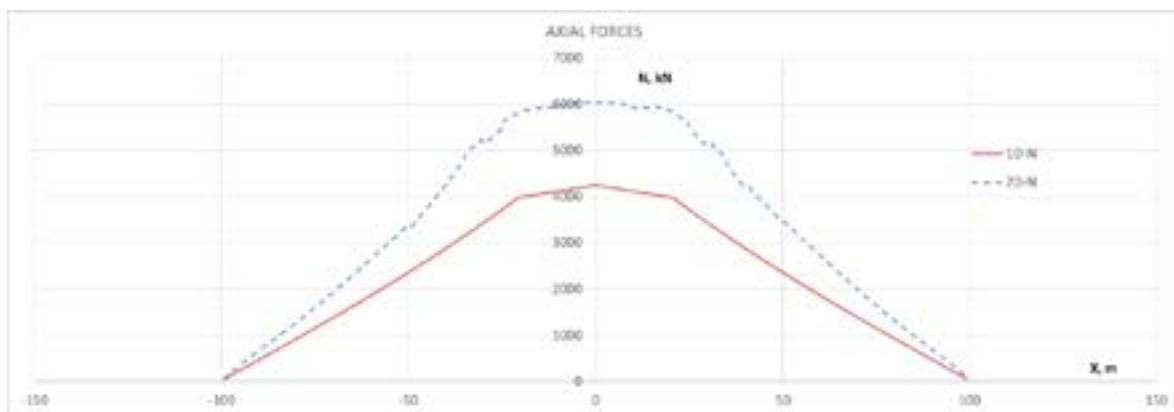
(a)



(b)



(c)



(d)

Figure 18 The combined load set case. Diagrams of displacements (a), shear forces (b), bending moments (c) and axial forces (d) in terms of distance x .

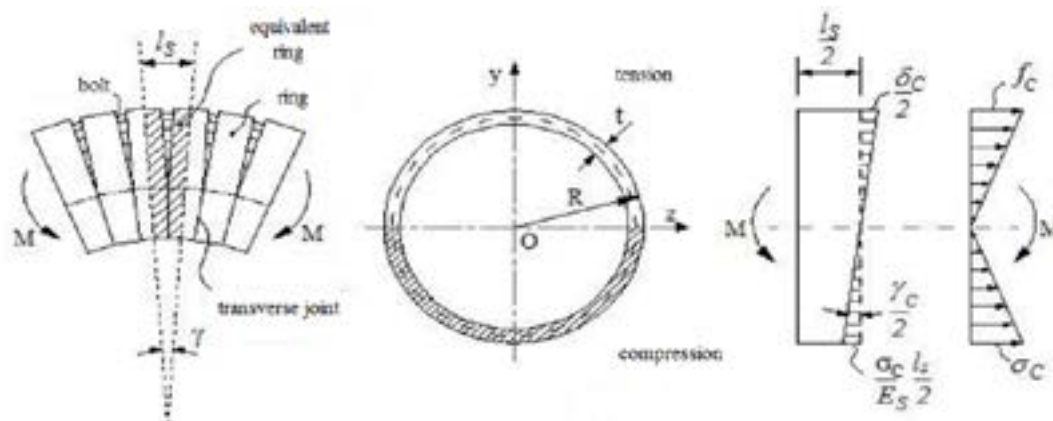


Figure 19 Stress distribution and angle displacement of the cross-section area in the ring

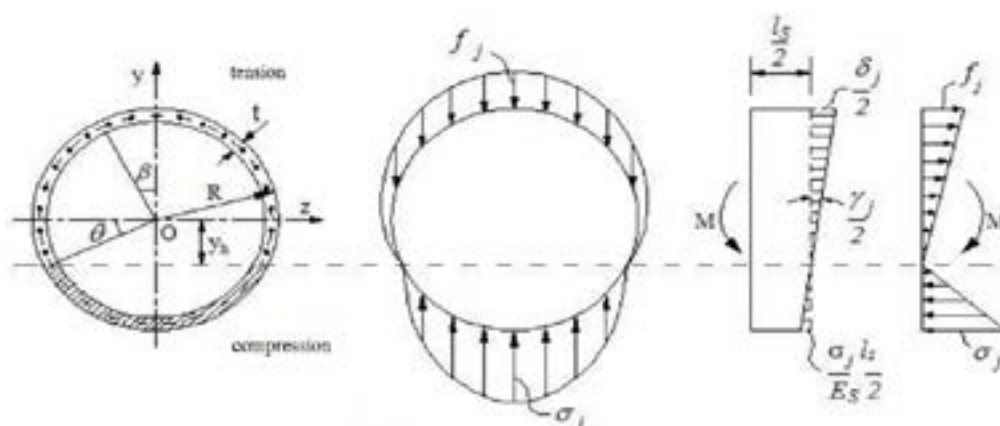


Figure 20 Stress distribution and angle displacement of the cross-section area in the transverse joint

References

- [1] ASAKURA T., TSUKADA K., MATSUNAGA T., MATSUOKA S., YASHIRO K., SHIBA Y., OYA T. Damage to mountain tunnels by earthquake and its mechanism. *Proceedings of Japan Society of Civil Engineers (JSCE)* [online]. 2000, **2000**(659), p. 27-38. eISSN 2187-5103. Available from: https://doi.org/10.2208/jscej.2000.659_27
- [2] DOWDING C.H., ROZEN A. Damage to rock tunnels from earthquake shaking. *Journal of Geotechnical Engineering Division ASCE*. 1978, **104**(2), p. 175-191. ISSN 1090-0241, eISSN 1943-5606.
- [3] KONTOGIANNI V., STIROS S. Earthquakes and seismic faulting: effects on tunnels. *Turkish Journal on Earth Sciences*. 2003, **12**, p. 153-156. ISSN 1300-0985, eISSN 1303-619X.
- [4] KURBATSKY E. Equivalent stiffness of the segment lining when bending is perpendicular to the tunnel axis / Эквивалентная жесткость сборной обделки при изгибе перпендикулярно оси тоннеля (in Russian). In: VI international Conference of Professors, Young Scientist and Students: proceedings. 2013. p. 3-6.
- [5] MAI, D. M. Seismic analysis of tunnels crossing the fault zone in elasto-plastic soils / Raschet tonneley, raspolozhennykh v uprugoplasticheskikh gruntakh, peresekayushchikh zony razloma, na seymicheskie vozdeystviya (in Russian). *Building and Reconstruction*. 2013, **1**(45), p. 19-26. ISSN 2073-7416.
- [6] SCOTT, R. F. *Foundation analysis*. New Jersey, Prentice-Hall: Englewood Cliffs, 1981. ISBN 978-0133291698.
- [7] TIMOSHENKO, S. *Strength of materials. Vol. II. Advanced theory and problems*. 3. ed. Melbourne (Florida): Krieger Publishing Company, 2002. ISBN 978-8123910772.
- [8] WINKLER, E. *On elasticity and fixity / Die Lere fon der Elastitsitet und Festigayt* (in German). Prague: Dominicus, 1867.
- [9] ZAINAGABDINOV, D., MAI, D. M. Mathematical models for automated monitoring of tunnels in fault zones / Matematicheskie modeli pri avtomatizirovannom monitoringe tonneley v zonakh razlomov (in Russian). *Modern Technologies. System analysis. Modelling*. 2013, **4**(40), p. 66-72. ISSN 1813-9108.
- [10] ZAINAGABDINOV D., MAI, D. M. Models for calculations crossing active faults tunnels / Modeli dlya rascheta tonneley, peresekayushchikh aktivnye razlomny (in Russian). *Naukovedenie* [online]. 2013, **3**, 25TBH313. Available from: <https://naukovedenie.ru/PDF/25tvn313.pdf>

ENSURING OPERATIONAL RELIABILITY OF OVERPASS ON "ALMATY-KAPSHAGAI" HIGHWAY SECTION IN KAZAKHSTAN

Assylkhan Jalairov¹, Dauren Kumar^{2,*}, Khaini-Kamal Kassymkanova², Gulshat Murzalina³, Gulnar Jangulova²

¹Department of Transport, Construction, Bridges and Tunnels, Kazakh University of Way Transport, Almaty, Republic of Kazakhstan

²Department of Cartography and Geoinformatics, Al-Farabi Kazakh National University, Almaty, Republic of Kazakhstan

³Faculty of General Construction, International Education Corporation, Almaty, Republic of Kazakhstan

*E-mail of corresponding author: daurendkb@gmail.com

Resume

The article presents results of the overpass condition survey, technical survey, static tests and assessment of the structure operational reliability, a double-decker overpass on Almaty-Kapshagai highway section in Kazakhstan.

Technical survey determined the dimensions of the overpass, the camber of reinforced concrete superstructures main beams and checked the values of the overpass roadway actual transverse and longitudinal slopes. The calculation and analytical assessment of the overpass load-bearing structures, for the strength of the bending moment, are performed. Static tests of the overpass split beam superstructure of a length of 33.0m were conducted. Trucks loaded with ballast were accepted as a test load.

Article info

Received 11 April 2021

Accepted 26 July 2021

Online 22 October 2021

Keywords:

bridge beam,
span,
support,
design scheme,
test load,
static tests,
deflection

Available online: <https://doi.org/10.26552/com.C.2022.1.D23-D36>

ISSN 1335-4205 (print version)

ISSN 2585-7878 (online version)

1 Introduction

The overpass is located on a straight section in the plan and on a longitudinal slope in $i = 5 ‰$ profile. The longitudinal axis intersection angle of the highway overpass with the existing highway is 66° . The bridge layout is accepted $33+33$ m. The overpass length is taken along the rear edges of backwalls and according to the project is 66.917m. The overpass dimensions, taking into account the speed change lanes are taken $17.0 + 2 \times 1.0$ m. The roadway width is $4 \times 3.5 = 14.0$ m and the safety lanes are 1.5m each.

The roadway structure is taken as a two-layer one, consisting of "TECHNOELASTMOST S" waterproofing material laid on top of an overhead slab and asphalt concrete pavement with a thickness of 70mm.

The "MAURER" D-100 type expansion joints are arranged along the roadway width above the end and intermediate supports, within the sidewalks - compensator type expansion joints. The railing is a metal safety fence with a height of 1.2m, the posts of which are welded to the embedded parts in the bridge construction monolithic sections.

The safety fence posts are bolted to the embedded parts installed in separate bollards. The coupling structure is made of cast-in-place and precast constructions. Prefabricated blocks grouting is performed at the ends of

the transition slabs, which slabs are made of the precast reinforced concrete of a length of 8.0m. The overpass coupling structure with approach embankment includes the device of draining backfill behind the supports, laying of reinforced concrete transition slabs of a length of 8m along the roadway entire width. The coupling of sidewalks with curbs-transition slabs is of a length of 2m.

The roadway and sidewalk drainage is designed according to the longitudinal scheme. The roadway transverse profile has $20 ‰$ of the two sloping surfaces from the roadway axis. Atmospheric water is diverted from the overpass roadway due to the longitudinal slopes.

The overpass superstructures consist of the VTK-33u prestressed beams of a length of 33m. A monolithic reinforced concrete overhead slab with joint grouting on the roadway slabs of VTK-33u beams is arranged on the top of the superstructures beams (the abbreviation "VTK" is from the Russian term "BTK - vysokotekhnologicheskaja konstrukcija", what means "high-tech construction" for bridges).

Fourteen beams are installed in transverse profile of the overpass superstructures. The overpass intermediate supports consist of six monolithic posts of oval profile with a width of 800mm, connected on top by a monolithic crossbar. The intermediate support



Figure 1 General view of the overpass from Kapshagai before repair



Figure 2 General view of the repaired superstructure No. 1 from Almaty

foundations are taken in the form of load distribution structures, supported by drilled piers with a diameter of 1500 mm. The abutment foundations are also taken in the form of load distribution structures, supported by drilled piers of a diameter of 1500 mm.

2 Materials and methods

The peculiarity of this structure was that during its construction, all fourteen VTK-33u beams of

superstructure No. 1 were damaged as a result of vehicle impact.

Figure 1 shows a general view of the road overpass before repair and Figure 2 shows the repaired superstructure No. 1 [1].

The following types of activities have been performed [2-8] during the highway overpass survey:

- familiarization with the project documentation in terms of construction solution adopted in the project and as-built documents for construction;
- control measurements of the bridge supporting

structures geometric parameters and their compliance with the project requirements;

- condition survey of the roadway structures, supports and superstructures;
- technical survey of the superstructures bottom beams (camber beam assessment in the middle of the superstructure) and the overpass vehicular deck top.

3 Results and discussion

A survey using geodetic tools was conducted to assess the position of the highway overpass elements in space.

Instrumental measurements allow to observe the vertical and horizontal deformations of superstructures and supports. Those measurements allow to timely detect hidden defects that cannot be discovered during the inspection, help explain the appearance of defects found during the inspection, as well as choose the most correct ways to repair and strengthen the structure [9-10].

The survey was conducted under the following weather conditions: ambient temperature - 4 °C, light wind, low clouds, good visibility. A technical survey of the bottom of the main beams of the reinforced concrete superstructures, to determine their camber was conducted in accordance with the work program. The technical survey was conducted at three points on each main beam - in the area of the beam support sections and in the middle of its span [11].

The technical survey results made it possible to determine some moments on each superstructures beam, results of which are shown in Table 1. As can be seen from this table, all the beams have the bending moments, with the exception of beam No. 14 in superstructure No. 1, which rests in an almost horizontal position. That is, in the longitudinal direction, the static scheme is two simple spans.

The data analysis given in Table 2 shows that the bending moments in beams No. 1, 2, 3, 4, 11, 12, 13 in superstructure No. 1, after laying the overhead slab and asphalt pavement, have an insignificant value and there is a deflection in beam No. 14 equal to 0.5 mm.

It should be noted that the above-mentioned beams were installed to replace the dismantled beams.

Minor bending moments in these beams indicate that prestressing forces in the tensioned reinforcement were lower than in beams No. 5 to 10.

A computational and analytical check was also performed [12-14].

The considered superstructure No. 1 is composed of fourteen VTK-33u reinforced concrete girder and diaphragm type beams. In the transverse direction, the beams are connected to monolithic joints on the loop outlets and with the use of a monolithic overhead slab with a thickness of 150 mm, involved in the behavior with the help of vertical outlets from the beam slab. The monolithic joint width is assumed to be 0.3 m, which corresponds to the accepted distance of 1.4 m between the beam axes.

Due to the fact that the superstructure is a slab-type structure, for the construction of influence lines, the transverse profile of the superstructure should be considered as a continuous beam on elastically settling supports, which are the main beams. The influence lines of pressures on beams are constructed as influence lines of beams support reactions on elastic supports [15-16].

The distance between the beams is $d = 1.4$ m and the effective span is $l = 32.4$ m.

Inertia moment of a 1 m wide superstructure slab is:

$$I_{pl} = \frac{bh_f^3}{12} = \frac{1 \cdot 0.3^3}{12} = 2.25 \cdot 10^{-3} m^4. \quad (1)$$

The inertia moment of the VTK-33u beam transverse profile, in the middle of the span with the overhead slab, according to this project, is assumed to be equal to:

Table 1 Bending moments data in the overpass superstructure beams

Beam number	Bending of beams, mm	
	Span structure No. 1	Span structure No. 2
1	-3.5	-29.5
2	-4.5	-34.0
3	-4.0	-42.0
4	-10.0	-34.5
5	-25.5	-39.5
6	-29.0	-33.5
7	-18.5	-31.5
8	-24.0	-29.5
9	-23.0	-31.0
10	-30.5	-37.5
11	-10.0	-37.5
12	-2.0	-40.5
13	-4.0	-37.0
14	0.5	-28.5

$$I_{beam} = 186.6 \cdot 10^{-3} m^4. \tag{2}$$

The stiffness parameter is:

$$\alpha = 12.8 \cdot \frac{d^3}{l^4} \cdot \frac{E_b I_{beam}}{E_b I_{pl}} = 12.8 \cdot \frac{1.4^3}{32.4^4} \times \frac{186.6 \cdot 10^{-3}}{2.25 \cdot 10^{-3}} = 0.00264. \tag{3}$$

The pressure influence line ordinates on the elastically settling supports were found according to formulas for an eight-span beam with cantilevers based on the calculation data. If the number of spans of the

transverse structure exceeds eight, eight spans can be taken into account, since the impact of subsequent spans is insignificant.

The calculation data of the pressure influence line ordinates, on the elastically settling supports (beams) are shown in Table 2.

The bridge superstructure was calculated for the most unfavorable load - the load from vehicles is taken in such a form that the cars of the prescribed weight were placed in two lanes, shifted to the edge of the bridge travelled way (including the safety lanes), to determine the forces in the beams from the temporary prescribed

Table 2 Data on the influence line ordinates

The number of the beam in the transverse direction	Ordinates of the lines of influence of pressure on the supports						
	R1	R2	R3	R4	R5	R6	R7
1	0.426	0.323	0.228	0.146	0.077		
2	0.323	0.268	0.209	0.152	0.099	0.077	
3	0.228	0.209	0.187	0.155	0.119	0.099	0.077
4	0.146	0.152	0.155	0.151	0.134	0.119	0.099
5	0.077	0.099	0.119	0.134	0.141	0.134	0.119
6	0.020	0.051	0.081	0.110	0.134	0.141	0.134
7	-0.030	0.007	0.044	0.081	0.119	0.134	0.141
8	-0.074	-0.034	0.007	0.051	0.099	0.119	0.134
9	-0.116	-0.074	-0.030	0.020	0.077	0.099	0.119
10						0.077	0.099
11							0.077
12							
13							
14							

Table 3 Data used for calculation and values of bending moments

Beam No.	Transverse location factor		Design load		Load safety factor		Dynamic coefficient	Influence line area	Calculated bending moments in the middle of the beam span	
	for load trolley	for intended load	for load trolley	for intended load	for load trolley	for intended load			for $\gamma_f > 1;$ $1+\mu > 1$	for $\gamma_f = 1;$ $1+\mu > 1$
			kN	kN/m					m ²	kN-m
1	0.378	0.337						1868	1573*	
2	0.356	0.309						1739	1464*	
3	0.330	0.277						1590	1339*	
4	0.294	0.238	140	14	<u>1.178</u>	<u>1.2</u>	1.095	131.2	1395	1175*
5	0.248	0.204			1.0	1.0			1185	998*
6	0.217	0.182							1044	880*
7	0.178	0.152							863	727*

* Values of the bending moments in the middle of the beam span with a load safety factor of one ($\gamma_f = 1.0$) and a full dynamic coefficient ($(1+\mu) > 1.0$)

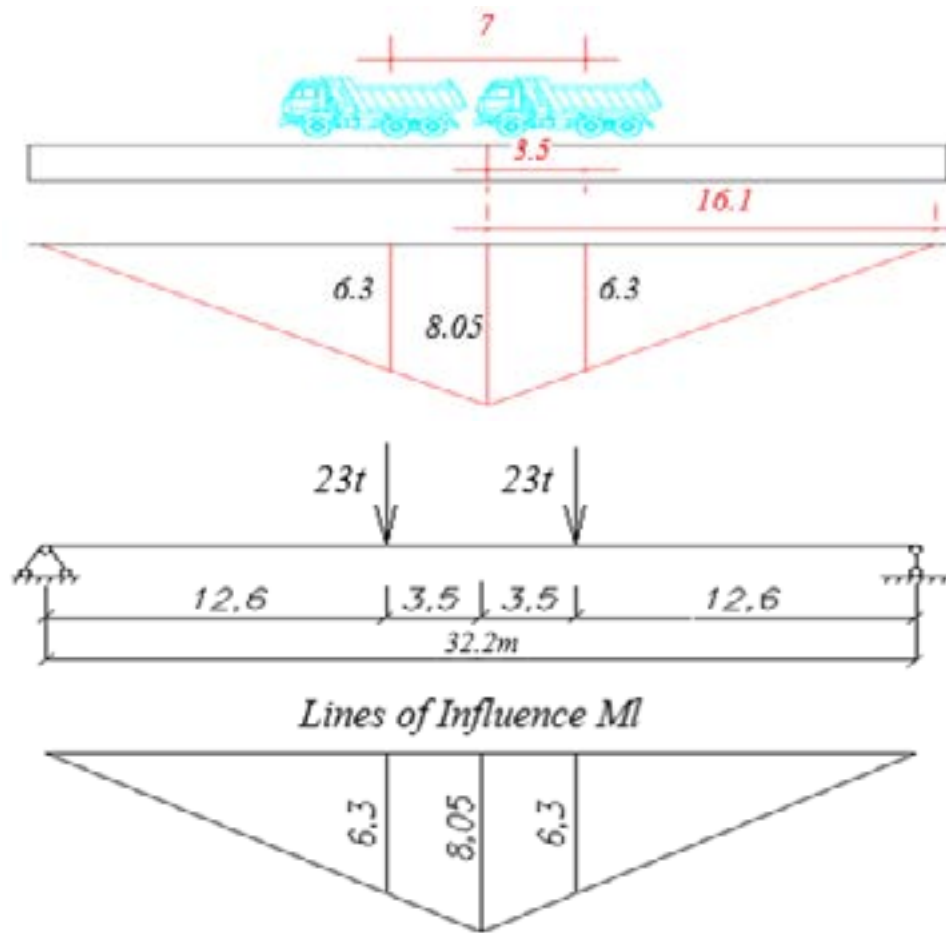


Figure 3 The influence line of the bending moment in the middle of the beam span and the position of the test load on the superstructure

Table 4 The transverse location factor (TLF) data from the action of the test load

First test stage		Second test stage		Third test stage	
Beam No.	TLF	Beam No.	TLF	Beam No.	TLF
1	0.378	14	0.378	1	-0.099
2	0.356	13	0.356	2	-0.025
3	0.330	12	0.330	3	0.051
4	0.294	11	0.294	4	0.131
5	0.248	10	0.248	5	0.214
6	0.217	9	0.217	6	0.245
7	0.178	8	0.178	7	0.262

load from cars. The outer track axis of the prescribed load from cars is moved from the curb edge for 0.55m. The distance between the lane load axes is assumed to be 3m. The load trolley of prescribed load from cars is installed in the middle of the superstructure No. 1.

Table 3 shows the calculation data and determined values of the bending moments in the middle of the beam span, with the load safety factor greater than one ($\gamma_f > 1.0$) and a full dynamic coefficient ($(1+\mu) > 1.0$) and with a load safety factor of one ($\gamma_f = 1.0$) and a full dynamic coefficient ($(1+\mu) > 1.0$).

Here is the test load calculation. The influence line of the bending moment in the middle of the beam span

and the position of the test load on the superstructure are shown in Figure 3.

Table 4 shows the transverse location factor (TLF) values from the action of the test load when the last row of trucks is located at a distance of 1.5m from the roadway safety fence and in the middle of the superstructure (Figures 4, 5 and 6).

The analysis of the transverse location factor values showed that at the accepted position of the test load at the first, second and third stages of the tests, the maximum load was on beams No. 1, No. 14 and No. 7, respectively.

Determined bending moments in the middle of the



Figure 4 Vehicles are located at the roadway safety fence of superstructure No. 1 from Kapshagai at the first stage of testing



Figure 5 Vehicles are located at the roadway safety fence technical of superstructure No. 1 from Almaty at the second stage of testing



Figure 6 Vehicles are located at the longitudinal axis of superstructure No. 1 at the third stage of testing



Figure 7 Location of deflection gauges under each of the fourteen beams in the middle of the superstructure No. 1

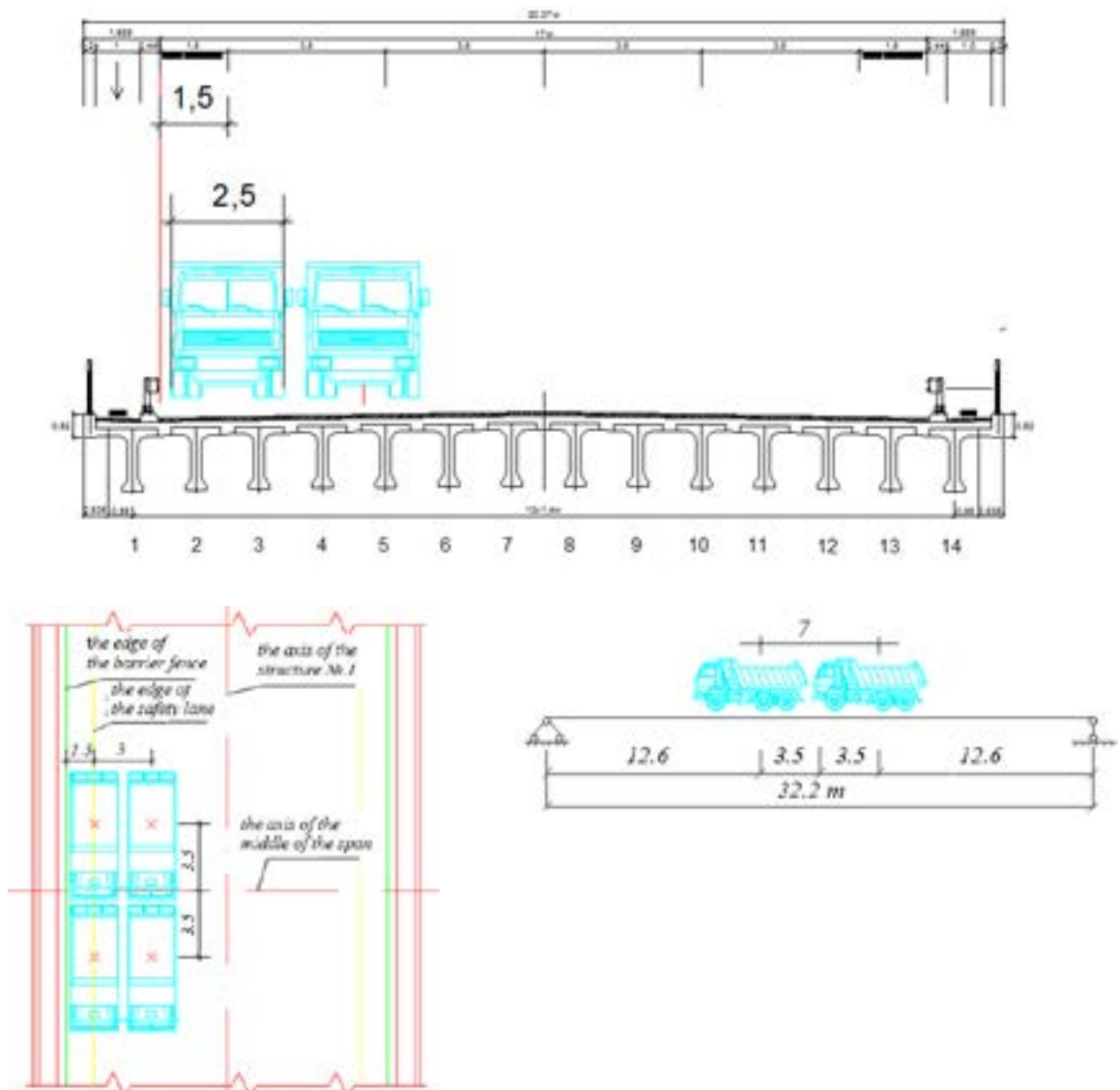


Figure 8 The first stage of the static tests on superstructure No. 1

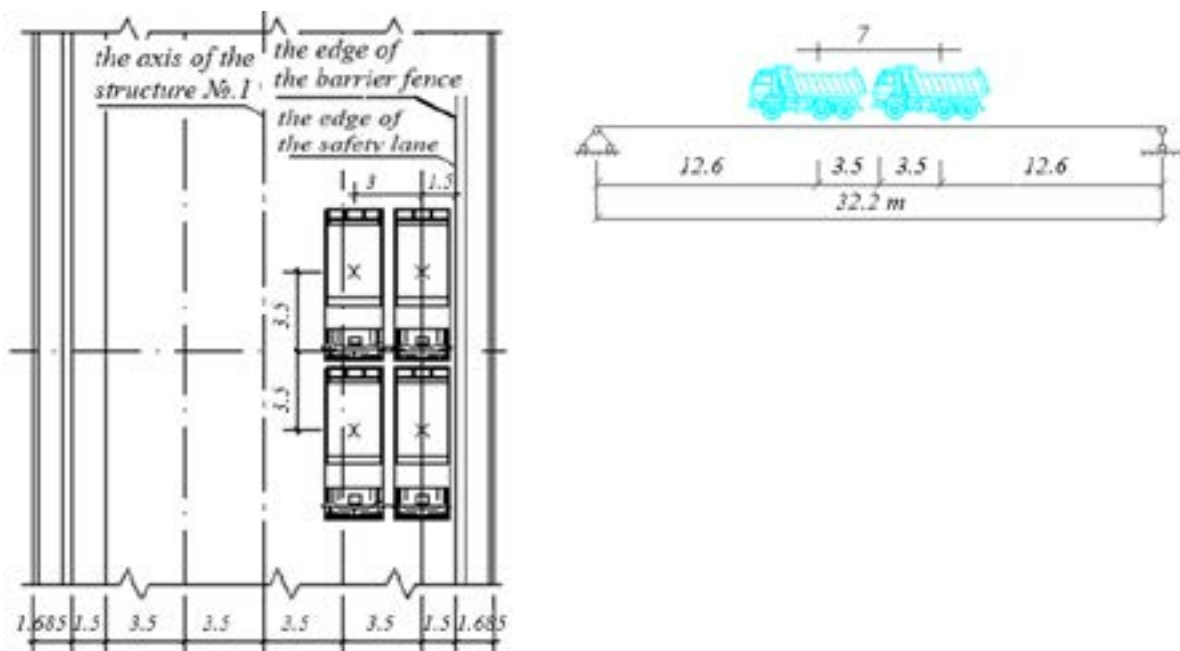


Figure 9 The second stage of the static tests on superstructure No. 1

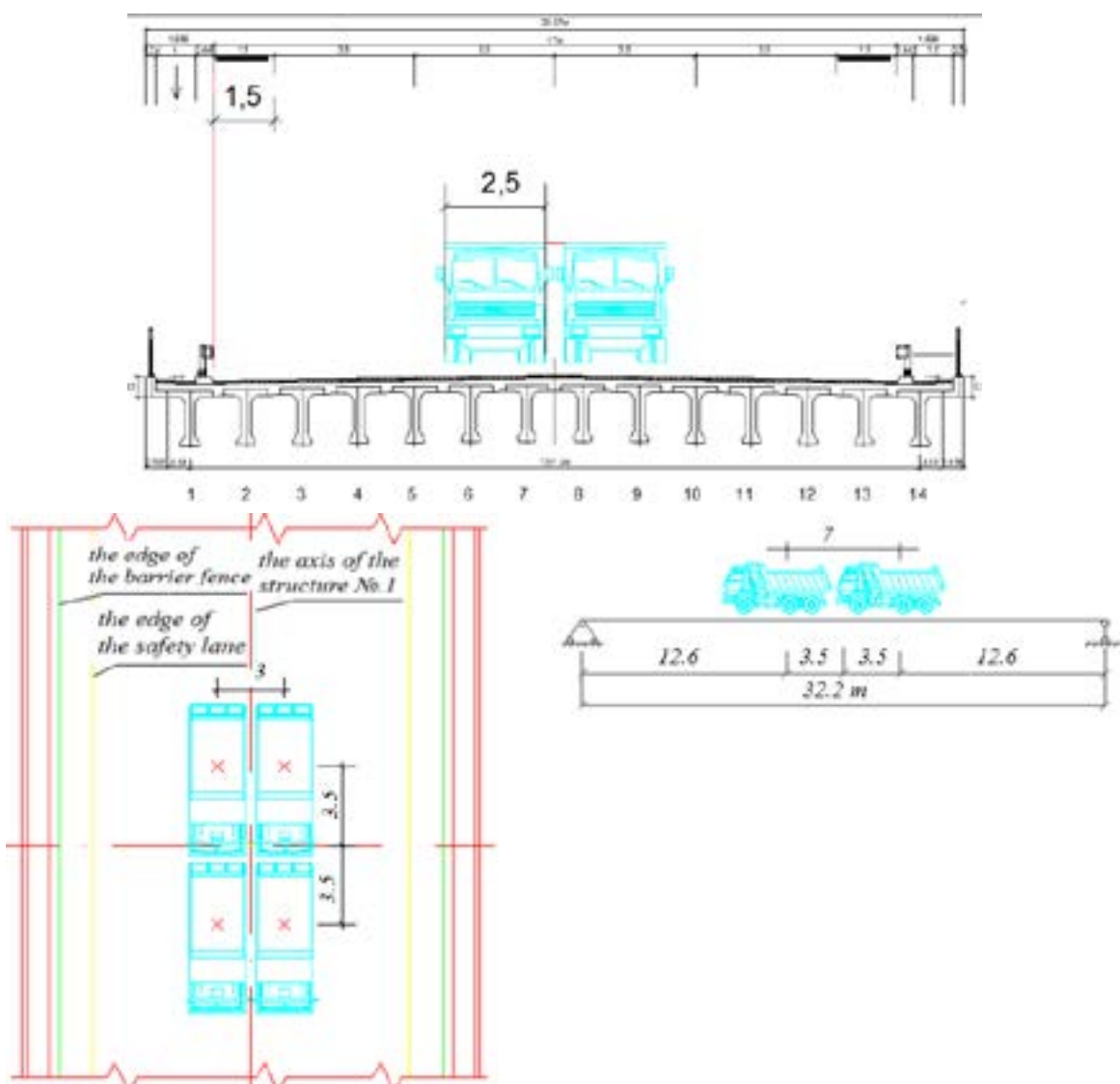


Figure 10 The third stage of the static tests on superstructure No. 1

beam for each test stage are:

- In beams No. 1 and No. 14 for the first and second stage of testing:

$$M_{(1\text{ and }14)} = 2 \cdot 23.0 \cdot 0.378 \cdot 6.34 \cdot 10 = 1102 \text{ kN} \cdot \text{m} . \quad (4)$$

- In beam No. 7 for the third stage of testing:

$$M_{(7)} = 2 \cdot 23.0 \cdot 0.262 \cdot 6.34 \cdot 10 = 764 \text{ kN} \cdot \text{m} . \quad (5)$$

The force arising in highway and city bridges from the action of the test load should be in the range of 70 to 100% of the calculated forces from the action of the live temporary vertical load adopted in the project, with the load safety factor equal to one ($\gamma_f = 1.0$) and a full dynamic coefficient ($(1+\mu) > 1.0$) in accordance with the regulatory documents of the Republic of Kazakhstan.

The calculated value of the bending moment from the action of temporary loads in the most loaded beam

with the load safety factor of more than one ($\gamma_f > 1.0$) and a full dynamic coefficient ($(1+\mu) > 1.0$) is $M_{ul} = 1868 \text{ kN} \cdot \text{m}$ in accordance with the calculation (see Table 4).

The permissible bending moment in the beam from the action of the temporary load with the load safety factor equal to one ($\gamma_f = 1.0$) and a full dynamic coefficient ($(1+\mu) > 1.0$) is $M_{ul} = 1573 \text{ kN} \cdot \text{m}$.

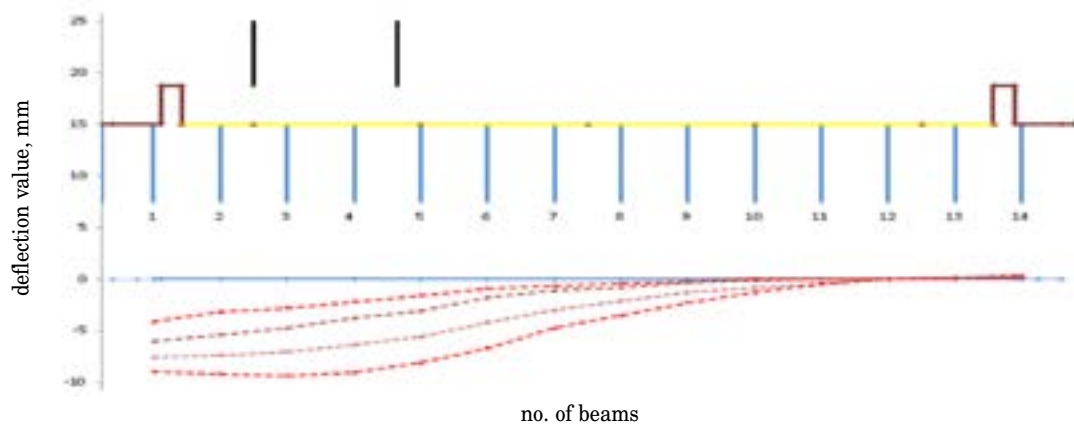
The calculated bending moment ratio from the action of the test load to the bending moment from the action of the temporary load with the load safety factor equal to one ($\gamma_f = 1.0$) and a full dynamic coefficient ($(1+\mu) > 1.0$) is:

For the first and second stages:

$$\frac{M_{(1\text{ and }14)}}{M_{ul}} = \frac{1102 \text{ kN} \cdot \text{m}}{1573 \text{ kN} \cdot \text{m}} = 0.7 . \quad (6)$$

For the third stage:

$$\frac{M_{(7)}}{M_{ul}} = \frac{764 \text{ kN} \cdot \text{m}}{1573 \text{ kN} \cdot \text{m}} = 0.5 . \quad (7)$$



Measurement type	Beam No.	zero count	1 stage	f, mm	2 stage	f, mm	3 stage	f, mm	4 stage	f, mm
			count	count	count	count	count	count		
Aistov	1	25	340	3.15	628	6.03	783	7.58	925	9
Aistov	2	0	320	3.2	538	5.38	736	7.36	920	9.2
Aistov	3	47	325	2.78	521	4.74	752	7.05	983	9.36
Aistov	4	770	991	2.21	1150	3.8	1409	6.39	1676	9.06
CRIBS	5	3	19	1.6	34	3.1	59	5.6	84	8.1
CRIBS	6	0	9	0.9	18	1.8	42	4.2	67	6.7
Aistov	7	26	88	0.62	136	1.1	328	3.02	502	4.76
Aistov	8	12	53	0.41	92	0.8	223	2.11	364	3.52
CRIBS	9	2	4	0.2	5	0.3	15	1.3	25	2.3
CRIBS	10	4	4	0	5	0.1	12	0.8	17	1.3
Aistov	11	44	43	-0.01	44	0	82	0.38	89	0.45
Aistov	12	46	45	-0.01	44	-0.02	47	0.01	47	0.01
Aistov	13	23	12	-0.11	11	-0.12	11	-0.12	10	-0.13
Aistov	14	36	25	-0.11	18	-0.18	5	-0.31	0	-0.36

Figure 11 Loading and unloading stages, the superstructure transverse profile and outline of the beam deflections during the loading and unloading at the first stage

Four loaded vehicles with a mass of 23 tons each were accepted for the static tests, taking into account the results of this calculation.

KamAZ 65115 and North Benz ND3250S trucks with ballast, the average mass of each was mainly 23 tons, were used as the test load when conducting the static tests.

The repaired superstructure No. 1 was subjected to the control tests. Aistov and V. A. Kucherenko CRIBS deflection gauges with the price of division on the scale of the device of 0.01 and 0.1mm, respectively, were used to determine the deflections in fourteen beams of superstructure No. 1. The superstructure No. 1 was loaded in stages and beams deflections [17-18] were recorded at each stage of loading.

Figure 7 shows the deflection gauges' location under fourteen beams in the middle of the superstructure No. 1.

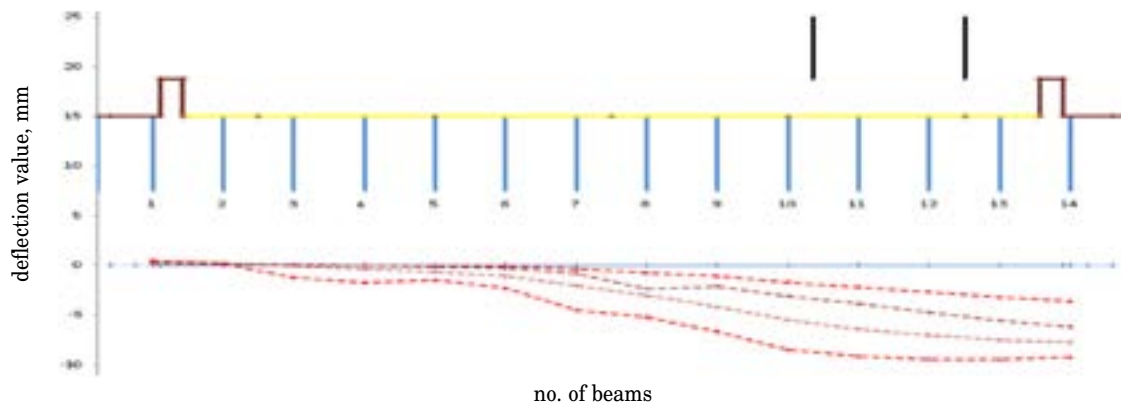
The static tests of the overpass were conducted in accordance with the work program in three stages [19-21].

Four vehicles were installed in stages on superstructure No. 1 at the first (Figure 8) and second (Figure 9) stages of the static tests. Meanwhile, the roll axis of the last vehicle was located at a distance of 1.5m from the roadway fence. The distances between the vehicles in overpass transverse and longitudinal directions were 3.0m and 7.0m, respectively.

Four trucks - two vehicles in one row were also installed on superstructure No. 1 at the third stage of testing. The axes of each vehicle row were separated from the roadway longitudinal axis at a distance of 1.5m. The distances between vehicles in the overpass transverse and longitudinal directions were 3.0m and 7.0m, respectively (Figure 10).

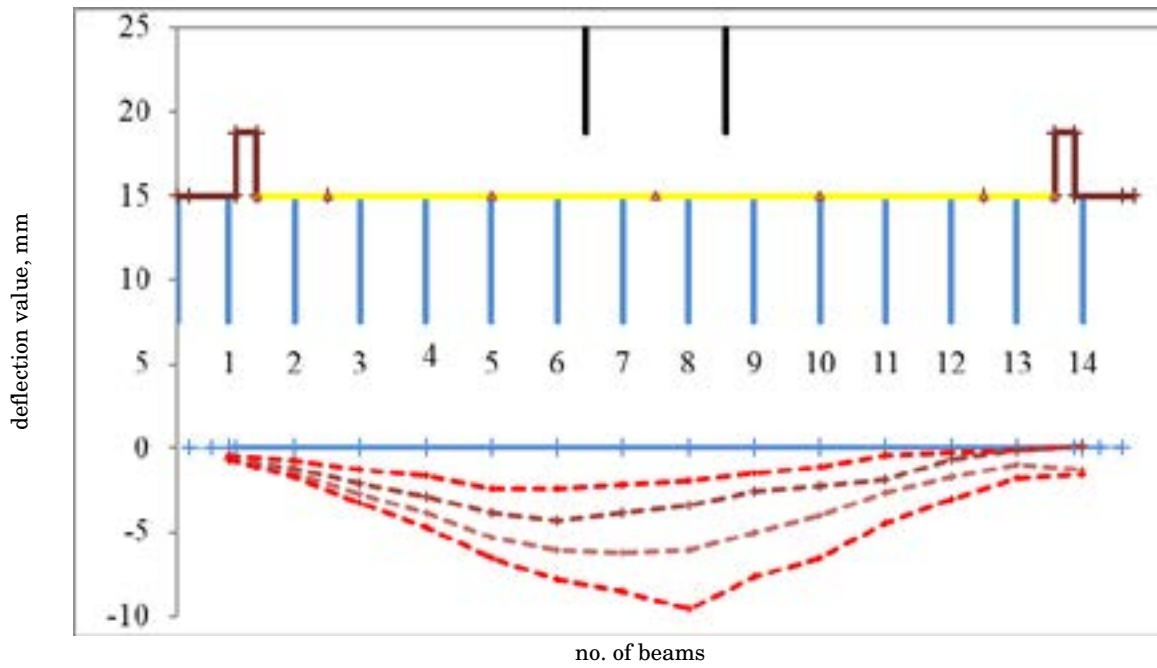
Experimental deflections have been determined in fourteen beams of a length of 33.0m in the middle of the repaired superstructure No. 1, according to the static tests results.

Figures 11, 12 and 13 show the loading and



Measurement type	Beam No.	zero count	1 stage	f, mm	2 stage	f, mm	3 stage	f, mm	4 stage	f, mm
			count	count	count	count	count			
Aistov	1	57	36	-0.21	27	-0.3	20	-0.37	9	-0.48
Aistov	2	21	10	-0.11	4	-0.17	2	-0.19	5	-0.16
Aistov	3	71	64	-0.07	62	-0.09	78	0.07	197	1.26
Aistov	4	785	786	0.01	787	0.02	821	0.36	961	1.76
CRIBS	5	3	4	0.1	5	0.2	10	0.7	18	1.5
CRIBS	6	0	1	0.1	3	0.3	11	1.1	23	2.3
Aistov	7	25	61	0.36	107	0.82	228	2.03	479	4.54
Aistov	8	6	82	0.76	243	2.37	313	3.07	528	5.22
CRIBS	9	1	12	1.1	22	2.1	43	4.2	68	6.7
CRIBS	10	2	19	1.7	33	3.1	57	5.5	87	8.5
Aistov	11	21	239	2.18	406	3.85	663	6.42	940	9.19
Aistov	12	25	292	2.67	496	4.71	729	7.04	971	9.46
Aistov	13	10	331	3.21	564	5.54	763	7.53	958	9.48
Aistov	14	31	393	3.62	651	6.2	806	7.75	958	9.27

Figure 12 Loading and unloading stages, the superstructure transverse profile and outline of the beam deflections during the loading and unloading at the second stage



Measurement type	Beam No.	zero count	1 stage	f, mm	2 stage	f, mm	3 stage	f, mm	4 stage	f, mm
			count	count	count	count				
Aistov	1	51	92	0.41	115	0.64	120	0.69	121	0.7
Aistov	2	21	93	0.72	139	1.18	175	1.54	198	1.77
Aistov	3	64	191	1.27	273	2.09	337	2.73	388	3.24
Aistov	4	783	952	1.69	1073	2.9	1168	3.85	1252	4.69
CRIBS	5	3	27	2.4	42	3.9	56	5.3	68	6.5
CRIBS	6	0	24	2.4	43	4.3	61	6.1	78	7.8
Aistov	7	32	252	2.2	417	3.85	654	6.22	885	8.53
Aistov	8	11	210	1.99	352	3.41	622	6.11	965	9.54
CRIBS	9	3	18	1.5	29	2.6	53	5	80	7.7
CRIBS	10	5	16	1.1	28	2.3	45	4	70	6.5
Aistov	11	69	115	0.46	257	1.88	334	2.65	515	4.46
Aistov	12	49	79	0.3	112	0.63	224	1.75	352	3.03
Aistov	13	39	49	0.1	55	0.16	133	0.94	220	1.81
Aistov	14	61	53	-0.08	48	-0.13	185	1.24	222	1.61

Figure 13 Loading and unloading stages, the superstructure transverse profile and outline of the beam deflections during the loading and unloading at the third stage

unloading stages, the superstructure transverse profile and the outline of beam deflections during the loading and unloading.

At the first stage of testing, the maximum deflection value has been recorded in beam No. 3, which was $f = 9.36\text{ mm}$.

At the second stage of testing, the maximum deflection value has been recorded in beam No. 13, which had a value equal to $f = 9.48\text{ mm}$.

At the third stage of testing, the maximum deflection value has been recorded in beam No. 8, which had

a value equal to $f = 9.54\text{ mm}$.

The values analysis of the deflection increments during the loading and unloading at the first, second and third stages of the static tests testified to the elastic behavior of the VTK-33u beams of a length of 33.0 m.

The overpass structural elements have been inspected prior to the static tests, as well as after their completion, which allowed to assess the impact of the tests on the bridge. The inspection revealed the absence of any damage in the load-bearing structures caused by the action of the test load.

Table 5 Results of the static tests

Static test stage	No. of the beam in which the maximum deflection is recorded	Actual maximum deflection value, f_e , mm	Estimated maximum deflection value, f_{cal} , mm	TLF	Design factor, K
1	3	9.36		0.330	0.5
2	13	9.48	54.3	0.356	0.5
3	8	9.54		0.262	0.7

The main criterion for the positive behavior of the overpass superstructures during the bridge acceptance static tests is the compliance of the beams elastic deflections measured under the influence of the test load with the deflection values determined by calculation from the action of the same test load [22-24].

Such indicator of the superstructure beam behavior during the static tests is the design factor determined by the formula:

$$K = \frac{f_e}{f_{cal}}, \quad (8)$$

where:

f_e is deflection in the beam measured under the test load;
 f_{cal} - deflection in the beam, determined by calculation from the action of the test load.

K - design factor values for the main load-bearing structures and their elements are from 0.7 to 1.0 and for the superstructures elements, in which the calculations do not take into account the joint behavior of the main beams with the elements of the roadway and road surfacing, as a rule, from 0.5 to 0.7 according to the static tests results.

The calculated deflection from the test load action in the middle of the span of a length of 33.0 m is determined by the formula:

$$f_{cal} = \frac{1.1 \cdot p \cdot l^3}{24 \cdot E_b \cdot I_{red}}, \quad (9)$$

where:

$P = 230 \text{ kN}$ is the truck load;

$l = 32.4 \text{ m}$ - calculated beam span;

$E_b = 352 \cdot 10^5 \text{ kN/m}^2$ - beam concrete modulus of elasticity;

$I_{red} = 0.1875 \text{ m}^4$ - inertia moment of the cross section in the middle of the beam.

Its behavior as a part of the superstructure should be taken into account when determining the deflection

in a beam. The test load proportion perceived by the beam is determined by the transverse location factor shown in Table 5.

The obtained design factor values indicate presence of load-bearing capacity reserves in the structural elements and evidence that the superstructure beams behavior corresponds to the accepted microflexibility approach.

4 Conclusions

Based on the survey results of damaged structures, the recommendations for the repair of some beams have been developed and a number of beams have been proposed to be dismantled and replaced by the new beams.

Defects that reduce the structure operational properties were not detected during the survey. The technical condition of the structural elements and, in general, the structure itself should be recognized as meeting the project requirements.

The overpass structures condition survey showed that there were no defects or damages affecting the safe movement of vehicles and pedestrians. The condition of the bridge load-bearing structures meets the project requirements.

Analysis of the deflection increments values, at the loading and unloading stages, in three test stages testified to the elastic behavior of the superstructure.

The survey and tests' results of Almaty-Kapshagai highway overpass showed that the actual stress-strain state of the load-bearing structures corresponds to the microflexibility approach.

The overpass design capacity (km 38+90) on Almaty-Kapshagai highway section is provided and it can be operated under A14, NK-120 and NK-180 [25] design loads without restrictions.

References

- [1] SIDDIKA, A., MAMUN, A., ALYOUSEF, R., AMRAN, M. Strengthening of reinforced concrete beams by using fiber-reinforced polymer composites: a review. *Journal of Building Engineering* [online]. 2019, **25**, p. 24-28 [accessed 2019-10-05]. ISSN 2352-7102. Available from: <https://doi.org/10.1016/j.job.2019.100798>
- [2] GOKHAN, D., NACI, C., ALPER, I., CEMAL, Y. Residual load bearing capacity and failure mechanism of impacted high-strength reinforced concrete shear beams. *Engineering Failure Analysis* [online]. 2021, **121**, p. 24-29 [accessed 2020-31-12]. ISSN 1350-6307. Available from: <https://doi.org/10.1016/j.engfailanal.2020.105185>

- [3] MISKIEWICZ, M., BRUSKI D., CHROSCIELEWSKI, J., WILDE, K. Safety assessment of a concrete viaduct damaged by vehicle impact and an evaluation of the repair. *Engineering Failure Analysis* [online]. 2019, **106**, p. 45-49 [accessed 2019-23-08]. ISSN 1350-6307. Available from: <https://doi.org/10.1016/j.engfailanal.2019.104147>
- [4] WEI, F., YANG, S., CANCAN, Y., WENBIAO, S. YANG, H. Assessing the response and fragility of concrete bridges under multi-hazard effect of vessel impact and corrosion. *Engineering Structures* [online]. 2020, **225**, p. 54-69 [accessed 2020-15-12]. ISSN 0141-0296. Available from: <https://doi.org/10.1016/j.engstruct.2020.111279>
- [5] ZEIN, S., NEAZ, S., ALEX, R., ABHEEK, B. Damage assessment of GFRP bar reinforced ultra-high-strength concrete beams under overloading impact conditions. *Engineering Structures* [online]. 2020, **213**, p. 54-69 [accessed 2020-15-06]. ISSN 0141-0296. Available from: <https://doi.org/10.1016/j.engstruct.2020.110581>
- [6] CHASSIAKOS, A. P., VAGIOTAS, P., THEODORAKOPOULOS, D. D. A knowledge-based system for maintenance planning of highway concrete bridges. *Advances in Engineering Software* [online]. 2005, **36**(11-12), p. 740-749 [accessed 2005-11-12]. ISSN 0965-9978. Available from: <https://doi.org/10.1016/j.advengsoft.2005.03.020>
- [7] MAHMOUD, D., MANSOUR, M., MAHDI, I., HUSSEIN, A., ARAFAT, H. An assessment model for identifying maintenance priorities strategy for bridges. *Ain Shams Engineering Journal* [online]. 2019, **10**(4), p. 695-704 [accessed 2019-23-08]. ISSN 2090-4479. Available from: <https://doi.org/10.1016/j.asej.2019.06.003>
- [8] TELES, D., OLIVEIRA, M., AMORIM, D. A simplified lumped damage model for reinforced concrete beams under impact loads. *Engineering Structures* [online]. 2019, **205**, 110070 [accessed 2019-9-12]. ISSN 0141-0296. Available from: <https://doi.org/10.1016/j.engstruct.2019.110070>
- [9] MUSAB RABI, M., CASHELLA, K. A., SHAMASS, R. Flexural analysis and design of stainless steel reinforced concrete beams. *Engineering Structures* [online]. 2019, **198**, 109432 [accessed 2019-14-08]. ISSN 0141-0296. Available from: <https://doi.org/10.1016/j.engstruct.2019.109432>
- [10] YU, Y., LEE, S., CHO, J.-Y. Deflection of reinforced concrete beam under low-velocity impact loads. *International Journal of Impact Engineering* [online]. 2021, **154**, 103878 [accessed 2021-27-03]. ISSN 0734-743X. Available from: <https://doi.org/10.1016/j.ijimpeng.2021.103878>
- [11] KOVACIC, B., KAMNIK R., PUSTOVGAR A. Analysis of precision of geodetic instruments for investigating vertical displacement of structures. In: 15th International scientific conference Underground Urbanisation as a Prerequisite for Sustainable Development: proceedings. Procedia Engineering 165. St. Petersburg: Peter the Great St. Petersburg Polytechnic University, 2016. ISSN 1877-7058, p. 906-917.
- [12] GHEITASI, A., OZBULUT, O. E., USMANI, S., ALIPOUR, M., HARRIS, D. K. Experimental and analytical vibration serviceability assessment of an in-service footbridge. *Case Studies in Nondestructive Testing and Evaluation* [online]. 2016, **6**(A), p. 79-88 [accessed 2016-9-11]. ISSN 2214-6571. Available from: <https://doi.org/10.1016/j.csndt.2016.11.001>
- [13] WANG, X., MAO, X., FRANGOPOL, D. M., DONG Y., WANG, H., TAO, P., QI, Z., TANG, S. Full-scale experimental and numerical investigation on the ductility, plastic redistribution and redundancy of deteriorated concrete bridges. *Engineering Structures* [online]. 2021, **234**, p. 79-88 [accessed 2021-1-21]. ISSN 0141-0296. Available from: <https://doi.org/10.1016/j.engstruct.2021.111930>
- [14] KRAKHMALNY, T. A., EVTUSHENKO, S. I., KRAKHMALNAYA, M. P. Improvement of a method of calculation of a residual resource of small reinforced concrete bridge constructions. In: International Conference on Industrial Engineering: proceedings. Procedia Engineering 150. Novocherkassk: Platov South-Russian State Polytechnic University, 2016. ISSN 1877-7058, p. 1797-1803.
- [15] SELIEM, H. M., EID, M., SHERIF, A. G. Assessment of vehicular live load and load factors for design of short-span bridges according to the new Egyptian code. *Housing and Building National Research Center* [online]. 2014, **11**, p. 57-67 [accessed 2014-24-02]. ISSN 1687-4048. Available from: <https://doi.org/10.1016/j.hbrcej.2014.02.009>
- [16] FAN, W., LIU, B., HUANG, X., SUN, S. An efficient modeling method was proposed to capture both flexural and shear behaviors of RC members under impact loading. *Engineering Structures* [online]. 2019, **195**, p. 22-50 [accessed 2019-4-06]. ISSN 0141-0296. Available from: <https://doi.org/10.1016/j.engstruct.2019.05.082>
- [17] RAPHAELA, W., ZGHEIBA, E., CHATEAUNEUF, A. Experimental investigations and sensitivity analysis to explain the large creep of concrete deformations in the bridge of Chevire. *Case Studies in Construction Materials* [online]. 2018, **9**, p. 22-30 [accessed 2018-17-05]. ISSN 2214-5095. Available from: <https://doi.org/10.1016/j.cscm.2018.e00176>
- [18] ALAYLIOGLU, H., ALAYLIOGLU, A. Dynamic structural assessment of a highway bridge via hybrid FE model and in situ testing. *Computers and Structures* [online]. 1997, **63**(3), p. 439-453 [accessed 1997-1-05]. ISSN 0045-7949. Available from: [https://doi.org/10.1016/S0045-7949\(96\)00364-1](https://doi.org/10.1016/S0045-7949(96)00364-1)
- [19] HENG, K., LI, R., LI, Z., WU, H. Dynamic responses of highway bridge subjected to heavy truck impact. *Engineering Structures* [online]. 2021, **232**, p. 22-30 [accessed 2021-1-04]. ISSN 0141-0296. Available from: <https://doi.org/10.1016/j.engstruct.2020.111828>

- [20] FAN, W., SHEN, D., HUANG, X., SUN, Y. Reinforced concrete bridge structures under barge impacts: FE modeling, dynamic behaviors and UHPFRC-based strengthening. *Ocean Engineering* [online]. 2020, **216**, p. 22-30 [accessed 2020-15-11]. ISSN 0029-8018. Available from: <https://doi.org/10.1016/j.oceaneng.2020.108116>
- [21] GANESH, P., MURTHY, A. R. Fatigue performance of damaged RC beams rehabilitated with GGBS based ultra high performance concrete. *International Journal of Fatigue* [online]. 2020, **138**, p. 22-30 [accessed 2020-17-05]. ISSN 0142-1123. Available from: <https://doi.org/10.1016/j.ijfatigue.2020.105707>
- [22] VICAN, J., GOGAL, J., ODRONINAK, J., MORAVCIK, M., KOTES, P. Determination of railway bridges loading capacity. In: XXIV R-S-P Seminar, Theoretical Foundation of Civil Engineering (24RSP): proceedings. *Procedia Engineering* 111. Zilina: University of Zilina, 2015. ISBN 1877-7058, p. 839-844.
- [23] SOUSA, H. BENTO, J., FIGUEIRAS, J. Construction assessment and long-term prediction of prestressed concrete bridges based on monitoring data. *Engineering Structures* [online]. 2013, **52**, p. 26-37 [accessed 2013-07]. ISSN 0141-0296. Available from: <https://doi.org/10.1016/j.engstruct.2013.02.003>
- [24] SIWOWSKI, T., RAJCHEL, M., KULPA, M. Design and field evaluation of a hybrid FRP composite - lightweight concrete road bridge. *Composite Structures* [online]. 2019, **230**, p. 26-37 [accessed 2019-24-09]. ISSN 0263-8223. Available from: <https://doi.org/10.1016/j.compstruct.2019.111504>
- [25] SNIP 3.06.07-86. Overpasses and underpasses. Inspection and testing requirements / Mosty i Truby. Pravila obsledovani i ispytani (in Kazakh).

DYNAMIC RESPONSE OF A ROAD BRIDGE SUBJECTED TO PASSING A HEAVY VEHICLE OVER A STANDARD IRREGULARITY - NUMERICAL MODELLING AND EXPERIMENTAL TESTING

Milan Moravčík

Faculty of Civil Engineering, University of Zilina, Zilina, Slovakia

*E-mail of corresponding author: mimo@fstav.uniza.sk

Resume

The paper presents an analysis of an actual problem related to dynamic effects to road bridges due to travelling a heavy vehicle over the bridge. Numerical simulations of the dynamic response are applied on a fictitious simple beam of the length $L_b = 52$ m with an artificial irregularity at mid-span, corresponding to a characteristic span $L_{(bs)} = 52$ m of the ten-span continuous box girder bridge. A heavy four-axle truck $m_v = 32$ t is used for dynamic excitation, travelling over the bridge at passing speed of 70 km / h. The obtained results are compared to results of the experimentally tested ten-span continuous pre-stressed reinforced concrete girder bridge at the same speed.

Article info

Received 5 May 2021

Accepted 21 June 2021

Online 27 October 2021

Keywords:

dynamic bridge deflection, moving vehicle load, modal superposition, numerical simulation, dynamic testing

Available online: <https://doi.org/10.26552/com.C.2022.1.D37-D45>

ISSN 1335-4205 (print version)

ISSN 2585-7878 (online version)

1 Introduction

Nowadays, one of the current problems in bridge engineering is evaluation of the dynamic response due to the intensive passages of heavy trucks and lorries over the bridge. This paper deals with validation of a simplified numerical modelling of a dynamic response of a bridge structure, induced by passing of a heavy truck vehicle over an artificial standard irregularity. Numerical modelling, as well as dynamic load tests of a heavy vehicle crossings over a bridge with the standard irregularity at mid-span [1], is an important procedure for checking the dynamic behavior and quality of a bridge structure under intense dynamic loading. Numerical simulations were created for a characteristic span $L_{(bs)} = 52$ m of the ten-span continuous box girder road bridge, modelled as a fictive simple beam associated to the characteristic span. This field has been experimentally tested for crossing of a heavy truck at the speed of 70 km/h. The overall view of the tested bridge is shown in Figure 1.

The solution of deflections of mid-span was obtained by application the linear theory of solving the motion equation, giving the beam deflection as a function of time [2-3]. The purpose of the numerical modelling has been:

(1) To verify the proposed simplified solution of the

dynamic response for a characteristic span of a continuous bridge structure, which is currently used the most, as a response of the fictive simple beam;

(2) To evaluate the intense dynamic response due to the moving of a heavy truck as an impact of the impulse load arising on the irregularity.

2 Numerical model

The simplified interaction model vehicle bridge is schematically shown in Figure 2a. The loading vehicle, used for dynamic excitation of the bridge is a four-axle heavy truck of the weight $m_v = 32$ t travelling over the bridge at speed 70 km/h, shown in Figure 2b.

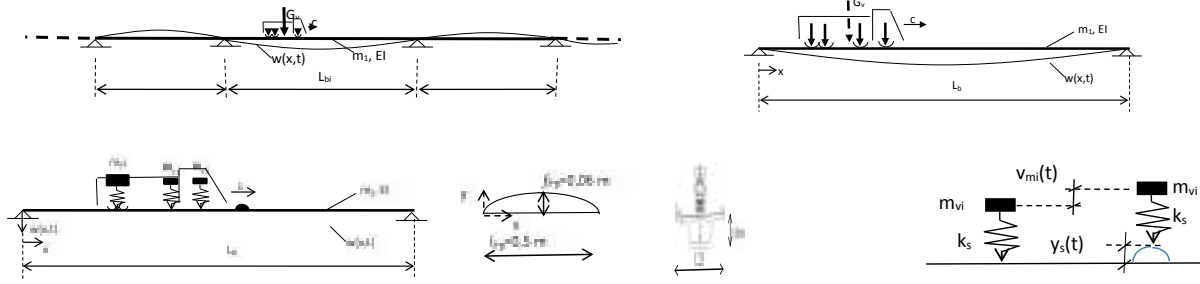
3 Physical modelling and formulation

The dynamic deflection of the simple bridge $L_b = 52$ m at mid-span, due to moving an axle mass m_{vi} crossing over the bridge at a speed c , obtained by superposition of a force vibration of a simple beam ${}^{(c)}w_{(1),(F_{vi})}(L_b/2, t)$ considering the first mode $j = 1$ only, subjected to a moving load F_{vi} and the impulse effect on the irregularity ${}^{(c)}w_{(M_0),(IF_{vi}Vel)}(t)$.

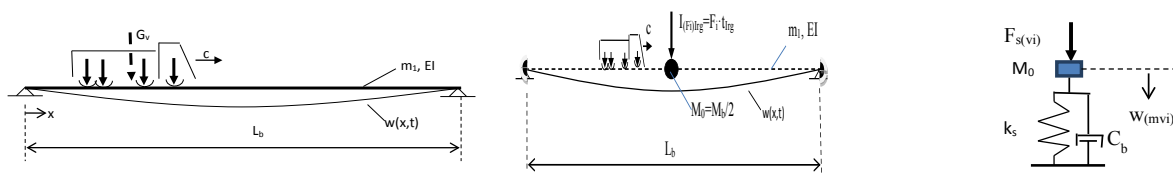


Figure 1 Overall view of the tested ten-span continuous concrete box-girder bridge

a) Moving of a heavy truck over a fictive simple beam bridge corresponding to a characteristic span $L_{(b5)} = 52$ m of the ten-span continuous bridge



Superposition: The moving load model + the modelling of effect of the standard irregularity



b) Loading model - the whole heavy truck model

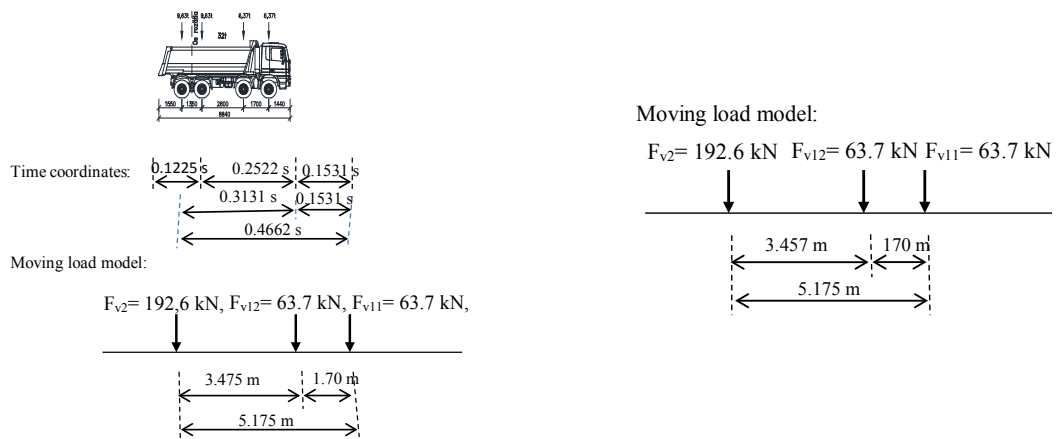


Figure 2 Schematic representation of the simplified dynamic analysis of a road bridge (due to crossing of a heavy car)

$${}^{(c)}w_{(F_{vi} + IF_{vi}Vel)}(L_b/2, t) = {}^{(c)}w_{(1),(F_{vi})}(L_b/2, t) + {}^{(c)}w_{(M_0),(IF_{vi}Vel)}(t). \tag{1}$$

3.1 Moving load problem - the dynamic deflection ${}^{(c)}w_{(1),(F_{vi})}(L_b/2, t)$ of the simple beam

The generally used method of modal superposition, together with use of the convolution integral, gives the closed form solution of the vertical dynamic displacements of the beam. This solution gives results that well correspond to the evaluated measurements of a dynamic response on real bridges of various structural arrangements. The beam is assumed to be of the Bernoulli-Euler type, Figure 3.

The beam displacement $w(x, t)$ are governed by the typical equation of motion

$$m_1 \frac{\partial^2 w(x, t)}{\partial t^2} + EI \frac{\partial^4 w(x, t)}{\partial x^4} = {}^{(c)}F_{vi} \delta(x - ct), \tag{2}$$

for $0 \leq ct \leq L_b$.

Many methods for solving this problem were developed and discussed in the literature (see e.g. [2-3]). One of the most well-known techniques is a solution based on the principle of modal superposition [4-6]. The solution Equation (2), represented in the series form, can be expressed as

$$w(x, t) = \sum_j q_j(t) \phi_j(x), j=1,2,\dots, \tag{3}$$

where $\phi_j(x)$ is the j -th modal shape function and $q_j(t)$ is the j -th modal amplitude.

For practical applications of a moving axle mass m_{vi} and for $m_{vi} \ll m_b$, it is concluded that the solution is of sufficient accuracy even if only the first mode of vibration ($j=1$) is considered. This solution gives results that well correspond to the evaluated measurements of a dynamic response on real bridges of various structural

arrangements. The excitation force ${}^{(c)}F_{vi}$ in Equation (2) represents the interaction force between the vehicle and the bridge structure. When the kinematic coupling a vehicle - bridge is neglected, the force ${}^{(c)}F_{vi}$ is simply an applied sprung axle force, (Figure 2b).

The solution to Equation (2) for a simple beam can be expressed in terms of the modal shapes $\phi_{(1)}(t)$ and associated modal coordinates $q_{(1)}(t)$ considering only the first mode $j = 1$. A beam deflection in the subsequent analysis is marked [4, 6] as ${}^{(c)}q_{(1),(F_{vi})}(t) \equiv {}^{(c)}w_{(1),(F_{vi})}(L_b/2, t)$.

$${}^{(c)}w_{(1),(F_{vi})}(L_b/2, t) = \frac{\hat{w}_{(1),(F_{vi})st}(L_b/2)}{1 - {}^{(c)}\alpha_{(1)}^2} \times (\sin({}^{(c)}\Omega_{(1)dr}(t - t_{(F_{vi})})) - {}^{(c)}\alpha_{(1)} \sin \omega_1(t - t_{(F_{vi})})) \times (H(t - t_{(F_{vi})in}) - H(t - t_{(F_{vi})out})). \tag{4}$$

The symbols used in Equation (4) have the following meaning: the driving frequency ${}^{(c)}\Omega_{(1)dr} = \frac{\pi c}{L_b}$, the non-dimensional parameter ${}^{(c)}\alpha_{(1)} = \frac{{}^{(c)}\Omega_{(1)dr}}{\omega_{(1)}}$,

the frequency vibration of the 1st mode of the beam

$$\omega_{(1)} = \frac{\pi^2}{L_b^2} \sqrt{\frac{EI}{m_1}} = \frac{3.14^2}{52^2} \sqrt{\frac{704802005}{22.16}} = 20.56 \text{ s}^{-1},$$

$$\text{the static displacement } \hat{w}_{(1),(F_{vi})st}(L_b/2, t) = \frac{2F_{vi} \cdot L_b^3}{\pi^4 \cdot EI^*}$$

due to the axle vehicle forces F_{vi} , the modal amplitude $\frac{\hat{w}_{(1),(F_{vi})st}(L_b/2)}{1 - {}^{(c)}\alpha_{(1)}^2}$, and the Heaviside function $H(t - t_{(F_{vi})})$.

3.2 Impulse load effect ${}^{(c)}I_{(sF_i, Vel)}$ arising on the irregularity considering the velocity of the spring compression ${}^{(c)}\hat{v}_{s(sup)} = {}^{(c)}\hat{v}_{lrg}$

Schematic illustration of the impulse load effect on the irregularity ${}^{(c)}I_{(sF_i, Vel)}$ on the dynamic response is shown in Figure 4.

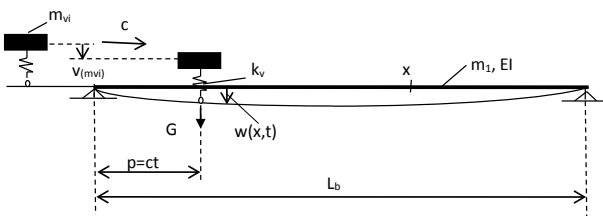


Figure 3 A single axle mass m_{vi} moving over a simple supported beam

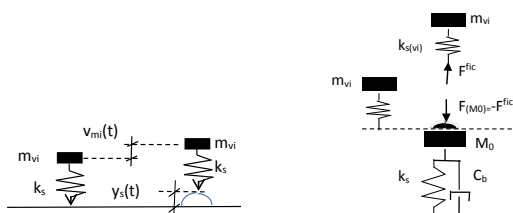
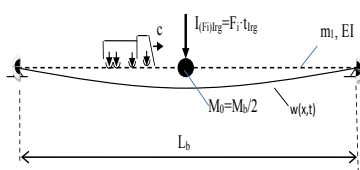
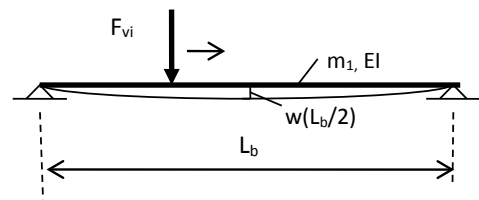


Figure 4 Schematic illustration of the impulse load effect on the irregularity ${}^{(c)}I_{(sF_i, Vel)}$ on the dynamic response

Table 1 The main parameters used in the simulations

Data of the bridge	Data of the vehicle
$L_b = 52 \text{ m}$	$m_v = 32 \text{ t}$
$A = 8.865 \text{ m}^2$	$m_{v11} = 6.37 \text{ t}$
$I = 10.97 \text{ m}^4$	$m_{v12} = 6.37 \text{ t}$
$m_{b,1} = 22.16 \text{ t/m}$	$m_{v2} = 19.26 \text{ t}$
$M_0 = 576.22 \text{ t}$	$k_{s11} = k_{s12} = 2545.4 \text{ kN/m}$
$EI_{(sb)}^* = 704802005 \text{ kNm}^2$	$k_{s2} = 5091 \text{ kN/m}$
${}^{(c=70)}\hat{w}_{(1),(Fv)st}(L_b/2) = \frac{2F_{(v320)}L_b^3}{\pi^4 EI_{(sb)}} = 0.0013$	
$\omega_{(1)} = \frac{\pi^2}{L_b^2} \sqrt{\frac{EI_{(sb)}}{m_1}} = 20.56 \text{ s}^{-1}$	

If the sprung mass system $1DOF_{(m_{vi})}$ (a single degree of freedom system) is subjected to the initial displacement ${}^{(c)}v_{(m_{vi})}(t=0) = v_0$ and the initial velocity $\dot{v}_{(m_{vi})}(t=0) = \dot{v}_0$, a free vibration displacement ${}^{(c)}v_{(m_{vi})}(t)$ of $1DOF_{(m_{vi})}$ may be expressed as follows [2, 3].

$${}^{(c)}v_{(m_{vi})}(t) = e^{-\omega b(t-t_{(Fvi)})} \frac{\hat{v}_0}{\omega_{(m_{vi})}} \sin \omega_{(m_{vi})}(t - t_{(Fvi)}). \quad (5)$$

The displacement amplitude ${}^{(c)}\hat{v}_{(m_{vi})}$ in Equation (5) can be expressed by means of the velocity ${}^{(c)}\hat{v}_{\text{sup}}$ from the impulse theorem

$$H_{(m_{vi})} = {}^{(c)}I_{(m_{vi})} \dots m_{vi} {}^{(c)}\hat{v}_{(m_{vi})} = {}^{(c)}F_{(m_{vi})Vel} {}^{(c)}t_{Irg}. \quad (6)$$

Thus, the amplitude of velocity from Equation (6) is

$${}^{(c)}\hat{v}_{(m_{vi})} = \frac{{}^{(c)}F_{(m_{vi})Vel} {}^{(c)}t_{Irg}}{m_{vi}}. \quad (7)$$

The displacement amplitude ${}^{(c)}\hat{v}_{(m_{vi})}$ of $1DOF_{(m_{vi})}$ from Equation (5) is expressed by means of the impulse ${}^{(c)}I_{(Fm_{vi})Vel}$, taking into account the rate of deformation ${}^{(c)}\hat{v}_{(m_{vi})}$ of the suspension:

$${}^{(c)}\hat{v}_{(m_{vi})} = \frac{\hat{v}_0}{\omega_{(m_{vi})}} = \frac{{}^{(c)}F_{(m_{vi})Vel} {}^{(c)}t_{Irg}}{m_{(vi)}\omega_{(m_{vi})}} = \frac{{}^{(c)}I_{(Fm_{vi})Vel}}{m_{(vi)}\omega_{(m_{vi})}}. \quad (8)$$

The amplitude of the dynamic deflection ${}^{(c)}\hat{w}_{(M_0),(IFvi)Vel}$ for $1DOF_{(M_0)}$ is expressed by means of a reactive impulse due to the impulse load ${}^{(c)}I_{(Fvi)Vel}$, Figure 3.

$${}^{(c)}\hat{w}_{(M_0),(IFvi)Vel}(t) = \frac{{}^{(c)}I_{(Fvi)Vel}}{\omega_0 M_0} \quad (9)$$

A dynamic deflection ${}^{(c)}\hat{w}_{(M_0),(IFvi)Vel}(t)$ of $1DOF_{(M_0)}$, with the amplitude Equation (9), can be expressed in the form [3, 6]:

$${}^{(c)}\hat{w}_{(M_0),(IFvi)Vel}(t) = \frac{{}^{(c)}I_{(Fvi)Vel}}{M_0 \omega_0} e^{-\omega b(t-t_{(Fvi)})} \sin \omega_0 \times (t - t_{(Fvi)}) \cdot (H(t - t_{(Fvi)(in)}) - H(t - t_{(Fvi)(out)})). \quad (10)$$

3.3 Simulation of the dynamic deflections for crossing of the three axle heavy truck

${}^{(c=70)}F_{(v320)} = 320 \text{ kN}$ with the speed $c = 70$

km/h = 19.44 m/s and the rate of deformation

${}^{(c=70)}\hat{y}_{Irg} = 9.33 \text{ m/s}$, ${}^{(c=70)}t_{Irg} = \frac{0.5}{19.44} = 0.0257$

for time $t > t_{Irg}$

The total dynamic displacement of the bridge due to moving an axle mass m_{vi} at the speed $c = 70 \text{ km/h} = 19.44 \text{ m/s}$ is obtained by superposition from Equation (1). In the subsequent analyses the components of the dynamic response ${}^{(c)}w_{(1),(Fvi)}(L_b/2, t)$ and ${}^{(c)}w_{(M_0),(IFvi)Vel}(t)$, the total dynamic deflection ${}^{(c)}w_{(Fvi+IFvi)Vel}(L_b/2, t)$ and the dynamic coefficient ${}^{(c)}\delta_{dyn(Fvi+sFvi)Vel}(L_b/2, t)$ are presented. The results of dynamic displacements from the above analytical relationships are presented graphically [8].

Input parameters

The main parameters used in the simulations are shown in Table 1.

Kinematic quantities ${}^{(c)}y_{Irg}(t)$, ${}^{(c)}\dot{y}_{Irg}(t)$ for the irregularity in the form of a parabolic plank, $l_{Irg} = 0.50 \text{ m}$, $h_{Irg} = 0.6 \text{ m}$, required for formulating an impulse load effect on the irregularity ${}^{(c)}I_{(Fi)Vel}$, for the speed $c = 70 \text{ km/h}$, are:

$${}^{(c=70)}y_{Irg}(t) = -0.96c^2t^2 + 0.48ct = -0.96 \times 19.44^2t^2 + 0.48 \cdot 19.44t = -362.8t^2 + 9.33t, \quad (11)$$

$${}^{(c=70)}\dot{y}_{Irg}(t) = -1.92 \cdot c^2t + 0.48c = -1.92 \times 19.44^2t + 0.48 \cdot 19.44 = -725.59t + 9.33. \quad (12)$$

Characteristics of an impulse effect for the axle force $F_{(v11)} = 63.7 \text{ kN}$

- Compression of the spring ${}^{(c=70)}\hat{v}_{(\text{sup})Vel}$ due to the velocity ${}^{(c=70)}\hat{v}_{\text{sup}} = 9.33 \text{ m/s}$ and

$${}^{(c=70)}\hat{v}_{(\text{sup})Vel} = {}^{(c=70)}\hat{v}_{\text{sup}} {}^{(c=70)}t_{(hIrg)} = 9.33 \cdot 0.0257 = 0.2398 \text{ m}, \quad (13)$$

- Force in the spring ${}^{(c=70)}F_{11(v_{sup} Vel)}$ due to the compression in the spring ${}^{(c=70)}\hat{v}_{(sup, Vel)}$

$${}^{(c=70)}F_{11(v_{sup} Vel)} = \frac{F_{v11} {}^{(c=70)}\hat{v}_{(sup, Vel)}}{t_{lrg}} = \frac{63.7 \cdot 0.2398}{0.06} = 254.56 \text{ kN}, \quad (14)$$

Impulse size ${}^{(c=70)}I_{(F_{11} Vel)}$ due to the sprung force ${}^{(c=70)}F_{11(v_{sup} Vel)}$ acting on the spring of $1DOF_{(m_{v1})}$

$${}^{(c=70)}I_{(F_{11} Vel)} = {}^{(c=70)}F_{11(v_{sup} Vel)} {}^{(c=70)}t_{lrg} = 254.56 \cdot 0.0257 = 6.5422 \text{ kNs}, \quad (15)$$

- Amplitude of displacement ${}^{(c=70)}\hat{w}_{(M_0), (IF_{v11} Vel)}(t)$ acting on the spring of $1DOF_{(m_{v1})}$

$${}^{(c=70)}\hat{w}_{(F_{v11} Vel)} = \frac{{}^{(c=70)}I_{(F_{v11} Vel)}}{\omega_{(m_{v11})} m_{(v11)}} = \frac{6.5422}{20 \cdot 6.37} = 0.0513 \text{ m}, \quad (16)$$

- Amplitude ${}^{(c=70)}\hat{w}_{(M_0), (F_{v11} Vel)}(t)$ acting on the spring of $1DOF_{(M_0)}$ for the impulse ${}^{(c=70)}I_{(F_{v11} Vel)} = 6.5422 \text{ kNs}$

$${}^{(c=70)}\hat{w}_{(M_0), (IF_{v11} Vel)}(t) = \frac{{}^{(c=70)}I_{(F_{v11} Vel)}}{\omega_0 M_0} = \frac{6.5422}{20.43 \cdot 576.16} = 0.00056 \text{ m}. \quad (17)$$

Characteristics of an impulse effect for the axle force ${}^{(c=70)}F_{(v2)} = 192.6 \text{ kN}$ is obtained analogously as for Equations (13) to (17).

Requirement of the same amplitudes of the deflection of continuous beam $\hat{w}_{(Fv320)st}(L_b/2, t)$ for the span No. 5 from the static calculation of the bridge is $\hat{w}_{(Fv320)st}(L_b/2, t) = 0.00133 \text{ m}$. The deflection of fictive simple beam $\hat{w}_{(Fv320)st}(L_b/2, t)$, with the fictive bending stiffness $E\hat{I}_{(sb)}$, for the force $F_v = 320 \text{ kN}$ it is image in Figure 5.

$$E\hat{I}_{(sb)} = \frac{F_v L_{(5)}^3}{48 \cdot w_{(F_v), (L_{(5)})}(x, \hat{p})} = \frac{320 \cdot 52^3}{48 \cdot 0.00133} = 704802005 \text{ kNm}^2. \quad (18)$$

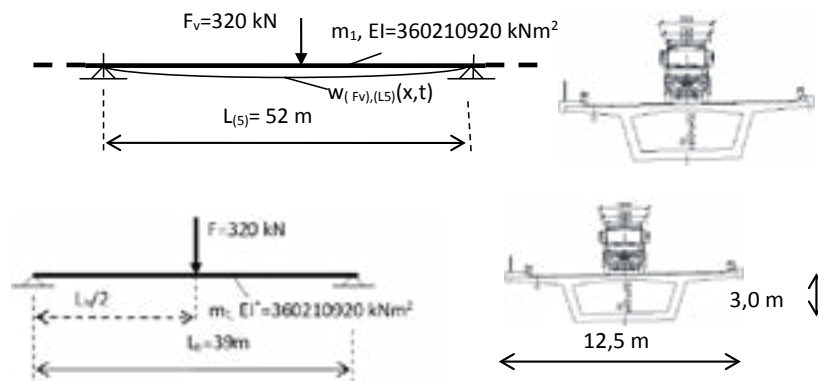


Figure 5 Associated fictitious simple beam for the analysis of the 5th span of bridge with the reduced bending stiffness $E\hat{I}_{(sb)}$

3.3.1 Time history of the dynamic deflections

${}^{(c)}w_{(F_{vi} + IF_{vi} Vel)}(L_b/2, t)$ due to the moving load F_{vi} for a time $t > t_{lrg}$

The dynamic deflections of the mid-span ${}^{(c)}w_{(F_{vi} + IF_{vi} Vel)}(L_b/2, t)$ from Equation (1) are applied for the speed $c = 70 \text{ km/h} = 19.44 \text{ m/s}$:

$${}^{(c=70)}w_{(F_{vi} + IF_{vi} Vel)}(L_b/2, t) = {}^{(c=70)}w_{(1), (F_{vi})}(L_b/2, t) + {}^{(c=70)}w_{(M_0), (IF_{vi} Vel)}(t). \quad (19)$$

3.3.1-1 Dynamic deflections ${}^{(c)}w_{(1), (Fv320)}(L_b/2, t)$ due to the moving axle load F_{v11}, F_{v12}, F_{v2}

a) Components of deflection

${}^{(c=70)}w_{(1), (F_{v11})}(L_b/2, t)$, ${}^{(c=70)}w_{(1), (F_{v12})}(L_b/2, t)$, ${}^{(c=70)}w_{(1), (F_{v2})}(L_b/2, t)$ belonging to axle loads, Figure 6.

b) Total deflection of the beam

${}^{(c=70)}w_{(1), (Fv320)}(L_b/2, t) \equiv {}^{(c=70)}q_{(1), (F_{v11} + F_{v12} + F_{v2})}(t)$ belong to the moving axle load $F_{v320} = F_{v11} + F_{v12} + F_{v2}$, Figure 7.

$${}^{(c=70)}w_{(1), (Fv320)}(L_b/2, t) = {}^{(c=70)}w_{(1), (F_{v11})}(L_b/2, t) + {}^{(c=70)}w_{(1), (F_{v12})}(L_b/2, t) + {}^{(c=70)}w_{(1), (F_{v2})}(L_b/2, t) \quad (20)$$

3.3.1-2 Dynamic deflections ${}^{(c=70)}w_{(M_0), (IF_{v320})}(L_b/2, t)$ due to the impulse load on the irregularity

$$I_{(v320)} = I_{(v11)} + I_{(v12)} + I_{(v2)}$$

Input characteristics are given from Equations (13) to (17).

a) Components of dynamic deflection

${}^{(c=70)}w_{(M_0), (IF_{v11} Vel)}(t)$, ${}^{(c=70)}w_{(M_0), (IF_{v12} Vel)}(t)$, ${}^{(c=70)}w_{(M_0), (IF_{v2} Vel)}(t)$ belong to the impulse load, Figure 8.

b) Total displacement ${}^{(c=70)}w_{(M_0), (IF_{v320} Vel)}(t)$ belong to the impulse load $F_v = 320 \text{ kN}$

${}^{(c=70)}w_{(M_0), (IF_{v320} Vel)}(t) = {}^{(c=70)}w_{(M_0), (IF_{v11} Vel)}(t) + {}^{(c=70)}w_{(M_0), (IF_{v12} Vel)}(t) + {}^{(c=70)}w_{(M_0), (IF_{v2} Vel)}(t)$, Figure 9.

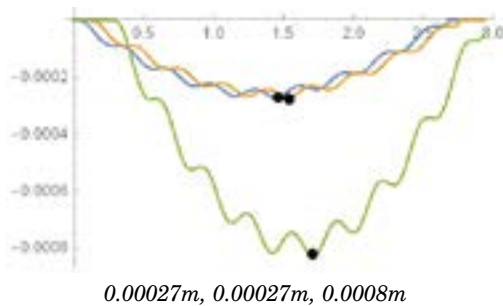


Figure 6 Axes: $x = t [s]$, $y =$ Components of deflection ${}^{(c=70)}w_{(1),(F_{v11})}(L_b/2, t)$, ${}^{(c=70)}w_{(1),(F_{v12})}(L_b/2, t)$, ${}^{(c=70)}w_{(1),(F_{v2})}(L_b/2, t)$ [m] belonging to axle loads F_{v1p} , F_{v2}

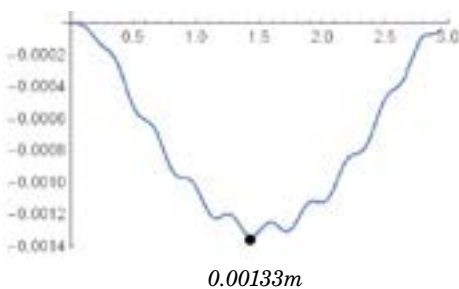


Figure 7 Axes: $x = t [s]$, $y = {}^{(c=70)}w_{(1),(F_{v320})}(L_b/2, t)$ [m], Total amplitude of deflection ${}^{(c=70)}\hat{w}_{(1),(F_{v320})}(L_b/2) = 0.00133$ m

3.3.2 Aggregate force effects acting on the beam deflection ${}^{(c=70)}w_{(M_0),(F_{v320} + IF_{v320} Vel)}(L_b/2, t)$

Aggregate force effects from Equation (19) for the whole truck obtain by the superposition of the moving load ${}^{(c=70)}w_{(1),(F_{v320})}(L_b/2, t)$ and the impulse load on the irregularity ${}^{(c=70)}w_{(M_0),(IF_{v320} Vel)}(L_b/2, t)$.

a) **Components** ${}^{(c=70)}w_{(1),(F_{v320})}(L_b/2, t)$, ${}^{(c=70)}w_{(M_0),(IF_{v320} Vel)}(L_b/2, t)$, Figure 10.

b) **Aggregate beam deflection** ${}^{(c=70)}w_{(M_0),(F_{v320} + IF_{v320} Vel)}(L_b/2, t)$
 ${}^{(c=70)}w_{(M_0),(F_{v320} + IF_{v320} Vel)}(L_b/2, t) =$
 $= {}^{(c=70)}w_{(1),(F_{v320})}(L_b/2, t) + {}^{(c=70)}w_{(M_0),(IF_{v320} Vel)}(t)$

Figure 11.

3.3.3 Dynamic impact factor (DAF)

${}^{(c=70)}\delta_{dyn}(F_{v320} + IF_{v320} Vel)(L_b/2, t)$ for the beam deflection

$${}^{(c=70)}\delta_{dyn}(F_{v320} + IF_{v320} Vel)(L_b/2, t) = \frac{{}^{(c=70)}w_{(F_{v320} + IF_{v320} Vel)max}(L_b/2, t)}{{}^{(c=70)}w_{(1),(F_{v320})st}(L_b/2, t)}, \text{ Figure 12.} \quad (21)$$

All the graphical solution (Figures 6 to 12) are the outputs from [8].

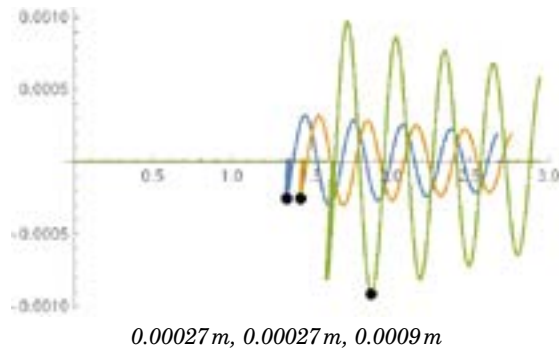


Figure 8 Axes: $x = t [s]$, $y =$ Components belong to the impulse load ${}^{(c=70)}w_{(M_0),(IF_{v11} Vel)}(t)$, ${}^{(c=70)}w_{(M_0),(IF_{v12} Vel)}(t)$, ${}^{(c=70)}w_{(M_0),(IF_{v2} Vel)}(t)$ [m]

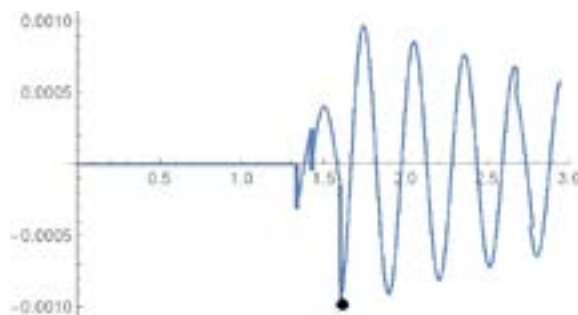


Figure 9 Axes: $x = t [s]$, $y = {}^{(c=70)}w_{(M_0),(IF_{v320} Vel)}(t)$ [m], Amplitude ${}^{(c=70)}\hat{w}_{(M_0),(IF_{v320} Vel)} = 0.001$ m

4 Dynamic load test of the 10-span RC highway bridge for passing a heavy truck $F_v = 320$ kN over the standard irregularity for the speed $c = 70$ km/h

In the previous section the dynamic response of a fictitious simple beam of length $L_b = 52$ m with the flexural stiffness $EI_{(sb)}$, corresponding to the characteristic span $L_{bi} = 52$ m of the ten-span continuous bridge, was analysed. In this section some results are presented from the dynamic testing of the 10-span highway bridge corresponding to the passage of a heavy testing vehicle with the total mass $m_v = 32$ t passing the bridge with a standard irregularity at speed $c = 70$ km/h = 19.44 m/s (the identical truck as in the numerical modelling), Figure 13. Dynamic tests were performed in accordance with standard [1].

4.1 Dynamic deflection ${}^{(c=70)}w_{(F_{v320})}^{obs}(L_{(b5)}/2, t)$ at the mid-span No. 5 due to crossing of the heavy truck $F_v = 32$ t - the irregularity located in the middle of span No. 5, $c = 70$ km/h

The time history of the dynamic deflection at the mid-span No. 5 ${}^{(c=70)}w_{(F_{v320})}^{obs}(L_{(b5)}/2, t)$ from [7] is shown in Figures 14, 15.

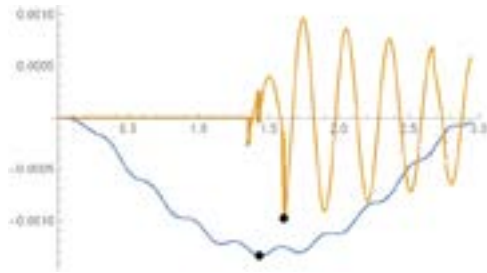


Figure 10 Axes: $x= t [s], y=Components$
 $(c=70)w_{(1),(Fv320)}(L_b/2,t), (c=70)w_{(M0),(IvFv320 Vel)}(t)$
 [m], Amplitudes $(c=70)\hat{w}_{(1),(Fv320)} = 0.00133 \text{ m},$
 $(c=70)\hat{w}_{(M0),(IvFv320 Vel)} = 0.001 \text{ m}$

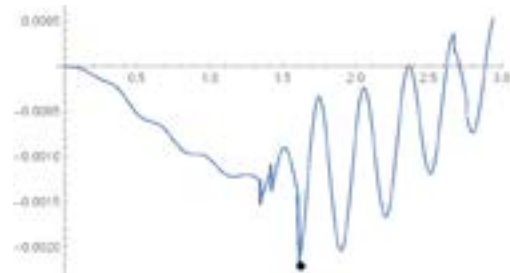
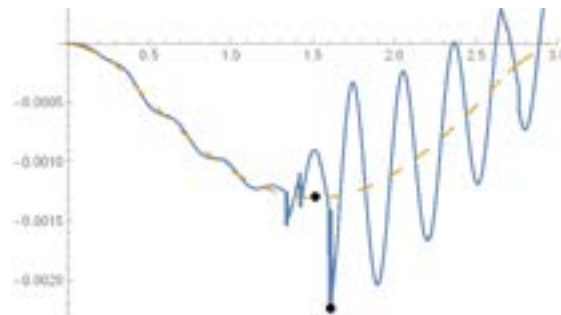


Figure 11 Axes: $x= t [s], y =$
 $(c=70)w_{(M0),(Fv320 + IvFv320 Vel)}(L_b/2,t) [m],$
 Amplitude $(c=70)\hat{w}_{(M0),(Fv320 + IvFv320 Vel)} = 0.0022 \text{ m}$

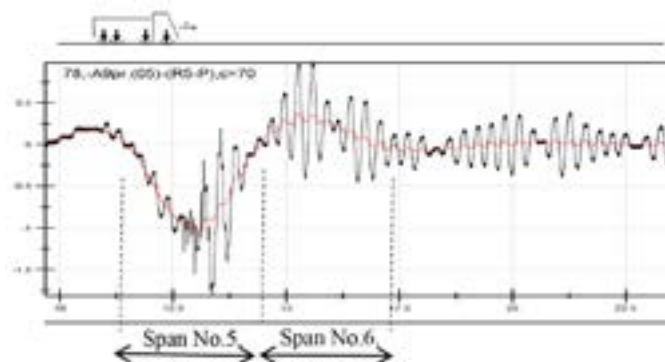


0.0022 m, 0.0013 m

Figure 12 Axes: $x= t [s], y=(DAF) (c=70)\delta_{dyn(Fv320 + IvFv320 Vel)}(L_b/2,t) [.]$
 $(c=70)\delta_{dyn(Fv320 + IvFv320 Vel)}(L_b/2,t) = \frac{(c=70)w_{(Fv320 + IvFv320 Vel)max}(L_b/2,t)}{(c=70)w_{(1),(Fv320)st}(L_b/2,t)} = \frac{0.0022}{0.0013} = 1.69$



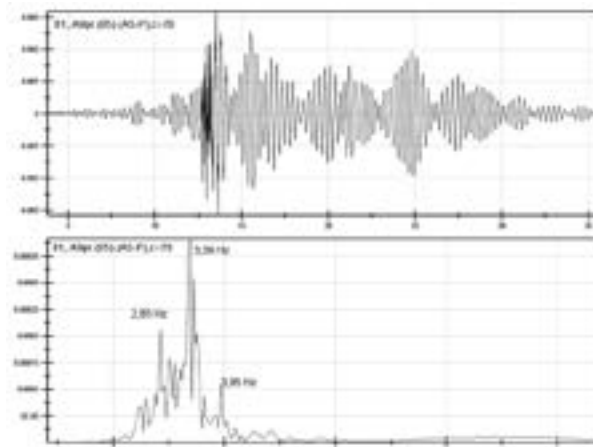
Figure 13 Dynamic load test of the Zvolen-Pstrusa highway bridge subjected to the heavy truck $F_v = 320 \text{ kN}$ passing over the standard irregularity



Measured dynamic amplifier factor for the 5th span $(c=70)w_{(Fv320)}^{obs}(L_{(b5)}/2,t) = \frac{1.75}{1.04} = 1.68$

Figure 14 The time history of the dynamic deflection $(c=70)w_{(Fv320)}^{obs}(L_{(b5)}/2,t)$ at the mid-span No. 5 of the ten-span tested continuous bridge for $c = 70 \text{ km/h}$ - The standard irregularity located in the middle of span No. 5

Frequency composition - dominant frequencies from the absolute transducer



$$f_{(1)}^{obs} = 2.85 \text{ Hz}, f_{(2)}^{obs} = f_{max}^{obs} = 3.39 \text{ Hz} \rightarrow \omega_{max}^{obs} = 21.29 \text{ s}^{-1}$$

Theoretical first circular frequency of the fictive beam $L_b = 52 \text{ m}$ used in numerical

$$\text{simulation is } \omega_{(1)} = \frac{\pi^2}{L_b^2} \sqrt{\frac{EI_{(sb)}}{m_1}} = 20.56 \text{ s}^{-1}$$

Figure 15 Frequency composition of the dynamic deflection of the measured continuous bridge ${}^{(c=70)}w_{(F_{v320})}^{obs}(L_{(b5)}/2, t)$ at the mid-span No. 5, obtained from the absolute transducer

5 Conclusions

One of the purposes of the numerical modelling was to verify the proposed simplified solution of a dynamic response of the characteristic span bridge structure as a response of a simple beam.

- (1) Comparison of numerical modelling of the response to the girder and experimental testing on a continuous bridge structure for a speed of 70 km/h shows a good agreement between the two results.
- (2) Evaluate the intense dynamic response due to the moving of the heavy truck as an impact of the impulse load arising on the irregularity:
 - Smooth passes of the test vehicle show low DAV values ${}^{(c=70)}\delta_{dyn(F_{v320})}^{sim}(L_b/2, t) = 1.03$. Passes of the tested vehicle over the bridge with the standard irregularity for the speed $c = 70 \text{ km/h}$ gives the strong response of the bridge. Measured dynamic amplifier factor for the 5th span ${}^{(c=70)}w_{(F_{v320})}^{obs}(L_{(b5)}/2t) = \frac{1.75}{1.04} = 1.68$
 - Simulation DAF from the Section 3.3.3 gave the value of DAF ${}^{(c=70)}\delta_{dyn(F_{v320} + IF_{v320} Vel)}^{sim}(L_b/2, t) = 1.69$
 - The ratio of DAFs for the pass of the tested

vehicle over the bridge with the standard irregularity and the smooth pass gives the value

$$\frac{{}^{(c=70)}\delta_{dyn(F_{v320}, Vel)}^{obs}(L_b/2, t)}{{}^{(c=70)}\delta_{dyn(F_{v320})}^{sim}(L_b/2, t)} = \frac{1.68}{1.03} = 1.64.$$

- The performed numerical simulation allows to evaluate also a dynamic coefficient of the force effect ${}^{(c=70)}\Delta_{dyn(F_{vi})}^{(Force)}$:

For the front axle force $F_{(v11)} = 63.7 \text{ kN}$:

$${}^{(c=70)}\Delta_{dyn(F_{v11})}^{(Force)} = \frac{{}^{(c=70)}F_{(v11)Vel}}{F_{(v11)}} = \frac{254}{63.7} = 4.0.$$

For the axle force $F_{(v2)} = 192.6 \text{ kN}$:

$${}^{(c=70)}\Delta_{dyn(F_{v2})}^{(Force)} = \frac{{}^{(c=70)}F_{(v2)Vel}}{F_{(v2)}} = \frac{769.76}{192.6} = 4.0.$$

By a dynamic coefficient of the force effect ${}^{(c=70)}\Delta_{dyn(F_{vi})}^{(Force)}$ one can determine a theoretical dynamic force ${}^{(c)}F_{(vi)dyn} = {}^{(c=70)}\Delta_{dyn(F_{vi})}^{(Force)} F_{(vi)}$. This result confirms the experimental measurement of the dynamic response on the bridge.

Acknowledgment

Presented result were obtained with the support of project VEGA No. 12/0045/19, Slovak Republic.

References

- [1] CSN 73 6209: Loading tests of bridges (in Czech). Prague: Standard CNI, 1996.
- [2] BIGGS, J. M. *Introduction to structural dynamics*. New York: Mc Graw-Hill, 1964. ISBN 978-0070052550.
- [3] KOLOUSEK, V. *Dynamics of building structures* (in Czech). Prague: SNTL, 1954.
- [4] MORAVCIK, M., MORAVCIK, M. Resonance vibration of railway bridges subjected to passing vehicles. *Communications - Scientific Letters of the University of Zilina* [online]. 2017, **19**(3), p. 96-101. ISSN 1335-4205, ISSN 2585-7878. Available from: <http://komunikacie.uniza.sk/index.php/communications/article/view/241>
- [5] FRYBA, L. *Vibration of solids and structures under moving loads*. London: Telford, 1999. ISBN 0-7277-2741-9.

-
- [6] YANG, Y. B., LIN, C. W. Vehicle bridge interaction dynamics and potential application. *Journal of Sound and Vibration* [online]. 2005, **284**(1-2), p. 205-226. ISSN 0022-460X. Available from: <https://doi.org/10.1016/j.jsv.2004.06.032>
- [7] MORAVCIK, M. Dynamic load test of a road bridge on R2 Zvolen-Pstrusa (in Slovak). Report. Zilina: University of Zilina, 2017.
- [8] Wolfram Mathematics. Version 10.3.1.

Dear colleague,

Journal Communications - Scientific Letters of the University of Zilina are a well-established open-access scientific journal aimed primarily at the topics connected with the field of transport. The main transport-related areas covered include Civil engineering, Electrical engineering, Management and informatics, Mechanical engineering, Operation and economics, Safety and security, Travel and tourism studies. The full list of main topics and subtopics is available at: <http://komunikacie.uniza.sk/index.php/communications/topics>

Journal Communications - Scientific Letters of the University of Zilina are currently indexed by EBSCO and SCOPUS.

We would like to invite authors to submit their papers for consideration. We have an open-access policy and there are no publication, processing or other fees charged for published papers. Our journal operates a standard double-blind review procedure, the successful completion of which is a prerequisite for paper publication.

The journal is issued four times a year (in January, in April, in July and in October).

I would also like to offer you the opportunity of using already published articles from past issues as source of information for your research and publication activities. All papers are available at our webpage: <http://komunikacie.uniza.sk>, where you can browse through the individual volumes.

For any questions regarding the journal Communications - Scientific Letters of the University of Zilina please contact us at: komunikacie@uniza.sk

We look forward to future cooperation.

Sincerely

Branislav Hadzima
editor-in-chief

MEASURING THE SPEED OF DOCKING SHIP WITH TOTAL STATION

Andrzej Felski

Institute of Navigation and Maritime Hydrography, Polish Naval Academy, Gdynia, Poland

*E-mail of corresponding author: a.felski@amw.gdynia.pl

Resume

The big modern ships are the largest mobile objects that exist in nowadays world. Their huge mass and length in combination with their limited maneuverability can result in the risk of extreme destructions of the infrastructure, as well as environment, in the case of even minor malfunction of any of its elements. The main danger is the kinetic energy of such a colossus and in these circumstances the accuracy of information on the ship's speed becomes particularly important. This is the reason of a growing interest in various systems designed to support harbor pilots during the maneuvers. The most popular ones are based on laser-measurement of the distance, as the rule, installed as static installation in the quay.

This article presents the results of the experiments of vessel's speed measurements when approaching the quay with use the geodetic total stations in a reflectorless variant.

Article info

Received 18 March 2021

Accepted 9 June 2021

Online 7 October 2021

Keywords:

pilot systems,
speed,
laser distance meter,
total station

Available online: <https://doi.org/10.26552/com.C.2022.1.E1-E10>

ISSN 1335-4205 (print version)

ISSN 2585-7878 (online version)

1 Introduction

Maneuvering a ship, especially a large one, is an operation that bears risks resulting from her enormous kinetic energy. Besides some differences between operations of mooring the ship and movement of the ship in canal or similar waterways, all of them are characterized by the similar risk of unwanted movement of a vessel. Such operations pose risks of collision not only with other vessels also with surrounding infrastructure, as well. The main threats come from small space, huge inertia of the object and its limited maneuverability. It is proper to mention that the energy of the moving object is a product of its mass and the speed upraised to the square and in many times the mass of the ship is 100000 tons or more. Even in the case of a speed of a few decimeters per second, the energy is enormous and in addition, what is extremely important, this is in absence of any effective brake-systems. In such circumstances a maneuvering support system seems to be very attractive.

The examples of how important are such problems can be seen in two papers of [1-2] where authors presented methods that can be used for estimating the navigational risk in the restricted areas. Similar problem of berthing velocity of a large vessel is discussed for example by Roubos et al. in [3-5].

There are several variants of such systems, which is why they are sometimes referred to as dock, harbor or pilot ones. To a certain extent, this classification

can be identified with application areas, since the dock systems are used primarily while approaching the quay, when harbor or pilot systems usually mean those that are used in the course of passing dangerous or crowded waterways. In addition, depending on the location of their basic elements, the systems can be divided into the shore based and ship based [6]. On the other hand, as far as the ship's engagement is concerned, active and passive systems can be distinguished. This classification is presented in Figure 1.

1.1 Ship based systems

Ship based systems with use of the GPS receivers, were tested already in the latter part of the XX century [7]. Nowadays, they are built as active systems and are most often called "portable pilot's units" (PPUs), based on laptops or tablets with dedicated software. In many cases this variant of devices has the ability to transmit data ashore via UHF. A typical portable pilot's system provides the pilot with his own, very accurate source of information about the position, heading (HDG) of the ship and her rate of turn (ROT). The most commonly used software in these devices is, in fact, a version of the simulation software being at the same time an overlay for an Electronic Chart Display and Information System (ECDIS). In some cases, the positions of surrounding ships come from an automatic identification system (AIS).



Figure 1 Classification of dock systems, [6]

Several levels of accuracy of the vessel's real-time positioning may be discussed, based on various augmented GPS variants [8], such as DGPS, EGNOS, RTK or PPP. Even though in this case the exact position of the ship is insufficient, more accurate position certainly allows to smooth out the information about the speed over ground (SOG) and course over ground (COG), calculated every second, which is the most important information for the pilot [9].

In such cases, the ship's heading (spatial orientation) is also extremely important, since the large ships length is sometime up to 400m and most often the position of the ship in fact refers to the position of a point near its stern. Therefore, if a ship is oriented not exactly along the axis of the seaway, it can occupy a much wider lane, which poses the threat of contact with its surroundings even when the controlled point (position) is exactly on the axis of the fairway.

DGPS - based PPUs provide sufficient accuracy for most of the tasks associated with passing along the shipping canals or recommended routes and usually no additional information or instructions from the shore are needed. The DGPS reference stations are numerous, especially in the northern hemisphere, therefore, this variant can be considered to be a very flexible, accessible and the cheapest option. They are rivalled by the Space Based Augmentation Systems (SBAS), in Europe (not only on seas, but also on rivers); this role is played by the European Global Navigation Overlay System (EGNOS). The SBAS class systems, with accuracy similar to DGPS, are also widely available in almost entire northern hemisphere.

The **RTK - based PPU**s require additional onshore stations and dedicated receivers. This variant assures the error below 0.4m, which suggests accuracy of speed at ± 10 mm/s. It is therefore a very accurate system that can be applied at any quay, or other restricted navigation area. In addition, this variant allows to obtain excellent accuracy of a real-time heading measurement; however, for this purpose at least two antennas spaced apart from each other at a distance of more than one meter are required. Unfortunately, this variant has significant limitations in the range of operation from the base station located on the land. The use of unified EUPOS reference networks, existing in many European countries, may be a solution. Moreover, many commercial

companies offer a similar networks of reference stations (for example Leica, Topcon etc.). These networks can provide corrections via the GSM, so there is no need to install an additional base station. Sometimes it may be difficult to obtain the right range, however, usually in ports area the GSM type systems are accessible.

1.2 Shore based systems

From the point of view of a harbour pilot, who will moor the ship in the particular harbour the deck system is inconvenient, because it demands delivering some additional devices to the vessel. This is difficult and not safe if a pilot is forced to clamber on the rope-ladder for dozen of meters. On the other hand, such systems are not unified, so with difficulty to await that vessel will transport on her deck many different devices, which will be useless in a specific harbour. This is why the shore based systems are attractive.

According to [10], the shore based systems, as a rule, consist of the following components:

- Quay located sensors of distance (usually laser, sometime radar or other microwaves system, eventually sonar);
- Control system located in some operator's building/room;
- System of data presentation, which can be in a form of large display situated on quay and presenting values of important parameters in digital form or lamp signaling safety or non-safety parameters. In certain options an additional portable display/receiver can be used in a form of laptop or tablet. Transmission of the data in addition to presented on the big quay display seems be more efficient, especially in poor visibility conditions, however, in such a situation skippers of tugs should possess additional receivers, as well.

The most common sensor in this kind of devices is a laser distance meter. The use of the laser to measure the distance is a common practice. For many years, surveyors use fully developed measuring systems, the so-called total stations. These are the combinations of distance measuring instruments and electronic theodolites. The high accuracy of the distance measurements and simultaneously measured angles of

azimuth and elevation can radically change the surveys of a position of the object. Unlike the ordinary lasers, which are used in harbor systems and must be installed in the quay, the total station could be transferred to another place.

In precise laser measuring techniques, as a rule, the reflective element is used, mainly in the form of a prisms combination. However, in the case of considered systems, the so-called reflectorless measurement is applied. It is assumed that in reflectorless measurements the laser beam will bounce off any surface of the ship's hull effectively enough to be able to measure the distance. This, of course, results in a smaller range, as reflected energy is smaller. If the average total station distance meter provides a range of up to 3km, the range of reflectorless measurements is limited to 200-300m. However, with regard to the system supporting the mooring of the ship in the port basin, this is not a problem, as distances of interests are usually shorter. This solution is characterized not only by the limited range, but by the limited accuracy, as well. While with reflector measurements a millimeter accuracy can be reached, the accuracy of reflectorless measurements is lower and dependent on the source of information. Usually it varies from 10 to 60mm with the standard frequency of shots in 2 seconds. However, the possibility that the object can move within 2 seconds by a distance greater than the accuracy of measurements has to be considered, which would significantly distort the result.

As a standard, a pair of stationary lasers is installed in the quay and connected to an IT system, which can ensure displaying results on different devices, transmission to other users, recording the measurements and their subsequent interpretation. In comparison to the solutions discussed earlier, this type is characterized by much higher accuracy, however, it is very inflexible, because it can be used only on a specified quay on which lasers and a display to present the results must be installed. In addition, systems of this type are the most expensive ones. The goal of this researches was to verify the usefulness of the total station in real harbor as a more flexible and possibly cheaper option.

Different variants of docking systems are in use since the sixties of the last century and many publications are accessible in the literature. For example, Trelleborg Marine and Infrastructure company [11-13] is a world leader in laser's shore systems. In these products, the speed and distance information are calculated based on the data measured by laser sensors located on the jetty and can be presented on the big display board, which are clearly visible from the ships' bridge. As this kind of systems are installed only stationary, they can be used only on a dedicated pier. In addition, laser sensors are installed close to salted water and this causes some exploitation problems, especially during the winter. This, aside from the costs of this installation, causes that they are rarely applied.

On the other hand, the demand on pilot supporting

aids are considerable. For example investigators from Marine Academy in Szczecin designed the Pilot-Docking System based on three laser distance measurements for the purpose of enumeration of the position of the agreed upon water-nymph of the ship [14]. In [10] authors discuss the general architecture of the same system.

Accessible papers discuss static systems installed on the pier. In this paper a hypothesis of the opportunity to use surveyors grade total station is tested. Author suggests that such an instrument is much more flexible as it can be installed for particular operation and the speed of the vessel approaching can be easily calculated based on such measurements. It should be noticed that the laser distance meters are in use for ship's berthing since the sixties. These systems are treated as mature, thus, in the last two decades this problem was in fact not discussed. However, investigation of the laser method is still provided, for example [16-18]. The constant evolution of surveying technology has contributed to a greater variety of available tools, for example total stations and laser scanners.

Of course, these devices are designed for surveying, different tasks than berthing vessels but some similarities can be observed in such tasks as, for example, modelled buildings with total stations without reflectors [19]. Authors emphasize that the total stations are incredibly versatile instruments with the near limitless measuring capabilities [15]. Surveying with a total station allows the surveyor to choose individual points to measure and each shot is made with relatively high precision of angular and distance measurements. Authors report their experience with modeling buildings and state that, since they provided measurements almost completely by the reflectorless mode, the obtained accuracy is estimated as 10mm. What is important, the errors in vertical axis were twice larger.

2 Experiments

Measurement of the ship's distance to the quay can be taken in several ways, but the method which does not require physical interaction with the ship, in the form of either an installation of any kind of infrastructure or transferring any person onto the ship, is preferred. That is possible with precise distance measurements, using the surveying total station located on the pier, especially since these instruments can work without any extra element installed on the vessel. Some experiments of such a type are reported in the paper. The measurement was done by the geodetic total stations, which are in fact precise laser distance meters, which can additionally measure angles in horizontal and vertical planes. Use of the two such aparati in two ways was verified:

- a) tracking two selected points on the hull of the ship approaching the quay;
- b) direct measurement of distances on lines perpendicular to the quay.

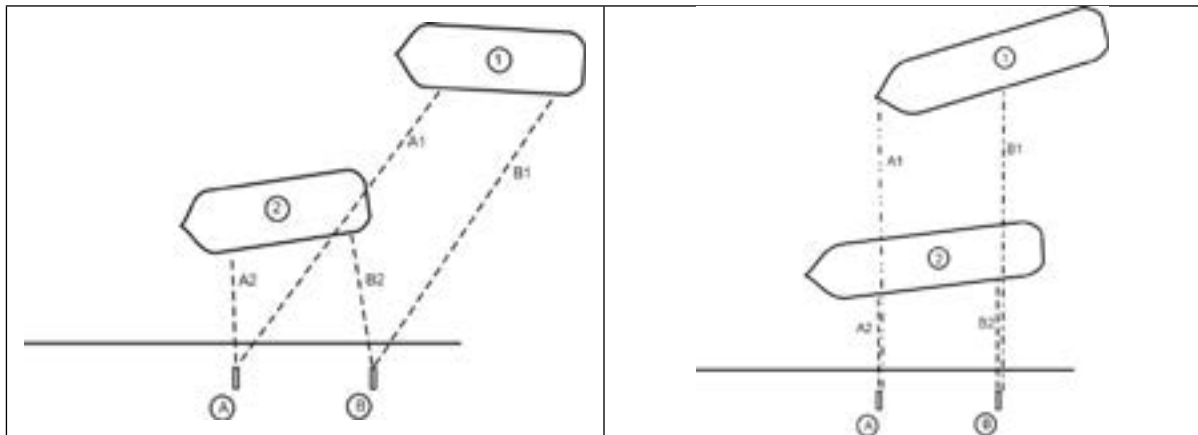


Figure 2 Differences between both possible methods of distance measurements

Table 1 The main parameters of total stations used in experiments

	TOPCON OS 103	TOPCON GT 500	TRIMBLE S3
Accuracy of distance measurement	3mm+2mm/km	2 mm + 2 mm/km	2 mm + 2 mm/km
Range of measurements	500 m	800 m	2200
Measurement time:			
Precise mode	0.9 s	0.9 s	1.2
Rough mode	0.7 s	0.6 s	
Tracking mode	0.3 s	0.4 s	0.4

Variant a) is attractive due to the fact that the total stations are perfectly suited to track movements, including the possibility of automatic implementation of this task, provided that it is possible to use the so-called robotic total station. However, in this case, the accuracy of measurement must account for the impact of both distance and angle measurements in the horizon plane (azimuth), as well as for the accuracy of tracking. In the course of measurements, assumption about the adverse impact of some ship's side colors on the range of the device was also confirmed. In some experiments two selected letters of the large lettering on the side of the ship were followed. For the ship with side lettering in black, when a back point was lit, there were numerous cases with no reflection.

On the other hand, variant b) allows to omit problems with aiming, however, as a consequence it also requires interpretation of results if the ship does not move towards the quay only. The complex hull shape sometimes causes significant and rapid changes in distance as the ship moves (please compare distances A1 and A2 in Figure 2 right).

Measurements were taken in both configurations on different days, for different large container ships in the length of more than 300 m and displacement of about 150 000 tons. The measurements were taken in a good visibility, with almost calm weather, in daytime as well as at night. Due to organizational limitations, three pieces of different types of total stations have been used and, unfortunately, they could not be used simultaneously, as well as in identical configuration.

Some technical data of these devices are presented in Table 1.

Technical capacities of used devices allowed to take distance even every second, but in reflectorless mode it was not working properly. In practice it was performed with 2 seconds cycle and based on the differences between successive distances, the speed was calculated (in meters per second).

3 Description of taken measurements

3.1 Point tracking measurement method

In one of the experiments, the ship had a large lettering (MAERSK) on the side, so it was decided to follow of the first and fine letter (variant on the left in Figure 2). The measurements were taken in daytime and it turned out that at the beginning of the experiment repeated gaps in measurements occurred. This was most likely due to the dubious accuracy of aiming the device (in the daytime the reflection on the side was invisible), which sometimes hit bright side next to the lettering and sometimes the black lettering itself, which did not give enough reflection at greater distances. The measurements were stable at distances in the range of 50 meters, which is in the harbor practice normal distance. The measurements were taken with a TRIMBLE S3 total station (station A) and a TOPCON S103 station (station B). For the purpose of measurements a local coordinate system was established as presented in Figure 3,

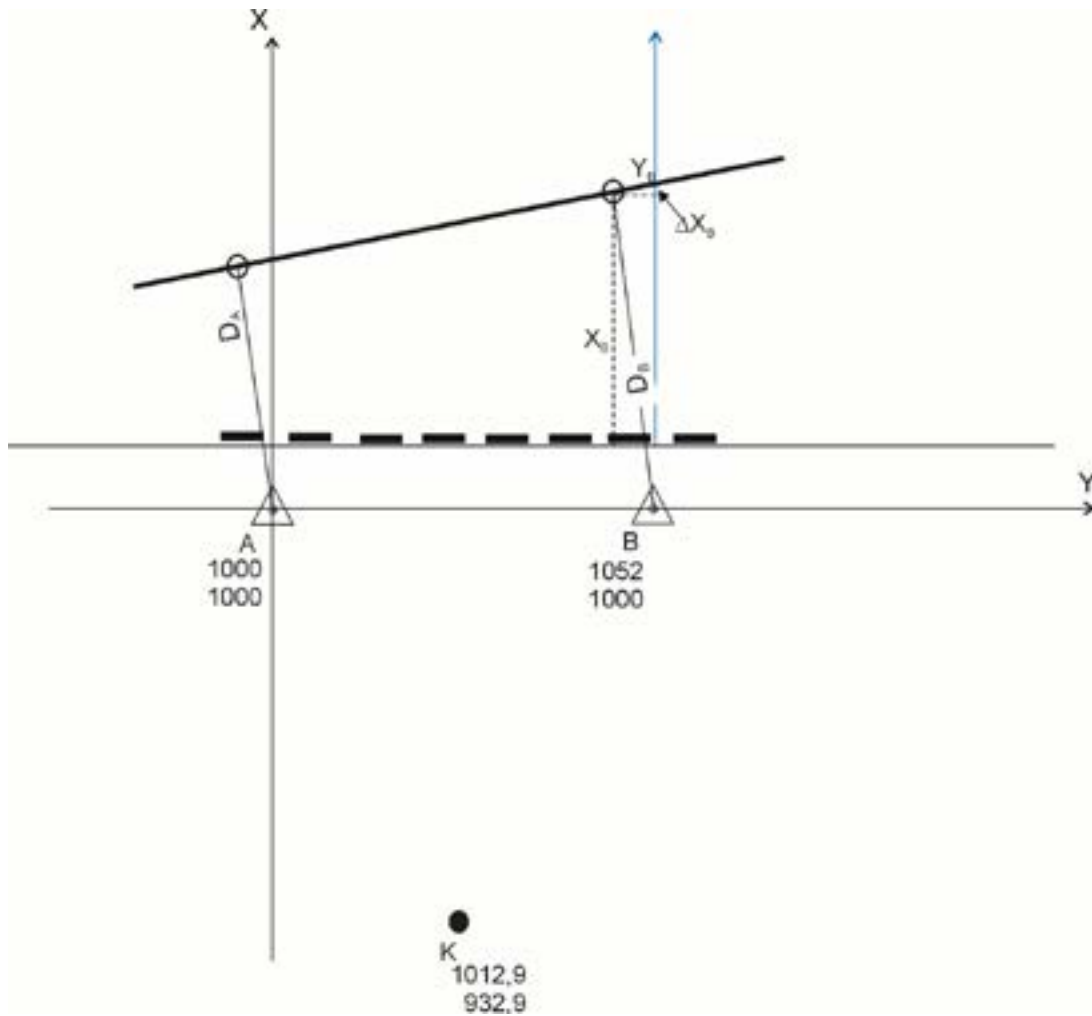


Figure 3 Situational sketch of measurements example taken in version 1, the line connecting the measurement points symbolizes the section of the ship's side

defining the coordinates of point A as (1000, 1000). Next, total station A was used to determine the coordinates for station B and control point K, which was a geodetic sign on the foundations of one of the lighthouses on the quay. Subsequently, the coordinates of station A and control point K were determined with use of the total station B. The results of the measurements taken with the first and the second total station resulted in identical coordinates for all the three points.

This experiment showed that the ship was eventually positioned at the quay in such a way that the selected points shifted to the left of the laser measurement lines installed on the quay. Moreover, for some time the ship moved non-parallel to the quay. For this reason, the coordinates of the measuring points had to be converted by projecting them onto the laser lines in the small-scale study. In both cases, the ΔX correction had to be taken into account (see Figure 3) resulting from the fact that the ship for some time was positioned at an angle to the assumed coordinate system. The additional difficulty at such a solution call out an adjacent installation, which periodically curtailed the tracked point. The considerable value of the azimuth variations suggests the necessity to install the instrument further from the

border of the wharf, however then many hindrances were found on the line of sight. In Figures 4 and 5 the distances (in meters) and calculated based on the speed of approaches (in m/s) in terms of time are presented.

The speed of approaching the quay was calculated as the quotient of the difference of successive distance measurements (D_i) and 2 seconds.

$$V_i = \frac{D_i - D_{i-1}}{2 \text{ sec}} \tag{1}$$

In Figure 5 significant changes of the speed can be noticed at the distances larger than 15 meters, where in the last stage changes in the speed are a result of a vessel touching the elastic fenders.

3.2 Direct measurements of distances on lines perpendicular to the quay

An example of measurements in the second version is presented on the example of measurements taken with a TOPCON GT 500 total station (station A) and a TOPCON OS 103 (station B) and presented in Figure 6. The basic assumption of the method is that

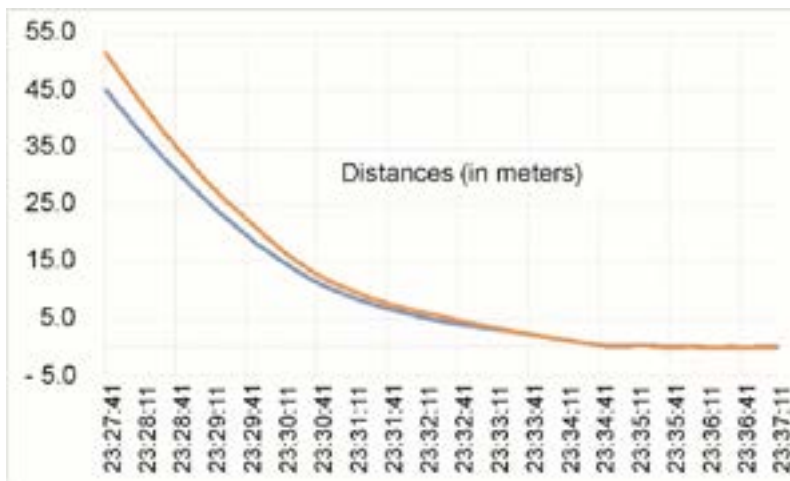


Figure 4 Changes in distance (in meters) measured with A and B total stations

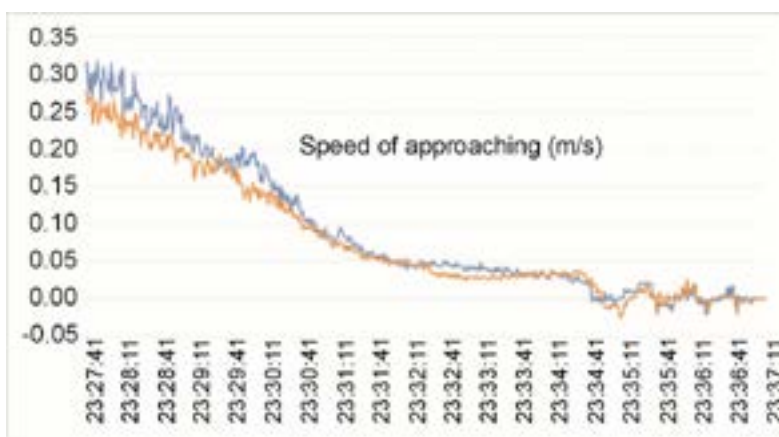


Figure 5 Speed of approaching (V) in m/s

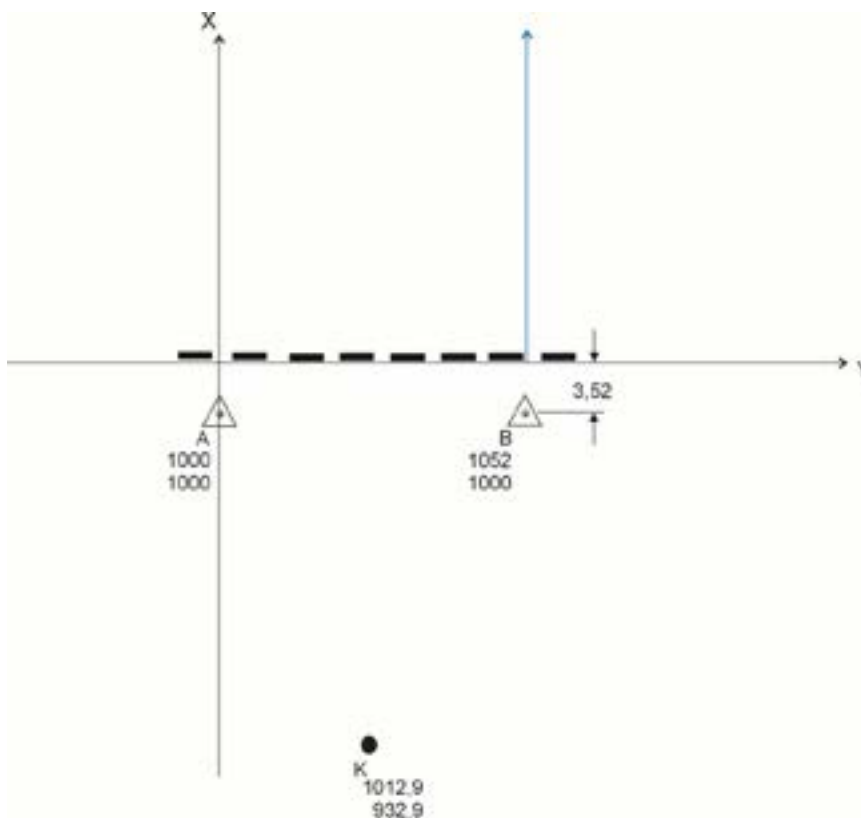


Figure 6 Situational sketch of measurements taken in version 2

repeatability of installation of the total station at the same place must retain the suitable accuracy

The next experiment was taken in the same place. Local coordinate system was re-established and the procedure of mutual determination of position coordinates was repeated, including the checkpoint K as in the previous experiment, obtaining identical coordinates. Next, the device at station A was turned with a measuring axis by 90 ° to the right from the orientation towards the station B. In station B the device was turned by 90 ° to the left from the orientation towards the device A. Coordinates was re-established with accuracy of 1mm. In both cases the distance from the total station to the edge of the quay was measured with a measuring tape. The distance was equal to 3.52m, which guarantees the mutual parallelism of the quay and base passing through both measurement stations and as a consequence the parallelism of the total stations axes. The measurement results for that day are shown in Figures 7 and 8.

4 Discussion

The presented examples allow to question the declared 3mm accuracy of distance measurements obtained with the use of the reflectorless method. It is worth noticing that in the case of lasers used in the stationary port-mounted systems, the manufacturer declares the accuracy of 10mm [19] and investigation described in [20] suggests the same value. The analysis of graphs 4 and 7 leads to the conclusion that the curves presenting distances are smooth, which corresponds to the practical experience of such maneuvers - ships with a mass of about 100000 tones have such a large inertia that it would be difficult to expect radical changes in the distance in subsequent 2-second measurement cycles. However, the declared accuracy of 3mm in the measurement cycle of two seconds, even at a few meters from the quay, cannot be observed on the speed vs. time plot (Figures 5 and 8). On both, large oscillations of the approaching speed of the ship are visible at distances

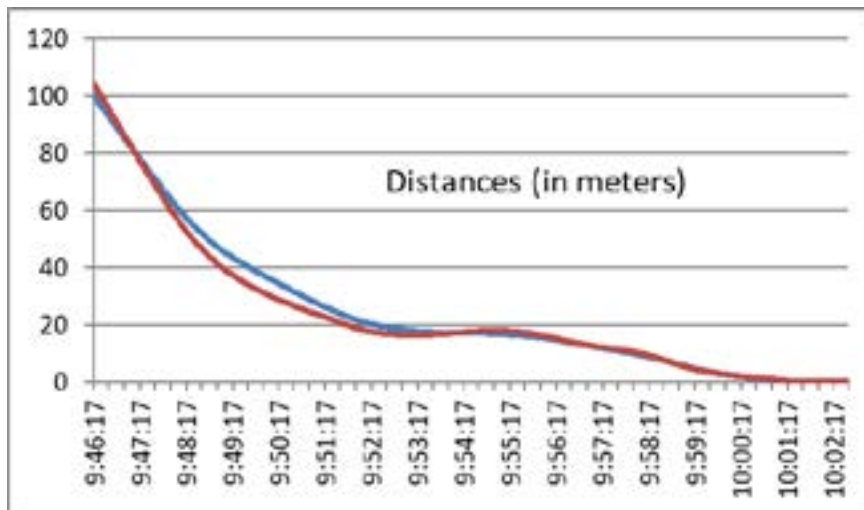


Figure 7 Distances (in meters) measured with A and B total stations

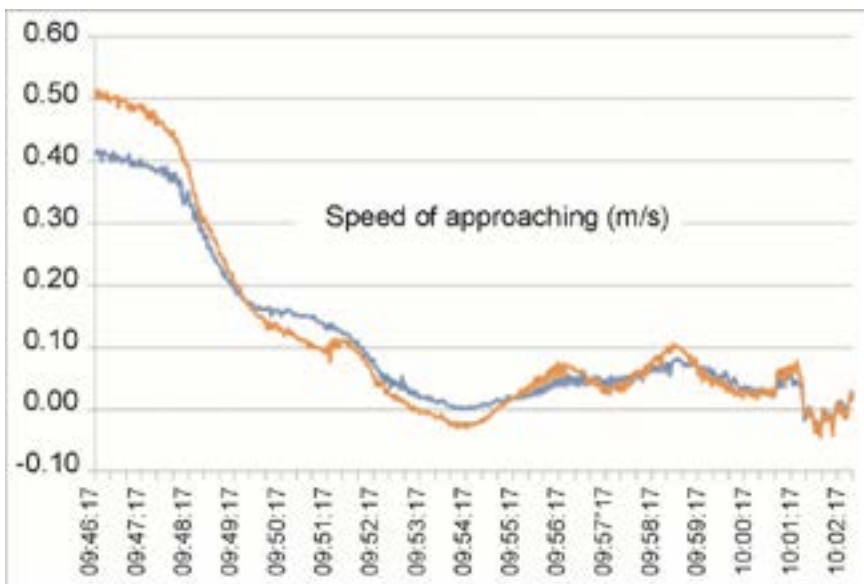


Figure 8 The approaching speed in m/s

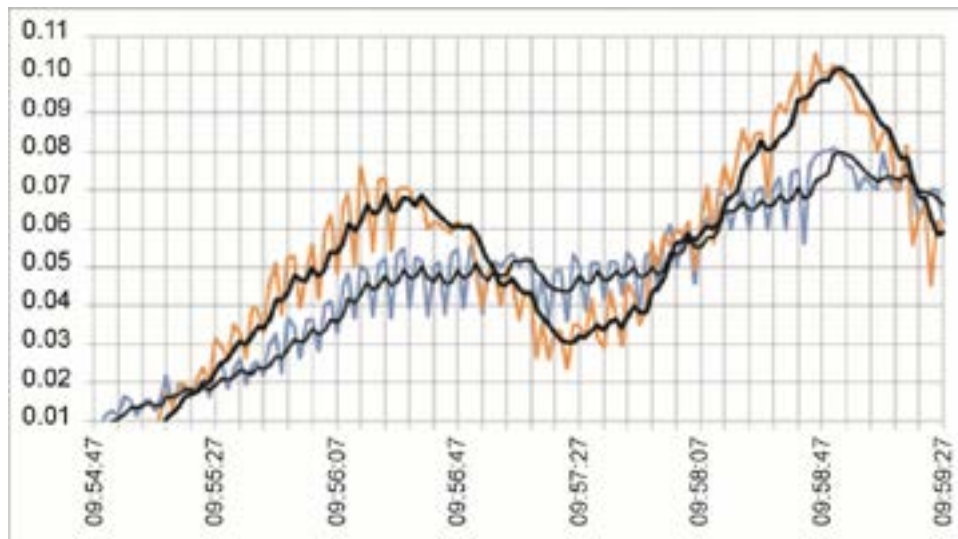


Figure 9 Speeds as a part of Figure 8 compared with the moving average of the adequate speed in m/s

ranging from 70 to 20 meters from the quay. This is absolutely the influence of the accuracy of the distance measurements.

An example of these oscillations is presented in Figure 9 (this is a part of a graph from Figure 8). Suggestions that the speed calculated based on the laser measurements of the distance should be filtered, can be seen, for example in [20]. In Figure 9 additionally smoothed data (which are counted as the moving average) is introduced. This is the part of the experiment when the vessel was not more than 20 meters to quay. The method of estimating the more integrated data is not a goal at the moment, so as an example the moving average is calculated as average for each last 5 values:

$$\Delta V_i = \left| V_i - \frac{1}{5} \sum_{j=1}^5 V_j \right|, \quad (2)$$

where:

V_i - is the consecutive measurement,

ΔV_i - deviations of consecutive measurements from the moving average value.

The experience proves that the accelerations occurring at this stage of mooring process do not cause essential changes of the speed of approaches and in the time of 10 sec this movement can be treated as stable. Assuming that such a value is the reference value, one can appraise that each value is different from the true one for not more than 10 mm/s. and mean value of such differences for all period of the experiment is 0.05 mm/s. In such a case and remembering that the cycle of measurement is 2 s, the error of measurements of the distance can be estimated as 10mm (0.005 m/s error in the window of 2 s.). The conclusion from the analysis of the distance measurements is that accuracy of the distance to the vessel in motion measurements with the total station in reflectorless mode can be evaluated as 10mm.

Besides the laser imperfection one can assume other sources of these errors. It is doubtful that this would have to be due to the hull accelerations, which is unlikely

with such a huge mass of the vessel. This issue requires deeper analysis; however, the following hypothetical reasons for this phenomenon can be indicated:

- imperfection of the surface of the ship's side: dents, welds, rust, etc.;
- vibrations of the metal plane due to the operation of the engine and other ship mechanisms;
- changes in distance to the point of sighting on the side caused by the oblique shape and slight hinges of the hull;
- painting of the hull, especially presence of black or very dark elements which did not have reflection at greater distances resulting in a lack of reading.

Occasionally irregular, but significant differences between successive measurements (even 100 mm, especially at longer distances) were found, which requires further analysis. Such differences occurred during daytime measurements and they did not occur at night. This may suggest that such systems operate in a more stable manner after dark. It is possible that this phenomenon was affected by the solar reflections during the day coming from other elements (moving) nearby.

5 Conclusions

Laser measuring technology is undoubtedly a great solution for mooring support systems. However, one should be aware of several limitations associated with a certain solutions causing erroneous judgments, if general information on laser distance meter capacity is relied on. The most important conclusion is that, in the systems currently used, the measurement is taken using the reflectorless method, which means that the accuracy of distance measurement is much worse than what could be assumed based on the commonly accessible materials. The most often suggested few millimeters accuracy of distance measurement is unattainable in these particular conditions.

The method of many measurements and averaging measured values in 1 or 2 - second cycles is easily accessible with commonly used devices. In such cases, the indicated value refers to the center of the measurement interval. Thus, the accuracy of the result is determined by the speed of the vessel movement and not by the accuracy of the laser since the latter value is many times lower.

An important issue in this type of measurement systems may be a problem of disturbances, primarily resulting from environmental conditions, especially accidental reflections and light reflections at greater distances from the quay. These systems are definitely better at night than during the day, assuming, of course, that no other artificial sources of light are present on site.

Application of lasers in the considered solutions has been known for many years, however it seems that development of technology still leaves a space for proposing several improvements. Development of the robotic total stations commonly used in surveying allows to suggest that similar measurements could be made, which seems possible providing that these devices are installed on the quay. Installation of the two total stations on the wharf is not a troublesome task and gives a chance to create a more elastic solution, especially in the places where such laser-system is indispensable once in a while.

Acknowledgements

Author acknowledges to Mr. Ireneusz Bojarowski for the help in making measurements for this article.

References

- [1] RUTKOWSKI, G. Safety of shipping when navigating on LNG tankers in gulf of Gdansk while approaching a prospective LNG terminal in Gdansk port Polnocny. *Archives of Transport*. 2006, **18**(2), p. 67-82. ISSN 0866-9546, eISSN 2300-8830.
- [2] RUTKOWSKI, G. Risk analysis when navigating in restricted sea areas. *Annual of Navigation*. 2006, **11**, p. 103-122. ISSN 1640-8632, eISSN 2300-6633.
- [3] ROUBOS, A., GROENEWEGEN, L., OLLERO, J., HEIN, CH., VAN DER WAL, A. Design values for berthing velocity of large seagoing vessel. In: 34th PIANC World Congress: proceedings [online] [accessed 2021-03-15]. 2018. Available from: https://www.researchgate.net/publication/329125486_DESIGN_VALUES_FOR_BERTHING_VELOCITY_OF_LARGE_SEAGOING_VESSELS
- [4] ROUBOS, A., GROENEWEGEN, L., PETERS, D. J. Berthing velocity of large seagoing vessels in the port of Rotterdam. *Marines Structures* [online]. 2017, **51**, p. 202-219. ISSN 0951-8339. Available from: <https://doi.org/10.1016/j.marstruc.2016.10.011>
- [5] Safe and reliable docking/berthing approach systems [online] [accessed 2021-03-12]. Available from: <http://www.mampaey.com>
- [6] FELSKI, A., NAUS, K., SWIERCZYNSKI, S., WAZ, M., ZWOLAN P. Present status and tendencies in docking systems' development. *Annual of Navigation* [online]. 2014, **21**, p. 35-48. ISSN 1640-8632, eISSN 2300-6633. Available from: <https://doi.org/10.1515/aon-2015-0003>
- [7] UENO, M., SANTERRE, R. Testing a GPS-based system for the support of ship berthing operations. In: U.S. Institute of Navigation ION GPS'99 Conference: proceedings. 1999. p. 1271-1279.
- [8] GRUNWALD, G., CIECKO, A., KRASUSKI, K., KAZMIERCZAK, R. The GPS/EGNOS positioning quality in APV-1 and LPV-200 flight procedures. *Communications-Scientific Letters of the University of Zilina* [online]. 2021, **23**(2), p. E23-E34. ISSN 1335-4205, eISSN 2585-7878. Available from: <https://doi.org/10.26552/com.C.2021.2.E23-E34>
- [9] HUANG, P., LIU, Y., DU, Z., CHEN, Q., CHEN, J. Design and implementation of large vessel navigation system based on Beidou CORS. *Polish Maritime Research* [online]. 2017, S3(95), **24**, p. 12-15. Available from: <https://doi.org/10.1515/pomr-2017-0098>.
- [10] GUCMA, L., BAK, A., GUCMA, M., JANKOWSKI, S., ZALEWSKI, P., PERKOWIC, M. Laser docking system integrated with pilot navigation support system. Background to high precision, fast and reliable vessel docking. In: 17th Saint Petersburg International Conference on Integrated Navigation Systems: proceedings. 2010.
- [11] Trelleborg [online] [accessed 2020-09-09]. Available from: <http://www.trelleborg.com/en/marine-systems/>
- [12] Kongsberg Maritime [online] [accessed 2020-05-20]. Available from: <http://www.km.kongsberg.com>
- [13] Navicom Dynamics [online] [accessed 20-05-2020]. Available from: <http://www.navicomdynamics.com>
- [14] ZALEWSKI, P. The position accuracy of the agreed upon waterline of the ship in the navigational-docking pilot system (in Polish). *Pomiary, Automatyka, Kontrola*. 2013, **59**(6), p. 578-581. ISSN 0032-4140.
- [15] BERKOVIC, G., SHAFIR, E. Optical methods for distance and displacement measurements. *Advances in Optics and Photonics* [online]. 2012, **4**(4), p. 441-471. ISSN 1943-8206. Available from: <https://doi.org/10.1364/AOP.4.000441>

- [16] AMANN, M. C., BOSCH, T., LESCURE, M., MYLLYLÄ, R., RIOUX, M. Laser ranging: a critical review of usual techniques for distance measurement. *Optical Engineering* [online]. 2001, **40**(1), p. 10-19. ISSN 0091-3286, eISSN 1560-2303. Available from: <https://doi.org/10.1117/1.1330700>
- [17] FONSECA J. A.-S. D., BAPTISTA, A., MARTINS, J., TORRES, J. P. N. Distance measurement systems using lasers and their applications. *Applied Physics Research* [online]. 2017, **9**(4), p. 33-43. ISSN 1916-9639, eISSN 1916-9647. Available from: <https://doi.org/10.5539/apr.v9n4p33>
- [18] OLEKSIUK, W., SANKEY, E. Comparison of laser scanner and total station survey [online] [accessed 2021-02-13]. Burnaby, British Columbia: British Columbia Institute of Technology, Geomatics Department, 2014. Available from: <https://spatialtechnologies.ca/wp-content/uploads/2014/04/Final-Report-by-Will-Oleksuik-and-Eric-Sankey.pdf>
- [19] User manual SP LAM laser distance meter [online] [accessed 27.05.2020]. Documentation number 012861-001-98-02-0507-en. Sensor partners BV, revision 0001. Drunen, 2007 Available at: <http://downloads.sensorpartners.com/manual-sensor-partners-LAM53xx.pdf>
- [20] ZALEWSKI, P., TOMCZAK, A. Laser range measurements filtration for PNDS purposes. *Scientific Journals Maritime University of Szczecin*. 2012, **32**(2), p. 182-185. ISSN 1733-8670, eISSN 2392-0378.

BATHYMETRIC MEASUREMENTS OF THE VISTULA SMIALA RIVER MOUTH WITH THE USE OF A HYDROGRAPHIC MANNED VESSEL

Michał Skrzypek*, Błażej Mach

Faculty of Navigation, Gdynia Maritime University, Gdynia, Poland

*E-mail of corresponding author: michalskrzypek1998@outlook.com

Resume

The aim of the article was to present the characteristics of conducting bathymetric measurements of a water area by means of a manned watercraft. The survey was performed in a body of water that is relatively shallow and frequently used by water sports enthusiasts. The results of the study described the shape of the bottom of the marina studied and identified dangerous places for vehicles moving on it. It was proved that using a manned vessel is dangerous or impossible to make measurements near the pier where the yachts were moored and areas where the depth was less than 1 meter. Using the points recorded by the Lowrance HDS Carbon 9 echo sounder, the authors of this paper generated 2D and 3D maps of the measured reservoir with the depths plotted on them. The created studies can be used when developing navigational aids to facilitate the driving of water vehicles.

Article info

Received 9 May 2021

Accepted 4 June 2021

Online 7 October 2021

Keywords:

bathymetric measurements,
Vistula Smiala river mouth,
hydrographic manned vessel

Available online: <https://doi.org/10.26552/com.C.2022.1.E11-E18>

ISSN 1335-4205 (print version)

ISSN 2585-7878 (online version)

1 Introduction

In the context of safe navigation of an inland vessel or water sports, it is crucial to know the bottom relief of a given body of water [1-2]. Nowadays yachts very often sail at depths not much bigger than their draught. Contact with sandy shoals should not cause more damage than a few scratches on the hull. In such situations the keel or even the hull may be seriously injured [3-4]. In order to avoid running aground it is very important to plan a route properly and to follow the navigation signs.

Information on the structure of a water body is obtained by taking hydrographic surveys [5-6]. Data recorded during the depth soundings have a direct impact on the safety of navigating vessels in approach lanes and ports [7]. Their results are used to construct maps of water bodies and other navigational aids used by captains. Knowledge of the shape of the bottom is especially important at mooring manoeuvres, where the depth of the body of water in a small area can become very shallow. It is worth adding that the information provided by bathymetric surveys must be as accurate and up-to-date as possible. Due to the high variability of small water bodies, including the port basins, a high frequency of depth measurements and updated hydrographic studies is required [8-9].

Hydrographic surveys are required to maintain sufficient positional accuracy during the data recording.

Systems supporting the Global Positioning System (GPS) satellite system such as Differential Global Positioning System (DGPS) or European Geostationary Navigation Overlay Service (EGNOS), which have much better characteristics and are used in maritime and air navigation, are used for this purpose [10-14]. One of their advantages is the ability to automatically record data. Therefore, when performing depth measurements, manned vessels are equipped with Global Navigation Satellite System (GNSS) receivers.

The traditional method of recording data on the structure of bodies of water is to perform depth soundings using a manned vessel [15]. Such a measurement campaign takes place by sailing over preplanned profiles. Information is collected through single beam or multibeam echosounders [16-19]. The device, using a converter, emits a beam of light, which then reflects off the bottom and returns to the transmitter. The measured "trace travel time" is converted into a depth value. The majority of hydrographic maps of Polish water reservoirs have been created based on the data collected by the above mentioned method. Such studies are unfortunately incomplete because they do not include ultra shallow areas. In parts of the basin where the depth drops below one meter, it is not possible to measure with a manned boat due to its size. In such cases, it is getting more common to use the latest technological solutions, which are unmanned units [20-24]. Hydrographic drones feature smaller size and



Figure 1 Location of the National Sailing Centre [25]



Figure 2 Hydrographic manned vessel "Navigator One AMG"[15]

greater mobility than traditional water vehicles. These features allow the bathymetric survey to be conducted safely in areas with limited accessibility.

The aim of this study is to carry out bathymetric measurements using a manned hydrographic survey unit in order to visualize the shape of the seabed in the area of the yacht marina. The survey is to provide reliable information on the structure of the bottom of the National Sailing Center in Gdansk and to identify terrain obstacles that are dangerous to sailors.

2 Materials and methods

Hydrographic surveys were conducted on August 29, 2019 during the afternoon at the yacht harbor of

the National Sailing Center of the Academy of Physical Education in Gdansk. The water area is located on the eastern bank of the estuary of the Vistula Smiala River and has a direct water connection with the Gulf of Gdansk. The National Sailing Centre of the Academy of Physical Education together with the Galion Sports Association forms a complex of marinas located 12km from the center of Gdansk, in the southern part of the Górkki Zachodnie district. Due to its optimal location, the marina is able to guarantee conditions for sailing training on inland and open waters. Additionally, the Vistula Smiala backwaters can be used to access the waterways of the Vistula Lagoon and the Ostroda-Ilawa Lake District via connections between the sea and inland waterways. On the west side, the National Sailing Center of the Academy of Physical Education

Table 1 Technical specifications Lowrance HDS Carbon 9[27]

Parameter	Lowrance HDS Carbon 9 Echosounder
Display	HD SolarMAX 16:9; 305 9" touch screen Resolution HD 1280 x 800
Backlighting	1250 LED rivets
Operating frequency	(50/200 CHIRP or 83/ 200 kHz CHIRP) + 455/ 800 kHz
Depth reading	up to 1524m/5,000 ft.
GPS receiver/ antenna	Internal high-sensitivity GPS + WAAS (Americas) or GPS + EGNOS + MSAS (non-Americas) 10 Hz (10 measurements per second)
Communication	NMEA 2000 Network, 2x Ethernet, NMEA 0183, Wi-Fi, Bluetooth
Data ports	Two SD/MMC slots for maps or recording sonar navigation data

**Figure 3** Lowrance HDS Carbon 9 Echosounder [27]

and Sport is situated next to the area called “Green Islands”. It is an ecological utility established in 2011 that provides protection for the nearby wet meadows and riverside reeds. On the other eastern side, the marina borders the Bird Paradise Nature Reserve. The park is located in the north-western part of Sobieszewo Island and covers an area of 188 hectares [25]. Figure 1 is a visual presentation of the described area.

The hydrographic manned vessel “Navigator One AMG”, which belongs to the Gdynia Maritime University was used for the measurements. The boat, which belongs to the Cathedral of Geodesy and Oceanography of the Faculty of Navigation, is the motor yacht “Pegazus 550”. The vessel is characterized by a length of 5.4 m, a width of 2.54 m, a draft of 0.3 m and a weight of 720 kg. “Navigator One AMG” is powered by a Suzuki 50 hp engine and is able to take 6 people on board. This unit stands out in its class for its impressive lateral stability, it is very expansive silhouette and its freeboard height of 90 cm. Figure 2 presents the mentioned hydrographic vessel.

Before surveying, sounding profiles were designed using the Trimble Business Center software with 10 m intervals. The speed of sound propagation in the water

was also measured and water levels were read from water gauge points. The measuring campaign was fully executed based on global standards and the 2020 International Hydrographic Organization (IHO) S-44 requirements [26].

A Lowrance HDS Carbon 9 echo sounder mounted on a manned vessel was used to record the survey points. It is equipped with a bright multitouch screen and an improved processor for advanced sonar techniques including CHIRP sonar and StructureScan® 3D. Transmitter combines wireless operation with highly accurate Lowrance navigation. The echosounder has an internal 10 Hz GPS antenna and the two micro SD card slots. Intuitive easy-to-use interface supports Gen3 features and functions as well as allows the user to operate the device via keyboard, touch screen or both. One of Carbon’s features is Genesis Live, which allows you to create bathymetric studies in real time. Bathymetric map is automatically generated when switching to Genesis Live data layer. There is no need to save data here as with the Garmin system. With the two-channel CHIRP sonar it is possible to detect objects placed very close to the seabed. Next GoFree™ feature enables integrated wireless connectivity to the

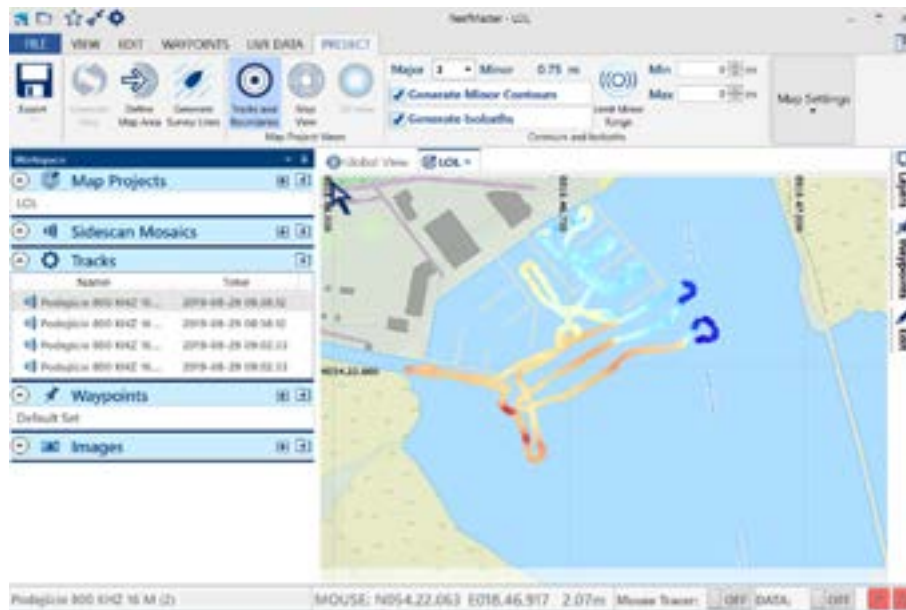


Figure 4 Screen shot of the Reef Master 2.0 software showing the trajectory of a manned vessel



Figure 5 Screen shot of the Reef Master 2.0 software showing properties of recorded points

HDS Gen3 Carbon display. The last noteworthy feature is StructureScan @ 3D, which allows to see objects in a three-dimensional view. This mapping allows users to determine the exact position of objects in relation to the unit from which the data is recorded. Using the touch screen commands it is possible to view the image from every angle. The specification of instruments is presented in the Table 1 [27]. Figure 3 present how is this device looks like.

Carbon sonar records depth using a cone-shaped beam which is sent towards the bottom. The beam bounces off the first obstacle it encounters and returns straight to the device. The sonar calculates the time needed for the wave to travel, which allows to read the direct distance of the object from the vessel equipped with the echo sounder. The transducer emits a beam at

an angle of 60 to 10 degrees and can control the range of the sound wave cone by changing the frequency of the scanning beam. Using the wide angle scanning (40 to 60 degrees), it is possible to record depth and bottom structure data quicker, at the expense of accuracy and detail. On the other hand, narrow-angle scanning (10 to 20 degrees) provides a more precise image but much less coverage of the area. The first method should be used in shallow waters and the second in deep waters.

3 Results

Reef Master 2.0 software was used to process the measurement data. It is an application for Windows computers that allows to create the 2D and 3D underwater

maps combined with graphical waypoint management and a multi-channel sonar viewer. App uses the National Marine Electronics Association (NMEA) 0183 data to create the real-time studies. The program allows to create maps with the option to adjust the contour intervals in US or metric units. Due to compatibility with the Lowrance side scan sonar data it is possible to create high resolution mosaics. The application allows for the quick and easy review of side scan sonar data and export of images in a wide range of formats.

Data processing had to start by creating a new file (naming it and assigning a location on the computer). The next step was to create a new chart project and import files recorded by the Lowrance HDS Carbon 9 system. Then the uploaded data was transferred to the map. To do this, right-click on the file containing the track information and use the “Add track to the

map” option. The program shows at what frequency the points were recorded (in this case 800 kHz). Once this is done, the application generates the registered points on the map. The depth levels are marked accordingly on the mosaic [27]. The program window showing the trajectory of the vessel used during the measurements, is presented in Figures 4 and 5.

By marking individual points of the vehicle trajectory with a mouse, it is possible to read out:

- recorded depth;
- latitude and longitude;
- the exact date and time of the registration;

The next step was to generate the 2D map. Using the “Define Map Area” function, one had to define the map boundary and use the “Generate Map” option to generate the map. The project created in this way had to be edited. For example, the application allows



Figure 6 The 2D map of National Sailing Center in Reef Master 2.0 software

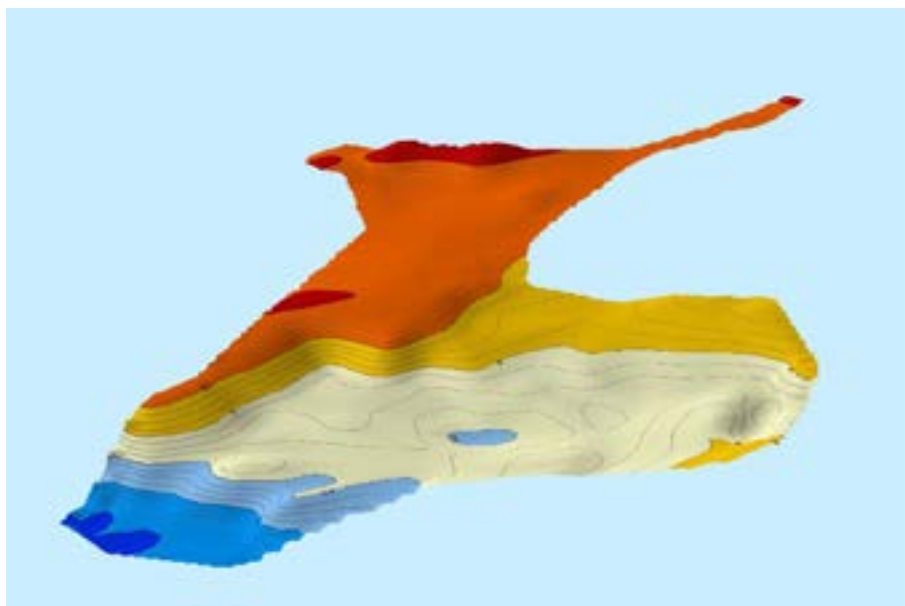


Figure 7 The 3D map of National Sailing Center in Reef Master 2.0 software



Figure 8 Area where no measurements were carried out

to import a file with data about the borders of a water body created, for example, in Google Earth Pro (in this case, using this option is pointless). The last step was to create the 3D map by selecting “3D View” and adjusting the scale of the model. The 2D and 3D map are presented in Figures 6 and 7, respectively.

4 Discussion of results

The completed hydrographic survey made it possible to prepare a bathymetric map with the isobaths of the marina at the National Sailing Center of the Academy of Physical Education and Sport in Gdansk. The depth in the northeastern part of the marina basin is between 4 and 5 meters. The largest recorded value is over 7 meters (west-central part of the map). The reservoir shallows to 2-3 meters near the approach to the port. Particularly shallow depths (less than 1m) were recorded in the southeastern part of the basin located closer to the “Green Islands” area. Such points should be appropriately indicated by navigational markings, as they pose a hazard to vessels with deeper draught. Unfortunately, due to the yachts moored to the piers of the marina, part of the harbor was not scanned. When manoeuvring the boat “Navigator One AMG” in such an area, collision and damage to vessels located there could occur. A fragment of the National Sailing Center, where no measurements were made, is presented in Figure 8.

Due to the submersion of the hydrographic survey vessel used, it was not possible to record data in ultra shallow areas. It is common in hydrographic survey mapping (with a lack of actual survey data of areas below 1 meter) to incorrectly assume a linear depth gradient. However, as much accuracy as possible is required in creating such maps because even the smallest differences in depths have a large impact on

their usefulness. In such cases, it is worth considering the use of unmanned hydrographic units, which have been available on the market for several years now. The USV (unmanned surface vehicle) is characterized by specific design features such as low draught and optimal time efficiency in performing the measurements. Such boats also allow data recording in the area of moored yachts. The small size is beneficial for collision-free maneuvering between the stationed units. It should be noted that the usefulness of the drawn up maps becomes quickly outdated, therefore it is recommended to carry out frequent control measurements, as well.

5 Conclusions

The aim of the article was to present the characteristics of conducting bathymetric works with the use of manned hydrographic unit in the marina areas. Due to the fact that the creation of the bathymetric maps and proper navigational marking of underwater obstacles have a significant direct impact on the safety of maritime and inland waterway transport, in the opinion of the authors of this paper it was justified to take up the presented topic.

The “Navigator One AMG” unit was used to conduct the hydrographic survey. The water vehicle was used to perform a measurement campaign of the marina at the National Sailing Center of the Academy of Physical Education and Sport in Gdansk. The acquired data were used to create the 2D and 3D map of the marina. However, the obtained models cannot be used for navigational purposes since only the Hydrographic Office of the Polish Navy is authorized to issue nautical aids and materials. Nevertheless, the measurements were performed taking into account the requirements of document S-44 issued by the

International Hydrographic Organization [IHO, 2020]. This document outlines the accuracy requirements that must be met when performing the hydrographic survey work, depending on the class of body of water in which the research is conducted. The instructions contained in Publication S-44 are the most common and frequently used in creation of the bathymetric studies, therefore the fact that they are included in the measurements carried out above, gives them a useful value. The methodology itself, as well as the measuring equipment used in the campaign, can serve as a practical aid in planning and carrying out surveys by institutions authorized to conduct such measurements

An important aspect, related to implementation of surveys on such bodies of water as marinas and other, relatively smaller bodies of water, are their limitations that prevent the use of manned vessels on their entire surface. For complementary measurements, unmanned hydrographic drones are often used, which allow measurements in ultra shallow areas (less than 1 m depth), as well as in places that do not allow the

use of classical, water-based survey vehicles. However, they have their limitations. When campaigning in open water, it may be impossible for an unmanned craft to stay on course due to the wave action and their light weight. Another problem is their relatively low seaworthiness, which makes measurements on larger bodies of water much more time consuming. The use of manned hydrographic boats in such small areas can complement surveys done by unmanned vessels in areas that require greater seaworthiness. In addition, the use of convention craft increases the safety of hydrographic drone surveys, as such a water vehicle can serve as a base unit to control the operation of equipment operating without an operator on board.

Acknowledgements

The work was carried out within the activities of loGISTic Science Club. Supervision during its preparation was exercised by Ph.D. Mariusz Specht.

References

- [1] SPECHT, M., SPECHT, C., MINDYKOWSKI, J., DABROWSKI, P., MASNICKI, R., MAKAR, A. Modelling of the tombolo phenomenon in Sopot using integrated geodetic and hydrographic measurement methods. *Remote Sensing*[online]. 2020, **12**(4), 737. ISSN 2072-4292. Available from: <https://doi.org/10.3390/rs12040737>
- [2] SPECHT, C., LEWICKA, O., SPECHT, M., DABROWSKI, P., BURDZIAKOWSKI, P. Methodology for carrying out measurements of the tombolo geomorphic landform using unmanned aerial and surface vehicles near Sopot Pier, Poland. *Journal of Marine Science and Engineering* [online]. 2020, **8**(6), 384. ISSN 2077-1312. Available from: <https://doi.org/10.3390/jmse8060384>
- [3] BOGALECKA, M. Running aground as a cause of accidents at sea / Wejscie na mielizne jako przyczyna wypadkow na morzu (in Polish). *Rocznik Bezpieczenstwa Morskiego*. 2013, **VII**, p. 113-123. ISSN 898-3189.
- [4] MALYSZKO, M., WIELGOSZ, M. Analysis of SAR DSS decision-making process on the example of ship aground / Analiza procesu decyzyjnego sar dss na przykladzie statku na mieliznie (in Polish). *Autobusy*. 2016, **17**(4), p. 33-38. ISSN 1509-5878, eISSN 2450-7725.
- [5] DIERSSEN, H., THEBERGE, A. Bathymetry: assessing methods. In: *Encyclopedia of natural resources. Vol. II - Water and air*[online]. WANG, Y. (ed.). Boca Raton: Taylor & Francis Group, 2014. eISBN 9780203757611. p. 1-8. Available from: <https://doi.org/10.1081/E-ENRW-120048588>
- [6] LUBIS, M., ANGGRAINI, K., KAUSARIAN, H., PUJIYATI, S. Marine seismic and side-scan sonar investigations for seabed identification with sonar system. *Journal of Geoscience, Engineering, Environment, and Technology*[online]. 2017, **2**(2), p. 166-170. ISSN 2541-5794, eISSN 2503-216X. Available from: <https://doi.org/10.24273/jgeet.2017.2.2.253>
- [7] MAKAR, A., SPECHT, C., SPECHT, M., DABROWSKI, P., SZAFRAN, M. Integrated geodetic and hydrographic measurements of the yacht port for nautical charts and dynamic spatial presentation. *Geosciences*[online]. 2020, **10**(5), 203. eISSN 2076-3263. Available from: <https://doi.org/10.3390/geosciences10050203>
- [8] Ministry of Transport, Construction and Maritime Economy. Ordinance of the Minister of Transport, Construction and Maritime Economy of 1 June 1998 on the technical conditions that should be met by marine hydraulic structures and their location (in Polish). Warsaw, Poland: Ministry of Transport, Construction and Maritime Economy: 1998.
- [9] Ministry of Transport, Construction and Maritime Economy. Ordinance of the Minister of Transport, Construction and Maritime Economy of 23 October 2006 on the technical conditions for the use of marine hydraulic structures and the detailed scope of inspections to be carried out on such structures (in Polish). Warsaw, Poland: Ministry of Transport, Construction and Maritime Economy, 2006.

- [10] SPECHT, C., SPECHT, M., DABROWSKI, P. Comparative analysis of active geodetic networks in Poland. In: 17th International Multidisciplinary Scientific GeoConferenceSGEM2017: proceedings[online]. 2017. Vol. 17, Iss. 22. ISBN 978-619-7408-02-7, ISSN 1314-2704, p. 163-176. Available from: <https://doi.org/10.5593/sgem2017/22/S09.021>
- [11] DZIEWICKI, M., SPECHT, C. Position accuracy evaluation of the modernized Polish DGPS. *Polish Maritime Research*[online]. 2009, **16**(4), p. 57-61. eISSN 2083-7429. Available from: <https://doi.org/10.2478/v10012-008-0057-x>
- [12] ARROYO-SUAREZ, E. N., RILEY, J. L., GLANG, G. F., MABEY, D. L. Evaluating a global differential GPS system for hydrographic surveying, In: OCEANS 2005 MTS/IEEE: proceedings[online]. IEEE, 2006. ISSN 0197-7385, ISBN 0-933957-34-3. Available from: <https://doi.org/10.1109/OCEANS.2005.1640155>
- [13] ERENER, A., GOKALP, E. Mapping the sea bottom using RTK GPS and lead-line in Trabzon harbor. In: FIG Working Week 2004 Workshop: proceedings. 2004.
- [14] STATECZNY, A., BURDZIAKOWSKI, P., NAJDECKA, K., DOMAGALSKA-STATECZNA, B. Accuracy of trajectory tracking based on nonlinear guidance logic for hydrographic unmanned surface vessels. *Sensors*[online]. 2020, **20**(3), 832. eISSN 1424-8220. Available from: <https://doi.org/10.3390/s20030832>
- [15] SPECHT, C., WEINTRIT, A., SPECHT, M., DABROWSKI, P. Determination of the Territorial Sea baseline - measurement aspect. *IOP Conference Series: Earth and Environmental Science*. 2017, **95**, 032011. ISSN 1755-1307, eISSN 1755-1315.
- [16] JIN, J., ZHANG, J., SHAO, F., LV, Z., LI, M., LIU, L., ZHANG, P. Active and passive underwater acoustic applications using an unmanned surface vehicle. In: OCEANS 2016MTS/IEEE: proceedings. IEEE, 2016.
- [17] SETO, M. L., CRAWFORD, A. Autonomous shallow water bathymetric measurements for environmental assessment and safe navigation using USVs. In: OCEANS 2015 MTS/IEEE: proceedings. IEEE, 2015.
- [18] STATECZNY, A., BURDZIAKOWSKI, P. Universal autonomous control and management system for multipurpose unmanned surface vessel. *Polish Maritime Research*[online]. 2019, **26**, p. 30-30. eISSN 2083-7429. Available from: <https://doi.org/10.2478/pomr-2019-0004>
- [19] ZWOLAK, K., WIGLEY, R., BOHAN, A., ZARAYSKAYA, Y., BAZHENOVA, E., DORSHOW, W., SUMIYOSHI, M., SATTIABARUTH, S., ROPEREZ, J., PROCTOR, A., WALLACE, C., SADE, H., KETTER, T., SIMPSON, B., TINMOUTH, N., FALCONER, R., RYZHOV, I., ELSAIED ABOU-MAHMOUD, M. The autonomous underwater vehicle integrated with the unmanned surface vessel mapping the Southern Ionian Sea. The Winning Technology Solution of the Shell Ocean Discovery XPRIZE. *Remote Sensing*[online]. 2020, **12**(8), 1344. eISSN 2072-4292. Available from: <https://doi.org/10.3390/rs12081344>
- [20] KUROWSKI, M., THAL, J., DAMERIUS, R., KORTE, H., JEINSCH, T. Automated survey in very shallow water using an unmanned surface vehicle. *IFAC Papers OnLine* [online]. 2019, **52**(21), p. 146-151. ISSN 2405-8963. Available from: <https://doi.org/10.1016/j.ifacol.2019.12.298>
- [21] LI, C., JIANG, J., DUAN, F., LIU, W., WANG, X., BU, L., SUN, Z., YANG, G. Modelling and experimental testing of an unmanned surface vehicle with rudderless double thrusters. *Sensors*[online]. 2019, **19**(9), 2051. eISSN 1424-8220. Available from: <https://doi.org/10.3390/s19092051>
- [22] MU, D., WANG, G., FAN, Y., QIU, B., SUN, X. Adaptive trajectory tracking control for under actuated unmanned surface vehicle subject to unknown dynamics and time-varying disturbances. *Applied Sciences*[online]. 2018, **8**(4), 547. eISSN 2076-3417. Available from: <https://doi.org/10.3390/app8040547>
- [23] WROBEL, K., WEINTRIT, A. With regard to the autonomy in maritime operations - hydrography and shipping, Interlinked. *TransNav the International Journal on Marine Navigation and Safety of Sea Transportation*[online]. 2020, **14**(3), p. 745-749. ISSN 2083-6473. Available from: <https://doi.org/10.12716/1001.14.03.29>
- [24] YANG, Y., LI, Q., ZHANG, J., XIE, Y. Iterative learning-based path and speed profile optimization for an unmanned surface vehicle. *Sensors*[online]. 2020, **20**(2), 439. eISSN 1424-8220. Available from: <https://doi.org/10.3390/s20020439>
- [25] SPECHT, M., SPECHT, C., SZAFRAN, M., MAKAR, A., DABROWSKI, P., LASOTA, H., CYWINSKI, P. The use of USV to develop navigational and bathymetric charts of yacht ports on the example of national sailing centre in Gdansk. *Remote Sensing*[online]. 2020, **12**(16), 2585. eISSN 2072-4292. Available from: <https://doi.org/10.3390/rs12162585>
- [26] IHO. IHO Standards for hydrographic surveys. 6. ed. IHO Publication No. 44. Monte Carlo, Monaco, 2020.
- [27] HDS Carbon 9 - Lowrance [online] [accessed 2021-04-15]. Available from: <https://www.lowrance.com/lowrance/type/fishfinders-chartplotters/hds-9-carbon-c-map-us-enhanced-basemap-medhigh3d-bundle>

BATHYMETRIC MEASUREMENTS OF A RETENTION RESERVOIR USING INTEGRATED HYDROGRAPHIC AND PHOTOGRAMMETRIC TECHNIQUES

Błażej Mach*, Michał Skrzypek

Faculty of Navigation, Gdynia Maritime University, Gdynia, Poland

*E-mail of corresponding author: Mach_b@interia.pl

Resume

The purpose of this paper was to determine the usability of unmanned hydrographic drones and photogrammetric techniques during the conduct of work, the results of which are potentially to serve as navigational materials in areas that, due to their characteristics, make it impossible to carry out research using crew vessels and direct shoreline determination. In order to prepare and carry out the measurement campaign with the greatest possible accuracy and safety, the authors of the article decided to determine the shoreline of the analyzed reservoir using photogrammetric methods. The use of satellite images allowed the border between land and water to be identified as precisely as possible, which had a direct impact on the accuracy of relating depth data to their location on Earth's globe. Use of unmanned vessels and orthophotos can find practical application when navigating vessels during maneuvers required high precision.

Article info

Received 9 May 2021

Accepted 4 June 2021

Online 14 October 2021

Keywords:

Unmanned Surface Vehicle (USV), hydrographic survey, Landsat satellite imagery, photogrammetric survey

Available online: <https://doi.org/10.26552/com.C.2022.1.E19-E27>

ISSN 1335-4205 (print version)

ISSN 2585-7878 (online version)

1 Introduction

A significant threat to maritime and inland waterway transport is the phenomenon of ships running aground [1-2]. The depth of even small water surfaces can change dynamically over several meters toward shore. Therefore, in order to safely maneuver a vessel on a water reservoir, it is important to know the shape of its bottom [3-4]. Depth information is obtained by taking hydrographic measurements. Their results allow ship captains to plan and execute the course of mooring maneuvers in the most optimal way. In addition to high accuracy, the actuality of the research is also important. Inland reservoirs, as well as small harbor facilities, are characterized by relatively high changeability, so it is required to update hydrographic studies with adequate frequency [5-6].

Manned hydrographic units are used in areas that are deeper than 1 meter. Unfortunately, in cases where the depth falls below the indicated value, the technical specifications of the vessels make it impossible to conduct the surveys effectively and safely. Therefore, there is a need to improve hydrographic survey methods to obtain accurate bathymetric surveys, in areas with high variability and low depth values. To fully cover the bottom of ultra-shallow water bodies, unmanned craft, both floating [7-11] and flying, are increasingly being used [12-16]. The construction and size of such drones allow surveys to be conducted in areas inaccessible to manned

vessels. Additionally, the technical characteristics of such hydrographic devices also allow for quick launching and therefore allow for easy, relatively fast and frequent update work.

Hydrographic surveys should not only provide adequate accuracy in measuring the depth of the body of water being surveyed, but also maintain the required positioning accuracy. For that reason, depth sounders, such as single beam echo-sounders (SBES) and multi-beam echo-sounders (MBES), are commonly used when conducting bathymetric surveys of marine and inland areas [17-20]. In addition, Global Navigation Satellite System (GNSS) receivers based on Differential Global Positioning System (DGPS) or Real Time Kinematic (RTK) solutions are used to determine position coordinates [21-25].

Bathymetric maps of ultra-shallow water areas, created by unmanned craft, answer the growing accuracy requirements of the International Hydrographic Organization. Such hydrographic studies also serve to supplement surveys made using the manned craft in areas that are difficult to reach, as well as operators making direct [26]. The accuracy requirements for both depth measurements and positioning are described in document S-44 issued by the International Hydrographic Organization [27].

Despite their small size and high mobility, drones have limitations that apply to all the watercraft. The fact is that the technical characteristics of this type of

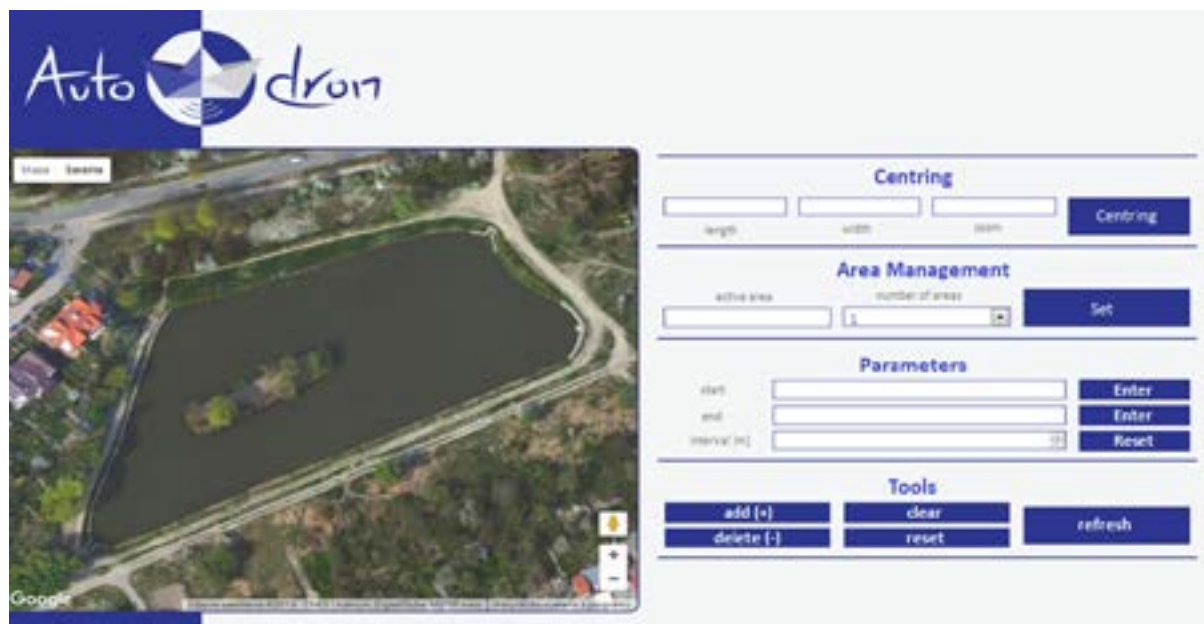


Figure 1 Examples of sounding lines during the bathymetric measurements [30]

equipment make it possible to perform measurements in places that are inaccessible for operators performing direct surveys, as well as for the manned units. Even so, it is impossible to fully cover the entire surface of the water surface where measurements are planned. Additional problems are measurement errors and vehicle deviations from the planned course. These cause that the obtained map of water reservoir is different from the actual state. In order to increase the accuracy of conducted campaigns, orthophotomaps can be used, thanks to which it is possible to obtain an image of the entire surface of the examined reservoir. Such a solution, thanks to relating objects presented on the photomap to localization coordinates, allows to determine the course of the coastline exactly on the land-water border. Another significant benefit of the photogrammetric methods is that they depict all or a significant area of the study area [28]. Consequently, it is possible not only to determine the coastline, but to find out if there are any other objects or surface elements on the surface of the reservoir, as well, that may affect the research being conducted. In addition, it is worth noting that orthophotos are easily available and provide relatively high accuracy. With the use of studies available through free programs, it is possible to determine the position of the indicated point with an accuracy of several m. These advantages make photogrammetric images extremely useful and helpful materials during the preparation and realization of survey campaigns, even though they are not directly used in depth measurements. Despite the many advantages of using the satellite imagery in coastline determination, attention must be paid to its actuality. Due to possible changes that may occur in and around the reservoir, before designing the survey lines based on orthophotomaps, it is necessary to ensure that the images represent the actual status of the reservoir.

Due to water movement, the shape of the coastline may be deformed and movable features such as floating platforms may change their position [29]. Such changes can affect the accuracy of results and if the differences were significant, designing survey profiles based on outdated data can even lead to a damage to the unit.

Due to the above, the aim of this paper was to present the results of bathymetric measurements of the Wilenska reservoir in Gdansk using the integrated hydrographic and photogrammetric methods. The results of the work can be used in carrying out measurements in similar areas, characterized by shallow depths and places inaccessible to other vessels and operators, as well as for the development of hydrographic studies. The use of hydrographic drones is especially useful when surveying such areas as marinas, harbor approach lanes, near-shore areas, small inland reservoirs, and the immediate surrounding of moored vessels, hydro-technical structures-such as caps and piers.

2 Materials and methods

2.1 Methodology of conducting bathymetric measurements using an USV

Preparing the vessel for the survey was based on defining the survey profiles along which the device was to move. Motion trajectories can take many forms. Depending on the need, trajectories can be used: parallel or spirals. A unit moving according to the parallel profiles measures from shore to shore, while the spiral lines resemble tapering squares. Figure 1 shows examples of survey lines [30].

The survey profiles presented above are for illustrative purposes only, therefore they may be freely modified, depending on the needs of the conducted

measurements. Another aspect, regarding the use of unmanned vessel for bathymetric surveys, is the need to consider the weather conditions in the area where the surveys are to take place. Due to the small size of a device there is a risk that its trajectory may be modified by waves or wind. Due to that, measurements should be made at the lowest possible values of the Douglas and Beaufort scales [30]. Other factors that may influence the measurement result are: the speed of sound propagation in water (fluctuation may be daily or seasonal) and the current water level [30]. After taking into account the above mentioned factors, as well as determining the water conditions, it is necessary to carry out a calibration of the equipment used, which can be divided into activities related to preparation of the echo sounder and the GNSS receiver [31]:

Preparing the echo sounder to take measurements involves the following steps:

- calibration (taring) of the vertical echo sounder
- measuring the speed of sound propagation in water;
- measuring the depth at which the sonar transducer is located;

Preparing a satellite receiver requires:

- inclinometer calibration;
- magnetometer calibration.

A manned base unit should also be used during the hydrographic surveys. Besides taking measurements in open areas, it also acts as a safety backup for the unmanned vehicle. When conducting measurements in a small water area, it is enough for the operator to monitor the drone from the shore position [31].

2.2 Bathymetric measurements of the retention reservoir bottom shape using the hydrographic method

The device used to perform the measurements described in this article was a HyDrone catamaran made by Seafloor System Inc. The basic element of the drone's construction are two floats made of the high-density polyethylene (HDPE), which is resistant to environmental conditions and mechanical factors [32]. The floats are connected by an H-shaped frame made of aluminum. The unit has the following dimensions: length 1.1 m, width 0.7 m, draft about 100 mm. The mass of the unit is approximately 25 kg.

A SonarMite v2.1 vertical echo-sounder was used for the measurements. The sonar operated at 200 kHz and the minimum depth that could be measured was 300 mm. When it is necessary to take measurements in shallower areas, it is recommended to use the direct method. Measurement uncertainty during sonar operation was 10 mm \pm 0.5% of the depth. The Trimble R10 GNSS receiver and the Trimble TSC3 controller were used to determine the position of the entire set. The satellite receiver provided reception of all GNSS global navigation satellite systems, so the positioning

accuracy reached 10 - 20 mm. Another advantage, resulting from the use of GNSS systems, was the ability to use an average of 16-20 satellites in the real time for receiving location data. The echo-sounder and satellite receiver were configured with a controller before the measurements were made. The transducer was connected to the echo sounder using a waterproof cable with IP67 protection class. The receiver and echo sounder with the controller were connected to each other via a Bluetooth system. In addition to manual control, 3DR's PiXHawk autopilot was used during research. To make the autonomous system usable, modifications had to be made. Before the rebuild, each float operated independently, which made it impossible to use an autonomous system [32]. The accuracy parameters given above fulfill the International Hydrographic Organization (IHO) standards as described in document S-44. When measurements were conducted, 1500 m/s was taken as the speed of sound in water. This value was not determined experimentally because the maximum depth of the studied water area was 1.5 m, so the measurement error was a few m. Carrying out the survey work took about 2 hours. Due to the minimal operating range of the echo sounder, the smallest measured depth value was 200 mm. To enable the collection of location data it was necessary to connect with the reference station in Gdansk. For this purpose, a commercial real-time RTK service was used, provided by VRSNet.pl company. The connection was made using the General Packet Radio Service (GPRS) cell phone network, and the data from the measurements were recorded on a memory card installed in the receiver in a file with the extension job.

2.3 Determination of the shoreline of a retention reservoir using the photogrammetric method

In order to carry out the measurements that were the objective of this research, the coastline of the retention reservoir at Wilenska Street in Gdansk Morena was measured. Due to the characteristics of the study area, photogrammetric images taken by a satellite were used to determine the shoreline. It was done by using the free computer program Google Earth Pro. Using the tool: Add Marked Sites; the border of surveyed water area was determined. This activity consisted of manually marking the contour of the water reservoir using points marks. These points had to be made with appropriate density and taking into consideration where the shoreline was more diverse. A satellite image, taken on 30/05/2018, was used to determine the shoreline. This image was taken by the Landsat 8 satellite, which is used by Google Earth when capturing satellite images. The use of Landsat 8 satellite enables the collection of images with a resolution of 15 m per pixel [33]. Data about the reservoir was exported from Google Earth Pro and entered into the Trimble Business Center software,



Figure 2 Mapped shoreline using the “Google Earth Pro” software

Table 1 Data processing parameters during reservoir shoreline measurements [32]

Parameter	Data
Country	Poland
System/zone	2000/18
Reference ellipsoid	WGS 84
Ellipsoid semi-major axis	6378137 [m]
Ellipsoid flattening	0.00335281067183
Projection	Gauss-Kruger
Latitude of origin	0
Central meridian	18
False Northing	0
False Easting	6 500 000
Scale factor	0.999923
Azimuth	North
Grid orientation	Rising northeast
Transformation of elevation	Geoid
Geoid model	PL-geoid-2011
Reference system	Kronstad

providing the reservoir shoreline. The result of the work is shown in Figure 2.

3 Results

In order to process the data, a measurement campaign was used that was carried out on 03.09.2016. Its aim was to create a numerical model of the bottom on the TIN triangular grid and a bathymetric map of the studied reservoir [32]. The campaign consisted of 2222 measurement points, which were acquired by an unmanned unit operating in both manual and automatic mode. In order to process the measurement points Trimble Business Center software was used, where the

processing of the obtained data took place, according to the parameters shown in Table 1.

Using the above parameters, World Geodetic System 1984 (WGS-84) ellipsoidal coordinates were transformed to plane coordinates in the PL-2000 system. Based on the available material, a bathymetric map was created and exported to .kmz format. This extension is supported by the Google Earth Pro, which was used because of its universality, intuitive interface and simplicity of data representation. The result of the study is shown in Figure 3.

The measurements made it possible to determine the size of the reservoir, as well as to create a bathymetric map and a model with isobaths. As per the results, the reservoir has a size of 1.19 ha, its maximum depth

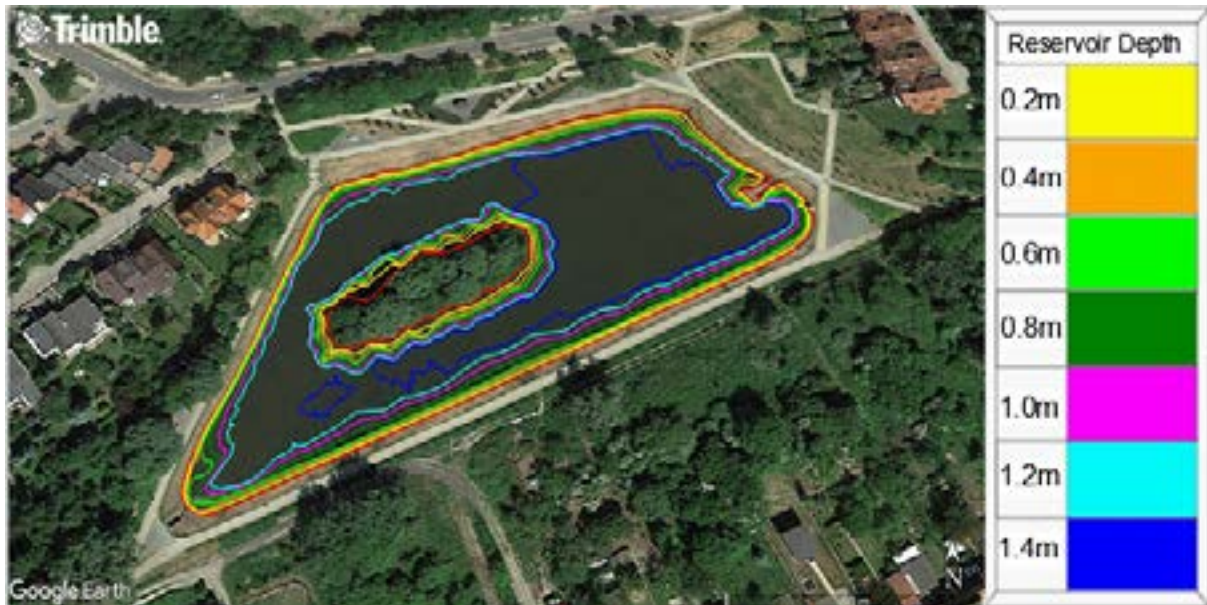


Figure 3 Isobaths applied to satellite image in Google Earth Pro with depth interpretation

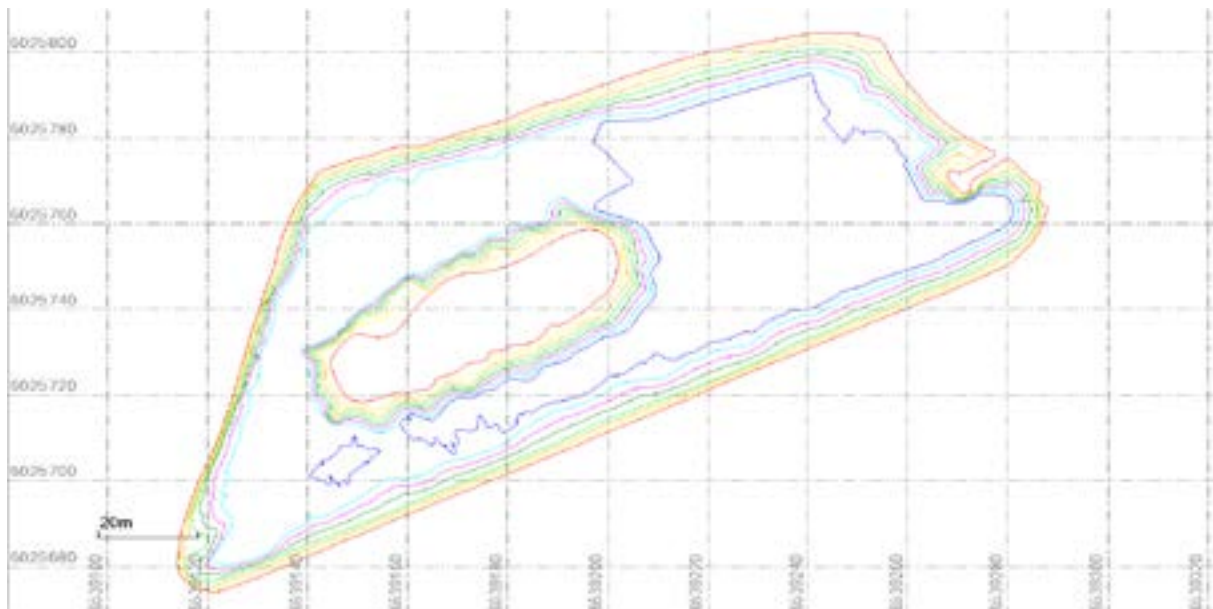


Figure 4 Bathymetric (contour) map of the retention reservoir at Wilenska Street, in the 2000 layout

reaches 1.57 m and its length is 525 m. A characteristic feature of the investigated artificial reservoir is its steepness, which causes that in the distance of 4–8 m from the shore a suddenly increased depth to the value of 1.4 m can be observed. Upon reaching this value, the tank bottom assumes a flat characteristic. In the area of the bottom flattens, the depth of the water body oscillates between 1.4 and 1.57 m, this range represents 50.29% of the surveyed area. This specification of the reservoir bottom regarding its steepness is an example of how important it is to conduct the bathymetric measurements in shallow water areas. Due to the significant change in depth, maneuvering vessels in such waters may be associated with a risk of damage. Figure 4. shows the map with the isobaths applied.

4 Discussion

Due to the low level of seaworthiness of the vessel used during the survey campaign, special attention should be paid during the planning of bathymetric surveys. Because of the technical limitations of the vessel used, the tests should be carried out in the as windless weather as possible and with the lowest waves of water. Therefore, the date of the survey cannot be chosen randomly, but has to consider weather forecasts and there is still a risk that the survey work will have to be postponed or cancelled. Another important aspect of planning and execution of the surveys is to ensure that the satellite images used for the sounding profiles are as up-to-date as possible and correspond with the actual

condition of the water surface. Attention should be paid to the shape of the shoreline, as well as the presence of various elements on and below the water surface, such as piers, ships and underwater elements of the quay structure. In the case of using outdated photos, there is a risk that due to the planning of the survey trajectory on their base, the unit may be damaged by terrain obstacles and in the worst case - completely broken. This is especially important in areas such as harbors and marinas where there are many moving parts, such as floating piers. The solution to this problem is to go to the place of measurement and directly verify the validity of available satellite images. In addition, the autopilot that was planned to be used to guide the vessel during the survey was not designed to operate in water conditions, due to which rounding of the sounding profiles occurred. In addition, the GPS receiver showed an inaccurate position with an error of several meters. The reason for this problem was the dedicated modem used for the pixhawk autopilot. Despite the difficulties mentioned, the measurements were carried out with acceptable accuracy. It is also worth noting that within 2 hours it was possible to measure an area of 1.17 ha. Therefore, it would take just over 3 hours to survey the entire area of a yacht marina like Puck. During the preparation, implementation and development of measurements, document S-44 was adopted as the document standardizing the methodology and accuracy of surveying [IHO, 2020]. Although this document does not include standards for performing this type of work in inland waters, it is the most widely used and internationally recognized document in the context of bathymetric surveying. Considering that potentially this drone is to be used in areas that are under IHO recommendations, the inclusion of the S-44 standard, in the research presented above will enable future use of the device to make measurements where the specific accuracy will be required. In the context of further development of the described device, it should also be noted that the values obtained above cover depths of less than 1 m. Research work in such shallow waters is significantly complicated by the construction of classical survey vessels. However, due to its low draft, as well as its small size, the unmanned hydrographic drone used for the purpose of this research works well in areas inaccessible to other crafts. The fact that the work was conducted in an area characterized by shallow depths makes the accuracy of the data obtained extremely important. When creating such accurate maps, even small differences between the actual state and the value obtained through measurements can affect the usefulness of such studies, as well as the safety of navigation. Bathymetric studies of ultra-shallow waters can become outdated relatively quickly due to wave motion and movement of the surface layer of the bottom, such as sand. In order to maintain the use value of this type of study, control measurements should be taken relatively frequently.

5 Conclusions

The use of such units, as the unmanned hydrographic drone described in this article, significantly contribute to increasing the detail of mapping and other bathymetric studies. Due to the unit's shallow draft, it was possible to collect depth data, with values of less than 1 m, and represent them on the Earth's surface. The acquired data were used to create maps whose depth level is currently unattainable for any institution involved in bathymetric measurements in Poland.

The results obtained during the measurement campaign ranged from 300 to 1570 mm. Such detailed maps significantly reduce navigators' uncertainty when guiding vessels in areas where accurate determination of the water supply under the keel is critical. During the ship mooring in port and other such maneuvering operations, the draft value often closely approximates the depth in a given area. For this reason, from the navigator's perspective, it is necessary that the information about the depth at which he operates is reliable and allows for safe operation of the vessel. Therefore, the use of unmanned hydrographic drones increases safety and reduces the time needed to plan and execute maneuvers in closed waters and activities related to port entry. Despite the fact that the crew of vessels in many cases has a depth sounder on board, the use of a map in which the smallest depth values occurring in a given area are included allows for more efficient, faster and safer planning of the vessel's course.

Usage of unmanned watercraft significantly increases cognitive capabilities when conducting bathymetric work in ultra-shallow waters. As a result of technological development, depth measurements are becoming more and more precise, therefore it is reasonable to increase the accuracy of the other acquired data, having a direct or indirect impact on the final effect of the studies created based on the conducted measurements. Due to increasing opportunities for depth measurements in the immediate nearshore and shallow areas of the reservoir, increasing the precision of the shoreline delineation is complementary to the depth and positioning results obtained. In order to determine the borders of the measured reservoir as precisely as possible, the authors of the paper decided to use orthophotomaps. A significant advantage of this method is the ability to obtain an image of the entire water body, resulting in the ability to quickly determine the border of the entire water area. Current satellite systems used to create this type of study provide a high degree of accuracy in determining the coastline (several tenths of a mm). However, the usefulness of photometric systems depends on their actuality. To make their use possible during the planning and realization of measurement campaigns, it is necessary for orthophotomaps to present the actual condition of the reservoir, as well as the equipment and infrastructure located on it. Special attention should be paid to items that may change their position.

To ensure that the bathymetric studies, created using a hydrographic drone, maintain the required level of map coverage with the actual condition of the water bottom, care must be taken to systematically work on updating the results. This fact causes that the most frequent updating works are recommended, nevertheless that their frequency depends on technical possibilities, needs, and the type of measured reservoir and its bottom, as well. Due to the small size of these units, their easy launch and ability to work in autonomous mode, measurement campaigns can be carried out in a relatively short time. The use of autonomous units is a good supplement to data collected by the conventional manned water vehicles. Therefore, the hydrographic drones provide

a solution for measurements in areas inaccessible to conventional vessels, their size, maneuverability and easiness of operation make it possible to measure in shallow and inaccessible areas. In addition, use of the photogrammetric systems allows, when the study area is extended to include the ultra-shallow places, to increase accuracy of the shoreline and other parts of the studied body of water determination.

Acknowledgements

The work was carried out within the activities of loGISTic Science Club. Supervision during its preparation was exercised by Ph.D. Mariusz Specht.

References

- [1] VANTORRE, M., ELOOT, K., DELEFORTRIE, G., LATAIRE, E. Maneuvering in shallow and confined water. In: *Encyclopedia of maritime and offshore engineering* [online]. John Wiley & Sons, 2017. ISBN 9781118476352, eISBN 9781118476406. Available from: <https://doi.org/10.1002/9781118476406.emoe006>
- [2] RUTKOWSKI, G. Determining the best possible speed of the ship in shallow waters estimated based on the adopted model for calculation of the ship's domain depth. *Polish Maritime Research*. 2020, **27**(3), p. 140-148. eISSN 2083-7429. Available from: <https://doi.org/10.2478/pomr-2020-0055>
- [3] SPECHT, M., SPECHT, C., MINDYKOWSKI, J., DABROWSKI, P., MASNICKI, R., MAKAR, A. Modeling of the tombolo phenomenon in Sopot using integrated geodetic and hydrographic measurement methods. *Remote Sensing* [online]. 2020, **12**(4), 737. ISSN 2072-4292. Available from: <https://doi.org/10.3390/rs12040737>
- [4] SPECHT, C., LEWICKA, O., SPECHT, M., DABROWSKI, P., BURDZIAKOWSKI, P. Methodology for carrying out measurements of the tombolo geomorphic landform using unmanned aerial and surface vehicles near Sopot Pier, Poland. *Journal of Marine Science and Engineering* [online]. 2020, **8**(6), 384. ISSN 2077-1312. Available from: <https://doi.org/10.3390/jmse8060384>
- [5] BODUS-OLKOWSKA, I., WAWRZY尼亚K, N., ZANIEWICZ, G. Bathymetric surveys for inland electronic navigation charts production of the Lower Odra RIS area / Pomiarы batymetryczne na potrzeby produkcji srodladowych elektronicznych map nawigacyjnych obszaru RIS Dolnej Odry (in Polish). *Logistyka*. 2011, **6**, p. 4551-4561. ISSN 1231-5478.
- [6] BANDINI, F., OLESEN, D., JAKOBSEN, J., KITTEL, C., WANG, S., GARCIA, M., BAUER-GOTTWEIN, P. Bathymetry observations of inland water bodies using a tethered single-beam sonar controlled by an unmanned aerial vehicle, Lyngby, Denmark: National Space Institute, Technical University of Denmark, 2017.
- [7] KUROWSKI, M., THAL, J., DAMERIUS, R., KORTE, H., JEINSCH, T. Automated survey in very shallow water using an unmanned surface vehicle. *IFAC PapersOnLine* [online]. 2019, **52**(21), p. 146-151. ISSN 2405-8963. Available from: <https://doi.org/10.1016/j.ifacol.2019.12.298>
- [8] LI, C., JIANG, J., DUAN, F., LIU, W., WANG, X., BU, L., SUN, Z., YANG, G. Modeling and experimental testing of an unmanned surface vehicle with rudderless double thrusters. *Sensors* [online]. 2019, **19**(9), 2051. eISSN 1424-8220. Available from: <https://doi.org/10.3390/s19092051>
- [9] MU, D., WANG, G., FAN, Y., QIU, B., SUN, X. Adaptive trajectory tracking control for underactuated unmanned surface vehicle subject to unknown dynamics and time-varying disturbances. *Applied Sciences* [online]. 2018, **8**(4), 547. eISSN 2076-3417. Available from: <https://doi.org/10.3390/app8040547>
- [10] WROBEL, K., WEINTRIT, A. With regard to the autonomy in maritime operations - hydrography and shipping, Interlinked. *TransNav the International Journal on Marine Navigation and Safety of Sea Transportation* [online]. 2020, **14**(3), p. 745-749. ISSN 2083-6473. Available from: <https://doi.org/10.12716/1001.14.03.29>
- [11] YANG, Y., LI, Q., ZHANG, J., XIE, Y. Iterative learning-based path and speed profile optimization for an unmanned surface vehicle. *Sensors* [online]. 2020, **20**(2), 439. eISSN 1424-8220. Available from: <https://doi.org/10.3390/s20020439>
- [12] ANGNUURENG, D. B., JAYSON-QUASHIGAH, P.-N., ALMAR, R., STIEGLITZ, T. C., ANTHONY, E. J., AHETO, D. W., ADDO, K. A. Application of shore-based video and unmanned aerial vehicles (drones): complementary tools for beach studies. *Remote Sensing* [online]. 2020, **12**(3), 394. eISSN 2072-4292. Available from: <https://doi.org/10.3390/rs12030394>

- [13] BURDZIAKOWSKI, P., SPECHT, C., DABROWSKI, P. S., SPECHT, M., LEWICKA, O., MAKAR, A. Using UAV photogrammetry to analyze changes in the coastal zone based on the Sopot Tombolo (Salient) Measurement Project. *Sensors* [online]. 2020, **20**(14), 4000. eISSN 1424-8220. Available from: <https://doi.org/10.3390/s20144000>
- [14] CONTRERAS-DE-VILLAR, F., GARCIA, F. J., MUNOZ-PEREZ, J. J., CONTRERAS-DE-VILLAR, A., RUIZ-ORTIZ, V., LOPEZ, P., GARCIA-LOPEZ, S., JIGENA, B. Beach leveling using a Remotely Piloted Aircraft System (RPAS): problems and solutions. *Journal of Marine Science and Engineering* [online]. 2021, **9**(1), 19. ISSN 2077-1312. Available from: <https://doi.org/10.3390/jmse9010019>
- [15] GENCHI, S. A., VITALE, A. J., PERILLO, G. M. E., SEITZ, C., DELRIEUX, C. A., Mapping topobathymetry in a shallow tidal environment using low-cost technology. *Remote Sensing* [online]. 2020, **2**(9), 1394. eISSN 2072-4292. Available from: <https://doi.org/10.3390/rs12091394>
- [16] LOWE, M. K., ADNAN, F. A. F., HAMYLTON, S. M., CARVALHO, R. C., WOODROFFE, C. D. Assessing reef-island shoreline change using UAV-derived orthomosaics and digital surface models. *Drones* [online]. 2019, **3**(2), 44. eISSN 2504-446X. Available from: <https://doi.org/10.3390/drones3020044>
- [17] JIN, J., ZHANG, J., SHAO, F., LV, Z., LI, M., LIU, L., ZHANG, P. Active and passive underwater acoustic applications using an unmanned surface vehicle. In: OCEANS 2016 MTS/IEEE: proceedings. IEEE, 2016.
- [18] SETO, M. L., CRAWFORD, A. Autonomous shallow water bathymetric measurements for environmental assessment and safe navigation using USVs. In: OCEANS 2015 MTS/IEEE: proceedings. IEEE, 2015.
- [19] STATECZNY, A., BURDZIAKOWSKI, P. Universal autonomous control and management system for multipurpose unmanned surface vessel. *Polish Maritime Research* [online]. 2019, **26**, p. 30-30. eISSN 2083-7429. Available from: <https://doi.org/10.2478/pomr-2019-0004>
- [20] ZWOLAK, K., WIGLEY, R., BOHAN, A., ZARAYSKAYA, Y., BAZHENOVA, E., DORSHOW, W., SUMIYOSHI, M., SATTIABARUTH, S., ROPEREZ, J., PROCTOR, A., WALLACE, C., SADE, H., KETTER, T., SIMPSON, B., TINMOUTH, N., FALCONER, R., RYZHOV, I., ELSAIED ABOU-MAHMOUD, M. The autonomous underwater vehicle integrated with the unmanned surface vessel mapping the Southern Ionian Sea. The Winning Technology Solution of the Shell Ocean Discovery XPRIZE. *Remote Sensing* [online]. 2020, **12**(8), 1344. eISSN 2072-4292. Available from: <https://doi.org/10.3390/rs12081344>
- [21] SPECHT, C., SPECHT, M., DABROWSKI, P. Comparative analysis of active geodetic networks in Poland. In: 17th International Multidisciplinary Scientific GeoConference SGEM 2017: proceedings [online]. 2017. Vol. 17, Iss. 22. ISBN 978-619-7408-02-7, ISSN 1314-2704, p. 163-176. Available from: <https://doi.org/10.5593/sgem2017/22/S09.021>
- [22] DZIEWICKI, M., SPECHT, C. Position accuracy evaluation of the modernized Polish DGPS. *Polish Maritime Research* [online]. 2009, **16**(4), p. 57-61. eISSN 2083-7429. Available from: <https://doi.org/10.2478/v10012-008-0057-x>
- [23] ARROYO-SUAREZ, E. N., RILEY, J. L., GLANG, G. F., MABEY, D. L. Evaluating a global differential GPS system for hydrographic surveying, In: OCEANS 2005 MTS/IEEE: proceedings [online]. IEEE, 2006. ISSN 0197-7385, ISBN 0-933957-34-3. Available from: <https://doi.org/10.1109/OCEANS.2005.1640155>
- [24] ERENER, A., GOKALP, E. Mapping the sea bottom using RTK GPS and lead-line in Trabzon harbor. In: FIG Working Week 2004 Workshop: proceedings. 2004.
- [25] STATECZNY, A., BURDZIAKOWSKI, P., NAJDECKA, K., DOMAGALSKA-STATECZNA, B. Accuracy of trajectory tracking based on nonlinear guidance logic for hydrographic unmanned surface vessels. *Sensors* [online]. 2020, **20**(3), 832. eISSN 1424-8220. Available from: <https://doi.org/10.3390/s20030832>
- [26] SUHARI, K., KARIM, H., GUNAWAN, P., PURWANTO, H. Small ROV marine boat for bathymetry surveys of shallow waters - potential implementation in Malaysia. *The International Archives of the Photogrammetry, Remote Sensing and Spatial Information Sciences* [online]. 2017, XLII-4/W5, p. 201-208. eISSN 2194-9034. Available from: <https://doi.org/10.5194/isprs-archives-XLII-4-W5-201-2017>
- [27] IHO. IHO Standards for hydrographic surveys. 6. ed. IHO Publication No. 44. Monte Carlo, Monaco, 2020.
- [28] BODUS-OLKOWSKA, I. Basic hydrography lesson script / Skrypt do zajęć z przedmiotu podstawy hydrografii (in Polish). In: *Basics of geodesy and hydrography / Zakład geodezji i hydrografii*. Szczecin: Akademia Morska w Szczecinie, Instytut Geoinformatyki, 2018
- [29] DUDZIŃSKA-NOWAK, A. Determining the development trends of the shore on the basis of remote sensing research / Określenie tendencji rozwojowych brzegu na podstawie badań teledetekcyjnych (in Polish). In: *Basics of remote sensing and maritime cartography / Zakład teledetekcji i kartografii morskiej*. Szczecin: Uniwersytecki Instytut Nauk o Morzu, Wydział Nauk o Ziemi, 2008.
- [30] SPECHT, M., SPECHT, C., WAZ, M., NAUS, K., GRZADZIEL, A., IWEN, D. Methodology for performing territorial sea baseline measurements in selected waterbodies of Poland. *Applied Sciences* [online]. 2019, **9**(15), 3053. eISSN 2076-3417. Available from: <https://doi.org/10.3390/app9153053>

- [31] GRZADZIEL, A. Metodyka wykonywania badan hydrograficznych przeszkod podwodnych / Single beam echo sounder in hydrographic surveys (in Polish). *Przegląd Morski / Maritime Review*. 2006, **7/8**, p. 29-45. ISSN 0137-7205.
- [32] SPECHT, C., SWITALSKI, E., SPECHT, M. Application of an autonomous/unmanned survey vessel (ASV/USV) in bathymetric measurements. *Polish Maritime Research* [online]. 2017, **24(3)**, p. 36-44. eISSN 2083-7429. Available from:
- [33] PIEKARCZYK, J. Satellite, aerial and terrestrial remote sensing / Teledetekcja satelitarna, lotnicza i naziemna (in Polish). In: *Basics of cartography and geomatics / Zakład kartografii i geomatyki*. Poznan: Instytut Geografii Fizycznej i Kształtowania Środowiska Przyrodniczego Uniwersytet im. Adama Mickiewicza, 2019

AIRCRAFT POSITION PREDICTION DURING THE CROSSWIND APPROACH

Marek Grzegorzewski*, Jerzy Biały

Institute of Navigation, Military University of Aviation, Deblin, Poland

*E-mail of corresponding author: m.grzegorzewski@law.mil.pl

Resume

Testing the impact of the drag coefficient on an F16 aircraft model, depending on the angle of attack α was performed. First, a navigation model was introduced describing the preliminary and computational assumptions of the model. The final part of the present paper contains the relationships between the wind angle and the wind correction angle at the angle of attack $\alpha = 0^\circ$, $\alpha = 11^\circ$, $\alpha = 13^\circ$ for a full-scale F-16 aircraft. The tables present results of all the calculations for individual angles of attack, taking into account variable wind angles relative to the longitudinal axis of the runway. The values show the corrections calculated for an 1/19 scale aircraft model and for a full-scale F16 aircraft. The "right" and "left" designations represent the direction from which the wind blows in relation to the aircraft.

Article info

Received 16 March 2021

Accepted 19 April 2021

Online 8 November 2021

Keywords:

GPS,
position prediction,
navigation

Available online: <https://doi.org/10.26552/com.C.2022.1.E28-E35>

ISSN 1335-4205 (print version)

ISSN 2585-7878 (online version)

1 Introduction

Accurate determination of the aircraft's position has always been one of the fundamental reasons for existence of the air navigation. This allows pilots to perform air operations safely and accurately. Landing is the most crucial moment of every flight. That is the phase which is the most burdensome for pilots, requiring the high degree of commitment and focus. Prediction of the aircraft's position during the landing approach may be used in order to reduce the pressure placed on pilots at that time. Accurate information provided to the pilot, concerning their current position, allows for more accurate and, what is important, the safer operations. In order to develop a method for the position prediction, experimental studies of aerodynamic characteristics were used, which were performed in the wind tunnel with a measurement space diameter $\varnothing = 1.1$ m, which belongs to the Military University of Technology, Warsaw Poland. The model used for determination of all the characteristics was an 1/19 scale F-16, which, at that time, had a closed engine inlet channel and an exhaust cone with asymmetric air flow. All the calculations and findings of the above work refer to the above-mentioned model in a "clean" configuration, i.e. all the control surfaces, high-lift devices and aerodynamic brakes are not deflected and the landing gear is retracted. Tests were performed for asymmetric flow at sideslip angles of up to $\beta = -30^\circ$ to 30° at every 2° for angle of attack, $\alpha = 0^\circ, \alpha = 11^\circ, \alpha = 13^\circ$, which, according to the Flight Manual,

correspond to the angles occurring during the landing approach. The measurements were conducted under the following conditions: velocity pressure $q = 1000$ [Pa] ($V \approx 40$ [m.s⁻¹]), Reynolds number $Re \approx 4.5 \times 10^5$. The test results were prepared in the form of graphs showing the courses of the drag coefficient as a function of the sideslip angle β , with a fixed angle of attack $\alpha = C_{\alpha\alpha} = f(\beta, \alpha = \text{const})$ [1].

2 Materials and methods

The objective of the calculations performed in the present work was to make it easier for the pilot to keep the aircraft aligned with the axis of the runway during the crosswind approach. The impact of a crosswind on the aircraft may be crucial during the precision approaches. Strong wind at a high angle in relation to the runway axis can prevent safe operation of even the heaviest and most powerful flying machines. The aim of the following calculations was to show how it acts on an aircraft during the most critical flight phase - landing.

2.1 Calculation assumptions

The first calculations concern a 1/19 scale model of an F-16 aircraft, as it was described in the introduction [2]. One of the basic assumptions is that the calculations were performed for the short periods of time and,

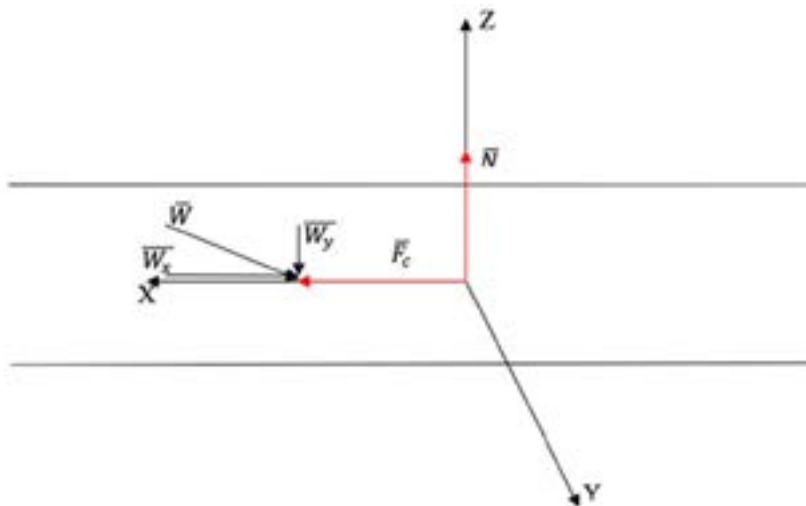


Figure 1 Presentation of trigonometric relationships for the F-16 model at the angle of attack $\alpha = 0^\circ$ and wind angle 5° where: \overline{F}_c - thrust, \overline{N} - lift

consequently, it can be assumed that the wind speed and direction do not change their values in relation to those assumed. The above-mentioned values are, among others, wind speed, which remains constant $V_w = 40 \text{ m}\cdot\text{s}^{-1}$, and its direction, the angle of which with respect to the runway axis was 5° , 10° and 15° , both to the left and to the right. Moreover, the wind direction was parallel to the runway and the wind neither blew onto the aircraft from below nor from above. The model of the aircraft during the tunnel tests was set under three angles of attack values in relation to the air flow: $\alpha = 0^\circ$, $\alpha = 11^\circ$ and $\alpha = 13^\circ$, which were also taken into consideration in the calculations. The approach speeds of the F-16 aircraft are closely related to the angle of attack, which varies depending on the angle α selected. For $\alpha = 0^\circ$, the approach speed is 152 knots (IAS - Indicated Airspeed), for $\alpha = 11^\circ$, - 144 knots (IAS) and for $\alpha = 13^\circ$, - 136 knots (IAS) [3]. Moreover, along with the approach speeds of the aircraft, there is also a change of its allowable mass at which the aircraft would retain the appropriate handling characteristics: $V = 152 \text{ kt} - 25000 \text{ lbs}$, $V = 144 \text{ kt} - 22500 \text{ lbs}$, $V = 136 \text{ kt} - 20000 \text{ lbs}$ [4]. In order to maintain the stability of the glide slope, the engines must generate adequate thrust to keep the speed within a safe range. Turbofan augmented engine, F110-GE-129, is a standard propulsion system used in F-16 aircraft. It is capable of generating 70 kN of thrust without and 131 kN with afterburning. When analyzing the graphs contained in the manual, one can formulate the following assumption: with the maximum thrust, without afterburning equal to 70 kN, the F-16 aircraft engine is able to accelerate to a maximum speed of 660 kt. Owing to this assumption, it would be possible to determine the thrust needed during the approach, depending on the approach speed required. Furthermore, an additional assumption facilitating the determination of the thrust, would be making the approach speed dependent on specific masses. Researchers conducting

tunnel tests assumed the velocity pressure $q = 1000 \text{ [Pa]}$ and found the area of the model surface $S = 0.0698 \text{ [m}^2\text{]}$. These are the data that, together with C_x coefficients, proportional to the respective angles of attack and sideslip would make it possible to calculate the slip forces acting on the F-16 aircraft using the formulas:

$$q = \frac{\rho V^2}{2}, P_x = q \cdot S \cdot C_x, \tag{1}$$

where:

q - velocity pressure (dynamic),

ρ - air density,

V - velocity of the body,

P_x - slip force (drag),

S - model area,

C_x - drag coefficient.

However, before calculating the aircraft's slip forces, its exact speed relative to the air flow ought to be calculated. To that end, the trigonometric relationships between vectors must be used.

The situation of the first instance, i.e. the angle of attack being $\alpha = 0^\circ$, and the angle between the wind and the runway axis being 5° was shown in Figure 1.

This illustration shows the location of the major X, Y and Z axes and the vectors of the slip forces acting on the aircraft. Thrust \overline{F}_c acts on the aircraft along its longitudinal axis X, lift \overline{N} acts along the vertical axis Z and the Y axis is the transverse (pitch) axis of the aircraft. The vector W_x is the vector of the slip force of the wind blowing straight against the nose of the aircraft, while W_y is the vector of the slip force of wind blowing sideways against the side of the aircraft at an angle of 90° . \overline{W} vector is the resultant vector of the two vectors, W_x and W_y , which allows to determine the influence of the crosswind depending on its angle in relation to the longitudinal runway axis. Moreover, the exact values of thrust that are required for calculation of the relevant corrections should be determined. To this end, having

the previously given values of $F_c = 70$ kN and $V = 660$ kt, the values F_c , required for specific speeds, may be determined based on the following proportions:

For $V = 152$ kts; 70000 N - 660 kts

$$x-152 \text{ kts} \\ x = \frac{70000\text{N} \cdot 152\text{kts}}{660\text{kts}} = 16121.21 \text{ N} \quad (2)$$

For $V = 144$ kts; 70000 N - 660 kts

x-144 kts.

Owing to the thrust values, calculated for an actual F-16 aircraft, in the calculations concerning the aircraft model, it would be possible to determine the thrust force proportional to the surface and mass of the 1/19 scale model.

2.2 Calculations of the slip forces acting on the 1/19 scale F-16 model [5]

Trigonometric formulas ought to be used in order to calculate the component vectors W_x and W_y . The resultant W may be determined by applying the difference of cosines for 90° angles and for the first situation examined 5° . Furthermore, values obtained from calculation of cosines should be multiplied by the speed of the wind blowing at a given moment. In this case it is $V_w = 40$ m.s⁻¹. Applying the above instructions, one obtains:

$$40 [\text{m}\cdot\text{s}^{-1}] \cos 90^\circ - (40 [\text{m}\cdot\text{s}^{-1}] \cos 5^\circ) = 0-39.85 = 39.85. \quad (3)$$

The solution of the above problem should then be subtracted, in accordance with the sign in front of the numerical value, from the speed of the aircraft depending on the given angle of attack α . In this case, for the first example the speed was 152 knots, which corresponds to the angle of $\alpha = 0^\circ$.

To begin with, it is necessary to convert the unit of 152 knots into the same unit as specified for the wind speed, i.e. meters per second. Using the calculation formulas below, one obtains:

$$V[\text{kt}] \cdot 1.852 = \\ V[\text{km} \cdot \text{h}^{-1}] \alpha \rightarrow V[\text{km} \cdot \text{h}^{-1}] \cdot 3.6 = V[\text{km} \cdot \text{h}^{-1}] \\ 152[\text{kts}] \cdot 1.852 = 281.5[\text{km} \cdot \text{h}^{-1}] \rightarrow \\ \rightarrow 281.5[\text{km} \cdot \text{h}^{-1}] \div 3.6 = 78.20[\text{m} \cdot \text{s}^{-1}]. \quad (4)$$

Having an exactly calculated speed value relative to the air flow, one can calculate the value of the speed over the ground, referred to as ground speed (GS), according to the formula:

$$\text{GS} = 78.20[\text{m} \cdot \text{s}^{-1}] - 39.85[\text{m} \cdot \text{s}^{-1}] = \\ = 38.35[\text{m} \cdot \text{s}^{-1}]. \quad (5)$$

After determining the GS, the mass and thrust of

the F-16 model should be determined in relation to an actual aircraft [6]. In order to do that, the proportions should be used. To calculate the mass of the model, the surface area, the mass of the aircraft and the surface area of the model should be combined with one another, as follows:

$$25000\text{lbs} \cdot 0.4536 = 11340 \text{ kg} \\ 27.87\text{m}^2 - 0.0698\text{m}^2 \\ 11340 \text{ kg} - x \\ x = \frac{11340 \cdot 0.0698\text{m}^2}{27.87\text{m}^2} = 28.40 \text{ kg} \quad (6)$$

where: 27.87 m²- surface area of the real F16 aircraft, 0.0698 m²- surface area of the 1/19 aircraft model, 11 340 kg - mass of the full-scale F-16 at velocity $V = 78.20$ m.s⁻¹.

The calculated mass is a computational assumption necessary in the subsequent action to determine the approximate thrust for a model, proportional to that required for an actual aircraft. This is done by using the basic formula for thrust:

$$F_c = m \cdot a. \quad (7)$$

Having the thrust of an actual F-16 for a given V at a given mass, the value of its acceleration is to be determined for the given conditions:

$$16121.21\text{N} = 11340 \text{ kg} \cdot a, \\ a = \frac{16121.21 \text{ N}}{11340 \text{ kg}} = 1.42 \text{ m}\cdot\text{s}^{-2}. \quad (8)$$

Then, knowing that the acceleration in the case under consideration is to be the same, one can determine the approximate thrust of the model:

$$F_c = 28.40 \text{ kg} \cdot 1.42\text{m}\cdot\text{s}^{-2} = 40.33\text{N}. \quad (9)$$

After solving the above problems, calculations of the slip force P_x should be commenced. In order to do that, the formula for force should be used which was presented in the previous subsection. The following values were used in the calculations given below: dynamic pressure $q = 1000$ [Pa], surface area of the model tested $S = 0.0698$ m² and the drag coefficient values C_x from Table 1 for wind blowing from the right -0.02931 and from the left -0.02945 at the angle of attack $\alpha = 0^\circ$. Having calculated values of thrust F_c and slip force P_x , it is possible to determine the value of the angular correction to be used by the pilot in order to continue the straight flight, undisturbed by the crosswind impact. For this purpose, the next trigonometric formula has to be used, this time for the tangent of an angle.

$$P_x = [P_d] \cdot 0.0698[\text{m}^2] \cdot 0.02931 = 2.05[\text{N}]. \quad (10)$$

Figure 2 presents the mutual orientation of thrust

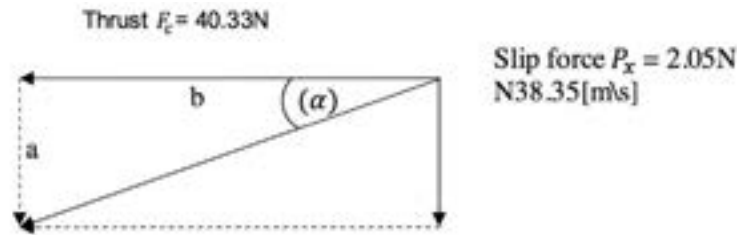


Figure 2 Presentation of the dependence of thrust and slip force vectors with the wind blowing at 5° from the right and the angle of attack $\alpha = 0^\circ$

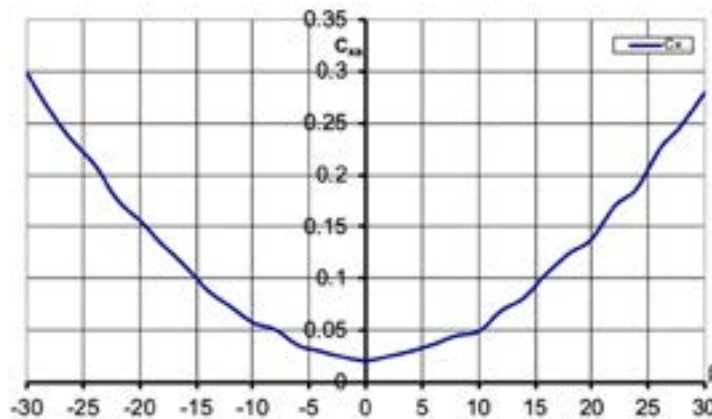


Figure 3 Drag coefficient graph of the F-16 model as a sideslip angle function for the angle of attack $\alpha = 0^\circ$

and slip force vectors. A resultant vector was drawn between them, which designates two triangles sharing an edge. In order to calculate a correction, required to correct the aircraft flight path, one should first determine the value of the angle tangent α and then convert it to an angular value indicating by how many degrees the aircraft should yaw.

Following the above guidelines, one obtains:

$$\tan \alpha = \frac{a}{b} \rightarrow \tan \alpha = \frac{2.05[N]}{40.33[N]} = 0.0508 \rightarrow 2.09^\circ. \quad (11)$$

Using a calculator converting the value of a tangent function into an angular value, one can obtain the value of 2.90° , which in this case means that in order to correct the crosswind impact, the pilot, must deflect the plane by the angle given against the wind, i.e. to the right. The same principle applies to the wind blowing from the left. The only change in the calculations would be a different value of the C_x coefficient.

3 Results

3.1 Analysis of the drag coefficient influence on the F-16 aircraft model depending on the angle of attack α [4]

3.1.1 Drag coefficient as a function of the sideslip angle for angle of attack $\alpha = 0^\circ$

The curve of a drag coefficient C_{xa} as a function of the sideslip angle is parabolic. The minimum value of

the drag coefficient may be observed for the sideslip angle $\beta \approx 0^\circ$ and its value is then $C_{xamin} = 0.02004$ (Figure 3). In the sideslip angle range from $\beta \approx -15^\circ$ to $\beta \approx 16^\circ$, the drag coefficient does not exceed 0.1. For sideslip angles greater than the above, the intensity of increase of C_{xa} grows, achieving at $\beta \approx -30^\circ$ the value of $C_{xa} = 0.29896$, whereas at $\beta \approx 30^\circ$ to $C_{xa} = 0.27966$.

3.1.2 Drag coefficient as a function of sideslip angle for the angle of attack $\alpha = 11^\circ$

It can be observed that the shape of the characteristics $C_{xa} = f(\beta)$ is parabolic in this case, as well. Here, however, there are significant differences in its course (Figure 4). The minimum drag coefficient $C_{xamin} = 0.16449$ is achieved at the sideslip angle $\beta \approx 4^\circ$. In the sideslip angle range from $\beta \approx -20$ to $\beta \approx 21$ drag coefficient does not exceed 0.3. At the sideslip angles defining the boundaries of the graph, the coefficient C_{xa} starts increasing much faster, which results in the fact that, for $\beta \approx -30^\circ$, the drag coefficient reaches $C_{xa} = 0.43481$ whereas at $\beta \approx 30^\circ$, reaches the value $C_{xa} = 0.41274$.

Another factor, which has an additional influence on the increase of the drag coefficient, is the value of the sideslip angle. In such a situation, as in the angle of attack change mentioned above, any deviation from the axis of the air flow causes an increase in drag. However, in this case the motion occurs in relation to the vertical axis (Z axis) of the aircraft. When

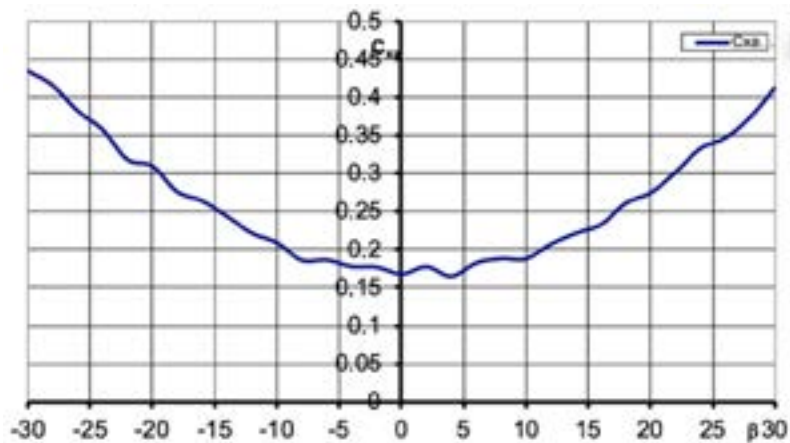


Figure 4 Drag coefficient graph of the F-16 model as a sideslip angle function for the angle of attack $\alpha = 11^\circ$

Table 1 Results of the correction angle calculations for the F16 model in 1/19 scale

$\alpha = 0^\circ V=152\text{kt}/78.20[\text{m}\cdot\text{s}^{-1}]$						
5 ⁰		10 ⁰		15 ⁰		
Left	Right	Left	Right	Left	Right	
-2.92 ⁰	2.90 ⁰	-4.79 ⁰	5.65 ⁰	-10.26 ⁰	10.98 ⁰	
$\alpha = 11^\circ V=144\text{kt}/74.08[\text{m}\cdot\text{s}^{-1}]$						
5 ⁰		10 ⁰		15 ⁰		
Left	Right	Left	Right	Left	Right	
-16.65 ⁰	17.90 ⁰	-18.83 ⁰	20.81 ⁰	-22.93 ⁰	-25.64 ⁰	
$\alpha = 13^\circ V=136\text{kt}/69.96[\text{m}\cdot\text{s}^{-1}]$						
5 ⁰		10 ⁰		15 ⁰		
Left	Right	Left	Right	Left	Right	
-23.32 ⁰	24.42 ⁰	-26.10 ⁰	26.52 ⁰	-29.12 ⁰	31.51 ⁰	

Table 2 Results of the correction angle calculations for the full scale F16

$\alpha = 0^\circ V=152\text{kt}/78.20 \left[\frac{\text{m}}{\text{s}} \right]$						
5 ⁰		10 ⁰		15 ⁰		
Left	Right	Left	Right	Left	Right	
-2.92 ⁰	2.86 ⁰	-4.80 ⁰	5.65 ⁰	-10.20 ⁰	10.98 ⁰	
$\alpha = 11^\circ V=144\text{kt}/74.08 \left[\frac{\text{m}}{\text{s}} \right]$						
5 ⁰		10 ⁰		15 ⁰		
Left	Right	Left	Right	Left	Right	
-16.70 ⁰	17.95 ⁰	-18.88 ⁰	20.86 ⁰	-22.98 ⁰	25.69 ⁰	
$\alpha = 13^\circ V=136\text{kt}/69.96 \left[\frac{\text{m}}{\text{s}} \right]$						
5 ⁰		10 ⁰		15 ⁰		
Left	Right	Left	Right	Left	Right	
-23.32 ⁰	24.42 ⁰	-26.11 ⁰	26.52 ⁰	-29.12 ⁰	31.51 ⁰	

comparing the above two graphs to each other, one can come to yet another conclusion, which is related to the difference between the minimum and maximum value of the drag coefficient, relative to the angle of attack and the sideslip angle. By analyzing the graph for the zero-degree angle of attack, it can be noticed that, in

comparison to the rest of the graphs, it has the largest difference between the minimum and the maximum value of the drag coefficient. This points to the fact that sideslips of an F-16 plane in straight and level flight at a zero-degree angle of attack are much more harmful to the aircraft characteristics than at 11⁰ angles.

4 Discussion

Tables 1 and 2 present results of all the calculations for individual angles of attack, taking into account variable wind angles relative to the longitudinal axis of the runway. The values show the corrections, calculated for an 1/19 scale aircraft model and for a full-scale F16 aircraft. The “right” and “left” designations represent the direction from which the wind blows in relation to the aircraft. The values above them, i.e. 5°, 10°, 15° are its angles.

When analyzing the results for the angle of attack $\alpha = 0^\circ$, one may notice that the discrepancy between the results for the model and the actual aircraft is not large. This points out to the fact that all the calculation assumptions were formulated correctly. Owing to that, the values are very similar to one another, the differences are slight and they should not significantly affect the precision and safety of the approach. Such accuracy of the results also shows that the 1/19 model aircraft has been tested correctly and that it is a real model of an actual aircraft. Particularly worth noting are the corresponding values of drag forces P_x calculated in the above work and those presented by the Military University of Technology, Warsaw Poland. The largest difference between the results obtained may be seen between the corrections for the wind blowing at 15° from the left, for the angle of attack $\alpha = 0^\circ$. In that case the difference was 0.06°; as mentioned before, its value is small and it has no significant effect on conducting the operation. A lot of calculation results were congruent with one another. In sixteen, out of thirty-six calculations performed, exactly the same value was obtained, which shows the validity of computational assumptions and

the fact that the model simulated the behavior of an actual F-16 in crosswind very precisely. It may be observed, in the results obtained, that the most rapid change between the correction values takes place where the biggest difference in the angles of attack occurred, i.e. between $\alpha = 0^\circ$ and $\alpha = 11^\circ$. In this situation, the arithmetic mean of differences (mean difference) of the corrections for the model is 14.2°, whereas for the actual F-16 it is -14.28°.

Comparing this to discrepancies in the change from $\alpha = 11^\circ$ to $\alpha = 13^\circ$, where the arithmetic mean of differences (mean difference) of the corrections for the model was 6.37° and -6.32° for the actual F-16, one may see that there was almost a two-fold increase in the value of the corrections. It is worth noting that with the angle of attack increase by 11° the increase of corrections is significantly lower than when the angle of attack increased by 2° between $\alpha = 11^\circ$ and $\alpha = 13^\circ$. As shown previously, taking into account, e.g. the aircraft model at the increase of $\alpha = 0^\circ$ -11° the value is 14.21°, whereas for the increase of $\alpha = 11^\circ$ to 13° it was 6.37°. This shows that the F-16 aircraft is very sensitive to crosswind at higher angles of attack. The result of this observation may also be influenced by the fact that for the angles of attack being $\alpha = 11^\circ, \alpha = 13^\circ$ the aircraft was flying at lower speeds, which could also have affected its inferior crosswind resistance.

Graphs presented in Figures 5 and 6 show the corrections, which were obtained from calculations. Due to the fact that the values obtained do not differ significantly from each other, it can be observed that the course of both charts is almost identical. The only difference between them is the slightly steeper course of the graph in the (-4.79) - (-10.26) range for the F-16

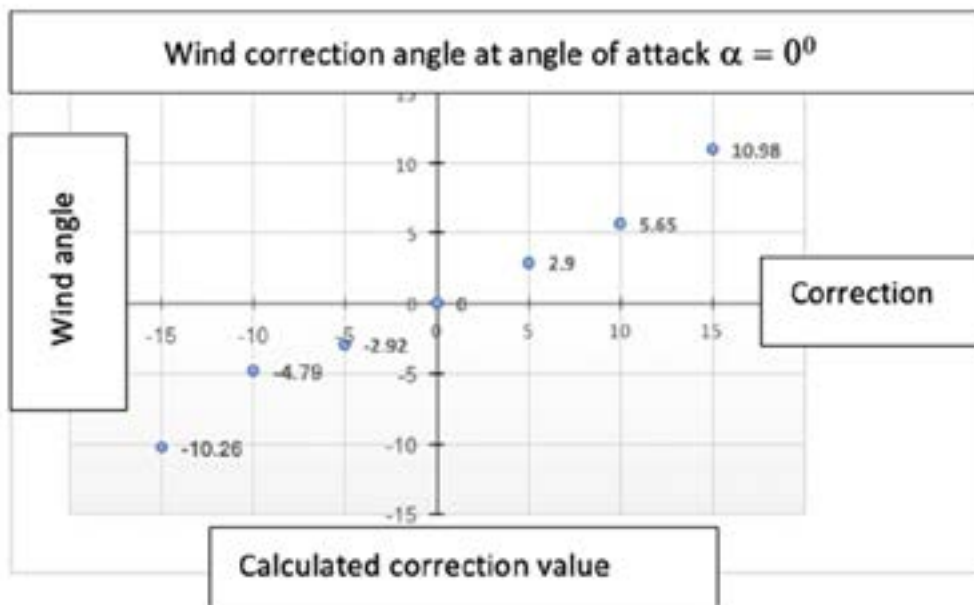


Figure 5 Relationship between the wing angle and wind correction angle at angle of attack $\alpha = 0^\circ$ for the 1:19 scale F16 model

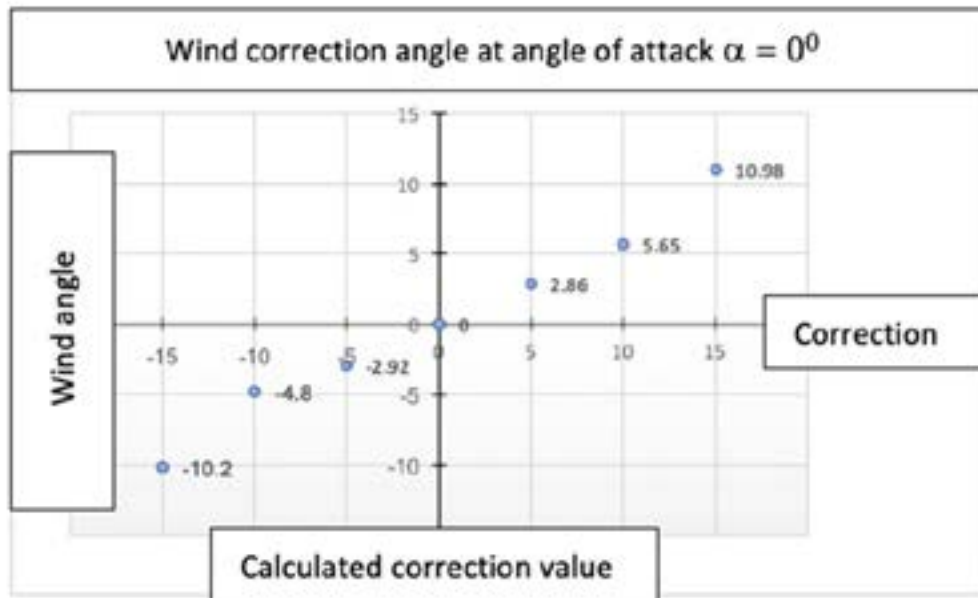


Figure 6 Relationship between the wind angle and wind correction angle at the angle of attack $\alpha = 0^\circ$ for the full-scale F16 aircraft

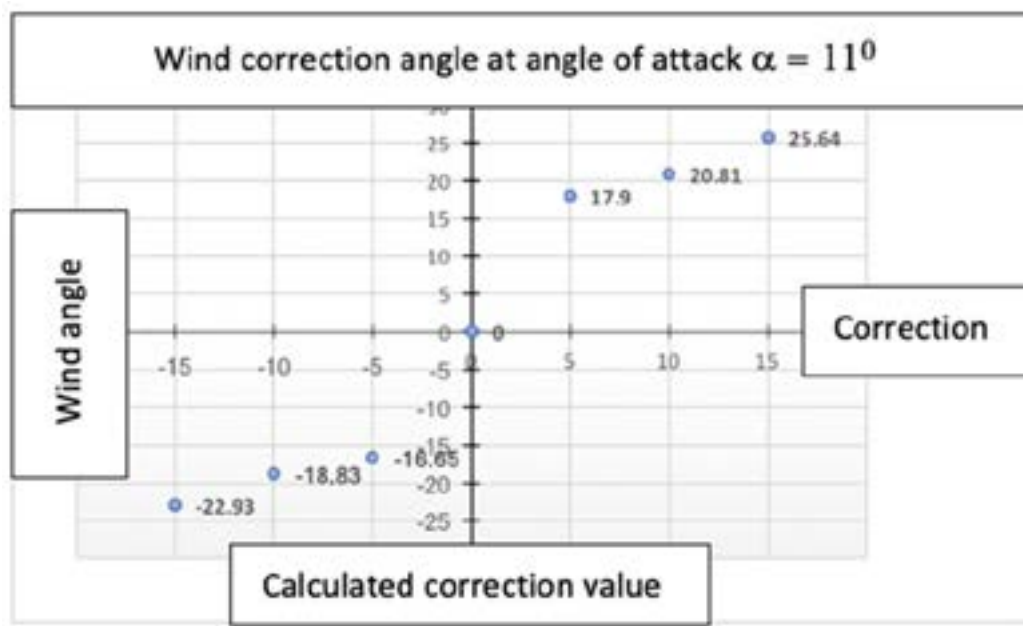


Figure 7 Relationship between the wind angle and wind correction angle at the angle of attack $\alpha = 11^\circ$ for the 1:19 scale F-16 model

aircraft model as compared to the full-scale aircraft.

Figures 7 and 8 show the corrections calculated for the angle of attack $\alpha = 11^\circ$. In this case, it may be noted that the graph of the 1/19 model runs below that of the full-scale F-16. This is caused by differences between the correction values being on average approximately 0.05° .

5 Conclusions

The presented work shows the importance of position prediction for the precise and safe execution of

the landing approach. Owing to the use of trigonometric relationships, exact parameters of the aircraft tested - in this case the F-16 - fundamental laws of aerodynamics and very precise tunnel tests' results, it is possible to determine the exact correction value to be introduced so that the aircraft can keep its trajectory in the longitudinal axis of the runway on which the landing has been planned. The impact of the crosswind, depending on its speed and direction, can significantly affect the flight trajectory of an aircraft and that can be seen by analyzing the results of the tests. The largest correction possible to determine was as much as 31.51° ,

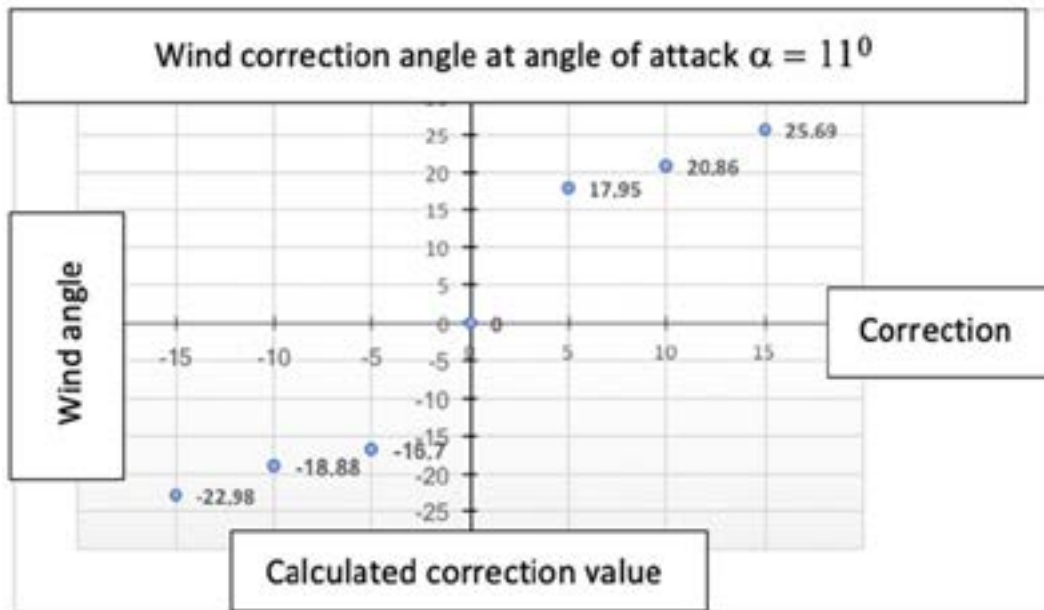


Figure 8 Relationship between the wind angle and wind correction angle at the angle of attack $\alpha = 11^\circ$ for the full-scale F-16 aircraft

which shows how crosswind can influence the flight path, of e.g. an airplane. Such a large value of deviation constitutes a very significant change of direction. It should be remembered, however, that the calculations were performed for the wind speed reaching $40 \text{ m}\cdot\text{s}^{-1}$ at which in real life no air operation would be allowed to take place, as such conditions would not ensure the safety of flight operations.

Acknowledgements

This research was funded by Polish Air Force University Statutory Project: Prediction of Position on the Glide Path Using Bessel Equations - Testing the F16 Aircraft Drag Coefficient in the Function of Wind Angle, grant number PBN 03077/2017/WAT. The APC was funded by Polish Air Force University, Deblin Poland.

References

- [1] ABLAMOWICZ, A., NOWAKOWSKI, W. *Fundamentals of aerodynamics and flight mechanics / Podstawy aerodynamiki i mechaniki lotu* (in Polish). Warszawa: Wydawnictwa Komunikacji i Łączności, 1980. ISBN 83-206-0054-5, p. 25-26.
- [2] GRZEGORZEWSKI, M. Navigating an Aircraft by Means of a Position Potential in Three-Dimensional Space / Nawigacja statku powietrznego za pomocą potencjału pozycji w przestrzeni 3D (in Polish). *Annual of Navigation*. 2005, 9, p. 47-69. ISSN 1640-8632.
- [3] LEITNER, R., ZAKOWSKI, W. *Mathematics - preparatory course for technical universities / Matematyka - Kurs przygotowawczy na wyższe uczelnie techniczne* (in Polish). Warszawa: Wydawnictwa Naukowo-Techniczne, 1968. p. 421-431.
- [4] LOCKHEED, M. US Air Force: F-16 C/D Block 50 and 52+ Supplemental Flight Manual. 1997. p. 144-146.
- [5] FRANT, M., MAJCHER, M., RAPALA, E. Experimental studies in wind tunnel on drag coefficient as a function of sideslip angle / Doswiadczenia badania w tunelu aerodynamicznym współczynnika oporu czołowego modelu samolotu F-16 w funkcji kąta ślizgu (in Polish). Warszawa: Wojskowa Akademia Techniczna, 2017. p. 3-12.
- [6] LOCKHEED, M. US Air Force: F-16 C/D Block 50 Flight Manual. 1996. p. 23, 212-215, 424.

PROCESSING OF THE RESULTS OF SATELLITE INLAND POSITIONING TRANSPORT USING MOBILE DEVICES AND THEIR VISUALIZATION

Malgorzata Kulas

Gdynia Maritime University, Gdynia, Poland

*E-mail of corresponding author: malgorzatakulas98@wp.pl

Resume

The issue of spatial data visualization is currently an important element in the positioning and navigation process. The constant trend in increasing the accuracy and availability of position modules affects the widespread use of the mobile devices in transport. The paper presents creation of a three-dimensional visualization model based on ground tracks recorded in NMEA (National Marine Electronics Association) and GPX (GPS Exchange Format) formats. Additionally, the study presents an analysis of the positioning accuracy including the sky obstructions presence and the instantaneous state of the satellite constellation. The significant deterioration in positioning accuracies was noted due to the presence of sky obstructions and low movement speed during data recording. The analysis of these parameters showed the dependence of the positioning accuracy with the number of visible satellites and the HDOP (Horizontal Dilution of Precision) parameter.

Available online: <https://doi.org/10.26552/com.C.2022.1.E36-E48>

Article info

Received 4 May 2021

Accepted 2 August 2021

Online 22 November 2021

Keywords:

land transport,
satellite positioning,
NMEA,
GPX,
KML,
visualization

ISSN 1335-4205 (print version)

ISSN 2585-7878 (online version)

1 Introduction

Satellite positioning is widely used in both maritime and land transport. The practical application of astronavigation in marine navigation has been almost eliminated by the global satellite navigation systems [1]. The issue of visualization of routes in the sea conditions is carried out through the use of the ECDIS (Electronic Chart Display and Information System) system [2]. Based on the readings of the GNSS (Global Navigation Satellite System) sensors, the current position of the ship is determined and then it is related to the electronic map [3]. Concerning the land transport, the issue of the spatial data visualization is related to connection of positional data with the environment. In the period of rapid development of information and geospatial technologies, on-line numerical maps are widely used [4-5]. Another level of detail is imaging based on photogrammetric imaging [6], LIDAR (Light Detection and Ranging) aerial laser scanning [7] and terrestrial laser scanning [8].

Presentation of the routes of movement of people and means of transport is related to the accuracy of satellite positioning. Positioning errors vary depending on the measurement mode and type of receivers. Authors in [9] focused mainly on the aspect of availability of the smartphone positioning service under different conditions and did not include the accuracy results of the devices. In [10] the research topic was determining the

positioning accuracy in the rail transport, however, the professional GNSS receivers and INS (Inertial Navigation System) and MEMS (Micro-Electro Mechanical System) inertial modules were used in the study. In [11] and [12] the methodology was presented, as well as verification of the real data for the accuracy analysis of dynamic and stationary satellite measurements. The cited works confirm the variability of the accuracy results in relation to the constant values presented in the official standards issued by the managers of navigation systems, e.g. GPS (Global Positioning System) [13]. The presence of the sky obstacles, which block the reception of satellite signals, is of particular importance from the point of view of positioning accuracy [14]. To increase the accuracy of the determined coordinates, supporting systems are used, e.g. active geodetic networks [15]. In [16] the accuracy of static and dynamic positioning of smartphones was examined in relation to the reference station of an active geodetic network. Similar studies were carried out in [17].

Presentation of the spatial data in numerical form is realized in the form of topography and land cover models. In the second case, especially in highly urbanized cities, different levels of details (LoD) are used [18]. The source of this data is photogrammetric images collected, among others by aerial [19] and surface drone vehicles [20]. The spatial data, after appropriate harmonization [21], are presented in the form of a three-dimensional model with various levels of detail, e.g. the Google Earth [4]. An additional advantage of the above solutions is the

ability to import external spatial data and display them together with the terrain model. This is an important tool for representing the location of different modes of transport.

The fusion of positioning technology with supporting systems has significantly changed the implementation of the land transport. These solutions are primarily used in personal navigation systems and vehicle fleet monitoring [22]. Vehicle tracking information provides useful data, such as congestion, determining the site of an accident, locating emergency vehicles and the public transport. The above operations significantly support the procedures for traffic management, tracking and managing the fleet of vehicles [23]. An interesting issue concerning the public transport is described in [24] by application of the GNSS and WiFi technologies in determining the position in underground/ subway public transportation conditions, whereas in [25] the methodology of using smartphones for indoor/outdoor navigation in the public transport was presented. The authors did not include the precision parameters for positioning of devices in the study. The application of the satellite positioning also has a key role in the rapidly growing industry of Intelligent Transport Systems (ITS) and autonomous vehicles [26]. In addition, location data is used to coordinate the fleet, determine transport routes, conduct and optimize the transport control [27].

This study is related to presentation of the process of integration of the spatial data from external sources with the spatial model of the Google Earth application. For this purpose, satellite measurements were carried out with use of the four different mobile devices at four locations in Poland and Sweden. The study also involved processing the recorded spatial source data of GNSS receivers into an import format used in the Google Earth application. Moreover, based on the recorded data, a basic positioning accuracy analysis of the used mobile devices was carried out. The study was divided into three main sections describing used data formats, data processing procedures and visualization results.

2 Materials and methods

The study used three formats commonly used in the GIS (Geographic Information System) environment: NMEA, GPX, and KML (Keyhole Markup Language). The advantage of the formats is recording of the latitude and longitude coordinates as well as the height relative to the adopted reference level. The name of the first format comes from the NMEA, the creator of standards for digital data exchange between the marine electrical devices [28]. The NMEA standards are open, but access to the full specification is limited and paid for. Currently, there are two versions of the standard: NMEA 0183 and NMEA 2000. Due to the emergence of more and more modern devices, the NMEA standards are constantly being improved, as well.

The NMEA 0183 standard enables one-way data exchange and defines requirements for data protocols, electrical signals, transmission time and sentence format. Devices using the NMEA 0183 use an asynchronous serial interface with strictly defined transmission parameters: speed 4800 bits per second with 8 data bits, one stop bit and no parity [29]. Data is transmitted in sentences with a defined structure and ASCII encoding is used for recording. In the NMEA 0183 transport and navigation applications, a Global Positioning System Fix Data (GGA) message is often used to provide the positioning information [30]. The NMEA 2000 differs from the previous version because it is multi-tasking and self-configuring. The format uses the binary encoding and offers the faster data transmission than the alphanumeric NMEA 0183. It also enables bi-directional data exchange between multiple transmitters and receivers. The NMEA 2000 messages are transmitted as a series of data frames. The standard is primarily used for transmission of the short data messages [28].

The other two formats: GPX and KML are open standards developed based on XML (Extensible Markup Language). The XML defines a set of rules for encoding ASCII documents in such a way that they are both human and machine-readable [31]. Created in 2002, the GPX format defines a set of tags to describe the GNSS survey data and geographic data and allows to indicate user-defined features and attributes. The format allows saving position data in the form of points, routes and tracks. The GPX is supported by many applications and websites and it is considered by many to be the standard format for exchange of the GPS data between the fixed and mobile devices, GNSS receivers and internet services [32].

The second XML-based format is KML (Keyhole Markup Language). According to the documentation of the format, it is used to store the spatial data, with help of which visualizations are created in mobile applications, internet maps, or browsers of three-dimensional Earth models, such as Google Earth [33]. The KML files, unlike the encrypted KMZ format, can be generated either by using the GIS software user interface or created from scratch using XML in a text editor. The KML's feature set includes placemarks, lines, polygons, 3D models, text annotations, images, icons, labels, web links [34]. Each point saved in the KML file is defined by longitude and latitude and optional data defining the view in the 3D space of the software. The location coding with KML is entered in the form of tuples, i.e. multi-element variables consisting of a sequence of real numbers representing the coordinates in the following order: longitude, latitude and altitude. Horizontal coordinates are defined on the WGS84 ellipsoid (World Geodetic System 1984) [35] and the elevation coordinate is measured with respect to the EGM96 geoid model (Earth Geopotential Model 1996) [36].

Measurements were analyzed after the registration

was completed and the files were copied to the computer. Processing of the spatial data saved in NMEA and GPX formats is related to the filtering of the content of source files and downloading from them, among others values of geographic coordinates and heights of subsequent points. The visualization of spatial data recorded by mobile devices in this study was carried out in the Google Earth software [6]. Since the Google Earth supports files in KML format, it was necessary to convert the input data to the appropriate form. In the first phase of data processing, the input data, in the form of NMEA messages and GPX file, was transformed into a time series of positional parameters of the measured points. The second phase of processing was to create a text file with a tag structure corresponding to the KML language [37].

Of all the NMEA 0183 messages recorded by mobile devices, the study analyzes used the GGA type containing position data of the receivers. The NMEA 0183 protocol messages are sentences with successive parameters separated by a comma separator. Geographic coordinates in the NMEA GGA format are stored in the form of a series of digits consisting of degrees and minutes. The first coordinate in the message is the latitude, which consists of the first two digits representing the full degree value and the remainder of the floating-point representing the number of arc minutes. The next parameter - the longitude consists of the first three digits that define the number of full degrees [12]. The latitude and longitude coordinates, after separating the whole parts of degrees and minutes, were converted to degrees with a decimal part:

$$\varphi = \varphi_{ST} + \frac{\varphi_{MIN}}{60}, \quad (1)$$

$$\lambda = \lambda_{ST} + \frac{\lambda_{MIN}}{60}, \quad (2)$$

where φ is latitude [°], φ_{ST} is a number of full degrees of latitude, φ_{MIN} number of angular minutes of latitude, λ longitude [°], λ_{ST} number of full degrees of longitude, λ_{MIN} number of angular minutes of longitude.

The processing of data from the GPX file consisted of extracting the position data based on selected tags. Unlike the NMEA GGA format, the GPX longitude and latitude angular coordinates are given in degrees and do not require additional numeric recalculation. The last stage of data processing from both recording formats is arranging the coordinates of the points in the order required in the KML format, i.e. longitude, latitude and altitude, respectively. The decimal separator in KML format is a period and the separator of values in a given record is a comma. The ordered coordinates of points constituted the body of the KML file. To read it properly in the Google Earth software, it was necessary to add a header and footer defined in the format documentation [37]. The implementation of individual stages of the data processing in the work is presented in Table 1.

It should be noted that the text file used for visualization, containing geospatial data processed from the NMEA and GPX formats, should be saved with the KML extension.

3 Measurements

Four mobile devices equipped with the GNSS modules were used to record the satellite data in the study: three smartphones and a smartwatch. The installed GNSS module determines the coordinates, which are then saved on the device's storage medium. In the case of smartphones, obtaining the position data in a file requires installation of a software that reads the signal from the GNSS receiver of the phone and saves it in text files in the NMEA format. The used smartwatch saves the designated coordinates in the GPX format using an appropriate application. The characteristics of the equipment used in the study are presented in Table 2.

The measurement data for visualization by the procedure described in the Materials and Methods section have been registered in Poland (3 routes) and Sweden (1 route). The test route selection criterion reflected the accuracy of the GNSS receivers recorded in the field conditions with varying degrees of satellite signal availability limited by the sky obstacles.

The first measurement on the Stara Kiszewa - Gdynia (Poland) route was made while driving a car using a Samsung Galaxy A30S smartphone with an active SIM card. The section is the longest recorded route with a length of 83.7km. Along the route, there are all variants of presence of the terrain barriers that hinder the accuracy of positioning: difficult, moderate and favorable. The initial part of the route runs through the rural areas characterized by sparse buildings, winding roads, roadside trees and sometimes wooded areas. The middle part of the route is an expressway with no major obstacles. The final part of the recorded route is located in the area of the high urban development in Gdynia.

The second measurement was made with an iPhone 7 smartphone on the route Glava - Arvika (southern Sweden) during the bus ride. The smartphone has an active SIM card. The 29km long route runs through agricultural land located between lakes and is characterized by a large forest area. There are no buildings along the entire length of the measurement route. The exceptions are the final route part in the city of Arvika and the village of Sulvik. Most of the measurements were made in difficult conditions with presence of tree obstacles, which significantly reduces the quality of satellite positioning.

The third test section in Gdynia between Gdynia Main Railway Station and seafront was covered on foot. A Huawei Mate 10 Lite mobile phone without an active SIM card was used to record the satellite data. The course of the route was planned in such a way as to ensure the most unfavorable measurement conditions.

Table 1 Results of the steps for processing the sample NMEA and GPX source data to create a KML export file

NMEA	No.	Result of the transformation stage													
	1	\$GPGGA,144436.00,5430.1520,N,01833.5260,E,1,13,0.818,41.778,M,,M,0,*70													
	2	\$GPGGA	144436	5430.152	N	1833.526	E	1	13	0.818	41.778	M	M	0	*70
	3	54		30.1520										33.5260	
	4	18.55877			54.50253						41.778				
5		18.558766666667,54.502533333333,41.778													
GPX	No.	Result of the transformation stage													
	<pre><trkpt lat="54.51764757279307" lon="18.52669391781092"> <ele>60.577198691309306</ele> <eleGPS>90</eleGPS> <speed>0.6120000064373017</speed> <time>2020-05-20T06:36:44</time> </trkpt> <trkpt lat="54.51764757279307" lon="18.52669391781092"> <ele>60.577198691309306</ele> 54.517647572793 18.5266939178109 60.5771986913093 18.52669391781092,54.51764757279307, 60.577198691309306</pre>														
	1														
	2														
	3														
4															
KML	<pre><?xml version="1.0" encoding="UTF-8"?> <kml xmlns="http://www.opengis.net/kml/2.2"> <Document> <name>Trasa.kml</name> <open>1</open> <Placemark> <name>Trasa</name> <LineString> <extrude>1</extrude> <tessellate>1</tessellate> <coordinates> 18.558766666667,54.502533333333,41.778 ... 18.531613333333,54.520615,44.492 </coordinates> </LineString> </Placemark> </Document> </kml></pre>														

Table 2 Selected technical parameters of the mobile devices used in the study [38-41]

	Samsung Galaxy A30S	iPhone 7	Huawei Mate 10 Lite	Samsung Gear S3 Frontier
Measuring device				
Systems available	GPS, GLONASS, Galileo, BeiDou	GPS	GPS, GLONASS, BeiDou	GPS, A-GPS, GLONASS
Application	NMEA Tools Pro	NMEA Gps	NMEA Tools Pro	GPX Tracker, Gear GPX receiver
Recording format	NMEA	NMEA	NMEA	GPX
Frequency	1 Hz	1 Hz	1 Hz	1 Hz
Recorded NMEA messages	BDGSA, BDGSV, GAGSA, GAGSV, GLGSA, GLGSV, GNGSA, GPGGA, GPGSA, GPGSV, GPRMC, GPVTG	GPGGA, GPGSA, GPGSV, GPRMC, GPVTG	BDGSA, BDGSV, GLGSA, GLGSV, GNGSA, GPGGA, GPGSA, GPGSV, GPRMC, QZGSA	not applicable

This applies especially to the part of the route running near the vicinity of high urban development. The remainder of the measurement was taken on the seaside boulevard along which the sky is more exposed on the south and south-east sides.

The last test measurement on the Gdynia - Sopot (Poland) route was performed with the Samsung Gear S3 Frontier smartwatch while driving. There are two types of terrain conditions along the route. In the initial section in Gdynia and the final section in the center of Sopot, the sky visibility is limited by buildings. The remaining part of the registered route is a straight course of the road and no buildings near the road. The only terrain obstacles in this section are roadside trees. The list of test routes along with the assessment of field conditions is presented in Table 3.

The recorded position data represents both different terrain conditions and different speed of movement of the user. Thanks to this, the data is a valuable research material, both in terms of presenting the procedure of transition from the level of saved files with the receiver positions to three-dimensional visualization, as well as for conducting a preliminary assessment of positioning accuracy.

4 Results

The NMEA format, in addition to position data, also contains additional information about the instantaneous state of the satellite constellation. The NMEA GGA messages include the following parameters: the number of available satellites and the HDOP factor. Figure 1 shows the parameter values for three routes, where registration was performed on smartphones with the use of NMEA stream recording applications. The graphs show jumps in parameter values in various terrain conditions of the routes traveled.

In the case of the first route Stara Kiszewa - Gdynia (Figure 1a), the number of satellites ranges from 5 to 24 satellites with an average value of 18.6 and for the

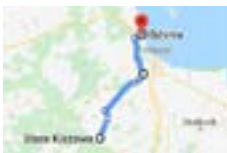
Gdynia Centrum route (Figure 1c) it ranged from 13 to 18 with an average value 16.0. For the Glava - Arvika route (Figure 1b) the number of GPS satellites along the entire length of the route was constant and amounted to 12. The average HDOP value for the Stara Kiszewa - Gdynia route was 0.58, for the Glava - Arvika route 2.54 and for the Gdynia Centrum route 0.72.

Based on the presented measurement data, it is noticeable that with the greater number of GNSS systems used, the number of visible satellites increases and the HDOP factor takes the lower values. In places located in wooded areas, under viaducts, or in the vicinity of high-rise buildings, the number of visible satellites decreased and the value of the HDOP increased. In addition, for the one-system (GPS) phone, the iPhone 7 has a significantly higher DOP value than the remaining multi-system smartphones, which represents the advantage of using multiple satellite navigation systems to improve the geometry of the satellite system in the user's sky.

The conducted analyses indicate that the number of available satellites and the value of the HDOP are interdependent. It should be noted, however, that the distribution of satellites in the sky, which determines the values of dilution of precision parameter, is of the key importance for the positioning accuracy. With increase in the number of visible satellites and their favorable distribution in the sky, the HDOP decreases and the accuracy of determining the horizontal position increases [43].

An important factor influencing the quality of the measurement is also the speed of the GNSS receiver during the measurement. Therefore, graphs were made to show the speed achieved during the measurement for each of the recorded routes. For this purpose, the \$GPRMC sentences from the NMEA files were used, which contained information about the speed given in knots. The values recorded in kn were converted to km/h. For the route saved using the GPX format, the speed was read from the <speed> tag, which contained the values recorded in the destination unit km/h, so

Table 3 List of test routes with a map orientation plan [42]

Route	Stara Kiszewa - Gdynia (Poland)	Glava - Arvika (Sweden)	Gdynia Centrum (Poland)	Gdynia - Sopot (Poland)
Map				
Recording device	Samsung Galaxy A30S	iPhone 7	Huawei Mate 10 Lite	Samsung Gear S3 Frontier
Length of the route	83.7km	29.2km	3.3km	11.1 km
Duration	1 hour 3 min. 2 sec.	38 min. 52 sec.	37 min. 2 sec.	18 min. 15 sec.
Field conditions	good, moderate and difficult	difficult	good and difficult	moderate

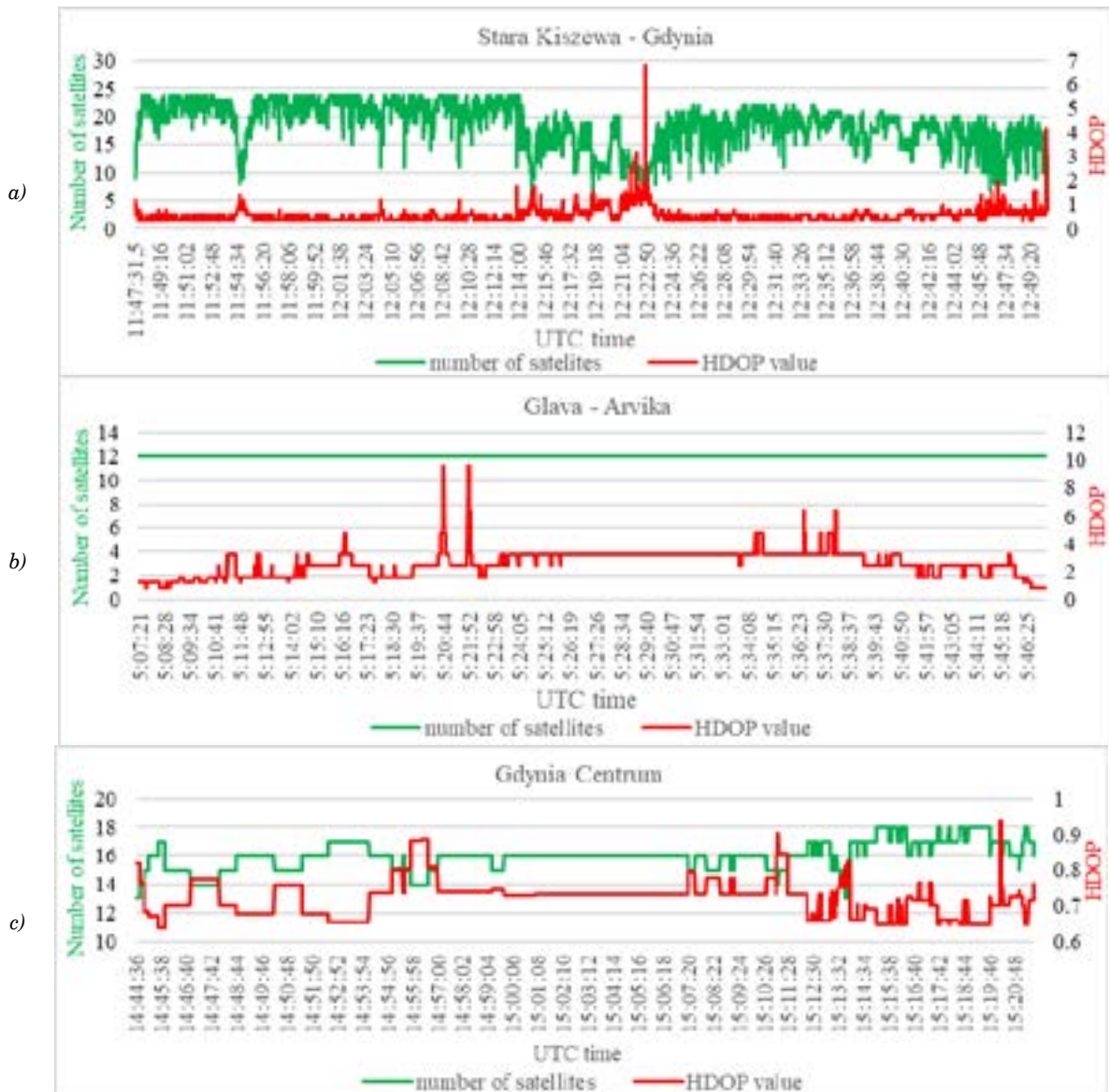


Figure 1 The number of satellites and HDOP from NMEA recording for each route: Stara Kiszewa - Gdynia (a); Glava - Arvika (b); Gdynia Centrum (c)

they did not require processing. Figure 2 presents the graphs of the speeds achieved during the registration of individual routes.

It should be noted that the specificity of the mobile devices and applications used do not allow for comparison of all the parameters that could have influenced the size of measurement errors. The applications and algorithms used in the measurement devices allow only the reading and recording of the signal from GNSS receivers in the established NMEA and GPX formats. Information related to the technology implemented in the GNSS receivers of the tested devices is not publicly available. Therefore, parameters such as ionospheric correction, tropospheric correction, correction from the EGNOS system, multipath signals mitigation and the Doppler shift were not included in the data analysis. In addition, information on the Kalman filter software used in the receiver and its settings are unknown and it is only

possible to observe the filtering results. The formats used for the data recording also make it impossible to read from the files in how many measuring epochs the position was not determined and with what quality the positions were determined (code / fixed).

In order to assess the size of the measurement errors, the cross-track errors at 100 equally distant route points based on the visualizations were determined in Google Earth. Based on the read values of position errors, graphs were made for each of the routes (Figure 3). In the case of the longest route Stara Kiszewa - Gdynia (Figure 2a) the mean value of the position error was 2.89 with a standard deviation of 3.24. For the route Glava - Arvika (Figure 2b) the mean value of the position error was the highest and amounted to 4.04 with a standard deviation of 4.06. For the Gdynia Centrum route (Figure 2c), the mean value of the position error was the lowest and amounted to 1.66 with a standard deviation of 2.50.

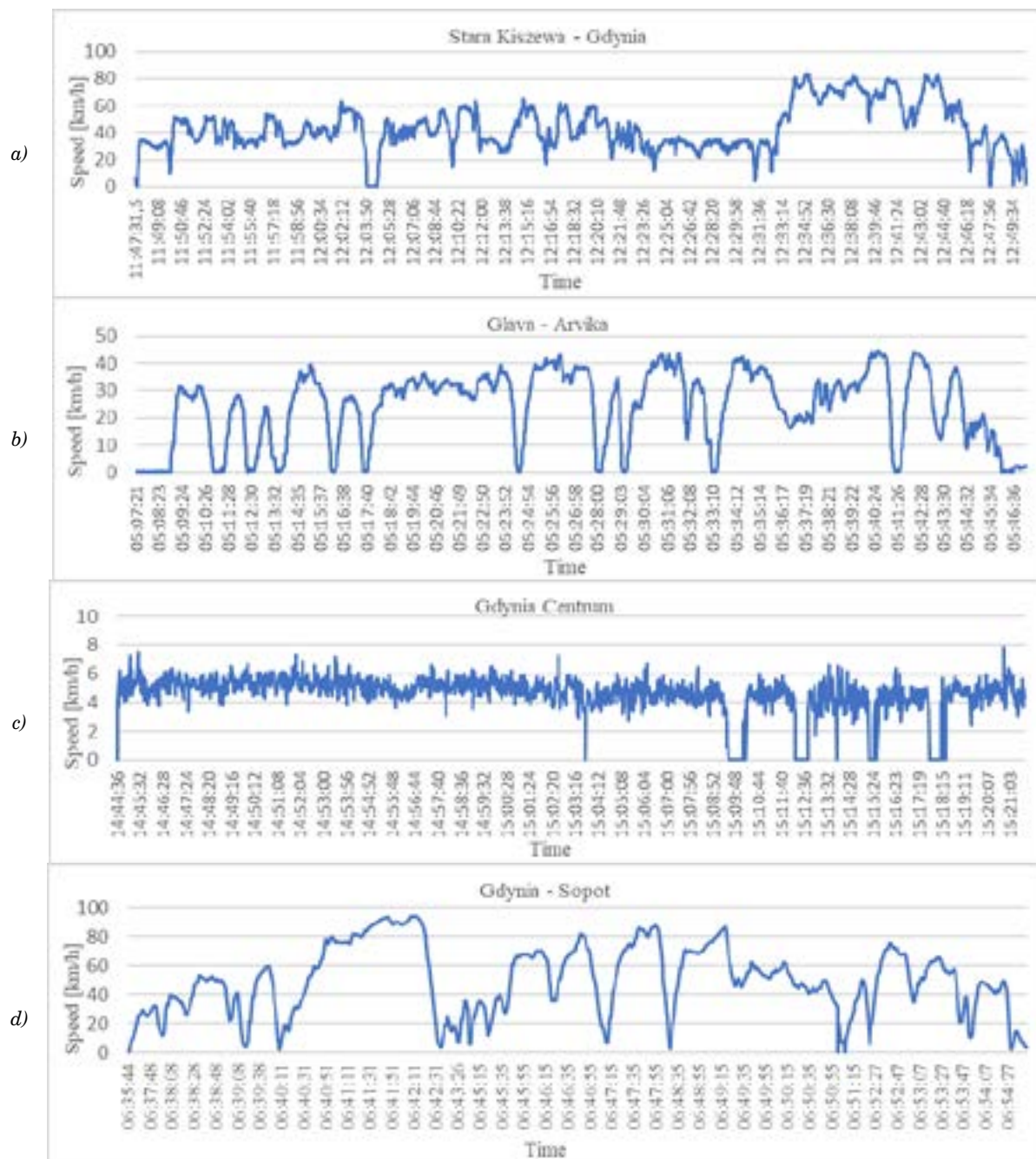


Figure 2 GNSS receivers speed on individual routes: Stara Kiszewa - Gdynia (a); Glava - Arvika (b); Gdynia Centrum (c); Gdynia - Sopot (d)

For the last Gdynia-Sopot route (Figure 2d) the mean value of the position error was 1.71 with the standard deviation 1.77.

4.1 Visualization of the route Stara Kiszewa - Gdynia

In the parts of the rural areas of the Stara Kiszewa - Gdynia route, slight deviations of the recorded track, related to the road, due to the lack of major obstacles are visible. Nevertheless, the presence of single trees near

the road or the course of the route through wooded areas causes a noticeable deterioration of accuracy. An example is the section of a winding road leading through the forest in Kolbudy (Figure 4a). Due to the sky obstacles, almost the entire recorded route (yellow) is outside the real position of the road (green). It is a fragment of the measurement representing the UTC range 12:13 - 12:29 shown in Figure 1a, which is characterized by the highest variation of the HDOP along the entire route, which, at the critical moment, reached the maximum value of 6.8. The number of available satellites has also sharply decreased from 21 to 6.

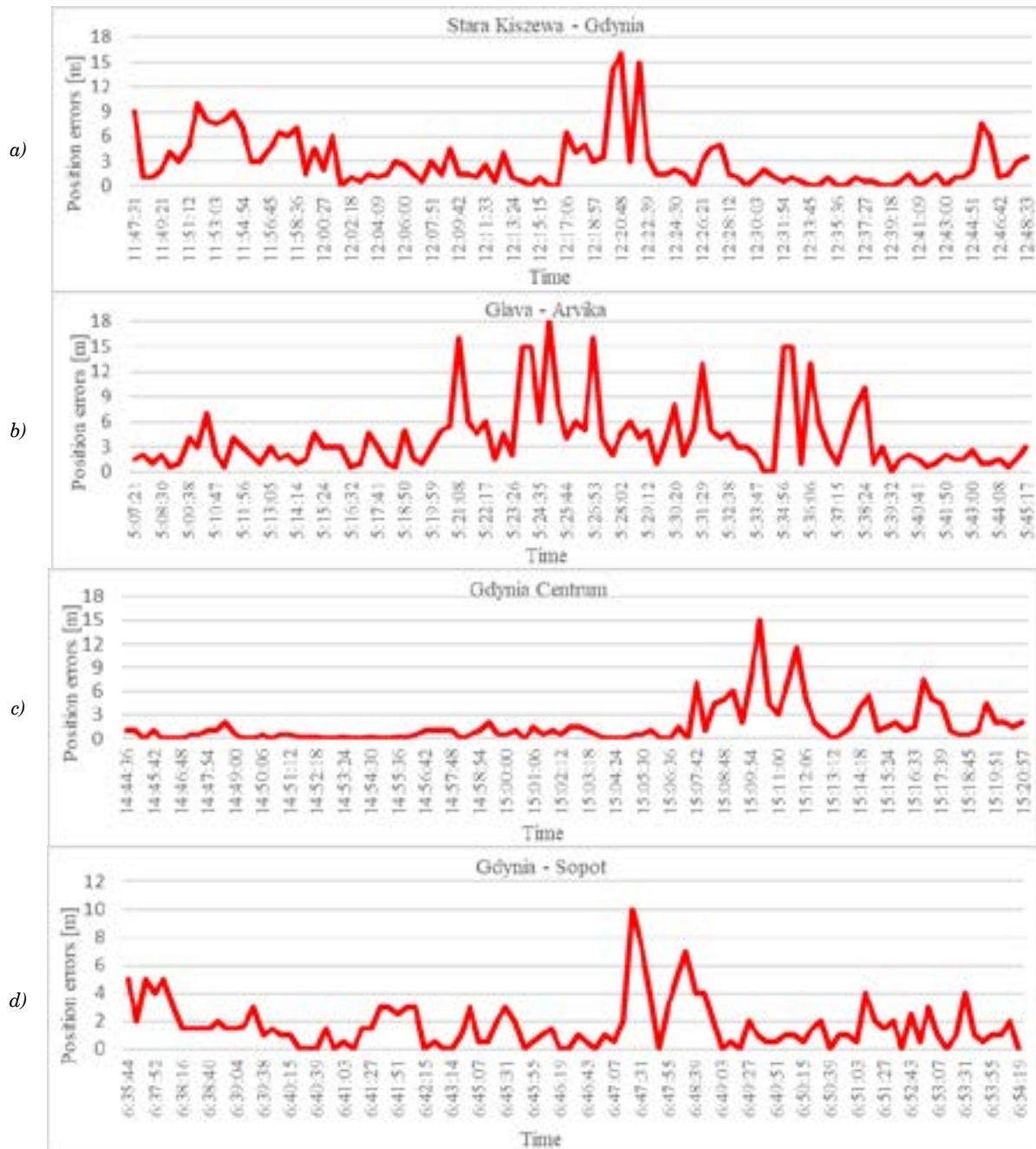


Figure 3 Position errors read on the basis of visualizations made in Google Earth on individual routes: Stara Kiszewa - Gdynia (a); Glava - Arvika (b); Gdynia Centrum (c); Gdynia - Sopot (d)

The section of the route located on the Tricity ring road (Figure 4b) was covered at high speed (Figure 2a, UTC period 12:34 - 12:44), thanks to which no significant disturbances influencing the visualization of the course of the track were recorded. This indicates convenient measurement conditions and high measurement accuracy, close to 1 meter, enabling the identification of the occupied road lane. The course of the curve is influenced by the working Kalman filter [45] smoothing out the outliers of the receiver position. With the predominantly no obstruction of the sky along the expressway, the HDOP values did not exceed 0.8 (Figure 1a).

The projection of the route from the UTC period 12:45 - 12:50 (Figure 1a) located along Morska Street in Gdynia (Figure 4c) has significant and frequent fluctuations in HDOP and the number of satellites due to the high urban development. The HDOP in the presented location was the second largest value of 4.2. In turn, the number of satellites reached the lowest value during the measurement and was 5. The unfavorable parameters of the satellite constellation in this section did not cause any major fluctuations thanks to use of the Kalman filter. The course of the visualized route is rectilinear, but almost the entire length is outside the real path.

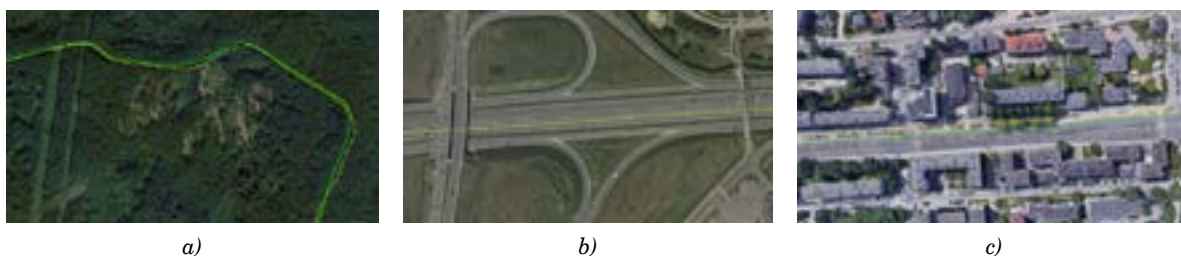


Figure 4 Selected fragments of the visualization of the route Stara Kiszewa - Gdynia: the section of a winding road in Kolbudy (a); the section located on the Tricity ring road (b); the section located along Morska Street in Gdynia (c) (Poland) [44]

4.2 Visualization of the route Glava - Arvika

Taking into account that the recorded route is located at the latitude of 59°N and GPS satellites operate in principle on orbit inclined to the equator by 55° angle, the quality of the measurement may be much lower and burdened with a greater error. Additionally, anomalies caused by the speed drop to 0 km/h while stopping at bus stops are visible along the entire length of the route (Figure 2b). Figure 5a shows clear jumps in position caused by the bus stopping and much smaller anomalies along the rest of the section. This situation is illustrated by the effect of the Kalman filter, which gives positive results for positioning in motion. The terrain conditions in this section are the best for the entire route. The road is surrounded by agricultural land and sparse surrounding trees. This is reflected in values of the HDOP coefficient, which is the lowest in the first minutes of the measurement and fluctuates slightly in the range from 0.8 to 1.6 (Figure 1b).

Figure 5b shows a fragment of the Glava - Arvika route in the forested area corresponding to the HDOP jumps, which falls in the period of UTC $5:33 - 5:38$ shown in Figure 1b. The value of the coefficient fluctuates considerably and doubles from 3.2 to 6.4 . The projection of the entire route section is inaccurate and is outside the road area. In extreme cases, the estimated error value, related to the road axis, is even 15 m . This is due to the presence of tall trees close to the road, irregular course of the route and bus stops located in this area, causing the vehicle to stop.

The last landmark of the route is its final section in the city of Arvika (Figure 5c). It shows deviations of the recorded position from the road, caused by urban buildings obscuring the sky and increasing the risk of

multipath errors. Figure 1b shows that the value of the HDOP coefficient in the UTC period from $5:45:38$ to $5:45:41$ slightly increases from 2.4 to 3.2 . At the end of the route, when the bus enters the station area, the HDOP coefficient decreases to the minimum value for the entire route of 0.8 .

4.3 Visualization of the Gdynia Centrum route

The Gdynia Centrum route was covered on foot at a low speed of 1.24 m/s on average (Figure 2c). In the section located on the Seaside Boulevard (Figure 6a), slight deviations of the recorded route from the rectilinear route are visible. There were no sky obstacles near the receiver during the registration. Figure 1c shows that fluctuations in both the HDOP and the number of satellites occur much less frequently in relation to the measurement section located between the buildings on Polish Home Army street in Gdynia (Figure 6b).

The discussed section of the route was covered in the closest possible vicinity of high urban development. There are large anomalies in the determined horizontal positions along the entire length of the route. Taking into account that the pedestrian with the receiver was walking along the sidewalk on the right side of the road, it can be assumed that the positioning error at extreme moments was 15 m . In Figure 1c the fluctuations of the HDOP are visible, which varies from 0.65 to 0.94 . During the period shown, the number of visible satellites ranged from 13 to 18 , while the number of all the satellites varied from 33 to 37 (Figure 6c). This indicates that the dense buildings obscured 60% of the satellites visible to an observer in Gdynia during the measurement.

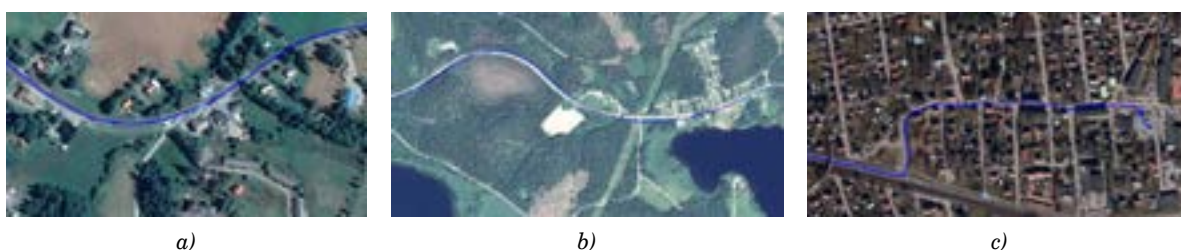


Figure 5 Selected fragments of the visualization of the route Glava - Arvika: the section of road with bus stop (a); the section located in the forested area (b); the section in the city of Arvika (c) (Sweden) [44]

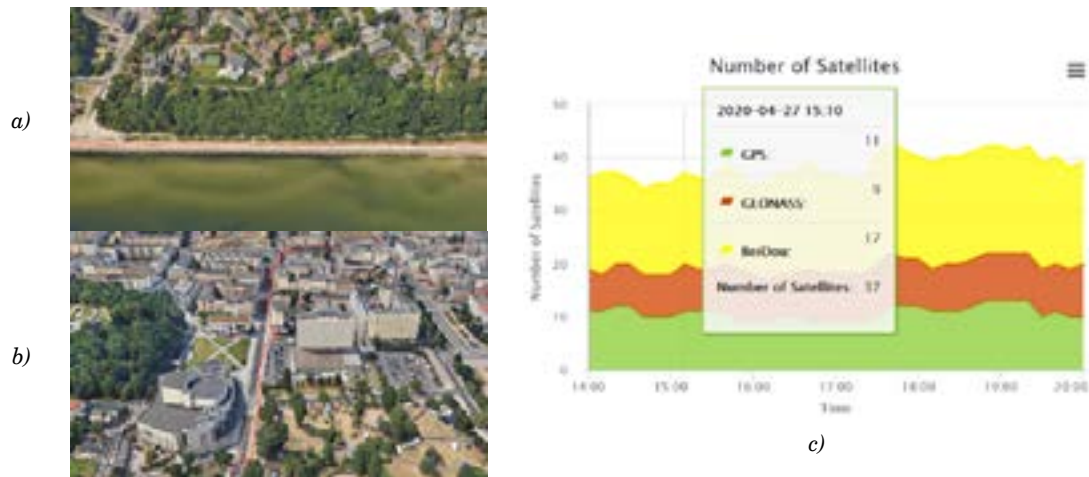


Figure 6 Selected fragments of the route visualization Gdynia Centrum: the section located on the Seaside Boulevard (a); the section along Polish Home Army street in Gdynia (b) (Poland) [44] and the Trimble GNSS Planning Online window showing the number of available satellites (c) [46]

4.4 Visualization of the Gdynia - Sopot route

The last test route was recorded using a smartwatch in GPX format. For this reason, in contrast to the three previous routes, it was not possible to evaluate the parameters of the satellite constellation. The assessment of factors influencing the positioning accuracy was made based on the conditions of the presence of sky obstacles found in the field and speed. Figure 7a shows a section of the route located on one of the main public roads in Gdynia, where the car reached a higher speed than in the rest of the route (Figure 2d, UTC period 06:40:30 - 06:42:20). Moreover, there are no larger sky obstacles near the road, which makes the measurement conditions very favorable. The outliers that appear from time to time are eliminated by the Kalman filter, thanks to which a measurement error close to 1 m was obtained.

In the further part of the public road in question, the measurement conditions significantly different from the previous measurement conditions were noted, where there are many trees near the road, forming natural sky obstacles (Figure 7b). This results in a sixfold deterioration in the accuracy of the measurement in relation to the earlier part of the road. The projection of the track is located outside the edge of the road and deviates from the axis of the road lane on which the car was moving by approximately 6 m.

The last section presented is a fragment of a public road in the neighboring city of Sopot (Poland). The route presented in Figure 7c is surrounded by high buildings causing disturbances in the rectilinear representation of the car route. The largest anomaly is located at the intersection of the roads and is associated with stopping of a vehicle and disruption of the Kalman filter (Figure 2d, UTC 06:51). The estimated error in the section shown was about 3 m at the extreme moment.

5 Conclusions

The paper presents the process of creating a visualization based on routes recorded by the mobile devices GNSS receivers. The NMEA and GPX formats require that saved positional data be processed and saved in KML format to be recognized by the Google Earth software. In addition to presenting the subsequent calculation steps, the study included the application of the presented procedure on results of the satellite measurements carried out on four routes located in Poland and Sweden. Measurements were made in various field conditions using three smartphones and one smartwatch. Apart from presenting the traveled routes, this article presents an analysis of the factors influencing the positioning accuracy. The dependence

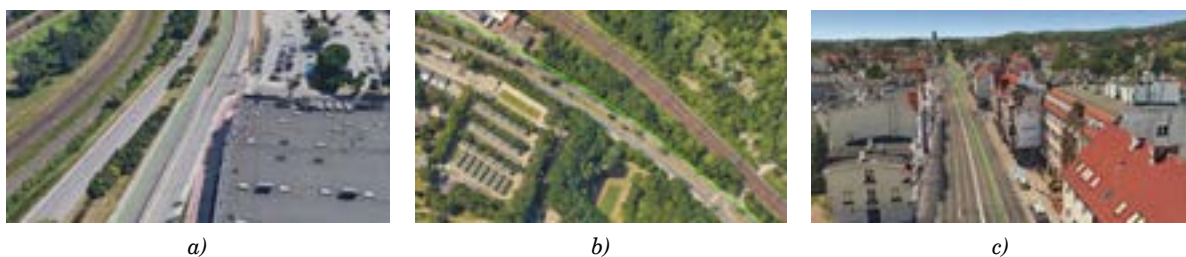


Figure 7 Selected fragments of the visualization of the Gdynia - Sopot route (Poland): the section along Victory Avenue street street in Gdynia (section with favorable measurement conditions (a), wooded section (b)); the section along Polish Home Army street in Sopot (c) [44]

of the quality of the obtained route mapping on the existing terrain barriers was noted on each of the routes. Depending on the size and distance of the shutters from the receiver, they increased the errors in the coordinates determined.

The study showed that with deterioration of the terrain conditions, the HDOP value increases and the number of satellites decreases, which is associated with a decrease in the accuracy of satellite positioning results. On the visualized measurement routes, it was also observed that with decrease in speed, the quality of the obtained mapping of the traveled route also decreased. This situation is due to the Kalman filter, which alters the current position coordinates with their previous values. This was especially noticeable in the places where the wheeled vehicles stopped and the route was covered on foot. Due to the different conditions of the measurements, it was not possible to precisely determine the average positioning accuracy of the devices used. The values of horizontal errors

were approximated based on the route of roads and streets on the map and assuming the correctness of georeferencing of satellite images. Based on the research, the estimated values of the mean positioning errors were 15 m in difficult conditions and 1 m in favorable conditions.

The conducted study presented the process of creating a visualization of traveled routes based on the position data recorded in the NMEA and GPX formats. Additionally, the visualization of routes in the Google Earth software, thanks to the extensive function of adjusting the view, enables the basic accuracy analysis of the recorded position data. The NMEA format, thanks to the range of recorded data wider than the GPX format, enables the comparison of the constellation parameters of satellites without mapping in the basic graphical form of the route. Descriptive attributes in the form of the number of satellites and the HDOP are an important source of information about the accuracy of the measurements.

References

- [1] WARD, N., SHAW, G., WILLIAMS, P., GRANT, A. The role of GNSS in e-navigation and the need for resilience. In: Proceedings of European Navigation Conference GNSS: proceedings [online]. 2010. Available from: <https://www.gla-rad.org/content/uploads/2018/01/the-role-of-gnss-in-e-navigation-and-the-need-for-resilience.pdf>
- [2] WEINTRIT, A. *The electronic chart display and information system (ECDIS): an operational handbook*. Boca Raton, USA: CRC Press, 2009. ISBN 9781439847640.
- [3] WEINTRIT, A., NEUMANN, T. *Safety of marine transport: marine navigation and safety of sea transportation*. Boca Raton, USA: CRC Press, 2015. ISBN 9781138028593.
- [4] MILLER, C. C. A beast in the field: the Google Maps mashup as GIS/2. *Cartographica: The International Journal for Geographic Information and Geovisualization* [online]. 2006, **41**(3), p. 187-199 [accessed 2021-03-24]. ISSN 0317-7173. Available from: <https://doi.org/10.3138/JOL0-5301-2262-N779>
- [5] WANG, M., LI, Q., HU, Q., ZHOU, M. Quality analysis of open street map data. *The International Archives of the Photogrammetry, Remote Sensing and Spatial Information Sciences* [online]. 2013, **XL-2/W1**, p. 155-158 [accessed 2021-03-24]. eISSN 2194-9034. Available from: <https://doi.org/10.5194/isprsarchives-XL-2-W1-155-2013>
- [6] GORELICK, N., HANCHER, M., DIXON, M., ILYUSHCHENKO, S., THAU, D., MOORE, R. Google earth engine: planetary-scale geospatial analysis for everyone. *Remote Sensing of Environment* [online]. 2017, **202**, p. 18-27 [accessed 2021-03-24]. ISSN 0034-4257. Available from: <https://doi.org/10.1016/j.rse.2017.06.031>
- [7] VERMA, V., KUMAR, R., HSU, S. 3D building detection and modeling from aerial LIDAR data. In: 2006 IEEE Computer Society Conference on Computer Vision and Pattern Recognition CVPR'06: proceedings. Vol. 2. 2006. ISBN 0-7695-2597-0, p. 2213-2220.
- [8] SPECHT, C., DABROWSKI, P., DUMALSKI, A., HEJBUDZKA, K. Modeling 3D objects for navigation purposes using laser scanning. *TransNav: International Journal on Marine Navigation and Safety of Sea Transportation* [online]. 2016, **10**(2), p. 301-306 [accessed 2021-03-24]. ISSN 2083-6473. Available from: <https://doi.org/10.12716/1001.10.02.12>
- [9] LOPEZ, A. J., SEMANJSKI, I., GAUTAMA, S., OCHOA, D. Assessment of smartphone positioning data quality in the scope of citizen science contributions. *Mobile Information Systems* [online]. 2017, **2017**, 4043237 [accessed 2021-08-28]. ISSN 1875-905X. Available from: <https://doi.org/10.1155/2017/4043237>
- [10] SPECHT, M., SPECHT, C., DABROWSKI, P., CZAPLEWSKI, K., SMOLAREK, L., LEWICKA, O. Road tests of the positioning accuracy of INS/GNSS systems based on MEMS technology for navigating railway vehicles. *Energies* [online]. 2020, **13**(17), 4463 [accessed 2021-08-28]. ISSN 1996-1073. Available from: <https://doi.org/10.3390/en13174463>
- [11] SPECHT, C., SZOT, T., DABROWSKI, P., SPECHT, M. Testing GNSS receiver accuracy in Samsung Galaxy series mobile phones at a sports stadium. *Measurement Science and Technology* [online]. 2020, **31**(6), 064006 [accessed 2021-03-24]. ISSN 0957-0233. Available from: <https://iopscience.iop.org/article/10.1088/1361-6501/ab75b2>

- [12] SZOT, T., SPECHT, C., SPECHT, M., DABROWSKI, P. S. Comparative analysis of positioning accuracy of Samsung Galaxy smartphones in stationary measurements. *PLoS one* [online]. 2019, **14**(4), e0215562 [accessed 2021-03-24]. ISSN 1932-6203. Available from: <https://doi.org/10.1371/journal.pone.0215562>
- [13] US DoD, 2020. Global Positioning System (GPS) Standard Positioning Service (SPS) Performance Standard - 5th ed. [online] [accessed 2021-03-20]. Available from: <https://www.gps.gov/technical/ps/2020-SPS-performance-standard.pdf>
- [14] NARKIEWICZ, J. *GPS and other satellite systems / GPS i inne systemy satelitarne* (in Polish). Warsaw: WKiL, 2007. ISBN 9788320616422.
- [15] SPECHT, C., SPECHT, M., DABROWSKI, P. Comparative analysis of active geodetic networks in Poland. In: International Multidisciplinary Scientific GeoConference SGEM: proceedings. 2017. ISBN 978-619-7408-02-7, p. 163-176.
- [16] MUSULIN, I., BRCIC, D., KOS, S. A research study of handheld multiconstellation GNSS receivers satellite positioning performance. In: Annual Baska GNSS Conference: proceedings. 2015. ISSN 1849-7306. p. 63-84.
- [17] SPECHT, C., DABROWSKI, P. S., PAWELSKI, J., SPECHT, M., SZOT, T. Comparative analysis of positioning accuracy of GNSS receivers of Samsung Galaxy smartphones in marine dynamic measurements. *Advances in Space Research* [online]. 2019, **63**(9), p. 3018-3028 [accessed 2021-08-28]. ISSN 0273-1177. Available from: <https://doi.org/10.1016/j.asr.2018.05.019>
- [18] TANG, L., YING, S., LI, L., BILJECKI, F., ZHU, H., ZHU, Y., YANG, F., SU, F. An application-driven LOD modeling paradigm for 3D building models. *ISPRS Journal of Photogrammetry and Remote Sensing* [online]. 2020, **161**, p. 194-207 [accessed 2021-03-24]. ISSN 0924-2716. Available from: <https://doi.org/10.1016/j.isprsjprs.2020.01.019>
- [19] BURDZIAKOWSKI, P., SPECHT, C., DABROWSKI, P. S., SPECHT, M., LEWICKA, O., MAKAR, A. Using UAV photogrammetry to analyze changes in the coastal zone based on the Sopot tombolo (Salient) measurement project. *Sensors* [online]. 2020, **20**(14), 4000 [accessed 2021-03-24]. ISSN 1424-8220. Available from: <https://doi.org/10.3390/s20144000>
- [20] SPECHT, C., LEWICKA, O., SPECHT, M., DABROWSKI, P., BURDZIAKOWSKI, P. Methodology for carrying out measurements of the tombolo geomorphic landform using unmanned aerial and surface vehicles near Sopot pier, Poland. *Journal of Marine Science and Engineering* [online]. 2020, **8**(6), 384 [accessed 2021-03-24]. ISSN 2077-1312. Available from: <https://doi.org/10.3390/jmse8060384>
- [21] DABROWSKI, P., SPECHT, C., SPECHT, M., BURDZIAKOWSKI, P., MAKAR, A., LEWICKA, O. Integration of multi-source geospatial data from GNSS Receivers, Terrestrial Laser Scanners and Unmanned Aerial Vehicles. *Canadian Journal of Remote Sensing* [online]. Paper accepted for publication. ISSN 0703-8992. Available from: <https://doi.org/10.1080/07038992.2021.1922879>
- [22] MACIUK, K. The applications of GNSS systems in logistics. *Budownictwo i Architektura* [online]. 2018, **17**(3), p. 181-188 [accessed 2021-03-24]. ISSN 1899-0665. Available from: https://doi.org/10.24358/Bud-Arch_18_173_13
- [23] ASTARITA, V., FESTA, D. C., GIOFRE, V. P. Mobile systems applied to traffic management and safety: a state of the art. *Procedia Computer Science* [online]. 2018, **134**, p. 407-414 [accessed 2021-03-24]. ISSN 1877-0509. Available from: <https://doi.org/10.1016/j.procs.2018.07.191>
- [24] STOCKX, T., HECHT, B., SCHONING, J. Subway PS: towards smartphone positioning in underground public transportation systems. In: 22nd International Conference on Advances in Geographic Information Systems ACM SIGSPATIAL 2014: proceedings. 2014. ISBN 978-1-4503-3131-9, p. 93-102.
- [25] REHRL, K., GOLL, N., LEITINGER, S., BRUNTSCH, S. Combined indoor/outdoor Smartphone navigation for public transport travelers [online]. 2005. Available from: people.cs.clemson.edu/~johnmc/courses/cpsc875/projects/rehrl2.pdf
- [26] JOUBERT, N., REID, T. G., NOBLE, F. Developments in modern GNSS and its impact on autonomous vehicle architectures. In: 2020 IEEE Intelligent Vehicles Symposium: proceedings. IEEE. 2020. ISBN 9781728166742, p. 2029-2036.
- [27] BUJAK, A., TOPOLSKA, K. Increasing the efficiency of the transport process by eliminating weak points in enterprise management process transport. *Logistyka* [online]. 2014, **6**, p. 4-5 [accessed 2020-05-03]. ISSN 1231-5478. Available from: <http://yadda.icm.edu.pl/yadda/element/bwmeta1.element.baztech-18e9add6-e2f8-4e42-b755-5707891105d0>
- [28] NMEA [online] [accessed 2020-04-10]. Available from: <https://www.nmea.org>
- [29] BETKE, K. The NMEA 0183 protocol [online]. 2001. Available from: <https://tronico.fi/OH6NT/docs/NMEA0183.pdf>
- [30] NMEA 0183 - Standard for interfacing marine electronic devices - NMEA [online] [accessed 2020-04-10]. 2002. Available from: <http://www.plaisance-pratique.com/IMG/pdf/NMEA0183-2.pdf>
- [31] NOLAN, D., LANG, D. T. *XML and web technologies for data sciences with R*. New York: Springer, 2014. ISBN 9781461478997.

- [32] GPX [online] [accessed 2020-05-19]. Available from: https://www.topografix.com/gpx_resources.asp
- [33] HOLDENER, A. T. *HTML5 geolocation*. USA: O'Reilly Media, Inc., 2011, ISBN 9781449304720.
- [34] OGC [online] [accessed 2020-04-17]. Available from: <https://www.ogc.org/standards/kml>
- [35] KUMAR, M. World geodetic system 1984: a modern and accurate global reference frame. *Marine Geodesy* [online]. 1988, **12**(2), p. 117-126 [accessed 2021-03-24]. ISSN 0149-0419. Available from: <https://doi.org/10.1080/15210608809379580>
- [36] LEMOINE, F. G., FACTOR, J. K., KENYON, S. C. The development of the joint NASA GSFC and the National Imagery and Mapping Agency (NIMA) geopotential model EGM96 (Vol. 206861) [online] [accessed 2021-03-24]. Greenbelt, Maryland, USA: National Aeronautics and Space Administration, Goddard Space Flight Center, 1998. p. 490-539. Available from: https://science.gsfc.nasa.gov/sed/content/uploadFiles/publication_files/EGM96_NASA-TP-1998-206861.pdf
- [37] KML Reference - Google [online] [accessed 2020-09-19]. Available from: <https://developers.google.com/kml/documentation/kmlreference>
- [38] Samsung A30S - Samsung [online] [accessed 2020-08-25]. Available from: <https://www.samsung.com/pl/smartphones/galaxy-a30s/SM-A307FZGVXEO/>
- [39] iPhone 7 - Apple [online] [accessed 2020-08-25]. Available from: <https://web.archive.org/web/20160914204242/https://www.apple.com/pl/iphone-7/>
- [40] Huawei Mate 10 Lite - Huawei [online] [accessed 2020-08-25]. Available from: <https://consumer.huawei.com/pl/support/phones/mate10-lite/>
- [41] Samsung Gear S3 Frontier - Samsung [online] [accessed 2020-06-03]. Available from: <https://www.samsung.com/us/mobile/wearables/smartwatches/samsung-gear-s3-frontier-sm-r760ndaaxar/>
- [42] Google Maps [online] [accessed 2020-03-19]. Available from: <https://www.google.com/maps>
- [43] SPECHT, C. *System GPS*. Pelplin: Bernardinum Sp. z o.o., 2007. ISBN 9788373804692.
- [44] Google Earth [online] [accessed 2020-09-19]. Available from: <https://www.google.com/intl/pl/earth/>
- [45] KALMAN, R. E. A new approach to linear filtering and prediction problems. *Journal of Basic Engineering* [online]. 1960, **82**(Series D) p. 35-45 [accessed 2021-03-24]. ISSN 0021-9223. Available from: <https://doi.org/10.1115/1.3662552>
- [46] Trimble GNSS planning [online] [accessed 2020-09-19]. Available from: <https://www.gnssplanning.com/#/settings>

Editor-in-Chief:

Branislav HADZIMA - SK

Associate Editor:

Jakub SOVIAR - SK

Executive Editor:

Sylvia DUNDEKOVA - SK

Language Editor:

Ruzica NIKOLIC - SK

Graphical Editor:

Juraj ZBYNOVEC - SK

Honorary Members:

Otakar BOKUVKA - SK

Jan COREJ - SK (in memoriam)

Milan DADO - SK

Pavel POLEDNAK - CZ

Scientific Editorial Board:

Greg BAKER - NZ

Abdelhamid BOUCHAR - FR

Pavel BRANDSTETTER - CZ

Mario CACCIATO - IT

Jan CELKO - SK

Andrew COLLINS - GB

Samo DROBNE - SI

Erdogan H. EKIZ - MA

Michal FRIVALDSKY - SK

Juraj GERLICI - SK

Vladimir N. GLAZKOV - RU

Ivan GLESK - GB

Mario GUAGLIANO - IT

Andrzej CHUDZIKIEWICZ - PL

Jaroslav JANACEK - SK

Zdenek KALA - CZ

Antonin KAZDA - SK

Michal KOHANI - SK

Jozef KOMACKA - SK

Matyas KONIORCZYK - HU

Tomas LOVECEK - SK

Frank MARKERT - DK

Jaroslav MAZUREK - SK

Marica MAZUREKOVA - SK

Vladimir MOZER - CZ

Jorge Carvalho PAIS - PT

Peter POCTA - SK

Maria Angeles Martin PRATS - ES

Pavol RAFAJDUS - SK

Che-Jen SU - TW

Giacomo SCELBA - IT

Janka SESTAKOVA - SK

Eva SVENTEKOVA - SK

Eva TILLOVA - SK

Anna TOMOVA - SK

Franco Bernelli ZAZZERA - IT

Executive Editorial Board:

Michal BALLAY - SK

Martin BOROS - SK

Kristian CULIK - SK

Jan DIZO - SK

Lukas FALAT - SK

Filip GAGO - SK

Lubica GAJANOVA - SK

Stefan HARDON - SK

Martin HOLUBCIK - SK

Maros JANOVEC - SK

Matus KOZEL - SK

Lenka KUCHARIKOVA - SK

Matus MATERNA - SK

Daniela MICHALKOVA - SK

Eva NEDELLIAKOVA - SK

Pavol PECHO - SK

Jozef PROKOP - SK

Marek PRUDOVIC - SK

Michal SAJGALIK - SK

Anna SIEKELOVA - SK

Simona SKRIVANEK KUBIKOVA - SK

Michal TITKO - SK

Vladislav ZITRICKY - SK

Address of the Editorial Office:

University of Žilina
EDIS - Publishing House
Univerzitná 8215/1
010 26 Žilina, Slovakia

E-mail: komunikacie@uniza.sk

Individual issues of the journal can be found on: <http://komunikacie.uniza.sk>

Each paper was reviewed by two reviewers.

Journal is excerpted in SCOPUS and EBSCO host.

Published quarterly by University of Žilina in EDIS - Publishing House of the University of Žilina.

Registered No: EV 3672/09

ISSN (print version) 1335-4205

ISSN (online version) 2585-7878

ICO 00397 563

The full author guidelines are available at: <http://komunikacie.uniza.sk/index.php/communications/guidelines>